Catalyst Design and Mechanistic Investigation of Electrochemical CO_2 Reduction Reaction for the Efficient Production of Fuels and Chemicals

A Thesis Submitted for the Degree of

Doctor of Philosophy

As a part of

Ph.D. Programme (Chemical Science)

by

Mr. Debabrata Bagchi

New Chemistry Unit

Jawaharlal Nehru Centre for Advanced Scientific Research

(A Deemed University)

Bangalore-560064 (INDIA)

July 2022

"*Education is the manifestation of the perfection already in man.*"

— Swami Vivekananda

"*No matter what you look at, if you look at it closely enough, you are involved in the entire universe.*"

— Michael Faraday

"*Science is not only a disciple of reason but also one of romance and passion.*"

— Stephen Hawking

"*I slept and dreamt that life was joy. I awoke and saw that life was service. I acted and behold, service was joy.*"

— Rabindranath Tagore

Dedicated to my beloved friend Arunava

Declaration

I hereby declare that the matter embodied in the thesis entitled ***"Catalyst Design and Mechanistic Investigation of Electrochemical CO_2 Reduction Reaction for the Efficient Production of Fuels and Chemicals"*** is the result of investigations carried out by me at the New Chemistry Unit, Jawaharlal Nehru Centre for Advanced Scientific Research, Bengaluru, India under the supervision of Prof. Sebastian C. Peter and that it has not been submitted elsewhere for the award of any degree or diploma. In keeping with the general practice in reporting scientific investigations, due acknowledgment has been made wherever the work described is based on the findings of other investigators. Any omission that might have occurred by oversight or error of judgment is regretted.

Date: 29th July, 2022 Debabrata Bagchi

Bengaluru, India

Certificate

I hereby declare that the matter embodied in the thesis entitled "***Catalyst Design and Mechanistic Investigation of Electrochemical CO_2 Reduction Reaction for the Efficient Production of Fuels and Chemicals***" has been carried out by Mr. Debabrata Bagchi at the New Chemistry Unit, Jawaharlal Nehru Centre for Advanced Scientific Research, Bengaluru, India under my supervision and that it has not been submitted elsewhere for the award of any degree or diploma.

Date: 29th July, 2022

Bengaluru, India

Prof. Sebastian C. Peter
Associate Professor
New Chemistry Unit, JNCASR
(Research Supervisor)

Acknowledgement

"*Actual Gratitute is the Symptom of Humility*"

— Radhanath Swami

I would like to thank all the people who helped me on this journey towards the successful accomplishment of my Ph.D. I firmly believe their constant help, support and enthusiasm have been the most important reasons why I have been able to finish this doctoral thesis work.

First and foremost, I want to express my sincere thanks and gratitude to my research advisor, **Prof. Sebastian C. Peter,** for encouraging and motivating me to dive into a challenging and exciting research area. His constant support, motivation, and encouragement inspire me to grapple with my projects independently. Not only have I acquired scientific knowledge from him, but I am also inspired by his leadership in handling a huge number of students. He also taught me to handle any kind of difficult situation and educated me to enhance my perseverance and patience to be positive and hopefully always. I also appreciate a lot the opportunity he has given me to carry out different advanced experiments in the country and even abroad, where I've learned a lot and advanced myself with scientific experience. Thank you, sir, for everything that helped enriches me a lot to be able to a complete researcher.

I would like to express my sincere thanks to **Prof. C. N. R. Rao, Bharat Ratna,** for being the embodiment of the inspiration, motivation, and encouragement in the scientific research in JNCASR. I also thank him for providing the wonderful infrastructure and necessary facilities to perform my research work.

I would like to thank **Prof. Subi J. George**, the Chairman, New Chemistry Unit (NCU), Jawaharlal Nehru Centre for Advanced Scientific Research, for the excellent and world-class research environment provided in the NCU.

I would like to express my thanks to all my course instructors Prof. Sebastian C. Peter, Prof. Chandrabhas Narayana, Prof. A. Sundaresan, Prof. Kanishka Biswas, Prof. Sarit Agasti, Dr. Premkumar Senguttuvan, Prof. Balasubramanian Sundaram, Prof. Shobhana Narasimhan and Prof. Amitabh Joshi for their excellent courses.

I would also take the opportunity to thank my collaborators: Prof. Umesh Waghmare, Prof. N. Ravishankar (IISc), Dr. C. P. Vinod (NCL Pune), Komalpreet Kaur, Prof. Ujjal K. Gautam (IISER Mohali), Dr. Tuhin Khan, Jayendran Iyer and Prof. Ali Haider (IIT Delhi).

My sincere thanks to all the technical staff of JNCASR: Mr. Sreenivas, Usha Ma'am, Mr. Anil, Ms. Selvi, Mr. Mahesh, Mr. Vasu, Mr. Deepak, Mr. Shivakumar, Mr. Rahul, Mr. Sachin, Mr. Arun and Ms. Meenakshi for their help with the various characterization techniques. I would like to thank Melissa, Naveen, JNCASR Administration, Academic Section, Complab, Students' Residence, Library, Dhanvantari, and Security.

I would like to thank the Council of Scientific and Industrial Research (CSIR) for the research fellowship. I would like to thank JNCASR, DST, DESY-Germany, and KEK Japan for various funding.

I would like to express my gratitude to my Lab Family, to whom I will always remain indebted: **Present members**: Dr. Sathyapal R. Churipard, Dr. Kousik Das, Dr. Mohd Riyaz, Dr. Veenu Mishra, Dr. Arjun Cherevotan, Ashutosh Kumar Singh, Risov Das, Bitan Ray, Devender Goud, Soumi Mondal, Subhajit Chakraborty, Nilutpal Dutta, Asish Borah, Dr. Bharath Velaga, Geetansh Chawla, Gouri Ramadas Nayanar, Mohammed Jasil P, Ragina K K.

Breathe Members: Rahul K. Ravindran, Shan Royson, and Manjunath Doddamani.

Past members: Dr. Soumyabrata Roy, Dr. Shreya Sarkar, Dr. Saurav Chandra Sarma, Dr. Rajkumar Jana, Dr. Sumanta Sarkar, Dr. Udumula Subbarao, Abhishek Rawat, Dr. Raghu Vamsy, Dr. Nithi Phukan, Jithu Raj, Vinay Naral, Kajol Tonk, Dundappa Mumbaraddi,

Vamseedhara Vemuri, Dr. Tapas Paramanik, Dr. Vijaykumar Marakkatti, Vidyanshu Mishra, Dr. M. Kanagaraj, Dr. Subba Reddy Mari, Dr. Suman Das, Dr. Rimzhim Gupta, Palaparthi Neehar, Manoj Kaja Sai, Dr. A. R. Rajamani, Merin Vargheese, Mohd Jabed Hossain, Chinthu Prasad, Sandeep Kumar, Subhankar Chowdhury, Anish Yadav, Sayanee Das, Ranjana Burman, Rahul Naskar, Chanchal Solanki, and Jyoti Vashist, **Visiting faculties:** Dr. Sudhakara Prasad, Dr. Ann Mary K. A., Dr. Debajyoti Mahanta, Dr. Sujin Jose, and Dr. C. K. Sumesh.

I extend my gratitude to Dr. Ashly P. C. for being an overwhelming host and for constant enthusiasm for lab trips and parties. She has always been encouraging and positive. I extend my love to the beautiful angels Caitlyn and Angelyn whose presence made all our activities more fun-filled and memorable.

I express my thanks to all my JNCASR friends and batchmates: Arunava Saha, Risov Das, Sanchita Karmakar, Paribesh Acharyya, Swadhin Garain, Souvik Sarkar, Rajib Dey, Sudip Mukherjee, Anupam Dey, Debattam Sarkar.

I extend my heartfelt gratitude and love to friends outside JNCASR: Snehashis Chowdhry, Souradip Swarnakar, Sumit Roy, Arijit Jana, Tathagata Datta, Soumyadeep Banerjee, Sayantan Mahapatra, Soumak Ghosh, Yudhisthir Mandal, Hemkalyan Ballav, Kanad Majumder for their gracious support throughout my life.

I am grateful to my Alma Mater J. N. High School, R. K. M. Vidyamandira, IIT Madras.

I am really indebted and fortunate to have all my teachers, especially Rajat Kumar Sarkar (Karimpur J. N. High School), Dr. Balai Chand Kundu (Presidency University), Dr. Nabakumar Bera (RKM Vidyamandira), Prof. Narayanan Chandrakumar (IIT Madras).

Most importantly, I am grateful to my Parents, all of my family members and Soumi for their love and affection.

Debabrata

Preface

The thesis is majorly divided into six chapters.

Chapter 1 gives an introduction to the immediate necessity of the production of sustainable chemicals from anthropogenic carbon dioxide due to the rapid depletion of fossil fuels. In this section, various ways of CO_2 conversion have been discussed. Among them, the utility of electrochemical CO_2 reduction (eCO_2RR) for the production of various hydrocarbons and oxygenates have been thoroughly depicted. The idea of the eCO_2RR is to use electricity that comes from reviewable energy sources like solar and wind and utilize that to perform CO_2 reduction reaction in the aqueous electrolyte. The various aspects of designing cost-effective catalysts, which are the central part of eCO_2RR have been properly described. The chapter also discusses the strategies and concepts used to improve the activity and selectivity of the eCO_2RR by tuning the electronic structure of the catalyst and how it affects the activity. The effect of alloying/substitution, morphology variation, phase transformation, charge distribution, and strain engineering in tuning the activity and durability have been described. Apart from catalysts-design the effect of different the process-parameters involved in eCO_2RR, especially in the flow cell in gas diffusion electrode (GDE) for the selective production of alcohols and hydrocarbons with higher current density, has also been discussed here.

Chapter 2 demonstrates the design strategy for the formation of an interface made up of an alloy (PdIn) and oxide (In_2O_3) by optimizing various synthetic conditions. The eCO_2RR performance of both the PdIn and PdIn@In_2O_3 catalysts has been assessed, and it was found that the activity of PdIn@In_2O_3 has been increased upon the formation of optimum oxide-derived surface, which drives the reaction towards the enhanced CO formation suppressing HER. The oxide-derived PdIn surface has shown excellent eCO_2RR activity and enhanced CO selectivity with Faradaic efficiency (FE) 92.13% at -0.9 V (vs. RHE). In contrast, pure PdIn alloy (without In_2O_3) suffers from lower CO_2RR performance, and its activity decreases over time due to surface oxidation of the Pd site during electrolysis. The In_2O_3 acts as protecting oxide layer for PdIn alloy and restricts the surface oxidation of Pd. The in situ time-dependent ATR FT-IR maps the real-time evolution of different adsorbed intermediates during eCO_2RR on the oxide-derived PdIn alloy surface. The oxidation state and local structure of the catalysts have been elucidated by XPS and EXAFS techniques. In situ EXAFS, powder XRD, Raman,

and ex-situ XPS allow us to investigate the potential dependent surface electronic structure and compositions. The current density has been further enhanced by using a flow cell with the optimum gas-GDE-electrolyte interface.

Chapter 3 discusses the design of two intermetallic compounds, $CuGa_2$ and Cu_9Ga_4, as new catalysts for the eCO_2RR to high energy density product like methanol. $CuGa_2$ exhibited the best performance towards the formation of methanol (FE of 77.26%) at an applied potential of -0.3 V vs. RHE. The unique 2D flake-type structure of $CuGa_2$ has promoted the formation of a higher amount of surface gallium oxide (Ga_2O_3), which is responsible for the higher catalytic performance than that of Cu_9Ga_4, which has 3D spherical morphology hindering the surface oxide formation. XRD, XPS, and XAS have been employed to map the global and local structure, and microscopic techniques (AFM, SEM, and TEM) have been performed for morphological and elemental analysis of both compounds. In-situ IR spectroscopy was carried out to determine the intermediates involved in the formation of methanol, and the reaction mechanism was predicted from the potential dependent IR spectral analysis. The electrochemical activity and selectivity have decreased as we proceed to the higher potential, and the degradation mechanism was studied by quasi in-situ powder XRD, in-situ XAFS and ex-situ XPS techniques. It was found that the progressive reduction of the surface oxide species in the case of $CuGa_2$ caused by applied reduction potential is the reason for the lower catalytic activity at a higher negative potential.

Chapter 4 describes a single-step facile technique for the synthesis of the WC nanosystem embedded on an N-doped graphitic matrix (@NGC), which has shown excellent activity towards eCO_2RR for the C_2 product like acetic acid production at low overpotential. The electrocatalytic activity has been further enhanced by the incorporation of atomically dispersed Cu in WC@NCG (Cu_1-WC@NGC) for acetic acid production with a record FE of 80.02% at an overpotential of -0.3 V (vs. RHE). Upon increasing the Cu loading, the eCO_2RR activity decreases because of the presence of elemental Cu attached to the WC carbide lattice. At higher overpotentials, the relative amount of WO_3 increases due to the charge transfer between Cu and WC, which drives the selectivity towards hydrogen evolution reaction (HER). In-situ IR study reveals the possible intermediates formed due to CO_2RR at lower potential and also maps the dominating occurrence of hydrogen evolution at higher potential.

Chapter 5 describes the synthesis and characterization of different kinds of Pd-Cu catalysts like alloy, intermetallic and bimetallic and demonstrates that type of the components play an important role in determining each catalyst's activity and selectivity. In this case, we

have showed how to tune the catalyst structure to switch the product selectivity from C1(like CO, HCOOH, CH_4) to C2 (C_2H_4, C_2H_5OH, CH_3COOH etc). The sample that features neighboring Cu atoms (bimetallic Pd-Cu compound) favors the production of C_2 products, i.e., ethanol and ethylene, while the sample that features the alternating Pd-Cu arrangement favors the production of monocarbon product like CO, formate and methane. In situ EXAFS study shows how Pd-Cu, Cu-O, and Cu-Cu bonds evolve during the course of eCO_2RR in the case of intermetallic, alloy, and bimetallic catalysts. Computational studies on different catalysts also show that the C-C coupling is more favorable on PdCu bimetallic catalyst than the PdCu intermetallic catalyst. This concept can provide a new insight for the design of even better Pd-Cu based catalysts for the conversion of CO_2 to desired products. In place of Pd, other transition metals can also be giving a new structure-product selectivity trend like this.

In **Chapter 6** reported a new strategy for the synthesis of ordered $PdCu_3$ nanocube ($PdCu_3$-C) and $PdCu_3$ nanosphere ($PdCu_3$-S) by changing the solvent ratio of oleylamine and oleic acid without using any strong reducing agent. In this case, we have advanced ourselves one step ahead and could be able to obtain C_3 product like n-propanol with high selectivity. $PdCu_3$-C and $PdCu_3$-S compounds crystallize in the cubic system having space group $Pm\bar{3}m$. Both of these compounds have shown excellent electrochemical CO_2RR performance with ethanol and n-propanol as the major multicarbon products. The ordered $PdCu_3$-C catalyst having (100) exposed plane has higher multi-carbon selectivity than the $PdCu_3$-S where (111) plane is exposed. Because of the ordered arrangement of the intermetallic catalysts, $PdCu_3$ shows excellent stability during the eCO_2RR process. The rational design favored the highest ever formation rate and Faradaic efficiency (FE) towards n-propanol. The key intermediates for the formation of n-propanol have been identified via in-situ ATR-FTIR and are well complemented by the density functional theory (DFT).

List of Abbreviations

ADT	Accelerated degradability test
AFM	Atomic force microscopy
AR	Analytical grade
ATR-FTIR	Attenuated Total Reflection Fourier-Transform Infrared Spectroscopy
BE	Binding energy
BM	Bimetallic
CA	Chronoamperometry
CE	Counter electrode
CO_2ER	CO_2 Electroreduction
CV	Cyclic voltammetry
DFT	Density functional theory
DMSO	Dimethyl sulfoxide
DOS	Density of states
ECO_2RR	Electrochemical CO_2 Reduction Reaction
ECSA	Electrochemically active surface area
EDAX (EDS)	Energy Dispersive X-ray Spectroscopy
EIS	Electrochemical impedance spectroscopy
EXAFS	Extended X-ray absorption fine structure spectroscopy
FCC	Face-Centred cubic
FE	Faradaic efficiency
FESEM	Field emission scanning electron microscopy
FT-IR	Fourier Transform Infrared Spectroscopy
GC (E)	Glassy carbon (electrode)
GC	Gas chromatography
GDE	Gas Diffusion Electrode
GC-MS	Gas chromatography – Mass spectrometry
GGA	Generalized gradient approximation
HAADF	High-Angle Annular Dark Field
HER	Hydrogen evolution reaction
HPLC	High Performance Liquid Chromatography
HRTEM	High resolution transmission electron microscopy
ICP	Inductive coupled plasma
IF	Infrared spectroscopy
IM	Intermetallic
IPA	Isopropyl alcohol
Ir-MMO	Iridium Mixed Metal Oxide

LSV	Linear sweep voltammetry
LUMO	Lowest unoccupied molecular orbital
MFC	Mass flow controller
NGC	N-doped Graphitic Carbon
NHE	Normal hydrogen electrode
NMR	Nuclear magnetic resonance
NP	Nanoparticles
OER	Oxygen evolution reaction
PBE	Perdew-Burke-Ernzerhof
PDOS	Partial density of states
PGM	Platinum group metals
PXRD	Powder X-ray diffraction
RDS	Rate determining step
RE	Reference electrode
RHE	Reversible hydrogen electrode
SAED	Selected area electron diffraction
SCE	Saturated calomel electrode
SEM	Scanning Electron Microscopy
STEM	Scanning Transmission Electron Microscopy
TCD	Thermal conductivity detector
TEM	Transmission electron microscopy
TGA	Thermogravimetric analysis
TM	Transition metal
TOF	Turn over frequency
UHP	Ultrahigh pure
UV	Ultraviolet
WE	Working electrode
XAFS	X-ray absorption fine structure spectroscopy
XANES	X-ray absorption near edge spectroscopy
XAS	X-ray absorption spectroscopy
XPS	X-ray photoelectron spectroscopy
XRD	X-ray diffraction

Table of Contents

Declaration……..v

Certificate……..vii

Acknowledgment……...ix

Preface…….....xiii

List of Abbreviation……xvii

Table of contents……...xx

Chapter 1. Introduction……....1

1.1. Background 4

1.2. Electrocatalytic CO_2 reduction reaction (eCO_2RR) 4

1.3. Critical challenges in eCO_2RR 6

1.3.1. Fundamental challenge 6

1.3.2. Solubility of CO_2 6

1.3.3. Optimization of electrocatalytic process parameters 7

1.3.4. Achieving the industrially-relevant current density 8

1.3.5. Requirement of multiple techniques 8

1.4. Catalyst Design for eCO_2RR 8

1.4.1. Modification of active metal site towards product selectivity 9

1.4.2. Controlling the particle size and shape 10

1.4.3. Role of support materials 11

1.4.4. Defect engineering 11

1.4.5. Single-atom and molecular catalysts 12

1.4.6. Tandem catalysts 13

1.4.7. Two-dimensional and other strategies form materials perspective catalyst 14

1.4.8. Electronic-structure modulated catalyst surface 15

1.5. Effect of Process Conditions on eCO_2RR 15

1.5.1. Effect of Cell design on eCO_2RR product selectivity 16

1.5.2. H-type cell 17

1.5.3. Flow cell with gas diffusion electrode configuration and membrane electrode assembly (MEA) 18
1.5.4. Differential electrochemical mass spectrometry (DEMS) cell 20
1.6. Mechanism of electrochemical CO_2RR 21
1.6.1. Branching mechanism of eCO_2RR to multiple products 22
1.6.2. Carbon monoxide Formic acid/ Formate 22
1.6.3. Methanol vs. Methane 24
1.6.4. Ethylene vs. Acetate 25
1.6.5. Ethylene vs. Ethanol 25
1.6.6. Acetone vs. n-Propanol 26
1.7. Fundamental terms in electrocatalysis 27
1.7.1. Onset potential 27
1.7.2. Overpotential 27
1.7.3. Electrochemically active surface area (ECSA) 28
1.7.4. Faradaic efficiency (FE) 28
1.8. Parameters to screen various electrocatalysts 28
1.8.1. Activity 28
1.8.2. Stability 28
1.8.3. Selectivity 38
1.9. Experimental and characterization tools for evaluating an electrocatalyst 29
1.9.1. Cyclic voltammetry (CV) 29
1.9.2. Linear sweep voltammetry (LSV) 29
1.9.3. Chronoamperometry (CA) 29
1.9.4. Bulk electrolysis with coulometry 29
1.9.5. EIS spectroscopy (AC impedance) 29
1.9.6. Powder X-ray diffraction (PXRD) 29
1.9.7. X-ray photoelectron spectroscopy (XPS) 30
1.9.8. X-ray absorption spectroscopy (XAS) 30
1.9.9. Electron Microscopy 31
1.10. Electrochemical CO_2 reduction reactor 32
1.10.1. General electrochemical setup for H-cell study 32
1.10.2. Flow cell reactor for eCO_2RR in gas diffusion electrode configuration (GDE) 33

1.10.3. Preparation of Gas diffusion Electrode (GDE) 33
1.11. CO_2 reduced product analysis 35
1.11.1. Gas chromatography (GC) 35
1.11.2. High-Performance Liquid Chromatography (HPLC) 36
1.11.3. Nuclear magnetic resonance spectroscopy (NMR) 36
1.12. Spectroscopic and analytical techniques for in situ mechanistic studies 37
1.12.1. In situ Electrochemical Attenuated Total Reflection Fourier Transform Infrared Spectroscopy (ATR-FTIR) 37
1.12.2. In situ X-ray absorption Spectroscopic studies 37
1.12.3. In situ Raman Spectroscopic studies 38
1.12.4. Differential electrochemical mass spectrometry (DEMS) 39
1.13. Density Functional Theory (DFT) 40
1.14. References 43

Chapter 2. Potential and Time Dependent Dynamic Nature of Oxide-derived PdIn Nanocatalyst During Electrochemical CO_2 Reduction ……...59
2.1. Introduction 62
2.2. Experimental Details 63
2.2.1. Chemicals and reagents 63
2.2.2. Synthesis of PdIn @In_2O_3 and PdIn 64
2.3. Characterization and Experimental Method 64
2.3.1. Powder X-ray Diffraction (PXRD) 64
2.3.2. Transmission Electron Microscope (TEM) 65
2.3.3. Inductively coupled plasma atomic emission spectroscopy (ICP-OES) 65
2.3.4. X-ray Photoelectron Spectroscopy (XPS) 65
2.3.5. Raman Spectroscopy 65
2.3.6. X-ray Absorption Spectroscopy 65
2.3.7. Electrochemical CO_2 Reduction Reaction (eCO_2RR) 66
2.3.8. Reference electrode calibration for H-cell and flow cell configurations 66
2.3.9. Flow cell optimization for eCO_2RR in gas diffusion electrode configuration 67
2.3.10. Gaseous product analysis 68
2.3.11. Liquid product analysis 68

2.3.12. Preparation of Gas diffusion Electrode (GDE) 68

2.3.13. In-situ Electrochemical Attenuated Total Reflection Fourier Transform Infrared Spectroscopy (ATR-FTIR) 69

2.4. Results & Discussion 69

2.4.1. Synthesis and characterizations 69

2.4.2. Electrochemical CO_2 reduction (eCO_2RR) in H-cell 72

2.4.3. In situ electrochemical ATR-FTIR study 77

2.4.4. Local and surface electronic structures on eCO_2RR 79

2.4.5. High current density using microflow cell 87

2.5. Conclusion 88

2.6. References 89

Chapter 3. Structure-Tailored Surface Oxide on Cu-Ga Intermetallics Enhances CO_2 Reduction Selectivity to Methanol at Ultra-Low Potential..... 96

3.1. Introduction 99

3.2. Experimental Details 101

3.2.1. Chemicals and reagents 101

3.2.2. Synthesis of $CuGa_2$ and Cu_9Ga_4 101

3.2.3. Ball milling 102

3.3. Characterization and Experimental Methods 103

3.3.1. Powder X-ray Diffraction (PXRD) 103

3.3.2. Transmission Electron Microscope (TEM) 103

3.3.3. Inductively coupled plasma atomic emission spectroscopy (ICP-OES) 103

3.3.4. X-ray Photoelectron Spectroscopy (XPS) 103

3.3.5. Elemental Analysis 103

3.3.6. X-ray Absorption Spectroscopy 104

3.3.7. Atomic Force Microscopy (AFM) 104

3.3.8. Electrochemical CO_2 Reduction Reaction (eCO_2RR) 104

3.3.9. Flow cell optimization for eCO_2RR in gas diffusion electrode configuration 105

3.3.10. Gaseous product analysis 105

3.3.11. Liquid product analysis 105

3.3.12. Preparation of Gas diffusion Electrode (GDE) 106

3.3.13. In situ Electrochemical Attenuated Total Reflection Fourier Transform Infrared Spectroscopy (ATR-FTIR) 106
3.4. Results & Discussion 106
3.4.1. Synthesis and characterizations 106
3.4.2. Electrochemical CO_2 reduction (eCO_2RR) in H-cell 110
3.4.3. Product quantification and Faradaic efficiency (FE) 111
3.4.4. In situ electrochemical ATR-FTIR study 113
3.4.5. Oxidation state and Local electronic structures from XAFS 115
3.4.6. Potential dependent in-situ XAFS analysis 117
3.4.7. Potential dependent Ex-situ XPS and powder XRD analysis 119
3.4.8. High current density using flow cell with GDE configuration 125
3.5. Conclusion 128
3.6. References 129

Chapter 4. Atomically Dispersed Copper on WC@NGC Boosts the Conversion of CO_2 to Acetic Acid..... 134
4.1. Introduction 137
4.2. Experimental Details 138
4.2.1. Chemicals and reagents 138
4.2.2. Synthesis of Cu_1-WC@NGC catalyst 138
4.3. Characterization and Experimental Method 139
4.3.1. Powder X-ray Diffraction (PXRD) 139
4.3.2. Transmission Electron Microscope (TEM) 140
4.3.3. Inductively coupled plasma atomic emission spectroscopy (ICP-OES) 140
4.3.4. X-ray Photoelectron Spectroscopy (XPS) 140
4.3.5. Scanning electron microscopy (SEM) and Energy Dispersive Spectrum (EDAX) 140
4.3.6. X-ray Absorption Spectroscopy 141
4.3.7. Raman Spectroscopy 141
4.3.8. Electrochemical CO_2 Reduction Reaction (eCO_2RR) 141
4.3.9. Flow cell optimization for eCO_2RR in gas diffusion electrode configuration 142
4.3.10. Gaseous product analysis 142

4.3.11. Liquid product analysis 143

4.3.12. Preparation of Gas diffusion Electrode (GDE) 143

4.3.13. In situ Electrochemical Attenuated Total Reflection Fourier Transform Infrared Spectroscopy (ATR-FTIR) 143

4.3.14. Computational Details 144

4.4. Results & Discussion 144

4.4.1. Synthesis and characterizations 144

4.4.2. Electrochemical CO_2 reduction (eCO_2RR) in H-cell 147

4.4.3. In situ electrochemical ATR-FTIR study 151

4.4.4. Oxidation state and Local electronic structures from Spectroscopic study 153

4.4.5. Post electrochemical characterization 156

4.4.6. High current density using flow cell with GDE configuration 159

4.4.7. Computational understanding of the reaction mechanism 159

4.5. Conclusion 161

4.6. References 161

Chapter 5. Operando Investigation of the Origin of C-C Coupling in Electrochemical CO_2 Reduction Upon Releasing Bonding and Structural Ordering in Pd-Cu Catalyst……..…169

5.1. Introduction 172

5.2. Experimental Details 173

5.2.1. Chemicals and reagents 173

5.2.2. Synthesis of Pd-Cu-based catalysts 173

5.3. Characterization and Experimental Method 173

5.3.1. Powder X-ray Diffraction (PXRD) 173

5.3.2. Transmission Electron Microscope (TEM) 173

5.3.3. Inductively coupled plasma atomic emission spectroscopy (ICP-OES) 174

5.3.4. X-ray Photoelectron Spectroscopy (XPS) 174

5.3.5. X-ray Absorption Spectroscopy 174

5.3.6. Electrochemical CO_2 Reduction Reaction (eCO_2RR) 174

5.3.7. Flow cell optimization for eCO_2RR in gas diffusion electrode configuration 175

5.3.8. Gaseous product analysis 175

5.3.9. Liquid product analysis 176

5.3.10. In situ Electrochemical Attenuated Total Reflection Fourier Transform Infrared Spectroscopy (ATR-FTIR) 176

5.3.11. Methodology of computational study 177

5.4. Results & Discussion 178

5.5. Electrochemical CO_2 reduction (eCO_2RR) 181

5.6. Mechanistic Studies 183

5.6.1. In situ ATR-FTIR spectroscopy 183

5.6.2. In situ Raman Study 185

5.7. Spectroscopic investigation of the active site 185

5.7.1. XPS study 185

5.7.2. Ex situ and in situ X-ray absorption spectroscopy 186

5.8. Computational understanding of the Reaction Mechanism 189

5.9. High current density using flow cell with GDE configuration 194

5.10. Conclusion 196

5.11. References 197

Chapter 6. Unravelling the Mechanism of Higher Alcohols Production on the Ordered Intermetallic Surface During CO_2 Electroreduction.....203

6.1. Introduction 206

6.2. Experimental Details 208

6.2.1. Chemicals and reagents 208

6.2.2. Synthesis of $PdCu_3$ 208

6.3. Characterization and Experimental Method 209

6.3.1. Powder X-ray Diffraction (PXRD) 209

6.3.2. Transmission Electron Microscope (TEM) 209

6.3.3. Inductively coupled plasma atomic emission spectroscopy (ICP-OES) 209

6.3.4. X-ray Photoelectron Spectroscopy (XPS) 209

6.3.5. Scanning electron microscopy (SEM) and Energy Dispersive Spectrum (EDAX) 210

6.3.6. X-ray Absorption Spectroscopy 210

6.3.7. Electrochemical CO_2 Reduction Reaction (eCO_2RR) 210

6.3.8. Flow cell optimization for eCO_2RR in gas diffusion electrode configuration 211
6.3.9. Gaseous product analysis 211
6.3.10. Liquid product analysis 212
6.3.11. In situ Electrochemical Attenuated Total Reflection Fourier Transform Infrared Spectroscopy (ATR-FTIR) 212
6.3.12. Methodology of computational study 212
6.4. Results & Discussion 213
6.4.1. Electrochemical CO_2 reduction (eCO_2RR) 216
6.4.2. Faradaic efficiency (FE) of CO_2 reduced products 218
6.5. Mechanistic Studies 223
6.5.1. In-situ IR spectroscopy and XPS study 223
6.5.2. Ex situ and in situ X-ray absorption spectroscopy 225
6.5.3. Mechanistic Insight on Product Selectivity 229
6.5.4. Differential electrochemical mass spectrometry (DEMS) 239
6.6. Conclusion 240
6.7. References 240

Summary and Future Outlook……247
List of Publications…… 250
Biography……253

Chapter 1

Introduction

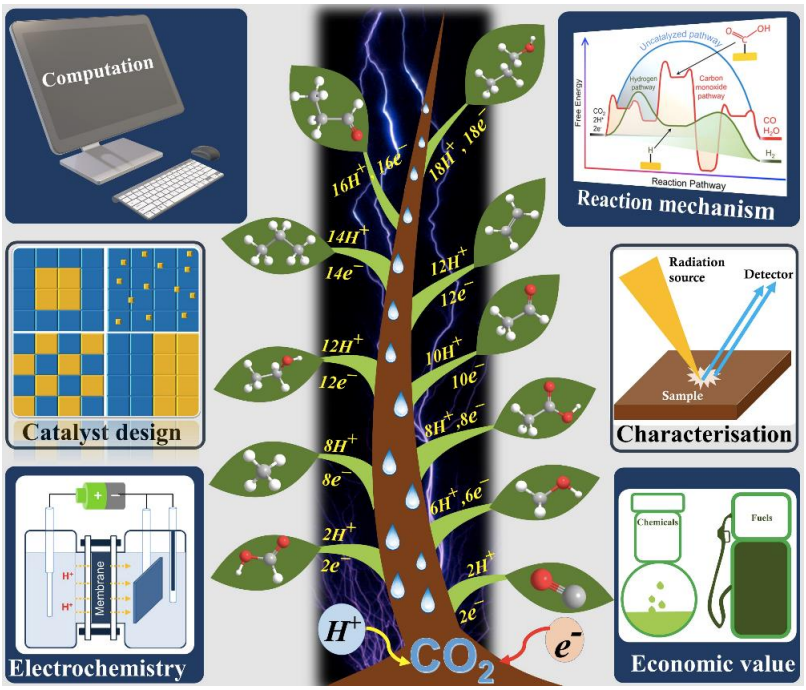

Part of this chapter is taken from

An Integrated Material Design and Catalytic Perspective on Electrochemical CO_2 Reduction. Bagchi, D. Roy, S. Sarma, S.C. and Peter, S. C. *Adv. Funct. Mater.* **2022**, 2209023

Table of Contents

1.1 Background 4

1.2 Electrocatalytic CO_2 reduction reaction (eCO_2RR) 4

1.3 Critical challenges in eCO_2RR 6

1.3.1 Fundamental challenge 6

1.3.2 Solubility of CO_2 6

1.3.3 Optimization of electrocatalytic process parameters 7

1.3.4 Achieving the industrially-relevant current density 8

1.3.5 Requirement of multiple techniques 8

1.4 Catalyst design for eCO_2RR 8

1.4.1 Modification of active metal site towards product selectivity 9

1.4.2 Controlling the particle size and shape 10

1.4.3 Role of support materials 11

1.4.4 Defect engineering 11

1.4.5 Single-atom and molecular catalysts 12

1.4.6 Tandem catalysts 13

1.4.7 Two-dimensional and other strategies form materials perspective catalyst 14

1.4.8 Electronic-structure modulated catalyst surface 15

1.5 Effect of Process Conditions on eCO_2RR 15

1.5.1 Effect of Cell design on eCO_2RR product selectivity 16

1.5.2 H-type cell 17

1.5.3 Flow cell with gas diffusion electrode configuration and membrane electrode assembly (MEA) 18

1.5.4 Differential electrochemical mass spectrometry (DEMS) cell 20

1.6 Mechanism of electrochemical CO_2RR 21

1.6.1 Branching mechanism of eCO_2RR to multiple products 22

1.6.2 Carbon monoxide Formic acid/ Formate 22

1.6.3 Methanol vs. Methane 24

1.6.4 Ethylene vs. Acetate 25

1.6.5 Ethylene vs. Ethanol 25

1.6.6 Acetone vs. *n*-Propanol 26

1.7 Fundamental terms in electrocatalysis 27

1.7.1 Onset potential 27

1.7.2 Overpotential 27

1.7.3 Electrochemically active surface area (ECSA) 28

1.7.4 Faradaic efficiency (FE) 28

1.8 Parameters to screen various electrocatalysts 28

1.8.1 Activity 28

1.8.2 Stability 28

1.8.3 Selectivity 28

1.9 Experimental and characterization tools for evaluating and characterizing an electrocatalyst 29

1.9.1 Cyclic voltammetry (CV) 29
1.9.2 Linear sweep voltammetry (LSV) 29
1.9.3 Chronoamperometry (CA) 29
1.9.4 Bulk electrolysis with coulometry 29
1.9.5 EIS spectroscopy (AC impedance) 29
1.9.6 Powder X-ray diffraction (PXRD) 29
1.9.7 X-ray photoelectron spectroscopy (XPS) 30
1.9.8 X-ray absorption spectroscopy (XAS) 30
1.9.9 Electron Microscopy 31

1.10 Electrochemical CO_2 reduction reactor 32

1.10.1 General electrochemical setup for H-cell study 32
1.10.2 Flow cell reactorfor eCO_2RR in gas diffusion electrode configuration (GDE) 33
1.10.3 Preparation of Gas diffusion Electrode (GDE) 33

1.11 CO_2 reduced product analysis 35

1.11.1 Gas chromatography (GC) 35
1.11.2 High-Performance Liquid Chromatography (HPLC) 36
1.11.3 Nuclear magnetic resonance spectroscopy (NMR) 36

1.12 Spectroscopic and analytical techniques for in situ mechanistic studies 37

1.12.1 In situ Electrochemical Attenuated Total Reflection Fourier Transform Infrared Spectroscopy (ATR-FTIR). 37
1.12.2 In situ X-ray absorption Spectroscopic studies 37
1.12.3 In situ Raman Spectroscopic studies 38
1.12.4 Differential electrochemical mass spectrometry (DEMS) 39

1.13 Density Functional Theory (DFT) 40

1.14 References 43

1.1 Background

The global energy demand is skyrocketing day by day as a consequence of levels of greenhouse gases and pollutants. Because of this, an earnest need for achieving a green and sustainable global economy. This requires the development of new energy technologies using renewable energy sources that can meet the global requirement without posing a threat to our society and environment. Electrochemical energy conversion plays a significant role in energy sustainability due to their high efficiencies and quite negligible chemical and noise pollution. The core of the electrochemical energy conversion technology involves the development and designing of highly efficient and durable materials that can effectively catalyze various electrochemical reactions needed to facilitate the transition towards a greener economy.

Most conventional energy derivation routes in our society exploit a highly spontaneous central reaction, involving the exothermic oxidative combustion of different hydrocarbons or carbon-containing oxygenates producing CO_2 and H_2O (**Eqn. 1.1**). While this reaction enables us to meet the energy demands of our growing society, its overexploitation has altered the natural carbon cycle adversely, creating detrimental effects on the environment. Thus, reversing this reaction, to fix CO_2 back in the form of fuels/chemicals/hydrocarbons, harvesting renewable electricity, is one of the most elegant ways to solve the intertwined problems of environmental degradation and increasing energy demands.

$$C_xH_y + zO_2 \rightleftharpoons xCO_2 + (y/2)H_2O \quad -\Delta G \qquad \textbf{(Eqn. 1.1)}$$

$$2H_2O \rightleftharpoons O_2 + 4H^+ + 4e^- \quad E^0 = 1.23 \text{ V (RHE)} \qquad \textbf{(Eqn. 1.2)}$$

$$2CO_2 + 12H^+ + 12e^- \rightleftharpoons C_2H_5OH + 3H_2O \quad E^0 = 0.08 \text{ V (RHE)} \qquad \textbf{(Eqn. 1.3)}$$

$$2CO_2 + 3H_2O \rightleftharpoons C_2H_5OH + 3O_2 \quad \Delta E = 1.15 \text{ V (RHE)}; \ \Delta G = +1270 \text{ kJ/mol} \qquad \textbf{(Eqn. 1.4)}$$

However, the direct reversal of such a thermodynamically downhill reaction is immensely energy expensive (**Eqn. 1.2-1.4**). One of the most efficient ways to close the anthropogenic carbon cycle is to use electrons and protons to convert CO_2 back in the form of fuels and chemical feedstocks. However, to lower the activation energy barriers for the reaction pathways, we need suitable catalysts that can efficiently convert CO_2 close to the thermodynamic energy requirements using sources like photons, temperature, or electromotive force.

1.2 Electrocatalytic CO_2 reduction reaction (eCO_2RR)

Electrocatalytic CO_2 reduction reaction (eCO_2RR) is one of the greenest and most efficient pathways of converting CO_2 to valuable fuels and chemicals. In this way, the application of external potential, which can be generated from cheap, renewable electricity like solar and wind, reduces CO_2 to CO and various hydrocarbons and oxygenates depending on the

catalyst surface where the eCO_2RR takes place. The most significant advantage of eCO_2RR over other possible routes lies in the wide range of products that can be categorically targeted through this process at defined potentials (**Figure 1.1a**). Electrocatalytic CO_2RR can occur through a 2-, 4-, 6-, 8-, 12-, or even an 18-electron reduction pathway to convert CO_2 into various gaseous (carbon monoxide, methane, ethane, and ethylene) and liquid products (formic acid, methanol, ethanol, acetic acid, propanol, etc.).[1, 2] However, lack of thorough mechanistic understanding impedes the utilization of the true potential of this technology which still faces significant challenges in areas like (a) low reaction rates or current densities (typically ≤ 200 $mAcm^{-2}$: one order less than requirements of commercial electrolyzers) & CO_2 mass transport limitations (b) slow electron-transfer (ET) kinetics, (c) unsatisfactory product selectivity for some of the desired reduction products (methanol, ethanol, and higher hydrocarbons)[3] & durability (typically ≤ 100 h).[4] Most of the electrocatalysts reported so far can produce below 200 mA cm^{-2}, which is far less than industrial electrolyzers, usually operating at more than 70% efficiency at current densities above 200 mA cm^{-2}.[5, 6] For these reasons, a lot of efforts have been devoted towards the design and synthesis of efficient, selective, cost-effective, and robust electrocatalysts which can reduce CO_2 at high rates with minimum overpotential (**Figure 1.1b**). Parallelly tremendous engineering have optimized other parameters like cell design, use of gas diffusion electrode (GDE) in flow cell configuration, use of suitable electrolyte, pH, CO_2-flowrate, temperature, etc. to enhance the overall performance. The overall goal of the eCO_2RR research is to design non-precious metal-based catalyst, which can selectivity produce one particular product with high rate. Then, we need to understand the reaction mechanism as well as active site of the catalysts by various ex situ and in situ studies[7, 8]

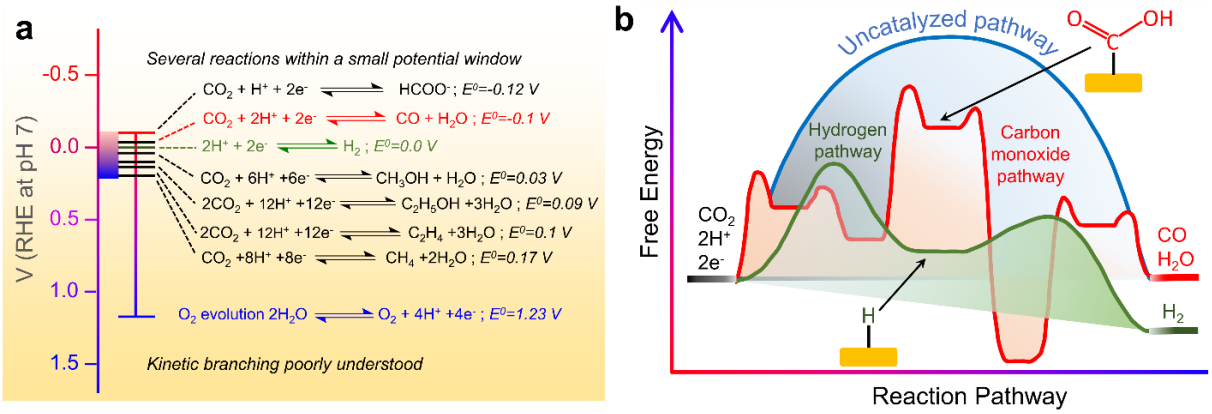

Figure 1.1. (a) eCO_2RR products within a small potential window and (b) schematic energy profile landscape of the uncatalyzed and catalyzed reaction pathways for CO and dihydrogen formation.

1.3 Critical challenges in eCO_2RR

1.3.1 Fundamental challenge

Carbon dioxide is a linear, stable, and chemically inert molecule with ultralow electron affinity and a large HOMO-LUMO energy gap (13.7 eV). Its transformation is generally dominated by nucleophilic attacks at the carbon center, which is an uphill process demanding a substantial input of energy (750 kJ mol^{-1} for dissociation of the C=O bond).[4] CO_2 has a standard formation enthalpy of -393.5 kJ/mol and hence exhibits high thermodynamic stability.[9] Electrocatalytic reduction of CO_2 to the majority of the products is a multi-electron-proton transfer process that proceeds through several intermediate steps during the transformation. Moreover, the potential for competing water reduction process falls in the same potential region.[10] The product window consists of closely-placed thermodynamic potential levels, which can be further resolved by the staggered kinetics of multiple electron transfer steps. Thus, any multistep eCO_2RR is an interplay between thermodynamic and kinetic factors, optimal control of which will let us exploit the true potential of this energy conversion pathway. The eCO_2RR in aqueous electrolytes is rather complex and bears considerable kinetic barriers compared to the competing hydrogen evolution reaction (HER).[11] Unfortunately, the reaction suffers from slow kinetics owing to the low local concentration of CO_2 especially in case of liquid-phase CO_2 reduction reaction for multi-step reaction mechanism. Another issue with CO_2 is that it can undergo reduction into several C_1-C_3 products, all of which lie within small thermodynamic potential window of ~200 mV (**Figure 1a**).[10] However, all the >2e^- reduction processes (other than CO/ formate), though thermodynamically more favorable, are severely limited (kinetically) due to the multiple proton-electron transfer steps involved in their formation. The hydrogenation of adsorbed C_1 intermediates is kinetically more facile than C–C bond formations, which limits the catalytic rate and selectivity of C_2-C_3 hydrocarbon/oxygenate production.[12] The maximum Faradic efficiency (FE) of the high energy-dense C_3 product (C_3H_7OH) in a direct electroreduction never crossed 30%.[13] **Figure 1.2** shows that close to ~98% FE towards C_1 products have been achieved. However, FE towards C_2 and C_3 products have been very less. Thus, insights into the mechanism of product formation in addition to the knowledge of catalyst design, must be exploited to further tune the catalyst for a selected product.

1.3.2 Solubility of CO_2

In addition to the bulk and surface structures of the catalysts, electrolytes, which are the primary proton donors (in RLS or past RLS)[14] or at times even sources of molecular CO_2, play a crucial role as the media for coupled electron-proton transfer (e^-/H^+).

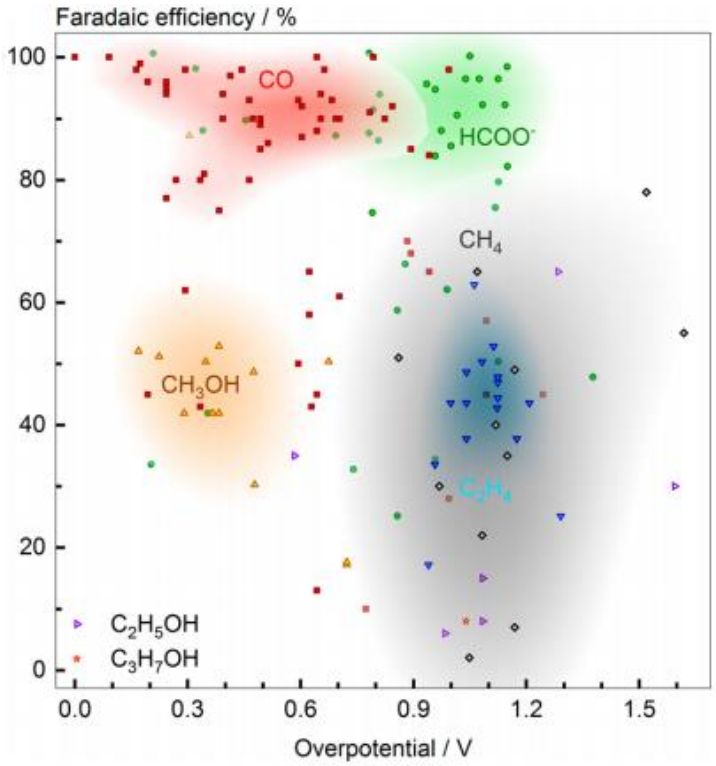

Figure 1.2. Performance map for the eCO_2RR toward the most commonly reported products. The maximum FE and it's corresponding overpotential are plotted for each reported catalyst. The background color intensity is positively correlated to the density of points, suggesting characteristic values of FE-overpotentials for different products. Reprinted from Larrazábal *et al.*,[15] with permission from the American Chemical Society.

In the case of aqueous electrolytes, e.g., bicarbonates, having low buffer capacity (which maintains the bulk but not local pH of the electrolytes),[14] the counter cations can alter the outer Helmholtz plane potential and can also influence the surface hydrogen coverage by transferring H_2O molecules from their solvation shell to the electrode.

1.3.3 Optimization of electrocatalytic process parameters

The effects of conditions like the types of electrocatalysts (composition, size, shape, oxidation state, and crystal structure), electrolytes (cation, anion, concentration), pH, temperature, pressure, and applied potential gets superimposed onto the thermodynamic and kinetic considerations. A good catalyst, in general, should entail, on the one hand, optimal adsorption (reactants & intermediates) and desorption energies (products) for a preferred pathway, and on the other should provide catalytic sites transferring electrons that are close to sites providing protons. Nonetheless, the adsorption energies (E_{ads}) of the intermediates in the multi-electron transfer pathways of eCO_2RR are found to follow linear-scaling relationships, which limit the overall catalytic efficiencies leading to multiple product formation.[16]

1.3.4 Achieving the industrially-relevant current density

The success of the entire process of electrochemical transformation of CO_2 to value-added fuels and chemicals depends on improvements in energy efficiency so that minimum operating costs can be required for its application on the industrial scale.[17] To decrease the capital cost of the CO_2 reduction technology, it is fundamentally important to increase the current density in industrial level (more than 100mA/cm^2). In the traditional liquid phase CO_2RR study, the current density has been limited because of poor CO_2 diffusion and lower solubility in the liquid electrolytes, which restricts its large-scale commercial application. In recent years, flow cell in gas diffusion configuration has been employed especially in alkaline electrolyte to enhance current density (even 1A/cm^2) and overall CO_2RR performance.[18] But alkaline electrolyte can consume CO_2 and form bicarbonate and carbonate and reduce the CO_2 conversion efficiency. So, choice of electrolyte is extremely crucial to achieve high current density without compromising CO_2RR activity.

1.3.5 Requirement of multiple techniques

For better catalytic efficiency and selectivity, it is really important to understand the reaction mechanism for each CO_2 reduced product as well as the knowledge about the fate of the catalyst surface during CO_2 reduction.[19] But, there is no single spectroscopic or microscopic technique available that can simultaneously probe the intermediate adsorbed over time as well as electronic and structural changes of the catalyst during CO_2RR. It is very crucial to have the perception of all sorts of in-situ spectroscopic, microscopic along with analytic techniques to systemically investigate CO_2 reduction in real-time. All in all, it is intuitive that the critical problems of CO_2 electroreduction (kinetic rates and product selectivity) can only be solved through efficient proton management, proper electrolytic conditions, informed catalyst design, and the meticulous choice of other parameters. However, the development of these interconnected approaches can only be achieved through iterative loops of catalytic design and subsequent mechanistic understanding of structure-activity/selectivity relationships.

1.4 Catalyst design for eCO_2RR

The central part of the eCO_2RR research is to design suitable, robust catalyst materials which would be able to convert CO_2 to selective products at a minimum applied potential producing higher current in the process. **Figure 1.3** summarize important classes/families, examples, and strategies of electrocatalyst designs explored in eCO_2RR. Catalysts design strategies can be classified as few major types viz. modification of active metal site,[20] controlling

particle size,[21] shape,[22] and morphology,[23] carbon-based,[24] role of catalyst support materials,[25, 26] defect engineering,[27] molecular,[28] single-atom catalyst,[29, 30] tandem catalysts.[31]

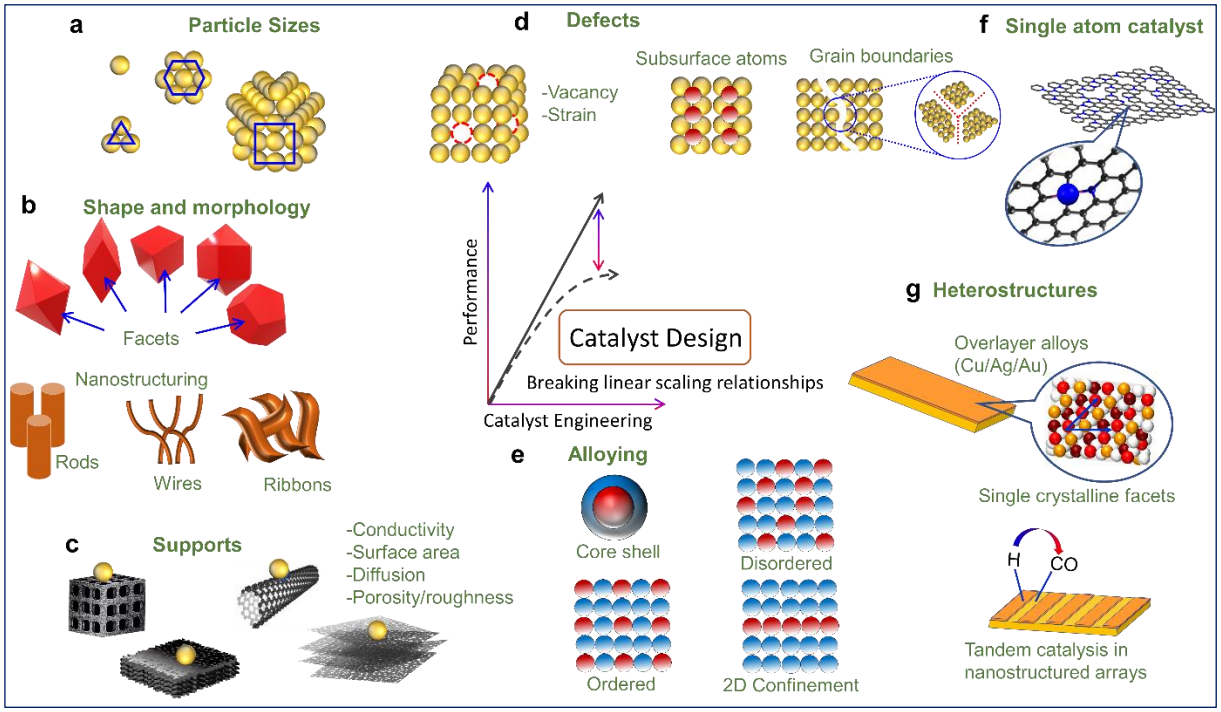

Figure 1.3. Catalyst designing strategies for eCO_2RR based on (a) particle sizes, (b) shape and morphology, (c) support, (d) defects, (e) alloying, (f) single atom catalyst, (g) heterostructures.

The linear-scaling relationships mentioned in the previous section can be envisioned to be broken by (a) reducing the coordination numbers of the pristine catalytic sites, (b) doping with secondary elements (p block), (c) incorporating exophilic sites, and introduction of surface ligands.[32]

1.4.1 Modification of active metal site towards product selectivity

Transition metal-based catalysts are most extensively explored for eCO_2RR. Among monometallic catalysts, CO selective metals (e.g., Au, Ag, and Pd), formic acid selective metals (e.g., Sn, Pb, In, and Pb), and Cu is for C_1-C_{2+} alcohols and hydrocarbons.[33] Since the landmark work by Hori *et al*. classifying elements, especially metals for particular product selectivity in CO_2 electroreduction, a plethora of catalyst engineering approaches (including bi-metals, ordered intermetallics, disordered alloys, metal oxides, chemical heterostructures, oxide derived metal surface, and sulfides, carbon-based materials, and organic frameworks) have been undertaken to improve catalytic current densities and product selectivities.[34, 35] It is well known that the eCO_2RR can produce as many as 16 different products ranging from C_1-C_3 hydrocarbons, as demonstrated on Cu surface across different potential windows by Jaramillo et. al.[36] Apart from the simpler ($2e^-$ reduced) products like CO or formate, which are generated

through the preferred binding modes of the CO_2 through C or O ends to the active site, most other products involve several intermediates, C-C bond formation and proton-electron transfer steps where the E_{ads} and activation energies of the transition states are critical to the mechanistic control of reaction pathways. CO is a common intermediate to all the higher reduction products, its binding energy becomes a matter of critical consideration. Recently, the multi-carbon selectivity on the Cu surface has been achieved by several new strategies like Cl-doping,[37] F-modification,[38] and methanethiol monolayers-Cu.

Metallic Cu (polycrystalline or single crystalline facets) has by far been the best catalyst for C_{2+} products, while Au and Ag have been found to be benchmark catalysts for CO production.[39] Higher carbon products beyond CO and formates have more significance in the material value chain owing to their energy density, chemical utility, market size, etc.[40] The on-top, edge, and step sites of polycrystalline Cu (corresponding to particular crystallographic planes) have been shown to have different selectivities for higher reduction products.[41] Controlling the local pH and reactant diffusion through introducing meso and microstructures in inverse opal Ag/Au porous catalysts, Surendranath and co-workers achieved high CO FE suppressing hydrogen generation.[42] Engelbrecht *et al.* undertook another approach to increase the CO FE through the application of pulsed electrochemical potential.[43] In a recent report on a Cu-hydride catalyst, the enhanced formic acid selectivity, in contrast to the usual $2e^-$ CO_2 reduction pathway, was proposed to proceed via a lattice hydride mechanism.[44] The most important relevance of such alternative mechanistic considerations ($*CO_2^{\delta-}$ or anionic hydride mediated) is the pH and cationic species dependence of the pathways owing to the high polarizability of the intermediates.

1.4.2 Controlling the particle size and shape

Controlling the particle of metallic nanoparticle, different dimension, CO_2RR activity can be tuned (**Figure 1.3a**). Sun *et al*. reported that CO selectivity of monodispersed Au nanoparticles decreases with decreasing nanoparticle size. By computational study, they proved that CO production is more favorable in the smaller nanoparticle, which contains more Au (211) sites (edge sites), while larger nanoparticle consisting of Au (111) and 13-atom Au clusters (corner sites) are more active sites for H_2 production.[45] Similar size-dependent activity has been shown for other metal NPs such as Ag,[46] Bi,[47] Sn,[48] and Zn[49] as well where CO_2RR efficiency decreases below a certain particle size.[50] Apart from the size, shape, and morphology (**Figure 1.3b**) of the catalyst plays a crucial impact on the CO_2 reduction activity. Shape engineering of the nanoparticle can be opted by careful synthesis, which would expose the preferred plane and

give rise to proper shape and morphology.[51] The exposed crystallographic facet has a strong role in controlling the intermediate adsorption during the electrochemical reaction and determining the CO_2RR performance.[52] In the case of Pd, octahedra predominantly formed by (111) facet exhibited more CO selectivity (FE up to 95%) than to Pd cubes having (100) facets.[53] Recently, facet-dependent selectivity of Cu catalysts have been investigated on cubic, spherical, and octahedral Cu nanoparticle by Buonsanti and co-workers. Cu cube shows higher selectivity for multicarbon products than others and reaches ethylene selectivity to 57%, whereas Cu octahedra exhibit much higher C_1 selectivity forming methane with FE of 51%.[54] It has been found that Cu octahedra are formed with (111) facet, and Cu cube predominantly has (100) facet. Garza *et al*. proposed that the C-C bond formation is more favorable on the Cu (100) surface than the Cu (111) surface and found *COCHO to be the main intermediate for C_2 products.[55]

1.4.3 Role of support materials

Dynamic changes of nanoelectrocatalysts can be avoided by using suitable support materials which have good conductivity and surface area for the electron transfer and diffusion of reactant, respectively. The physical and chemical property like porosity, toughness of support have also been investigated (**Figure 1.3c**) towards CO_2RR the synergic effect between support and active metal play a very important role in monitoring electrochemical performance.[56] The active Cu^+ species under eCO_2RR, is found to be more stable in the presence of Cu foil support than the carbon support,[57] and Cu cube supported on Cu foil has shown higher FE for C_{2+} products at lower overpotential than those on the carbon support.[58] Au displayed better CO production on CeO_x support than on carbon support.[59] Au nanoparticle with C_3N_4 support shows enhanced CO_2RR activity than the carbon support. In this case, C_3N_4 induces a negative charge on the Au surface, which stabilizes the COOH* intermediate.[60] It has been observed that the CO_2RR activity can be further increased by the incorporation of carbon quantum dot in combination with C_3N_4, which enhances the conductivity and CO_2 adsorption.[61] In corporation of metal catalyst into the MOF support is an interesting strategy to enhance the catalytic activity.[62] It has been shown that Ag nano catalyst has shown better CO selectivity after incorporating it into MOF moiety.[63]

1.4.4 Defect engineering

Modification of catalyst surface by creating defects, strain, or grain boundary are a few important strategies to tune catalytic activity (**Figure 1.3d**).[64, 65] Ajayan *et al*. studied N-doped graphene foam (NGF) having different amounts of N-defects and found that defective NGF showed better CO selectivity than Ag or Au in the same CO_2RR conditions.[27] They also

observed that catalytic activity was majorly dependent on the pyridinic-N defect rather than graphitic-N or pyrrolic-N. Wang and co-workers reported F-doped carbon (FC), which has shown an extremely high CO FE of 90%. From DFT calculations, they prove that doped F defects increase the COOH* adsorption and prevent hydrogen evolution.[66] Kanan and co-workers extensively studied the role of grain-boundary on the CO_2RR performance. Initially, they observed that continuous metal film consisting of Cu having 10-100 nm crystallites connected grain boundaries (GB) shows extremely good CO_2RR activity.[67] Later, they provided the quantitative correlation between CO_2RR activity and GB density. Their results show that GB-rich Cu on carbon nanotube showed significant enhancement in the formation of multi-carbon products.[68] Electrocatalyst defects, such as atomic vacancies and dopants, facilitate the adsorption of unusual eCO_2RR intermediates and thus selectively enhance the corresponding pathway towards oxygenates.[24, 69] Sargent and co-workers[70] studied the role of defects in a core-shell Cu electrocatalyst in detail, taking *C_2H_3O as an example, which is the potential penultimate intermediate for ethylene and ethanol production (**Figure 1.3e**). It has been proposed that the binding energies of *CO, *CHO, *CH_2O, and *COOH can be independently modulated by inducing lattice strain in metal catalysts.[71] Huang *et al.* have reported the synthesis of Pd octahedral and icosahedra nanoparticles and demonstrated that Pd icosahedra exhibits superior activity (FE_{CO} ~91.1%) towards CO production due to tensile strain on the surface.[72]

1.4.5 Single-atom and molecular catalysts

Single-atom catalysts (SACs) are atomically dispersed transition metal atoms on 2D support and connected with a heteroatom (like N, C, P, or S) (**Figure 1.3f**).[73] Thus, over SACs only a particular type of intermediate species is stabilized, leading to high selectivity towards a particular product. When the catalyst size reduces to isolated atoms, CO becomes the major product of CO_2 reduction and tuning the metal coordination plays a key role in enhancing catalyst activity and selectivity.[74, 75] The promotional effect of single atomic sites have recently been demonstrated from a slightly different perspective by Jiang *et al.*, where high FE for CO production was achieved by dispersing single Ni sites on a graphene matrix.[76] Many other theoretical and experimental findings have confirmed this viewpoint.[77] Due to their high activity and selectivity, SACs have attracted increasing interest, with a significant reduction in noble metal use and high atomic efficiency. Due to unfavorable chemisorption of atomic hydrogen on and near M-N_x sites, isolated active single M-N_x sites have the vital advantage of largely suppressing the competing Hydrogen Evolution Reaction (HER) process.[78, 79]

Interestingly, in contrast to the initial concerted proton-electron transfer (CPET) step for metallic or bulk electrocatalysts, molecular electrocatalysts are believed to proceed through the electron-transfer mediated CO_2 binding step followed by subsequent proton transfer or CPET to produce *COOH or *COOH-.[80] Due to a different r.d.s. in these catalysts, e.g., in the case of graphite-immobilized Co-protoporphyrin, the pH dependence of CO_2 reduction and competitive HER pathways determined the overall product selectivity between H_2 (pH 1) and CO (pH 3) at different pH.[81, 82] Compared to SAC, dual atomic site catalysts (DAC) are also very tunable and efficient, which are recently explored for eCO_2RR as well.[83, 84] Li and co-workers reported a very interesting strategy for the synthesis of Pd_2 DAC, which has shown significant advancement in the CO selectivity than Pd_1 SAC.[85] Recently, an advanced SAC with Co–N–Ni bimetallic sites has been found to be extremely selective towards CO production showing FE of 96.4% at an over the potential of only 370 mV.[86] In the case of molecular catalysts, such mechanistic pathways are triggered by the potential induced oxidation state variation of the metal centers or the ligands.[87, 88] For example, in post-transition metalloporphyrins of Rh, Sn, and In, the formate or formic acid production has been predicted to proceed through an anionic hydride as the key intermediate[89] with a nucleophilic attack on CO_2 carbon, producing the HCOO- species.

1.4.6 Tandem catalysts

Depending on the mode of adsorption of the intermediates and strength of interaction with the active site, eCO_2RR can lead to different types of products. Lum *et al.* verified this in oxide-derived Cu catalysts, where they have observed product-specific active sites.[90] In a catalyst containing multiple active sites, a greater selectivity towards a particular product is compromised. This necessitates the presence of a similar type of active site in a catalyst to achieve higher selectivity. An interesting experimental approach that has been explored to enhance C_2/C_3 product formation in eCO_2RR is tandem catalysis (**Figure 1.3e**).[91] Through the sequential reduction of CO on separated Au and Cu sites/regions, Lum *et al.* and Morales-Guio *et al.* showed interesting examples of this approach.[92] The basis of a similar approach at a molecular level can be drawn from the insightful work by Surendranath and co-workers where on polycrystalline Cu metal surface, the reduction of CO to CH_4 or ethylene was found to follow the Langmuir-Hinshelwood mechanism, thus emphasizing the role of the proton adsorption/spill-over site on the catalytic surface.[93] This work demonstrated that selective subsequent reduction of CO intermediate during direct eCO_2RR, would require single atomic sites for H spillover, surrounded by islands of moderately strong CO binding sites. The atoms

chosen for the single site H adsorption/spillover should be the ones that predominantly exhibit Tafel desorption in hydrogen evolution. Such single atomic sites, lacking adjacent H adsorption sites, is likely to transfer the adsorbed protons for further reduction of CO in the surrounding catalytic islands. For tandem catalysis, one may explore nanolithography to construct different arrays and compositions of Cu-Ag-Au electrodes to study their effect on product selectivity. Integration of these electrodes in the working setup of a floating electrode can substantially get rid of the mass transport limitations.[65]

1.4.7 Two-dimensional and other strategies form materials perspective catalyst

Recently, 2D nanostructured catalysts having a large number of low-coordinated surface atoms have attracted much attention towards eCO_2RR. 2D materials like metals, oxides, chalcogenides, nitrides, carbides, phosphates, halides, and covalent organic have been started applied in eCO_2RR. Xie and co-workers reported freestanding 4-atom-thick Co sheets for highly selective formate production at ultra-low potential.[94] Ultrathin Bi displayed excellent formate selectivity with an FE of 86% at 16.5 mA/cm^2.[95] Recently, Au–Cu bimetallic thin films having different metal ratios were studied for eCO_2RR.[96] Four different chaclcogenides materials viz. MoS_2, $MoSe_2$, WS_2 and WSe_2, have been explored for CO_2RR and it is found that WSe_2 nanoflakes exhibit the highest with an exceptional current density of 330 mA/cm^2 and an FE of 85% for CO generation activity at an overpotential of 65 mV than other catalysts.[97] Among MOF-based catalysts, Co-based MOF is found to be the best catalyst for CO selectivity (FE of 99% at -0.8V).[98] Among metal-oxide 2D structures, Moreover, Co_3O_4 layers having 1.72 nm thickness displayed a maximum current density of 0.68 mA/cm^2 and FE of 64.3% for formate production. Oxygen (II)-vacancy-rich Co_3O_4 nanosheets (0.84 nm) displayed 85% formate selectivity for 40 h.[94] By making heterostructure of two materials, the eCO_2RR selectivity and performance can be improved. For example, Fe_2P has been reported for CO_2 to ethylene glycol with excellent selectivity. It has been proposed from DFT that phosphino-hydrides helps to convert *formate to *formaldehyde, the key intermediate for C–C coupling, facilitates the ethylene glycol production.[99] Ni_2P has been found to be the only catalyst which could generate, methylglyoxal (C3), and 2,3-furandiol (C4) along with formic acid (C_1) via CO_2RR.[100] Among metal carbides, Mo_2C is capable of reducing CO_2 into CH_4 at low potentials (~ -0.55).[101] Asadi and co-workers reported 2D-W_2C as one of the promising catalysts for methane production with FE of 82.7% at -421.63 mA/cm^2.[102] A representative trend of catalyst-structure with high activity and selectivity have been discussed. In the meantime a significant efforts have been achieved to acquire a better understanding of the mechanisms, especially at the molecular level

and to gain idea about active site and betterment in electrochemical performance by systematic optimization of other process parameters which will be discussed in the successive sections.

1.4.8 Electronic-structure modulated catalyst surface

Polycrystalline metal surfaces of Cu, Ag and Au contain multiple structurally/electronically distinct sites with varying coordination numbers, which lead to the formation of different products. Epitaxially grown single crystalline surfaces of these metals on suitable substrates can offer better control on the type of single crystal facets one could probe for selective product formation.[41] For example, both low and high-index planes of Cu can be grown on Ag and Au electrodes. Electrodeposition is another way to synthesize such overlayer alloys (**Figure 1.3f**).[103] However, as shown in the study by Chorkendorff and co-workers,[104] such overlayer surfaces grown through underpotential deposition may allow reaction intermediates like CO (having strong binding affinities) to break the layer and expose the underlying metal surfaces leading to decreased product selectivity and increased H_2 production. The smoothness and rigidity of the films grown through layer deposition techniques may surpass such limitations of structural engineering. The underlying metal substrates like Au and Ag will modulate the electronic properties of the Cu single crystal facets for optimal intermediate or transition state adsorption. The sample scope can be broadened by inter-combining the substrate and thin-film composition between Cu, Ag, and Au. Controlling the thickness of the overlayer films will allow one to modulate the relative ratios of different single crystalline facets on the catalyst surface. For tandem catalysis, one may explore nanolithography to construct different arrays and compositions of Cu-Ag-Au electrodes to study their effect on product selectivity. Integration of these electrodes in the working setup of a floating electrode can substantially get rid of the mass transport limitations.[65] Metals other than Ag and Au, generally follow the theoretically predicted trend (optimum formate binding energy)[105] pretty well, where the post-transition metals, like Pb and Sn, prefer binding through oxygen leading to formate selectivity, while the transition metals primarily form CO by binding through carbon. The anomalies in the former case of Ag and Pd are explained on the basis of kinetic effects.[106]

Gaining the knowledge of catalyst design, it is foremost to know how these strategies can be linked with the formation of specific products with high selectivity through the generation of branching intermediates, which will be discussed in the next section.

1.5 Effect of Process Conditions on eCO_2RR

In addition to the catalyst design, the complexity of multiple and branched intermediate reaction routes is strongly dependent on the effects of local pH, cationic species, electrolytes

(buffer capacity), operating current densities, etc., which often results in poor product selectivity.[106]

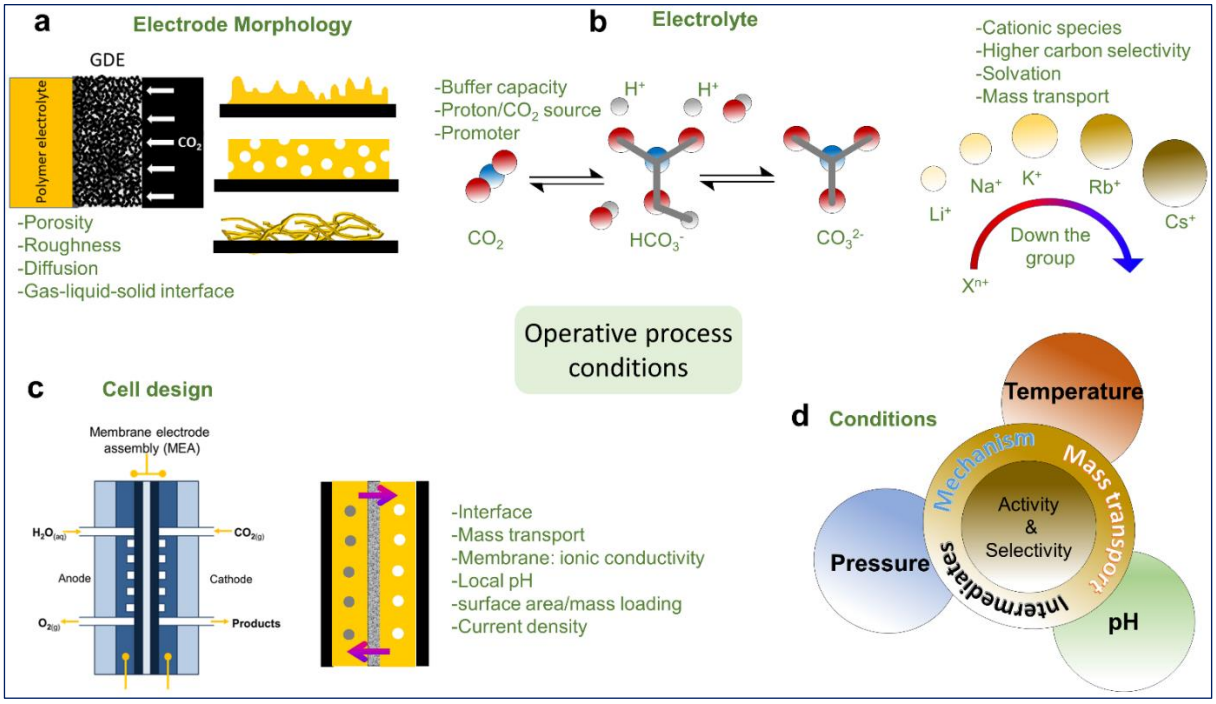

Figure 1.4. Effect of (a) electrode morphology, (b) electrolyte, (c) cell design, (d) other operating conditions on eCO_2RR performance.

This section discusses some of the most critical research findings pertaining to the effect of operational conditions like electrolyte nature, ionic species, pH, buffer strength of electrolytes, cell type, and mass transport conditions on the catalytic outcomes of eCO_2RR (**Figure 1.4**).[107, 108] Till now, the categorical effects of these process conditions on catalytic activity and selectivity are weakly understood. The establishment of standard protocols for applying operative conditions during electrocatalytic reduction is very important for the unification of mechanistic concepts in the field.[108]

1.5.1 Effect of Cell design on eCO_2RR product selectivity

In the case of eCO_2RR, the typical catalytic system consists of four components, including a cathode where CO_2 reduction takes place and an anode where oxygen evolution reaction (OER) occurs, an electrolyte allowing rapid mass transport of the reactants and products, and a polymer electrolyte membrane to separate cathodic and anodic counterparts. During the electrolytic reaction, ions are transported across the membrane from one side to the other side and electrons travel through the external circuit.

Designing appropriate cells for eCO_2RR is one of the most crucial parts of the entire process as it has an important role in controlling current density, FE, detection of products, and

stability of the catalyst. In the 1980s, Yoshio *et al*. first introduced the systemic work on CO_2 reduction.[109] Later on, different cell designs were applied to this field.

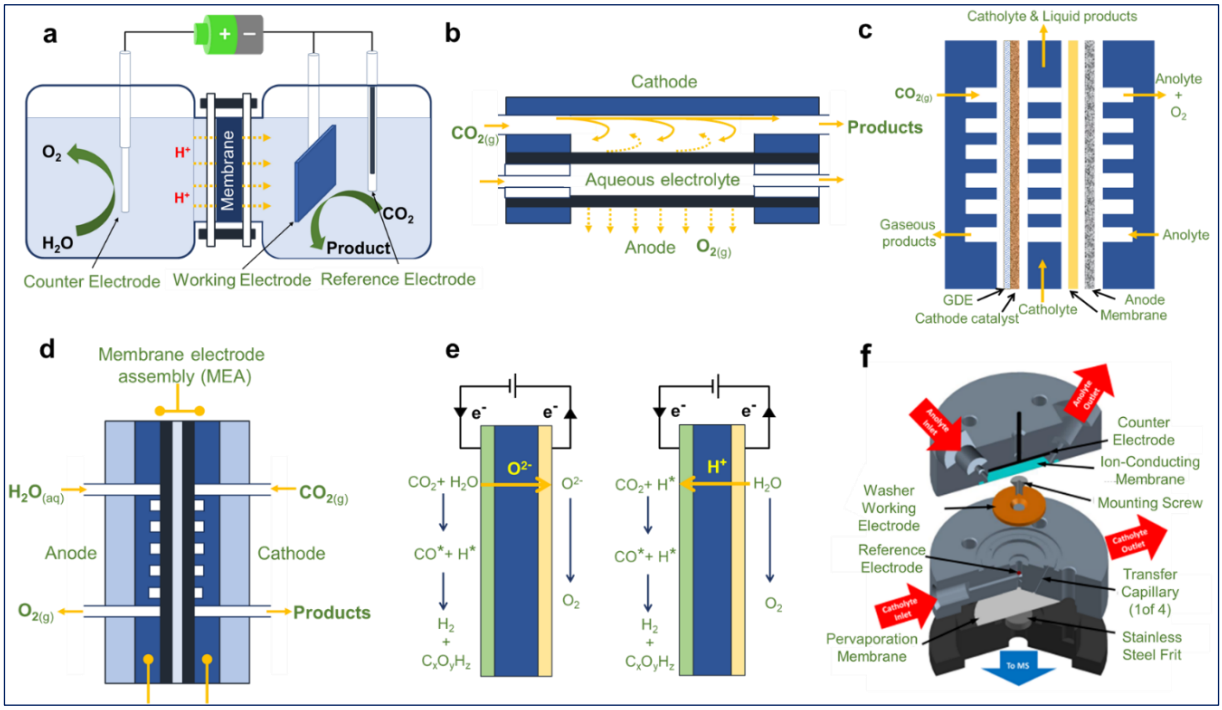

Figure 1.5. A schematic diagram of the (a) typical H-type electrochemical cell, (b) microfluidic flow cell, (c) flow cell for CO_2RR in GDE configuration. (c) Membrane electrode assembly (MEA) configuration in flow cell. (d) Schematic of solid oxide electrolysis cells (SOEC) based on the oxygen ionic conductors (left) and the protonic conductors (right). (e) modified differential electrochemical mass spectrometry (DEMS) cell for eCO_2RR. Reprinted from Clark *et al*.,[115] with permission from the American Chemical Society.

For now, reactor vessels can be mainly categorized into H-type cell (**Figure 1.5a**),[36, 110] liquid flow cell with GDE (**Figure 1.5b**),[111, 112] flow cell with membrane electrode assembly (MEA) (**Figure 1.5c-e**),[113, 114] and differential electrochemical mass spectrometry (DEMS) cell (**Figure 1.5f**).[115, 116]

1.5.2 H-type cell

To date, the commercially available H-type cell is still the most acclaimed lab-scale reactor for eCO_2RR, in which the working electrode and reference electrode are set in a cathodic compartment while the counter electrode is set in the anodic compartment, as illustrated in **Figure 1.5a**.[117] Subsequently, these two compartments are usually connected through a channel and separated by an ion-exchange membrane to prevent the product crossover. During electrolysis, CO_2 gas is continuously purged into the cathodic compartment via a glass frit and then analyzed through an on-line gas chromatograph (GC) to detect the gaseous products. For

liquid product detection, at a constant potential, the duration of the electrolysis process together with the volume of the cell should be carefully considered to reach the detection limits of HPLC or NMR, as most liquid-phase products have low FEs, especially for Cu-based catalysts.[118]

Therefore, smaller electrode compartment volumes and longer electrolysis times are recommended for the determination of liquid products with low FE values in H-type cells. Operating cells with high catalyst surface area to electrolyte volume ratios (S/V) can give rise to better sensitivity towards the detection of liquid products. A pressure cell similar to H-cell was also designed to study the effect of applied CO_2 pressure on product selectivity. The high-pressure CO_2 reactor, which was basically made using stainless steel autoclave, showed that CO_2 pressures helped to produce C_2H_4 formation in the case of oxide-derived copper catalyst**.**[119, 120] Although the H-type cell is suitable for quantifying and detecting various CO_2-reduced products with significant sensitivity, it is recommended to use more efficient cells to prevent mass-transport limitations at higher overpotential.

1.5.3 Flow cell with gas diffusion electrode configuration and membrane electrode assembly (MEA)

Flow cell can minimize the mass transfer limitations of an H-cell by continuously circulating the reactants and products to and away from the electrodes and can substantially enhance CO_2 concentrations at the electrocatalyst surface.[121] Initially, microfluidic flow cell (MFC) had been first employed for CO_2 reduction by Kenis and co-workers.[122] The basic setup includes a thin flowing electrolyte channel situated between cathode and anode (**Figure 1.5b**)**.** The reactant gas CO_2 is passed through the cathode which is in contact with GDE and O_2 is coming out from the anode side. The main difference between this MFC and the flow cell containing membrane (**Figure 1.5c**) is that the former set-up separates reduction and oxidation products by the diffusion of products instead of a membrane. The flowing stream can simultaneously adjust operating conditions such as electrolyte composition, pH, water supply process. Recently many works have been reported to produce different CO_2-reduced products using a similar type of cell, giving current density more than 100 mA/cm^2.[123, 124] Recently flow cell containing membrane has been extensively explored for CO_2 reduction, can quantify gaseous and liquid products quite sensitively.[7, 125] Using such kind of cell, a current density of more than 200 mA/cm^2 was also obtained with ethanol and ethylene as the main product having FE of 46% in the alkaline electrolyte and GDE.[126] The main advantage of flow cell over H-cell is that flow cell can be used in an alkaline medium whereas, in the case of H-cell, CO_2 dissolved in an alkaline electrolyte is rapidly consumed and form a neutral-pH carbonate mixture. There

has been lot of improvement happened based on flow cell reactor engineering to enhance the catalytic performance. Sargent and co-workers reported that in strongly alkaline conditions (10 M KOH), Cu catalyst supported on polymer-based gas diffusion could produce ethylene (FE of ~70%) with a current density of ~473 mA cm^{-2}, which is the highest reported selectivity towards C_2H_4 production.[125] The eCO_2RR performance of flow cell can be affected by various parameters, including feed CO_2 concentration, gas flow rate, GDE structure, and channel length. It has been reported that with increasing the channel length from 0.01 m to 0.35 m, CO partial current density decreased from 35 mA cm^{-2} to 10 mA cm^{-2} and CO FE decreased from 89% to 57%, while CO_2 conversion increased from 13% to 99%. We have seen that flow cell has been found a promising candidate for increasing the eCO_2RR activity towards higher carbon products. However, the pressure sensitivity coming from different parts of the membrane for this kind of cell is the main difficulty for its large-scale utilization. Recently Sinton and co-workers reported the use of permeable CO_2 regeneration layer to enable CO_2 regeneration at the catalyst surface, which can enhance the CO_2 conversion efficiency.[127]

Flow cell with membrane electrode assembly (MEA) is the most common type of flow cell for practical utilization (**Figure 1.5d**), consists of cathode and anode current collectors, cathode and anode flow plates, and MEA. MEA is prepared by hot-pressing, membrane and cathodic gas-diffusion electrode (GDE). Besides, the electrocatalysts in flow cells are usually coated on a carbon paper or carbon cloth gas diffusion layer (GDL), which can provide high surface area and good contact with CO_2 molecules, thus enhancing the upper limit of eCO_2RR rates and current densities.[128, 129] The reactant phase, electrode substrate, and type of membrane in the MEA flow cells have a profound effect on the efficiency and selectivity of eCO_2RR.[130]

Highly-porous gas diffusion layers (GDLs), where catalysts are coated, attached with the membrane, support the catalyst, and maximizes the CO_2-catalyst contact efficiency which in turn controls the current density, efficiency, and selectivity towards eCO_2RR. A series of recent studies demonstrated the effect of manipulating certain GDL variables on electrochemical performance in a CO_2 flow cell.[131] These experiments were performed in a flow cell reactor in which the prepared GDE materials served as the interface between a gaseous CO_2 inlet stream and electrolyte. The performance of GDL relies on (1) high electrical conductivity, (2) high porosity for proper gas diffusion, (3) high hydrophobicity to protect flooding of water into the gas chamber, (4) smoothness of the surface to accommodate the catalyst layer.[8] Bitar *et al.*[132] compared the catalytic performance of the GDE-In/C and an indium foil under identical operating conditions. The HCOOH partial current density on the GDE-In/C was found to be

seven times higher than that on the indium foil with a FE of 45% at -1.65 V vs. Ag/AgCl, demonstrating the excellent mass transfer efficiency of GDE.

Three classes of membranes have been used in flow cells viz. cation-exchange membrane (CEM), anion-exchange membranes (AEM)[133] and bipolar membrane (BPM).[134] The types of the membrane determine the transport of ions through it, which affects the pH of the electrolyte and affects the kinetics of the eCO_2RR. Wu *et al.* achieved a FE of 70% for HCOOH over Sn catalyst by using an electrolyte buffer layer, in the absence of which the system showed nearly 100% FE for hydrogen. This revealed that insertion of a buffer layer into MEA might be an efficient way to suppress HER.[135]

1.5.4 Differential electrochemical mass spectrometry (DEMS) cell

Differential electrochemical mass spectrometry (DEMS) is a very sensitive analytical technique that enables us to detect and to analyze CO_2 reduced products rapidly (~seconds), within the time limit of the electrolysis process (even while taking linear sweep voltammogram, LSV). Bell and co-workers first introduced this technique. In the DEMS cell, the ion-conducting membrane is sandwiched between the working electrode and the counter electrode to ensure uniform conductivity. The CO_2-reduced products are delivered into the collection chamber, which is then detected and quantified by mass spectrometry. Bell and co-workers represented transient selectivity of all the CO_2 reduced products and observed that copper electrocatalyst experiences no deactivation during 1 h of the electrolysis process at a fixed potential.[115] As the volatile component or intermediate product can also be detected in a very short time limit, DEMS cell is quite useful to provide the mechanism of eCO_2RR for the formation of multi carbon products. Moreover, the local pH, CO_2 concentration at the electrode-electrolyte interface, which has a crucial role in determining eCO_2RR activity, can be tracked with the help of DEMS cell. Jia *et al.* reported for the first time formation of formic acid, acetic acid, lactic acid, and methane at around the theoretical reduction potential using Pt-Ru black as eCO_2RR catalyst.[136] It had been observed that the amount of H_2 and CO produced on Ag catalyst matches properly with what is obtained by gas chromatographic analysis from a typical H-cell while other operational conditions remain the same.[116] In addition, they also found the reaction of CO_2 with OH^- evolved at the cathode surface and have explained that the influence of this slows down the chemical reaction, which can be minimized by conducting product analysis during a rapid potential sweep by DEMS analysis (**Figure 1.5f**). In the same study over Cu surface, they confirmed that electrolyte which has contact with electrode has a higher concentration of aldehyde (acetaldehyde and propionaldehyde) than the respective alcohols (ethanol and n-

propanol) and at more overpotentials, the concentration of ethanol near the cathode increases at the expense of propionaldehyde. These observations prove that acetaldehyde is a precursor of ethanol and propionaldehyde, and that the latter is a precursor of n-propanol. All these discoveries suggest that DEMS is a promising reactor to get an insight into the local reaction environment and the mechanism of eCO_2RR.

1.6 Mechanism of electrochemical CO_2RR

Efficient electrochemical CO_2 activation is impeded both thermodynamically and kinetically due to the chemical inertness and stability of the CO_2 molecule. The direct outer electron sphere single electron reduction of CO_2 to $CO_2^{\cdot-}$ radical anion occurs at high negative potential of -1.9V vs. NHE in absence of a catalyst and hence, is a significantly energy demanding process.[35] This is attributed to the high reorganizational energy required to bend the otherwise linear CO_2 molecule. Hence, a catalyst with low activation energy is highly desirable to propagate the reaction process at specific potentials bypassing the formation of $CO_2^{\cdot-}$ radical anion. Depending on the number of protons and electrons transferred electrochemical reduction of CO_2 leads to the formation of a wide variety of products like formic acid (HCOOH), acetic acid (CH_3COOH), ethanol (C_2H_5OH), isopropanol (C_3H_8OH), acetone (CH_3COCH_3) etc.[36]

$$CO_2 + 2H^+ + 2e^- \rightarrow HCOOH \qquad E^0 = -0.61\text{V} \qquad \text{Eqn. } \mathbf{1.5}$$

$$CO_2 + 2H_2O + 2e^- \rightarrow HCOOH + OH^- \qquad E^0 = -1.491V \qquad \text{Eqn. } \mathbf{1.6}$$

$$CO_2 + 2H^+ + 2e^- \rightarrow CO + H_2O \qquad E^0 = -0.53V \qquad \text{Eqn. } \mathbf{1.7}$$

$$CO_2 + 2H_2O + 2e^- \rightarrow CO + OH^- \qquad E^0 = -1.347V \qquad \text{Eqn. } \mathbf{1.8}$$

$$2CO_2 + 2H^+ + 2e^- \rightarrow H_2C_2O_4 \qquad E^0 = -0.913V \qquad \text{Eqn. } \mathbf{1.9}$$

$$CO_2 + 2e^- \rightarrow C_2O_4^{2-} \qquad E^0 = -1.003V \qquad \text{Eqn. } \mathbf{1.10}$$

$$CO_2 + 4H^+ + 4e^- \rightarrow HCHO + H_2O \qquad E^0 = -0.48V \qquad \text{Eqn. } \mathbf{1.11}$$

$$CO_2 + 3H_2O + 4e^- \rightarrow HCHO + OH^- \qquad E^0 = -1.311V \qquad \text{Eqn. } \mathbf{1.12}$$

$$CO_2 + 6H^+ + 6e^- \rightarrow CH_3OH \qquad E^0 = -0.38V \qquad \text{Eqn. } \mathbf{1.13}$$

$$CO_2 + 5H_2O + 6e^- \rightarrow CH_3OH + OH^- \qquad E^0 = -1.225V \qquad \text{Eqn. } \mathbf{1.14}$$

$$CO_2 + 8H^+ + 8e^- \rightarrow CH_4 + 2H_2O \qquad E^0 = -0.24V \qquad \text{Eqn. } \mathbf{1.15}$$

$$CO_2 + 6H_2O + 8e^- \rightarrow CH_4 + 8OH^- \qquad E^0 = -1.072V \qquad \text{Eqn. } \mathbf{1.16}$$

$$CO_2 + 12H^+ + 12e^- \rightarrow C_2H_4 + 4H_2O \qquad E^0 = -0.349V \qquad \text{Eqn. } \mathbf{1.17}$$

$$CO_2 + 8H_2O + 12e^- \rightarrow C_2H_4 + 12OH^- \qquad E^0 = -1.177V \qquad \text{Eqn. } \mathbf{1.18}$$

$$CO_2 + 12H^+ + 12e^- \rightarrow C_2H_5OH + 3H_2O \qquad E^0 = -0.329V \qquad \text{Eqn. } \mathbf{1.19}$$

$$CO_2 + 9H_2O + 12e^- \rightarrow C_2H_5OH + 12OH^- \qquad E^0 = -1.157V \qquad \text{Eqn. } \mathbf{1.20}$$

$$CO_2 + 14H^+ + 14e^- \rightarrow C_2H_6 + 4H_2O \qquad E^0 = -0.27V \qquad \text{Eqn. } \mathbf{1.21}$$

$$CO_2 + 18H^+ + 18e^- \rightarrow C_3H_7OH + H_2O \qquad E^0 = -0.31V \qquad \text{Eqn. } \mathbf{1.22}$$

$$2H^+ + 2e^- \rightarrow H_2 \qquad E^0 = -0.42V \qquad \text{Eqn. } \mathbf{1.23}$$

CO_2 to CO conversion takes place via the formation of the *COOH intermediate which is generated by the transfer of concerted proton/electron from the electrolyte to the adsorbed CO_2 on the catalyst surface.[37] The adsorbed *COOH intermediate undergoes further reduction by proton/electron and desorbs from the surface of the catalyst as CO and H_2O. However, *CO is the intermediate for the formation of CH_3OH and CH_4.[38] After undergoing a series of hydrogenation reactions the *CO intermediate forms $^*OCH_3$ intermediates. In the next proton-electron coupling reaction, proton combines with the carbon atom rather than the oxygen atom resulting in a competition between methane and methanol formation. There are two pathways for the formation of formate or formic acid: via direct carbon bonded *COOH intermediates from stabilized CO_2^- radical anions or through proton-electron coupled transfer process via the *OCHO intermediate.[38] C2 and C_2^+ product formation however involves a variety of intermediates that includes *CO, $^*CH_2$ and $^*CH_3$ along with the C-C coupling reaction which is the most crucial step.[39] The formation of C_2 products like acetaldehyde, ethylene and ethanol requires high overpotential and have low FE as compared to C_1 products due to the large kinetic barrier of the C-C bond in comparison to that of the C-H and C-O bonds. The overall mechanism of eCO_2RR along for the selective product formation can be categorized in the following way by considering the branching mechanism.

1.6.1 Branching mechanism of eCO_2RR to multiple products

It is rather apparent that we are still far away from desired catalytic rates or product selectivity in eCO_2RR suitable for practical applications. Better catalytic design and process condition development (electrolyte, pH, potential range) can only be achieved through a deeper and holistic understanding of complete reaction pathways to specific products. eCO_2RR involves a number of intermediates, proper tuning of which can yield us a selective product. Mechanistic branching from a particular intermediate can generate a number of products. Thus, a critical understanding of this 'branching-intermediate' is necessary to develop a catalyst that can prefer a specific pathway over the other.

1.6.2 Carbon monoxide Formic acid/ Formate

Both CO and HCOOH are industrially relevant raw products that can be further processed downstream for the synthesis of basic organic chemical products and intermediates.[137] Formate/formic acid is also regarded as a valuable hydrogen carrier for fuel cells.[138, 139] It has been identified that a class of metals like Au,[110] Ag,[133] Pd,[140], and Zn[141] produces CO with high

current efficiency and selectivity while elemental Pb, Hg, In, Cd, Sn, and Tl forms formate/formic acid as one of the major electrochemical CO_2 reduced products.[142] This depends mainly on the C or O binding ability of a catalyst surface.[143, 144] The first step in the CO_2 reduction process is the reductive adsorption of CO_2 on the catalyst surface. Adsorbed $CO_2^{\cdot-}$ intermediate can then undergo protonation at the C or the O site. Thus, $CO_2^{\cdot-}$ is the branching-intermediate for the formation of CO or formate/formic acid (**Figure 1.6**).

a) **Protonation at the O-site** leads to the formation of a *COOH intermediate, where * indicates the surface-adsorbed species. The adsorbed *COOH intermediate undergoes further reduction to *CO via a CPET process. If the adsorption strength of *CO on the catalyst surface is weaker, it can leave the catalyst surface, thus forming CO as the major product. Thus, the selectivity is completely determined by the interaction of CO with the catalyst surface. Henceforth, an ideal electrocatalyst should have appropriate adsorption strength for the key intermediates, which would facilitate both the CO_2 activation (*COOH formation) and the *CO desorption steps.[145] *COOH is determined to be the key intermediate for CO production on metal surfaces.[146]

b) **Protonation at the C-site** favors the selective transformation of CO_2 to $HCOO^-$. Thus, *OCHO is the key intermediate for the CO_2RR to $HCOO^-$ transformation, and the optimal adsorption energy of *OCHO on metal surface supports its high selectivity for $HCOO^-$. The catalyst surface should have the active site for the adsorption of oxygen-bound intermediates. Metals like Au, Ag, Pt, and Cu lie on the weak-binding side, indicating that *OCHO may not interact strongly enough with the surface for high selectivity towards $HCOO^-$.[147] Sn has near-optimal adsorption energy, as reflected by its appearance on the top of the volcano plot.[148] This volcano suggests that *OCHO is a key intermediate for $HCOO^-$ production on transition metals as well as Sn and provides an explanation for Sn's high selectivity toward $HCOO^-$.

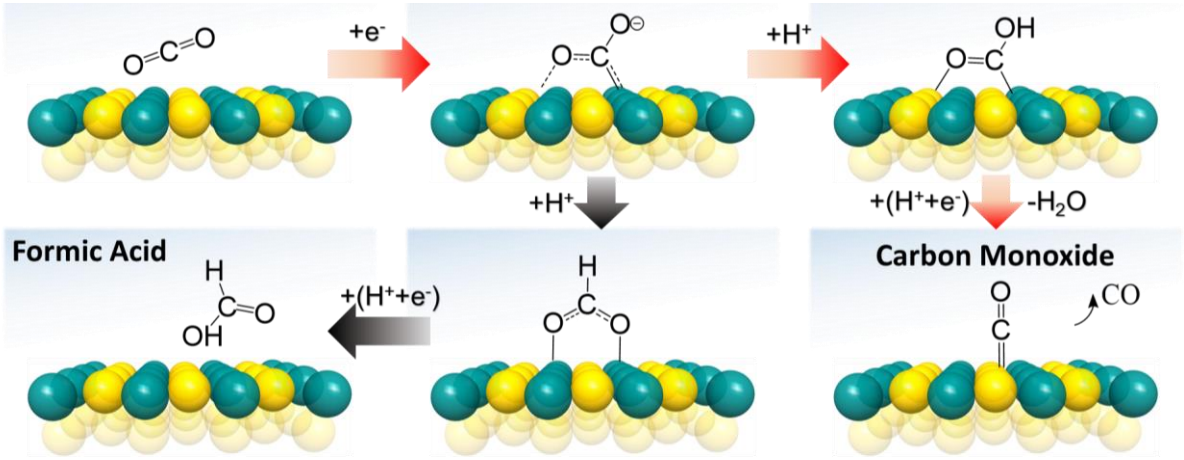

Figure 1.6. Formation mechanism of CO and HCOOH from CO_2 via different intermediate.

1.6.3 Methanol vs. Methane

Methanol is a renewable fuel that has an energy density of 15.6 MJ L^{-1} compared to 34.2 MJ L^{-1} of gasoline. On the other hand, methane is one of the major constituents of natural gas, has a potential impact on electricity generation by burning it as a fuel in a gas turbine or steam generator. Compared to other hydrocarbon fuels, both these chemicals produce less CO_2 for each unit of heat released.[149, 150] Strong binding of *CO on the catalyst surface ensures its further reduction to either methanol or methane.[30] Methane and methanol both share a common pathway till the formation of *COH intermediate. Thus, *COH is the branching-intermediate**,** and protonation at the C-site favors the formation of CH_3OH. Protonation at the O-site followed by the release of water leads to the formation of methane as the selective product (**Figure 1.7**). The Cu-based alloy catalysts are, except $PdCu_3$ and $PtCu_3$, mostly more energetically favorable to yield methane than methanol products.[151] This involves desorption of OH forming *CH_2, which undergoes two hydrogenation steps in order to form CH_4 as the product.[152] Yang and co-workers synthesized and analyzed Cu_xAu_{1-x} (x = 0.25, 0.5, and 0.75) alloys and observed that the fraction x directed the product selectivity in CO_2 reduction. Increasing x shifted the preference from CO to CH_4 generation. This was attributed to the fact that the presence of Cu adjacent to Au stabilizes the oxygen end of the bonded *COOH intermediate.[11] Wang *et al*. reported that Cu−Bi exhibited high CH_4 selectivity (FE of 70.6% at −1.2 V) and proposed that incorporation of Bi into Cu lattice stabilizes the *COH intermediate, which is responsible for the enhanced CH_4 formation.[153]

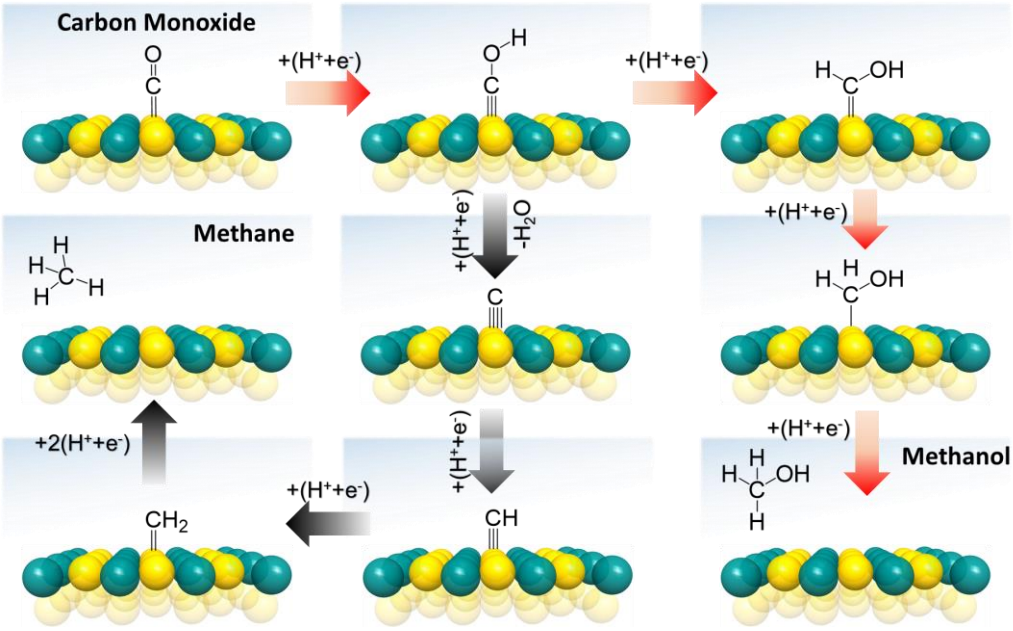

Figure 1.7. Formation mechanism of methane and methanol from CO_2 via *COH branching intermediate.

1.6.4 Ethylene vs. Acetate

The production of ethylene (C_2H_4) is an important index for measuring the level of development of the petrochemical industry. Higher CO_2 reduced product such as ethylene (which can be produced from ethane as well) is industrially relevant due to their use in polyethylene production. Besides, it can be used directly as a fuel for welding or a mixed component in natural gas. The reaction mechanisms describing the selectivity towards acetate vs. other C2 products remains controversial. Recently, Heenen et al. reported that acetate formation has strong pH dependence and proceeds through the formation of ketene (*CHCO) instead of $*CH_2$.[154] The mechanistic pathway has been observed to share the same branching intermediate (*CHCO) as ethylene, which is generated from the proton-coupled electron transfer steps of *CO. The mechanistic pathway is as shown in **Figure 1.8**. Ketene formation is followed by desorption from the surface and reaction with OH- to form acetate. Since proton donation is required for acetate formation, so H_2O mainly acts as the proton donor.

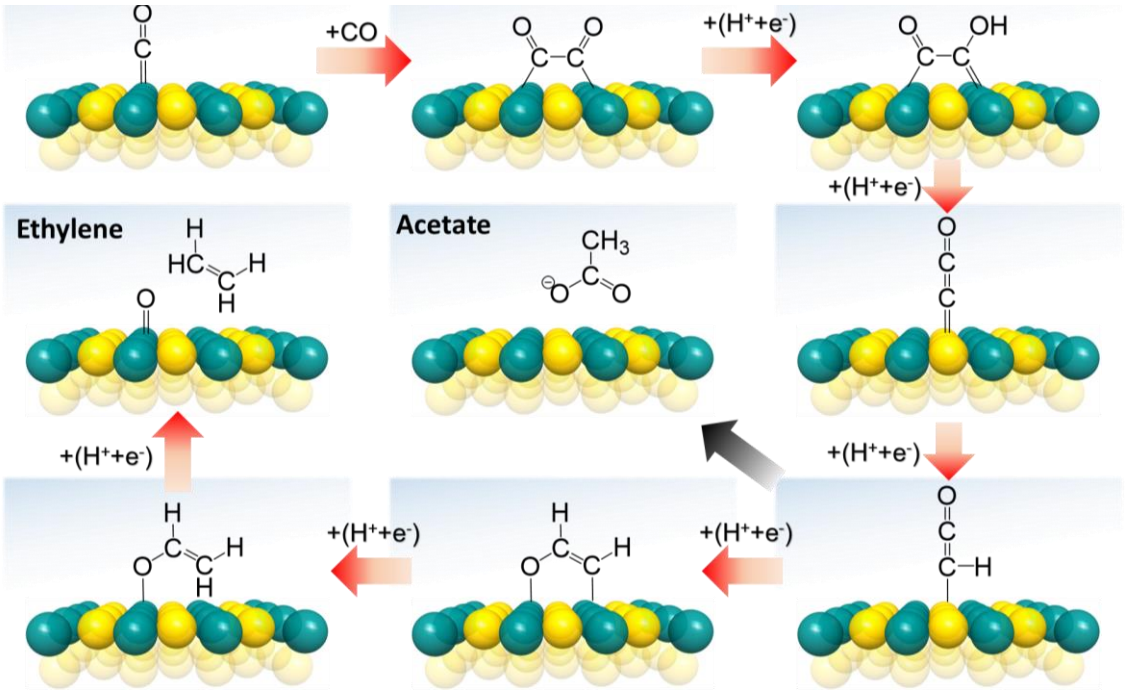

Figure 1.8. Formation mechanism of ethylene and acetate from CO_2 via *CHCO branching intermediate.

1.6.5 Ethylene vs. Ethanol

Ethanol is another energy-dense fuel used as an additive to automotive gasoline and ingredient for the synthesis of several industrially relevant organic compounds. Ethylene and ethanol share a common intermediate $*CH_2CHO$. Thus, $*CH_2CHO$ is the branching-intermediate. Ethanol is formed when further protonation takes place at carbon, and ethylene is formed upon the removal of the oxygen atom (**Figure 1.9**).

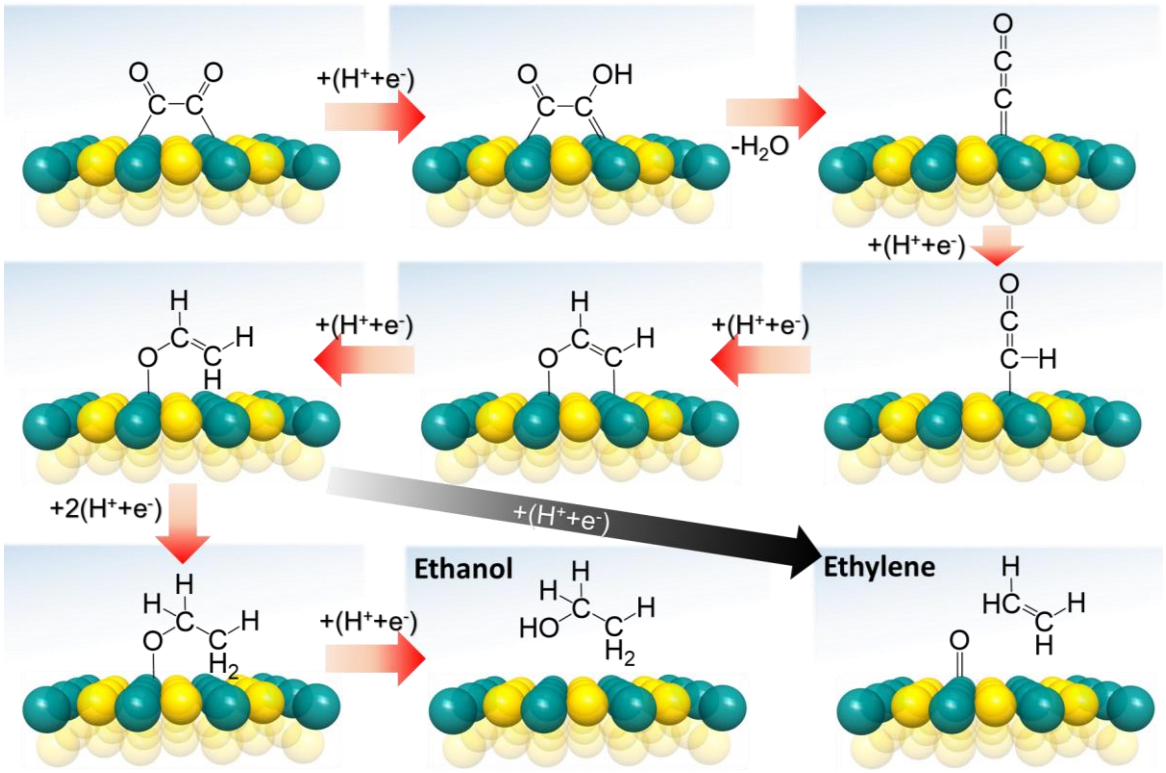

Figure 1.9. Formation mechanism of ethylene and ethanol from CO_2 via C_2H_3O branching intermediate.

1.6.6 Acetone vs. *n*-Propanol

Acetone is the smallest polar ketone because of which it has huge industrial importance, especially in the pharmaceutical industry. n-propanol is also an important solvent, and isomers of propanol like isopropanol are extensively used for sanitizers which has a potential impact in protecting against virus attacks, including the current threat of coronavirus. These C3 compounds are being produced with good FEs on Cu–ZnO electrodes requiring 18 and 16e-s, respectively. **Figure 1.10** demonstrates the probable mechanism for reducing CO_2 to n-propanol and acetone through electrochemical reduction. The steps are identical to the mechanism predicted for ethanol until C–C bond formation. At this stage, HCO_{ads} (formed by the addition of $3e^-$, $3H^+$ to CO_2) react with C_2 species to form an adsorbed C_3 intermediate. Several pathways from here on may lead to the formation of n-propanol/2-propanol and acetone. An increase of CO partial pressure favors n-propanol formation at the expense of C_2 (main ethylene) generation. The low C_3 selectivity on Cu catalysts is associated with the low rate of C–C bond formation, including C_1–C_1 and C_1–C_2 coupling. Prior studies confirm the enhancement in the production of C_{2+} products upon the creation of nanocavity confinement structure.[155] $FE_{n\text{-}PrOH}$ can also be enhanced by coating with a conducting substrate like PANI that facilitates the availability of CO and favors C-C coupling.[156]

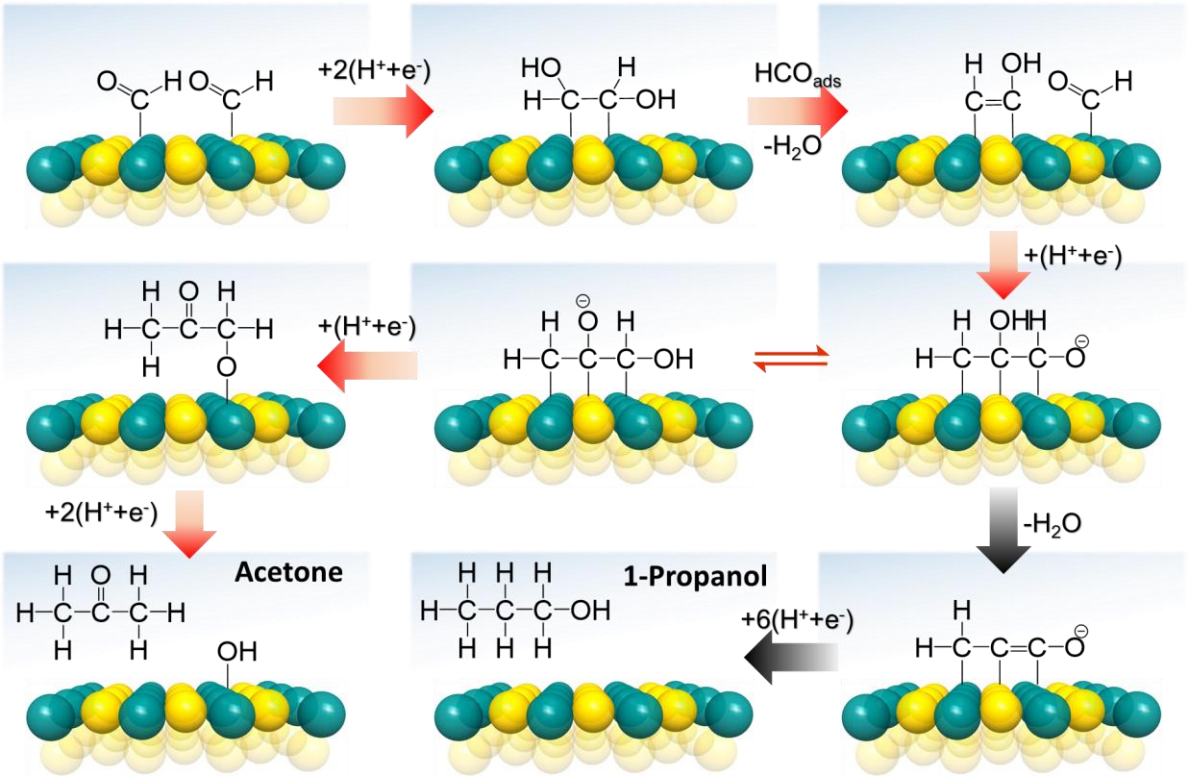

Figure 1.10. Formation mechanism of acetone and n-propanol from CO_2 via ($C_3H_4O_2^-$) branching intermediate.

As we have seen how important it is to know about detailed mechanistic aspect through the formation of branching intermediates for each one those CO_2 reduced products and formation of one product over another. Apart from designing suitable catalyst materials, adequate optimization of the other parameters and process conditions related to CO_2 also control the proper adsorption of intermediates and thereby affect the overall CO_2RR performance.

1.7 Fundamental terms in electrocatalysis

1.7.1 Onset potential

It is defined as the least negative (for cathodic reaction) or positive potential (for anodic reaction) in which a reaction product or Faradaic current is detected. However, in electrochemical CO_2 reduction the onset potential towards formation of a particular product is often poorly defined.

1.7.2 Overpotential

It is defined as the potential difference between the thermodynamically determined reduction/oxidation potential (E_{eq}) for a particular half-cell reaction and the experimentally observed potential (E) for the same redox event. It is related to cell's voltage efficiency. The overpotential (η) of an electrode reaction is defined as:

$$\eta = E - E_{eq} \qquad \text{Eqn. } \mathbf{1.24}$$

1.7.3 Electrochemically active surface area (ECSA)

It is defined as the active area of the electrode material that is accessible to the electrolyte for charge transfer. The ECSA will facilitate quantification of the reacting interface area and hence, provide more accurate performance comparison of catalysts. For Pt-based catalysts ECSA can be calculated from the charge associated with one monolayer of under-deposited hydrogen desorption in cyclic voltammetry (CV) while for other catalysts it is calculated by running CVs at high scan rate.

1.7.4 Faradaic efficiency (FE)

It is the ratio of the experimentally detected product to the theoretically predicted product amount that can be calculated from the current density based on 100% Faradaic yield. The details regarding FE calculation will be discussed in subsequent chapters.

1.8 Parameters to screen various electrocatalysts

1.8.1 Activity

The activity of an electrocatalyst is defined as its ability to speed up the electrochemical reaction. According to Sabatier principle an optimal level of intermediate adsorption and desorption is needed to enhance the performance of the catalyst. TF is one of the crucial parameters that defines the activity of a catalyst.

1.8.2 Stability

The durability of a catalyst is one of the most pivotal factors, which defines the potential a catalyst. The catalyst exhibits stable current and produces similar product selectivity, can be considered as the stable one. Usually, for industrial relevant current density (more than 100mA/cm^2) is desired to show higher stability for almost 100h. Comparison of several techniques like cyclic voltammetry (CV), linear sweep voltammetry (LSV), electrochemical impedance spectroscopy (EIS), double-layer capacitance before and after the durability is utilized for long-term assessment of the catalyst along FE of the major product.

1.8.3 Selectivity

Electrocatalysis is solely dependent on the materials used as catalysts and also on the applied potential for certain chemical reactions. In electrochemical CO_2 reduction reaction (eCO_2RR) different products are formed based on the applied potential and the elements used as electrocatalysts. A potentially good electrocatalyst is one which has high selectivity towards one particular product over a wide pH range for a long time of electrolysis with higher current density.

1.9 Experimental and characterization tools for evaluating and characterizing an electrocatalyst

1.9.1 Cyclic voltammetry (CV)

CV is the most commonly used electrochemical technique that measures the current developed in an electrochemical cell when voltage is applied under specific conditions. The characteristic electrochemical response of a catalyst is determined from the oxidation and reduction potentials that can be qualitatively obtained from CV. During the CV experiment the potential is linearly ramped and after attaining the final potential, the potential is reverted back to the initial potential.

1.9.2 Linear sweep voltammetry (LSV)

Using this technique working electrode potential is scanned in a particular range at a constant scan rate with fixed directionality which is dependent on the reaction that is being performed.

1.9.3 Chronoamperometry (CA)

CA is another electrochemical technique that can help in determining the reaction kinetics and mechanism. At the beginning of the experiment the potential is maintained at a fixed potential (E_i) which is then stepped up to a new potential (E_1) at t = 0 and the corresponding current response as a function of time is recorded.

1.9.4 Bulk electrolysis with coulometry

In this technique under the application of a constant potential the integrated charge is recorded as a function of time. However, a preelectrolysis step can be applied to reduce interference and background current.

1.9.5 EIS spectroscopy (AC impedance)

In this technique, the base potential is held constant at a constant potential. A sine waveform is superimposed onto the base potential, and its frequency is scanned from high to low with 12 components per decade. Current and potential are sampled and analyzed to obtain the real and imaginary parts of the impedance. During the experiment, you can switch between a Bode plot and a Nyquist plot by right-clicking. After the experiment, impedance data can be presented in various forms.

1.9.6 Powder X-ray diffraction (PXRD)

The most commonly used characterization technique for crystal structure determination is PXRD. This technique not only provides an insight to the crystal structure but information related to crystallite size, residual strain and preferential orientation can also be obtained. The

Miller planes are formed due to the periodic arrangement of atoms in a crystalline solid. Since in a crystal structure the interatomic and interplanar distance between atoms and layers are in the order of 0.1 nm X-rays have the characteristic wavelength of 0.01-10 nm and hence is appropriate to interact with the atoms in solid materials. Interference between X-rays diffracted by layers with different depths is an integral multiple of the X-ray wavelength (λ) the signal received by the detector is termed as constructive interference. However, non-integral multiple of wavelength λ results in destructive interference with no signal. This forms the basis of Bragg's law which is defined as follows:

$$n\lambda = 2d \sin \theta \qquad \text{Eqn.}\mathbf{1.25}$$

where, n is the integral multiple of wavelength, λ is the wavelength of incident radiation, d is the interplanar distance and θ is the angle of diffraction. With respect to the sample surface at specific θ a miller plane is diffracted in a crystal structure.

1.9.7 X-ray photoelectron spectroscopy (XPS)

XPS is an analytical technique that uses X-ray under ultra-high vacuum to examine the presence of a particular element both qualitatively and quantitatively. Using photoelectric effect the binding energy (B. E.) of the electrons corresponding to a particular element in a sample can be evaluated. With the sample being exposed to X-rays that have a defined energy ($h\nu$) electrons are knocked out from the sample and their kinetic energy (E_{kin}). Hence, binding energy (B. E.) can be calculated as follows:

$$B.E. = h\nu - E_{kin} - \varphi \qquad \text{Eqn.}\mathbf{1.26}$$

where, φ is the work function of the sample surface. The binding energy values can help in the qualitative determination of the elemental composition and chemical environment.

1.9.8 X-ray absorption spectroscopy (XAS)

In this technique high intensity X-rays typically generated by a synchrotron light source excites the core-level electrons (K, L or M shell) of a particular element from the ground state to an excited electronic state. This process of excitation leaves an empty core, which within a short span of 10^{-15} secs is filled by an electron from the higher energy shell. Fluorescence is known to occur when this electron returns to a lower energy state from the higher one. The energy released is equal to the energy difference between the two orbitals and hence, the absorption energy is specific for each element. The incident X-ray is partly absorbed by the sample while the remaining is transmitted by the sample and the probability of X-ray absorption is defined by the X-ray absorption coefficient. This absorption coefficient being element specific increases with binding energy of the core-level electrons and hence is directly proportional to

the atomic number of the elements. In a XAS measurement incident X-ray beam passes through an ionization chamber which measures the initial intensity (I_0). The fluorescence detector kept at angle of 45° from the sample detects the photoelectrons that are produced upon interaction of the incident radiation with the sample surface. The remaining radiation enters into a second ionization chamber where the transmitted radiation (I_t) is measured. A reference foil is placed after the second ionization chamber and intensity of the transmitted X-rays through the reference material is determined in a third ionization chamber (I_r). The X-ray absorption coefficient can be determined on the basis of measured intensity of incident and transmitted radiation. When the incident radiation has an energy equal to that of the energy required to excite a core-level electron a sharp increase of μ is expected which is defined as the absorption edge in a typical XAS spectrum. This absorption edge is element specific.

A typical XAS spectra comprises of two regions: X-ray near edge structure (XANES) and Extended X-ray absorption fine structure (EXAFS). XANES gives information about the oxidation state of the absorbing atoms. EXAFS gives important information about the local structure of the element i.e. bonding environment and coordination number. XANES region ranges from -50 to +100 eV of the absorption edge whereas EXAFS region begins after 50 eV from the absorption edge. A Fourier transform of the data expressed in k-space (momentum space) leads to expression of data in R-space where, R is the radial distance of the neighboring atom from the absorbing atom.

1.9.9 Electron Microscopy

Scanning electronic microscopy (SEM) and transmission electron microscopy (TEM) play an inevitable role in the characterization of catalysts. EM uses electron beams generated from the cathode (a tungsten filament or lanthanum hexaboride). When the beams are focused on the sample, the primary beam interacts with the atoms of the material causing scattering with various emissions, including secondary electrons (SE), backscattered electrons (BSE), and characteristic X-rays.[157] All these three radiations are usually significant for SEM analysis. These signals are associated with various types of information from the microscopy. The volume of electron beams interacting with the material depends on the energy of the incident beam, the type of material, and the atomic number of the elements.[158] The secondary electrons are very important in SEM while TEM uses the transmitted electrons. The number of secondary electrons emitted depends on other factors, like the acceleration and the characteristic voltage of the material (e.g., topography of the sample). These signals are responsible for information about the surface of the sample like morphology and topography. The basic distinction between SEM

and TEM is closely related to the intensity of the beam and how it is controlled and optimized by optical electronic column. The inelastic scattered electrons, secondary electrons are excluded from analysis through the lens objective. In addition, the speed with which the electrons pass through the electron optic column in TEM is typically much larger compared to SEM. Here the SEM is employed to understand the morphology of solid materials and characterize them in nanoscale. SEM technique commonly offers the image on the nanometre (nm) to micrometre (μm) scale and were specially employed in non-crystalline catalysts to observe distribution and sizes of mesopores. Aberration corrected FEI Titan G2 60−300 kV microscope has been used to investigate the nature of single-atom catalyst. High-Angle Annular Dark Field Scanning Transmission Electron Microscopy (HAADF STEM) imaging and X-ray Energy Dispersive Spectroscopy (XEDS) have been performed at an accelerating voltage of 300 kV with a probe convergence angle of 24.5 mrad using 70μm aperture. Similarly, TEM is also employed to understand the active metal nanoparticle distribution over the mesoporous solids. For TEM, a grid laden with sample was prepared before measurements. A small amount of each powder sample was dispersed into 500 μL ethanol and sonicated for 30 minutes. 5 to 10 μL from the dispersion was dropped on a carbon- coated grid and dried at for 8 hours before imaging. TEM images and selected area electron diffraction (SAED) patterns were collected using a JEOL JEM-2010 TEM instrument.

1.10 Electrochemical CO_2 reduction reactor

1.10.1 General electrochemical setup for H-cell study

All the electrochemical measurements were performed using a CHI 6008E electrochemical workstation. Electrochemical CO_2RR was carried out in a three-electrode system, which involves a working electrode (glassy carbon or carbon cloth), a counter electrode (graphitic carbon rod), and a reference electrode (Ag/AgCl). The cell compartments (**Figure 1.11**) are separated by a proton exchange membrane (Nafion 117), and the electrolyte used is 0.5 M $KHCO_3$ solution. The electrolyte solutions were purged with CO_2 gas for 1 hour prior to the measurement. The electrocatalyst was prepared by dispersing 2 mg of catalyst and 0.2 mg of Vulcan (activated carbon) in 200 μL of mixed solvent solution (IPA: H_2O = 1:1 v/v) and 10 μL of 1 wt% Nafion binder. From the prepared catalyst, 100 μL was coated on the carbon cloth and dried. The electrochemical cell was designed to have a large electrode area (0.7 cm x 0.7 cm) and a small electrolyte volume (10 mL) in each of the two compartments, along with a gas headspace of approximately 10 mL above the electrolyte on each side of the membrane.

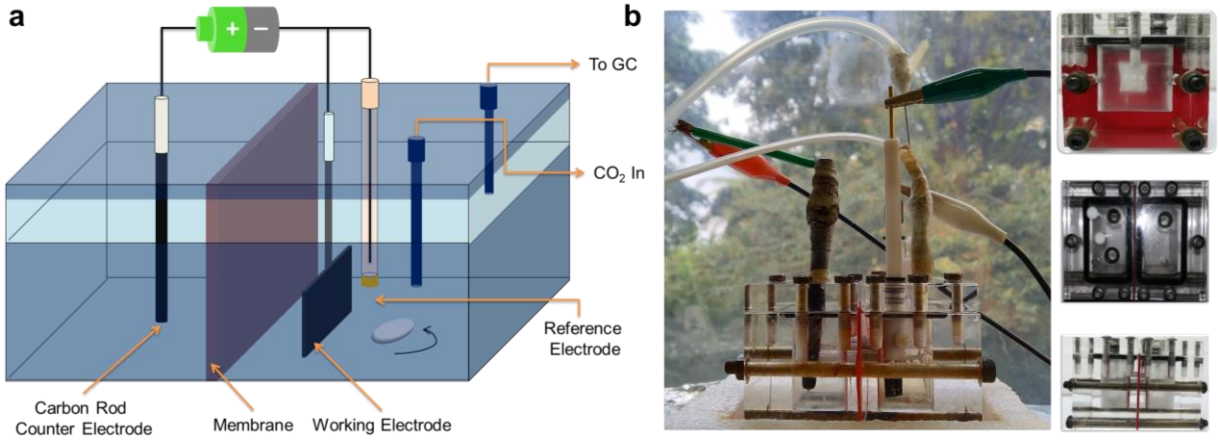

Figure 1.11. (a) Schematic illustration of the electrochemical reactor used for eCO_2RR. (b) Optical image of the reactor used in eCO_2RR.

The flow of CO_2 was regulated by a mass flow controller at 20 standard cubic centimeters per minute (sccm), flowed through the working electrode compartment of the cell during electrolysis. CO_2 flow through the cell was necessary in order to see large current efficiencies for CO_2 reduction products. The flow rate of 20 sccm was chosen to ensure sufficient CO_2 transport to the surface while preventing interference from gas bubbles striking the surface. The chronoamperometric study has been performed at different applied potential for 2h to evaluate the CO_2RR performance.

1.10.2 Flow cell reactorfor eCO_2RR in gas diffusion electrode configuration (GDE)

To increase the CO_2 diffusion and overall current density, the eCO_2RR experiments were carried out in a filter-press type Micro Flow Cell (Electrocell A/S), where a Ti sheet coated with Ir-MMO (iridium-mixed metal oxide) has been used as an Anode plate (Electrocell S/A). An anionic exchange membrane (Fumasep FAB-PK-130) was employed in the case of CO_2RR in 1M KOH medium. As shown in **Figure 1.12**, the cell has three compartments, (CO_2 gas, cathodic and anodic compartment), which is schematically shown in **Figure 1.13**. The electrolyte was recirculated continuously into the cell (both in cathode and anode) by two separate peristaltic pumps (Ravel, RH-P100L-100) to accumulate liquid products.

The flow of CO_2 was regulated by a mass flow controller (Brooks) at different flowrate (standard cubic centimeters per minute (sccm)) to optimize the most suitable flow rate, flowed through the working electrode compartment of the cell during electrolysis. For the final study, the gas flow is fixed to 50 sccm, and electrolyte flow was set to 20 sccm.

1.10.3 Preparation of Gas diffusion Electrode (GDE)

The PTFE-based gas diffusion electrode was fabricated by drop-casting the catalyst onto a cut piece of expanded polytetrafluoroethylene (ePTFE) (purchased from Sterlitech). The PTFE

used here is aspire laminated and having proper hydrophobicity. It also has a polyester backer, and the pore size is 200 nm. The ePTFE was pretreated by first performing an RCA cleaning process reported earlier.[18] It was first treated with a mixture of H_2O:HCl:H_2O_2 (5:1:1) at 80 °C for 2 minutes, then a mixture of H_2O:NH_4OH:H_2O_2 (5:1:1) for 2 minutes.

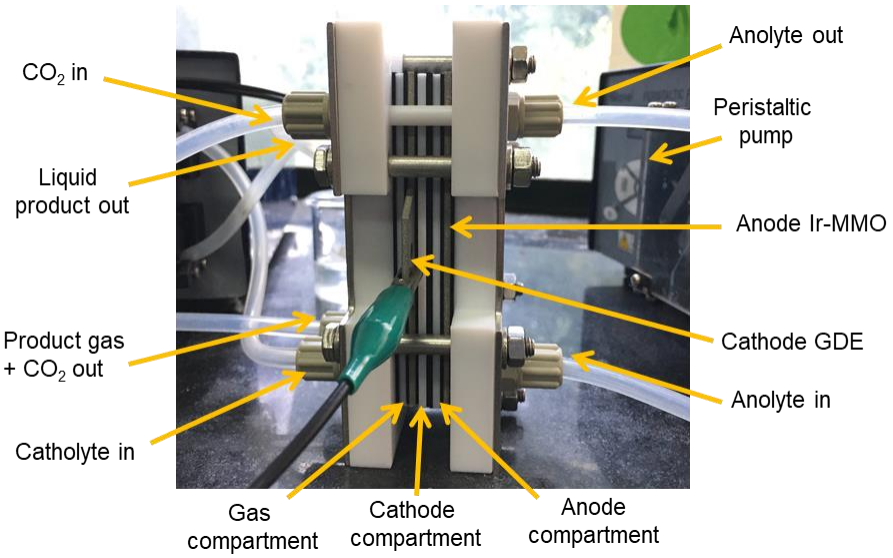

Figure 1.12. Optical photograph of the micro-flow cell used for performing full-cell eCO_2RR activity in flow-cell configuration with gas diffusion electrode.

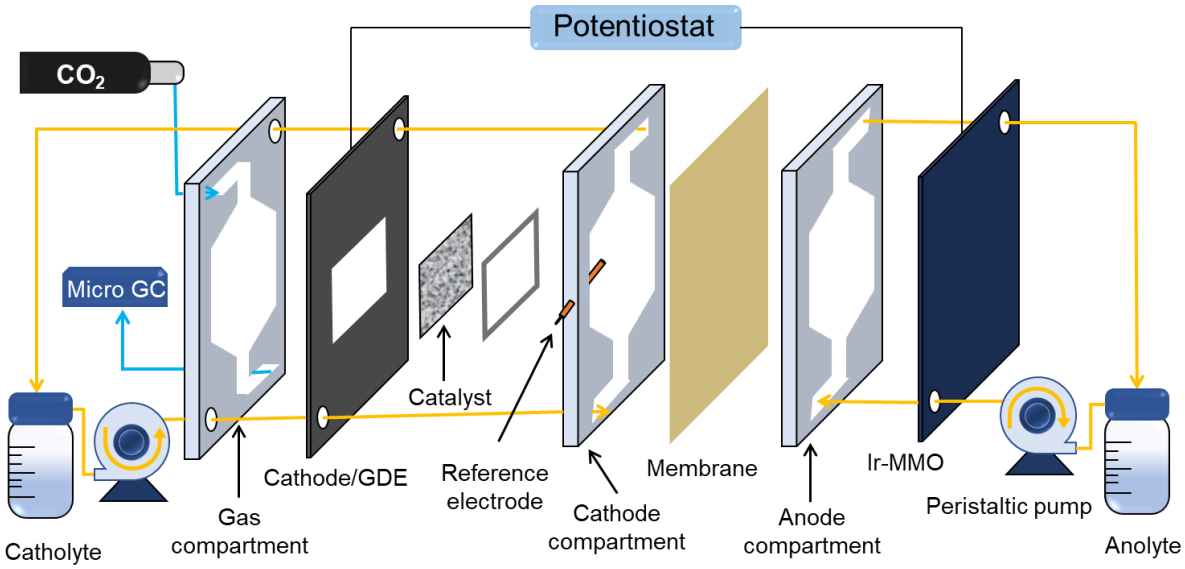

Figure 1.13. Schematic illustration of flow-cell used in the electrochemical CO_2 reduction.

This flow has been optimized to prevent both the liquid and gas cross-over during the electrolysis through the GDE and maintain proper interface of gas-electrolyte and ion. For the product quantification and Faradaic efficiency calculation, chronoamperometric study for fixed hours has been performed at each individual potential and for stability study, long-term chronoamperometric was performed.

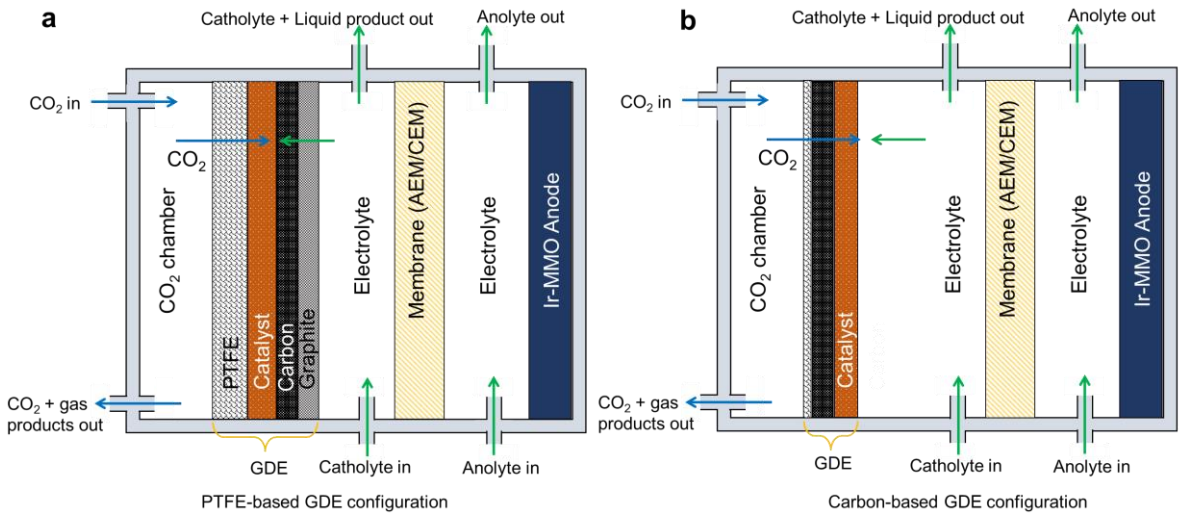

Figure 1.14. Scheme of the different compartments of Flow cell along with the components of Gas diffusion electrode for the optimized CO_2RR study in case of (a) PTFE-based and (b) C-based GDE configuration.

After rinsing and drying, the catalyst was coated on that, and vulcan was coated successively at different coating amounts. Graphite powder was coated on top of that to enhance further conductivity of the GDE. For the carbon-based GDE, a gas diffusion layer (GDL) (Freudenberg H23C2) that contains a micropourous carbon black layer and a fiber based PTFE bounded back bone is used as catalyst support. The catalyst material was prepared by dispersing 1 mg of catalyst powder in 200 mL of 2-propanol and water (v/v 1:1) mixture and coated on 1 cm^2 GDL. Additionally, 10 mL of 1 wt% nafion ionomer was added to the catalyst ink as binder. The gas diffusion electrode (GDE) was then dried for over night. The schematic illustration of the gas-GDE-catalysts-electrolyte interface for both PTFE-based and C-based GDE have been pictorially depicted in **Figure 1.14a** and **1.14b,** respectively. We have used both the PTFE-based and C-based GDE and found that the current density is found to be higher in C-based GDE. But the electrochemical stability for long-term electrolysis, PTFE-based GDE is better.

1.11 CO_2 reduced product analysis

1.11.1 Gas chromatography (GC)

Chromatography is one of the powerful analytical techniques used to separate and analyze quantitatively and qualitatively the chemical compounds in a gas or liquid sample, or in a feed stream if equipped with an on-line sampling device. In the experimental setup we used for continuous flow electrochemical reactor both in H-type cell and flow cell, the gas stream from sampler of reactor is continuously analyzed by the gas chromatograph (GC). This type of analysis is commonly known as online analysis. All the gaseous products were analyzed by online 490-Micro Gas Chromatography (GC), which has four channels for detecting different

gaseous products. Each channel has a specific column for analyzing relevant gases *viz*. Molsieve 5Å (for channel 1 and 2), Pora PLOT U (in channel 3) and CP-Sil 5 CB (for channel 4). The carrier gases were Ar and H_2. Each GC channel is equipped with a thermal conductivity detector (TCD). This detector responds to the difference in thermal conductivity between a reference cell (carrier gas only) and a measurement cell (carrier gas containing sample components).

Calculation of Faradaic Efficiency (FE) for gaseous products,

$$FE_{gas} = \frac{ppm \times flow\ rate \times \frac{number\ of\ electron \times Faraday\ contant \times pressure}{R \times Temperature}}{I_{average}} \times 100$$

Where ppm is the concentrations detected by GC, R is a gas constant (8.31 j $K^{-1}mol^{-1}$). The software ChemStation 7890A used to analyze the chromatograph were provided by Agilent. The gas and liquid calibration of GCs were done by standard calibration gas mixture.

1.11.2 High-Performance Liquid Chromatography (HPLC)

The liquid products were analyzed by HPLC (Agilent 1220 Infinity II LC system). The HPLC compartment contains autosampler, quaternary pump, column, refractive index detector (RID), and variable wavelength detector (VWD). Hi-Plex H column has been used to detect the organic liquid products like acids and alcohols. The flow rate through the Hi-Plex H column is kept at 0.5 ml/min while analyzing samples. Five mM H_2SO_4 is used as the mobile phase during analysis. The column temperature was kept at 50 °C. VWD uses a light signal to detect chromophores in the analytes. It can be used the products include ketones/carboxylic acids/aldehydes. Acquisition frequency is given as 10 Hz with a peak width of 0.05 min. It is good enough to record sufficient data points. RID is the primary detector in this HPLC configuration. It is a highly sensitive detector which works based on the difference in refractive index of the sample and analyte.

1.11.3 Nuclear magnetic resonance spectroscopy (NMR)

The liquid products were analyzed by ^1H NMR (600 MHz, JEOL). The following protocol was applied. Five hundred mL of the electrolyte and 30 µL of an internal standard solution were transferred into a centrifuge tube. The internal standard solution consisted of 50 mM phenol (99.5 %) and 10 mM dimethyl sulfoxide (99.9 %) made in D_2O solvent. The mixture is transferred into an NMR tube. Solvent suppression was used to decrease the intensity of the water peak. The FEs of liquid products were calculated from the NMR and HPLC peak area.

$$FE_{liquid} = \frac{Concentration\ of\ Liquid \times V \times number\ of\ electron \times Faraday\ contant}{Charge} \times 100\%$$

Where *Concentration of Liquid* (mol.L^{-1}) is obtained from the previously calibrated NMR and HPLC, *V* (L) is the volume of the electrolyte, *Faraday constant* = 96484 A.s.mol^{-1}, *Charge* (A.s) has been calculated from the CA curve at the corresponding potential.

1.12 Spectroscopic and analytical techniques for in situ mechanistic studies

1.12.1 In situ Electrochemical Attenuated Total Reflection Fourier Transform Infrared Spectroscopy (ATR-FTIR).

In situ electrochemical FTIR spectroscopic studies were performed using a purged VERTEX FT-IR spectrometer equipped with the A530/P accessory and a mid-band MCT detector. A silicon hemispherical window (F530-8) was used with the working electrode placed gently on top of the window as the single reflection attenuated total reflection (ATR) accessory for the FTIR study. The in situ experimental setups is depicted in **Figure 1.15**. The measurement parameters were 4 cm^{-1} resolution and 100 scans. This setup enabled the detection of eCO_2RR intermediate formation and change of adsorption of various intermediates on the electrode surface and within the thin-layer electrolyte. In the beginning of the IR-experiment, we have taken a spectrum of the overall electrochemical cell and then take a background spectrum so that the contribution of the electrolyte can be subtracted in the next spectrum while applying the potential during performing CO_2RR. The spectra were analyzed by the OPUS software and the absorption spectra have been directly plotted at various potential and time.

1.12.2 In situ X-ray absorption Spectroscopic studies

In situ XAS study has been performed in PETRA-III beamline, DESY, Germany. The XAS spectra have been taken while performing the CO_2RR reaction in 0.5M $KHCO_3$ in CO_2 purged solution. Both potential and time dependent XAS study were carried out. During in situ study, the chronoamperometric technique has been applied at different potential (e.g., -0.1V, -0.3V, -0.5V, -0.7V, -0.9, -1.1V) with respect to RHE and XAS data has been collected. The schematic representation of the in situ XAS set-up and its real-time photograph have been depicted in **Figure 1.16a** and **1.16b** respectively. The spectra have been detected in the fluorescence mode as seen in the **Figure 1.16a-b**.

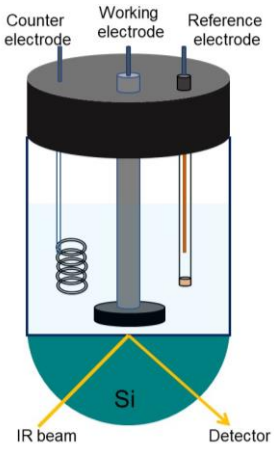

Figure 1.15. Schematic illustration of in situ ATR FT-IR configurations for eCO_2RR.

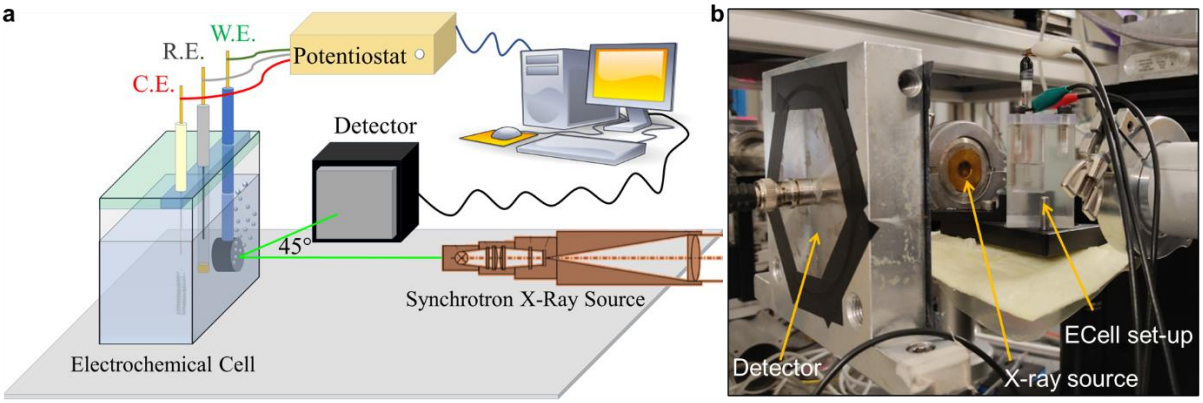

Figure 1.16. (a) Schematic illustration of in situ XAS study. (b) Photograph of different component of in situ XAS experiment in the CO_2RR condition.

1.12.3 In situ Raman Spectroscopic studies

In situ electrochemical Raman spectroscopic studies were performed using inVia Raman microscope using both 532 nm and 785 nm lasers with 50x magnification. Since better results were observed with 785 nm laser corresponding to electrochemically adsorbed CO_2RR intermediates, we continued all our in-situ Raman experiments using this laser. We have home-customized a cell where 2 ml CO_2-purged $KHCO_3$ was taken so that a thin film of electrolyte covers on the carbon paper having the catalyst coated on it. Pt coil and Ag/AgCl were used as counter and reference electrodes, respectively. CA was conducted for 15-20 mins and Raman data was taken at 2 mins each with data acquisition time of 10 secs and using 0.1 % of the power of the laser. Background data was taken with the complete cell setup with electrolyte and without giving the electrode potential. **Figure 1.17** show the cell setup during in-situ Raman measurements.

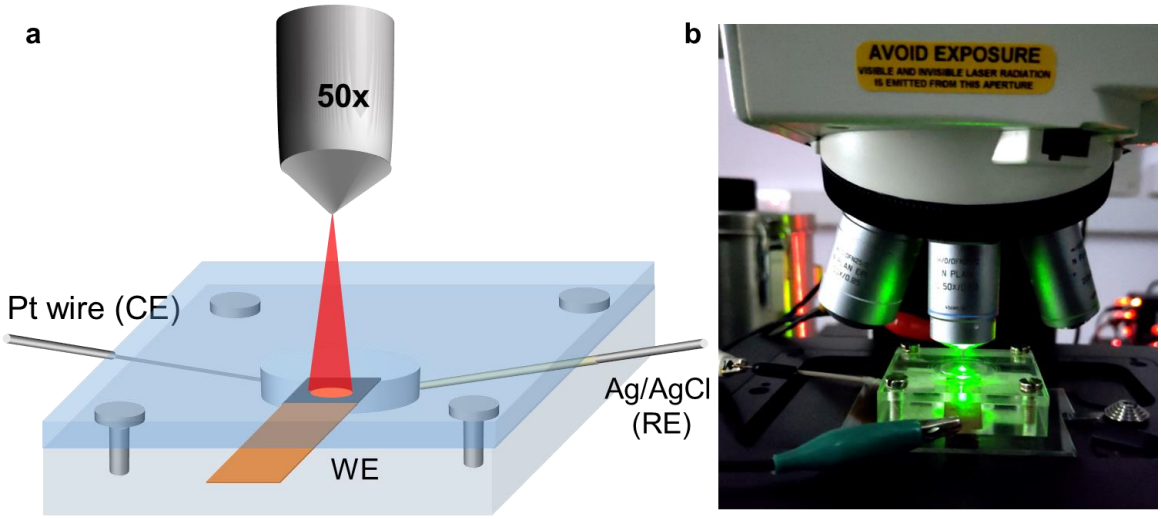

Figure 1.17. (a) Schematic illustration of in situ Raman spectroscopic study. (b) Photograph of the in-situ Raman spectroscopy set up.

1.12.4 Differential electrochemical mass spectrometry (DEMS)

This analytical technique combines electrochemical hall-cell setup with mass spectrometer and helps in the instantaneous detection of volatile or gaseous reactants, intermediates, or products. We have used HIDEN Analytical HPR-40 DEMS system with Type A and Type B cell for electrochemical reactions. **Figure 1.18a** and **1.18b** show the images of type A and type B cells, respectively. Type A cell is a single compartments cell whereas type B cell is more advanced two compartment cell with electrolyte flow in both chambers are controlled by a dual-syringe pump.

Ag/AgCl and Pt wire are used as reference and counter electrodes, respectively. Quadrupole mass spectrometer from RGA series is used with mass range up to 200 amu. Before starting eCO_2RR, the pressure inside the mass spectrometer should be in 10^{-6} mbar range. CO_2-purged $KHCO_3$ were taken in dual-syringe pump and continuously with 1 ml/min flow rate and CA was conducted at different potentials and mass spectrometry data was continuously been taken with QGA software and we obtained a plot of mass ion current for each constituent with respect to time. Different m/z value corresponding to different intermediate or product species gave their individual mass ion currents at different times.

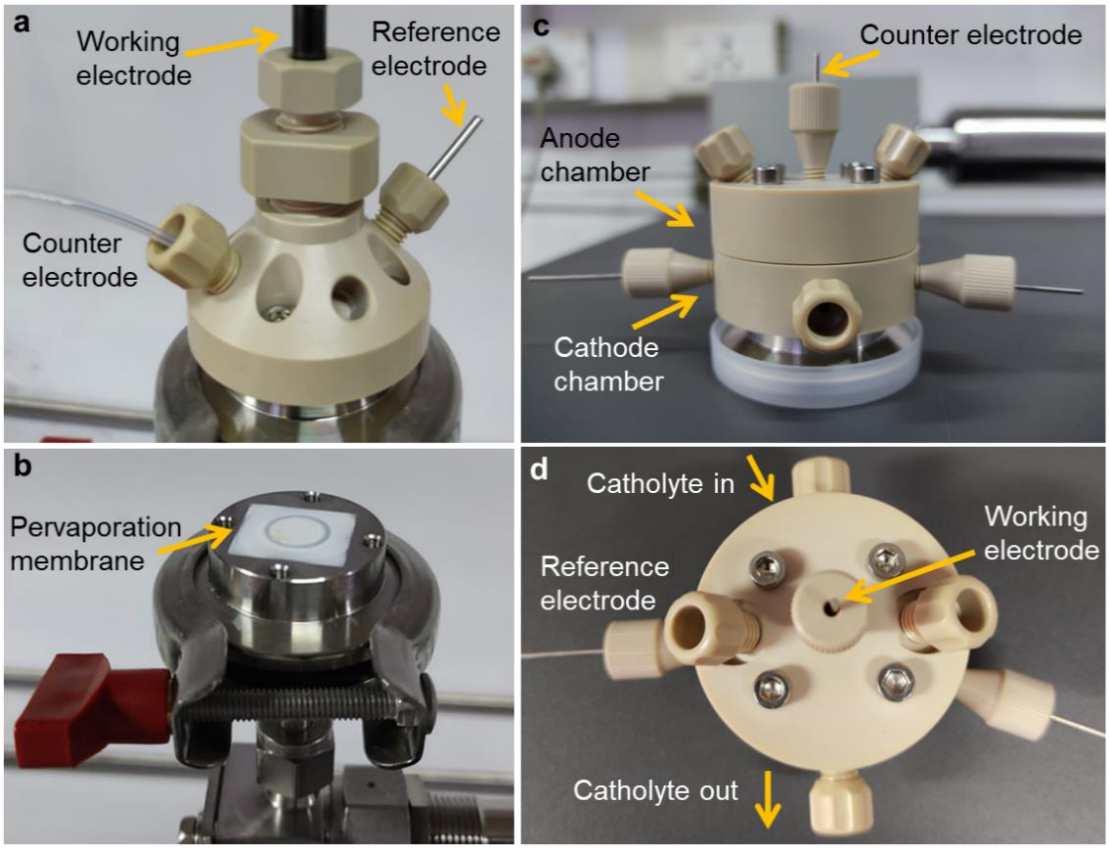

Figure 1.18. Photograph of the (a) DEMS Type-A cell (one compartment), (b) Pervaporation membrane (c-d) DEMS Type-B cell (two compartment).

1.13 Density Functional Theory (DFT)

DFT has been used to calculate the formation energies and adsorption energy of different c-bound and o-bound intermediate generated during the course of eCO_2RR. The rate determining step along with its activation energy also have been determined for the formation of different C_1, C_2 and C_3 products derived from CO_2. The calculations have been performed on systems containing a large number of atoms which required the optimization of the electronic/geometric structures prior to any property calculations.

Electronic optimization: It is a single-point energy calculation in which atoms are kept in a fixed position and its corresponding energy at that configuration is obtained.

Geometry optimization: This calculation facilitates in perceiving the most stable configuration since the system goes through several configurations driven by minimum energy and investigating the most stable ground state configuration.

Adsorption energy: The first step in any catalytic reaction involves the adsorption of reactant molecule on the catalyst surface. The binding energies for the systems under consideration can be obtained as follows:

$$E_b = E_{(ads/slab)} - E_{(slab)} - E_{(ads)} \quad \text{Eqn.}\mathbf{1.27}$$

where, $E_{(ads/slab)}$ is the energy of the final optimized adsorption configuration on the slab, $E_{(ads)}$ is the energy of the adsorbed molecule and E(slab) is the energy of the catalyst surface.

Descriptors: A descriptor can be defined as an experimentally determined or theoretically calculated catalytic property that can be directly correlated to the reaction thermodynamics or kinetics.

d-band centre is one such descriptor commonly used in catalysis which predicts the chemical reactivity of a metal catalyst in terms of a d-band model. Interaction of the adsorbate molecule with the metal results in bonding and anti-bonding states. The valence state of the adsorbate couples with the metal s states, which then turns to the metal d-states for coupling. The adsorbate interaction with the metal d states separates the metal d-band into bonding and anti-bonding states. Electronic modulation of the catalyst surface will cause either an upward or downward shift of the *d*-band with respect to the Fermi level. Filled bonding states and unfilled anti-bonding states will strengthen adsorbate binding to the catalyst surface hence, metals with higher *d*-band centre relative to the Fermi level will have unfilled antibonding orbitals and have a higher tendency of adsorption in comparison to the metals with lower *d*-band centre.

Adsorption free energy: Gibbs's free energy can indicate the reaction pathways. For example, in HER, hydrogen binding energy (ΔG_{H^*}) is a pivotal factor in determining the activity and kinetics of an electrocatalyst. $\Delta G_{H^*} > 0$ indicates weak hydrogen binding strength and hence, the activation of reactant/intermediate on the catalyst surface is difficult. Hydrogen binding strength is strong when $\Delta G_{H^*} < 0$ and may lead to poisoning since H_2 desorption is not facile and the intermediates will be occupied at the active sites. A maximum value is achievable when $\Delta G_{H^*} = 0$. Not only for HER adsorption energy like oxygen adsorption energy for OER and ORR, CO adsorption energy for eCO_2RR can be used as an activity descriptor for electrocatalysts. Adsorption energy (ΔG) can be calculated as follows:

$$\Delta G = \Delta E + \Delta ZPE - T\Delta S + \Delta G_U + \Delta G(pH) + \Delta G_{field} \quad \text{Eqn.}\mathbf{1.28}$$

where, ΔE is the ground-state energy, ΔZPE is the zero point correction, $T\Delta S$ is the entropy term, ΔG_U is related to the electrode potential, $\Delta G(pH)$ is related to the pH value of the electrolyte and ΔG_{field} is associated with the electrical double layer effect.

Free-energy diagram: The adsorption free energy can only provide information regarding the thermodynamics of the reaction intermediates without considering the kinetics. Free-energy diagram can impart the extra reaction-rate limiting steps that cannot be considered in adsorption free energy calculations. It takes into account the kinetic barrier between each step

in addition to the thermodynamics associated with the adsorption energy of each intermediate. Since overall reaction rate is dependent on the kinetic barrier between two intermediates, combination of both thermodynamics and kinetics is essential in determining the activity of electrocatalyst. The foundation of the free-energy diagram lies in the adsorption energy (ΔG) calculation. From these calculations the most probable mechanistic pathway for the formation of one particular product can be predicted. Moreover, the comparison of C-C coupling on different metal surface have been also evaluated.

Work function (φ) refers to the minimum work required to extract an electron from the Fermi level of a metal to the outside. The shift of Fermi level with respect to the equilibrium φ is dependent on the energy of the electrons in the Fermi level. Increase in φ of a metal can be related to higher exchange currents due to enhancement in activation of free energy. It has major implications in the electron and proton transfer rates. When the work function increases the adsorption energy becomes more endergonic.

The above-mentioned experimental techniques have been employed in summarizing our work in **Chapter 2-3.** While combination of both experimental and theoretical techniques have been utilized in comprehending our work in **Chapter 4-6**. In this thesis we have tried to provide a perception of the structure-property relations combining both experimental and theoretical techniques.

The overall goal of the work consists the unification of the most important mechanistic understanding of the electrochemical CO_2 reduction from a perspective of catalyst engineering, identification of appropriate electrocatalytic conditions, and its effect on the reaction mechanism. Firstly, we try to understand the most viable product scope of this process along with elucidating the detailed mechanistic pathways for all those products from the combined theoretical-experimental approaches. Furthermore, important experimental findings like cell design, potentials, pH, and choice of membranes were critically studied as these can guide product selectivity by controlling reaction pathways. Moreover, advantages of flow-cell and use of different types of GDE have been also discussed. Instrumentation for conducting eCO_2RR experiments and ways to accurately analyze products at fast and real timescales are defined. This discussion has been followed by one of the central and most important aspects of the work which tries to categorically understand unified catalyst structure-activity-selectivity relationships. By designing a plethora of catalysts design, we have tried to develop trends of activity-selectivity relationships to the nature of catalyst design, composition, and electronic structures. We started our journey by the production of CO in the second chapter which is the

simplest CO_2 reduced molecule on PdIn@In_2O_3 surface. Then, we could be able to produce more reduced product like methanol on structurally ordered $CuGa_2$ surface and provided the role of surface Ga_2O_3 on eCO_2RR. In the fourth chapter, atomically dispersed Cu has been stabilized on highly stable and conducting WC lattice, which could produce C2 product like acetic acid with high selectivity. In the next chapter, we have targeted more reduced product and investigated how the product selectivity can be switched from C1 (like CO, HCOOH, CH_4) to C2 (C_2H_5OH, C_2H_4, CH_3COOH etc.) by careful tuning of catalyst surface consisting of Pd-Cu systems. We could be able to even develop much more efficient catalyst in the next chapter i.e. $PdCu_3$ ordered intermetallic catalyst and showed how the crystallographic facets along with morphology plays an important role in the production of more reduced product like n-propanol in eCO_2RR. Throughout these works, we tried to find out some insights into the most reliable and powerful ex situ and in situ spectroscopic techniques like XRD, TEM, XPS, XAFS, IR, Raman etc, for the development of a standard CO_2 electroreduction instrumentation protocol for effective mechanistic studies as well as active site determination. The work can be immensely helpful for designing new cathode materials for CO_2 electroreduction to specific products is extremely critical for mechanistic studies, which is still an evolving field in itself.

1.14 References

1. Nguyen, T. N.; Guo, J.; Sachindran, A.; Li, F.; Seifitokaldani, A.; Dinh, C.-T., Electrochemical CO_2 Reduction to Ethanol: from Mechanistic Understanding to Catalyst Design. *J. Mater. Chem. A* **2021,** *9*, 12474-12494.

2. Karapinar, D.; Creissen, C. E.; Rivera de la Cruz, J. G.; Schreiber, M. W.; Fontecave, M., Electrochemical CO_2 Reduction to Ethanol with Copper-Based Catalysts. *ACS Energy Lett.* **2021,** *6*, 694-706.

3. Chen, C.; Khosrowabadi Kotyk, J. F.; Sheehan, S. W., Progress toward Commercial Application of Electrochemical Carbon Dioxide Reduction. *Chem* **2018,** *4*, 2571-2586.

4. Sun, Z.; Ma, T.; Tao, H.; Fan, Q.; Han, B., Fundamentals and Challenges of Electrochemical CO_2 Reduction Using Two-Dimensional Materials. *Chem* **2017,** *3*, 560-587.

5. He, J.; Dettelbach, K. E.; Salvatore, D. A.; Li, T.; Berlinguette, C. P., High-Throughput Synthesis of Mixed-Metal Electrocatalysts for CO_2 Reduction. *Angew. Chem. Int. Ed.* **2017,** *56*, 6068-6072.

6. Jin, S.; Wu, M.; Gordon, R. G.; Aziz, M. J.; Kwabi, D. G., pH Swing Cycle for CO_2 Capture Electrochemically Driven through Proton-Coupled Electron Transfer. *Energy Environ. Sci.* **2020,** *13*, 3706-3722.

7. Corral, D.; Feaster, J. T.; Sobhani, S.; DeOtte, J. R.; Lee, D. U.; Wong, A. A.; Hamilton, J.; Beck, V. A.; Sarkar, A.; Hahn, C.; Jaramillo, T. F.; Baker, S. E.; Duoss, E. B., Advanced Manufacturing for Electrosynthesis of Fuels and Chemicals from CO_2. *Energy Environ. Sci.* **2021**.

8. Rabiee, H.; Ge, L.; Zhang, X.; Hu, S.; Li, M.; Yuan, Z., Gas Diffusion Electrodes (GDEs) for Electrochemical Reduction of Carbon Dioxide, Carbon Monoxide, and Dinitrogen to Value-Added Products: a Review. *Energy Environ. Sci.* **2021,** *14*, 1959-2008.

9. Curtiss, L. A.; Raghavachari, K.; Redfern, P. C.; Pople, J. A., Assessment of Gaussian-2 and Density Functional Theories for the Computation of Enthalpies of Formation. *J. Chem. Phys.* **1997,** *106*, 1063-1079.

10. Nitopi, S.; Bertheussen, E.; Scott, S. B.; Liu, X.; Engstfeld, A. K.; Horch, S.; Seger, B.; Stephens, I. E. L.; Chan, K.; Hahn, C.; Nørskov, J. K.; Jaramillo, T. F.; Chorkendorff, I., Progress and Perspectives of Electrochemical CO_2 Reduction on Copper in Aqueous Electrolyte. *Chem. Rev.* **2019,** *119*, 7610-7672.

11. Kim, D.; Resasco, J.; Yu, Y.; Asiri, A. M.; Yang, P., Synergistic Geometric and Electronic Effects for Electrochemical Reduction of Carbon Dioxide Using Gold–Copper Bimetallic Nanoparticles. *Nat. Commun.* **2014,** *5*, 4948.

12. Zheng, Y.; Vasileff, A.; Zhou, X.; Jiao, Y.; Jaroniec, M.; Qiao, S.-Z., Understanding the Roadmap for Electrochemical Reduction of CO_2 to Multi-Carbon Oxygenates and Hydrocarbons on Copper-Based Catalysts. *J. Am. Chem. Soc.* **2019,** *141*, 7646-7659.

13. Lee, S.; Kim, D.; Lee, J., Electrocatalytic Production of C_3-C_4 Compounds by Conversion of CO_2 on a Chloride-Induced Bi-Phasic Cu_2O-Cu Catalyst. *Angew. Chem. Int. Ed.* **2015,** *127*, 14914-14918.

14. Wuttig, A.; Yoon, Y.; Ryu, J.; Surendranath, Y., Bicarbonate Is Not a General Acid in Au-Catalyzed CO_2 Electroreduction. *J. Am. Chem. Soc.* **2017,** *139*, 17109-17113.

15. Larrazábal, G. O.; Martín, A. J.; Pérez-Ramírez, J., Building Blocks for High Performance in Electrocatalytic CO_2 Reduction: Materials, Optimization Strategies, and Device Engineering. *J. Phys. Chem. Lett.* **2017,** *8*, 3933-3944.

16. Hong, X.; Chan, K.; Tsai, C.; Nørskov, J. K., How Doped MoS_2 Breaks Transition-Metal Scaling Relations for CO_2 Electrochemical Reduction. *ACS Catal.* **2016,** *6*, 4428-4437.

17. Jouny, M.; Luc, W.; Jiao, F., General Techno-Economic Analysis of CO_2 Electrolysis Systems. *Ind. Eng. Chem. Res.* **2018,** *57*, 2165-2177.

18. Corral, D.; Feaster, J. T.; Sobhani, S.; DeOtte, J. R.; Lee, D. U.; Wong, A. A.; Hamilton, J.; Beck, V. A.; Sarkar, A.; Hahn, C.; Jaramillo, T. F.; Baker, S. E.; Duoss, E. B., Advanced Manufacturing for Electrosynthesis of Fuels and Chemicals from CO_2. *Energy Environ. Sci.* **2021,** *14*, 3064-3074.

19. Li, X.; Wang, S.; Li, L.; Sun, Y.; Xie, Y., Progress and Perspective for In Situ Studies of CO_2 Reduction. *J. Am. Chem. Soc.* **2020,** *142*, 9567-9581.

20. Chen, Y.; Li, C. W.; Kanan, M. W., Aqueous CO_2 Reduction at Very Low Overpotential on Oxide-Derived Au Nanoparticles. *J. Am. Chem. Soc.* **2012,** *134*, 19969-19972.

21. Mistry, H.; Reske, R.; Zeng, Z.; Zhao, Z.-J.; Greeley, J.; Strasser, P.; Cuenya, B. R., Exceptional Size-Dependent Activity Enhancement in the Electroreduction of CO_2 over Au Nanoparticles. *J. Am. Chem. Soc.* **2014,** *136*, 16473-16476.

22. Liu, S.; Tao, H.; Zeng, L.; Liu, Q.; Xu, Z.; Liu, Q.; Luo, J.-L., Shape-Dependent Electrocatalytic Reduction of CO_2 to CO on Triangular Silver Nanoplates. *J. Am. Chem. Soc.* **2017,** *139*, 2160-2163.

23. Kim, H.; Park, H. S.; Hwang, Y. J.; Min, B. K., Surface-Morphology-Dependent Electrolyte Effects on Gold-Catalyzed Electrochemical CO_2 Reduction. *J. Phys. Chem. C* **2017,** *121*, 22637-22643.

24. Song, Y.; Chen, W.; Zhao, C.; Li, S.; Wei, W.; Sun, Y., Metal-Free Nitrogen-Doped Mesoporous Carbon for Electroreduction of CO_2 to Ethanol. *Angew. Chem. Int. Ed.* **2017,** *56*, 10840-10844.

25. Ma , S.; Lan , Y.; Perez, G. M. J.; Moniri, S.; Kenis , P. J. A., Silver Supported on Titania as an Active Catalyst for Electrochemical Carbon Dioxide Reduction. *ChemSusChem* **2014,** *7*, 866-874.

26. Jin, L.; Liu, B.; Wang, P.; Yao, H.; Achola, L. A.; Kerns, P.; Lopes, A.; Yang, Y.; Ho, J.; Moewes, A.; Pei, Y.; He, J., Ultrasmall Au Nanocatalysts Supported on Nitrided Carbon for Electrocatalytic CO_2 Reduction: the Role of the Carbon Support in High Selectivity. *Nanoscale* **2018,** *10*, 14678-14686.

27. Wu, J.; Liu, M.; Sharma, P. P.; Yadav, R. M.; Ma, L.; Yang, Y.; Zou, X.; Zhou, X.-D.; Vajtai, R.; Yakobson, B. I.; Lou, J.; Ajayan, P. M., Incorporation of Nitrogen Defects for Efficient Reduction of CO_2 via Two-Electron Pathway on Three-Dimensional Graphene Foam. *Nano Lett.* **2016,** *16*, 466-470.

28. Boutin, E.; Merakeb, L.; Ma, B.; Boudy, B.; Wang, M.; Bonin, J.; Anxolabéhère-Mallart, E.; Robert, M., Molecular Catalysis of CO_2 Reduction: Recent Advances and

Perspectives in Electrochemical and Light-Driven Processes with Selected Fe, Ni and Co Aza Macrocyclic and Polypyridine Complexes. *Chem. Soc. Rev.* **2020,** *49*, 5772-5809.

29. Wang, Y.; Liu, Y.; Liu, W.; Wu, J.; Li, Q.; Feng, Q.; Chen, Z.; Xiong, X.; Wang, D.; Lei, Y., Regulating the Coordination Structure of Metal Single Atoms for Efficient Electrocatalytic CO_2 Reduction. *Energy Environ. Sci.* **2020,** *13*, 4609-4624.

30. Yang, H.; Wu, Y.; Li, G.; Lin, Q.; Hu, Q.; Zhang, Q.; Liu, J.; He, C., Scalable Production of Efficient Single-Atom Copper Decorated Carbon Membranes for CO_2 Electroreduction to Methanol. *J. Am. Chem. Soc.* **2019,** *141*, 12717-12723.

31. Morales-Guio, C. G.; Cave, E. R.; Nitopi, S. A.; Feaster, J. T.; Wang, L.; Kuhl, K. P.; Jackson, A.; Johnson, N. C.; Abram, D. N.; Hatsukade, T.; Hahn, C.; Jaramillo, T. F., Improved CO_2 Reduction Activity Towards C_{2+} Alcohols on a Tandem Gold on Copper Electrocatalyst. *Nat. Catal.* **2018,** *1*, 764-771.

32. Li, Y.; Sun, Q., Recent Advances in Breaking Scaling Relations for Effective Electrochemical Conversion of CO_2. *Adv. Energy Mater.* **2016,** *6*, 1600463.

33. Kuhl, K. P.; Hatsukade, T.; Cave, E. R.; Abram, D. N.; Kibsgaard, J.; Jaramillo, T. F., Electrocatalytic Conversion of Carbon Dioxide to Methane and Methanol on Transition Metal Surfaces. *J. Am. Chem. Soc.* **2014,** *136*, 14107-14113.

34. Sun, Z.; Hu, Y.; Zhou, D.; Sun, M.; Wang, S.; Chen, W., Factors Influencing the Performance of Copper-Bearing Catalysts in the CO_2 Reduction System. *ACS Energy Lett.* **2021,** *6*, 3992-4022.

35. Cai, Z.; Wu, Y.; Wu, Z.; Yin, L.; Weng, Z.; Zhong, Y.; Xu, W.; Sun, X.; Wang, H., Unlocking Bifunctional Electrocatalytic Activity for CO_2 Reduction Reaction by Win-Win Metal–Oxide Cooperation. *ACS Energy Lett.* **2018,** *3*, 2816-2822.

36. Kuhl, K. P.; Cave, E. R.; Abram, D. N.; Jaramillo, T. F., New Insights Into the Electrochemical Reduction of Carbon Dioxide on Metallic Copper Surfaces. *Energy Environ. Sci.* **2012,** *5*, 7050-7059.

37. Li, M.; Ma, Y.; Chen, J.; Lawrence, R.; Luo, W.; Sacchi, M.; Jiang, W.; Yang, J., Residual Chlorine Induced Cationic Active Species on a Porous Copper Electrocatalyst for Highly Stable Electrochemical CO_2 Reduction to C_{2+}. *Angew. Chem. Int. Ed.* **2021,** *60*, 11487-11493.

38. Ma, W.; Xie, S.; Liu, T.; Fan, Q.; Ye, J.; Sun, F.; Jiang, Z.; Zhang, Q.; Cheng, J.; Wang, Y., Electrocatalytic Reduction of CO_2 to Ethylene and Ethanol through Hydrogen-Assisted C–C Coupling over Fluorine-Modified Copper. *Nat. Catal.* **2020,** *3*, 478-487.

39. Wang, Z.; She, X.; Yu, Q.; Zhu, X.; Li, H.; Xu, H., Minireview on the Commonly Applied Copper-Based Electrocatalysts for Electrochemical CO_2 Reduction. *Energy & Fuels* **2021,** *35*, 8585-8601.

40. Bushuyev, O. S.; De Luna, P.; Dinh, C. T.; Tao, L.; Saur, G.; van de Lagemaat, J.; Kelley, S. O.; Sargent, E. H., What Should We Make with CO_2 and How Can We Make It? *Joule* **2018,** *2*, 825-832.

41. Hahn, C.; Hatsukade, T.; Kim, Y.-G.; Vailionis, A.; Baricuatro, J. H.; Higgins, D. C.; Nitopi, S. A.; Soriaga, M. P.; Jaramillo, T. F., Engineering Cu Surfaces for the Electrocatalytic Conversion of CO_2: Controlling Selectivity toward Oxygenates and Hydrocarbons. *Proc. Natl. Acad. Sci.* **2017,** *114*, 5918-5923.

42. Yoon, Y.; Hall, A. S.; Surendranath, Y., Tuning of Silver Catalyst Mesostructure Promotes Selective Carbon Dioxide Conversion into Fuels. *Angew. Chem. Int. Ed.* **2016,** *55*, 15282-15286.

43. Engelbrecht, A.; Uhlig, C.; Stark, O.; Hammerle, M.; Schmid, G.; Magori, E.; Wiesner-Fleischer, K.; Fleischer, M.; Moos, R., On the Electrochemical CO_2 Reduction at Copper Sheet Electrodes with Enhanced Long-Term Stability by Pulsed Electrolysis. *J Electrochem Soc* **2018,** *165*, J3059-J3068.

44. Tang, Q.; Lee, Y.; Li, D.-Y.; Choi, W.; Liu, C. W.; Lee, D.; Jiang, D.-e., Lattice-Hydride Mechanism in Electrocatalytic CO_2 Reduction by Structurally Precise Copper-Hydride Nanoclusters. *J. Am. Chem. Soc.* **2017,** *139*, 9728-9736.

45. Zhu, W.; Michalsky, R.; Metin, Ö.; Lv, H.; Guo, S.; Wright, C. J.; Sun, X.; Peterson, A. A.; Sun, S., Monodisperse Au Nanoparticles for Selective Electrocatalytic Reduction of CO_2 to CO. *J. Am. Chem. Soc.* **2013,** *135*, 16833-16836.

46. Kim, C.; Jeon, H. S.; Eom, T.; Jee, M. S.; Kim, H.; Friend, C. M.; Min, B. K.; Hwang, Y. J., Achieving Selective and Efficient Electrocatalytic Activity for CO_2 Reduction Using Immobilized Silver Nanoparticles. *J. Am. Chem. Soc.* **2015,** *137*, 13844-13850.

47. Zhang, Z.; Chi, M.; Veith, G. M.; Zhang, P.; Lutterman, D. A.; Rosenthal, J.; Overbury, S. H.; Dai, S.; Zhu, H., Rational Design of Bi Nanoparticles for Efficient Electrochemical CO_2 Reduction: The Elucidation of Size and Surface Condition Effects. *ACS Catal.* **2016,** *6*, 6255-6264.

48. Zhang, S.; Kang, P.; Meyer, T. J., Nanostructured Tin Catalysts for Selective Electrochemical Reduction of Carbon Dioxide to Formate. *J. Am. Chem. Soc.* **2014,** *136*, 1734-1737.

49. Jeon, H. S.; Sinev, I.; Scholten, F.; Divins, N. J.; Zegkinoglou, I.; Pielsticker, L.; Cuenya, B. R., Operando Evolution of the Structure and Oxidation State of Size-Controlled Zn Nanoparticles during CO_2 Electroreduction. *J. Am. Chem. Soc.* **2018,** *140*, 9383-9386.

50. Zhao, S.; Jin, R.; Jin, R., Opportunities and Challenges in CO_2 Reduction by Gold- and Silver-Based Electrocatalysts: From Bulk Metals to Nanoparticles and Atomically Precise Nanoclusters. *ACS Energy Lett.* **2018,** *3*, 452-462.

51. Huang, J.; Buonsanti, R., Colloidal Nanocrystals as Heterogeneous Catalysts for Electrochemical CO_2 Conversion. *Chem. Mater.* **2019,** *31*, 13-25.

52. Choi, C.; Kwon, S.; Cheng, T.; Xu, M.; Tieu, P.; Lee, C.; Cai, J.; Lee, H. M.; Pan, X.; Duan, X.; Goddard, W. A.; Huang, Y., Highly Active and Stable Stepped Cu Surface for Enhanced Electrochemical CO_2 Reduction to C_2H_4. *Nat. Catal.* **2020,** *3*, 804-812.

53. Zhu, W.; Kattel, S.; Jiao, F.; Chen, J. G., Shape-Controlled CO_2 Electrochemical Reduction on Nanosized Pd Hydride Cubes and Octahedra. *Adv. Energy Mater.* **2019,** *9*, 1802840.

54. De Gregorio, G. L.; Burdyny, T.; Loiudice, A.; Iyengar, P.; Smith, W. A.; Buonsanti, R., Facet-Dependent Selectivity of Cu Catalysts in Electrochemical CO_2 Reduction at Commercially Viable Current Densities. *ACS Catal.* **2020,** *10*, 4854-4862.

55. Garza, A. J.; Bell, A. T.; Head-Gordon, M., Mechanism of CO_2 Reduction at Copper Surfaces: Pathways to C2 Products. *ACS Catal.* **2018,** *8*, 1490-1499.

56. Tsujiguchi, T.; Kawabe, Y.; Jeong, S.; Ohto, T.; Kukunuri, S.; Kuramochi, H.; Takahashi, Y.; Nishiuchi, T.; Masuda, H.; Wakisaka, M.; Hu, K.; Elumalai, G.; Fujita, J.-i.; Ito, Y., Acceleration of Electrochemical CO_2 Reduction to Formate at the Sn/Reduced Graphene Oxide Interface. *ACS Catal.* **2021,** *11*, 3310-3318.

57. Gao, D.; Zegkinoglou, I.; Divins, N. J.; Scholten, F.; Sinev, I.; Grosse, P.; Roldan Cuenya, B., Plasma-Activated Copper Nanocube Catalysts for Efficient Carbon Dioxide Electroreduction to Hydrocarbons and Alcohols. *ACS Nano* **2017,** *11*, 4825-4831.

58. Grosse, P.; Gao, D.; Scholten, F.; Sinev, I.; Mistry, H.; Roldan Cuenya, B., Dynamic Changes in the Structure, Chemical State and Catalytic Selectivity of Cu Nanocubes during CO_2 Electroreduction: Size and Support Effects. *Angew. Chem. Int. Ed.* **2018,** *57*, 6192-6197.

59. Gao, D.; Zhang, Y.; Zhou, Z.; Cai, F.; Zhao, X.; Huang, W.; Li, Y.; Zhu, J.; Liu, P.; Yang, F.; Wang, G.; Bao, X., Enhancing CO_2 Electroreduction with the Metal–Oxide Interface. *J. Am. Chem. Soc.* **2017,** *139*, 5652-5655.

60. Zhang, L.; Mao, F.; Zheng, L. R.; Wang, H. F.; Yang, X. H.; Yang, H. G., Tuning Metal Catalyst with Metal–C_3N_4 Interaction for Efficient CO_2 Electroreduction. *ACS Catal.* **2018,** *8*, 11035-11041.

61. Zhao, S.; Tang, Z.; Guo, S.; Han, M.; Zhu, C.; Zhou, Y.; Bai, L.; Gao, J.; Huang, H.; Li, Y.; Liu, Y.; Kang, Z., Enhanced Activity for CO_2 Electroreduction on a Highly Active and Stable Ternary Au-CDots-C_3N_4 Electrocatalyst. *ACS Catal.* **2018,** *8*, 188-197.

62. Kung, C.-W.; Audu, C. O.; Peters, A. W.; Noh, H.; Farha, O. K.; Hupp, J. T., Copper Nanoparticles Installed in Metal–Organic Framework Thin Films are Electrocatalytically Competent for CO_2 Reduction. *ACS Energy Lett.* **2017,** *2*, 2394-2401.

63. Guntern, Y. T.; Pankhurst, J. R.; Vávra, J.; Mensi, M.; Mantella, V.; Schouwink, P.; Buonsanti, R., Nanocrystal/Metal–Organic Framework Hybrids as Electrocatalytic Platforms for CO_2 Conversion. *Angew. Chem. Int. Ed.* **2019,** *58*, 12632-12639.

64. Ma, Z.; Tsounis, C.; Kumar, P. V.; Han, Z.; Wong, R. J.; Toe, C. Y.; Zhou, S.; Bedford, N. M.; Thomsen, L.; Ng, Y. H.; Amal, R., Enhanced Electrochemical CO_2 Reduction of Cu@Cu_xO Nanoparticles Decorated on 3D Vertical Graphene with Intrinsic sp^3-type Defect. *Adv. Funct. Mater.* **2020,** *30*, 1910118.

65. Nguyen, D. L. T.; Lee, C. W.; Na, J.; Kim, M.-C.; Tu, N. D. K.; Lee, S. Y.; Sa, Y. J.; Won, D. H.; Oh, H.-S.; Kim, H.; Min, B. K.; Han, S. S.; Lee, U.; Hwang, Y. J., Mass Transport Control by Surface Graphene Oxide for Selective CO Production from Electrochemical CO_2 Reduction. *ACS Catal.* **2020,** *10*, 3222-3231.

66. Xie, J.; Zhao, X.; Wu, M.; Li, Q.; Wang, Y.; Yao, J., Metal-Free Fluorine-Doped Carbon Electrocatalyst for CO_2 Reduction Outcompeting Hydrogen Evolution. *Angew. Chem. Int. Ed.* **2018,** *57*, 9640-9644.

67. Verdaguer-Casadevall, A.; Li, C. W.; Johansson, T. P.; Scott, S. B.; McKeown, J. T.; Kumar, M.; Stephens, I. E. L.; Kanan, M. W.; Chorkendorff, I., Probing the Active Surface Sites for CO Reduction on Oxide-Derived Copper Electrocatalysts. *J. Am. Chem. Soc.* **2015,** *137*, 9808-9811.

68. Feng, X.; Jiang, K.; Fan, S.; Kanan, M. W., A Direct Grain-Boundary-Activity Correlation for CO Electroreduction on Cu Nanoparticles. *ACS Cent. Sci.* **2016,** *2*, 169-174.

69. Liu, Y.; Chen, S.; Quan, X.; Yu, H., Efficient Electrochemical Reduction of Carbon Dioxide to Acetate on Nitrogen-Doped Nanodiamond. *J. Am. Chem. Soc.* **2015,** *137*, 11631-11636.

70. Zhuang, T.-T.; Liang, Z.-Q.; Seifitokaldani, A.; Li, Y.; De Luna, P.; Burdyny, T.; Che, F.; Meng, F.; Min, Y.; Quintero-Bermudez, R.; Dinh, C. T.; Pang, Y.; Zhong, M.; Zhang, B.; Li, J.; Chen, P.-N.; Zheng, X.-L.; Liang, H.; Ge, W.-N.; Ye, B.-J.; Sinton, D.; Yu, S.-H.; Sargent, E. H., Steering Post-C–C Coupling Selectivity Enables High Efficiency Electroreduction of Carbon Dioxide to Multi-Carbon Alcohols. *Nat. Catal.* **2018,** *1*, 421-428.

71. Jansonius, R. P.; Reid, L. M.; Virca, C. N.; Berlinguette, C. P., Strain Engineering Electrocatalysts for Selective CO_2 Reduction. *ACS Energy Lett.* **2019,** *4*, 980-986.

72. Huang, H.; Jia, H.; Liu, Z.; Gao, P.; Zhao, J.; Luo, Z.; Yang, J.; Zeng, J., Understanding of Strain Effects in the Electrochemical Reduction of CO_2: Using Pd Nanostructures as an Ideal Platform. *Angew. Chem. Int. Ed.* **2017,** *56*, 3594-3598.

73. Kaiser, S. K.; Chen, Z.; Faust Akl, D.; Mitchell, S.; Pérez-Ramírez, J., Single-Atom Catalysts across the Periodic Table. *Chem. Rev.* **2020,** *120*, 11703-11809.

74. Qu, Q.; Ji, S.; Chen, Y.; Wang, D.; Li, Y., The Atomic-Level Regulation of Single-Atom Site Catalysts for the Electrochemical CO_2 Reduction Reaction. *Chem. Sci.* **2021,** *12*, 4201-4215.

75. Zhang, N.; Zhang, X.; Tao, L.; Jiang, P.; Ye, C.; Lin, R.; Huang, Z.; Li, A.; Pang, D.; Yan, H.; Wang, Y.; Xu, P.; An, S.; Zhang, Q.; Liu, L.; Du, S.; Han, X.; Wang, D.; Li, Y., Silver Single-Atom Catalyst for Efficient Electrochemical CO_2 Reduction Synthesized from Thermal Transformation and Surface Reconstruction. *Angew. Chem. Int. Ed.* **2021,** *60*, 6170-6176.

76. Jiang, K.; Siahrostami, S.; Zheng, T.; Hu, Y.; Hwang, S.; Stavitski, E.; Peng, Y.; Dynes, J.; Gangisetty, M.; Su, D.; Attenkofer, K.; Wang, H., Isolated Ni Single Atoms in Graphene Nanosheets for High-Performance CO_2 Reduction. *Energy Environ. Sci.* **2018,** *11*, 893-903.

77. Lee, S. Y.; Jung, H.; Kim, N.-K.; Oh, H.-S.; Min, B. K.; Hwang, Y. J., Mixed Copper States in Anodized Cu Electrocatalyst for Stable and Selective Ethylene Production from CO_2 Reduction. *J. Am. Chem. Soc.* **2018,** *140*, 8681-8689.

78. Möller, T.; Ju, W.; Bagger, A.; Wang, X.; Luo, F.; Ngo Thanh, T.; Varela, A. S.; Rossmeisl, J.; Strasser, P., Efficient CO_2 to CO Electrolysis on Solid Ni–N–C Catalysts at Industrial Current Densities. *Energy Environ. Sci.* **2019,** *12*, 640-647.

79. Derrick, J. S.; Loipersberger, M.; Chatterjee, R.; Iovan, D. A.; Smith, P. T.; Chakarawet, K.; Yano, J.; Long, J. R.; Head-Gordon, M.; Chang, C. J., Metal–Ligand

Cooperativity via Exchange Coupling Promotes Iron- Catalyzed Electrochemical CO_2 Reduction at Low Overpotentials. *J. Am. Chem. Soc.* **2020,** *142*, 20489-20501.

80. Göttle, A. J.; Koper, M. T. M., Proton-Coupled Electron Transfer in the Electrocatalysis of CO_2 Reduction: Prediction of Sequential vs. Concerted Pathways Using DFT. *Chem. Sci.* **2017,** *8*, 458-465.

81. Shen, J.; Kortlever, R.; Kas, R.; Birdja, Y. Y.; Diaz-Morales, O.; Kwon, Y.; Ledezma-Yanez, I.; Schouten, K. J. P.; Mul, G.; Koper, M. T. M., Electrocatalytic Reduction of Carbon Dioxide to Carbon Monoxide and Methane at an Immobilized Cobalt Protoporphyrin. *Nat. Commun.* **2015,** *6*, 8177.

82. Shen, J.; Kolb, M. J.; Göttle, A. J.; Koper, M. T. M., DFT Study on the Mechanism of the Electrochemical Reduction of CO_2 Catalyzed by Cobalt Porphyrins. *J. Phys. Chem. C* **2016,** *120*, 15714-15721.

83. Xie, H.; Wan, Y.; Wang, X.; Liang, J.; Lu, G.; Wang, T.; Chai, G.; Adli, N. M.; Priest, C.; Huang, Y.; Wu, G.; Li, Q., Boosting Pd-catalysis for Electrochemical CO_2 Reduction to CO on Bi-Pd Single Atom Alloy Nanodendrites. *Appl. Catal. B* **2021,** *289*, 119783.

84. Xie, H.; Wang, F.; Liu, T.; Wu, Y.; Lan, C.; Chen, B.; Zhou, J.; Chen, B., Copper−Iron Dimer for Selective C–C Coupling in Electrochemical CO_2 Reduction. *Electrochim Acta* **2021,** *380*, 138188.

85. Zhang, N.; Zhang, X.; Kang, Y.; Ye, C.; Jin, R.; Yan, H.; Lin, R.; Yang, J.; Xu, Q.; Wang, Y.; Zhang, Q.; Gu, L.; Liu, L.; Song, W.; Liu, J.; Wang, D.; Li, Y., A Supported Pd_2 Dual-Atom Site Catalyst for Efficient Electrochemical CO_2 Reduction. *Angew. Chem. Int. Ed.* **2021,** *60*, 13388-13393.

86. Pei, J.; Wang, T.; Sui, R.; Zhang, X.; Zhou, D.; Qin, F.; Zhao, X.; Liu, Q.; Yan, W.; Dong, J.; Zheng, L.; Li, A.; Mao, J.; Zhu, W.; Chen, W.; Zhuang, Z., N-Bridged Co–N–Ni: New Bimetallic Sites for Promoting Electrochemical CO_2 Reduction. *Energy Environ. Sci.* **2021,** *14*, 3019-3028.

87. Guo, Y.; Wang, Y.; Shen, Y.; Cai, Z.; Li, Z.; Liu, J.; Chen, J.; Xiao, C.; Liu, H.; Lin, W.; Wang, C., Tunable Cobalt-Polypyridyl Catalysts Supported on Metal–Organic Layers for Electrochemical CO_2 Reduction at Low Overpotentials. *J. Am. Chem. Soc.* **2020,** *142*, 21493-21501.

88. Ummireddi, A. K.; Sharma, S. K.; Pala, R. G., Inhibition of Hydrogen Evolution without Debilitating Electrochemical CO_2 Reduction via the Local Suppression of Proton Concentration

and Blocking of Step-edges by Pyridine Functionalization on Cu Electrocatalysts. *Catal. Sci. Technol.* **2021**.

89. Solis, B. H.; Maher, A. G.; Dogutan, D. K.; Nocera, D. G.; Hammes-Schiffer, S., Nickel Phlorin Intermediate Formed by Proton-Coupled Electron Transfer in Hydrogen Evolution Mechanism. *Proc. Natl. Acad. Sci.* **2016,** *113*, 485.

90. Lum, Y.; Ager, J. W., Evidence for Product-Specific Active Sites on Oxide-Derived Cu Catalysts for Electrochemical CO_2 Reduction. *Nat. Catal.* **2019,** *2*, 86-93.

91. Jia, H.; Yang, Y.; Chow, T. H.; Zhang, H.; Liu, X.; Wang, J.; Zhang, C.-y., Symmetry-Broken Au–Cu Heterostructures and their Tandem Catalysis Process in Electrochemical CO_2 Reduction. *Adv. Funct. Mater.* **2021,** *n/a*, 2101255.

92. Lum, Y.; Ager, J. W., Sequential Catalysis Controls Selectivity in Electrochemical CO_2 Reduction on Cu. *Energy Environ. Sci.* **2018,** *11*, 2935-2944.

93. Schreier, M.; Yoon, Y.; Jackson, M. N.; Surendranath, Y., Competition between H and CO for Active Sites Governs Copper-Mediated Electrosynthesis of Hydrocarbon Fuels. *Angew. Chem. Int. Ed.* **2018,** *57*, 10221-10225.

94. Gao, S.; Lin, Y.; Jiao, X.; Sun, Y.; Luo, Q.; Zhang, W.; Li, D.; Yang, J.; Xie, Y., Partially Oxidized Atomic Cobalt Layers for Carbon Dioxide Electroreduction to Liquid Fuel. *Nature* **2016,** *529*, 68-71.

95. Zhang, W.; Hu, Y.; Ma, L.; Zhu, G.; Zhao, P.; Xue, X.; Chen, R.; Yang, S.; Ma, J.; Liu, J.; Jin, Z., Liquid-Phase Exfoliated Ultrathin Bi Nanosheets: Uncovering the Origins of Enhanced Electrocatalytic CO_2 Reduction on Two-Dimensional Metal Nanostructure. *Nano Energy* **2018,** *53*, 808-816.

96. Liu, K.; Ma, M.; Wu, L.; Valenti, M.; Cardenas-Morcoso, D.; Hofmann, J. P.; Bisquert, J.; Gimenez, S.; Smith, W. A., Electronic Effects Determine the Selectivity of Planar Au–Cu Bimetallic Thin Films for Electrochemical CO_2 Reduction. *ACS Appl. Mater. Interfaces* **2019,** *11*, 16546-16555.

97. Asadi, M.; Kim, K.; Liu, C.; Addepalli Aditya, V.; Abbasi, P.; Yasaei, P.; Phillips, P.; Behranginia, A.; Cerrato José, M.; Haasch, R.; Zapol, P.; Kumar, B.; Klie Robert, F.; Abiade, J.; Curtiss Larry, A.; Salehi-Khojin, A., Nanostructured Transition Metal Dichalcogenide Electrocatalysts for CO_2 Reduction in Ionic Liquid. *Science* **2016,** *353*, 467-470.

98. Zhang, Z.; Xiao, J.; Chen, X.-J.; Yu, S.; Yu, L.; Si, R.; Wang, Y.; Wang, S.; Meng, X.; Wang, Y.; Tian, Z.-Q.; Deng, D., Reaction Mechanisms of Well-Defined Metal–N4 Sites in Electrocatalytic CO_2 Reduction. *Angew. Chem. Int. Ed.* **2018,** *57*, 16339-16342.

99. Calvinho, K. U. D.; Alherz, A. W.; Yap, K. M. K.; Laursen, A. B.; Hwang, S.; Bare, Z. J. L.; Clifford, Z.; Musgrave, C. B.; Dismukes, G. C., Surface Hydrides on Fe_2P Electrocatalyst Reduce CO_2 at Low Overpotential: Steering Selectivity to Ethylene Glycol. *J. Am. Chem. Soc.* **2021,** *143*, 21275-21285.

100. Calvinho, K. U. D.; Laursen, A. B.; Yap, K. M. K.; Goetjen, T. A.; Hwang, S.; Murali, N.; Mejia-Sosa, B.; Lubarski, A.; Teeluck, K. M.; Hall, E. S.; Garfunkel, E.; Greenblatt, M.; Dismukes, G. C., Selective CO_2 Reduction to C_3 and C_4 Oxyhydrocarbons on Nickel Phosphides at Overpotentials as Low as 10 mV. *Energy Environ. Sci.* **2018,** *11*, 2550-2559.

101. Zhou, H.; Chen, Z.; Kountoupi, E.; Tsoukalou, A.; Abdala, P. M.; Florian, P.; Fedorov, A.; Müller, C. R., Two-dimensional Molybdenum Carbide 2D-Mo_2C as a Superior Catalyst for CO_2 Hydrogenation. *Nat. Commun.* **2021,** *12*, 5510.

102. Esmaeilirad, M.; Baskin, A.; Kondori, A.; Sanz-Matias, A.; Qian, J.; Song, B.; Tamadoni Saray, M.; Kucuk, K.; Belmonte, A. R.; Delgado, P. N. M.; Park, J.; Azari, R.; Segre, C. U.; Shahbazian-Yassar, R.; Prendergast, D.; Asadi, M., Gold-Like Activity Copper-Like Selectivity of Heteroatomic Transition Metal Carbides for Electrocatalytic Carbon Dioxide Reduction Reaction. *Nat. Commun.* **2021,** *12*, 5067.

103. Lee, S. Y.; Chae, S. Y.; Jung, H.; Lee, C. W.; Nguyen, D. L. T.; Oh, H.-S.; Min, B. K.; Hwang, Y. J., Controlling the C_{2+} Product Selectivity of Electrochemical CO_2 Reduction on an Electrosprayed Cu Catalyst. *J. Mater. Chem. A* **2020,** *8*, 6210-6218.

104. Varela, A. S.; Schlaup, C.; Jovanov, Z. P.; Malacrida, P.; Horch, S.; Stephens, I. E. L.; Chorkendorff, I., CO_2 Electroreduction on Well-Defined Bimetallic Surfaces: Cu Overlayers on Pt(111) and Pt(211). *J. Phys. Chem. C* **2013,** *117*, 20500-20508.

105. Bagger, A.; Ju, W.; Varela, A. S.; Strasser, P.; Rossmeisl, J., Electrochemical CO_2 Reduction: A Classification Problem. *ChemPhysChem* **2017,** *18*, 3266-3273.

106. Birdja, Y. Y.; Pérez-Gallent, E.; Figueiredo, M. C.; Göttle, A. J.; Calle-Vallejo, F.; Koper, M. T. M., Advances and Challenges in Understanding the Electrocatalytic Conversion of Carbon Dioxide to Fuels. *Nat. Energy* **2019,** *4*, 732-745.

107. Singh, M. R.; Clark, E. L.; Bell, A. T., Effects of Electrolyte, Catalyst, and Membrane Composition and Operating Conditions on the Performance of Solar-Driven Electrochemical Reduction of Carbon Dioxide. *Phys. Chem. Chem. Phys.* **2015,** *17*, 18924-18936.

108. Clark, E. L.; Resasco, J.; Landers, A.; Lin, J.; Chung, L.-T.; Walton, A.; Hahn, C.; Jaramillo, T. F.; Bell, A. T., Standards and Protocols for Data Acquisition and Reporting for Studies of the Electrochemical Reduction of Carbon Dioxide. *ACS Catal.* **2018,** *8*, 6560-6570.

109. Yoshio, H.; Katsuhei, K.; Shin, S., Production of CO and CH_4 in Electochemical Reduction of CO_2 at metal Electrodes in Aqueous Hydrogencarbonate Solution. *Chem. Lett.* **1985,** *14*, 1695-1698.

110. Liu, M.; Pang, Y.; Zhang, B.; De Luna, P.; Voznyy, O.; Xu, J.; Zheng, X.; Dinh, C. T.; Fan, F.; Cao, C.; de Arquer, F. P. G.; Safaei, T. S.; Mepham, A.; Klinkova, A.; Kumacheva, E.; Filleter, T.; Sinton, D.; Kelley, S. O.; Sargent, E. H., Enhanced Electrocatalytic CO_2 Reduction via Field-Induced Reagent Concentration. *Nature* **2016,** *537*, 382-386.

111. Narayanan, S. R.; Haines, B.; Soler, J.; Valdez, T. I., Electrochemical Conversion of Carbon Dioxide to Formate in Alkaline Polymer Electrolyte Membrane Cells. *J Electrochem Soc* **2011,** *158*, A167.

112. Wang, G.; Pan, J.; Jiang, S. P.; Yang, H., Gas Phase Electrochemical Conversion of Humidified CO_2 to CO and H_2 on Proton-Exchange and Alkaline Anion-Exchange Membrane Fuel Cell Reactors. *J. CO_2 Util.* **2018,** *23*, 152-158.

113. Gabardo, C. M.; O'Brien, C. P.; Edwards, J. P.; McCallum, C.; Xu, Y.; Dinh, C.-T.; Li, J.; Sargent, E. H.; Sinton, D., Continuous Carbon Dioxide Electroreduction to Concentrated Multi-carbon Products Using a Membrane Electrode Assembly. *Joule* **2019,** *3*, 2777-2791.

114. Weng, L.-C.; Bell, A. T.; Weber, A. Z., Towards Membrane-Electrode Assembly Systems for CO_2 Reduction: a Modeling Study. *Energy Environ. Sci.* **2019,** *12*, 1950-1968.

115. Clark, E. L.; Singh, M. R.; Kwon, Y.; Bell, A. T., Differential Electrochemical Mass Spectrometer Cell Design for Online Quantification of Products Produced during Electrochemical Reduction of CO_2. *Anal. Chem.* **2015,** *87*, 8013-8020.

116. Clark, E. L.; Bell, A. T., Direct Observation of the Local Reaction Environment during the Electrochemical Reduction of CO_2. *J. Am. Chem. Soc.* **2018,** *140*, 7012-7020.

117. Zhao, C.; Wang, J., Electrochemical Reduction of CO_2 to Formate in Aqueous Solution Using Electro-Deposited Sn Catalysts. *Chem. Eng. Sci.* **2016,** *293*, 161-170.

118. Lum, Y.; Yue, B.; Lobaccaro, P.; Bell, A. T.; Ager, J. W., Optimizing C–C Coupling on Oxide-Derived Copper Catalysts for Electrochemical CO_2 Reduction. *J. Phys. Chem. C* **2017,** *121*, 14191-14203.

119. Kas, R.; Kortlever, R.; Yılmaz, H.; Koper, M. T. M.; Mul, G., Manipulating the Hydrocarbon Selectivity of Copper Nanoparticles in CO_2 Electroreduction by Process Conditions. *ChemElectroChem* **2015,** *2*, 354-358.

120. Raciti, D.; Wang, C., Recent Advances in CO_2 Reduction Electrocatalysis on Copper. *ACS Energy Lett.* **2018,** *3*, 1545-1556.

121. Kortlever, R.; Shen, J.; Schouten, K. J. P.; Calle-Vallejo, F.; Koper, M. T. M., Catalysts and Reaction Pathways for the Electrochemical Reduction of Carbon Dioxide. *J. Phys. Chem. Lett.* **2015,** *6*, 4073-4082.

122. Whipple, D. T.; Finke, E. C.; Kenis, P. J. A., Microfluidic Reactor for the Electrochemical Reduction of Carbon Dioxide: The Effect of pH. *Electrochem. Solid-State Lett.* **2010,** *13*, B109.

123. De Luna, P.; Quintero-Bermudez, R.; Dinh, C.-T.; Ross, M. B.; Bushuyev, O. S.; Todorović, P.; Regier, T.; Kelley, S. O.; Yang, P.; Sargent, E. H., Catalyst Electro-Redeposition Controls Morphology and Oxidation State for Selective Carbon Dioxide Reduction. *Nat. Catal.* **2018,** *1*, 103-110.

124. Wang, M.; Torbensen, K.; Salvatore, D.; Ren, S.; Joulié, D.; Dumoulin, F.; Mendoza, D.; Lassalle-Kaiser, B.; Işci, U.; Berlinguette, C. P.; Robert, M., CO_2 Electrochemical Catalytic Reduction with a Highly Active Cobalt Phthalocyanine. *Nat. Commun.* **2019,** *10*, 3602.

125. Dinh, C.-T.; Burdyny, T.; Kibria, M. G.; Seifitokaldani, A.; Gabardo, C. M.; García de Arquer, F. P.; Kiani, A.; Edwards, J. P.; De Luna, P.; Bushuyev, O. S.; Zou, C.; Quintero-Bermudez, R.; Pang, Y.; Sinton, D.; Sargent, E. H., CO_2 Electroreduction to Ethylene via Hydroxide-Mediated Copper Catalysis at an Abrupt Interface. *Science* **2018,** *360*, 783-787.

126. Hollinger, A. S.; Maloney, R. J.; Jayashree, R. S.; Natarajan, D.; Markoski, L. J.; Kenis, P. J. A., Nanoporous Separator and Low Fuel Concentration to Minimize Crossover in Direct Methanol Laminar Flow Fuel Cells. *J. Power Sources* **2010,** *195*, 3523-3528.

127. O'Brien, C. P.; Miao, R. K.; Liu, S.; Xu, Y.; Lee, G.; Robb, A.; Huang, J. E.; Xie, K.; Bertens, K.; Gabardo, C. M.; Edwards, J. P.; Dinh, C.-T.; Sargent, E. H.; Sinton, D., Single Pass CO_2 Conversion Exceeding 85% in the Electrosynthesis of Multicarbon Products via Local CO_2 Regeneration. *ACS Energy Lett.* **2021,** *6*, 2952-2959.

128. Yang, K.; Kas, R.; Smith, W. A.; Burdyny, T., Role of the Carbon-Based Gas Diffusion Layer on Flooding in a Gas Diffusion Electrode Cell for Electrochemical CO_2 Reduction. *ACS Energy Lett.* **2021,** *6*, 33-40.

129. Liu, K.; Smith, W. A.; Burdyny, T., Introductory Guide to Assembling and Operating Gas Diffusion Electrodes for Electrochemical CO_2 Reduction. *ACS Energy Lett.* **2019,** *4*, 639-643.

130. Weekes, D. M.; Salvatore, D. A.; Reyes, A.; Huang, A.; Berlinguette, C. P., Electrolytic CO_2 Reduction in a Flow Cell. *Acc. Chem. Res.* **2018,** *51*, 910-918.

131. Jhong, H.-R. M.; Brushett, F. R.; Kenis, P. J. A., Fuel Cells: The Effects of Catalyst Layer Deposition Methodology on Electrode Performance. *Adv. Energy Mater.* **2013,** *3*, 541-541.

132. Bitar, Z.; Fecant, A.; Trela-Baudot, E.; Chardon-Noblat, S.; Pasquier, D., Electrocatalytic Reduction of Carbon Dioxide on Indium Coated Gas Diffusion Electrodes—Comparison with Indium Foil. *Appl. Catal. B* **2016,** *189*, 172-180.

133. Lu, Q.; Rosen, J.; Zhou, Y.; Hutchings, G. S.; Kimmel, Y. C.; Chen, J. G.; Jiao, F., A Selective and Efficient Electrocatalyst for Carbon Dioxide Reduction. *Nat. Commun.* **2014,** *5*, 3242.

134. Vermaas, D. A.; Smith, W. A., Synergistic Electrochemical CO_2 Reduction and Water Oxidation with a Bipolar Membrane. *ACS Energy Lett.* **2016,** *1*, 1143-1148.

135. Wu, J.; Risalvato, F. G.; Sharma, P. P.; Pellechia, P. J.; Ke, F.-S.; Zhou, X.-D., Electrochemical Reduction of Carbon Dioxide. *J Electrochem Soc* **2013,** *160*, F953-F957.

136. Jia, S.; Matsuda, S.; Tamura, S.; Shironita, S.; Umeda, M., Study of CO_2 Reduction at Pt-Ru Electrocatalyst in Polymer Electrolyte Cell by Differential Electrochemical Mass Spectrometry and Liquid Chromatography. *Electrochim Acta* **2018,** *261*, 340-345.

137. Khodakov, A. Y.; Chu, W.; Fongarland, P., Advances in the Development of Novel Cobalt Fischer−Tropsch Catalysts for Synthesis of Long-Chain Hydrocarbons and Clean Fuels. *Chem. Rev.* **2007,** *107*, 1692-1744.

138. Bejtka, K.; Zeng, J.; Sacco, A.; Castellino, M.; Hernández, S.; Farkhondehfal, M. A.; Savino, U.; Ansaloni, S.; Pirri, C. F.; Chiodoni, A., Chainlike Mesoporous SnO_2 as a Well-Performing Catalyst for Electrochemical CO_2 Reduction. *ACS Appl. Energy Mater.* **2019,** *2*, 3081-3091.

139. Dai, C.; Sun, L.; Song, J.; Liao, H.; Fisher, A. C.; Xu, Z. J., Selective Electroreduction of Carbon Dioxide to Formic Acid on Cobalt-Decorated Copper Thin Films. *Small Methods* **2019,** *3*, 1900362.

140. Gao, D.; Zhou, H.; Wang, J.; Miao, S.; Yang, F.; Wang, G.; Wang, J.; Bao, X., Size-Dependent Electrocatalytic Reduction of CO_2 over Pd Nanoparticles. *J. Am. Chem. Soc.* **2015,** *137*, 4288-4291.

141. Rosen, J.; Hutchings, G. S.; Lu, Q.; Forest, R. V.; Moore, A.; Jiao, F., Electrodeposited Zn Dendrites with Enhanced CO Selectivity for Electrocatalytic CO_2 Reduction. *ACS Catal.* **2015,** *5*, 4586-4591.

142. Fan, K.; Jia, Y.; Ji, Y.; Kuang, P.; Zhu, B.; Liu, X.; Yu, J., Curved Surface Boosts Electrochemical CO_2 Reduction to Formate via Bismuth Nanotubes in a Wide Potential Window. *ACS Catal.* **2020,** *10*, 358-364.

143. Lee, M.-Y.; Ringe, S.; Kim, H.; Kang, S.; Kwon, Y., Electric Field Mediated Selectivity Switching of Electrochemical CO_2 Reduction from Formate to CO on Carbon Supported Sn. *ACS Energy Lett.* **2020,** *5*, 2987-2994.

144. Van Daele, K.; De Mot, B.; Pupo, M.; Daems, N.; Pant, D.; Kortlever, R.; Breugelmans, T., Sn-Based Electrocatalyst Stability: A Crucial Piece to the Puzzle for the Electrochemical CO_2 Reduction toward Formic Acid. *ACS Energy Lett.* **2021,** *6*, 4317-4327.

145. Jiang, K.; Siahrostami, S.; Akey, A. J.; Li, Y.; Lu, Z.; Lattimer, J.; Hu, Y.; Stokes, C.; Gangishetty, M.; Chen, G.; Zhou, Y.; Hill, W.; Cai, W.-B.; Bell, D.; Chan, K.; Nørskov, J. K.; Cui, Y.; Wang, H., Transition-Metal Single Atoms in a Graphene Shell as Active Centers for Highly Efficient Artificial Photosynthesis. *Chem* **2017,** *3*, 950-960.

146. Pan, Z.; Wang, K.; Ye, K.; Wang, Y.; Su, H.-Y.; Hu, B.; Xiao, J.; Yu, T.; Wang, Y.; Song, S., Intermediate Adsorption States Switch to Selectively Catalyze Electrochemical CO_2 Reduction. *ACS Catal.* **2020,** *10*, 3871-3880.

147. Feaster, J. T.; Shi, C.; Cave, E. R.; Hatsukade, T.; Abram, D. N.; Kuhl, K. P.; Hahn, C.; Nørskov, J. K.; Jaramillo, T. F., Understanding Selectivity for the Electrochemical Reduction of Carbon Dioxide to Formic Acid and Carbon Monoxide on Metal Electrodes. *ACS Catal.* **2017,** *7*, 4822-4827.

148. Lu, X.; Wu, Y.; Yuan, X.; Huang, L.; Wu, Z.; Xuan, J.; Wang, Y.; Wang, H., High-Performance Electrochemical CO_2 Reduction Cells Based on Non-noble Metal Catalysts. *ACS Energy Lett.* **2018,** *3*, 2527-2532.

149. Don, W. G.; Robert, H. P., *Perry's Chemical Engineers' Handbook, Eighth Edition*. 8th ed. / ed.; McGraw-Hill Education: New York, 2008.

150. Pan, H.; Barile, C. J., Electrochemical CO_2 Reduction to Methane with Remarkably High Faradaic Efficiency in the Presence of a Proton Permeable Membrane. *Energy Environ. Sci.* **2020,** *13*, 3567-3578.

151. Hirunsit, P.; Soodsawang, W.; Limtrakul, J., CO_2 Electrochemical Reduction to Methane and Methanol on Copper-Based Alloys: Theoretical Insight. *J. Phys. Chem. C* **2015,** *119*, 8238-8249.

152. Jiao, Y.; Zheng, Y.; Chen, P.; Jaroniec, M.; Qiao, S.-Z., Molecular Scaffolding Strategy with Synergistic Active Centers To Facilitate Electrocatalytic CO_2 Reduction to Hydrocarbon/Alcohol. *J. Am. Chem. Soc.* **2017,** *139*, 18093-18100.

153. Wang, Z.; Yuan, Q.; Shan, J.; Jiang, Z.; Xu, P.; Hu, Y.; Zhou, J.; Wu, L.; Niu, Z.; Sun, J.; Cheng, T.; Goddard, W. A., Highly Selective Electrocatalytic Reduction of CO_2 into Methane on Cu–Bi Nanoalloys. *J. Phys. Chem. Lett.* **2020,** *11*, 7261-7266.

154. Hendrik H. Heenen, G. K., † Haeun Shin,‡ Sean Overa,‡; Joseph A. Gauthier, F. J., ∗,‡ and Karen Chan∗,†, Mechanism for Acetate Formation in CO_2 Reduction on Cu: Selectivity Trends with pH and Nanostructuring Derive from Mass Transport. *Catalysis*.

155. Zhuang, T.-T.; Pang, Y.; Liang, Z.-Q.; Wang, Z.; Li, Y.; Tan, C.-S.; Li, J.; Dinh, C. T.; De Luna, P.; Hsieh, P.-L.; Burdyny, T.; Li, H.-H.; Liu, M.; Wang, Y.; Li, F.; Proppe, A.; Johnston, A.; Nam, D.-H.; Wu, Z.-Y.; Zheng, Y.-R.; Ip, A. H.; Tan, H.; Chen, L.-J.; Yu, S.-H.; Kelley, S. O.; Sinton, D.; Sargent, E. H., Copper Nanocavities Confine Intermediates for Efficient Electrosynthesis of C_3 Alcohol Fuels from Carbon Monoxide. *Nat. Catal.* **2018,** *1*, 946-951.

156. Wei, X.; Yin, Z.; Lyu, K.; Li, Z.; Gong, J.; Wang, G.; Xiao, L.; Lu, J.; Zhuang, L., Highly Selective Reduction of CO_2 to C_{2+} Hydrocarbons at Copper/Polyaniline Interfaces. *ACS Catal.* **2020,** *10*, 4103-4111.

157. Schmal, M.; Moya, S., Nanostructured Catalysts. In *Heterogeneous Catalysis and its Industrial Applications*, Springer: 2016; pp 285-327.

158. Bond, G. C.; Keane, M. A.; Kral, H.; Lercher, J. A. J. C. R., Compensation Phenomena in Heterogeneous Catalysis: General Principles and a Possible Explanation. *J. Catal. Rev.* **2000,** *42*, 323-383.

Chapter 2

Potential and Time Dependent Dynamic Nature of Oxide-derived PdIn Nanocatalyst During Electrochemical CO_2 Reduction

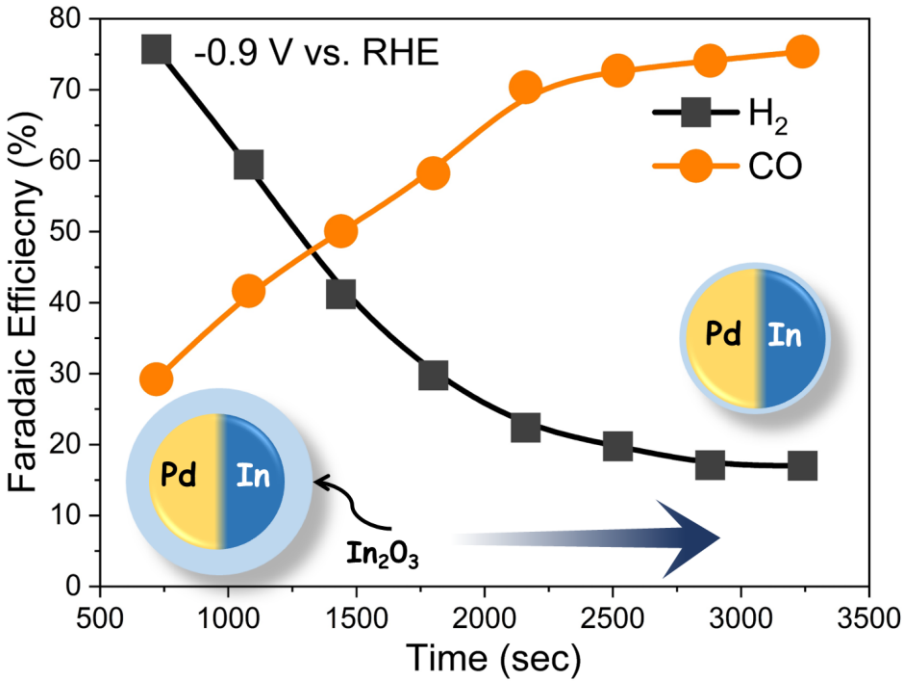

Bagchi, D.; Sarkar, S.; Singh, A. K.; Vinod, C. P.; Peter, S. C. *ACS Nano* **2022**. *16*, 6185–6196

Summary

Tremendous efforts have been carried out for designing efficient catalyst materials to selectively produce the desired product in high yield from CO_2 by the electrochemical process. In this chapter, we have focused on the production of simplest CO_2 reduced product i.e. CO and try to investigate how the product selctivity can be improved by constructing an interface between a metal-based alloy (PdIn) nanoparticle and an oxide (In_2O_3), which was synthesized by a facile solution method. The oxide-derived PdIn surface has shown excellent eCO_2RR activity and enhanced CO selectivity with Faradaic efficiency (FE) 92.13% at -0.9 V (vs. RHE). On the other hand, surface PdO formation due to charge transfer on the bare PdIn alloy reduces the CO_2RR activity. With the support of in situ (EXAFS and IR) and ex-situ (XPS, Raman) spectroscopic techniques, the optimum presence of the Pd-In-O interface has been identified as a crucial parameter for enhancing eCO_2RR towards CO in the reducing atmosphere. The influence of eCO_2RR duration is reported that affects the overall performance by switching the product selectivity from H_2 (from water reduction) to CO (from eCO_2RR) on the oxide-derived alloy surface. This work also succeeded in the multifold enhancement of the current density by employing the gas diffusion electrode (GDE) and optimizing its process parameters in a flow cell configuration.

In this chapter, DB (author) has conceptualized the idea and synthesised the catalysts, performed all the electrochemical studies (both flow cell and H-cell) and other ex-situ (XRD, Raman, XPS, TEM), in-situ studies (FTIR, EXAFS), analyzed the data, and written the draft. SS has helped in flow cell optimization. AKS assisted in in-situ EXAFS experiment. CPV procured the XPS data. SCP conceptualized the idea, supervised the work, reviewed and edited the draft.

Table of Contents

2.1 Introduction 63

2.2 Experimental Details 64

2.2.1 Chemicals and reagents 64

2.2.2 Synthesis of PdIn @In_2O_3 and PdIn 65

2.3 Characterization and Experimental Methods 65

2.3.1 Powder X-ray Diffraction (PXRD) 65

2.3.2 Transmission Electron Microscope (TEM) 66

2.3.3 Inductively coupled plasma atomic emission spectroscopy (ICP-OES) 66

2.3.4 X-ray Photoelectron Spectroscopy (XPS) 66

2.3.5 Raman Spectroscopy 66

2.3.6 X-ray Absorption Spectroscopy 66

2.3.7 Electrochemical CO_2 Reduction Reaction (eCO_2RR) 67

2.3.8 Reference electrode calibration for H-cell and flow cell configurations 67

2.3.9 Flow cell optimization for eCO_2RR in gas diffusion electrode configuration 68

2.3.10 Gaseous product analysis 69

2.3.11 Liquid product analysis 69

2.3.12 Preparation of Gas diffusion Electrode (GDE) 69

2.3.13 In-situ Electrochemical Attenuated Total Reflection Fourier Transform Infrared Spectroscopy (ATR-FTIR) 70

2.4 Results & Discussion 70

2.4.1 Synthesis and characterizations 70

2.4.2 Electrochemical CO_2 reduction (eCO_2RR) in H-cell 73

2.4.3 In situ electrochemical ATR-FTIR study 78

2.4.4 Local and surface electronic structures on eCO_2RR 80

2.4.5 High current density using microflow cell 88

2.5 Conclusion 89

2.6 References 90

2.1 Introduction

The real challenge in eCO_2RR lies in designing highly active and robust catalyst materials which will have optimized activation and adsorption of inert CO_2 molecules and other intermediate species.[1, 2] The major competing reaction during CO_2RR is the hydrogen evolution reaction (HER) which happens in a similar potential range.[3] P-block metals like In, Sb, Pb, Sn, Bi are considered to be efficient materials for CO_2 reduction because of their high overpotential HER.[4] Among them, due to the low toxicity Sn and In-based catalysts have been widely explored for CO_2 reduction.[5, 6] Production of CO with high selectivity via eCO_2RR is very advantageous as it can be easily separated and utilized as an all-round feedstock for the production of different kinds of high energy-density fuels and chemicals.[7] However, for the CO product to be transformed to value-added chemicals or fuels, it must react with H_2, which is usually obtained from some other processes. Instead, if an electrochemical process produces a mixture of CO and H_2 (syngas) with a particular CO:H_2 ratio, the mixture can be used directly in existing thermocatalytic processes like Fischer−Tropsch and methanol synthesis.[8]

Owing to it's this kind of nature of producing both CO and HCOOH depending on the potential regions Pd based catalysts have gained significant interest.[9] However, selective CO formation requires high overpotential due to the formation of Pd-CO bonds.[10] Kuhl et al. investigated the correlation between current density due to CO_2 reduction and the CO-binding strength of different metals and found that weak CO bonding metals (Ag, Au, and Zn) exhibit higher CO selectivity whereas metals (Pt, Fe, Ni), which binds CO strongly, give rise to lower CO selectivity.[11-13] Similarly, pure Pd-metal suffers from low CO selectivity and a high barrier of overpotential.[14-16] Thus, it has been a necessity to tune the electronic structure of Pd catalyst by means of different techniques like alloying,[17] intermetallics,[18] single atoms supported on N/C coordinated matrix,[18, 19] dual atomic site catalysts,[20] heterostructure,[21] core-shell structure,[22] etc. Notably, the introduction of secondary metal into Pd lattice reduces the possibility of multiple functionalities at interfacial sites by modifying the electronic structure of the pristine metal hence, modulating the d-band centre.[23] To improve the catalyst selectivity as well as the tolerance to CO-poisoning of Pd catalyst, Indium is a suitable non-expensive candidate which can drive the eCO_2RR process by stabilizing the formate intermediate.[24] Among all the bimetallic indium-based alloy catalysts, Cu-In has been well-studied, and it has been reported that alloying In with Cu lattice can alter the CO_2RR selectivity from HCOOH to CO.[25] DFT studies show that the adsorption characteristics of adjacent Cu sites have been greatly perturbed by the introduction of In, leading to enhanced adsorption of *COOH and

suppression of HER. It is previously reported that in aqueous electrolytes, In catalysts having surface oxides can dissociate water molecules and form surface In-OH which can interact with CO_2 to form In-CO_3^- that facilitates the formation of CO_2 reduced products.[26] Ding et al. have reported fully reduced electrodeposited metallic In in acetonitrile electrolyte containing imidazolium ionic liquid, which gives rise to CO selectivity.[27] Ye et al. reported PdIn/SiO_2 for the thermochemical CO_2 hydrogenation and production of CO due to the formation of PdIn bimetallic on a silica support.[28] But the real active site and surface oxidation state had not been extensively discussed in the previous case. However, there are no reports mentioning the behavior of Pd-In-O surface towards eCO_2RR in different applied potential and over the long electrolysis process, which may provide a pathway to comprehend how different CO_2 adsorbed species evolve during the electrolysis process.[29]

In this chapter, we demonstrate the design strategy for the formation of an interface made up of an alloy (PdIn) and oxide (In_2O_3) by optimizing various synthetic conditions. The eCO_2RR performance of both the PdIn and PdIn@In_2O_3 catalysts have been assessed, and it was found that activity of PdIn@In_2O_3 has been increased upon the formation of optimum oxide-derived surface, which drives the reaction towards the enhanced CO formation suppressing HER. In contrast, pure PdIn alloy (without In_2O_3) suffers from lower CO_2RR performance, and its activity decreases over time due to surface oxidation of the Pd site during electrolysis. In_2O_3 acts as protecting oxide layer for PdIn alloy and restricts the surface oxidation of Pd. The in situ time-dependent ATR FT-IR maps the real-time evolution of different adsorbed intermediates during eCO_2RR on the oxide-derived PdIn alloy surface. The oxidation state and local structure of the catalysts have been elucidated by XPS and EXAFS techniques. In situ EXAFS, powder XRD, Raman, and ex-situ XPS allow us to investigate the potential dependent surface electronic structure and compositions. The current density has been further enhanced by using a flow cell with the optimum gas-GDE-electrolyte interface. The utilization of GDE and flow cell not only increase the current density, it has also improved the overall performance of the CO_2 reduction supressing hydrogen evolution reaction as the CO_2 gas has been directly reduced here instead of reducing the dissolved CO_2 in electrolyte.

2.2 Experimental Details

2.2.1 Chemicals and reagents

The following chemicals were used: Indium nitrate ($InCl_3$, Alfa Aesar), potassium tetrachloropalladate(II) (K_2PdCl_4, Alfa Aesar), lithium triethylborohydride (Li(Et_3BH), Sigma Aldrich), polyvinyl pyrrolidine (PVP, Alfa Aesar), tetraethylene glycol (TEG, Merck). All the

chemicals used were commercially available certified reagents and used without further purifications unless mentioned.

2.2.2 Synthesis of PdIn @In_2O_3 and PdIn

In a stainless steel autoclave $InCl_3$ and K_2PdCl_4 were mixed in ratios of 1:1 (PdIn@In_2O_3) with respect to Pd:In, lithium triethylborohydride as the reducing agent ($Li(Et_3BH)$, 1.6 mL) and polyvinyl pyrrolidine (PVP, 70 mg) as the stabilizing agent. The mixture was dissolved in TEG (35 mL) and stirred for 1 hour. The sealed vessel was heated to 220 °C for 24 hours and was cooled to room temperature. To eliminate the in-situ formation of In_2O_3, controlled colloidal synthesis procedure has been employed keeping the precursor ratio same as 1:1 (PdIn). The colloidal synthesis was performed in N_2 atmosphere at 220 °C for 3 hours (**Figure 2.1.**). All the cases nanoparticles were obtained after centrifugation using ethanol and water at a centrifugal speed of 8000 rpm for 8 min for 4-6 times, and dried at 50 °C.

2.3 Characterization and Experimental Methods

2.3.1 Powder X-ray Diffraction (PXRD)

PXRD measurements were done at room temperature on a Rigaku Miniflex X-ray diffractometer with a Cu−K_α X-ray source (λ = 1.5406 Å), equipped with a position-sensitive detector in the angular range of $10° \leq 2\theta \leq 90°$ with the step size 0.02° and a scan rate of 0.5 s/step calibrated against corundum standards. The experimental XRD patterns were compared to the patterns simulated from the data reported in the literature.

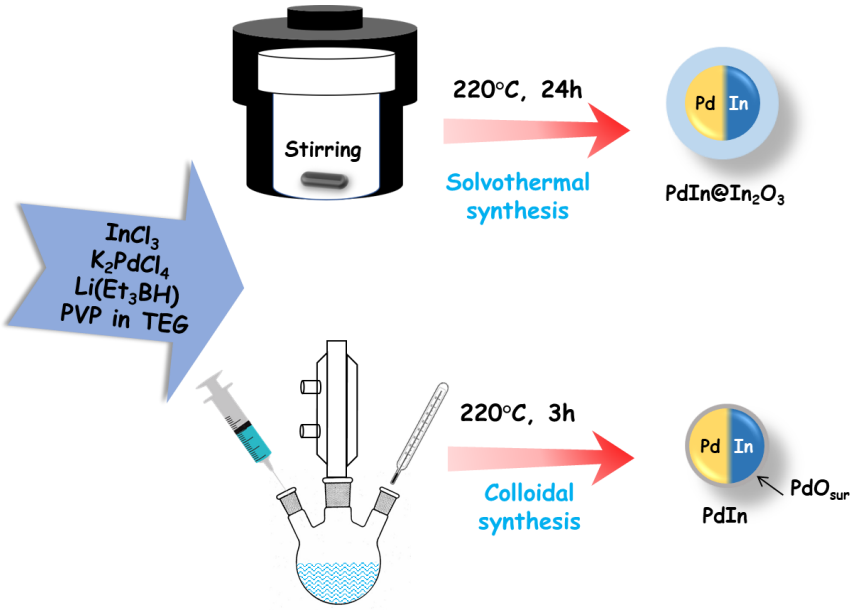

Figure 2.1. Schematic illustration of solvothermal and colloidal synthesis process of PdIn @In_2O_3 and PdIn, respectively, and the reaction conditions employed during the synthesis techniques.

2.3.2 Transmission Electron Microscope (TEM)

Transmission electron microscope (TEM), high-resolution TEM (HRTEM) images and selected area electron diffraction (SAED) patterns were collected using TECNAI and JEOL 200 kV TEMs. TEM samples for these measurements were prepared by sonicating the nanocrystalline powders in ethanol and dropping a small volume onto a carbon-coated copper grid.

2.3.3 Inductively coupled plasma atomic emission spectroscopy (ICP-OES)

ICP-OES was performed using a Perkin Elmer Optima 7000 DV instrument. The samples were digested in concentrated aqua regia, followed by dilution with distilled water. In a typical experiment, 2 mg of the sample was dissolved in 1 ml aqua regia and left overnight (12 hrs) for digestion. The digested sample was then diluted to 10 ml volume with deionized water. The solid particles were separated by thorough centrifugation before measurements.

2.3.4 X-ray Photoelectron Spectroscopy (XPS)

XPS measurements were carried out using Thermo K-alpha+ spectrometer using micro focused and monochromated Al Kα radiation with energy 1486.6 eV. The pass energy for the spectral acquisition was kept at 50 eV for individual core-levels. The electron flood gun was utilized for providing charge compensation during data acquisition. Further, the individual core-level spectra were checked for charging using C1s at 284.6 eV as standard and corrected if needed. The peak fitting of the individual core-levels was done using CASA XPS software with a Shirley type background.

2.3.5 Raman Spectroscopy

Raman experiments were performed in backscattering geometry using a custom-built Raman spectrometer equipped with a 532 nm laser excitation. Unpolarized Raman spectra were obtained with a laser power of ~2 mW at room temperature. Raman spectroscopy has been utilized to probe the In_2O_3 species which is the important active site for the catalytic conversion of CO_2 in this case. We have tested the electrode after carrying out CO_2 reduction at each potential.

2.3.6 X-ray Absorption Spectroscopy

X-ray absorption near-edge spectroscopy (XANES) and quick-Extended X-ray Absorption Fine Structure (quick-EXAFS) experiments at 300 K were performed at PETRA III, beamline P64, of DESY, Germany. Measurements of Pd-*K* and In-*K* at ambient pressure were performed in fluorescence as well as transmission mode using gas ionization chambers to monitor the incident and transmitted X-ray intensities. Monochromatic X-rays were obtained

using a Si (111) double crystal monochromator, which was calibrated by defining the inflection point (first derivative maxima) of Cu foil as 8980.5 eV. The beam was focused by employing a Kirkpatrick-Baez (K-B) mirror optic. A rhodium-coated X-ray mirror was used to suppress higher-order harmonics. A CCD detector was used to record the transmitted signals. Pellets for the ex-situ measurements were made by homogeneously mixing the sample with an inert cellulose matrix to obtain an X-ray absorption edge jump close to one.

2.3.7 Electrochemical CO_2 Reduction Reaction (eCO_2RR)

All the electrochemical measurements were performed using a CHI 6008E electrochemical workstation. Electrochemical CO_2 reduction reaction (eCO_2RR) is carried out in a three-electrode system, which involves a working electrode (glassy carbon or carbon cloth), counter electrode (graphitic carbon rod), and reference electrode (Ag/AgCl). The cell compartments are separated by a proton exchange membrane (Nafion 117), and the electrolyte used is 0.5M $KHCO_3$ solution. The electrolyte solutions were purged with CO_2 gas for 1 hour prior to the measurement. The electrocatalyst was prepared by dispersing 2 mg of catalyst and 0.2 mg of Vulcan (activated carbon) in 200 µL of mixed solvent solution (IPA:H_2O = 1:1 v/v) and 10 µL of 1 wt% nafion binder.

From the prepared catalyst 100 µL was coated on the carbon cloth and dried. The electrochemical cell was designed to have a large electrode area (0.7 cm x 0.7 cm) and a small electrolyte volume (10 mL) in each of the two compartments, along with a gas headspace of approximately 5 mL above the electrolyte on each side of the membrane. CO_2, regulated by a mass flow controller at 10 standard cubic centimeters per minute (sccm), flowed through the working electrode compartment of the cell during electrolysis. CO_2 flow through the cell was necessary in order to see large current efficiencies for CO_2 reduction products, presumably because of mass transport limitations in a quiescent cell. The flow rate of 10 sccm was chosen to ensure sufficient CO_2 transport to the surface while preventing interference from gas bubbles striking the surface. The gaseous product has been detected in the online mode with the help of gas chromatographic technique.

2.3.8 Reference electrode calibration for H-cell and flow cell configurations

The reference electrode (Ag/AgCl) has been calibrated with respect to standard hydrogen electrode and its calibration potential has been calculated from the average potential with respect to zero current in the hydrogen reduction/oxidation region as mentioned in the **Figure 2.2a-2.2b** (for H-cell) and **Figure 2.2c-2.2d** (for Flow-cell).

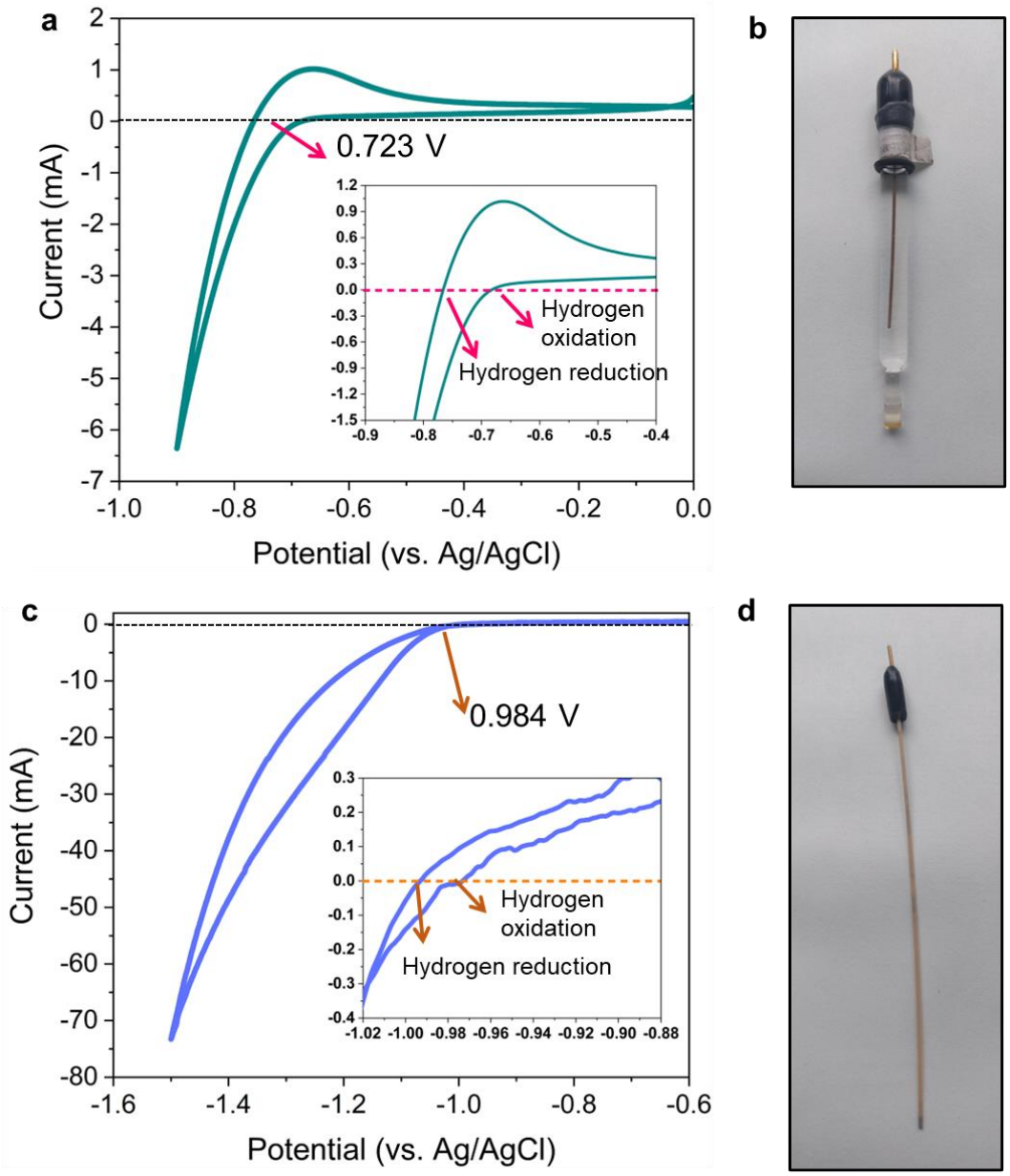

Figure 2.2. (a) RHE calibration of Ag/AgCl electrode under hydrogen saturated 0.5M $KHCO_3$. (b) Photograph of the Ag/AgCl electrode (reference) used in H-cell configuration. (c) RHE calibration of Ag/AgCl electrode under hydrogen saturated 1M KOH. (d) Photograph of the Ag/AgCl electrode (reference) used in flow cell configuration.

2.3.9 Flow cell optimization for eCO_2RR in gas diffusion electrode configuration

To increase the CO_2 diffusion and increase the overall current density, the electrochemical carbon dioxide experiments were carried out in a filter-press type Micro Flow Cell (Electrocell A/S), where a Ti sheet coated with Ir-MMO (iridium-mixed metal oxide) is used as an Anode plate (Electrocell S/A). An anionic exchange membrane (Fumasep FAB-PK-130) was employed in the case of CO_2RR in KOH medium. As discussed in **Figure 1.12**, the

cell has three compartments, viz. CO_2 gas compartment, cathodic and anodic compartment (**Figure 1.13**). The electrolyte was recirculated continuously into the cell (both in cathode and anode) by two separate peristaltic pumps (Ravel, RH-P100L-100) to accumulate liquid products. The flow of CO_2 was regulated by a mass flow controller (Brooks) at different flowrate (standard cubic centimeters per minute (sccm)) to optimize the most suitable flow rate, flowed through the working electrode compartment of the cell during electrolysis. For the final study, the gas flow is fixed to 50 sccm, and electrolyte flow was set to 20 sccm. To achieve C-based GDE, Freudenberg H23C2 has been used as the gas diffusion layer (GDL) and catalyst ink was coated with loading of 1mg/cm^2 (**Figure 1.14**).

2.3.10 Gaseous product analysis

All the gaseous products were analyzed by online 490-Micro Gas Chromatography (GC), which has four channels for detecting different gaseous products. Each channel has a specific column for analyzing relevant gases *viz*. Molsieve 5Å (for channel 1 and 2), Pora PLOT U (in channel 3) and CP-Sil 5 CB (for channel 4). The carrier gases were Ar and H_2. Each GC channel is equipped with a thermal conductivity detector (TCD). This detector responds to the difference in thermal conductivity between a reference cell (carrier gas only) and a measurement cell (carrier gas containing sample components).

Calculation of Faradaic Efficiency (FE) for gaseous products,

$$FE_{gas} = \frac{ppm \times flow\ rate \times \frac{number\ of\ electron \times Faraday\ contant \times pressure}{R \times Temperature}}{I_{average}} \times 100$$

Where ppm is the concentrations detected by GC, R is a gas constant (8.31 j K^{-1}mol^{-1}).

2.3.11 Liquid product analysis

The liquid products were analyzed by ^{1}H NMR (600 MHz, JEOL). The following protocol was applied. 500 mL of the electrolyte and 30 µL of an internal standard solution were transferred into a centrifuge tube. The internal standard solution consisted of 50 mM phenol (99.5 %) and 10 mM dimethyl sulfoxide (99.9 %) made in D_2O solvent. The mixture is transferred into an NMR tube. Solvent suppression was used to decrease the intensity of the water peak.

2.3.12 Preparation of Gas diffusion Electrode (GDE)

The PTFE-based GDE was fabricated by drop-casting the catalyst onto a cut piece of expanded polytetrafluoroethylene (ePTFE) (purchased from Sterlitech). The PTFE used here is aspire laminated and having proper hydrophobicity. It also has a polyester backer, and the pore size is 200 nm. The ePTFE was pretreated by first performing an RCA cleaning process

reported earlier.[30] It was first treated with a mixture of H_2O:HCl:H_2O_2 (5:1:1) at 80 °C for 2 minutes, then a mixture of H_2O:NH_4OH:H_2O_2 (5:1:1) for 2 minutes. After rinsing and drying, the catalyst was coated on that, and vulcan was coated successively at different coating amounts. Graphite powder was coated on top of that to enhance further conductivity of the GDE.

2.3.13 In-situ Electrochemical Attenuated Total Reflection Fourier Transform Infrared Spectroscopy (ATR-FTIR)

In-situ electrochemical FTIR spectroscopic studies were performed using a purged VERTEX FT-IR spectrometer equipped with the A530/P accessory and a mid-band MCT detector. A silicon hemispherical window (F530-8) was used with the working electrode placed gently on top of the window as the single reflection attenuated total reflection (ATR) accessory for FTIR study. The in-situ experimental setups is depicted in **Figure 1.15**. The measurement parameters were 4 cm^{-1} resolution and 100 scans. This setup enabled the detection of eCO_2RR intermediate formation and change of adsorption of various intermediates on the electrode surface and within the thin-layer electrolyte. In the beginning of the IR-experiment, we have taken a spectrum of the overall electrochemical cell and then take a background spectrum so that the contribution of the electrolyte can be subtracted in the next spectrum while applying the potential during performing CO_2RR. The spectra were analyzed by the OPUS software and the absorption spectra have been directly plotted at various potential and time.

2.4 Results & Discussion

2.4.1 Synthesis and characterizations

PdIn@In_2O_3 was synthesized by solvothermal synthesis, while PdIn was obtained by the colloidal synthesis in an inert atmosphere by keeping all the other conditions remain the same (**Figure 2.1**). In the case of colloidal synthesis, PdIn alloy nanoparticle has been formed. PdIn crystallizes in the FCC crystal structure, having $Fm\bar{3}m$ space group. Whereas solvothermal synthesis leads to the formation of In_2O_3 along with FCC PdIn alloy, which was confirmed from the powder XRD of PdIn@In_2O_3 and PdIn (**Figure 2.3a**). In_2O_3 crystallizes in Sm_2O_3 type structure having $I2_13$ space group, which is confirmed from the corresponding diffraction peaks of (222), (400), and (622) in the XRD pattern of PdIn@In_2O_3. The XRD peak corresponding to major crystallographic planes of FCC structure i.e. (111) and (200) of Pd have been shifted to lower 2θ value indicating incorporation of indium (larger atomic radius 220 *pm*) into Pd lattice (smaller atomic radius 163 *pm*) (**Figure 2.3b-c**).

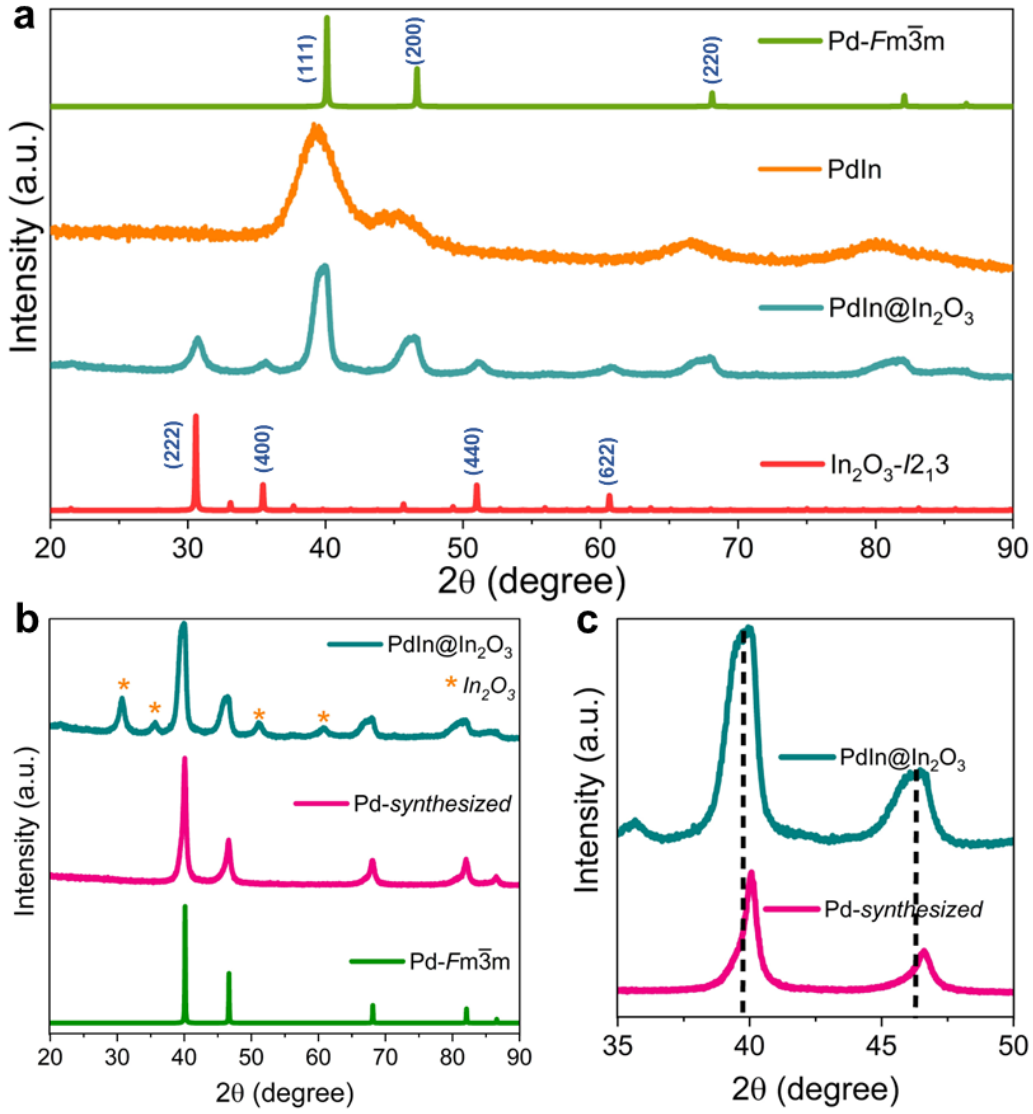

Figure 2.3. (a) Comparison of the powder XRD patterns of PdIn@In_2O_3 and PdIn with the simulated XRD patterns of Pd and In_2O_3. (b) Comparison of the powder XRD patterns of PdIn@In_2O_3 and as synthesized Pd nanoparticle with the simulated XRD patterns of Pd. (c) Zoomed image of the two major crystallographic peaks corresponding to (111) and (200) of Pd.

TEM images and particle distribution curve of PdIn@In_2O_3 (**Figure 2.4a-b**) and PdIn (**Figure 2.4c-d**) indicate the proper distribution of ~5 nm-sized particles of PdIn@In_2O_3 and slightly lesser (~4 nm) sized particle in case of PdIn catalyst, which is also reflected as the XRD peaks due to its broadening (**Figure 2.3a**). High-resolution TEM image of PdIn@In_2O_3 depicts the presence of (111) plane of PdIn alloy lattice having d-spacing 0.247 nm and (310) plane of In_2O_3 having d-spacing of 0.287 nm (**Figure 2.4e**) whereas PdIn alloy contains plane (111) having d-spacing of 0.249 nm (**Figure 2.4f**).

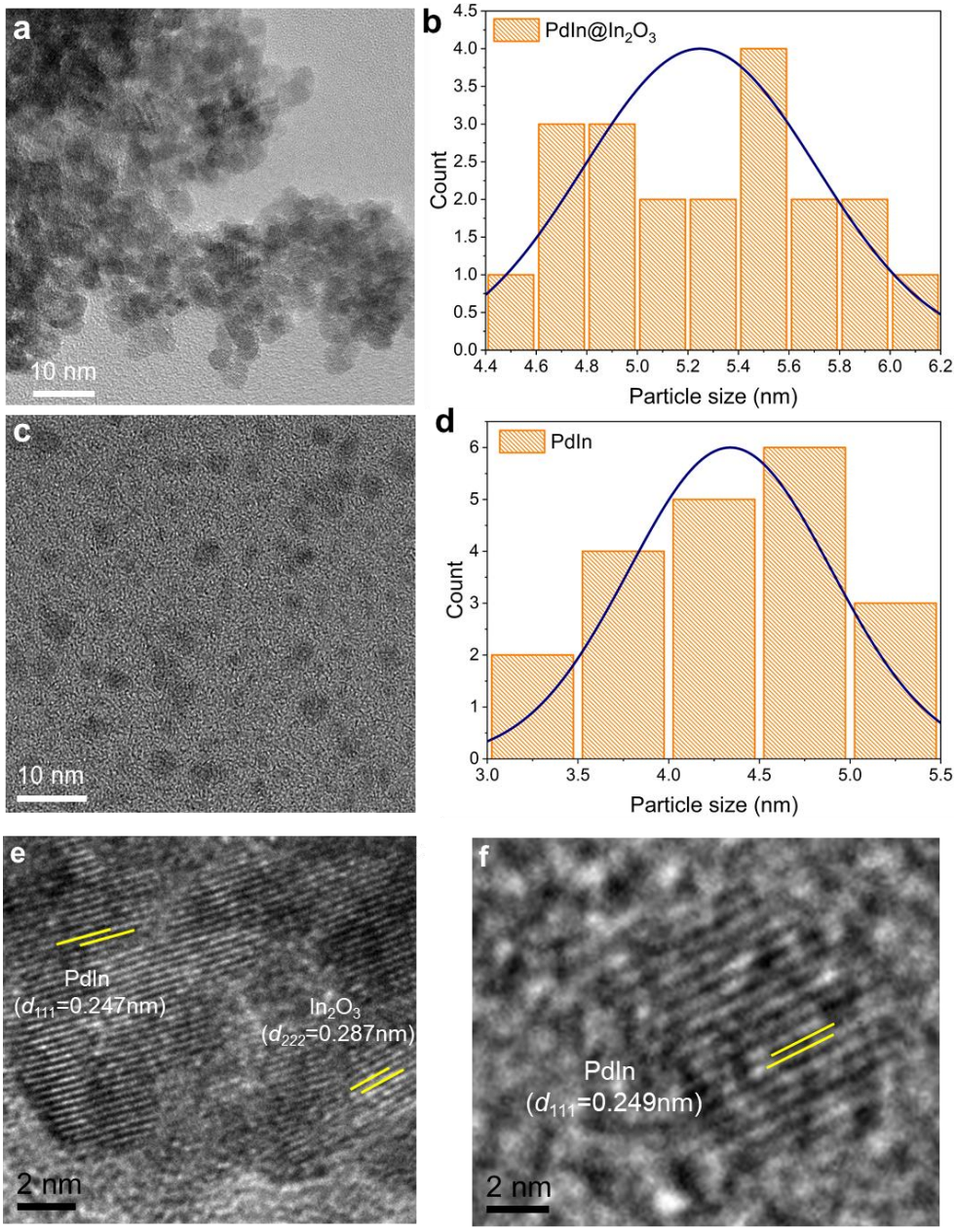

Figure 2.4. TEM images of (a) PdIn@In_2O_3 and (b) the histogram profile of particle distribution. TEM images of (c) PdIn and (d) the histogram profile of particle distribution. High resolution TEM image of (e) PdIn@In_2O_3 and (f) PdIn.

TEM color mapping image of PdIn@In_2O_3 depicted the uniform distribution of individual elements Pd, In, and O on the surface of the nanocatalyst (**Figure 2.5a-d**). Furthermore, the selected area electron diffraction (SAED) patterns of PdIn@In_2O_3 were indexed with (222) and (400) planes of In_2O_3 and (111), (200) planes of PdIn alloy (**Figure 2.5e**). On the other hand, SAED patterns presented in **Figure 2.5f** confirm the presence of (111), (200), (220), and (311) planes. The elemental composition of both the catalysts has been verified using ICP-OES (**Figure 2.6a-b** and **Table 2.1**).

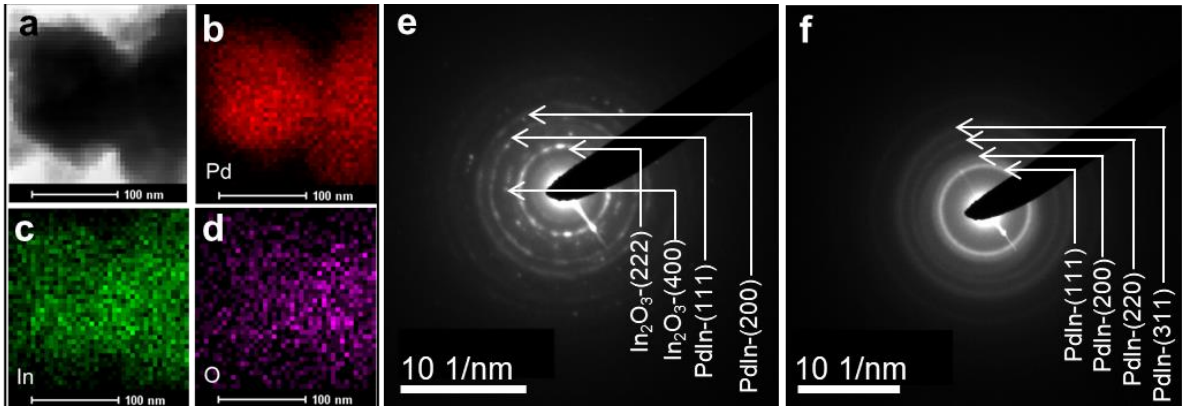

Figure 2.5. (a)-(d) TEM color mapping shows the proper distribution of different elements like Pd, In, and O on the surface of PdIn@In_2O_3. Selected area electron diffraction (SAED) pattern of (e) PdIn@In_2O_3 and (f) PdIn.

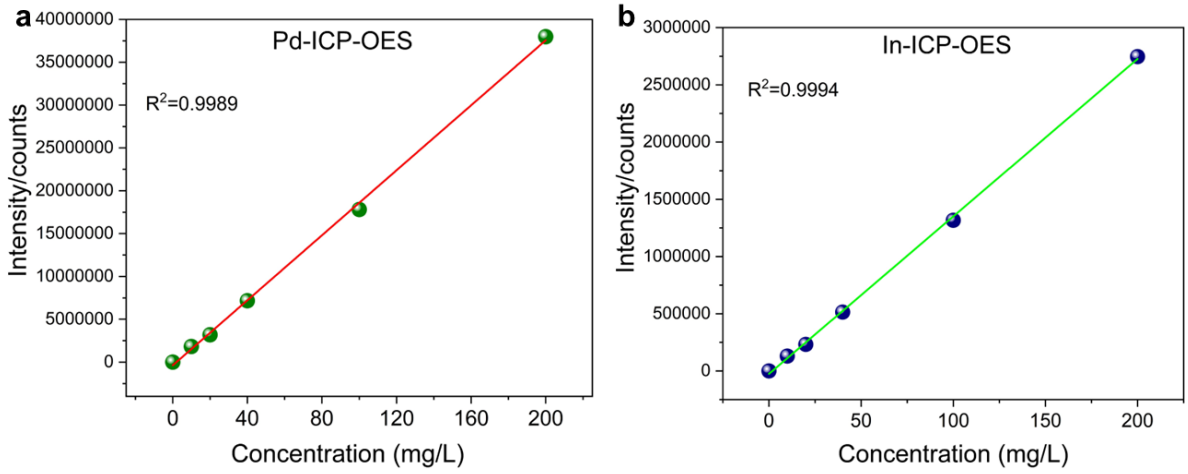

Figure 2.6. ICP-OES Calibration curves for (a) Pd and (b) In quantification at different concentration range.

Tables 2.1. Calculation of amount of Pd and In present in PdIn @In_2O_3 and PdIn catalysts through ICP-OES.

Sample	Elements	mg/L	Atomic %
PdIn @In_2O_3	Pd	81.40	51.694
	In	65.52	48.305
PdIn	Pd	51.18	55.82
	In	43.40	44.18

2.4.2 Electrochemical CO_2 reduction (eCO_2RR) in H-cell

Electrochemical CO_2RR was carried out on both the PdIn and PdIn@In_2O_3 catalysts in 0.5 M $KHCO_3$ with continuous CO_2 purging at 20 cm^3/min flow rate in the homemade H-type

electrochemical cell. Toray carbon paper was used as the working electrode with a surface area of 1 cm^2. In the first step, a linear sweep voltammetric study has been performed in the CO_2RR potential region, and it was found that in the CO_2 atmosphere, PdIn@In_2O_3 exhibited much lower current densities in CO_2 atmosphere compared to N_2-saturated 0.5 M $KHCO_3$, suggesting that in the N_2 atmosphere, HER is extremely favorable in this kind of Pd-based catalyst (**Figure 2.7a**).[31] The hump at around -0.3V (vs. RHE) indicates the CO adsorption in CO_2RR conditions.[32] The obtained higher obtained current density of PdIn compared to that of PdIn@In_2O_3 under CO_2RR condition may be attributed to the fact that the hydrogen evolution rate is high in the case of PdIn as the CO_2RR activity was found to be higher in the PdIn@In_2O_3 catalyst (**Figure 2.7b**).

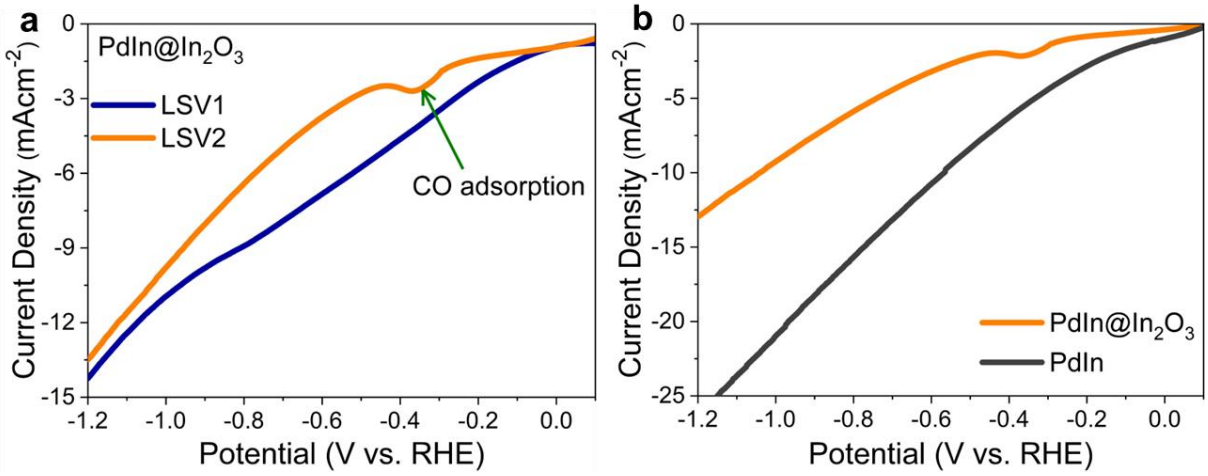

Figure 2.7. (a) Linear sweep voltammogram (LSV) taken in eCO_2RR condition and in N_2 atmosphere PdIn@In_2O_3. (b) Comparison of LSVs of PdIn@In_2O_3 and PdIn catalysts in the eCO_2RR condition.

For the evaluation of the electrochemical behavior and the quantification of CO_2-reduced products, chronoamperometric test at different potentials (-0.5 V, -0.7 V, -0.9 V, and -1.1 V vs. RHE) was performed in CO_2 saturated 0.5 M $KHCO_3$ solution for 1h under the CO_2 flow of 20 cm^3/min. The detection and quantification of gaseous products were performed by GC (**Figure 2.8**) and liquid products by NMR (**Figure 2.9**). **Figure 2.10a** shows the potential dependent average FE of CO, H_2, and HCOOH on PdIn@In_2O_3 catalyst, and it is found that maximum average FE of CO_2 reduced product (FE_{CO}: 54.4%) has been achieved at -0.9V, which is double compared to PdIn alloy catalyst (FE_{CO}: 27.6% at -0.9V), as presented in **Figure 2.10b**.

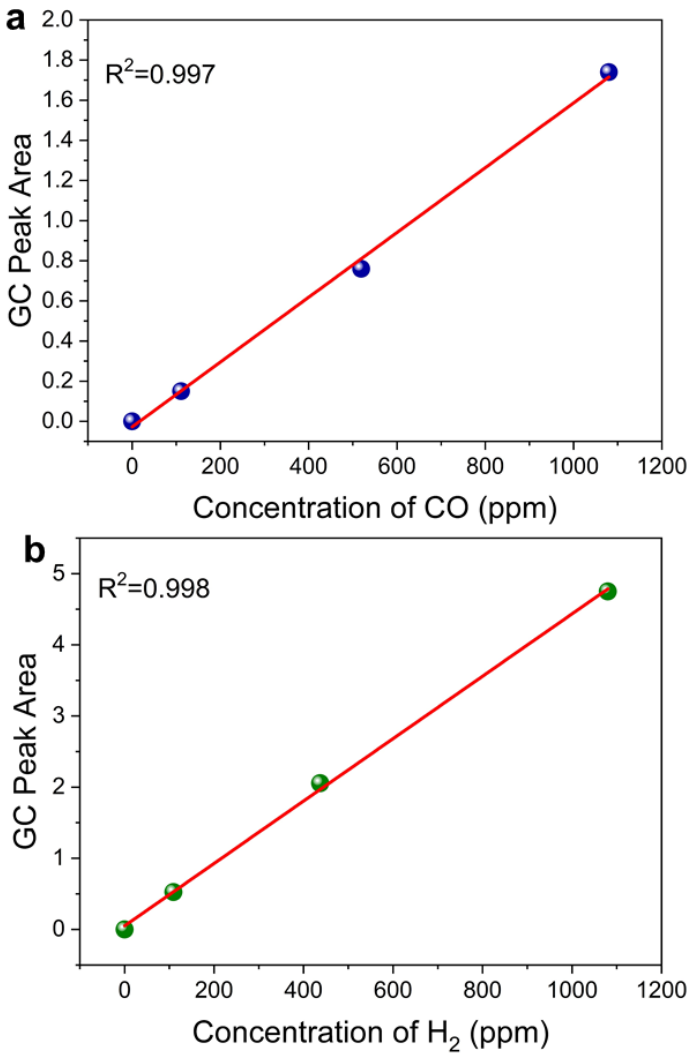

Figure 2.8. GC Calibration curves for (a) CO and (b) H_2 quantification at different concentration (ppm) range.

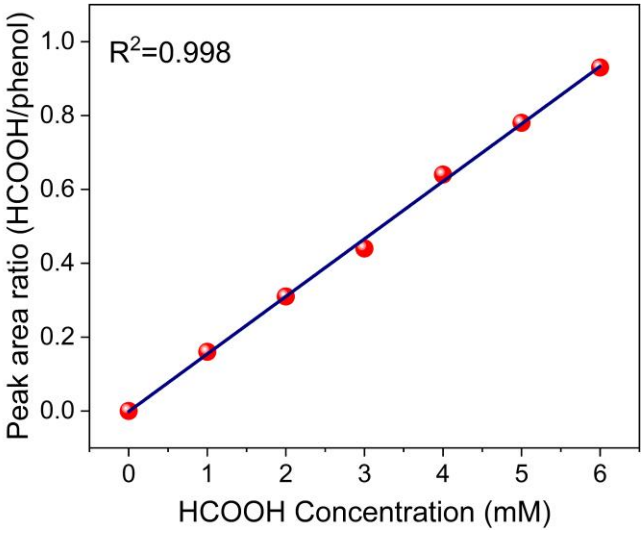

Figure 2.9. NMR Calibration curves for HCOOH quantification at different concentration (mM) range.

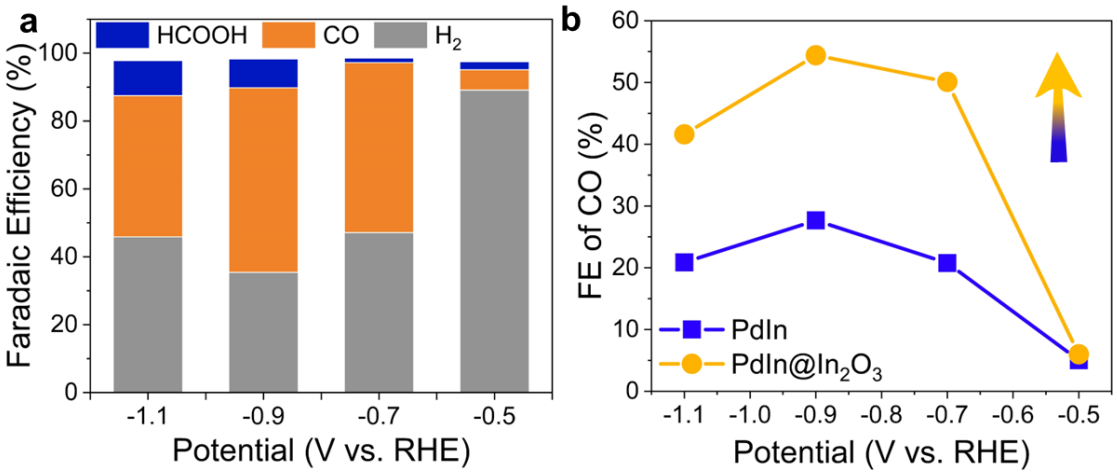

Figure 2.10. (a) Average Faradaic efficiency (FE) for H_2, HCOOH, and CO at the different applied potentials on PdIn@In_2O_3. (b) comparison of FE of CO on PdIn@In_2O_3 and PdIn catalysts.

In order to understand the influence of time on the eCO_2RR, we have performed the experiment using PdIn@In_2O_3 for a longer duration (~54 mins) and calculated FE of CO and H_2 at regular intervals. Interestingly, the production of CO has been gradually increased with concomitant suppression of hydrogen production as time progressed (**Figure 2.11**). While the FE_{CO} is found to be 29.2% at 12 min, it has increased to the value of 75.36% at 54 min of electrolysis at -0.9V. On the contrary, the FE of H_2 has decreased from the value of 75.7% (at 12 min) to 17.01% (at 54 min). This indicates that PdIn@In_2O_3 catalyst modifies its surface to an oxide-derived reduced state, which has an optimum Pd-In-O interface, responsible for better CO production in the reducing atmosphere during CO_2 reduction.

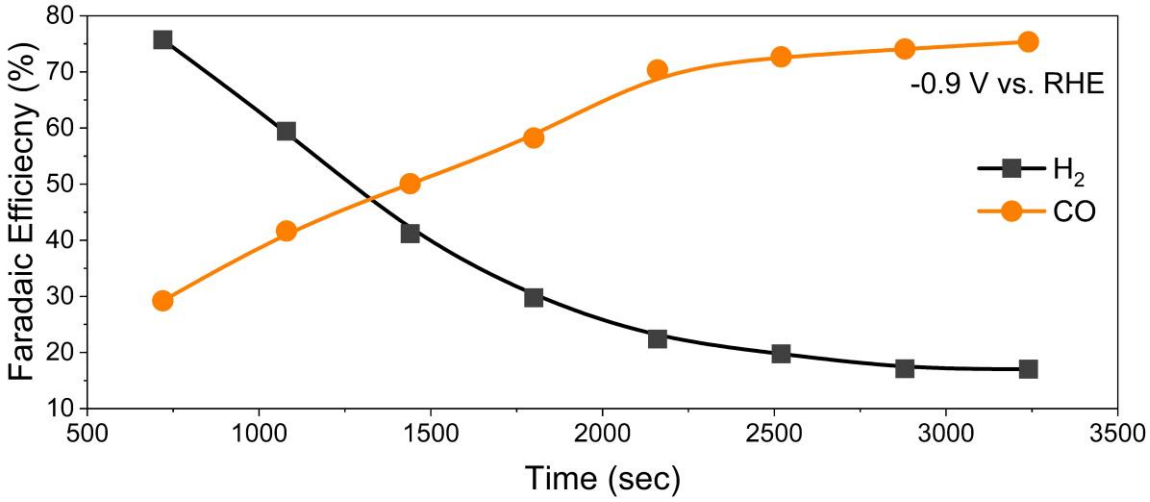

Figure 2.11. Time-dependent evolution of H_2 and CO at potential -0.9V (vs. RHE) on PdIn@In_2O_3 surface.

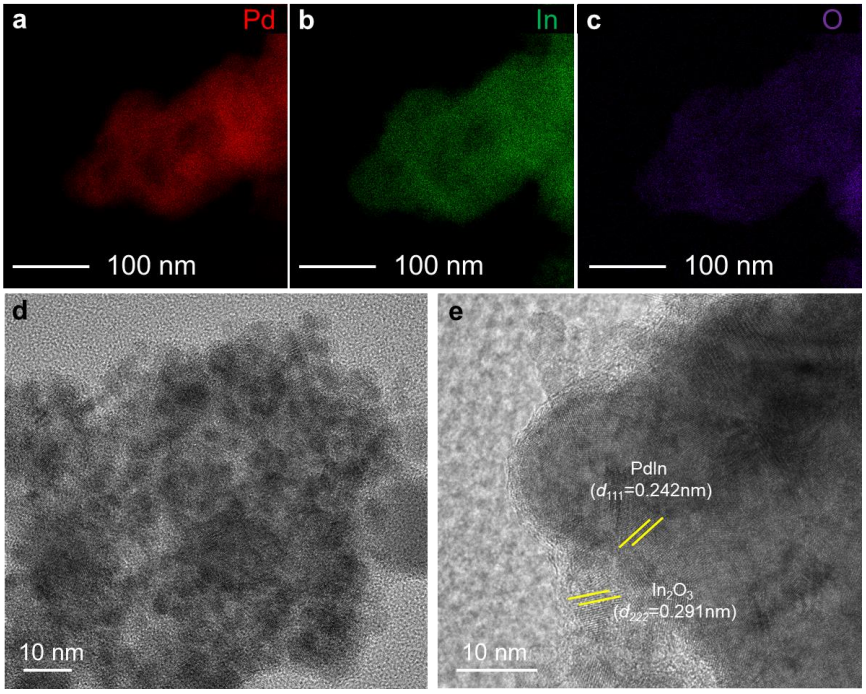

Figure 2.12. Post electrochemical TEM color mapping shows the distribution of different elements like (a) Pd, (b) In, and (c) O on the surface of PdIn@In_2O_3 after CA at -0.9V (vs. RHE) for 1 h electrolysis during electrochemical CO_2 reduction. (b) Low-resolution TEM and high-resolution TEM of the catalyst after performing electrolysis in the same condition.

The post electrochemical elemental mapping shows uniform distribution of Pd, In and O (slightly less than it was before catalysis) (**Figure 2.12a-c**). The low-resolution TEM image further shows that the PdIn and In_2O_3 phases are homogeneously distributed over the surface (**Figure 2.12d**). The interface between PdIn alloy and In_2O_3 has been found to be very clear in HRTEM image (**Figure 2.12e**).

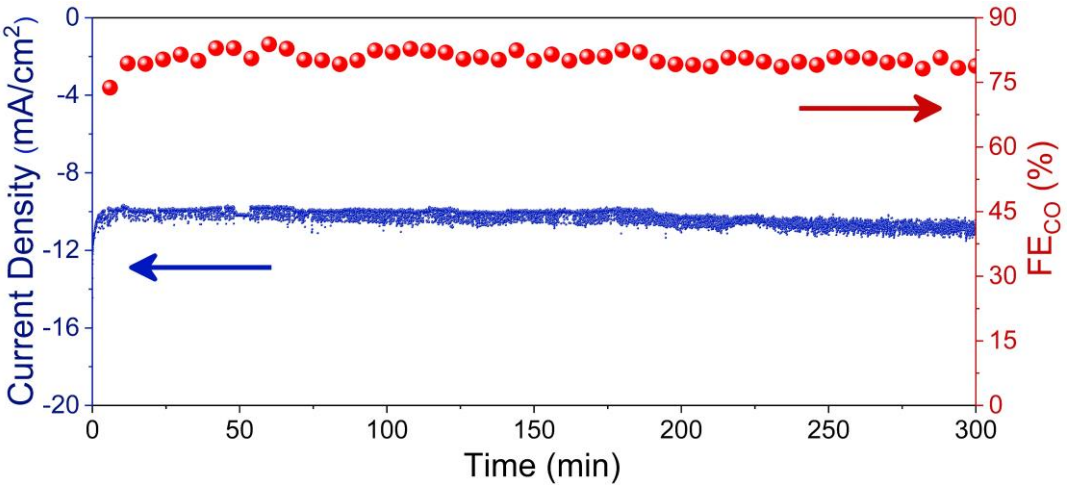

Figure 2.13. Long-term chronoamperometry study and the obtained FE at each time interval on PdIn@In_2O_3 during CO_2RR condition at -0.9V after activating the catalysts at -0.9V for 5h.

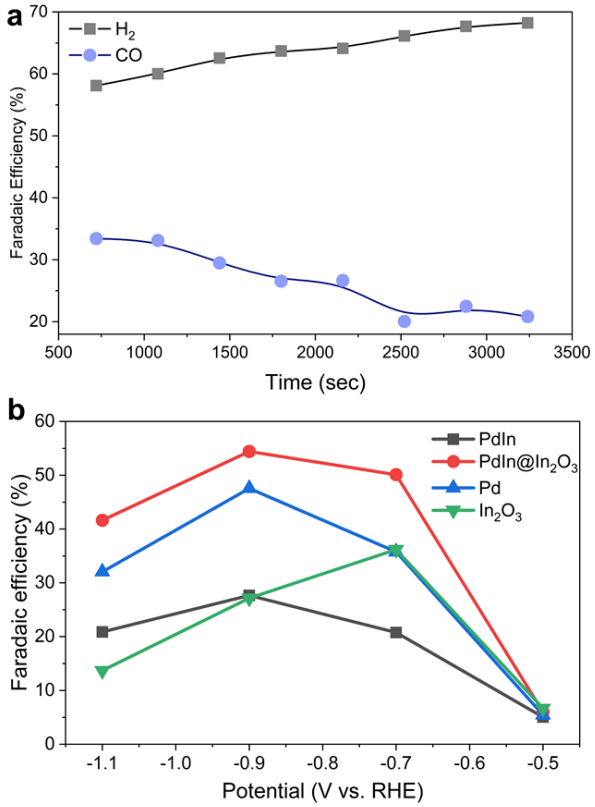

Figure 2.14. (a) Time dependent evolution of H_2 and CO at potential -0.9V (vs. RHE) on PdIn surface. (b) comparison of FE of CO on PdIn@In_2O_3 and PdIn catalysts with pristine Pd and In_2O_3 nanoparticle at different potential.

The catalytically modified oxide-derived PdIn alloy was found to be extremely stable and produced higher CO selectivity (~80%) during the CA study at -0.9 V for a long time (300 min), as shown in **Figure 2.13**. On the other hand, PdIn produces more hydrogen as time increases time with the consequent reduction in CO selectivity (**Figure 2.14a-b**). The catalytic activity has also been compared with that of pristine Pd and In_2O_3 nanoparticles applying similar conditions and found that Pd and In_2O_3 both have lower CO selectivity than that of PdIn@In_2O_3.

2.4.3 In situ electrochemical ATR-FTIR study

In situ ATR-FTIR spectroscopy was performed to monitor the real-time evolution of possible intermediates formed during CO_2RR and to propose the reaction mechanism during the electrochemical reduction of CO_2 on the PdIn and PdIn@In_2O_3 catalysts in CO_2 saturated 0.5 M $KHCO_3$ solutions.[33] **Figure 2.15a** displays a series of spectra taken while CO_2RR was performed at -0.3V, -0.5V, -0.7V, and -0.9V (vs. RHE) on PdIn@In_2O_3 surface. The peak around 1580 cm^{-1} corresponds to the crucial COOH* intermediate. The peak at 1280 cm^{-1} is the characteristic peak of C-OH stretch.[34]

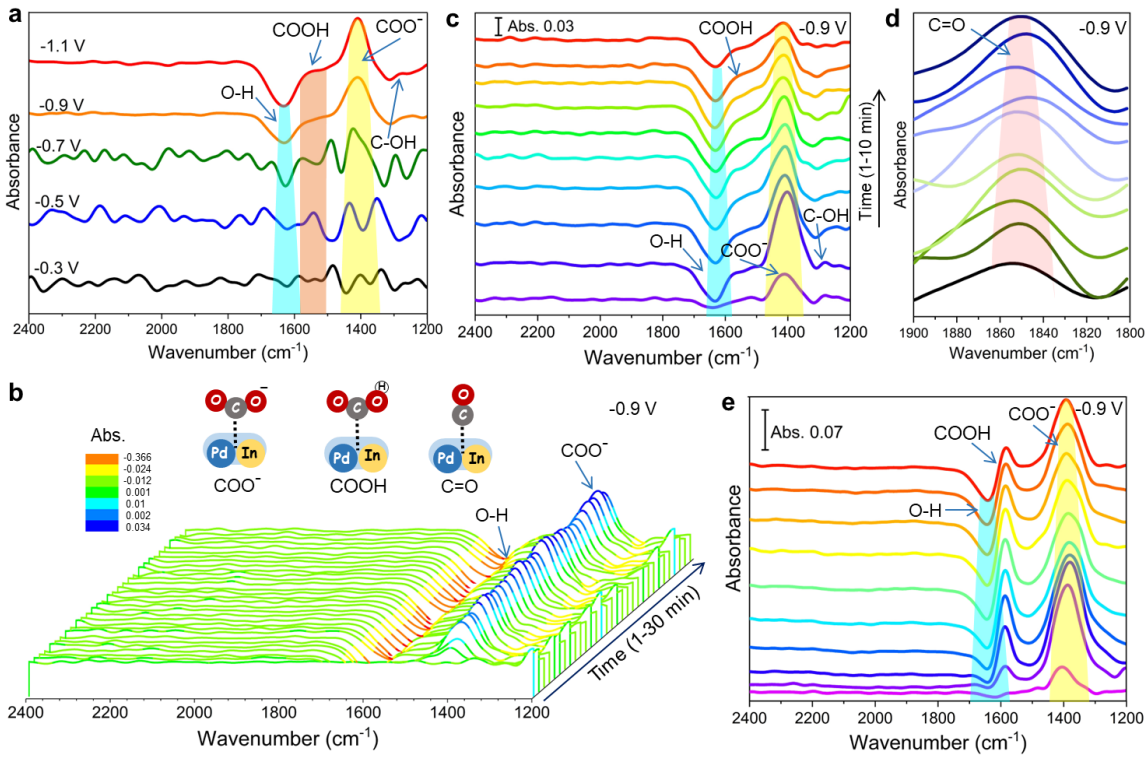

Figure 2.15. (a) In situ infrared (IR) spectra along with the binding mode of different intermediates adsorbed on catalyst surface during eCO_2RR performed on $PdIn@In_2O_3$ catalyst, Time-dependent in situ IR spectra taken at -0.9V (vs. RHE) in eCO_2RR condition on $PdIn@In_2O_3$,during first CA (b) and (c) during the second CA at -0.9V. (d) Time-dependent evolution of C=O peak during the CA taken on $PdIn@In_2O_3$ catalyst in the eCO_2RR conditions and (e) Time-dependent in situ infrared spectra were taken at -0.9V on the PdIn alloy catalyst.

The inverse peak at around 1630 cm^{-1} represents the H−O−H bend of water which also splits in the reducing atmosphere, and the peak reverse band 3300 cm^{-1} represents the stretching vibration of O-H bonds of water.[35, 36] The intensity of these two bands is intensified at -1.1V than at -0.9V indicates predominant HER in the extremely higher potential. The inverse peak likely to be broadened in the higher potential indicates a combination of the H−O−H bend and a C=O asymmetric stretching at 1660 cm^{-1}, which corresponds to the COOH* intermediate.[34, 37, 38] The peaks at 1280 and 1660 mutually indicate the formation of COOH* on the surface of the catalyst.[39] Literature reports suggest that the band at around 1407 cm^{-1} corresponds to the symmetric stretch of $*COO^-$ and C-O stretching of *COOH on the catalyst surface, which has become prominent in the relatively higher reduction potential (-0.9V-1.1V).[38, 40] The formation of CO can not be achieved from the O-bound COOH intermediate. So, it can be concluded that the C atom of COO^- is directly bonded to the catalyst surface.[1, 41] As displayed in **Figure 2.15a**, the IR intensity corresponding to the peak of C-O bond of the C-bound COO^- at 1407

cm^{-1} gradually increases with the increase of the applied cathodic potentials as the reaction proceeds further, indicating that more CO_2 was being reduced at the higher cathodic potential (-0.9V), where FE of the CO_2 reduced product was found to be higher than -0.3V. In **Figure 2.15b**, the peak intensity of the C-O bond increases over the period of time in the first chronoamperometric study at -0.9 V (vs. RHE). As observed from the CO_2RR activity in the initial CA, the production of CO has been increased, and subsequently, the hydrogen evolution is also decreased, which has been reflected in the higher evolution of COO^- ion in the initial CA in the **Figure 2.15b**. As it can be seen in the second CA (**Figure 2.15c**), the evolution of C-O and C=O peaks corresponding to the formate slowly decreasing, which is the direct indication of conversion of the adsorbed species to CO_2 reduced products, which is reflected in the product distribution and FE calculation. **Figure 2.15d** indicates the proper evolution of catalyst-CO stretch on the catalytic surface at -0.9 V (**Tables 2.2**).[42, 43] In the case of PdIn alloy catalyst, the intensity of *COOH and $*COO^-$ has not been changed much over time, as shown in **Figure 2.15e** reflects its product distribution also.

Tables 2.2. Vibrational frequencies of various surface bound species during CO_2 reduction on PdIn@In_2O_3.

Sl No	Vibrational frequency (cm^{-1})	Moiety	Vibration mode	Ref.
1.	1288	COOH	C-O-H stretch	34
2.	1630	H_2O	H-O-H bend	36, 43
3.	3300	H_2O	O-H stretch	36, 43
4.	1660	COOH	C=O asymmetric stretch	37, 38
5.	1407	COO^-	C-O symmetric stretch	38, 40
6.	1850	CO	Metal-C=O	42, 43

2.4.4 Local and surface electronic structures on eCO_2RR

To understand the surface composition and the electronic state of PdIn and PdIn@In_2O_3 catalysts, high-resolution XPS and XAS have been performed. The Pd 3d core-level XPS spectra of PdIn@In_2O_3 are dominated by the characteristic peak at binding energy position (335.7 eV) corresponding to metallic Pd $3d_{5/2}$ state of Pd-alloy and substantially low quantity (<10%) of surface Pd-oxide (BE can also be seen as presented in **Figure 2.16a)**.[44] On the contrary, core level Pd 3d XPS of the PdIn alloy catalyst shows the characteristic Pd $3d_{5/2}$ peak at relatively higher binding energy along with a substantial amount (20%) of surface oxide (PdO) species.[45]

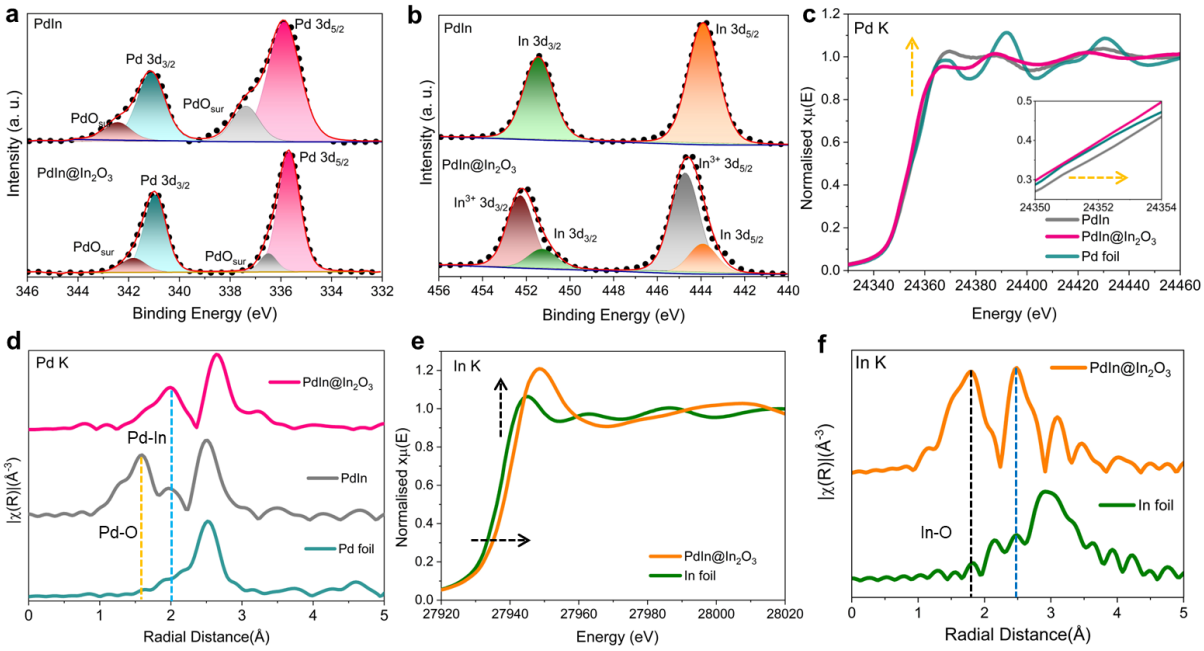

Figure 2.16. XPS spectra for PdIn and PdIn@In_2O_3 including (a) Pd 3d core level and (b) In 3d core level. (c) Comparison of normalized XANES spectra of Pd *K*-edge of PdIn and PdIn@In_2O_3 with the respective metal foil. Fourier transformed R-space data showing the radial distances of (d) Pd *K*-edge. for PdIn and PdIn@In_2O_3 with the reference samples. (e) Comparison of normalized XANES spectra of In *K*-edge of PdIn@In_2O_3 with the respective metal foil. (f) Fourier transformed R-space data showing the radial distances of In-O and In-In bonds for PdIn@In_2O_3 and the reference In foil.

This suggests that PdIn alloy catalyst has a significant amount of surface PdO whereas, in the case of PdIn@In_2O_3, surface PdO was found to be negligible.[46] In core levels of PdIn alloy is dominated by the existence of metallic In $3d_{5/2}$ with a binding energy of 443.82 eV whereas In 3d core level of PdIn@In_2O_3 consists of the characteristic peak at binding energy of 444.58 eV corresponding to In_2O_3 with a minor contribution from metallic In features from PdIn alloy environment (**Figure 2.16b**).[44, 47] The overall peak position and line shapes of Pd 3d and In 3d suggest that Pd in PdIn@In_2O_3 is covered by In_2O_3 at the surface and is being protected from surface oxidation. On the other hand, Pd in PdIn bare alloy is exposed on the surface and easily gets oxidized and formed PdO_{sur}. XANES data for both the catalysts have been analyzed to understand the oxidation state and local electronic structure. In **Figure 2.16c**, the absorption edge corresponding to the white line of Pd K edge involves 1s→4p dipole transition, shifts towards higher photon energy value in case of PdIn than the Pd foil and PdIn@In_2O_3 catalyst, indicates the presence of higher valent Pd species in the PdIn catalyst, which is corroborating the XPS data.[48] The presence of PdO in the PdIn catalyst has also been

verified in the Fourier transformed R-space data of Pd K edge where the characteristic bond at 1.586 Å corresponding to Pd-O has been observed along with the Pd-In bond (at 1.96Å) as shown in **Figure 2.16d**.[49] The XANES of In-K edge indicates that In has a higher oxidation state than that of In foil (**Figure 2.16e**).[50] Fourier transformed R-space data also suggests the proper In-O bond present at around 1.6 Å in the PdIn@In_2O_3 sample (**Figure 2.16f**).[51]

The real-time in situ XAS study has also been performed at a different time interval to see the electronic structural evolution and charge transfer kinetics between Pd and In spite of the catalysts.[52, 53] The time-dependent XANES spectra of In K-edge of PdIn@In_2O_3 sample at -0.9V potential shows that the white line intensity for In decreases indicates the increase in the electron density on the In site as CO_2RR progresses (**Figure 2.17a**). During the CO_2RR structure, the bond distance corresponding to In-O bond does not change much, as presented in **Figure 2.17b**. On the other hand, the white line intensity of Pd K-edge XANES spectra does slightly increase due to the charge transfer process during CO_2RR (**Figure 2.18a**). This charge transfer process does not change the bulk structure of PdIn, and consequently, there is negligible change in the bond distance in the FT-transform R-space spectra in **Figure 2.18b**. On the contrary, in the case of bare PdIn catalyst, during the staring of electrolysis, there is a decrease of the white line due to reduction of Pd site as mentioned in **Figure 2.18c**. But as the white line has increased upon the reaction progresses due to charge transfer. During the catalysis process, the pristine bulk structure and the bond distances do not change much, as seen in **Figure 2.18d**, and only the surface is being affected, which has been characterized by the XPS technique discussed later.

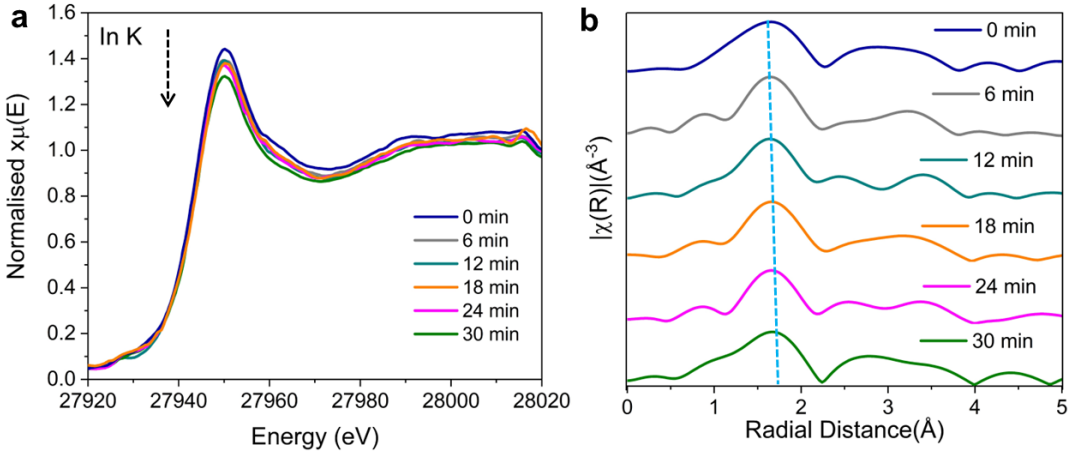

Figure 2.17. In-situ XAS performed during CO_2RR condition on PdIn@In_2O_3 catalyst. (a) time-dependent XANES spectra OF In *K*-edge obtained during chronoapmerometric study at -0.9 V. (b) Fourier transformed R-space data showing the radial distances of In-O bond at different time during CO_2RR.

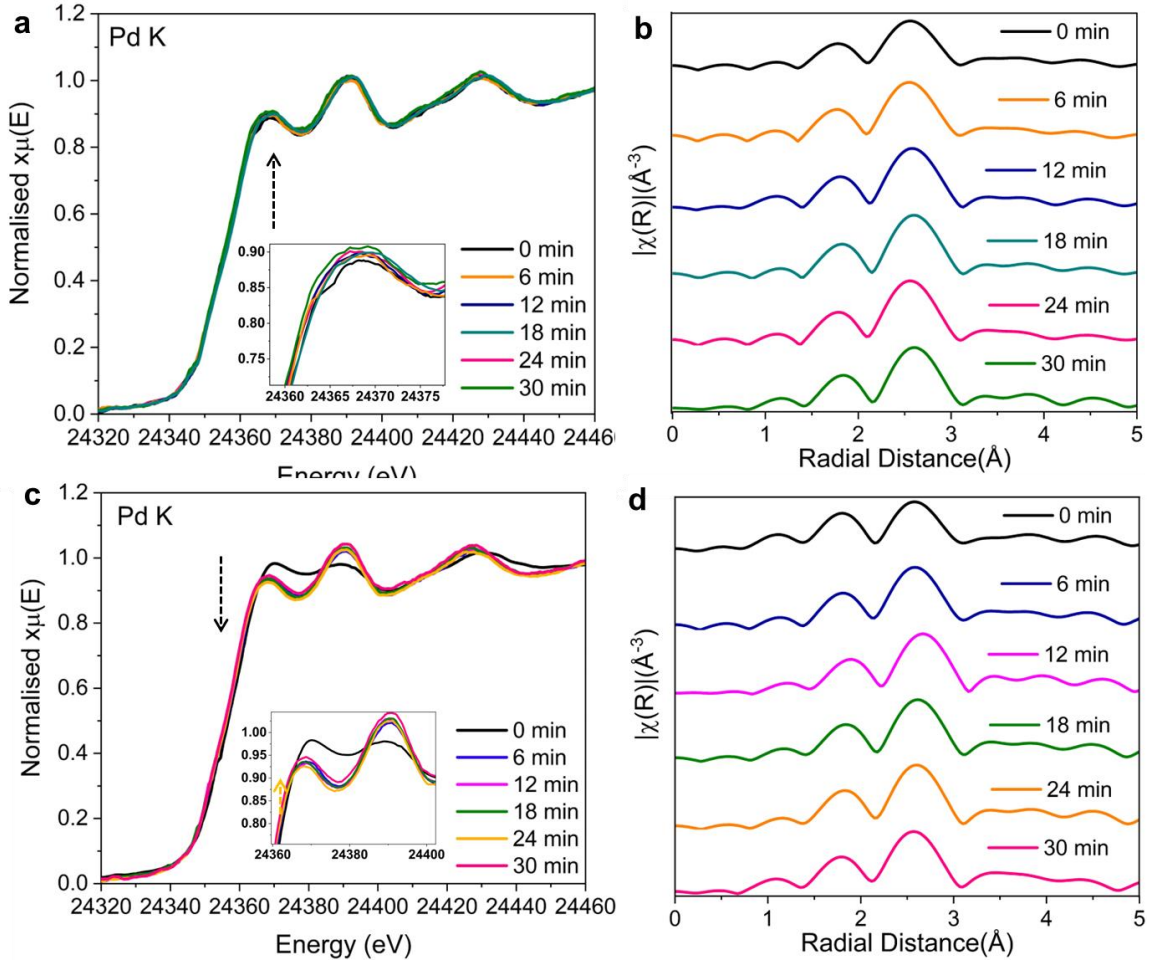

Figure 2.18. In-situ XAS performed during CO_2RR condition on PdIn@In_2O_3 catalyst. (a) time-dependent XANES spectra OF Pd *K*-edge obtained during chronoapmerometric study at -0.9 V. (b) Fourier transformed R-space data showing the radial distances of different bonds during CO_2RR. In-situ XAS performed during CO_2RR condition on PdIn catalyst. (c) time-dependent XANES spectra OF Pd *K*-edge obtained during chronoapmerometric study at -0.9 V. (d) Fourier transformed R-space data showing the radial distances of different bonds during CO_2RR.

Potential dependent XPS of both PdIn alloy and oxide-derived samples were studied to map the electronic structure and oxidation state during CO_2 reduction under each reduction potential. PdIn@In_2O_3 sample shows the core level In 3d peak at 444.58 eV corresponding to In_2O_3, which shifted to lower binding energy as the negative potential increased from -0.5 V to -1.1 V (vs. RHE) (**Figure 2.19a**). The peak at 335.7 eV of Pd core level XPS signal is also shifted to lower binding energy at higher reduction potential (**Figure 2.19b**) and optimum binding energy close to metallic Pd was achieved at an extremely higher reduction potential (-1.1V) (**Figure 2.19c, Table S4**). At -0.9V, the surface contains optimum synergy between

oxide derived In electronic state and metallic Pd, which give rise to the best electrocatalytic performance. On the other hand, in the case of PdIn alloy, the oxidation state of In was found to be lower than that of oxide-derived catalyst, and the change of binding energy is not significant as we move to the higher overpotential (**Figure 2.19d**). Interestingly, at the higher negative potential in the CO_2RR atmosphere, the surface PdO gradually appears, as indicated in the potential dependent Pd 3d XPS (**Figure 2.19e** and **Figure 2.19f**).

It can be concluded that Pd in the PdIn alloy is prone to get oxidized in the CO_2 condition, and thereby, its activity degrade over time. On the other hand, due to the protective layer of In_2O_3, the oxide-derived catalyst mask the Pd active site from the surface oxidation during the reaction conditions, and as the reaction progresses, the Pd site is being exposed, and an optimum Pd-In-O is crucial to exhibit the best catalytic performance at -0.9V. Moreover, the O 1s core-level XPS signal shows that the peak at 530.5 eV generated from oxygen defect in the In-O-In ($O_{lattice}$) in the PdIn@In_2O_3 catalyst before applying any potential (**Figure 2.19a**), which has been drastically reduced at -0.9V (**Figure 2.19b**).[54, 55]

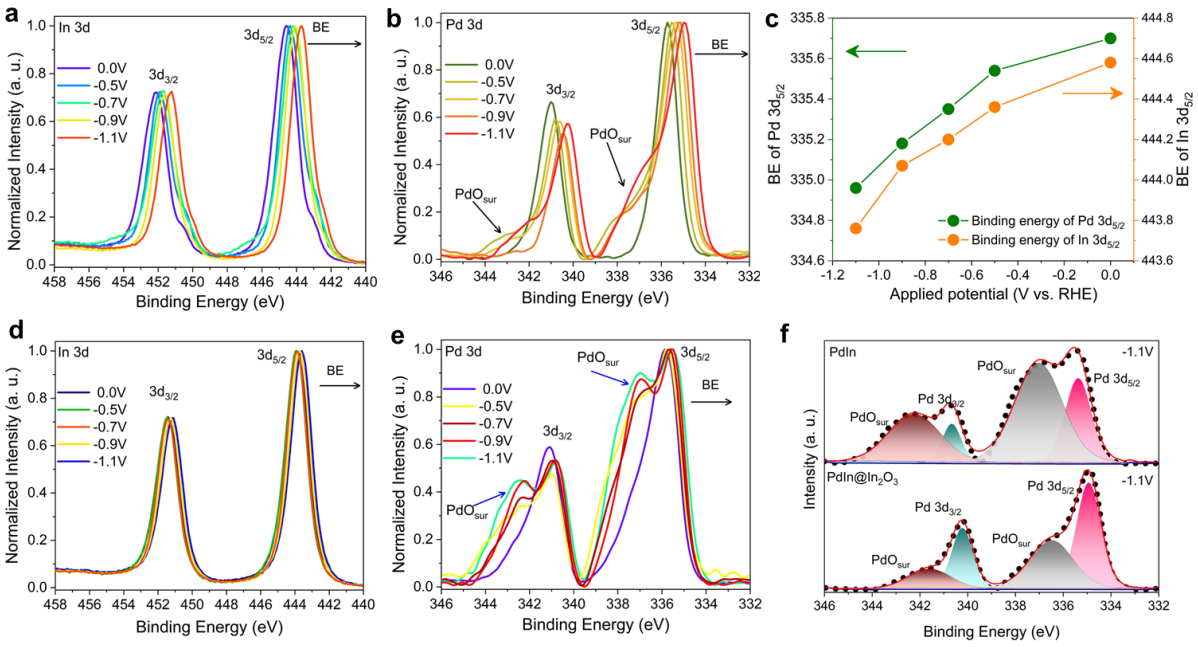

Figure 2.19. Potential dependent XPS spectra for PdIn@In_2O_3 of (a) In 3d core level and (b) In 3d core level. (c) Variation of binding energy (eV) of Pd 3d core level and In 3d core level obtained from XPS analysis for PdIn@In_2O_3 at different applied potential after eCO_2RR. Potential dependent XPS spectra for PdIn alloy catalyst of (d) In 3d core level and (e) Pd 3d core level. (f) Fitted XPS data of Pd core level of PdIn and PdIn@In_2O_3 catalysts after performing eCO_2RR at -1.1V (vs. RHE).

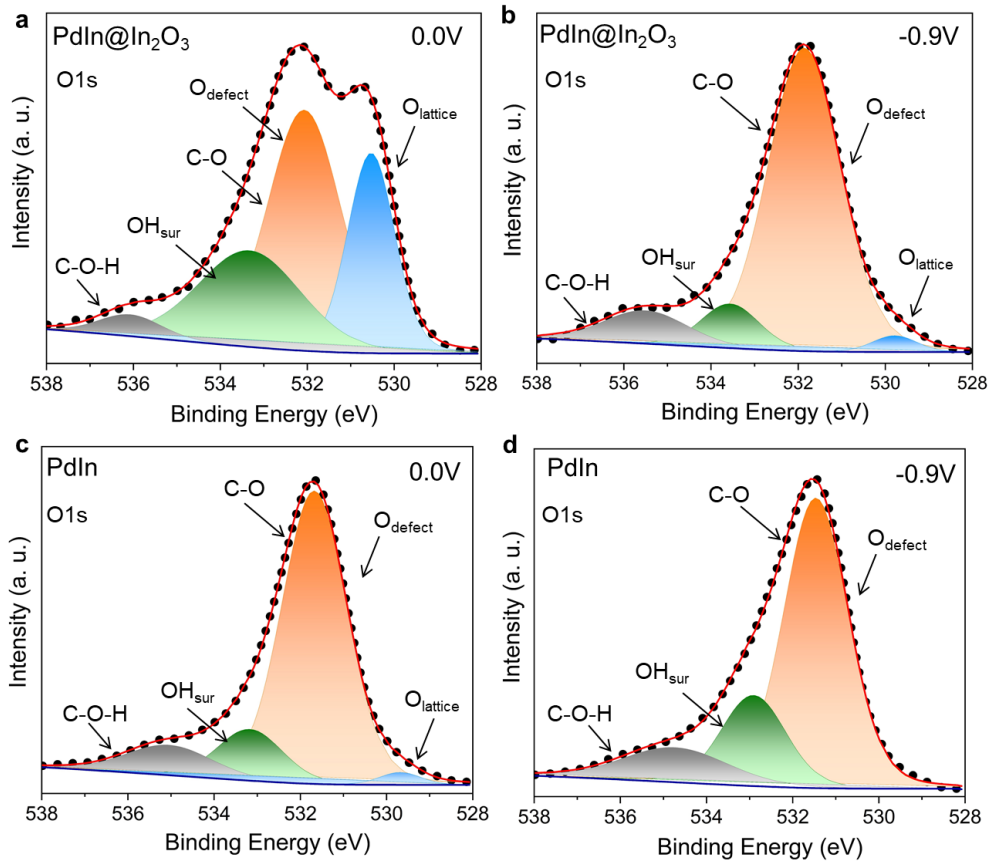

Figure 2.19. High-resolution XPS spectra of O 1s core level of PdIn@In_2O_3 sample (a) without applying potential, (b) after applying -1.6 V during eCO_2RR conditions. O 1s core level of PdIn sample (c) without applying potential, (d) after applying -1.6 V during eCO_2RR conditions.

On the other hand, O1s spectra of PdIn alloy do not show any significant presence of $O_{lattice}$ peak of In-O-In (**Figure 2.19c**), clearly suggesting the absence of In_2O_3 before and in the CO_2RR atmosphere (**Figure 2.19d**).[56, 57] The XPS peak corresponding to the O_{defect} of In_2O_3 is overlapping with that of the C-O peak of the carbon electrode used during CO_2RR study.[58] It is very crucial to get an idea about the actual active crystallographic phase responsible for the catalytic reaction as the crystal structure and phase can be changed during eCO_2RR at the negative potential. To understand the structural changes during eCO_2RR, powder XRD of the working electrodes was recorded immediately after the electrolysis at each potential (**Figure 2.20**). It has been observed that the diffraction peak corresponding to In_2O_3 in the PdIn@In_2O_3 catalyst gradually decreases from pristine catalysts (without applying potential) to -0.5V and completely disappeared at a higher negative potential, suggesting the oxide-derived surface is the main reason for enhancement in the CO_2RR activity (**Figure 2.20a-b**). On the other hand, the alloy catalyst does not show any significant change in the powder XRD at various applied potentials (**Figure 2.20c**).

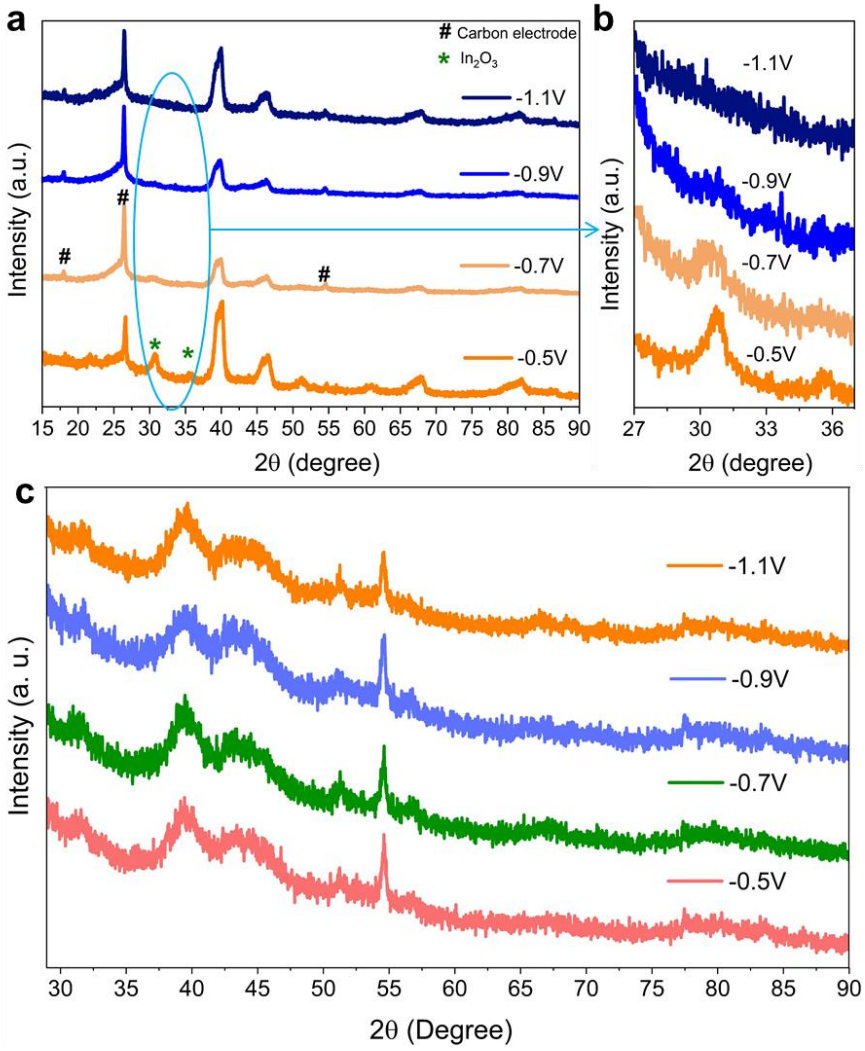

Figure 2.20. Post electrochemical powder XRD analysis of (a) PdIn@In_2O_3 and (b) PdIn at different applied potential.

The cubic In_2O_3 structure belongs to the $I2_13$ space group. So, it is obvious to have a vibrational mode with symmetry A_g, E_g, and T_g (Raman active) and T_u vibrations (IR active). The potential-dependent Raman spectra were recorded in the spectral range of 200–1000 cm^{-1} to investigate the structural changes of PdIn@In_2O_3 (**Figure 2.21a**), and it is found that the Raman bands correspond to E_{1g}, $A_{1g,}$ and E_{2g} have been found.[59, 60] The major peak at 632.7 cm^{-1} corresponding to the stretching vibrations of the [InO_6] octahedrons (**Figure 2.21b**), has shifted to lower energy (618.7 cm^{-1} at -0.7V), indicating a weakening of In-O bonds as the negative potential applied. This peak has shifted to further low energy, and its intensity also decreases in the higher negative potential (-0.9-1.1V), suggesting the gradual reduction of the In_2O_3 species in the extremely higher negative potential. These features of the Raman band were not observed in the case of the PdIn catalyst.

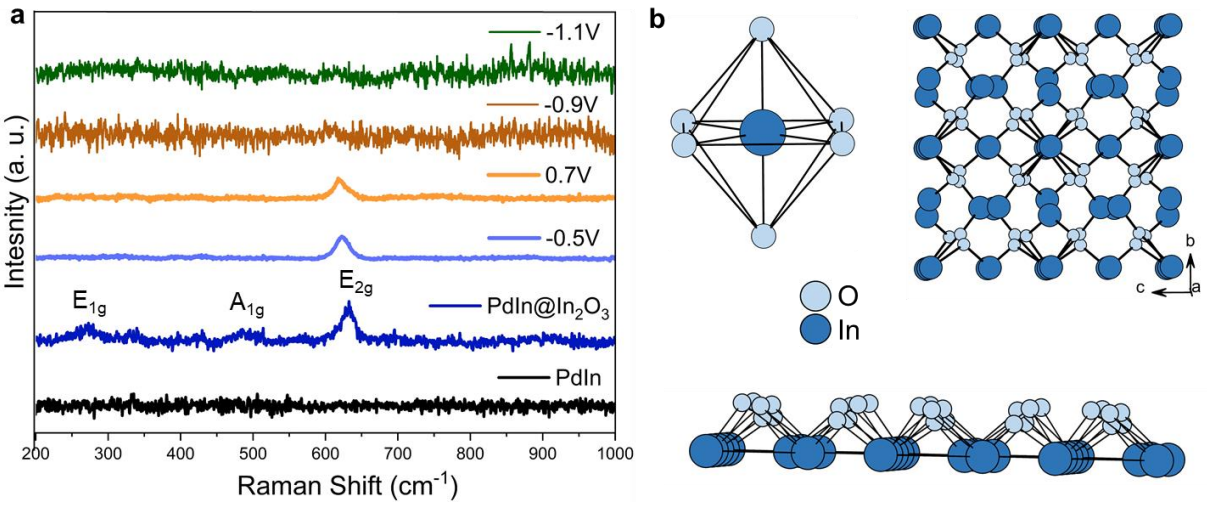

Figure 2.21. (a) Post electrochemical Raman spectroscopic analysis of PdIn and PdIn@In_2O_3 after performing eCO_2RR at respective appllied potential. (b) Different structural arrangements of In_2O_3 (space group: $I2_13$).

The surface reconstruction mechanism of PdIn and PdIn@In_2O_3 catalysts under eCO_2RR conditions have been depicted in **Figure 2.22a**. The in situ IR showed the formation of three crucial C-bound intermediates viz. *COOH, *COO^- and CO. From that observation, the probable mechanistic pathway for the electrochemical conversion of CO_2 to CO on oxide-derived PdIn surface can be illustrated in **Figure 2.22b**.

At first, CO_2 adsorbs on the PdIn@In_2O_3 surface and is converted to *COO^- by taking up one electron while applying negative potential. The surface adsorbed *COO^- transforms into *COOH by taking one proton from the electrolyte. Finally, *COOH gives rise to CO and H_2O by proton-coupled electron transfer (PCET).

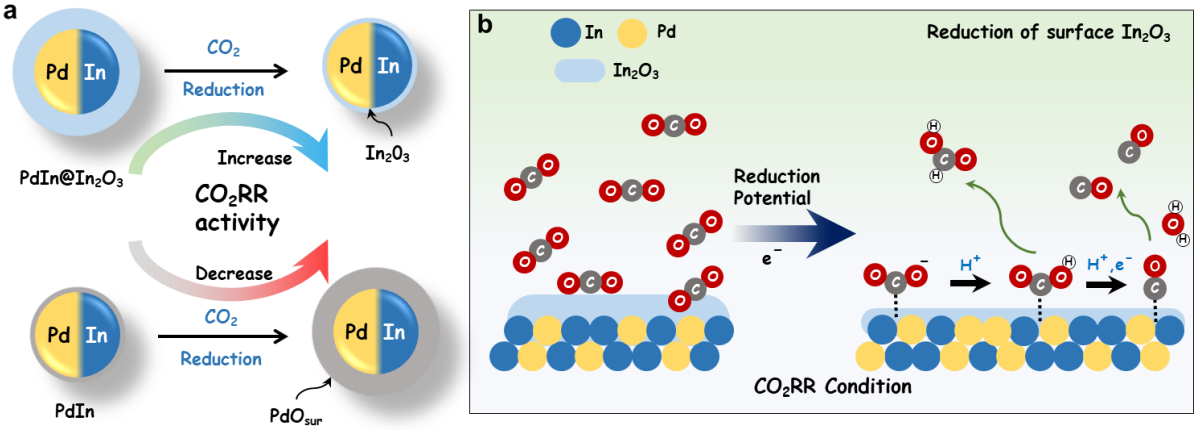

Figure 2.22. (a) Schematic representation of structural change for both PdIn and PdIn@In_2O_3 during the eCO_2RR performance. (b) Mechanistic illustration of electrochemical reduction of CO_2 to CO on oxide derived PdIn@In_2O_3 catalyst surface.

2.4.5 High current density using microflow cell

To avoid the mass transport issue in the H-cell mentioned in the previous section and to achieve higher current density, we have employed electrochemical microflow to evaluate CO_2RR performance on PdIn@In_2O_3 catalysts in two-electrode configuration at different cell potential (**Figure 2.23**). To improve stability and to decouple the hydrophobicity and proper current collection, we have utilized a PTFE-based gas diffusion electrode instead of a traditional carbon-based GDE.[30, 61] The GDE configuration has been optimized with different loadings of carbon and graphite on PTFE coated catalyst layer (CA: catalyst) where the PTFE layer acts as the stable hydrophobic gas diffusion layer which restricts flooding, and the carbon and graphite layers stabilize the catalyst surface along with an increase in the conductivity.[61, 62] Linear sweep voltammogram at different GDE configurations has been presented in **Figure 2.23a**, suggesting a six-fold increment in the higher current density (~140 mA/cm^2 @-4V, **Figure 2.23b**) achieved in the Flow cell compared to the traditional H-cell. The trend of catalytic activity has been found to be similar than that of H-cell with much higher current dnesity as depicted in the **Figure 2.23bc-d**.

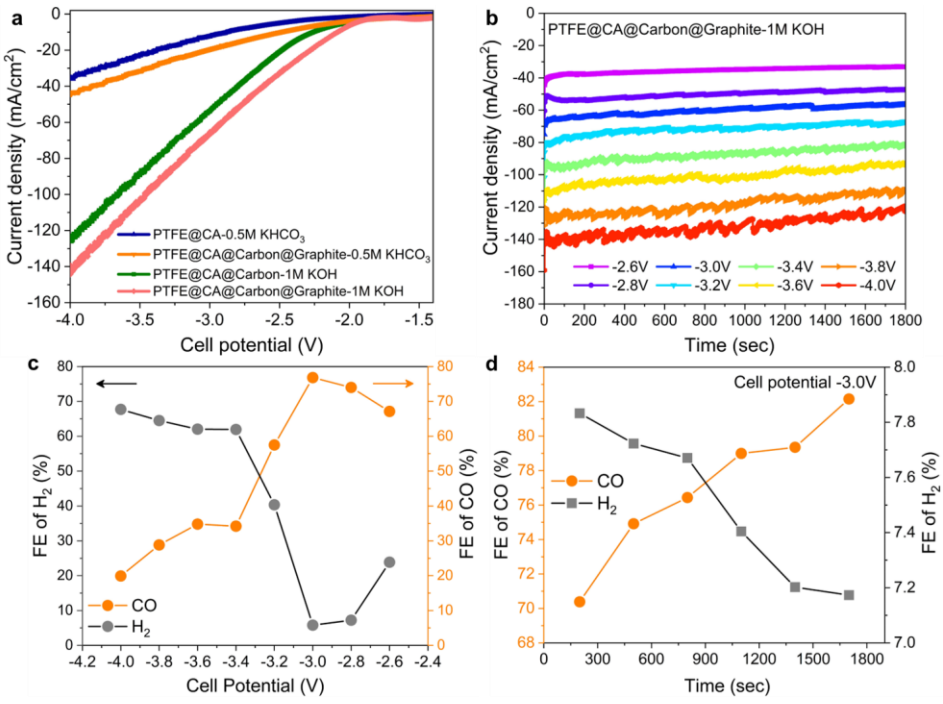

Figure 2.23. (a) Linear sweep voltammetry scan in various GDE configuration and CO_2RR conditions. (b) Chronoamperometric study at each applied potential in flow cell configuration. (c) Faradaic efficiency of CO at each cell potential in two-electrode configuration. (d)Time-dependent evolution of H_2 and CO at cell potential of -3.0 V on PdIn@In_2O_3 surface in the flow cell configuration while performing CO_2RR condition on GDE.

In the 3-electrode configuration of flow cell, C-based GDE has been utilized where the current density has been further improved (**Figure 2.24a**) and the product distribution has been shown in **Figure 2.24b**. The catalyst is also shown excellent stability over the long period of electrolysis **Figure 2.24c** .

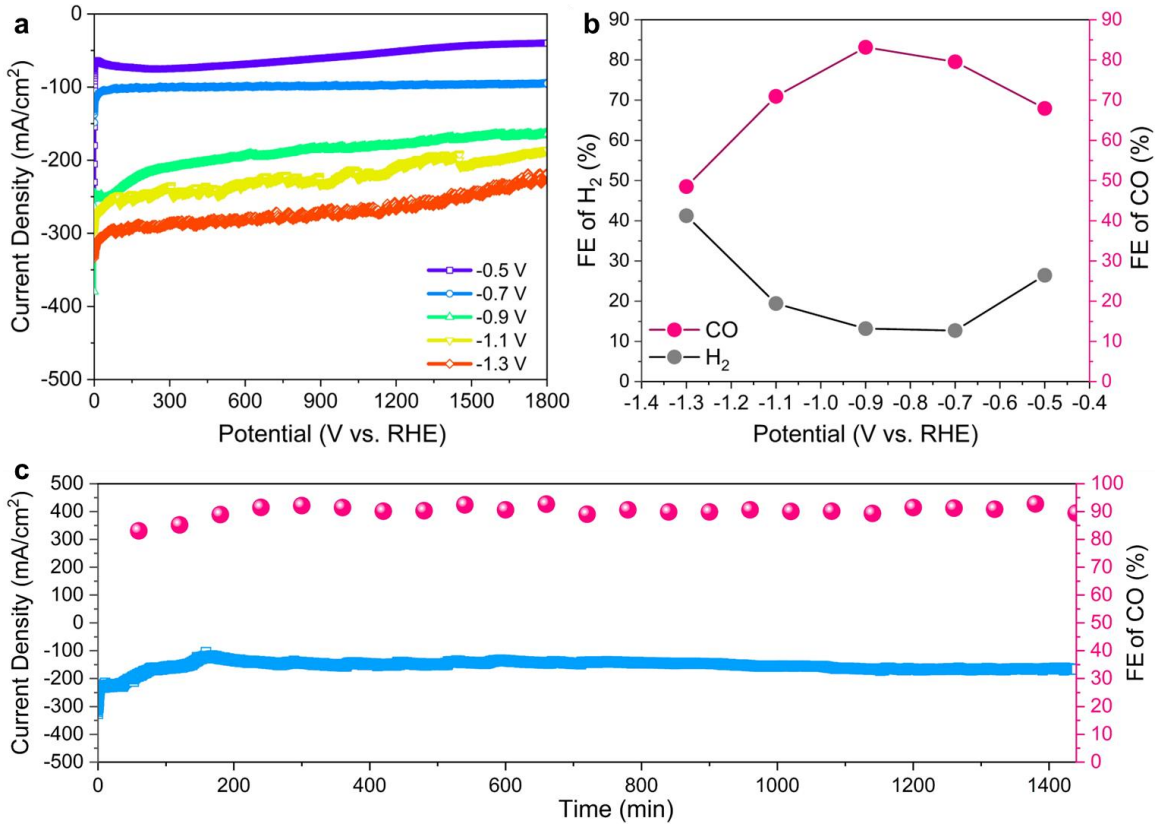

Figure 2.24. (a) Faradaic efficiency of CO at each cell potential on PdIn@In_2O_3 surface in in three-electrode set up with C-based GDE. (b) Long-term chronoamperometry study and the obtained FE at each time interval on PdIn@In_2O_3 during CO_2RR condition at -0.9V at -0.9V for 24 h.

2.5 Conclusion

In this work, a catalyst comprised of an alloy (PdIn) and oxide (In_2O_3) has been developed for the selective conversion of CO_2 to CO by rational design. Since the eCO_2RR research is still in the early stage of development, several material design strategies are not yet exploited for the best performance towards the desired product. Our strategy resulted in a generation of a metal-oxide interface during the operando condition, which enhances the conversion of CO_2 to CO substantially. It is found that In_2O_3 provides a protecting layer to the PdIn alloy surface so that it cannot get oxidized further during the electrolysis process, and an optimum surface In_2O_3 is crucial, which gives rise to better CO selectivity than the pristine

PdIn catalyst, which suppresses the undesired competitive HER in favor of high production of CO. The current density has been improved six-fold by introducing the flow cell in the GDE configuration by optimizing the catalyst, reactant gas, and electrolyte interface. We have also achieved the catalytic stability for almost 24h with higher current density (>100mA/cm^2) and extremely high FE of around 90% for CO production. The overall performance can be taken further and can be integrated with tandem catalysis process for the production of higher hydrocarbon from CO with higher yield. The mechanism and adsorption of crucial intermediates have been mapped as a function of time and potential with the help of in situ IR spectroscopy, which reveals the formation of C-bound *COOH, *COO$^-$ and *CO intermediates gives rise to CO as a major product along with HCOOH as the minor CO_2-reduced product via two-step PCET process. The overall electrochemical study, in situ mechanistic investigations, and potential-dependent structural illustration of catalysts' surface may inspire exploration and principles for a structure-property relationship, which could be advantageous for the development of more efficient electrocatalysts for CO_2 reduction.

2.6 References

1. Kortlever, R.; Shen, J.; Schouten, K. J. P.; Calle-Vallejo, F.; Koper, M. T. M., Catalysts and Reaction Pathways for the Electrochemical Reduction of Carbon Dioxide. *J. Phys. Chem. Lett.* **2015,** *6*, 4073-4082.
2. Roy, S.; Cherevotan, A.; Peter, S. C., Thermochemical CO_2 Hydrogenation to Single Carbon Products: Scientific and Technological Challenges. *ACS Energy Lett.* **2018,** *3*, 1938-1966.
3. Goyal, A.; Marcandalli, G.; Mints, V. A.; Koper, M. T. M., Competition between CO_2 Reduction and Hydrogen Evolution on a Gold Electrode under Well-Defined Mass Transport Conditions. *J. Am. Chem. Soc.* **2020,** *142*, 4154-4161.
4. Gu, J.; Héroguel, F.; Luterbacher, J.; Hu, X., Densely Packed, Ultra Small SnO Nanoparticles for Enhanced Activity and Selectivity in Electrochemical CO_2 Reduction. *Angew. Chem., Int. Ed.* **2018,** *57*, 2943-2947.
5. Ma, W.; Xie, S.; Zhang, X.-G.; Sun, F.; Kang, J.; Jiang, Z.; Zhang, Q.; Wu, D.-Y.; Wang, Y., Promoting Electrocatalytic CO_2 Reduction to Formate via Sulfur-Boosting Water Activation on Indium Surfaces. *Nat. Commun.* **2019,** *10*, 892.
6. Li, F.; Chen, L.; Knowles, G. P.; MacFarlane, D. R.; Zhang, J., Hierarchical Mesoporous SnO2 Nanosheets on Carbon Cloth: A Robust and Flexible Electrocatalyst for CO_2 Reduction with High Efficiency and Selectivity. *Angew. Chem. Int. Ed.* **2017,** *56*, 505-509.

7. Chen, Z.; Huang, A.; Yu, K.; Cui, T.; Zhuang, Z.; Liu, S.; Li, J.; Tu, R.; Sun, K.; Tan, X.; Zhang, J.; Liu, D.; Zhang, Y.; Jiang, P.; Pan, Y.; Chen, C.; Peng, Q.; Li, Y., Fe_1N_4–O_1 Site with Axial Fe–O Coordination for Highly Selective CO_2 Reduction over a Wide Potential Range. *Energy Environ. Sci.* **2021,** *14*, 3430-3437.
8. Khodakov, A. Y.; Chu, W.; Fongarland, P., Advances in the Development of Novel Cobalt Fischer−Tropsch Catalysts for Synthesis of Long-Chain Hydrocarbons and Clean Fuels. *Chem. Rev.* **2007,** *107*, 1692-1744.
9. Gao, D.; Zhou, H.; Cai, F.; Wang, J.; Wang, G.; Bao, X., Pd-Containing Nanostructures for Electrochemical CO_2 Reduction Reaction. *ACS Catal.* **2018,** *8*, 1510-1519.
10. Hammer, B.; Morikawa, Y.; Nørskov, J. K., CO Chemisorption at Metal Surfaces and Overlayers. *Phys. Rev. Lett.* **1996,** *76*, 2141-2144.
11. Kuhl, K. P.; Hatsukade, T.; Cave, E. R.; Abram, D. N.; Kibsgaard, J.; Jaramillo, T. F., Electrocatalytic Conversion of Carbon Dioxide to Methane and Methanol on Transition Metal Surfaces. *J. Am. Chem. Soc.* **2014,** *136*, 14107-14113.
12. Shan, W.; Liu, R.; Zhao, H.; He, Z.; Lai, Y.; Li, S.; He, G.; Liu, J., In Situ Surface-Enhanced Raman Spectroscopic Evidence on the Origin of Selectivity in CO_2 Electrocatalytic Reduction. *ACS Nano* **2020,** *14*, 11363-11372.
13. Lee, H.-E.; Yang, K. D.; Yoon, S. M.; Ahn, H.-Y.; Lee, Y. Y.; Chang, H.; Jeong, D. H.; Lee, Y.-S.; Kim, M. Y.; Nam, K. T., Concave Rhombic Dodecahedral Au Nanocatalyst with Multiple High-Index Facets for CO_2 Reduction. *ACS Nano* **2015,** *9*, 8384-8393.
14. Zeng, J.; Zhang, W.; Yang, Y.; Li, D.; Yu, X.; Gao, Q., Pd–Ag Alloy Electrocatalysts for CO_2 Reduction: Composition Tuning to Break the Scaling Relationship. *ACS Appl. Mater. Inter.* **2019,** *11*, 33074-33081.
15. Li, M.; Wang, J.; Li, P.; Chang, K.; Li, C.; Wang, T.; Jiang, B.; Zhang, H.; Liu, H.; Yamauchi, Y.; Umezawa, N.; Ye, J., Mesoporous Palladium–Copper Bimetallic Electrodes for Selective Electrocatalytic Reduction of Aqueous CO_2 to CO. *J. Mater. Chem. A* **2016,** *4*, 4776-4782.
16. Ni, W.; Xue, Y.; Zang, X.; Li, C.; Wang, H.; Yang, Z.; Yan, Y.-M., Fluorine Doped Cagelike Carbon Electrocatalyst: An Insight into the Structure-Enhanced CO Selectivity for CO_2 Reduction at High Overpotential. *ACS Nano* **2020,** *14*, 2014-2023.

17. Gunji, T.; Ochiai, H.; Ohira, T.; Liu, Y.; Nakajima, Y.; Matsumoto, F., Preparation of Various Pd-Based Alloys for Electrocatalytic CO_2 Reduction Reaction—Selectivity Depending on Secondary Elements. *Chem. Mater.* **2020,** *32*, 6855-6863.
18. He, Q.; Lee, J. H.; Liu, D.; Liu, Y.; Lin, Z.; Xie, Z.; Hwang, S.; Kattel, S.; Song, L.; Chen, J. G., Accelerating CO_2 Electroreduction to CO Over Pd Single-Atom Catalyst. *Adv. Funct. Mater.* **2020,** *30*, 2000407.
19. Leverett, J.; Daiyan, R.; Gong, L.; Iputera, K.; Tong, Z.; Qu, J.; Ma, Z.; Zhang, Q.; Cheong, S.; Cairney, J.; Liu, R.-S.; Lu, X.; Xia, Z.; Dai, L.; Amal, R., Designing Undercoordinated Ni–N_x and Fe–N_x on Holey Graphene for Electrochemical CO_2 Conversion to Syngas. *ACS Nano* **2021,** *15*, 12006-12018.
20. Zhang, N.; Zhang, X.; Kang, Y.; Ye, C.; Jin, R.; Yan, H.; Lin, R.; Yang, J.; Xu, Q.; Wang, Y.; Zhang, Q.; Gu, L.; Liu, L.; Song, W.; Liu, J.; Wang, D.; Li, Y., A Supported Pd_2 Dual-Atom Site Catalyst for Efficient Electrochemical CO_2 Reduction. *Angew. Chem. Int. Ed.* **2021,** *60*, 13388-13393.
21. Xie, J.-F.; Chen, J.-J.; Huang, Y.-X.; Zhang, X.; Wang, W.-K.; Huang, G.-X.; Yu, H.-Q., Selective Electrochemical CO_2 Reduction on Cu-Pd Heterostructure. *Appl. Catal. B.* **2020,** *270*, 118864.
22. Wang, P.; Yang, H.; Xu, Y.; Huang, X.; Wang, J.; Zhong, M.; Cheng, T.; Shao, Q., Synergized Cu/Pb Core/Shell Electrocatalyst for High-Efficiency CO_2 Reduction to C_{2+} Liquids. *ACS Nano* **2021,** *15*, 1039-1047.
23. Mun, Y.; Lee, S.; Cho, A.; Kim, S.; Han, J. W.; Lee, J., Cu-Pd alloy Nanoparticles as Highly Selective Catalysts for Efficient Electrochemical Reduction of CO_2 to CO. *Appl. Catal. B.* **2019,** *246*, 82-88.
24. Pavesi, D.; Ali, F. S. M.; Anastasiadou, D.; Kallio, T.; Figueiredo, M.; Gruter, G.-J. M.; Koper, M. T. M.; Schouten, K. J. P., CO_2 Electroreduction on Bimetallic Pd–In Nanoparticles. *Catal. Sci. Technol.* **2020,** *10*, 4264-4270.
25. Rasul, S.; Anjum, D. H.; Jedidi, A.; Minenkov, Y.; Cavallo, L.; Takanabe, K., A Highly Selective Copper–Indium Bimetallic Electrocatalyst for the Electrochemical Reduction of Aqueous CO_2 to CO. *Angew. Chem. Int. Ed.* **2015,** *54*, 2146-2150.
26. Zha, B.; Li, C.; Li, J., Efficient Electrochemical Reduction of CO_2 into Formate and Acetate in Polyoxometalate Catholyte with Indium Catalyst. *J. Catal.* **2020,** *382*, 69-76.

27. Ding, C.; Li, A.; Lu, S.-M.; Zhang, H.; Li, C., In Situ Electrodeposited Indium Nanocrystals for Efficient CO_2 Reduction to CO with Low Overpotential. *ACS Catal.* **2016,** *6*, 6438-6443.
28. Ye, J.; Ge, Q.; Liu, C.-j., Effect of PdIn Bimetallic Particle Formation on CO_2 Reduction over the Pd–In/SiO_2 Catalyst. *Chem. Eng. Sci.* **2015,** *135*, 193-201.
29. Lum, Y.; Ager, J. W., Evidence for Product-Specific Active Sites on Oxide-Derived Cu Catalysts for Electrochemical CO_2 Reduction. *Nat. Catal.* **2019,** *2*, 86-93.
30. Corral, D.; Feaster, J. T.; Sobhani, S.; DeOtte, J. R.; Lee, D. U.; Wong, A. A.; Hamilton, J.; Beck, V. A.; Sarkar, A.; Hahn, C.; Jaramillo, T. F.; Baker, S. E.; Duoss, E. B., Advanced Manufacturing for Electrosynthesis of Fuels and Chemicals from CO_2. *Energy Environ. Sci.* **2021,** *14*, 3064-3074.
31. Tan, W.; Cao, B.; Xiao, W.; Zhang, M.; Wang, S.; Xie, S.; Xie, D.; Cheng, F.; Guo, Q.; Liu, P., Electrochemical Reduction of CO_2 on Hollow Cubic Cu_2O@Au Nanocomposites. *Nanoscale Res. Lett.* **2019,** *14*, 63.
32. Jiang, B.; Zhang, X.-G.; Jiang, K.; Wu, D.-Y.; Cai, W.-B., Boosting Formate Production in Electrocatalytic CO_2 Reduction over Wide Potential Window on Pd Surfaces. *J. Am. Chem. Soc.* **2018,** *140*, 2880-2889.
33. Kim, Y.; Park, S.; Shin, S.-J.; Choi, W.; Min, B. K.; Kim, H.; Kim, W.; Hwang, Y. J., Time-resolved Observation of C–C Coupling Intermediates on Cu Electrodes for Selective Electrochemical CO_2 Reduction. *Energy Environ. Sci.* **2020,** *13*, 4301-4311.
34. Garand, E.; Wende, T.; Goebbert, D. J.; Bergmann, R.; Meijer, G.; Neumark, D. M.; Asmis, K. R., Infrared Spectroscopy of Hydrated Bicarbonate Anion Clusters: $HCO_3^-(H_2O)_{1-10}$. *J. Am. Chem. Soc.* **2010,** *132*, 849-856.
35. Loring, J. S.; Thompson, C. J.; Wang, Z.; Joly, A. G.; Sklarew, D. S.; Schaef, H. T.; Ilton, E. S.; Rosso, K. M.; Felmy, A. R., In Situ Infrared Spectroscopic Study of Forsterite Carbonation in Wet Supercritical CO_2. *Environ. Sci. Technol.* **2011,** *45*, 6204-6210.
36. Mizaikoff, B., Waveguide-Enhanced Mid-Infrared Chem/Bio Sensors. *Chem. Soc. Rev* **2013,** *42*, 8683-8699.
37. Han, S. W.; Ha, T. H.; Kim, C. H.; Kim, K., Self-Assembly of Anthraquinone-2-carboxylic Acid on Silver: Fourier Transform Infrared Spectroscopy, Ellipsometry, Quartz Crystal Microbalance, and Atomic Force Microscopy Study. *Langmuir* **1998,** *14*, 6113-6120.

38. Fan, M.; Andrade, G. F. S.; Brolo, A. G., A Review on the Fabrication of Substrates for Surface Enhanced Raman Spectroscopy and their Applications in Analytical Chemistry. *Anal. Chim. Acta* **2011,** *693*, 7-25.
39. Firet, N. J.; Smith, W. A., Probing the Reaction Mechanism of CO_2 Electroreduction over Ag Films via Operando Infrared Spectroscopy. *ACS Catal.* **2017,** *7*, 606-612.
40. Smith, E. L.; Porter, M. D., Structure of Monolayers of Short Chain n-Alkanoic Acids ($CH_3(CH_2)_nCOOH$, n = 0-9) Spontaneously Adsorbed from the Gas Phase at Silver as Probed by Infrared Reflection Spectroscopy. *J. Phys. Chem. A* **1993,** *97*, 8032-8038.
41. Xia, X. H.; Liess, H. D.; Iwasita, T., Early Stages in the Oxidation of Ethanol at Low Index Single Crystal Platinum Electrodes. *J. Electroanal. Chem.* **1997,** *437*, 233-240.
42. Katayama, Y.; Nattino, F.; Giordano, L.; Hwang, J.; Rao, R. R.; Andreussi, O.; Marzari, N.; Shao-Horn, Y., An In Situ Surface-Enhanced Infrared Absorption Spectroscopy Study of Electrochemical CO_2 Reduction: Selectivity Dependence on Surface C-Bound and O-Bound Reaction Intermediates. *J. Phys. Chem. C* **2019,** *123*, 5951-5963.
43. Zhu, S.; Li, T.; Cai, W.-B.; Shao, M., CO_2 Electrochemical Reduction As Probed through Infrared Spectroscopy. *ACS Energy Lett.* **2019,** *4*, 682-689.
44. Furukawa, S.; Endo, M.; Komatsu, T., Bifunctional Catalytic System Effective for Oxidative Dehydrogenation of 1-Butene and n-Butane Using Pd-Based Intermetallic Compounds. *ACS Catal.* **2014,** *4*, 3533-3542.
45. McGuirk, G. M.; Ledieu, J.; Gaudry, É.; de Weerd, M. C.; Fournée, V., Surface Structures of In-Pd Intermetallic Compounds. I. Experimental Study of In Thin Films on Pd(111) and Alloy Formation. *J. Chem. Phys.* **2014,** *141*, 084702.
46. Skála, T.; Veltruská, K.; Moroseac, M.; Matolı; x; nová, I.; Korotchenkov, G.; Matolı; x; n, V., Study of Pd–In Interaction during Pd Deposition on Pyrolytically Prepared In_2O_3. *Appl. Surf. Sci.* **2003,** *205*, 196-205.
47. Rameshan, C.; Lorenz, H.; Mayr, L.; Penner, S.; Zemlyanov, D.; Arrigo, R.; Haevecker, M.; Blume, R.; Knop-Gericke, A.; Schlögl, R.; Klötzer, B., CO_2-Selective Methanol Steam Reforming on In-Doped Pd Studied by In Situ X-ray Photoelectron Spectroscopy. *J. Catal.* **2012,** *295*, 186-194.
48. He, C.; Tao, J.; Shen, P. K., Solid Synthesis of Ultrathin Palladium and Its Alloys' Nanosheets on RGO with High Catalytic Activity for Oxygen Reduction Reaction. *ACS Catal.* **2018,** *8*, 910-919.

49. Tang, Y.; Zhang, S.; Rawal, T. B.; Nguyen, L.; Iwasawa, Y.; Acharya, S. R.; Liu, J.; Hong, S.; Rahman, T. S.; Tao, F., Atomic-Scale Structure and Catalysis on Positively Charged Bimetallic Sites for Generation of H_2. *Nano Lett.* **2020,** *20*, 6255-6262.
50. Dong, Y.; Ghuman, K. K.; Popescu, R.; Duchesne, P. N.; Zhou, W.; Loh, J. Y. Y.; Jelle, A. A.; Jia, J.; Wang, D.; Mu, X.; Kübel, C.; Wang, L.; He, L.; Ghoussoub, M.; Wang, Q.; Wood, T. E.; Reyes, L. M.; Zhang, P.; Kherani, N. P.; Singh, C. V.; Ozin, G. A., Tailoring Surface Frustrated Lewis Pairs of $In_2O_{3-x}(OH)_y$ for Gas-Phase Heterogeneous Photocatalytic Reduction of CO_2 by Isomorphous Substitution of In^{3+} with Bi^{3+}. *Adv. Sci* **2018,** *5*, 1700732.
51. Buchholz, D. B.; Ma, Q.; Alducin, D.; Ponce, A.; Jose-Yacaman, M.; Khanal, R.; Medvedeva, J. E.; Chang, R. P. H., The Structure and Properties of Amorphous Indium Oxide. *Chem. Mater.* **2014,** *26*, 5401-5411.
52. Roy, S.; Bagchi, D.; Dheer, L.; Sarma, S. C.; Rajaji, V.; Narayana, C.; Waghmare, U. V.; Peter, S. C., Mechanistic Insights into the Promotional effect of Ni Substitution in Non-Noble Metal Carbides for Highly Enhanced Water Splitting. *Appl. Catal. B: Environ.* **2021,** *298*, 120560.
53. Bagchi, D.; Raj, J.; Singh, A. K.; Cherevotan, A.; Roy, S.; Manoj, K. S.; Vinod, C. P.; C. Peter, S., Structure-Tailored Surface Oxide on Cu-Ga Intermetallics Enhances CO_2 Reduction Selectivity to Methanol at Ultra-Low Potential. *Adv. Mater.* **2022,** *34*, 2109426.
54. Detweiler, Z. M.; Wulfsberg, S. M.; Frith, M. G.; Bocarsly, A. B.; Bernasek, S. L., The Oxidation and Surface Speciation of Indium and Indium Oxides Exposed to Atmospheric Oxidants. *Surf. Sci.* **2016,** *648*, 188-195.
55. Araújo, T. P.; Shah, A.; Mondelli, C.; Stewart, J. A.; Curulla Ferré, D.; Pérez-Ramírez, J., Impact of Hybrid CO_2-CO Feeds on Methanol Synthesis over In_2O_3-Based Catalysts. *Appl. Catal. B.* **2021,** *285*, 119878.
56. Rui, N.; Wang, Z.; Sun, K.; Ye, J.; Ge, Q.; Liu, C.-j., CO_2 Hydrogenation to Methanol over Pd/In_2O_3: Effects of Pd and Oxygen Vacancy. *Appl. Catal. B.* **2017,** *218*, 488-497.
57. Gan, J.; Lu, X.; Wu, J.; Xie, S.; Zhai, T.; Yu, M.; Zhang, Z.; Mao, Y.; Wang, S. C. I.; Shen, Y.; Tong, Y., Oxygen Vacancies Promoting Photoelectrochemical Performance of In_2O_3 Nanocubes. *Sci. Rep.* **2013,** *3*, 1021.
58. Wu, Y.; Lin, Y.; Xu, J., Synthesis of Ag–Ho, Ag–Sm, Ag–Zn, Ag–Cu, Ag–Cs, Ag–Zr, Ag–Er, Ag–Y and Ag–Co Metal Organic Nanoparticles for UV-Vis-NIR Wide-Range Bio-Tissue Imaging. *Photochem. Photobiol. Sci.* **2019,** *18*, 1081-1091.

59. Berengue, O. M.; Rodrigues, A. D.; Dalmaschio, C. J.; Lanfredi, A. J. C.; Leite, E. R.; Chiquito, A. J., Structural Characterization of Indium Oxide Nanostructures: a Raman Analysis. *J. Phys. D Appl. Phys.* **2010,** *43*, 045401.
60. Wang, C. Y.; Dai, Y.; Pezoldt, J.; Lu, B.; Kups, T.; Cimalla, V.; Ambacher, O., Phase Stabilization and Phonon Properties of Single Crystalline Rhombohedral Indium Oxide. *Cryst. Growth Des.* **2008,** *8*, 1257-1260.
61. Dinh, C.-T.; Burdyny, T.; Kibria, M. G.; Seifitokaldani, A.; Gabardo, C. M.; García de Arquer, F. P.; Kiani, A.; Edwards, J. P.; De Luna, P.; Bushuyev, O. S.; Zou, C.; Quintero-Bermudez, R.; Pang, Y.; Sinton, D.; Sargent, E. H., CO_2 Electroreduction to Ethylene via Hydroxide-Mediated Copper Catalysis at an Abrupt Interface. *Science* **2018,** *360*, 783-787.
62. Niu, Z.-Z.; Chi, L.-P.; Liu, R.; Chen, Z.; Gao, M.-R., Rigorous Assessment of CO_2 Electroreduction Products in a Flow Cell. *Energy Environ. Sci.* **2021,** *14*, 4169-4176.

Chapter 3

Structure-Tailored Surface Oxide on Cu-Ga Intermetallics Enhances CO_2 Reduction Selectivity to Methanol at Ultra-Low Potential

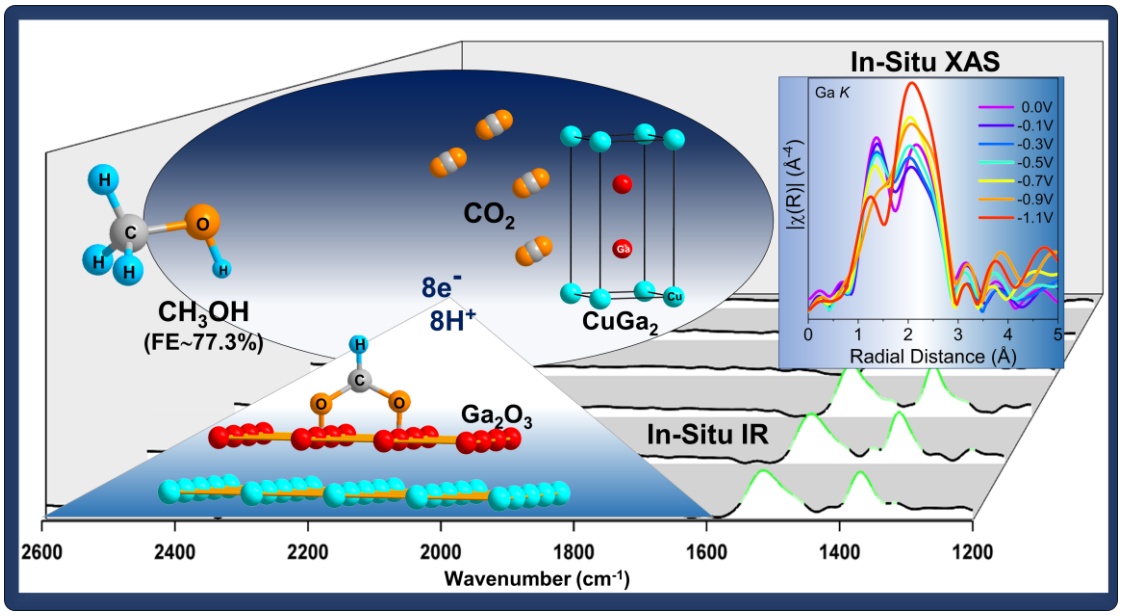

Bagchi, D.; Raj, J.; Singh, A. K.; Cherevotan, A.; Roy, S.; Manoj, K. S.; Vinod, C. P.; Peter, S. C., *Adv. Mater.* **2022,** *34*, 2109426.

Summary

In this chapter, we advanced ourselves further and tried to obtain more reduced and energy-dense chemicals, i.e., methanol via eCO_2RR. We have introduced an unexplored strategy of nanoparticle synthesis i.e., top-down approach and synthesized two intermetallic compounds formed by copper and gallium metals ($CuGa_2$ and Cu_9Ga_4). Among them, $CuGa_2$ selectively converts CO_2 to methanol with remarkable Faradaic efficiency (FE) of 77.26% at an extremely low potential of -0.3 V vs. RHE. The high performance of $CuGa_2$ compared to Cu_9Ga_4 has been driven by its unique two-dimensional structure that retains surface and sub-surface oxide species (Ga_2O_3) even in the reduction atmosphere. The Ga_2O_3 species have been mapped by XPS and XAFS techniques and electrochemical measurements. The eCO_2RR activity and selectivity to methanol have been decreased at higher potential due to the lattice expansion caused by the reduction of the Ga_2O_3, which has been probed by in-situ XAFS, quasi in-situ powder XRD and ex-situ XPS measurements. The mechanism of the formation of methanol from CO_2 at various potentials has been visualized by in-situ IR spectroscopy and source of carbon of methanol at the molecular level confirmed from the isotope labelling experiments in the presence of $^{13}CO_2$. Finally, to minimize the mass transport limitations and improve the overall eCO_2RR performance, PTFE-based gas diffusion electrode (GDE) has been employed in the flow cell configuration.

In this chapter, DB (author) has conceptualized the idea and synthesised the catalysts, performed all the electrochemical studies (both flow cell and H-cell) and other ex-situ (XRD, XPS, TEM, SEM), in-situ studies (FTIR, EXAFS), analyzed the data, and written the draft. JR has helped in flow cell optimization. AKS assisted in in-situ EXAFS experiment. AC assisted in in-situ FTIR experiment. SR and KSM helped in syntheising the catalyst. CPV procured the XPS data. SCP conceptualized the idea, supervised the work, reviewed and edited the draft.

Table of Contents

3.1. Introduction 100

3.2. Experimental Details 102

3.2.1. Chemicals and reagents 102
3.2.2. Synthesis of $CuGa_2$ and Cu_9Ga_4 102
3.2.3. Ball milling 103

3.3. Characterization and Experimental Methods 104

3.3.1. Powder X-ray Diffraction (PXRD) 104
3.3.2. Transmission Electron Microscope (TEM) 104
3.3.3. Inductively coupled plasma atomic emission spectroscopy (ICP-OES) 104
3.3.4. X-ray Photoelectron Spectroscopy (XPS) 104
3.3.5. Elemental Analysis 104
3.3.6. X-ray Absorption Spectroscopy 105
3.3.7. Atomic Force Microscopy (AFM) 105
3.3.8. Electrochemical CO_2 Reduction Reaction (eCO_2RR) 105
3.3.9. Flow cell optimization for eCO_2RR in gas diffusion electrode configuration . 106
3.3.10. Gaseous product analysis 106
3.3.11. Liquid product analysis 106
3.3.12. Preparation of Gas diffusion Electrode (GDE) 107
3.3.13. In situ Electrochemical Attenuated Total Reflection Fourier Transform Infrared Spectroscopy (ATR-FTIR) 107

3.4. Results & Discussion 107

3.4.1. Synthesis and characterizations 107
3.4.2. Electrochemical CO_2 reduction (eCO_2RR) in H-cell 111
3.4.3. Product quantification and Faradaic efficiency (FE) 112
3.4.4. In situ electrochemical ATR-FTIR study 114
3.4.5. Oxidation state and Local electronic structures from XAFS 116
3.4.6. Potential dependent in-situ XAFS analysis 118
3.4.7. Potential dependent Ex-situ XPS and powder XRD analysis 120
3.4.8. High current density using flow cell with GDE configuration 126

3.5. Conclusion 129

3.6. References 130

3.1. Introduction

The major challenge in the electrochemical process is that more than sixteen different kinds of products, including alcohols, aldehydes, olefins, and hydrocarbons, can be expected from the electroreduction of CO_2,[1, 2] which leads to complex chemical reaction and poor selectivity towards any desired product. In this study, we have designed a new kind of catalyst materials which can selectively produce higher energy C_1 product like methanol. Out of all the CO_2 reduced product, methanol is one of the most used green fuels having an energy density of 15.6 MJ L^{-1}, and it is also a very crucial intermediate for the production of daily used materials such as silicone, paint, plastics, adhesives, foams, plywood subfloors, solvents, and windshield washer fluid.[3] Compared to hydrogen, the most significant advantage of methanol is that it can be stored at atmospheric pressure and can be used directly in internal combustion engines because of its high octane rating and can be directly utilized in fuel cells (Direct Methanol Fuel Cells).[4] Efficient production of methanol from CO_2 is a very challenging task as CO_2 is a very stable molecule having extremely low Gibbs free energy (ΔG = −394.4 kJ/mol), and its conversion back to methanol having relatively higher Gibbs free energy (ΔG = −159.2 kJ/mol) is an endothermic process. This leads to the requirement of higher overpotential for the electroreduction of CO_2 to methanol.[5] Hence it is essential to make advancements in catalyst design to overcome the kinetic barrier associated with multistep reaction mechanism for the efficient production of methanol.

Although the electrocatalysis community has made much advancement for the eCO_2RR to methanol, certain constraints exist, such as poor selectivity, low Faradaic efficiencies (FEs), the durability of catalyst, and over-dependence of expensive noble metal catalysts. Moreover, mechanistic investigation and the degradation mechanism of catalysts have not been reported in detail. Therefore, it is still very demanded to have a low-cost catalyst that can efficiently convert CO_2 to methanol at extremely low energy input to make it an environmentally viable process.

Among the various catalyst systems, Cu–Zn–Al mixed oxide has been commercialized for methanol production via the thermocatalytic route.[6] This inspired the electrochemists to test Cu and Zn based compounds in the early stage of the eCO_2RR. Still, formic acid was obtained as the primary product with poor FEs towards methanol. Le et al. reported FEs up to 38% of methanol in 0.5 M $KHCO_3$ at electrodeposited cuprous thin films electrodes.[7] Recently, Jia et al. designed electrodeposited nanostructured Cu-Au alloy on nano-porous Cu film (NCF) where they demonstrated that the selectivity for alcohol production ($FE_{methanol+ethanol}$ of about

28%) from CO_2 is greatly dependent on the nanostructures and compositions of constituent elements.[8] Cu/Bi metal-organic framework-based compound has also been used to produce methanol from eCO_2RR, but only 8.6% FE of methanol.[9] Wang et al. reported pyridine derivative (PYD) doped metal composite [PYD] @ Cu-Pd with 26% FE of methanol under low potential.[10] Ensafi et al. reported 39% FE of methanol by using self-assembled monolayer electrode of 2-pyridinethiol@Pt-Au nanoparticles at an applied potential of −0.20 V (vs. Ag/AgCl).[11] Zhang et al. reported a 2D hierarchical Pd/SnO_2 structure for efficient production of methanol (FE of 54.8% for methanol at -0.24 V vs. RHE). They explained the role of Pd-O-Sn interfaces in enhancing the overall activity.[12, 13] In addition to these, there are several transition metal-based bimetallic, alloy, or oxide catalysts for CO_2 electroreduction to methanol,[8, 14, 15,16-18,19] but, to the best of our knowledge, the exclusive production of methanol at lower overpotential has not been reported so far, and it involves the great challenge in designing the catalysts.[18]

Ni_5Ga_3 phase was observed to outperform the industrial state-of-the-art catalyst Cu/ZnO/Al_2O_3 for methanol formation via the thermochemical pathway.[20] Since then, several works have been reported, especially on Ni-Ga-based catalysts, to investigate the role of Ga and different oxidized species of Ga towards the enhancement of thermochemical CO_2RR activity and stability.[21, 22] However, to the best of our knowledge, Ga based materials have never been reported for methanol selectivity upon eCO_2RR.

In this work, we have developed two intermetallic compounds, $CuGa_2$ and Cu_9Ga_4, as new catalysts for the eCO_2RR. $CuGa_2$ exhibited the best performance towards the formation of methanol (FE of 77.26%) at an applied potential of -0.3 V vs. RHE. The unique 2D flake type structure of $CuGa_2$ has promoted the formation of a higher amount of surface gallium oxide (Ga_2O_3), which is responsible for the higher catalytic performance than that of Cu_9Ga_4, which has 3D spherical morphology hindering the surface oxide formation. XRD, XPS, and XAS have been employed to map the global and local structure, and microscopic techniques (AFM, SEM, and TEM) have been performed for morphological and elemental analysis of both compounds. In-situ IR spectroscopy was carried out to determine the intermediates involved in the formation of methanol, and the reaction mechanism was predicted from the potential dependent IR spectral analysis. The electrochemical activity and selectivity have been decreased as we proceed to the higher potential, and the degradation mechanism was studied by quasi in-situ powder XRD and ex-situ XPS techniques. It was found that the progressive

reduction of the surface oxide species in the case of $CuGa_2$ caused by applied reduction potential is the reason for the lower catalytic activity at a higher negative potential.

3.2. Experimental Details

3.2.1. Chemicals and reagents

Cu metal (pieces, 99.99%) and Ga metal (pieces, 99.99%) were purchased from Alfa Aesar. Potassium bicarbonate (99.95 %), which has been used as the electrolyte during CO_2 reduction, was bought from Sigma Aldrich. All the organic solvents like methanol, ethanol, 2-propanol, acetone and acid-like formic acid, acetic acid of HPLC grade and were purchased from SDFCL. DMSO, phenol, and D_2O were purchased from Sigma Aldrich. All the chemicals used were commercially available certified reagents and used without further purifications unless mentioned.

3.2.2. Synthesis of $CuGa_2$ and Cu_9Ga_4

The intermetallics $CuGa_2$ and Cu_9Ga_4 were synthesized by high-temperature solid-state synthesis process following the phase diagram (**Figure 3.1a**), taking the corresponding metals (Cu and Ga) in their respective mole ratio.

A proper mole ratio of Cu and Ga metal (1:2 in case of $CuGa_2$ and 9:4 in case of Cu_9Ga_4) was taken in a 9 mm diameter quartz tube, which was flame sealed under a vacuum of 10^{-3} Torr to prevent oxidation during heating. The tube was then placed in a vertically aligned tube furnace (**Figure 3.1b**) and heated to 700 °C for $CuGa_2$ and 800 °C for Cu_9Ga_4 over a period of 5 h, maintained at that temperature for 5 h to allow proper homogenization, followed by cooling to 200 °C for $CuGa_2$ and 300 °C for Cu_9Ga_4 at a ramp rate of 2 °C /min and kept there isothermally for 24 h.

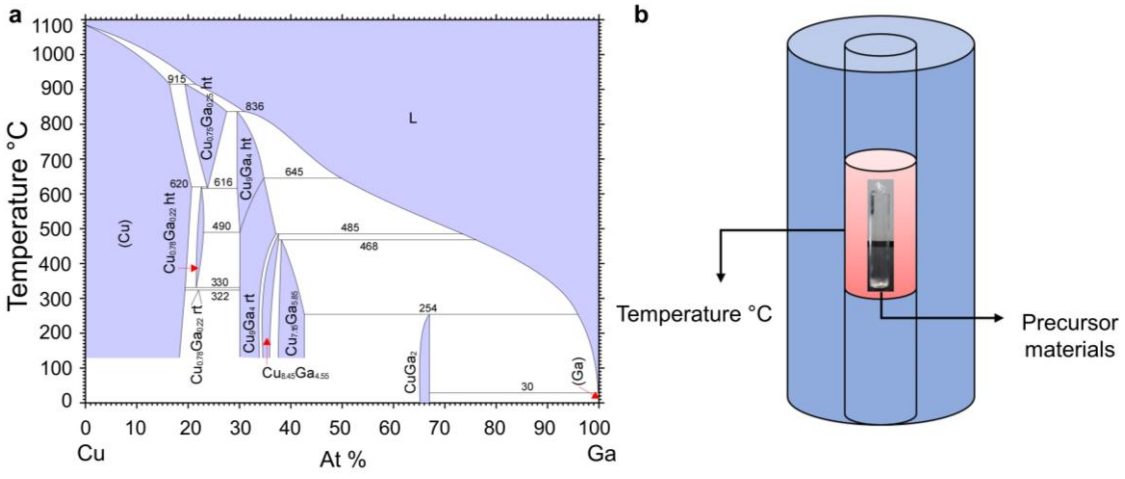

Figure 3.1. (a) Cu-Ga phase diagram.[23] (b) Schematic of annealing process for the high temperature synthesis of $CuGa_2$ and Cu_9Ga_4.

Finally, the system was allowed to cool down to room temperature in 10 h. The detailed temperature profile for the annealing process has been depicted in **Figure 3.2a-b**.

To reduce the dimension of the bulk intermetallic compounds, a top-down approach of nanomaterial synthesis technique has been employed (**Figure 3.3**).[24] After obtaining the proper intermetallic compounds ($CuGa_2$ and Cu_9Ga_4) by annealing, the samples were removed from the quartz tubes and mixed with Vulcan (2:1 weight ratio), and loaded into a planetary ball miller (Fritsch Planetary Micro Mill Pulverisette-7 premium line) having two steel bowls of 25 mL capacity with agate balls of 20 mm diameter. The milling was performed for total 30 cycles at 500 RPM with 15 minutes break in between to avoid the overheating of the sample. Each cycle was performed for 15 minutes, and for every 4-5 cycles, the milling bowl was opened and mixed the interior and milled again for uniform particle distribution. Vulcan was used as the conducting matrix of the ball milled intermetallic catalyst. This is very crucial strategy to utilize the top-down approach of nanoparticle synthesis and use them in electrocatalysis.

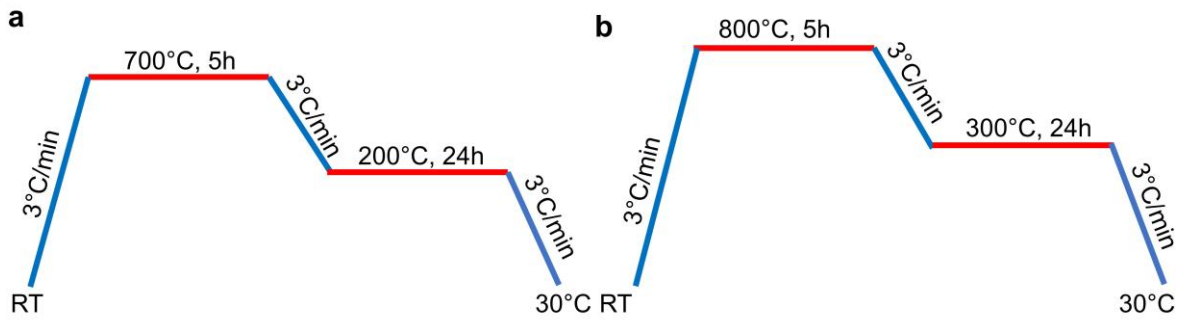

Figure 3.2. (a) Temperature profile of the annealing process during synthesis of (a) $CuGa_2$ and (b) Cu_9Ga_4.

3.2.3. Ball milling

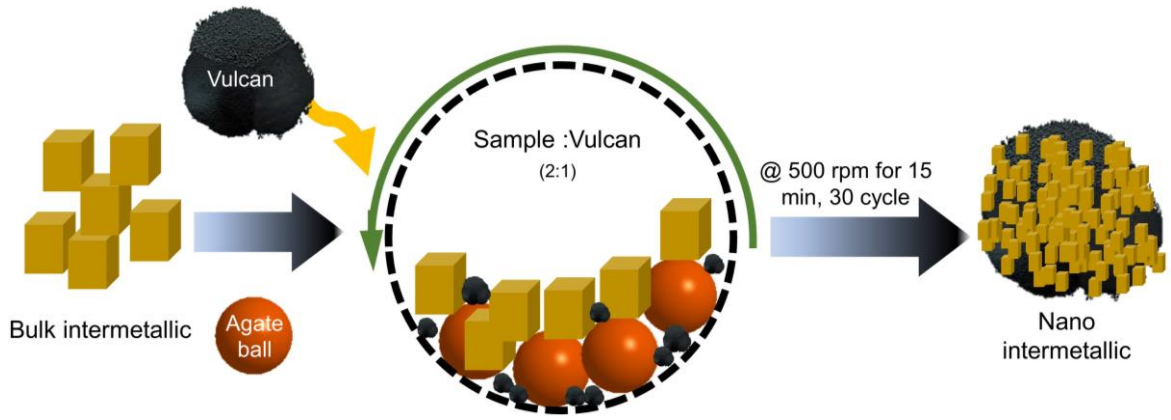

Figure 3.3. Schematic representation of top-down approach for the synthesis of $CuGa_2$ and Cu_9Ga_4 catalysts by ball milling.

3.3. Characterization and Experimental Methods

3.3.1. Powder X-ray Diffraction (PXRD)

PXRD measurements were done at room temperature on a Rigaku Miniflex X-ray diffractometer with a Cu−K_α X-ray source (λ = 1.5406 Å), equipped with a position-sensitive detector in the angular range of $10° \leq 2\theta \leq 90°$ with the step size 0.02° and a scan rate of 0.5 s/step calibrated against corundum standards. The experimental XRD patterns were compared to the patterns simulated from the data reported in the literature.

3.3.2. Transmission Electron Microscope (TEM)

Transmission electron microscope (TEM), high-resolution TEM (HRTEM) images and selected area electron diffraction (SAED) patterns were collected using TECNAI and JEOL 200 kV TEMs. TEM samples for these measurements were prepared by sonicating the nanocrystalline powders in ethanol and dropping a small volume onto a carbon-coated Cu grid.

3.3.3. Inductively coupled plasma atomic emission spectroscopy (ICP-OES)

ICP-OES was performed using a Perkin Elmer Optima 7000 DV instrument. The samples were digested in concentrated aqua regia, followed by dilution with distilled water. In a typical experiment, 2 mg of the sample was dissolved in 1 ml aqua regia and left overnight (12 hrs) for digestion. The digested sample was then diluted to 10 ml volume with deionized water. The solid particles were separated by thorough centrifugation before measurements.

3.3.4. X-ray Photoelectron Spectroscopy (XPS)

XPS measurements were carried out using Thermo K-alpha+ spectrometer using micro focused and monochromated Al Kα radiation with energy 1486.6 eV. The pass energy for the spectral acquisition was kept at 50 eV for individual core-levels. The electron flood gun was utilized for providing charge compensation during data acquisition. Further, the individual core-level spectra were checked for charging using C1s at 284.6 eV as standard and corrected if needed. The peak fitting of the individual core-levels was done using CASA XPS software with a Shirley type background.

3.3.5. Elemental Analysis

Quantitative microanalysis on all the samples was performed with an FEI NOVA NANOSEM 600 instrument equipped with an EDAX instrument. Data were acquired with an accelerating voltage of 20 kV and a 100 s accumulation time. The EDAX analysis was performed using the P/B-ZAF standard less method (where Z = atomic no. correction factor, A = absorption correction factor, F = fluorescence factor, P/B = peak to background model) on selected spots and points.

3.3.6. X-ray Absorption Spectroscopy

X-ray absorption near-edge spectroscopy (XANES) and quick-Extended X-ray Absorption Fine Structure (quick-EXAFS) experiments at 300 K were performed at PETRA III, beamline P64, of DESY, Germany. Measurements of Cu-*K* and Ga-*K* at ambient pressure were performed in fluorescence as well as transmission mode using gas ionization chambers to monitor the incident and transmitted X-ray intensities. Monochromatic X-rays were obtained using a Si (111) double crystal monochromator, which was calibrated by defining the inflection point (first derivative maxima) of Cu foil as 8980.5 eV. The beam was focused by employing a Kirkpatrick-Baez (K-B) mirror optic. A rhodium-coated X-ray mirror was used to suppress higher-order harmonics. A CCD detector was used to record the transmitted signals. Pellets for the ex-situ measurements were made by homogeneously mixing the sample with an inert cellulose matrix to obtain an X-ray absorption edge jump close to one.

3.3.7. Atomic Force Microscopy (AFM)

A Bruker, Forevision (MMV 1045901 model) instruments microscope in tapping mode with 10 nm diameter containing antimony doped Silicon tip was used to carry out AFM studies. The sample was coated on a Si wafer to perform the study.

3.3.8. Electrochemical CO_2 Reduction Reaction (eCO_2RR)

All the electrochemical measurements were performed using a CHI 6008E electrochemical workstation. Electrochemical CO_2 reduction reaction (eCO_2RR) is carried out in a three-electrode system, which involves a working electrode (glassy carbon or carbon cloth), counter electrode (graphitic carbon rod), and reference electrode (Ag/AgCl). The cell compartments are separated by a proton exchange membrane (Nafion 117), and the electrolyte used is 0.5M $KHCO_3$ solution. The electrolyte solutions were purged with CO_2 gas for 1 hour prior to the measurement. The electrocatalyst was prepared by dispersing 2 mg of catalyst and 0.2 mg of Vulcan (activated carbon) in 200 µL of mixed solvent solution (IPA:H_2O = 1:1 v/v) and 10 µL of 1 wt% nafion binder. From the prepared catalyst 100 µL was coated on the carbon cloth and dried. The electrochemical cell was designed to have a large electrode area (0.7 cm x 0.7 cm) and a small electrolyte volume (10 mL) in each of the two compartments, along with a gas headspace of approximately 5 mL above the electrolyte on each side of the membrane. CO_2, regulated by a mass flow controller at 10 standard cubic centimeters per minute (sccm), flowed through the working electrode compartment of the cell during electrolysis. CO_2 flow through the cell was necessary in order to see large current efficiencies for CO_2 reduction products, presumably because of mass transport limitations in a quiescent cell. The flow rate

of 10 sccm was chosen to ensure sufficient CO_2 transport to the surface while preventing interference from gas bubbles striking the surface.

3.3.9. Flow cell optimization for eCO$_2$RR in gas diffusion electrode configuration

To increase the CO_2 diffusion and increase the overall current density, the electrochemical carbon dioxide experiments were carried out in a filter-press type Micro Flow Cell (Electrocell A/S), where a Ti sheet coated with Ir-MMO (iridium-mixed metal oxide) is used as an Anode plate (Electrocell S/A). An anionic exchange membrane (Fumasep FAB-PK-130) was employed in the case of CO_2RR in KOH medium. As discussed in **Figure 1.12.**, the cell has three compartments, viz. CO_2 gas compartment, cathodic and anodic compartment (**Figure 1.13**). The electrolyte was recirculated continuously into the cell (both in cathode and anode) by two separate peristaltic pumps (Ravel, RH-P100L-100) to accumulate liquid products. The flow of CO_2 was regulated by a mass flow controller (Brooks) at different flowrate (standard cubic centimeters per minute (sccm)) to optimize the most suitable flow rate, flowed through the working electrode compartment of the cell during electrolysis. For the final study, the gas flow is fixed to 50 sccm, and electrolyte flow was set to 20 sccm.

3.3.10. Gaseous product analysis

All the gaseous products were analyzed by online 490-Micro Gas Chromatography (GC), which has four channels for detecting different gaseous products. Each channel has a specific column for analyzing relevant gases *viz*. Molsieve 5Å (for channel 1 and 2), Pora PLOT U (in channel 3) and CP-Sil 5 CB (for channel 4). The carrier gases were Ar and H_2. Each GC channel is equipped with a thermal conductivity detector (TCD). This detector responds to the difference in thermal conductivity between a reference cell (carrier gas only) and a measurement cell (carrier gas containing sample components).

Calculation of Faradaic Efficiency (FE) for gaseous products,

$$FE_{gas} = \frac{ppm \times flow\ rate \times \frac{number\ of\ electron \times Faraday\ contant \times pressure}{R \times Temperature}}{I_{average}} \times 100$$

Where ppm is the concentrations detected by GC, R is a gas constant (8.31 j $K^{-1}mol^{-1}$).

3.3.11. Liquid product analysis

The liquid products were analyzed by ^{1}H NMR (600 MHz, JEOL). The following protocol was applied. 500 mL of the electrolyte and 30 µL of an internal standard solution were transferred into a centrifuge tube. The internal standard solution consisted of 50 mM phenol (99.5 %) and 10 mM dimethyl sulfoxide (99.9 %) made in D_2O solvent. The mixture is

transferred into an NMR tube. Solvent suppression was used to decrease the intensity of the water peak.

3.3.12. Preparation of Gas diffusion Electrode (GDE)

The gas diffusion electrode (GDE) was fabricated by drop-casting the catalyst onto a cut piece of expanded polytetrafluoroethylene (ePTFE) (purchased from Sterlitech). The PTFE used here is aspire laminated and having proper hydrophobicity. It also has a polyester backer, and the pore size is 200 nm. The ePTFE was pretreated by first performing an RCA cleaning process reported earlier.[25] It was first treated with a mixture of H_2O:HCl:H_2O_2 (5:1:1) at 80°C for 2 minutes, then a mixture of H_2O:NH_4OH:H_2O_2 (5:1:1) for 2 minutes. After rinsing and drying, the catalyst was coated on that, and vulcan was coated successively at different coating amounts. Graphite powder was coated on top of that to enhance further conductivity of the GDE.

3.3.13. In situ Electrochemical Attenuated Total Reflection Fourier Transform Infrared Spectroscopy (ATR-FTIR)

In situ electrochemical FTIR spectroscopic studies were performed using a purged VERTEX FT-IR spectrometer equipped with the A530/P accessory and a mid-band MCT detector. A silicon hemispherical window (F530-8) was used with the working electrode placed gently on top of the window as the single reflection attenuated total reflection (ATR) accessory for the FTIR study. The in situ experimental setups is depicted in **Figure 1.15**. The measurement parameters were 4 cm^{-1} resolution and 100 scans. This setup enabled the detection of eCO_2RR intermediate formation and change of adsorption of various intermediates on the electrode surface and within the thin-layer electrolyte. In the beginning of the IR-experiment, we have taken a spectrum of the overall electrochemical cell and then take a background spectrum so that the contribution of the electrolyte can be subtracted in the next spectrum while applying the potential during performing CO_2RR. The spectra were analyzed by the OPUS software and the absorption spectra have been directly plotted at various potential and time.

3.4. Results & Discussion

3.4.1. Synthesis and characterizations

The intermetallics $CuGa_2$ (tetragonal system, space group: *P*4/*mmm*) and Cu_9Ga_4 (cubic phase, space group: $P\bar{4}3m$) were synthesized by high-temperature solid-state reaction (as mentioned before). The pure phases of both the compounds were subjected to ball milling (**Figure 3.3**) to reduce the particle size. Before ball milling, the sample was mixed with Vulcan

(2:1 weight ratio) to enhance the conductivity and uniform distribution of nanoparticles for electrochemical studies. The phase purity of both compounds was confirmed by the powder XRD technique (**Figure 3.4**). **Figure 3.5a-b** represents the unit cell of two dimensional (2D) $CuGa_2$ and three dimensional (3D) Cu_9Ga_4 crystal structures, respectively. The crystal structure of $CuGa_2$ is comprised of the alternate layers made up of Cu (1D sheet) and Ga (square net). Such kind of structural arrangement provides the accessibility of more metal atoms at the surface for the eCO_2RR.[26] Scanning electron microscopy (SEM) of both Cu_9Ga_4 and $CuGa_2$ has confirmed the nanoparticle distribution. The expected composition and uniform distribution of nanoparticles were confirmed by the Energy Dispersive spectrum (EDS) (**Figure 3.6-3.7**).

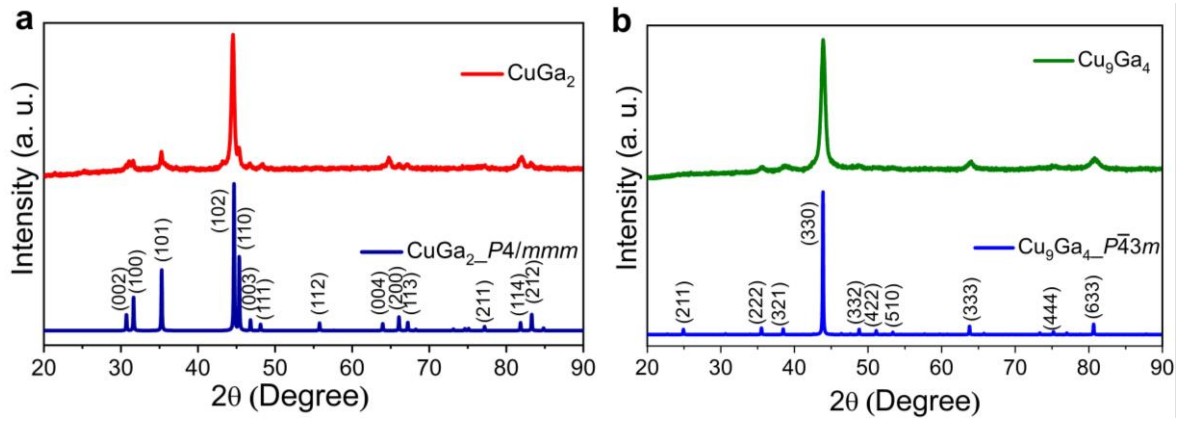

Figure 3.4. Experimental and simulated powder XRD comparison of $CuGa_2$ (a) and Cu_9Ga_4 (b).

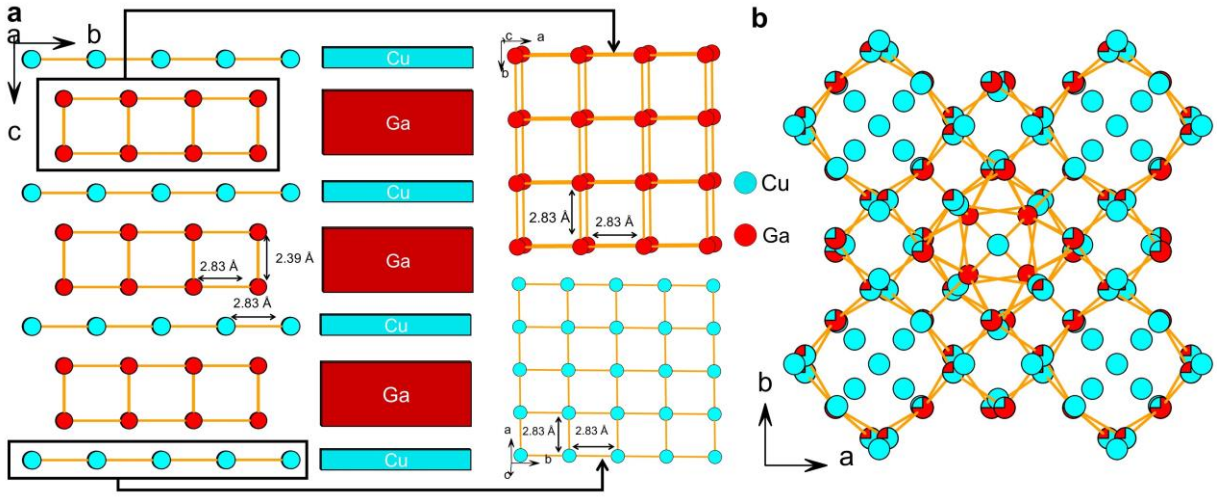

Figure 3.5. Crystal structure of Cu-Ga based intermetallics. (a) Crystal structure of $CuGa_2$ (cubic phase, space group: *P*4/*mmm*). The individual layers Cu (1D sheet) and Ga (2D square net) are shown separately. (b) Crystal structure of Cu_9Ga_4 (space group: $P\bar{4}3m$).

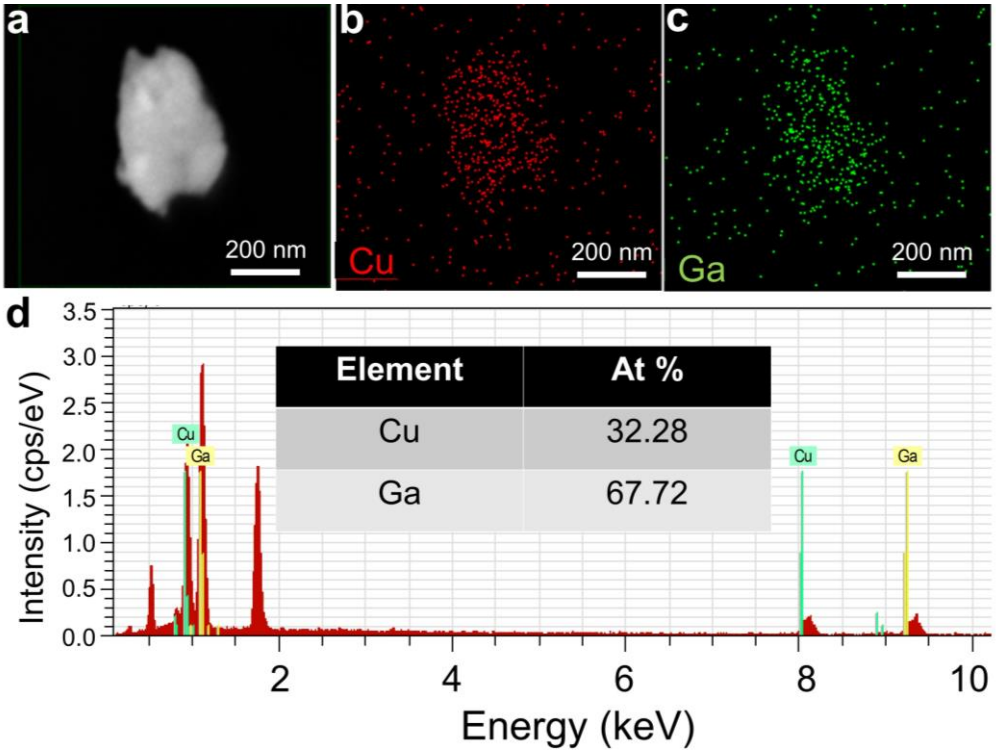

Figure 3.6. (a) Scanning electron microscopy (SEM) image of $CuGa_2$, (b-c) SEM colour mapping on the particle of $CuGa_2$. (d) EDS spectrum of $CuGa_2$ and inset table represents elemental composition $CuGa_2$.

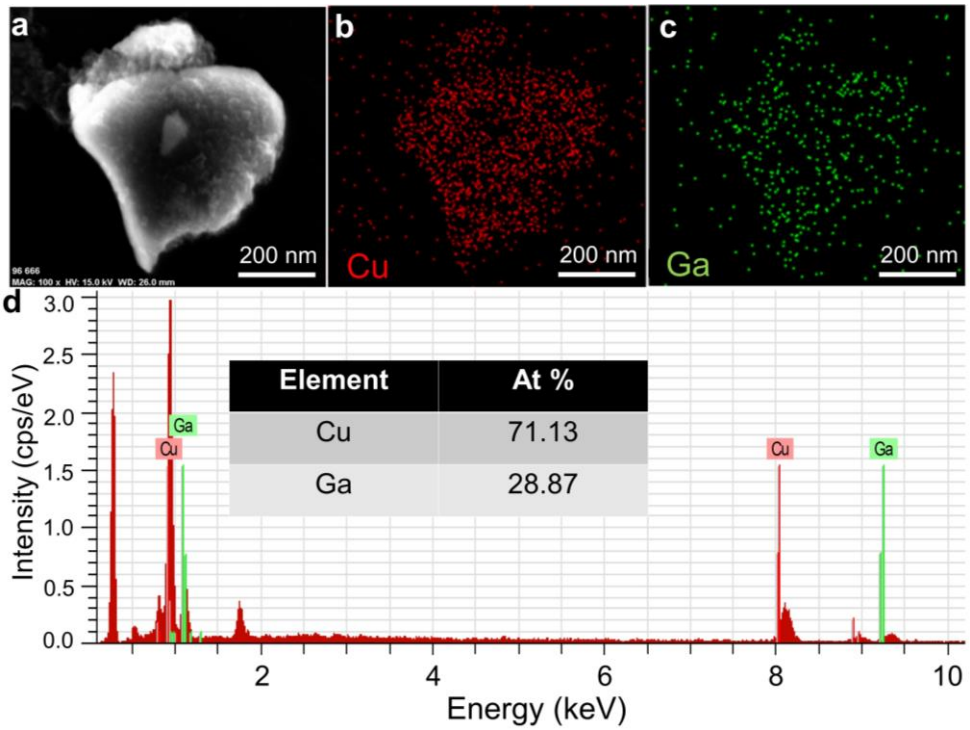

Figure 3.7. (a) Scanning electron microscopy (SEM) image of Cu_9Ga_4, (b-c) SEM colour mapping on the particle of Cu_9Ga_4 and (d) EDS spectrum of Cu_9Ga_4 and inset table represents elemental composition Cu_9Ga_4.

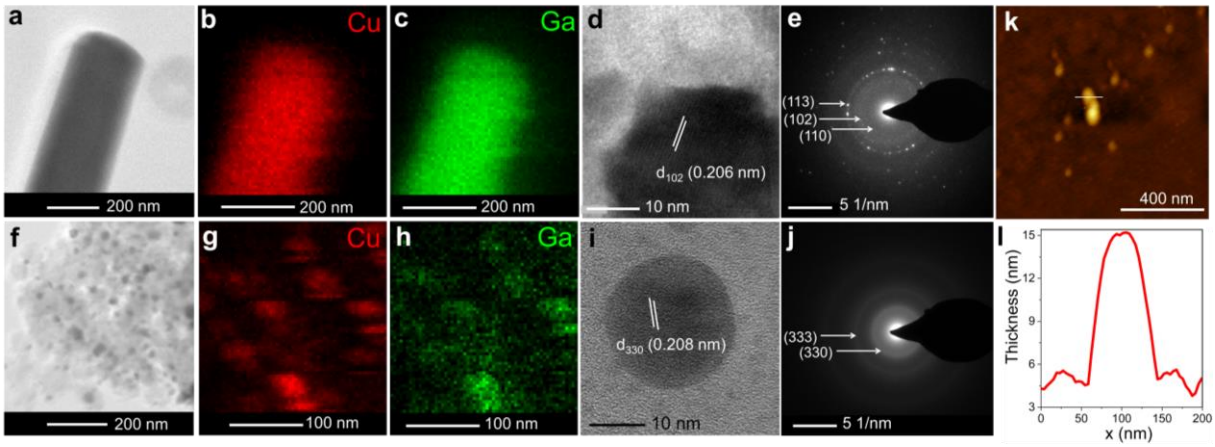

Figure 3.8. Transmission electron microscopic images and atomic force microscopic analysis. (a) Low-resolution TEM image of $CuGa_2$. (b-c) elemental mapping of $CuGa_2$. (d) High-resolution TEM image of $CuGa_2$. (e) SAED pattern of $CuGa_2$. (f) Low-resolution TEM image of Cu_9Ga_4. (g-h) Elemental mapping of Cu_9Ga_4. (i) HRTEM image of Cu_9Ga_4. (j) SAED pattern of Cu_9Ga_4. (k-l) AFM image of $CuGa_2$ and its corresponding cross-sectional thickness profile.

Figure 3.8 shows transmission electron microscopy (TEM) images and elemental mapping of the as-synthesized catalyst $CuGa_2$ (**Figure 3.8a-e**) and Cu_9Ga_4 (**Figure 3.8f-j**). HRTEM images clearly show the 2D flake kind of morphology of $CuGa_2$ (**Figure 3.8a**) whereas Cu_9Ga_4 showed a 3D spherical morphology (**Figure 3.8f)**, which is in good agreement with the crystal structures. TEM color mapping image of individual elements are depicted in **Figure 3.8b-c**, **3.8g-h**. High-resolution TEM images represent the lattice fringes corresponding to most exposed planes (102) and (330) for $CuGa_2$ and Cu_9Ga_4, respectively. Selected area electron diffraction (SAED) patterns indicate the polycrystalline nature of $CuGa_2$ (**Figure 3.8e**) and Cu_9Ga_4 (**Figure 3.8j**). Atomic force microscopy (AFM) confirmed the thickness of the $CuGa_2$ nanoflakes in the range of 12-15 nm (**Figure 3.8k-l**) and 50-85 nm for Cu_9Ga_4 (**Figure 3.8a-b**).

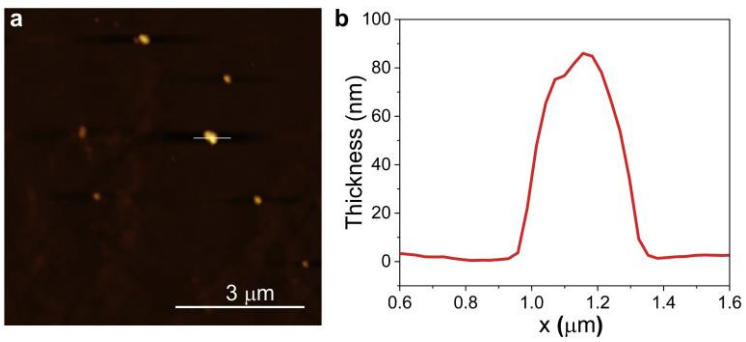

Figure 3.8. (a) AFM image of Cu_9Ga_4 nanocrystal and (b) its corresponding cross-sectional thickness profile.

3.4.2. Electrochemical CO_2 reduction (eCO_2RR) in H-cell

Electrochemical CO_2RR was carried out on both the catalysts in 0.5 M $KHCO_3$ with continuous CO_2 purging at 20 cm^3/min flow rate. Toray carbon paper was used as the working electrode with a surface area of 1 cm^2. In the first step, a linear sweep voltammetric study has been performed in the CO_2RR potential region, and it was found that in the CO_2 atmosphere, both catalysts exhibited much lower onset potentials and higher current densities than that in N_2-saturated 0.5 M $KHCO_3$, suggesting that the catalytic activity majorly originated from CO_2 reduction compared to hydrogen evolution (HER) (**Figure 3.9a**). To evaluate the electrochemical behavior of both compounds, chronoamperometric test has been performed. **Figure 3.9b** depicts the observed current density at each applied potential of both catalysts. The higher current density observed in the case of Cu_9Ga_4 at higher potential could be attributed to more reduction processes occurring at its surface compared to $CuGa_2$.

However, at relatively lower overpotential (-0.1V, -0.3V vs. RHE), the current densities for both catalysts are similar. The flat nature of chronoamperometry curves on both catalysts shown at different potentials in CO_2-saturated 0.5 M $KHCO_3$ solution (**Figure 3.10a-b**), indicating good electrochemical stability. Electrochemically active surface area (ECSA) is a critical kinetic factor influencing the activity of any electrocatalytic reaction.

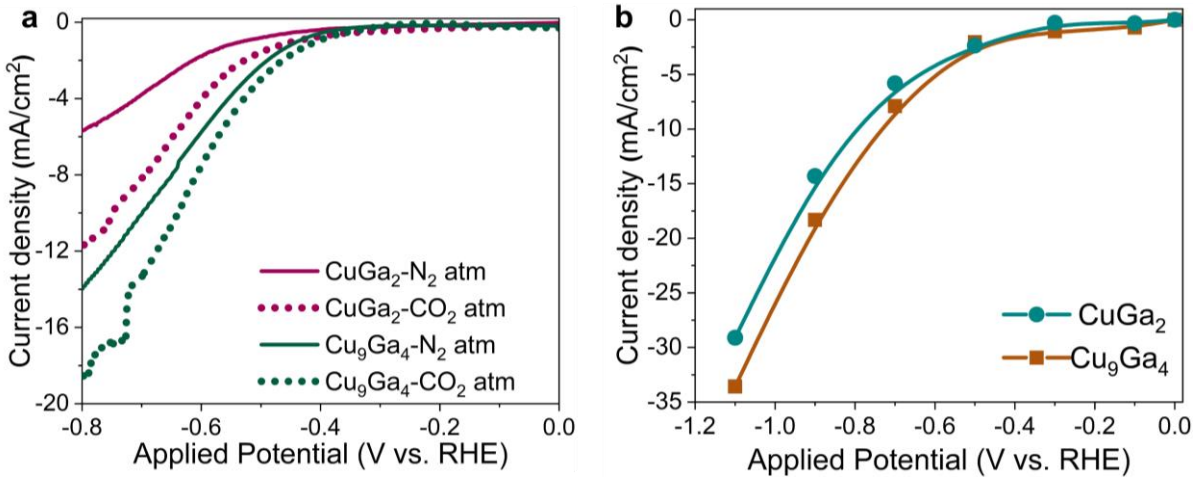

Figure 3.9. Electrochemical CO_2RR performance. (a) Linear sweep voltammogram taken in eCO_2RR condition and in N_2 atmosphere in $CuGa_2$ and Cu_9Ga_4 where hydrogen evolution is the major reaction. (b) Current density vs. applied potential on $CuGa_2$ and Cu_9Ga_4 (data derived from the chronoamperometric study at each potential during eCO_2RR in 0.5 M $KHCO_3$ solution). Faradaic efficiency for each CO_2 reduced liquid product methanol and formic acid as a function of potential during eCO_2RR on (c) $CuGa_2$ and (d) Cu_9Ga_4.

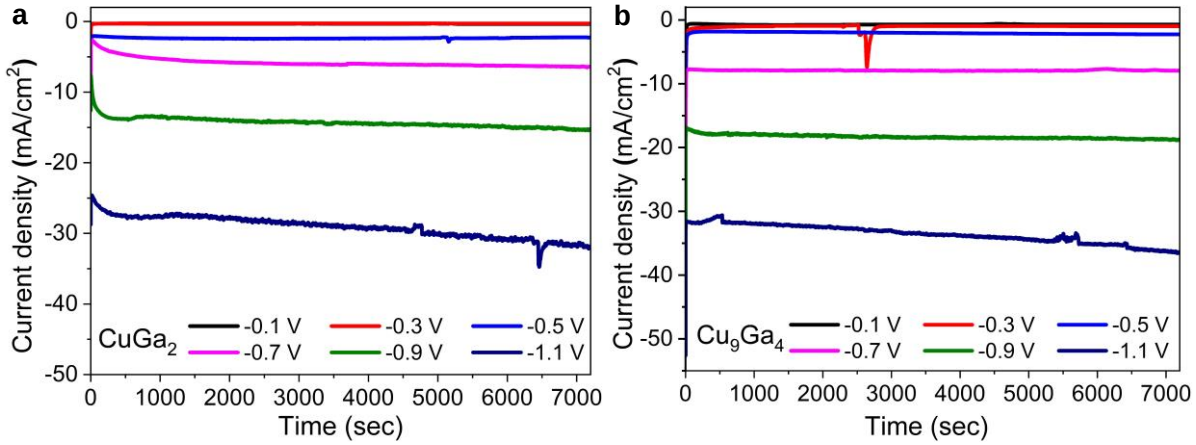

Figure 3.10. Chronoamperometric study (current density as a function of time) on (a) $CuGa_2$ and (b) Cu_9Ga_4 catalysts during electrochemical CO_2RR in 0.5 M $KHCO_3$.

To understand the role of ECSA in activity enhancement, double layer capacitances (C_{dl}) of the catalysts were determined (**Figure 3.11a-b)** As shown in **Figure 3.11c**, Cu_9Ga_4 (9.15 mF/cm^2) exhibits larger C_{dl} values than $CuGa_2$ (1.7 mF/cm^2). From these, the roughness factors have been found to be 129.6 and 24.08 for Cu_9Ga_4 and $CuGa_2$ respectively. Although the ECSA and roughness were found to be higher for Cu_9Ga_4 than $CuGa_2$, the eCO_2RR activity was found to be more in case of $CuGa_2$ can be correlated to the fact that the enhanced eCO_2RR activity is not solely due to the surface area effect; instead, the electronic and structural effects also contributed substantially.

3.4.3. Product quantification and Faradaic efficiency (FE)

Figure 3.12a-b shows the FEs and eCO_2RR product distributions as the function of applied potentials from -0.1 V to -1.1 V over both catalysts. The product distribution and their corresponding FEs are given in **Table 3.1**.

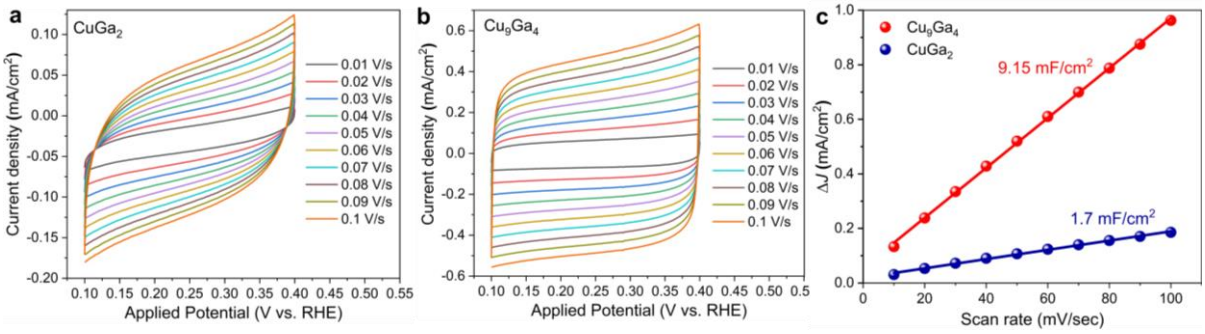

Figure 3.11. Cyclic voltammograms (CVs) of (a) $CuGa_2$, (b) Cu_9Ga_4, sweeping over the potential from 0.1 V to 0.4 V (vs. RHE) for the determination of double-layer capacitance (C_{dl}) and thereby estimation of effective surface area (ECSA). (c) Plots of ΔJ vs. scan rate for Cu_9Ga_4 and $CuGa_2$ where the slope of the fitted line gives the corresponding C_{dl} values.

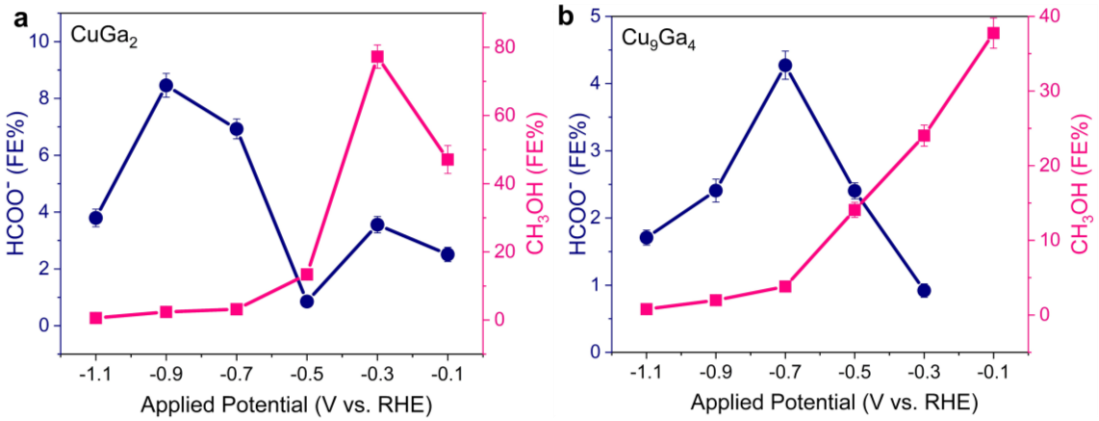

Figure 3.12. Electrochemical CO_2RR performance. Faradaic efficiency for each CO_2 reduced liquid product methanol and formic acid as a function of potential during eCO_2RR on (a) $CuGa_2$ and (b) Cu_9Ga_4.

Both the compounds show a similar product distribution trend producing methanol with substantial FE in lower overpotential (-0.1 to -0.5 V vs. RHE) and formic acid in relatively higher overpotential (-0.7 to -1.1V vs. RHE) (**Figure 3.13**).

Cu_9Ga_4 has produced methanol with FE of 37.75% at -0.1 V, and its activity gradually decreased as the overpotential is increased. $CuGa_2$ catalyst exhibited a volcano-shaped dependence of both methanol and formic acid on applied potential, and the maximum FE (77.26%) of methanol was achieved at -0.3 V potential with respect to RHE (**Figure 3.12a** & **Table 3.1**). C_2 product (acetic acid) has been observed at extremely low overpotential (−0.1 V vs. RHE) with FE of 40.80% and gradually decreased at a higher potential.

Table 3.1. Faradaic efficiency of CO_2 reduced products on catalysts surface at different applied potential (vs. RHE).

Catalyst	Product	FE (%) at different applied potential (vs. RHE)					
		−0.1 V	**−0.3 V**	**−0.5 V**	**−0.7 V**	**−0.9 V**	**−1.1 V**
$CuGa_2$	**CH_3OH**	47.07	77.25	13.38	3.16	2.39	0.59
	HCOOH	2.51	3.55	0.85	6.92	8.46	3.79
	CH_3COOH	40.80	16.41	5.94	1.79	1.13	0.41
	CO	-	-	0.57	42.05	18.20	12.11
Cu_9Ga_4	**CH_3OH**	37.75	24.03	14.07	3.82	1.97	0.78
	HCOOH	-	0.91	2.40	4.27	2.40	1.70
	CH_3COOH	21.87	13.29	6.81	1.31	0.88	0.36

	CO	-	-	3.86	12.38	7.42	6.41

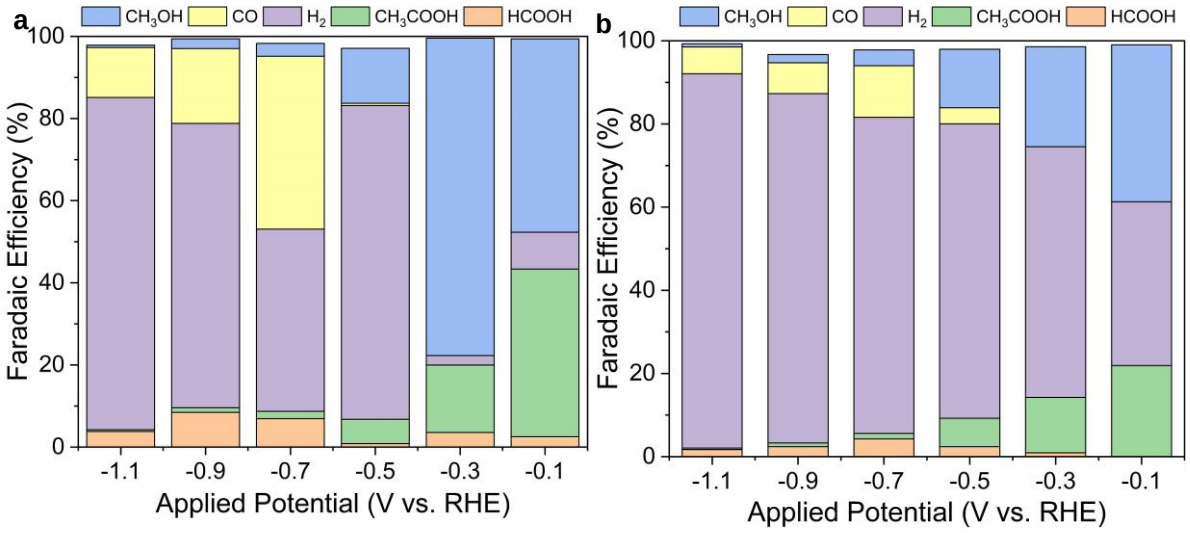

Figure 3.13. Faradaic efficiency for all the liquid and gaseous products found during CO_2 reduction as a function of potential during on (a) $CuGa_2$ and (b) Cu_9Ga_4 catalysts.

At relatively higher potential, CO has been formed with a good yield (FE of 42.05% at -0.7 V) on $CuGa_2$. Potential dependent product distributions have been plotted in **Figure 3.13** and listed in **Table 3.1**. Analysis of FEs of all the products suggested that the $CuGa_2$ catalyst is a much more active material for eCO_2RR compared to Cu_9Ga_4. The enhanced activity of $CuGa_2$ can be attributed to its unique tetragonal structure accompanied by 2D morphology (as shown in AFM and TEM analysis) and can expose more active sites for the CO_2 reduction. To have an in-depth depth mechanistic analysis and understand the driving force behind the enhanced CO_2 reduction and methanol selectivity in $CuGa_2$, we have performed comprehensive studies with the help of in-situ and ex-situ characterization techniques.[27, 28]

3.4.4. In situ electrochemical ATR-FTIR study

In-situ attenuated total reflection (ATR) Fourier transform (FT) Infra-Red (IR) spectroscopy was performed to probe the reaction pathways and intermediates involved in the eCO_2RR over $CuGa_2$ and Cu_9Ga_4 catalysts.[29] **Figure 3.14a** shows the potential-dependent in-situ IR spectra using $CuGa_2$ as the catalyst in CO_2 saturated 0.5 M $KHCO_3$ medium. The notable peaks observed at 1519 cm^{-1} and 1373 cm^{-1} can be assigned as the stretching frequency of the asymmetric and symmetric stretching modes of the OCO group of $HCOO^-$.[30] The time-dependent evolution of these two crucial intermediates has been depicted in **Figure 3.14b** where the absorption intensity has been gradually increased over time during the chronoamperometric study at -0.3 V (vs. RHE) indicates accumulation of more amount of adsorbed intermediate and thereby formation of corresponding CO_2 reduced products. A

similar observation has been found in the case of Cu_9Ga_4 catalyst as well (**Figure 3.15**), but the peak positions have been shifted to 1520 cm^{-1} and 1386 cm^{-1}. The negative band at 1628 cm^{-1} can be assigned to O-H bending originated during the water reduction.[31] This feature is more pronounced in the case of Cu_9Ga_4 signifies more HER. The reversed band at 2343 cm^{-1} can be assigned as the consumption of CO_2 in the solution during CO_2RR, which is slightly blue-shifted compared to Cu thin film electrode.[32] $CuGa_2$ exhibited both CO_{bridge} and CO_{atop} adsorbed intermediate, respectively, at 1808 cm^{-1} and 2006 cm^{-1} (**Figure 3.15)**. As expected, the absorption intensity of these two intermediate is negligible as their formation is very dynamic and not stable during the catalytic process.[33] All the IR spectra is having the band centered at 2073 cm^{-1} corresponding to H_{ad}.[34] The peak observed at 1415 cm^{-1} can be assigned to C-O stretching of $HCOO^-$.[31] The frequency for the O-C-H bending of HCO_{ad} is at ~1250 cm^{-1}, and the bidentate $HCOO_{ad}$ peak (~1225 cm^{-1}) have also been detected on $CuGa_2$ (**Figure 3.15**).

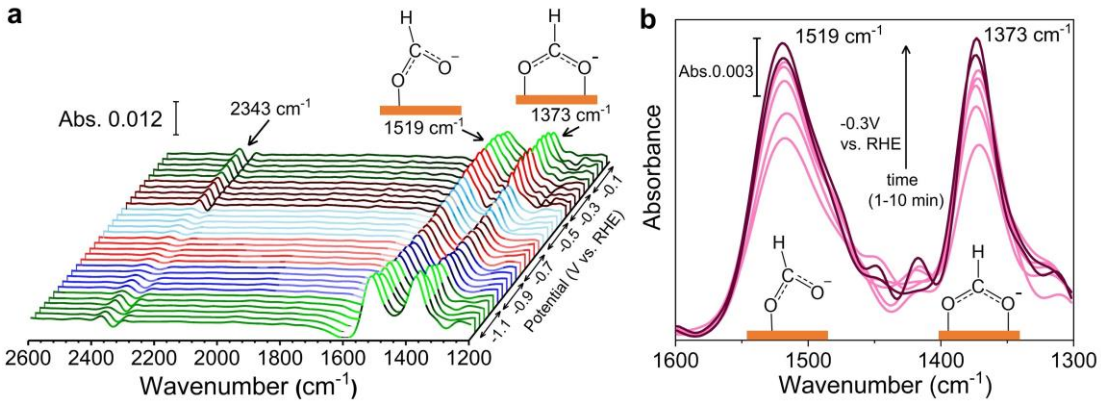

Figure 3.14. Mechanistic investigation of CO_2RR by in-situ IR study. (a) In-situ IR spectra obtained during the eCO_2RR using $CuGa_2$ catalyst. (b) IR spectra corresponding to CHO and COOH intermediate formed during methanol production at a different time during CA at -0.3 V (vs. RHE). (c) Plausible reaction mechanism for eCO_2RR to methanol on Cu-Ga based ordered intermetallic catalysts.

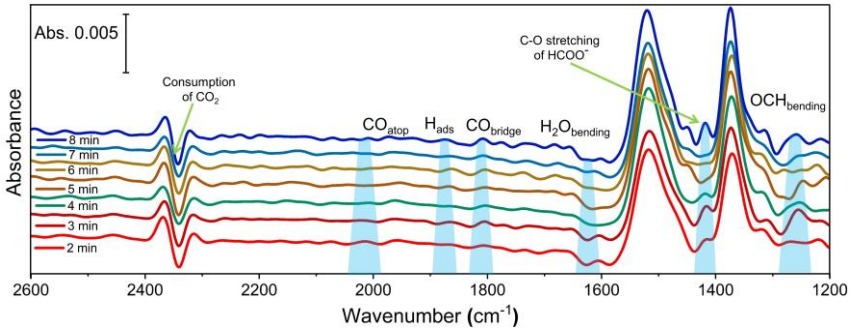

Figure 3.15. Real-time FT-IR spectra recorded during the chronoamperometry at -0.3 V (vs. RHE) of $CuGa_2$ catalyst in a CO_2-saturated 0.5 M $KHCO_3$ solution.

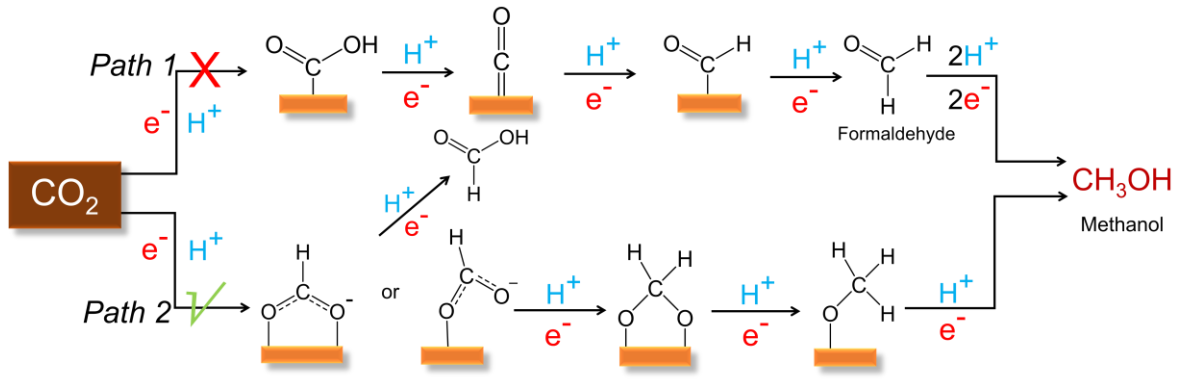

Figure 3.16. Plausible reaction mechanism for eCO_2RR to methanol on Cu-Ga based ordered intermetallic catalysts.

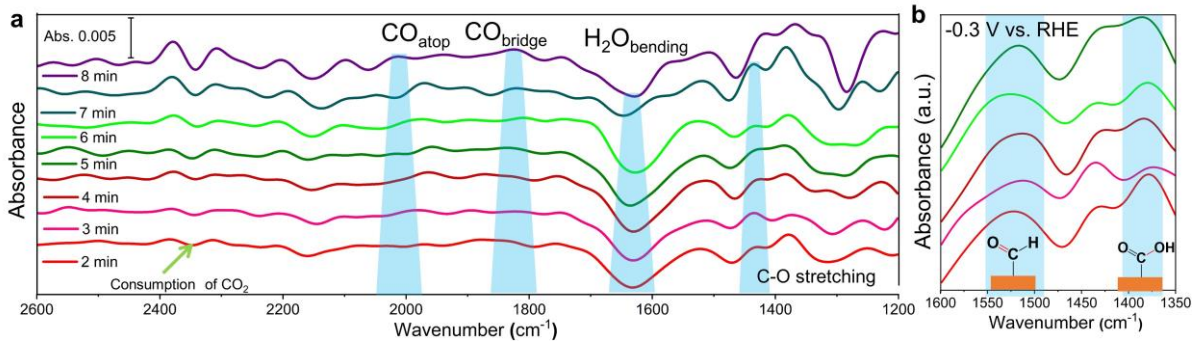

Figure 3.17. (a) Real-time FT-IR spectra recorded during the chronoamperometry at -0.3 V (VS RHE) of Cu_9Ga_4 catalyst in a CO_2-saturated 0.5 M $KHCO_3$ solution. (b) Evolution of IR spectra corresponding to major intermediate formed during eCO_2RR.

Based on the in-situ IR spectroscopic measurements, the conversion of CO_2 to methanol mechanism can be explained by two possible reaction pathways based on the C and O affinity trends on the catalyst surface (**Figure 3.16**). The observed asymmetric and symmetric stretching modes of the COO group of the $HCOO^-$ species (both are O-bound intermediate) ensures that *path 2* is the more probable mechanism for the formation of methanol during the course of CO_2RR. Moreover, the formation of HCOOH (minor product) is only possible through the second pathway. On the other hand, the formation of CO at the higher overpotential indicates the first pathway. The absorption intensity corresponding to the two major intermediates for methanol formation is relatively less in the case of Cu_9Ga_4 (**Figure 3.17**) compared to $CuGa_2$ indicates a lower formation of methanol on Cu_9Ga_4, which has been already verified in the product analysis section.

3.4.5. Oxidation state and Local electronic structures from XAFS

To elucidate the local structure, oxidation state, and coordination atmosphere of Cu and Ga, X-ray absorption (XAS) study has been performed. In **Figure 3.18a**, the absorption edge

corresponding to the white line involves 1s→4p dipole transition, shifts towards higher photon energy value than the Cu foil in both the compounds (Cu_9Ga_4:8998.86 eV & $CuGa_2$:9000.62 eV), indicates the presence of Cu having a higher oxidation state in the catalysts than the elemental state.[35] The presence of Cu_2O or CuO can be ruled out as the Cu-O bond (around 1.6 Å) is not observed in the R-space data of the EXAFS plot (**Figure 3.18b**). On the other hand, in the XANES of Ga *K*-edge of Cu_9Ga_4 (**Figure 3.18c**), there is an absorption maximum at 10378.37 eV and a shoulder at about 10382.46 eV, which are expected from the two types of Ga present in the system (Wyckoff position:4e & 12i). Whereas, $CuGa_2$ shows only one absorption edge (10378.92 eV) as it has only one type of Ga site (Wyckoff position:2h) in the crystal structure.

The position of absorption maxima of both the samples resembles that of Ga metal. The structural parameters obtained after fitting (**Figure 3.19**) the first coordination shell (**Table 3.2**) confirmed that the coordination number of Cu with respect to Ga (in the first coordination sphere) is higher (6.24) in the case of $CuGa_2$ compared to Cu_9Ga_4 (3.63), which can facilitate more Ga site to be exposed for oxidation and forming Ga_2O_3.

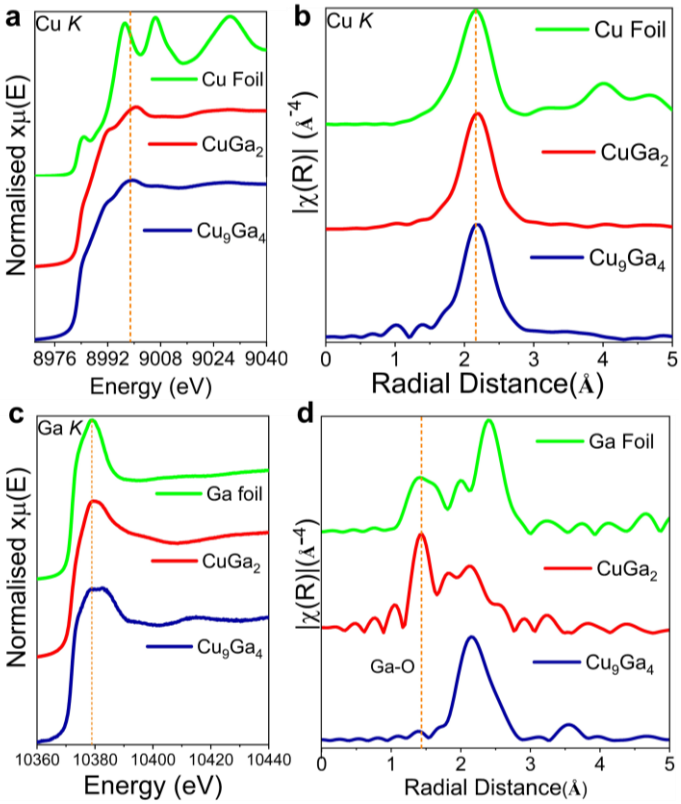

Figure 3.18. XAS analysis of Cu-Ga catalysts. Comparison of (a) normalized XANES spectra, (b) Fourier transformed R-space data of Cu *K*-edge of $CuGa_2$, Cu_9Ga_4 with the respective metal foil. Comparison of (c) normalized XANES spectra, (d) Fourier transformed R-space data of Ga *K*-edge of $CuGa_2$, Cu_9Ga_4 with the standard sample.

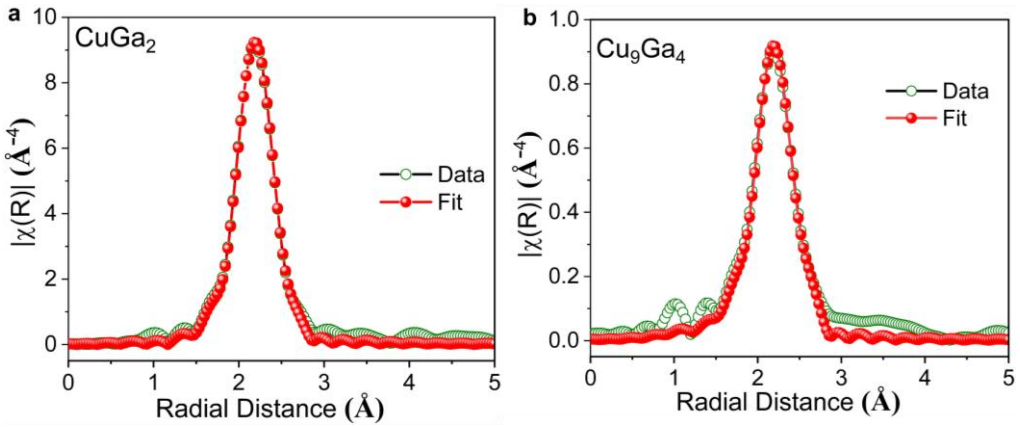

Figure 3.19. Fitted Fourier transformed R-space data of Cu *K*-edge for (a) $CuGa_2$ and (b) Cu_9Ga_4 catalysts. Olive represents the experimental data, and red represents the overall fit.

The peak observed at around 1.43 Å can be attributed to the presence of Ga_2O_3 in the $CuGa_2$ catalyst, which is absent in the case of the Cu_9Ga_4 catalyst (**Figure 3.18d**). On the other hand, the nature of the Cu-Cu bond distance is quite close in both systems but slightly different than that of elemental Cu (**Figure 3.19a-b**).

Table 3.2. Refined parameters were obtained after EXAFS fitting of Cu-k edge in $CuGa_2$ and Cu_9Ga_4.

	Path	**CN**	**S_0^2**	**σ^2 (Å^2)**	***E*$_0$ (eV)**	**ΔR (Å)**	**R (bond dis.) (Å)**
$CuGa_2$	Cu-Ga	6.24	1.0	0.026(1)	2.72	-0.0037(3)	2.6366(3)
	Cu-Cu	3.12	1.0	.0081(1)	2.72	-0.2888(1)	2.5411(1)
Cu_9Ga_4	Cu-Cu_3	4.381	1.0	0.0079(1)	0.32	0.0633(1)	2.5805(1)
	Cu-Cu_5	0.8	1.0	0.0030(1)	0.32	0	2.54910
	Cu-Cu_6	0.8	1.0	0.0030(1)	0.32	0	2.59580
	Cu-Ga_2	3.630	1.0	0.0049(1)	0.32	-0.0529(1)	2.5658(1)

3.4.6. Potential dependent in-situ XAFS analysis

The real-time in-situ XAFS was performed to map the change of oxidation state and the coordination atmosphere around both Ga and Cu at different applied potentials. The XAFS signal has been detected in the fluorescence mode in the operando study. In the case of Fourier transformed R-space data of Ga *K-edge* of $CuGa_2$, it has been observed that the intensity of the peak corresponding to the Ga-O bond at around 1.43 Å gradually reduced as the negative potential increases from -0.1V to -1.1V (**Figure 3.20a**). It is also seen that the second major peak (at around 2.2-2.3 Å), which can be corresponding to Ga-Ga bond, increases its intensity at the higher potentials.

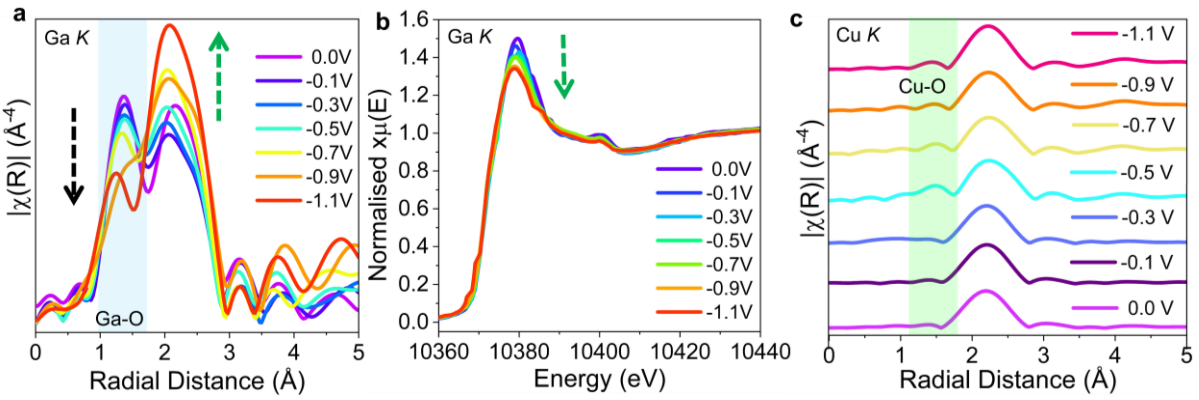

Figure 3.20. Potential dependent in-situ XAS and ex-situ XPS characterizations in CO_2RR conditions. (a) Fourier transformed R-space data of Ga *K-edge* of $CuGa_2$ catalyst at different potential during in-situ XAS. (b) Comparison of normalized XANES spectra of Ga *K*-edge during in-situ XAS. (c) Fourier transformed R-space data of Cu *K-edge* of $CuGa_2$ catalyst at different potential during in-situ XAS.

Figure 3.20b shows that the white line intensity of the XANES spectra of Ga *K*-edge decreases in the higher negative potential, indicating the reduction of Ga^{3+}, which is also correlated to the fact that the absorption energy also shifts to the lower photon energy (**Figure 3.20b**). The coordination numbers (CN) corresponding to Ga-Ga and Ga-O bond derived from EXAFS fitting of Ga *K*-edge, at each potential in the CO_2RR conditions, suggest that the CN_{Ga-Ga} progressively increases as the reduction potential increases (**Figure 3.21a**, **Table 3.3**). Consequently, the CN_{Ga-O} also decreases and the catalyst surface contains more metallic in nature in the higher negative potential as evident.

Table 3.3. Calculated coordination numbers (CN) corresponding to Ga-Ga and Ga-O bonds derived from EXAFS fitting of Ga-*K* edge of $CuGa_2$ during in-situ XAS in CO_2RR condition.

Applied potential (V vs. RHE)	**CN_{Ga-Ga}**	**CN_{Ga-O}**	**CN_{Ga-Ga} / CN_{Ga-O}**
0.0 V	3.35	1.68	1.98
-0.1V	3.71	1.66	2.22
-0.3V	4.35	1.64	2.64
-0.5V	5.02	1.61	3.10
-0.7V	6.45	1.60	4.01
-0.9V	6.59	1.59	4.14
-1.1V	7.20	1.49	4.83

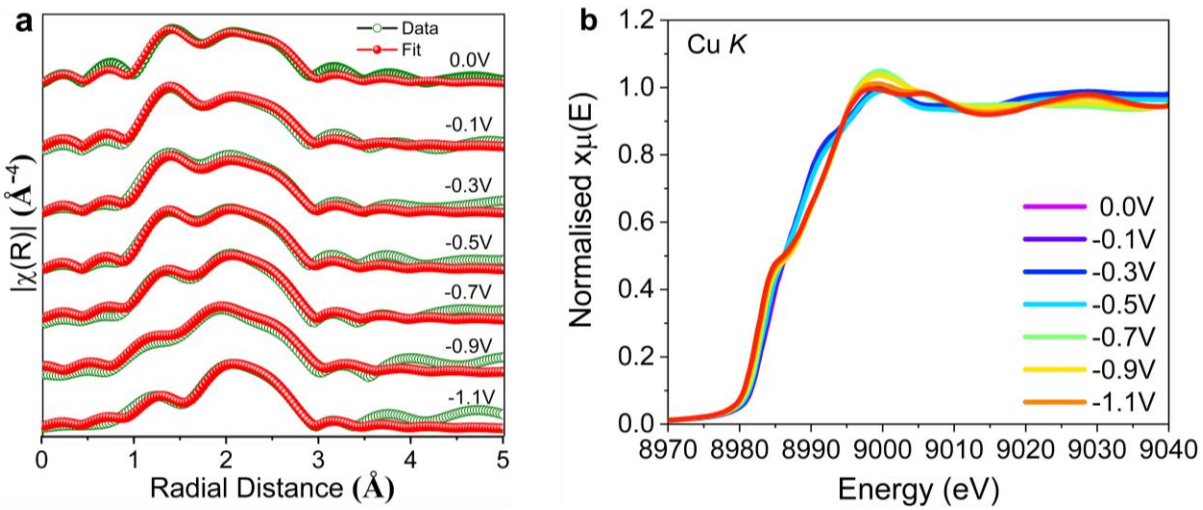

Figure 3.21. (a) Fitted Fourier transformed R-space data of Ga *K*-edge for $CuGa_2$ at different applied potential during in-situ XAS in CO_2RR condition. (b) Comparison of normalized XANES spectra of Cu K-edge during in-situ XAS study.

On the other hand, the coordination atmosphere of Cu does not change much except there is an evolution of Cu-O bond during the CO_2RR as indicated in **Figure 3.20c** and a corresponding shift of the absorption energy in the XANES spectra of Cu *K*-edge towards higher photon energy (**Figure 3.21b**). The in-situ XAFS study clearly indicates that Ga_2O_3 is the main active species for the methanol selectivity at the lower potential and the selectivity reduces at the higher negative potentials due to the reduction of surface Ga_2O_3.

3.4.7. Potential dependent Ex-situ XPS and powder XRD analysis

To gain insight into the potential-dependent surface composition and the associated oxidation state of each element, ex-situ XPS has been employed before and after eCO_2RR. XPS spectra of Cu 2*p* for both the catalysts (**Figure 3.22a-b**) show that Cu is in a slightly (higher than +1) oxidized state as the corresponding Cu $2p_{3/2}$ peak originates at around 933.4 eV, and the satellite peak of Cu^{2+} is also observed at around 944.38 eV (**Figure 3.23a**).[36, 37] The Cu $2p_{3/2}$ signal shifts observed at 933.4 eV in the absence of applied potential to 935.08 eV at -0.1 V indicates the charge transfer from Cu to Ga during eCO_2RR in the case of Cu_9Ga_4 catalyst. However, at higher reduction potential (-0.5 V to -0.9 V vs. RHE) the Cu $2p_{3/2}$ peak gradually shifts back to the lower binding energy suggesting the reduction of surface oxidized copper species in those extreme conditions. A similar observation was found in the case of $CuGa_2$ as well (**Figure 3.23b**).

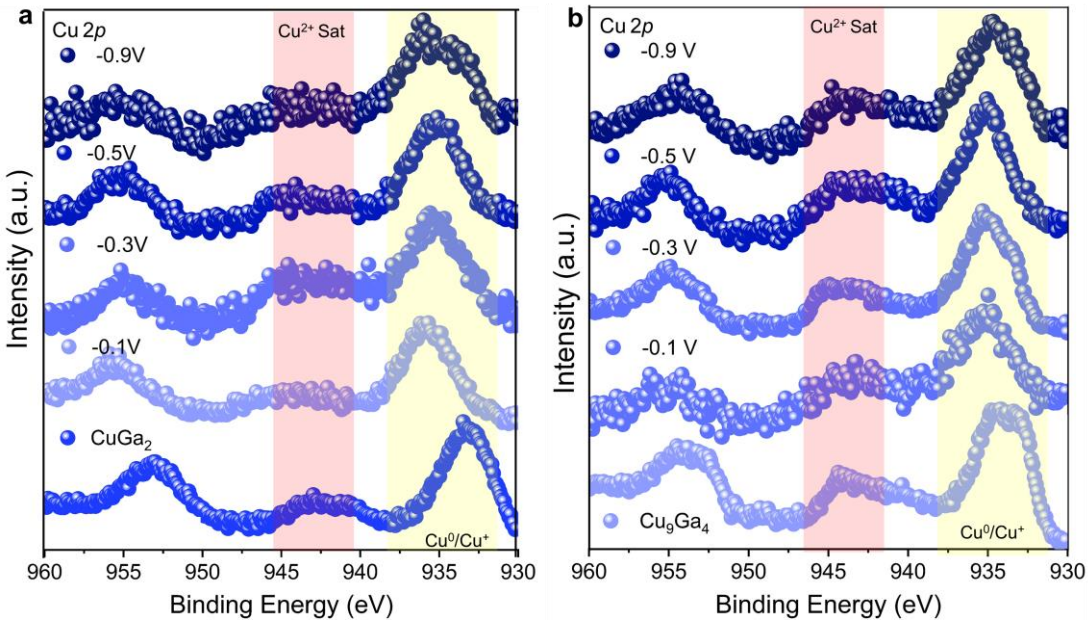

Figure 3.22. High-resolution XPS spectra of Cu 2*p*, for (a) Cu_9Ga_4 and (b) $CuGa_2$ pristine catalysts and the catalyst coated carbon electrode after application of a potential of -0.1V, -0.5V, and -0.9V during the chronoamperometric study for eCO_2RR.

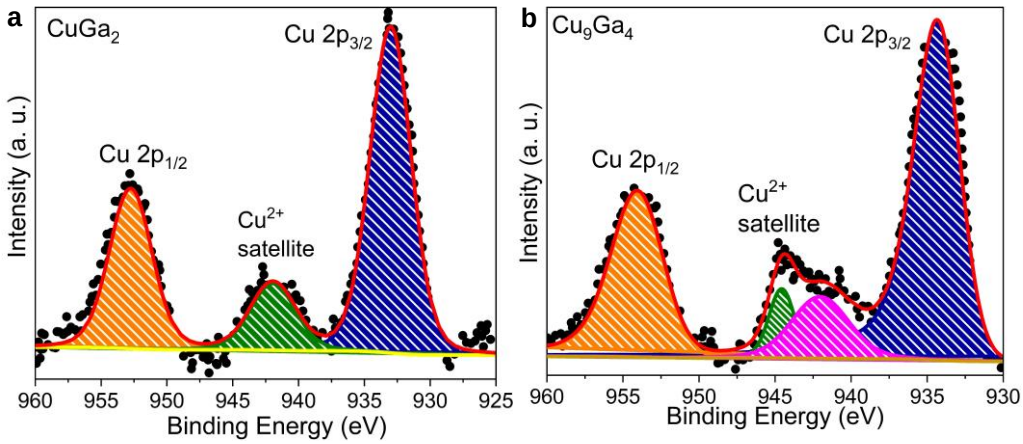

Figure 3.23. Cu 2*p* XPS spectra of (a) $CuGa_2$ and (b) Cu_9Ga_4. Cu $2p_{3/2}$ and $2p_{1/2}$ states are represented by the royal blue and orange curves, and the satellite peak of Cu^{2+} is represented by olive and magenta curves.

On the other hand, the analysis of the 3*d* region for Ga showed the $3d_{5/2}$ peak at around 20.4 eV in the case of both Cu_9Ga_4 and $CuGa_2$, which is very close to that of Ga_2O_3 reported in the literature (**Figure 3.24a-b**).[38] After applying the negative potential (-0.1V), the spectrum shows a typical signature peak of metallic Ga ($3d_{5/2}$) at about 18.2 eV and a broader shoulder of Ga_2O_3 at 20.2 eV ($3d_{5/2}$) (**Figure 3.24a**). The characteristic broad peak at around 22.5 eV corresponds to O 2*s*. As the negative potential increases further (from -0.5 V to -0.9 V), the

oxidation state of Ga decreases where the metallic Ga phase is predominantly observed at 18 eV. On the other hand, in the case of $CuGa_2$, the peak related to Ga_2O_3 persistent in the wide range of negative potential (-0.1 V to -0.5V).

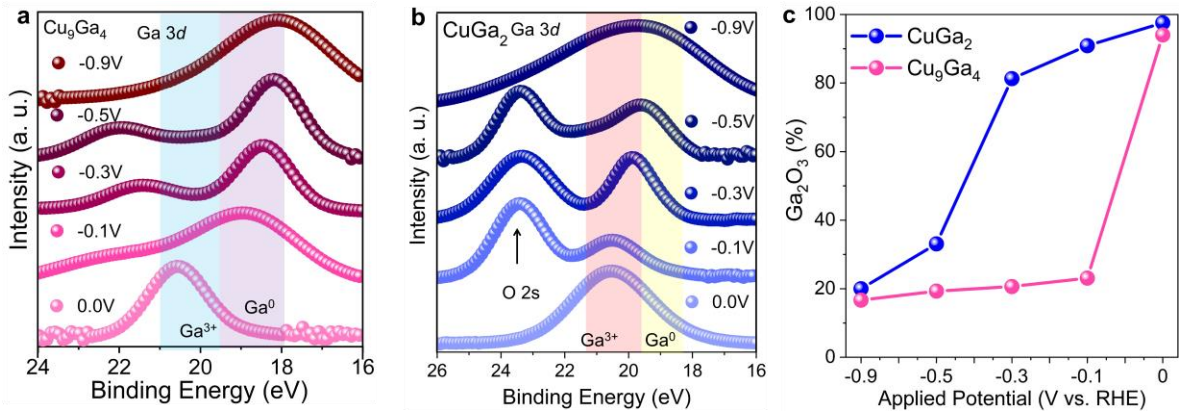

Figure 3.24. Potential dependent XPS characterizations in CO_2RR conditions. (a) High-resolution XPS spectra of Ga 3*d* for Cu_9Ga_4. (b) $CuGa_2$ for pristine catalysts and after eCO_2RR at different applied potential (-0.1V, -0.3V, -0.5V, and -0.9V) during the chronoamperometric study. (c) Comparison of the amount of surface Ga_2O_3 on $CuGa_2$ and Cu_9Ga_4 catalysts at different applied potentials during eCO_2RR study.

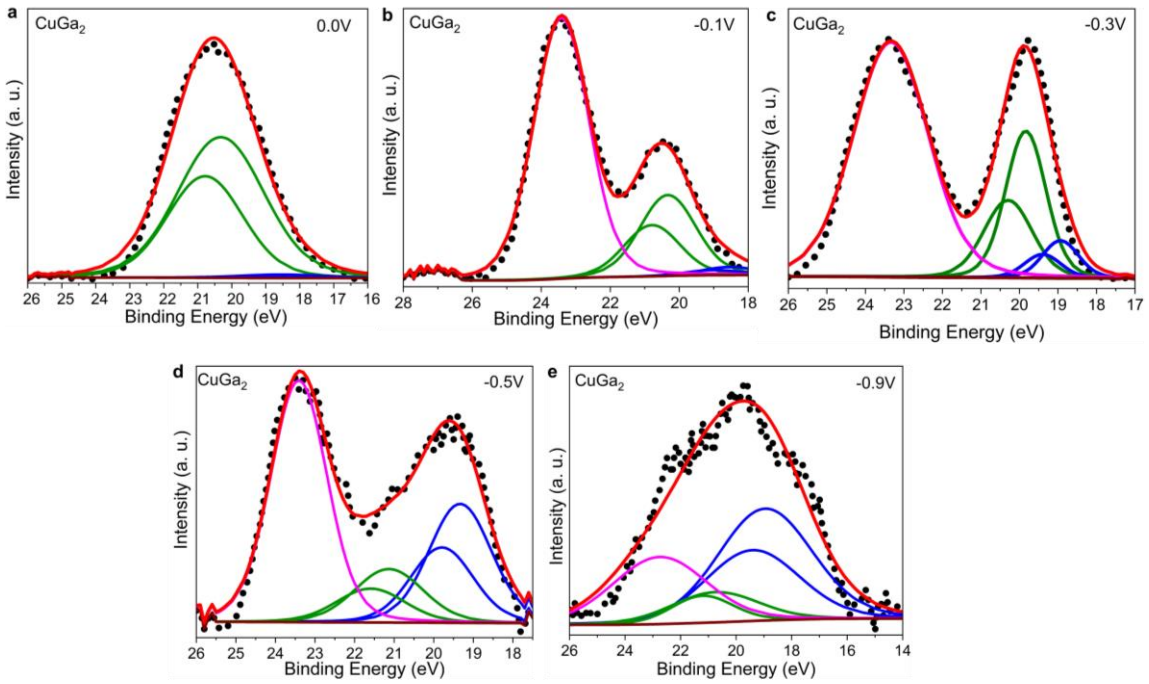

Figure 3.25. Ga 3*d* XPS spectra of (a) pristine $CuGa_2$ at (b) -0.1V, (c) -0.3V, (d) -0.5 and (e) -0.9V applied potential. Ga $3d_{5/2}$ and $3d_{3/2}$ states are represented by the blue curves, Ga_2O_3 $3d_{5/2}$ and $3d_{3/2}$ states are represented by the green curve. The O 2*s* spectra are denoted by the magenta curve.

In the significantly higher negative potential, the Ga 3*d* peak has been shifted to lower binding energy, indicating a lowering oxidation state of Ga in $CuGa_2$. The enrichment of Ga_2O_3 on the surface of the catalysts was quantified using the XPS data (**Table 3.4, Figure 3.25-3.26**). **Figure 3.24c** shows the relative % of Ga_2O_3 on the catalysts as a function of potential, and it is evident that the amount of surface oxide species observed is more on $CuGa_2$ surface than that of Cu_9Ga_4 at a negative potential.

Table 3.4. Amount (%) of Ga_2O_3 present on the surface of the catalyst was obtained from XPS considering Ga $3d_{5/2}$ and Ga_2O_3 using the following equation

$$Ga_2O_3 = \frac{Ga_2O_3}{Ga_2O_3 + Ga(0)} \times 100\%$$

$CuGa_2$		**Cu_9Ga_4**	
Potential	**Ga_2O_3 (%)**	**Potential**	**Ga_2O_3 (%)**
0.0 V	97.57	0.0 V	94.03
-0.1 V	90.90	-0.1 V	23.07
-0.3 V	81.30	-0.3 V	20.63
-0.5 V	33.08	-0.5 V	19.29
-0.9 V	20	-0.9 V	16.66

The existence of Ga_2O_3 in the higher potential can be originated from the subsurface oxide present in the system, which is in good agreement with the R-space EXAFS data of Ga *K*-edge.

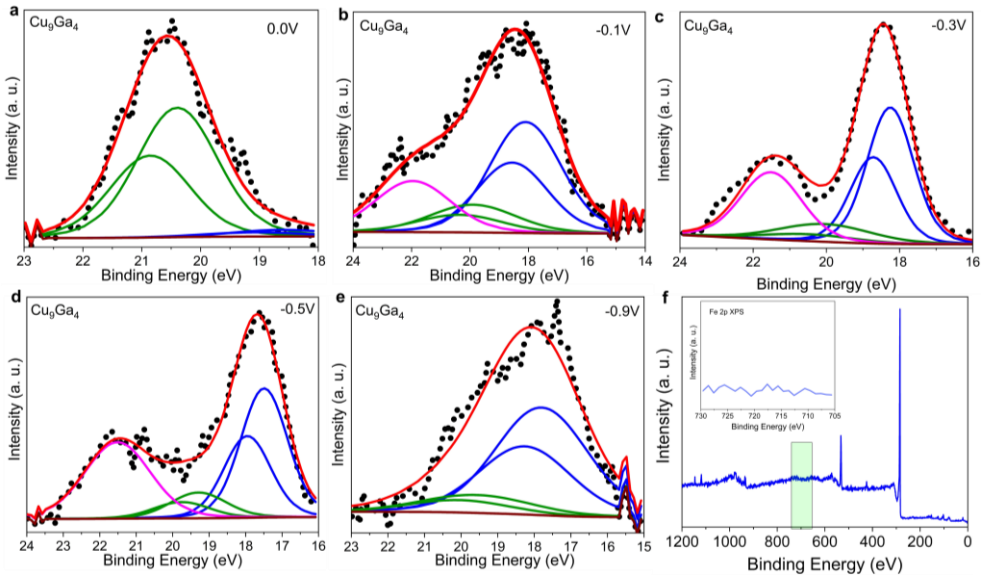

Figure 3.26. Ga 3*d* XPS spectra of (a) pristine Cu_9Ga_4 at (b) -0.1V, (c) -0.3V, (d) -0.5V and (e) -0.9V applied potential. Ga $3d_{5/2}$ and $3d_{3/2}$ states are represented by the blue curves, Ga_2O_3 $3d_{5/2}$ and $3d_{3/2}$ states are represented by the green curve. The O 2*s* spectra are denoted by the magenta curve. (f) Overall XPS survey spectra of Cu_9Ga_4 and (g) XPS spectra centered on Fe 2p to detect any Fe impurity coming during ball milling process.

The possibility of Fe impurity in the ball-milled sample has been ignored as there is no indication of Fe 2p peaks in XPS spectra presented in **Figure 3.26f**. The presence of a substantial amount of Ga_2O_3 in the lower potential facilitates the absorption of the key intermediate for the formation of methanol.[39, 40] As discussed earlier, two crucial intermediates asymmetric and symmetric stretching modes of the COO group of the $HCOO^-$ observed in the in-situ IR measurements are stabilized by the presence of surface Ga_2O_3. The adsorbed H from the Cu site can spill over to the Ga site and combine with the adsorbed formate intermediate to produce methanol selectively. It is indeed evident that a large amount of Ga_2O_3 at the surface of the $CuGa_2$ catalyst facilitates the efficient conversion of CO_2 to methanol with high FE.

It is very important to know the actual active crystallographic phase responsible for the catalytic reaction as the crystal structure and phase can be changed during eCO_2RR at the negative potential.[41] To understand the structural changes during eCO_2RR, powder XRD of the working electrodes was recorded immediately after the electrolysis at each potential (**Figure 3.27**). In the case of $CuGa_2$, the intensity of the most exposed crystallographic plane (102) has been decreased gradually as the overpotential is increased in comparison to the second major plane (110). The intensity ratio of these two peaks (102:110) decreases as a function of applied potential (**Figure 3.28b**), which confirms that the (102) plane has been affected mostly upon negative potential during eCO_2RR conditions with concomitant reduction of Ga_2O_3 to Ga. Subsequently, crystal lattice expanded in the perpendicular direction of the (102) plane, where (110) plane resides (**Figure 32**) and the powder XRD peak corresponding to the (110) plane shifted to lower 2θ value (**Figure 3.28a**).

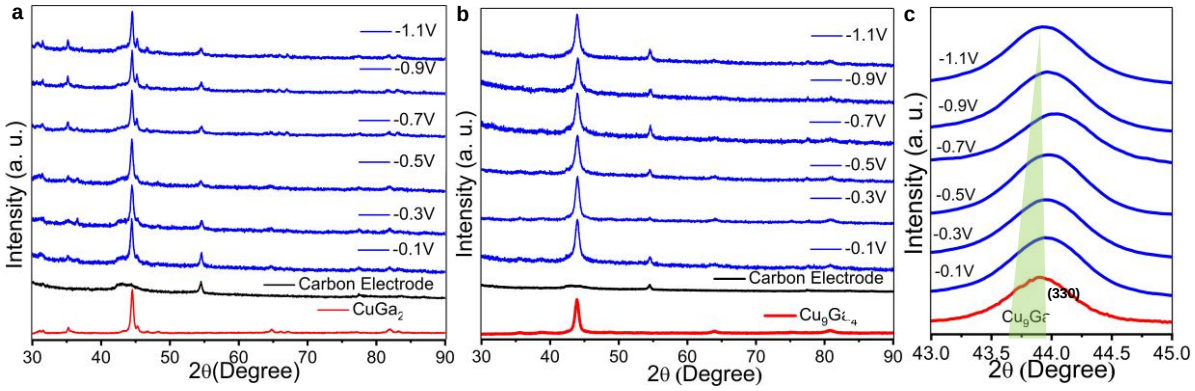

Figure 3.27. Post electrochemical powder XRD analysis of (a) $CuGa_2$, and (b) post electrochemical powder XRD analysis of Cu_9Ga_4 recorded after electrolysis at each potential. (c) the potential dependent peak shifting corresponding to the major crystallographic plane (330).

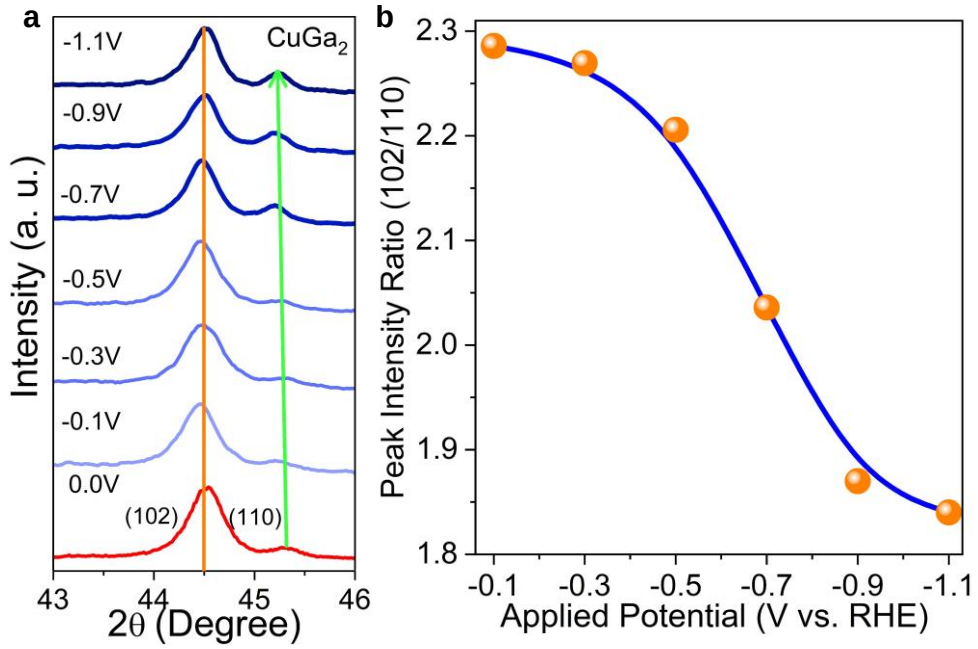

Figure 3.28. Post-electrochemical powder XRD. (a) Potential dependent peak shifting corresponding to the major crystallographic plane in $CuGa_2$. (b) The ratio of the peak intensity of two major crystallographic planes (102) and (110) as a function of potential in $CuGa_2$ catalyst.

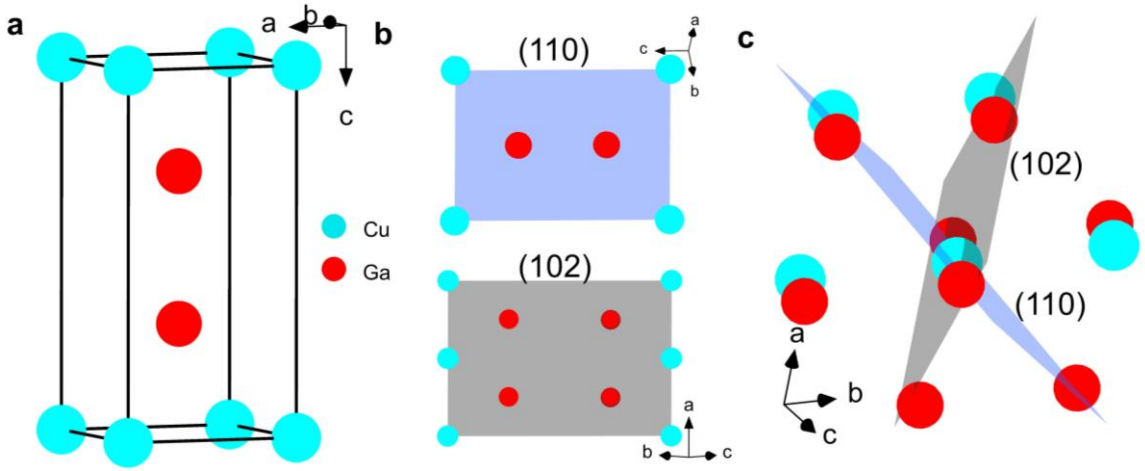

Figure 3.29. Unit cell representation of (a) $CuGa_2$ lattice. (b) Pictorial representation of two major crystallographic planes of $CuGa_2$ lattice.

In the higher overpotential, the intensity of the active crystallographic plane decreased which is directly affecting the electrocatalytic property. Because of the bulk 3D structure of Cu_9Ga_4, the major crystallographic plane (330) has been slightly affected by applying potential and shifted to right at lower negative potential suggesting the contraction of the lattice (**Figure 3.29b-c**). At extremely higher potential, the observed shift is not prominent.

3.4.8. High current density using flow cell with GDE configuration

To achieve higher current density by minimizing the CO_2 mass transport issue in the H-cell mentioned in the previous section, electrochemical microflow with gas diffusion electrode (GDE) configuration has been employed. To improve the stability of the GDE and to manage the hydrophobicity and proper current collection, a PTFE-based GDE has been utilized instead of a traditional carbon-based GDE.[25, 42] The GDE has been optimized with proper loadings of carbon and graphite on PTFE coated catalyst layer where the PTFE layer acts as the stable hydrophobic gas diffusion layer which prevents the electrolyte flooding, and the carbon and graphite layers stabilizes the catalyst surface along with an increase in the conductivity.[42] In flow cell configuration, 1M KOH medium instead of $KHCO_3$ has been used as the electrolyte to enhance the ionic mobility for better current density.[43] The obtained current density in the flow cell increases multiple (~5-200 mA/cm^2) times than that of the H-cell, as can be seen from the LSV (**Figure 3.30**) plot and the CA (**Figure 3.31**) at each individual potential.

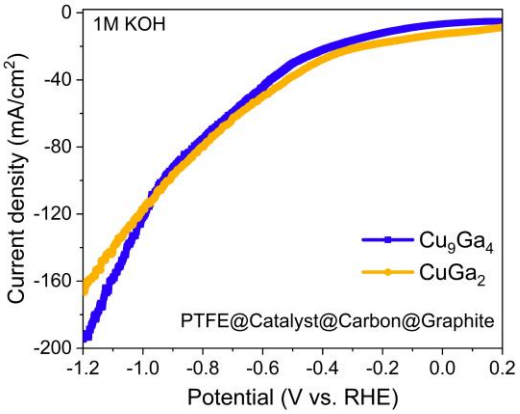

Figure 3.30. Linear sweep voltammogram taken in eCO_2RR condition $CuGa_2$ and Cu_9Ga_4 catalysts in flow cell configuration using GDE in 1M KOH.

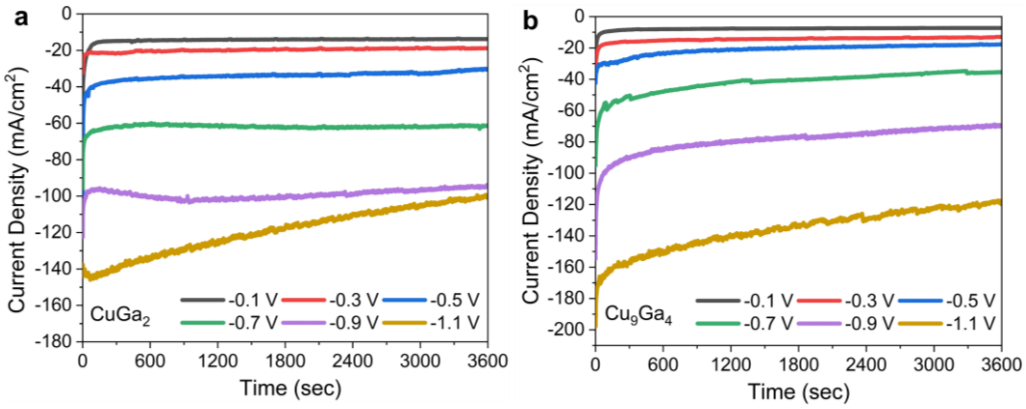

Figure 3.31. Chronoamperometric study (current density as a function of time) on (a) $CuGa_2$ and (b) Cu_9Ga_4 catalysts during electrochemical CO_2RR using flow cell in 1M KOH.

By analyzing the product distribution, it is observed that the FEs for the CO_2 reduced product, especially methanol, have been improved in the flow compared to their respective experiments in the H-cell configuration (**Figure 3.32**). The maximum observed FE for the main product (methanol: ~78%) in the case of $CuGa_2$ with a current density of 21.4 mA/cm^2 has been found to be quite stable in the long term electrolysis process (**Figure 3.33**). From the post-elecyrochemical powder XRD (**Figure 3.33)** and the SEM-EDX (**Figure 3.34)** mapping, it is found that catalyst is extremely stable even after long-term electrolysis process, which had been also reflected in the stability of the catalytic performance.

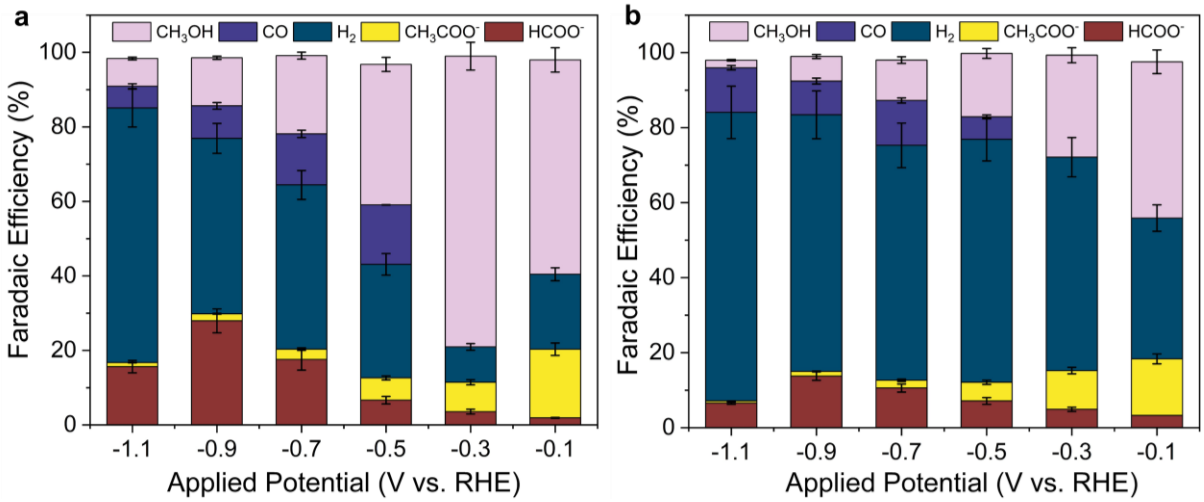

Figure 3.32. Faradaic efficiency for all the liquid and gaseous products found during CO_2 reduction as a function of potential during on (a) $CuGa_2$ and (b) Cu_9Ga_4 catalysts in the flow cell configuration in 1M KOH.

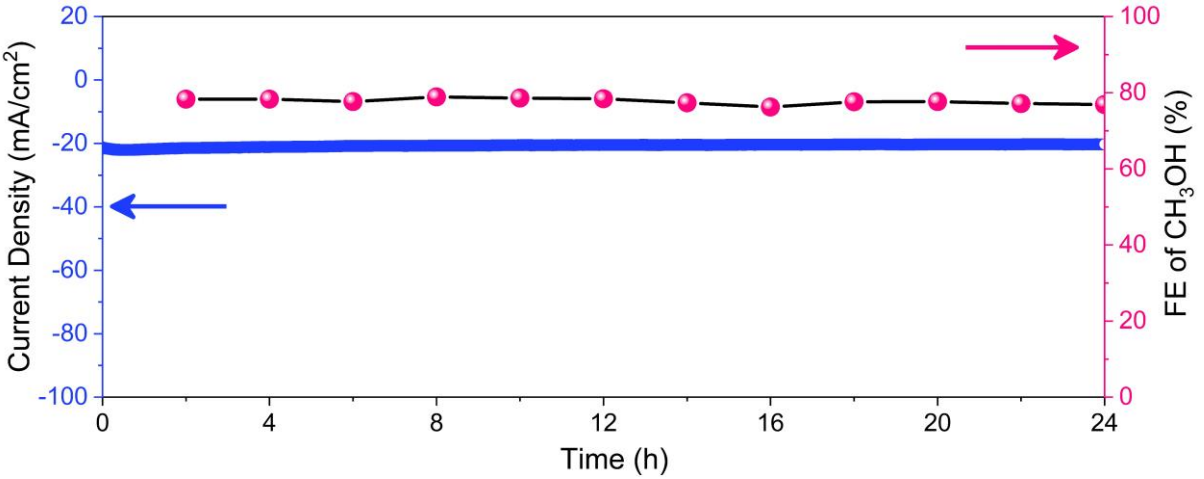

Figure 3.33. Chronoamperometric stability study (current density as a function of time) on $CuGa_2$ at -0.3 V (vs. RHE) and FE of methanol in flow cell configuration in CO_2RR condition.

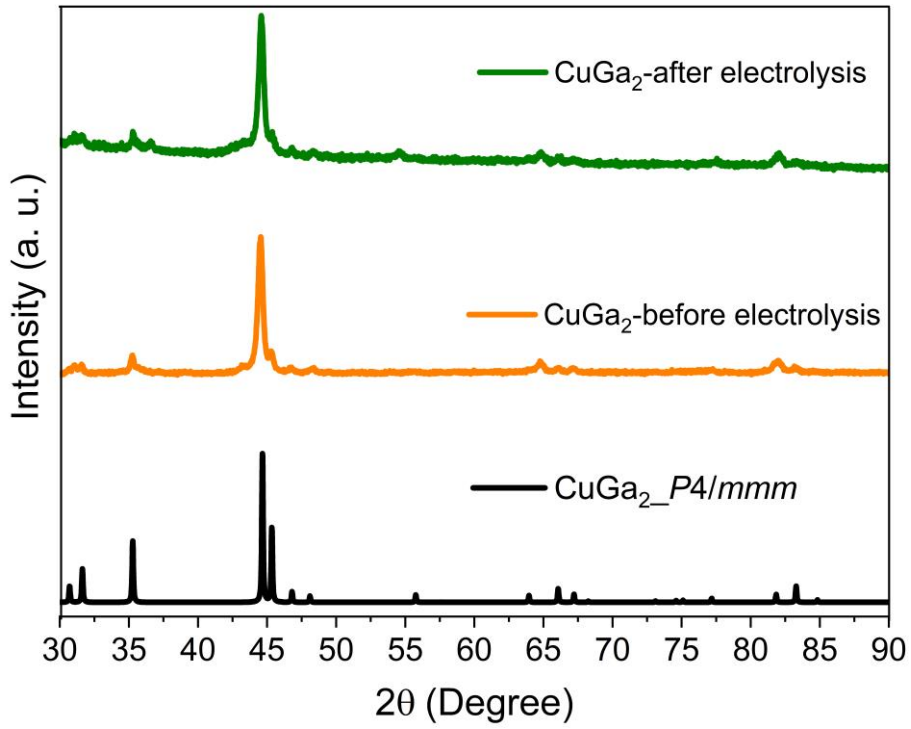

Figure 3.33. Post electrochemical powder XRD analysis of $CuGa_2$ taken after long-term stability study (CA at -0.3V for 24h) and compared that with the powder XRD pattern of pristine catalyst and the simulated XRD pattern of $CuGa_2$.

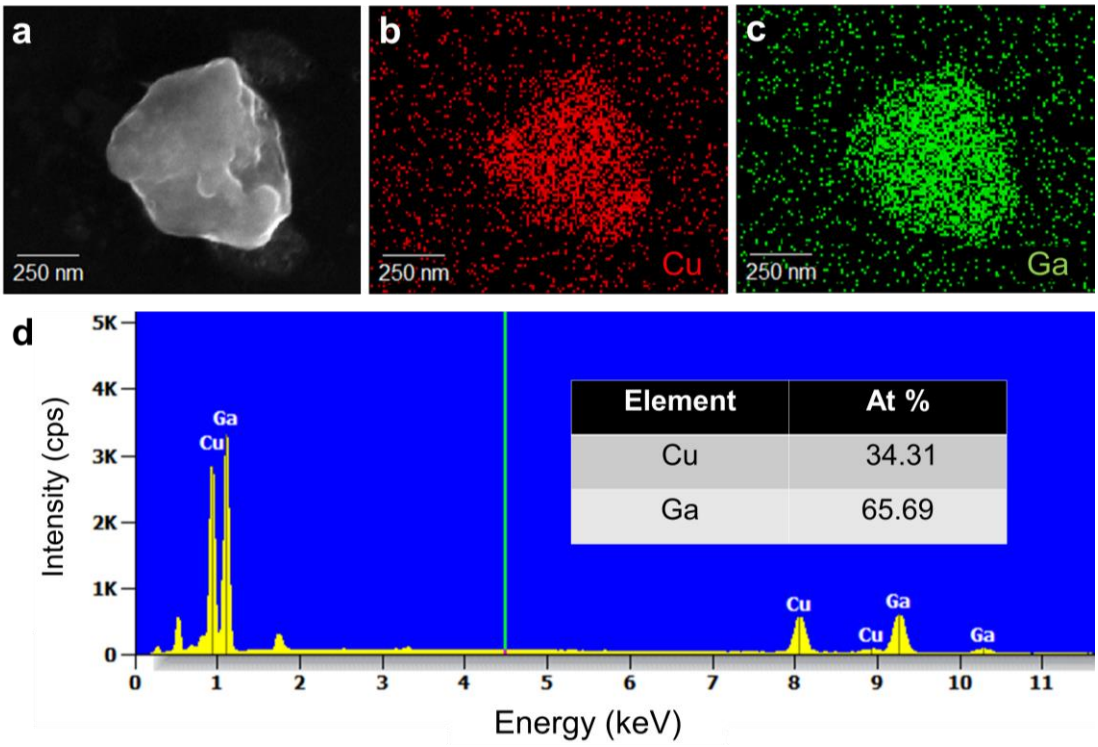

Figure 3.34. (a) Scanning electron microscopy (SEM) image of $CuGa_2$, (b-c) SEM colour mapping on the particle of $CuGa_2$. (d) EDS spectrum of $CuGa_2$ and inset table represents elemental composition $CuGa_2$.

3.5. Conclusion

In conclusion, a material has been designed for the efficient conversion of CO_2 selectively to methanol at ultra-low potential using rational strategy. In an aqueous environment, the developed catalyst $CuGa_2$ exhibited excellent production of methanol with an FE of 77.26% at -0.3 V vs. RHE), which is much higher than many other transition metal-based catalysts reported in the literature (**Figure 3.35**). The current density and overall CO_2RR performance have been improved by utilizing flow cell and optimization of gas-GDE-electrolyte interface. We have implemented the fundamental crystallographic knowledge to design a material with a more exposed surface, which could able to retain the oxide layer generated at the surface of the catalyst during the eCO_2RR and drive the conversion of CO_2 to methanol in high efficiency. The overall performance can be even further enhanced if we can stabilize the surface oxide even in the highly reduction potential, which is challenge. In that condition we could even achieve more than 100 mA/cm^2 current densities. We have developed another catalyst made up of the same metals, Cu_9Ga_4, having a 3D crystal structure with less exposed surface hinders the formation of the oxide layer, which confirms the crucial need of the exposed surface in our strategy. The evolution of crystal structure, operando probing of surface-oxide layer, in-situ mechanism at different surfaces under different electrochemical potential are mapped in detail with the assistance of diffraction (XRD, TEM, AFM), spectroscopic (XPS, XAFS, IR, EDAX), and electrochemical studies both in-situ and ex-situ conditions. We have also proved that at higher potential, the oxide layer was reduced to metal, which alters the mechanism and reduces the efficiency of the catalyst. It is expected that the present study can be a useful platform for the catalytic community to gain further new ideas to develop sustainable, low-cost, and efficient catalyst materials for the production of methanol via the electrochemical route.

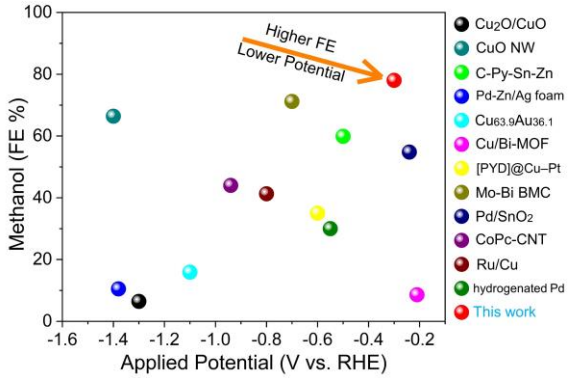

Figure 3.35. Comparison of Faradaic efficiency of different reported catalysts and the present $CuGa_2$ catalyst.[3, 8-10, 12, 44-51]

3.6. References

1. Kuhl, K. P.; Cave, E. R.; Abram, D. N.; Jaramillo, T. F., New Insights into the Electrochemical Reduction of Carbon Dioxide on Metallic Copper Surfaces. *Energy Environ. Sci.* **2012,** *5*, 7050-7059.
2. Chen, X.; Chen, J.; Alghoraibi, N. M.; Henckel, D. A.; Zhang, R.; Nwabara, U. O.; Madsen, K. E.; Kenis, P. J. A.; Zimmerman, S. C.; Gewirth, A. A., Electrochemical CO_2-to-Ethylene Conversion on Polyamine-Incorporated Cu Electrodes. *Nat. Catal.* **2021,** *4*, 20-27.
3. Albo, J.; Alvarez-Guerra, M.; Castaño, P.; Irabien, A., Towards the Electrochemical Conversion of Carbon Dioxide into Methanol. *Green Chem.* **2015,** *17*, 2304-2324.
4. Al-Rowaili, F. N.; Jamal, A.; Ba Shammakh, M. S.; Rana, A., A Review on Recent Advances for Electrochemical Reduction of Carbon Dioxide to Methanol Using Metal–Organic Framework (MOF) and Non-MOF Catalysts: Challenges and Future Prospects. *ACS Sustain. Chem. Eng* **2018,** *6*, 15895-15914.
5. Ganesh, I., Conversion of Carbon Dioxide into Methanol – a Potential Liquid Fuel: Fundamental Challenges and Opportunities (a Review). *Renew. Sust. Energ. Rev.* **2014,** *31*, 221-257.
6. Velu, S.; Suzuki, K.; Okazaki, M.; Kapoor, M. P.; Osaki, T.; Ohashi, F., Oxidative Steam Reforming of Methanol over CuZnAl(Zr)-Oxide Catalysts for the Selective Production of Hydrogen for Fuel Cells: Catalyst Characterization and Performance Evaluation. *J. Catal.* **2000,** *194*, 373-384.
7. Le, M.; Ren, M.; Zhang, Z.; Sprunger, P. T.; Kurtz, R. L.; Flake, J. C., Electrochemical Reduction of CO_2 to CH_3OH at Copper Oxide Surfaces. *J. Electrochem. Soc.* **2011,** *158*, E45.
8. Jia, F.; Yu, X.; Zhang, L., Enhanced Selectivity for the Electrochemical Reduction of CO_2 to Alcohols in Aqueous Solution with Nanostructured Cu–Au Alloy as Catalyst. *J. Power Sources* **2014,** *252*, 85-89.
9. Albo, J.; Perfecto-Irigaray, M.; Beobide, G.; Irabien, A., Cu/Bi Metal-Organic Framework-Based Systems for an Enhanced Electrochemical Transformation of CO_2 to Alcohols. *J. CO_2 Util.* **2019,** *33*, 157-165.
10. Yang, H.-P.; Qin, S.; Yue, Y.-N.; Liu, L.; Wang, H.; Lu, J.-X., Entrapment of a Pyridine Derivative within a Copper–Palladium Alloy: a Bifunctional Catalyst for Electrochemical

Reduction of CO_2 to Alcohols with Excellent Selectivity and Reusability. *Catal. Sci. Technol.* **2016,** *6*, 6490-6494.

11. Ensafi, A. A.; Alinajafi, H. A.; Jafari-Asl, M.; Rezaei, B., Self-Assembled Monolayer of 2-Pyridinethiol@Pt-Au Nanoparticles, a New Electrocatalyst for Reducing of CO_2 to Methanol. *J. Electroanal. Chem.* **2017,** *804*, 29-35.
12. Zhang, W.; Qin, Q.; Dai, L.; Qin, R.; Zhao, X.; Chen, X.; Ou, D.; Chen, J.; Chuong, T. T.; Wu, B.; Zheng, N., Electrochemical Reduction of Carbon Dioxide to Methanol on Hierarchical Pd/SnO_2 Nanosheets with Abundant Pd–O–Sn Interfaces. *Angew. Chem. Int. Ed.* **2018,** *57*, 9475-9479.
13. Zhang, W.; Qin, Q.; Dai, L.; Qin, R.; Zhao, X.; Chen, X.; Ou, D.; Chen, J.; Chuong, T. T.; Wu, B.; Zheng, N., Electrochemical Reduction of Carbon Dioxide to Methanol on Hierarchical Pd/SnO_2 Nanosheets with Abundant Pd–O–Sn Interfaces. **2018,** *57*, 9475-9479.
14. Qu, J.; Zhang, X.; Wang, Y.; Xie, C., Electrochemical Reduction of CO_2 on RuO_2/TiO_2 Nanotubes Composite Modified Pt Electrode. *Electrochim. Acta* **2005,** *50*, 3576-3580.
15. Tayyebi, E.; Hussain, J.; Skúlason, E., Why do RuO_2 Electrodes Catalyze Electrochemical CO_2 Reduction to Methanol rather than Methane or Perhaps Neither of Those? *Chem. Sci.* **2020,** *11*, 9542-9553.
16. Hoffman, Z. B.; Gray, T. S.; Moraveck, K. B.; Gunnoe, T. B.; Zangari, G., Electrochemical Reduction of Carbon Dioxide to Syngas and Formate at Dendritic Copper–Indium Electrocatalysts. *ACS Catal.* **2017,** *7*, 5381-5390.
17. Li, C. W.; Kanan, M. W., CO_2 Reduction at Low Overpotential on Cu Electrodes Resulting from the Reduction of Thick Cu_2O Films. *J. Am. Chem. Soc.* **2012,** *134*, 7231-7234.
18. Nitopi, S.; Bertheussen, E.; Scott, S. B.; Liu, X.; Engstfeld, A. K.; Horch, S.; Seger, B.; Stephens, I. E. L.; Chan, K.; Hahn, C.; Nørskov, J. K.; Jaramillo, T. F.; Chorkendorff, I., Progress and Perspectives of Electrochemical CO_2 Reduction on Copper in Aqueous Electrolyte. *Chem. Rev.* **2019,** *119*, 7610-7672.
19. Watanabe, M.; Shibata, M.; Katoh, A.; Sakata, T.; Azuma, M., Design of alloy electrocatalysts for CO_2 reduction: Improved Energy Efficiency, Selectivity, and Reaction Rate for the CO_2 Electroreduction on Cu Alloy Electrodes. *J. electroanal. chem.* **1991,** *305*, 319-328.

20. Studt, F.; Sharafutdinov, I.; Abild-Pedersen, F.; Elkjær, C. F.; Hummelshøj, J. S.; Dahl, S.; Chorkendorff, I.; Nørskov, J. K., Discovery of a Ni-Ga Catalyst for Carbon Dioxide Reduction to Methanol. *Nat. Chem.* **2014,** *6*, 320-324.
21. Gallo, A.; Snider, J. L.; Sokaras, D.; Nordlund, D.; Kroll, T.; Ogasawara, H.; Kovarik, L.; Duyar, M. S.; Jaramillo, T. F., Ni_5Ga_3 Catalysts for CO_2 Reduction to Methanol: Exploring the Role of Ga Surface Oxidation/Reduction on Catalytic Activity. *Appl. Catal. B* **2020,** *267*, 118369.
22. Duyar, M. S.; Gallo, A.; Snider, J. L.; Jaramillo, T. F., Low-Pressure Methanol Synthesis from CO_2 over Metal-Promoted Ni-Ga Intermetallic Catalysts. *J. CO_2 Util.* **2020,** *39*, 101151.
23. Okamoto, H., Supplemental Literature Review of Binary Phase Diagrams: Al-Nd, Al-Sm, Al-V, Bi-Yb, Ca-In, Ca-Sb, Cr-Nb, Cu-Ga, Ge-O, Pt-Sn, Re-Y, and Te-Yb. *J. Phase Equilib. Diff.* **2016,** *37*, 350-362.
24. Williams, B. P.; Qi, Z.; Huang, W.; Tsung, C.-K., The Impact of Synthetic Method on the Catalytic Application of Intermetallic Nanoparticles. *Nanoscale* **2020,** *12*, 18545-18562.
25. Corral, D.; Feaster, J. T.; Sobhani, S.; DeOtte, J. R.; Lee, D. U.; Wong, A. A.; Hamilton, J.; Beck, V. A.; Sarkar, A.; Hahn, C.; Jaramillo, T. F.; Baker, S. E.; Duoss, E. B., Advanced Manufacturing for Electrosynthesis of Fuels and Chemicals from CO_2. *Energy Environ. Sci.* **2021,** *14*, 3064-3074.
26. Luc, W.; Fu, X.; Shi, J.; Lv, J.-J.; Jouny, M.; Ko, B. H.; Xu, Y.; Tu, Q.; Hu, X.; Wu, J.; Yue, Q.; Liu, Y.; Jiao, F.; Kang, Y., Two-Dimensional Copper Nanosheets for Electrochemical Reduction of Carbon Monoxide to Acetate. *Nat. Catal.* **2019,** *2*, 423-430.
27. Neri, G.; Walsh, J. J.; Teobaldi, G.; Donaldson, P. M.; Cowan, A. J., Detection of Catalytic Intermediates at an Electrode Surface During Carbon Dioxide Reduction by an Earth-Abundant Catalyst. *Nat. Catal.* **2018,** *1*, 952-959.
28. Handoko, A. D.; Wei, F.; Jenndy; Yeo, B. S.; Seh, Z. W., Understanding Heterogeneous Electrocatalytic Carbon Dioxide Reduction through Operando Techniques. *Nat. Catal.* **2018,** *1*, 922-934.
29. Zhu, S.; Li, T.; Cai, W.-B.; Shao, M., CO_2 Electrochemical Reduction As Probed through Infrared Spectroscopy. *ACS Energy Lett.* **2019,** *4*, 682-689.

30. Collins, S. E.; Chiavassa, D. L.; Bonivardi, A. L.; Baltanás, M. A., Hydrogen Spillover in Ga_2O_3–Pd/SiO_2 Catalysts for Methanol Synthesis from CO_2/H_2. *Catal. Lett.* **2005,** *103*, 83-88.
31. Figueiredo, M. C.; Ledezma-Yanez, I.; Koper, M. T. M., In Situ Spectroscopic Study of CO_2 Electroreduction at Copper Electrodes in Acetonitrile. *ACS Catal.* **2016,** *6*, 2382-2392.
32. Zhu, S.; Jiang, B.; Cai, W.-B.; Shao, M., Direct Observation on Reaction Intermediates and the Role of Bicarbonate Anions in CO_2 Electrochemical Reduction Reaction on Cu Surfaces. *J. Am. Chem. Soc.* **2017,** *139*, 15664-15667.
33. Chou, T.-C.; Chang, C.-C.; Yu, H.-L.; Yu, W.-Y.; Dong, C.-L.; Velasco-Vélez, J.-J.; Chuang, C.-H.; Chen, L.-C.; Lee, J.-F.; Chen, J.-M.; Wu, H.-L., Controlling the Oxidation State of the Cu Electrode and Reaction Intermediates for Electrochemical CO_2 Reduction to Ethylene. *J. Am. Chem. Soc.* **2020,** *142*, 2857-2867.
34. Heyes, J.; Dunwell, M.; Xu, B., CO_2 Reduction on Cu at Low Overpotentials with Surface-Enhanced in Situ Spectroscopy. *J. Phys. Chem. C* **2016,** *120*, 17334-17341.
35. Klysubun, W.; Thongkam, Y.; Pongkrapan, S.; Won-in, K.; T-Thienprasert, J.; Dararutana, P., XAS Study on Copper Red in Ancient Glass Beads from Thailand. *Anal. Bioanal. Chem.* **2011,** *399*, 3033-3040.
36. Biesinger, M. C., Advanced Analysis of Copper X-Ray Photoelectron Spectra. *Surf. Interface Anal.* **2017,** *49*, 1325-1334.
37. Biesinger, M. C., Advanced Analysis of Copper X-Ray Photoelectron Spectra. **2017,** *49*, 1325-1334.
38. García-Trenco, A.; White, E. R.; Regoutz, A.; Payne, D. J.; Shaffer, M. S. P.; Williams, C. K., Pd_2Ga-Based Colloids as Highly Active Catalysts for the Hydrogenation of CO_2 to Methanol. *ACS Catal.* **2017,** *7*, 1186-1196.
39. Calatayud, M.; Collins, S. E.; Baltanás, M. A.; Bonivardi, A. L., Stability of Formate Species on β-Ga_2O_3. *Phys. Chem. Chem. Phys.* **2009,** *11*, 1397-1405.
40. Collins, S. E.; Baltanás, M. A.; Bonivardi, A. L., An Infrared Study of the Intermediates of Methanol Synthesis from Carbon Dioxide over Pd/β-Ga_2O_3. *J. Catal.* **2004,** *226*, 410-421.
41. Wang, Y.; Wang, Z.; Dinh, C.-T.; Li, J.; Ozden, A.; Golam Kibria, M.; Seifitokaldani, A.; Tan, C.-S.; Gabardo, C. M.; Luo, M.; Zhou, H.; Li, F.; Lum, Y.; McCallum, C.; Xu, Y.; Liu, M.; Proppe, A.; Johnston, A.; Todorovic, P.; Zhuang, T.-T.; Sinton, D.;

Kelley, S. O.; Sargent, E. H., Catalyst Synthesis under CO_2 Electroreduction Favours Faceting and Promotes Renewable Fuels Electrosynthesis. *Nat. Catal.* **2020,** *3*, 98-106.

42. Dinh, C.-T.; Burdyny, T.; Kibria, M. G.; Seifitokaldani, A.; Gabardo, C. M.; García de Arquer, F. P.; Kiani, A.; Edwards, J. P.; De Luna, P.; Bushuyev, O. S.; Zou, C.; Quintero-Bermudez, R.; Pang, Y.; Sinton, D.; Sargent, E. H., CO_2 Electroreduction to Ethylene via Hydroxide-Mediated Copper Catalysis at an Abrupt Interface. *Science* **2018,** *360*, 783-787.
43. Gabardo, C. M.; O'Brien, C. P.; Edwards, J. P.; McCallum, C.; Xu, Y.; Dinh, C.-T.; Li, J.; Sargent, E. H.; Sinton, D., Continuous Carbon Dioxide Electroreduction to Concentrated Multi-carbon Products Using a Membrane Electrode Assembly. *Joule* **2019,** *3*, 2777-2791.
44. Azenha, C.; Mateos-Pedrero, C.; Alvarez-Guerra, M.; Irabien, A.; Mendes, A., Enhancement of the Electrochemical Reduction of CO_2 to Methanol and Suppression of H_2 Evolution over CuO Nanowires. *Electrochim. Acta* **2020,** *363*, 137207.
45. Huang, W.; Yuan, G., A Composite Heterogeneous Catalyst C-Py-Sn-Zn for Selective Electrochemical Reduction of CO_2 to Methanol. *Electrochem. Commun.* **2020,** *118*, 106789.
46. Wu, Y.; Jiang, Z.; Lu, X.; Liang, Y.; Wang, H., Domino Electroreduction of CO_2 to Methanol on a Molecular Catalyst. *Nature* **2019,** *575*, 639-642.
47. Popić, J. P.; Avramov-Ivić, M. L.; Vuković, N. B., Reduction of Carbon Dioxide on Ruthenium Oxide and Modified Ruthenium Oxide Electrodes in 0.5 M $NaHCO_3$. *J. Electroanal. Chem.* **1997,** *421*, 105-110.
48. Seshadri, G.; Lin, C.; Bocarsly, A. B., A New Homogeneous Electrocatalyst for the Reduction of Carbon Dioxide to Methanol at Low Overpotential. *J. Electroanal. Chem.* **1994,** *372*, 145-150.
49. Sun, X.; Zhu, Q.; Kang, X.; Liu, H.; Qian, Q.; Zhang, Z.; Han, B., Molybdenum–Bismuth Bimetallic Chalcogenide Nanosheets for Highly Efficient Electrocatalytic Reduction of Carbon Dioxide to Methanol. *Angew. Chem. Int. Ed.* **2016,** *55*, 6771-6775.
50. Low, Q. H.; Loo, N. W. X.; Calle-Vallejo, F.; Yeo, B. S., Enhanced Electroreduction of Carbon Dioxide to Methanol Using Zinc Dendrites Pulse-Deposited on Silver Foam. *Angew. Chem. Int. Ed.* **2019,** *58*, 2256-2260.
51. Roy, A.; Jadhav, H. S.; Gil Seo, J., Cu_2O/CuO Electrocatalyst for Electrochemical Reduction of Carbon Dioxide to Methanol. *Electroanalysis* **2020,** *32*, 1-9.

Chapter 4

Atomically Dispersed Copper on WC@NGC Boosts the Conversion of CO_2 to Acetic Acid

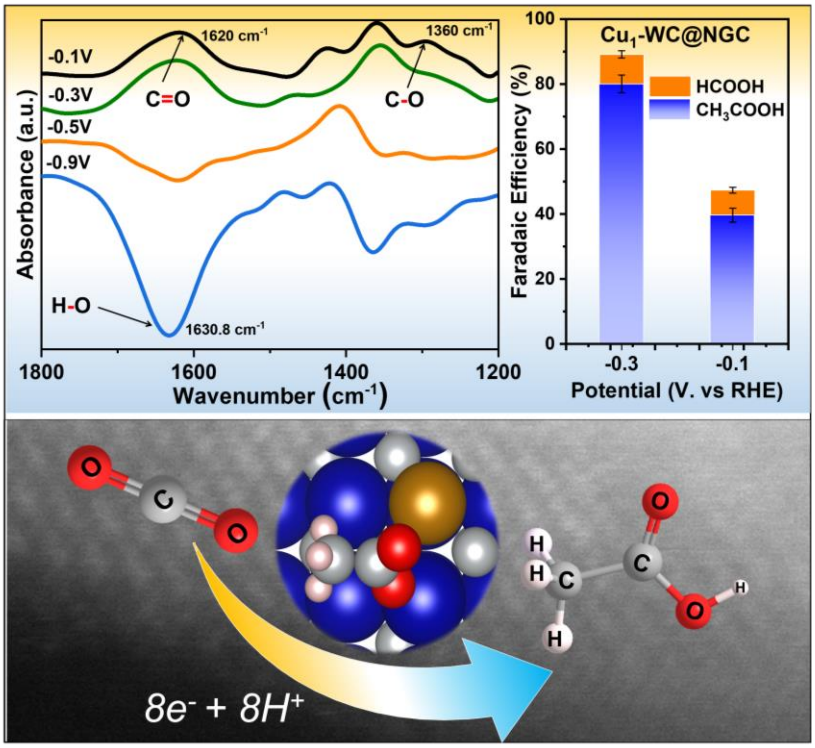

Bagchi, D.; Riyaz, M.; Raj, J.; Roy, S.; Singh, A. K.; Cherevotan, A.; Vinod, C. P.; Peter, S. C. (*manuscript under revision*)

Summary

In comparison to the previous chapter, we have targeted more reduced and energy-dense products in this work. Here, we have successfully produced C_2 product like acetic acid, which involves 8 electrons and 8 protons to achieve after eCO_2RR. In this work, we report an useful strategy to enhance eCO_2RR by constructing tungsten carbide (WC) nanoparticles embedded on N-doped graphitic carbon (NGC), which has shown excellent activity towards the formation of acetic acid at significantly lower potential. The activity has further enhanced by loading ultra-low atomically dispersed copper atoms into the catalyst system, which exhibits 80.02% Faradaic efficiency (FE) towards acetic acid at the overpotential of -0.3 V (vs. RHE). The potential-dependent in-situ Infra-Red (IR), X-ray photoelectron spectroscopy (XPS), Raman spectroscopy, and ex-situ extended X-ray absorption fine structure (EXAFS) studies confirm that synergic optimization of electronic structure between atomically dispersed Cu atoms and WC lattice is playing the crucial role in the formation of acetic acid with high FE at lower overpotential. The predominant occurrence of hydrogen evolution at higher potential (-0.5 to -1.1 vs. RHE) due to enhanced charge transfer between Cu and WC was mapped by in-situ IR spectroscopy and ex-situ XPS.

In this chapter, DB (author) has conceptualized the idea and synthesised the catalysts, performed all the electrochemical studies (both flow cell and H-cell) and other ex-situ (XRD, XPS, TEM, SEM, HAADF-STEM, Raman spectroscopy), in-situ studies (FTIR, EXAFS), analyzed the data, and written the draft. MR performed the computational study. JR has helped in flow cell optimization. SR helped to synthesize the catalyst. AKS assisted in in-situ EXAFS experiment. AC assisted in in-situ FTIR experiment. CPV procured the XPS data. SCP conceptualized the idea, supervised the work, reviewed and edited the draft.

Table of Contents

4.1. Introduction 138

4.2. Experimental Details 139

4.2.1. Chemicals and reagents 139

4.2.2. Synthesis of Cu_1-WC@NGC catalyst 139

4.3. Characterization and Experimental Methods 140

4.3.1. Powder X-ray Diffraction (PXRD) 140

4.3.2. Transmission Electron Microscope (TEM) 141

4.3.3. Inductively coupled plasma atomic emission spectroscopy (ICP-OES) 141

4.3.4. X-ray Photoelectron Spectroscopy (XPS) 141

4.3.5. Scanning electron microscopy (SEM) and Energy Dispersive Spectrum (EDAX) ……..141

4.3.6. X-ray Absorption Spectroscopy 142

4.3.7. Raman Spectroscopy 142

4.3.8. Electrochemical CO_2 Reduction Reaction (eCO_2RR) 142

4.3.9. Flow cell optimization for eCO_2RR in gas diffusion electrode configuration . 143

4.3.10. Gaseous product analysis 143

4.3.11. Liquid product analysis 144

4.3.12. Preparation of Gas diffusion Electrode (GDE) 144

4.3.13. In situ Electrochemical Attenuated Total Reflection Fourier Transform Infrared Spectroscopy (ATR-FTIR) 144

4.3.14. Computational Details 145

4.4. Results & Discussion 145

4.4.1. Synthesis and characterizations 145

4.4.2. Electrochemical CO_2 reduction (eCO_2RR) in H-cell 148

4.4.3. In situ electrochemical ATR-FTIR study 152

4.4.4. Oxidation state and Local electronic structures from Spectroscopic study 154

4.4.5. Post electrochemical characterization 157

4.4.6. High current density using flow cell with GDE configuration 160

4.4.7. Computational understanding of the reaction mechanism 160

4.5. Conclusion 162

4.6. References 162

4.1. Introduction

The extensive search for efficient cathode materials for eCO_2RR have led to exploration of a plethora of systems ranging from metal-based catalysts such as Cu,[1-3] Pd,[4, 5] Au,[6] Ag,[7, 8] Sn,[9, 10] Bi,[11, 12] Zn,[13] Co,[14] and In[15, 16] to metal-free carbon-based catalyst[17, 18] and carbon-metal nanocomposites.[19, 20] Except for Cu, most of the metallic catalysts primarily produce C_1 products like carbon monoxide or formate via eCO_2RR.[21] The selective conversion of CO_2 to C_2 and C_{2+} products is extremely challenging as those involve multiple energy-intensive electron and proton transfer steps, which are difficult to achieve on the monometallic system or through standard synthesis strategies. In this study, we developed an unique catalyst materials which can selectively produce C_2 product like acetic acid. Acetic acid is one of the most sought-after multicarbon products because of its high energy density value and application in different fields like food, pharma, chemical, textile, medicinal, cosmetics sectors, etc.[22, 23] There are a very few catalysts reported so far for the production of acetic acid via eCO_2RR. Copper nanostructure on carbon converted CO_2 to acetic acid with 56% Faradaic efficiency (FE).[22] Wang et al. reported Cu-Ag bimetallic nanoparticles exhibiting similar conversion, but only 21.2% FE.[24] Later, an enhanced FE of 60.9% had been achieved by Genovese et al. on Fe^{III}oxyhydroxide supported on N-doped carbon.[25] De et al. reported Mn-carrole based molecular catalyst with a 63% FE in a moderate acidic medium (pH 6).[26] To date, mostly carbon-based catalysts such as N-doped nanodiamond/Si rod array (NDD/Si RA),[27] Cu NP on carbon nanotubes,[22] and molecular catalysts[25] have been reported for the acetic acid production via the electrochemical route.

Transition metal carbides (TMCs), especially tungsten carbide (WC), have been widely explored as electrocatalysts and support materials for water splitting[28, 29] and fuel cell catalysis[30, 31] owing to their noble-metal like electronic structure at the Fermi level along with extreme hardness property and chemical and thermal stability.[32] More recently, several studies showed that TMCs also have the ability to capture, store and activate CO[33] for transformation to valuable fuels and chemicals.[34] Based on first-principles calculations, few transition metal,[35] especially Cu coated WC[36] has been theoretically proposed to be an active catalyst for CO_2 reduction. The computational investigation suggested that the performance of Cu/WC(0001) for CO_2 reduction is governed by the shift of the d-band center and the charge distribution on the surface, which can be tuned by the presence of W or C-termination of WC(0001).[36] Recently, Cu single-atom catalysts have been extensively studied for electrochemical CO_2

reduction.[37, 38] Single-atom Cu and host combination can be an important player in electrocatalysis.[39]

In this work, we demonstrated a single-step facile technique for the synthesis of the WC nanosystem embedded on an N-doped graphitic matrix (@NGC), which has shown excellent activity towards eCO_2RR for acetic acid production at low overpotential. The electrocatalytic activity has been further enhanced by the incorporation of atomically dispersed Cu in WC@NCG (Cu_1-WC@NGC) for the acetic acid production with a record FE of 80.02% at an overpotential of -0.3 V (vs. RHE). Upon increasing the Cu loading, the eCO_2RR activity decreases because of the presence of elemental Cu attached to the WC carbide lattice. At higher overpotentials, the relative amount of WO_3 increases due to the charge transfer between Cu and WC, which drives the selectivity towards hydrogen evolution reaction (HER). In-situ IR study reveals the possible intermediates formed due to CO_2RR at lower potential and also maps the dominating occurrence of hydrogen evolution at higher potential.

4.2. Experimental Details

4.2.1. Chemicals and reagents

Phosphotungstic acid ($H_3PW_{12}O_{40}$) and copper chloride hexahydrate ($CuCl_2$. $6H_2O$) were purchased from SDFCL. Melamine ($C_3H_6N_6$) was purchased from Sigma Aldrich. Sulfuric acid (H_2SO_4) and potassium hydroxide (KOH) were purchased from SDFCL. All the organic solvents like methanol, ethanol, 2-propanol, acetone and acid-like formic acid, acetic acid of HPLC grade and were purchased from SDFCL. DMSO, phenol, and D_2O were purchased from Sigma Aldrich. All the reagents were used without further purification. Deionized water (TKA, 18.2 MΩ.cm) was used throughout the syntheses and all measurements.

4.2.2. Synthesis of Cu_1-WC@NGC catalyst

Phosphotungstic acid, copper (II) chloride and melamine were mixed properly in ratio of 5:1:20 to achieve the mole ratio W:Cu:Melamine also 5:1:20. Mixing process was carried out by mortar pestle (grinding time is about 15 min).

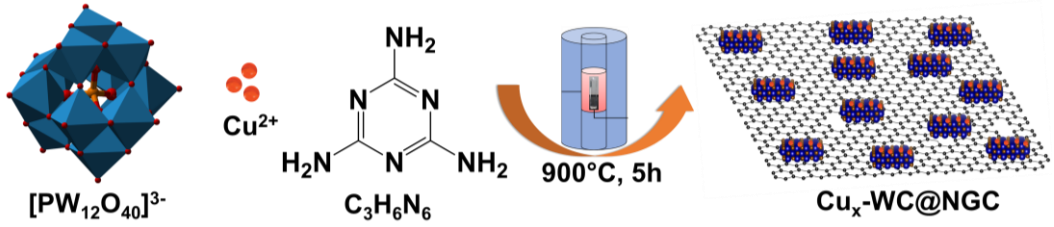

Scheme 4.1. Schematic illustration of the synthesis of Cu_x-WC@NGC catalyst.

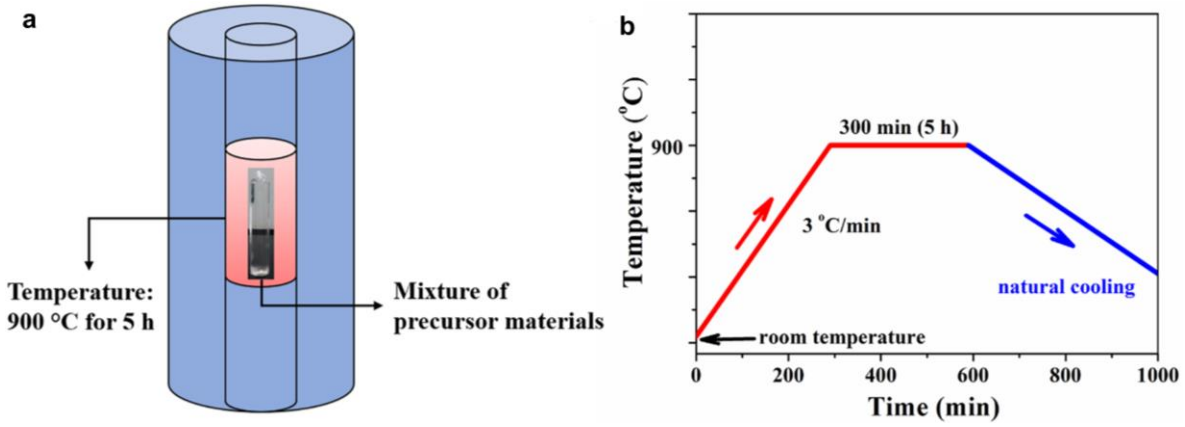

Figure 4.1. (a) Schematic diagram of the annealing process used for the synthesis of WC@NGC and Cu-WC@NGC. (b) Temperature program applied for the synthesis of WC@NGC and Cu-WC@NGC.

A quantity of 100 mg homogeneous mixture was then placed in a vacuum sealed quartz tube (of diameter 13 mm) and annealed at 900 °C in a tube furnace for 5 h with a heating rate of 3 °C/min. In this process melamine would be thermally converted first to carbon nitride (g-C_3N_4) around 500 °C and then to N-doped graphitic carbon (NGC) as the temperature increases. It will also act as the carbon source for carbonization and reduction of the transition metal salts following a similar reactions[40] (**Eqn. 4.1**). The schematic diagram for the synthesis of Cu_1-WC@NGC and temperature program applied during the synthesis are given in **Figure 4.1**.

$$H_3PW_{12}O_{40}.xH_2O + CuCl_2 + C_3H_6N_6 \rightarrow Cu\text{-}WO_3 + CH_4 \rightarrow Cu\text{-}WC + C(\text{N-doped})$$ **Eqn. 4.1.**

The obtained samples after carbonization were subsequently etched with 0.5 M H_2SO_4 at 80 °C for 12 h. Then the acid-etched solution was washed several times with deionized water and ethanol alternatively by centrifuging at 8000 rpm to remove unstable and inactive species. Then the sample was properly dried to obtain the desired Cu single atom containing tungsten carbide nano-systems on nitrogen doped graphitic carbon coded as Cu_1-WC@NGC. For comparative studies, WC@NGC (without Cu) and Cu_nWC@NGC were synthesised having corresponding mole ratio of the same precursors (i.e. W:Cu:Melamine) as 5:5:20, maintaining all other synthetic conditions the same.

4.3. Characterization and Experimental Methods

4.3.1. Powder X-ray Diffraction (PXRD)

PXRD measurements were done at room temperature on a Rigaku Miniflex X-ray diffractometer with a Cu−K_α X-ray source (λ = 1.5406 Å), equipped with a position-sensitive detector in the angular range of $10° \leq 2\theta \leq 90°$ with the step size 0.02° and a scan rate of 0.5

s/step calibrated against corundum standards. The experimental XRD patterns were compared to the patterns simulated from the data reported in the literature.

4.3.2. Transmission Electron Microscope (TEM)

Transmission electron microscope (TEM), high-resolution TEM (HRTEM) images and selected area electron diffraction (SAED) patterns were collected using TECNAI and JEOL 200 kV TEMs. TEM samples for these measurements were prepared by sonicating the nanocrystalline powders in ethanol and dropping a small volume onto a carbon-coated copper grid.

Aberration corrected FEI Titan G2 60−300 kV microscope has been used to investigate the nature of single-atom catalyst. High-Angle Annular Dark Field Scanning Transmission Electron Microscopy (HAADF STEM) imaging and X-ray Energy Dispersive Spectroscopy (XEDS) have been performed at an accelerating voltage of 300 kV with a probe convergence angle of 24.5 mrad using 70μm aperture.

4.3.3. Inductively coupled plasma atomic emission spectroscopy (ICP-OES)

ICP-OES was performed using a Perkin Elmer Optima 7000 DV instrument. The samples were digested in concentrated aqua regia, followed by dilution with distilled water. In a typical experiment, 2 mg of the sample was dissolved in 1 ml aqua regia and left overnight (12 hrs) for digestion. The digested sample was then diluted to 10 ml volume with deionized water. The solid particles were separated by thorough centrifugation before measurements.

4.3.4. X-ray Photoelectron Spectroscopy (XPS)

XPS measurements were carried out using Thermo K-alpha+ spectrometer using micro focused and monochromated Al Kα radiation with energy 1486.6 eV. The pass energy for the spectral acquisition was kept at 50 eV for individual core-levels. The electron flood gun was utilized for providing charge compensation during data acquisition. Further, the individual core-level spectra were checked for charging using C1s at 284.6 eV as standard and corrected if needed. The peak fitting of the individual core-levels was done using CASA XPS software with a Shirley type background.

4.3.5. Scanning electron microscopy (SEM) and Energy Dispersive Spectrum (EDAX)

The FESEM measurement was performed using Leica scanning electron microscopy equipped with an energy-dispersive X-ray spectroscopy (EDX) instrument (Bruker 120 eV EDAX instrument). Data were acquired by using an accelerating voltage of 15 kV, and the typical time taken for data accumulation is 100 s. The elemental analyses were performed using the P/B-ZAF standardless method (where P/B = peak to background model, Z = atomic no.

correction factor, A = absorption correction factor, and F = fluorescence factor) for Cu, Ga at multiple areas on the sample coated Si wafer.

4.3.6. X-ray Absorption Spectroscopy

X-ray absorption near-edge spectroscopy (XANES) and quick-Extended X-ray Absorption Fine Structure (quick-EXAFS) experiments at 300 K were performed at PETRA III, beamline P64, of DESY, Germany. Measurements of Cu-*K* and W-L_3 at ambient pressure were performed in fluorescence as well as transmission mode using gas ionization chambers to monitor the incident and transmitted X-ray intensities. Monochromatic X-rays were obtained using a Si (111) double crystal monochromator, which was calibrated by defining the inflection point (first derivative maxima) of Cu foil as 8980.5 eV. The beam was focused by employing a Kirkpatrick-Baez (K-B) mirror optic. A rhodium-coated X-ray mirror was used to suppress higher-order harmonics. A CCD detector was used to record the transmitted signals. Pellets for the ex-situ measurements were made by homogeneously mixing the sample with an inert cellulose matrix to obtain an X-ray absorption edge jump close to one.

4.3.7. Raman Spectroscopy

Raman experiments were performed in backscattering geometry (180°) using a commercial Raman spectrometer [LabRam HR evolution (Horiba)] equipped with a solid-state frequency-doubled 532 nm CW Nd-YAG laser and 800 mm focal length monochromator. The room temperature Raman spectra were collected with a laser power of less than 0.5 mW at the sample.

4.3.8. Electrochemical CO_2 Reduction Reaction (eCO_2RR)

All the electrochemical measurements were performed using a CHI 6008E electrochemical workstation. Electrochemical CO_2 reduction reaction (eCO_2RR) is carried out in a three-electrode system, which involves a working electrode (glassy carbon or carbon cloth), counter electrode (graphitic carbon rod), and reference electrode (Ag/AgCl). The cell compartments are separated by a proton exchange membrane (Nafion 117), and the electrolyte used is 0.5M $KHCO_3$ solution. The electrolyte solutions were purged with CO_2 gas for 1 hour prior to the measurement. The electrocatalyst was prepared by dispersing 2 mg of catalyst and 0.2 mg of Vulcan (activated carbon) in 200 µL of mixed solvent solution (IPA:H_2O = 1:1 v/v) and 10 µL of 1 wt% nafion binder. From the prepared catalyst 100 µL was coated on the carbon cloth and dried. The electrochemical cell was designed to have a large electrode area (0.7 cm x 0.7 cm) and a small electrolyte volume (10 mL) in each of the two compartments, along with a gas headspace of approximately 5 mL above the electrolyte on each side of the membrane.

CO_2, regulated by a mass flow controller at 10 standard cubic centimeters per minute (sccm), flowed through the working electrode compartment of the cell during electrolysis. CO_2 flow through the cell was necessary in order to see large current efficiencies for CO_2 reduction products, presumably because of mass transport limitations in a quiescent cell. The flow rate of 10 sccm was chosen to ensure sufficient CO_2 transport to the surface while preventing interference from gas bubbles striking the surface.

4.3.9. Flow cell optimization for eCO_2RR in gas diffusion electrode configuration

To increase the CO_2 diffusion and increase the overall current density, the electrochemical carbon dioxide experiments were carried out in a filter-press type Micro Flow Cell (Electrocell A/S), where a Ti sheet coated with Ir-MMO (iridium-mixed metal oxide) is used as an Anode plate (Electrocell S/A). An anionic exchange membrane (Fumasep FAB-PK-130) was employed in the case of CO_2RR in KOH medium. As discussed in **Figure 1.12**, the cell has three compartments, viz. CO_2 gas compartment, cathodic and anodic compartment (**Figure 1.13**). The electrolyte was recirculated continuously into the cell (both in cathode and anode) by two separate peristaltic pumps (Ravel, RH-P100L-100) to accumulate liquid products. The flow of CO_2 was regulated by a mass flow controller (Brooks) at different flowrate (standard cubic centimeters per minute (sccm)) to optimize the most suitable flow rate, flowed through the working electrode compartment of the cell during electrolysis. For the final study, the gas flow is fixed to 50 sccm, and electrolyte flow was set to 20 sccm. To achieve C-based GDE, Freudenberg H23C2 has been used as the gas diffusion layer (GDL) and catalyst ink was coated with loading of 1mg/cm^2.

4.3.10. Gaseous product analysis

All the gaseous products were analyzed by online 490-Micro Gas Chromatography (GC), which has four channels for detecting different gaseous products. Each channel has a specific column for analyzing relevant gases *viz*. Molsieve 5Å (for channel 1 and 2), Pora PLOT U (in channel 3) and CP-Sil 5 CB (for channel 4). The carrier gases were Ar and H_2. Each GC channel is equipped with a thermal conductivity detector (TCD). This detector responds to the difference in thermal conductivity between a reference cell (carrier gas only) and a measurement cell (carrier gas containing sample components).

Calculation of Faradaic Efficiency (FE) for gaseous products,

$$FE_{gas} = \frac{ppm \times flow\ rate \times \frac{number\ of\ electron \times Faraday\ contant \times pressure}{R \times Temperature}}{I_{average}} \times 100$$

Where ppm is the concentrations detected by GC, R is a gas constant (8.31 j $K^{-1}mol^{-1}$).

4.3.11. Liquid product analysis

The liquid products were analyzed by ^1H NMR (600 MHz, JEOL). The following protocol was applied. 500 mL of the electrolyte and 30 µL of an internal standard solution were transferred into a centrifuge tube. The internal standard solution consisted of 50 mM phenol (99.5 %) and 10 mM dimethyl sulfoxide (99.9 %) made in D_2O solvent. The mixture is transferred into an NMR tube. Solvent suppression was used to decrease the intensity of the water peak.

4.3.12. Preparation of Gas diffusion Electrode (GDE)

The gas diffusion electrode (GDE) was fabricated by drop-casting the catalyst onto a cut piece of expanded polytetrafluoroethylene (ePTFE) (purchased from Sterlitech). The PTFE used here is aspire laminated and having proper hydrophobicity. It also has a polyester backer, and the pore size is 200 nm. The ePTFE was pretreated by first performing an RCA cleaning process reported earlier.[41] It was first treated with a mixture of H_2O:HCl:H_2O_2 (5:1:1) at 80 °C for 2 minutes, then a mixture of H_2O:NH_4OH:H_2O_2 (5:1:1) for 2 minutes. After rinsing and drying, the catalyst was coated on that, and vulcan was coated successively at different coating amounts. Graphite powder was coated on top of that to enhance further conductivity of the GDE.

4.3.13. In situ Electrochemical Attenuated Total Reflection Fourier Transform Infrared Spectroscopy (ATR-FTIR)

In situ electrochemical FTIR spectroscopic studies were performed using a purged VERTEX FT-IR spectrometer equipped with the A530/P accessory and a mid-band MCT detector. A silicon hemispherical window (F530-8) was used with the working electrode placed gently on top of the window as the single reflection attenuated total reflection (ATR) accessory for the FTIR study. The in situ experimental setups is depicted in **Figure 1.15**. The measurement parameters were 4 cm^{-1} resolution and 100 scans. This setup enabled the detection of eCO_2RR intermediate formation and change of adsorption of various intermediates on the electrode surface and within the thin-layer electrolyte. In the beginning of the IR-experiment, we have taken a spectrum of the overall electrochemical cell and then take a background spectrum so that the contribution of the electrolyte can be subtracted in the next spectrum while applying the potential during performing CO_2RR. The spectra were analyzed by the OPUS software and the absorption spectra have been directly plotted at various potential and time.

4.3.14. Computational Details

All DFT calculations were performed using the Viana Ab Initio Simulation Package (VASP).[42, 43] The Perdew-Becke Ernzerhof (PBE)[44] exchange-correlation functional was used in combination with plane-wave augmented pseudopotential,[45] representing the interaction between ionic cores and valence electrons. The kinetic energy cutoff of 450 eV is applied to truncate the plane-wave basis used to describe the Kohn-Sham orbitals, and a convergence threshold of 0.03 eV/Å is accounted for forces on the atoms for ionic minimization. Grimme's D3 correction parameter[46] was employed to include the long-range interactions. The Monkhorst-Pack[47] mesh k-points of (3 × 3 × 1) were used for the p(3 × 3) surface slab of WC and Cu-doped WC containing four atomic layers, with a vacuum thickness of 15 Å. The atoms in the top two layers were allowed to relax while the bottom two layers were fixed at the bulk equilibrium position.

The Adsorption energy (E_{ads}) of the adsorbate was calculated as:

$$E_{ads} = E_{slab+x} - (E_{slab} + E_x)$$

Where E_{slab+x}, E_{slab} and E_x are the total energy of slab with adsorbate, the energy of bare slab and the energy of adsorbate in the gas phase respectively. The reaction free energies were approximated as:

$$\Delta G = \Delta E + \Delta ZPE - T\Delta S$$

Where ΔE is the DFT calculated change in reaction energy, ΔZPE is the zero-point energy change, and TΔS is the entropy change at 300 K. The values are compiled from reference.[35, 48]

4.4. Results & Discussion

4.4.1. Synthesis and characterizations

Atomically dispersed Cu-loaded WC@NGC catalyst has been synthesized by a facile one-step synthetic procedure (**Fugure 4.1)**. The precursors, phosphotungstic acid ($H_3PW_{12}O_{40}$), copper chloride ($CuCl_2$), and melamine ($C_3H_6N_6$), were properly mixed at various molar ratios of W:Cu (5:1, 5:5). The mixture is vacuum-sealed in a quartz tube and pyrolyzed at 900 °C (**Figure 4.1a-b**), resulting in the formation of well-dispersed WC nanoparticles embedded on nitrogen-doped graphitic carbon (Cu_1-WC@NGC). Powder XRD shows that the hexagonal phase of tungsten carbide (WC, $P\bar{6}m2$ space group) has been formed during the annealing process (**Figure 4.2a**). At the higher Cu loading (Cu_5W_5), the small peaks at 2θ of 43.3° and 50.4° indicate the formation of elemental Cu.

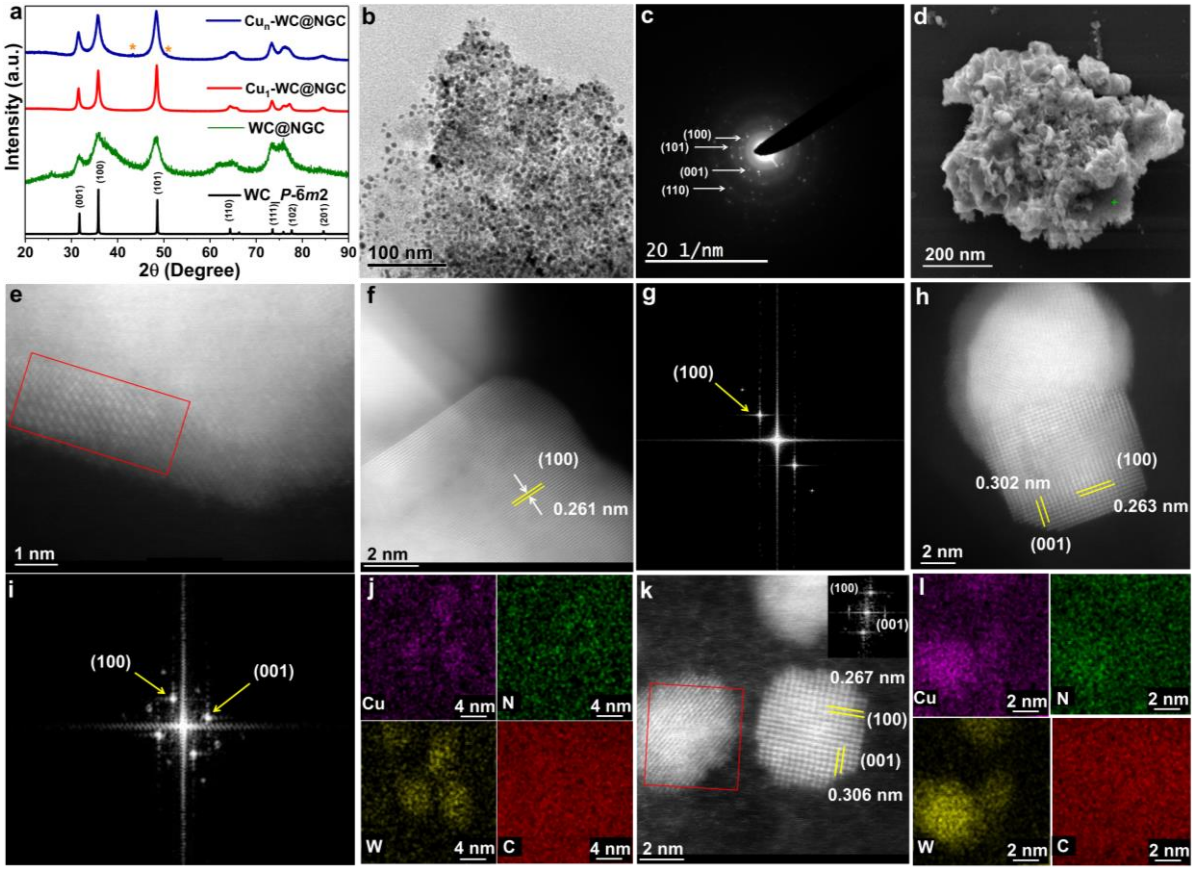

Figure 4.2. (a) Powder XRD patterns of pristine WC@NGC and Cu-loaded samples and comparison with the simulated pattern of WC, (b) TEM image of Cu_1-WC@NGC, (c) SAED pattern of Cu_1-WC@NGC. (d) High-resolution (HR) HAADF-STEM image of Cu_1-WC@NGC. Red rectangular highlight shows potential regions where bright spots indicate the Cu atoms are atomically dispersed on WC lattice. (f) HR HAADF-STEM image and (corresponding fast Fourier transform (FFT) analysis of WC. (h) A HR HAADF-STEM image of a sample of Cu_1-WC@NGC indicates d-spacing corresponding to two main exposed planes, (100) and (001) of WC lattice and their (i) FFT analysis. (j) STEM-EDS elemental mapping of Cu_1-WC@NGC shows the uniform distribution of W, N, C, and atomically dispersed Cu. (k) HAADF-STEM image of Cu_n-WC@NGC represents a cluster of Cu on the WC lattice (FFT analysis in the inset). (l) STEM-EDS elemental mapping of Cu_n-WC@NGC.

TEM images show that the Cu-loaded WC (particle size ~10-30 nm) nanoparticles are embedded and well-dispersed over the thin layer graphitic carbon matrix (**Figure 4.2b**). Selected area electron diffraction (SAED) patterns display the concentric rings of diffractions, characteristic of the low index exposed planes (100, 101, 001, 110) in Cu_1-WC@NGC catalyst (**Figure 4.2c**). SEM images of Cu_1-WC@NGC show the microstructural arrangement where the carbide nanoparticles are found to be grafted on the carbon matrix (**Figure 4.2d**).

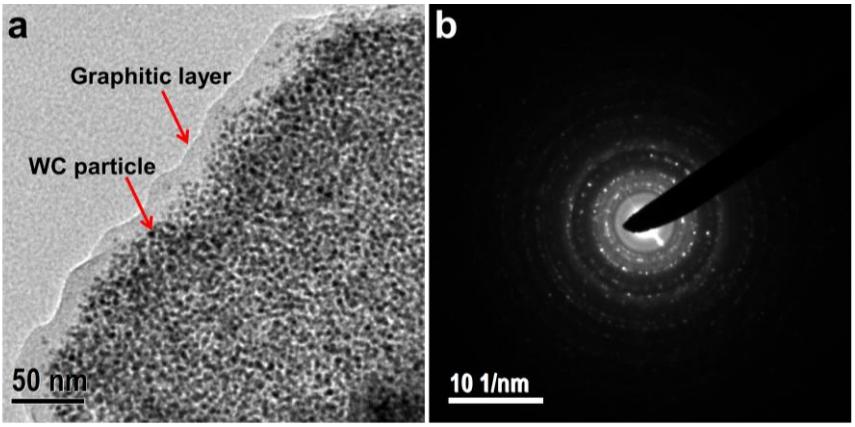

Figure 4.3. (a) TEM image of WC@NGC showed the WC nanoparticle embedded on graphitic layer and (b) SAED pattern of WC@NGC showed the polycrystalline nature.

TEM images of WC@NGC show the uniform distribution of WC nanoparticles which is anchored on the graphitic layer (**Figure 4.3a**). The existence of atomically dispersed Cu and WC can facilitate the electron and charge transfer process during electrocatalysis. The atomic resolution scanning transmission electron microscopy (STEM) analysis carried out in the high-angle annular dark-field (HAADF) mode displayed the atomically distributed Cu sites dispersed on the WC lattice (bright specks corresponding to atomically dispersed Cu single site) (**Figure 4.2e**). The high-resolution HAADF-STEM of WC shows its most exposed plane (100), having a d-spacing of 0.261 nm (**Figure 4.2f**). The fast Fourier transform (FFT) indicates the main reflections from the (100) plane of the WC lattice (**Figure 4.2g**). The high-resolution HAADF-STEM of Cu_1-WC@NGC shows the existence of the two most exposed planes of WC viz. (100) and (001) having d-spacing of 0.263 nm and 0.302 nm, respectively (**Figure 4.2h**). In the Cu_1-WC@NGC catalyst, the d-spacing corresponding to (100) plane has increased from that of pristine WC lattice, indicating a lattice expansion due to incorporation of larger sized Cu^{2+} ion (ionic radius: 73 pm) in the carbide lattice where W^{4+} is having ionic radius (66 pm). The FFT of the HRTEM also indicates the presence of (100) and (001) crystallographic planes of WC (**Figure 4.2i**).

The EDS elemental mapping of the Cu_1-WC@NGC displays the uniform distribution of W, C, N, and atomically distributed Cu on the surface (**Figure 4.2j**). It was found that the atomic percentage of Cu in Cu_1-WC@NGC is 0.47% (**Figure 4.4**), confirmed from SEM-EDS. The weight percentage of Cu in Cu_1-WC@NGC is also determined by ICP-OES measurement and found to be 0.63%. On the other hand, in the higher Cu loading sample, the bigger-sized bright spots indicated multiatomic Cu cluster in the Cu_n-WC@NGC (**Figure 4.2k).** The EDS elemental mapping also shows the higher distribution of Cu element along with W, C, and N on the surface of Cu_n-WC@NGC as indicated by **Figure 4.2l** and **Figure 4.5.**

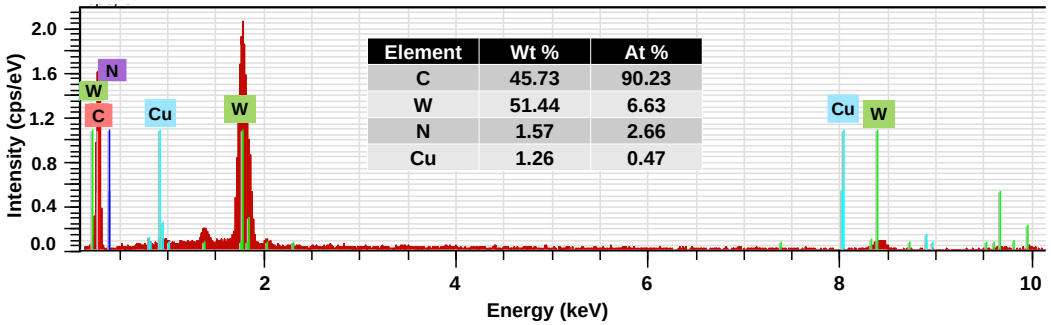

Figure 4.4. EDS spectrum of Cu_1-WC@NGC and inset table represents elemental composition Cu_1-WC@NGC.

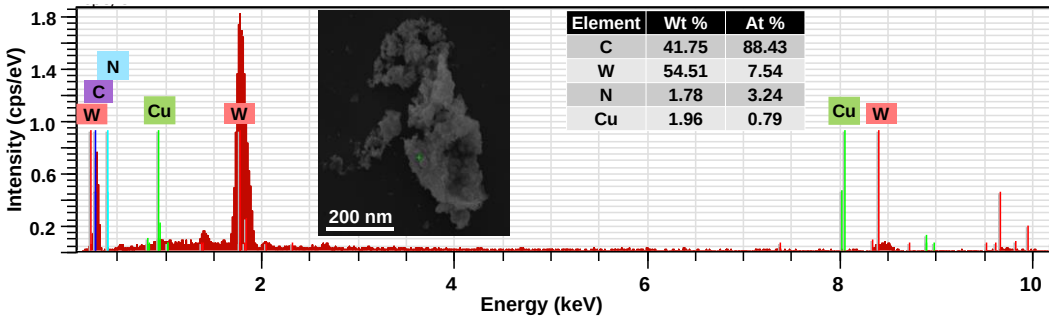

Figure 4.5. SEM images and EDS spectrum of Cu_n-WC@NGC and inset table represents elemental composition Cu_n-WC@NGC.

4.4.2. Electrochemical CO_2 reduction (eCO_2RR) in H-cell

Electrochemical CO_2RR studies were performed on all the WC-based catalysts in 0.5 M $KHCO_3$ with continuous CO_2 purging at 20 sccm flow rate in the customized cell presented in the previous section. Toray carbon paper has been used as the working electrode, which is having a surface area of 1 cm^2. Linear sweep voltammetric study has been performed in the CO_2RR potential region, and it was found that in the CO_2 atmosphere, both the WC@NGC and Cu_1-WC@NGC catalysts exhibited much lower onset potentials and higher current densities than those in N_2-saturated 0.5 M $KHCO_3$, suggesting that the catalytic activity is originated from CO_2 reduction not only from HER (**Figure 4.6a**).

To evaluate the electrochemical behaviour along with CO_2-derived product distribution of the carbide catalysts, chronoamperometric (CA) test at potential starting from -0.1 V, -0.3 V, -0.5 V, -0.7 V, -0.9 V, and -1.1 V (vs. RHE) was performed in CO_2 saturated 0.5 M $KHCO_3$ solution for one hour under the CO_2 flow of 20 sccm (**Figure 4.7**). **Figure 4.7** depicts the observed current density at each applied potential on WC@NGC and Cu_1-WC@NGC catalysts. Cu_1-WC@NGC has shown higher current density, especially at the higher overpotential than WC@NGC, which can be attributed to more Faradaic reactions occurring on the catalyst surface.

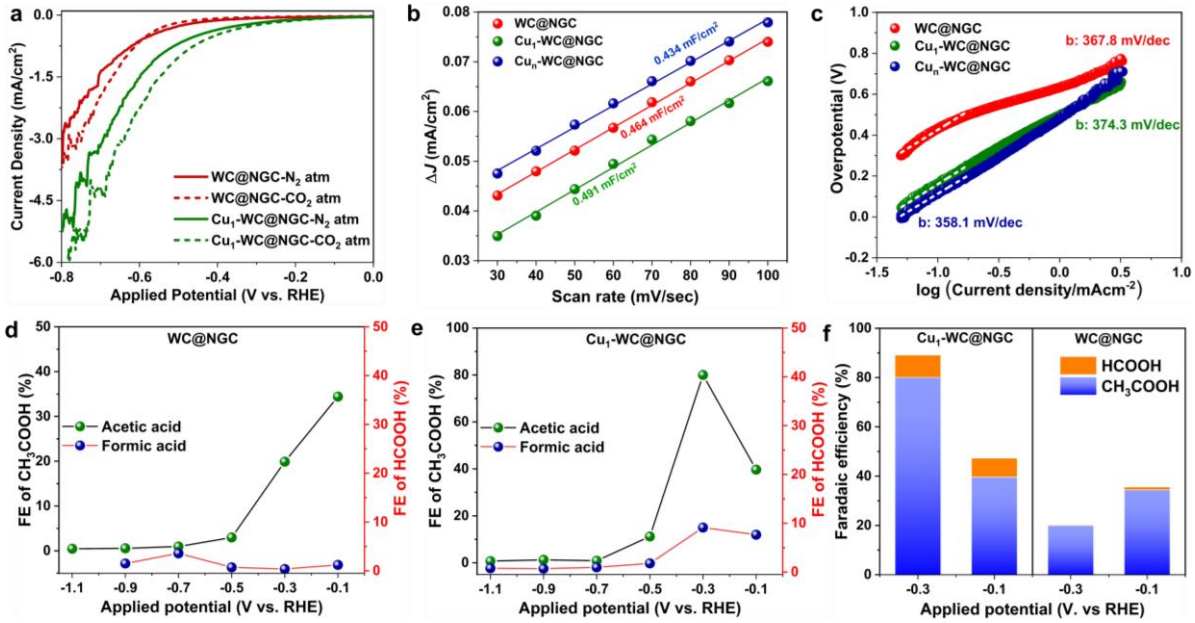

Figure 4.6. (a) Linear sweep voltammogram taken in eCO_2RR condition and in N_2 atmosphere on WC@NGC and Cu_1-WC@NGC catalysts. (b) Determination of double-layer capacitance (C_{dl}) and thereby estimation of electrochemical active surface area (ECSA). (c) Tafel plots of tungsten-based catalysts in eCO_2RR condition. Faradaic efficiency for each CO_2 reduced major liquid products as a function of potential during eCO_2RR on (d) WC@NGC, (e) Cu_1-WC@NGC catalyst. (f) Comparison of FE of CH_3COOH and HCOOH at the lower potential on WC@NGC and Cu_1-WC@NGC.

At relatively lower overpotential (-0.1V, -0.3V vs. RHE), the current densities for both catalysts are similar. The flat nature of CA curves on different carbide-based catalysts (**Figure 4.7a-b**) have been shown at different potentials in CO_2-saturated 0.5 M $KHCO_3$ solution, indicating the good electrochemical stability of our catalyst. Electrochemically active surface area (ECSA) is a critical kinetic factor influencing the activity of any electrocatalytic reaction. To deconvolute the role of ECSA in activity enhancement, double layer capacitances (C_{dl}) of the catalysts are determined (**Figure 4.8**). As shown in **Figure 4.6b**, Cu_1-WC@NGC catalyst (0.491 mF/cm^2) exhibit larger C_{dl} values than the WC@NGC catalyst (0.464 mF/cm^2) and Cu_nWC@NGC (0.434 mF/cm^2). The trend of ECSA is almost similar to that of the CO_2RR activity suggests that ECSA has a crucial role in controlling the activity of CO_2 reduction in these particular carbide-based catalysts. Tafel plots of different catalysts at the low voltage domain show comparable Tafel slope values indicate that these three catalysts follow similar electrocatalytic kinetics at this potential range.[49]

After each CA study, all the CO_2-reduced products were analyzed and quantified to evaluate the CO_2 reduction performance. The gaseous products were quantified by the gas

chromatographic (GC) technique, and the liquid products were analyzed by HPLC and NMR. **Figure 4.6d-f** shows the FEs and product distributions as the function of applied potentials from −0.1 V to −1.1 V over tungsten carbide-based catalysts. Both the WC@NGC and Cu_1-WC@NGC compounds show a similar product distribution trend (**Figure 4.6d-f**), producing acetic acid with substantial FE in lower overpotential (-0.1 to -0.5 V vs. RHE) along with formic acid as the minor product. WC@NGC has produced CH_3COOH with an FE of 34.4 % at -0.1 V, and its activity gradually decreased (FE: 19.9 % at -0.3V) as the overpotential is increased.

In the case of the atomically dispersed Cu-loaded WC@NGC catalyst, the catalytic activity has drastically increased, and FE of CH_3COOH has been found to be 80.02 % at -0.3V (vs. RHE). Once the amount of Cu loading is increased further and thereby forming the Cu nanoparticle embedded WC@NGC system, i.e., Cu_n-WC@NGC shows less activity than that of Cu_1-WC@NGC with respect to the production of acetic acid (**Figure 4.9a-d**).

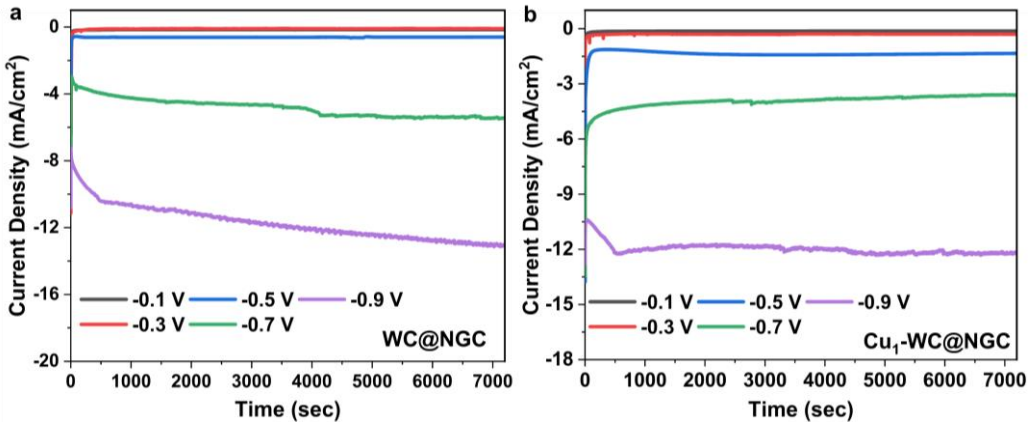

Figure 4.7. Chronoamperometric study (current density as function of time) on **(a)** WC@NGC and **(b)** Cu_1-WC@NGC during electrochemical CO_2RR in 0.5 M $KHCO_3$.

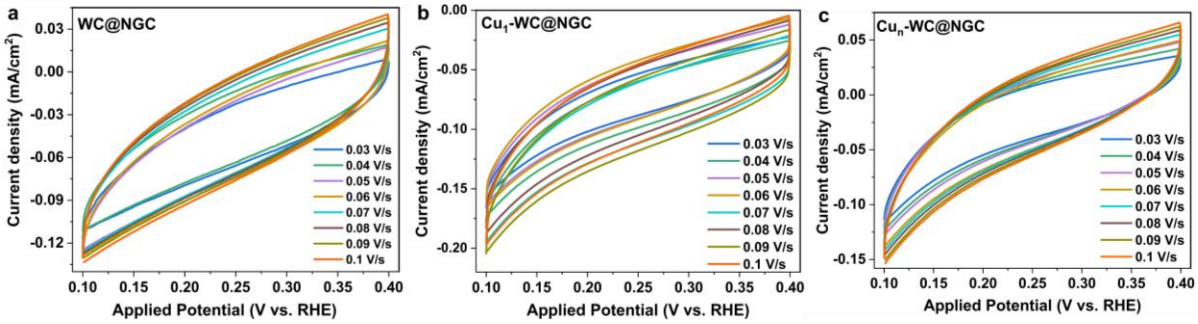

Figure 4.8. Cyclic voltammograms (CVs) of (a) WC@NGC, (b) Cu_1-WC@NGC and (c) Cu_n-WC@NGC sweeping over the potential area from 0.1 V (vs. RHE) to 0.4 V (vs. RHE) for the determination of double-layer capacitance (C_{dl}) and thereby estimation of effective surface area (ECSA).

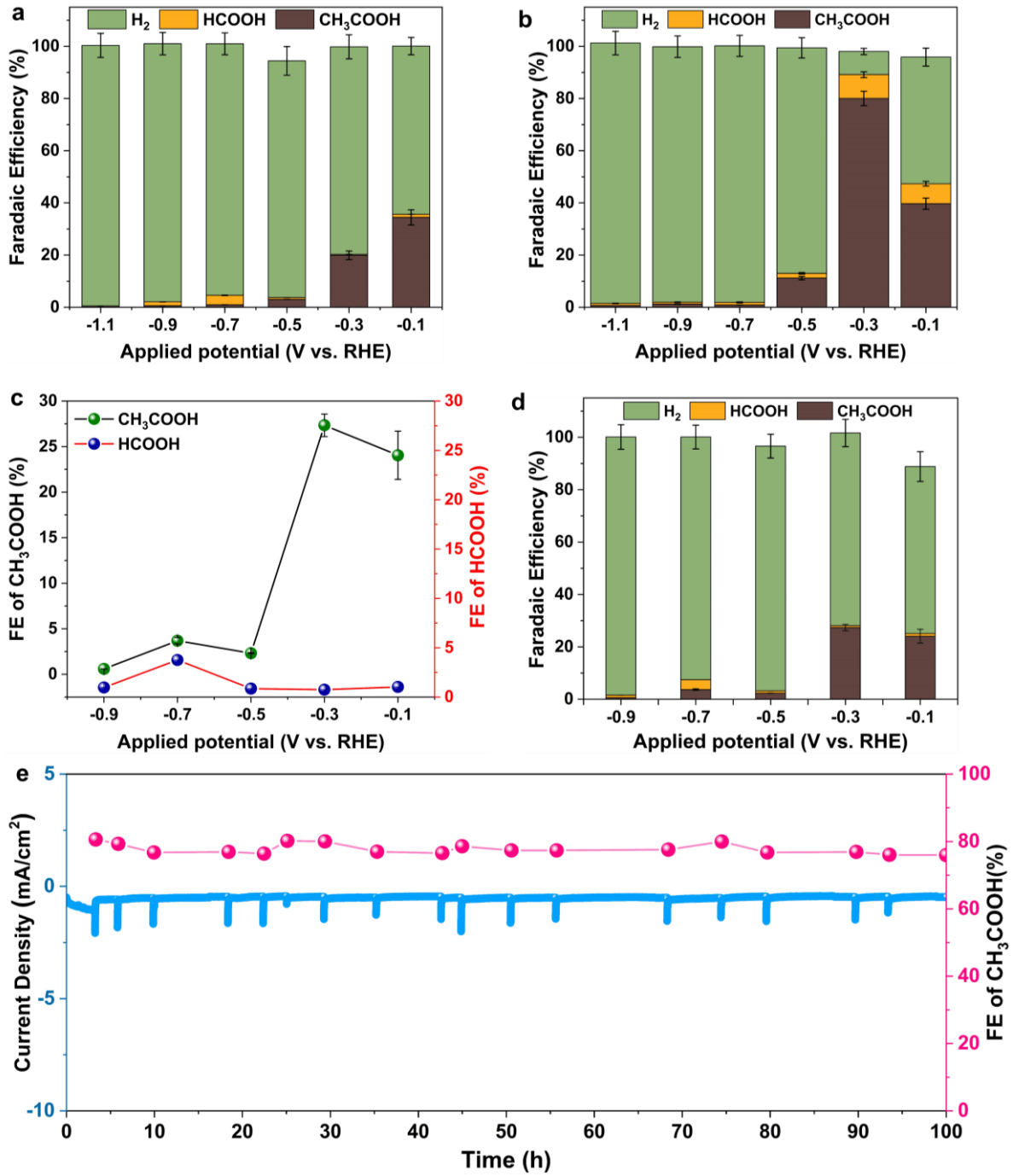

Figure 4.9. Faradaic efficiency for each CO_2 reduced products (acetic acid and formic acid) and hydrogen due to water splitting at different potential as on (a) WC@NGC, (b) Cu_1WC@NGC (c-d) Cu_nWC@NGC catalyst. (e) Chronoamperometric long-term stability study (current density as a function of time) on Cu_1WC@NGC at -0.3 V (vs. RHE) and FE of acetic acid in 0.5M $KHCO_3$.

As the overpotential is increased beyond -0.5V (vs. RHE), FE of the CO_2 reduced products has been decreased as HER enhanced much significantly. **Figure 4.9e** shows the long-term stability for the production of acetic acid on Cu_1-WC@NGC in the CO_2RR condition.

4.4.3. In situ electrochemical ATR-FTIR study

In-situ ATR-FTIR spectroscopy was carried out to detect the crucial intermediates formed during eCO_2RR and to propose the reaction mechanism. **Figure 4.10a** displays the time-dependent spectra were taken while eCO_2RR was performed at -0.1V and -0.3V (vs. RHE). The negative band at 2343 cm^{-1} observed at all the applied potentials, which can be attributed to the CO_2 consumption.[50]

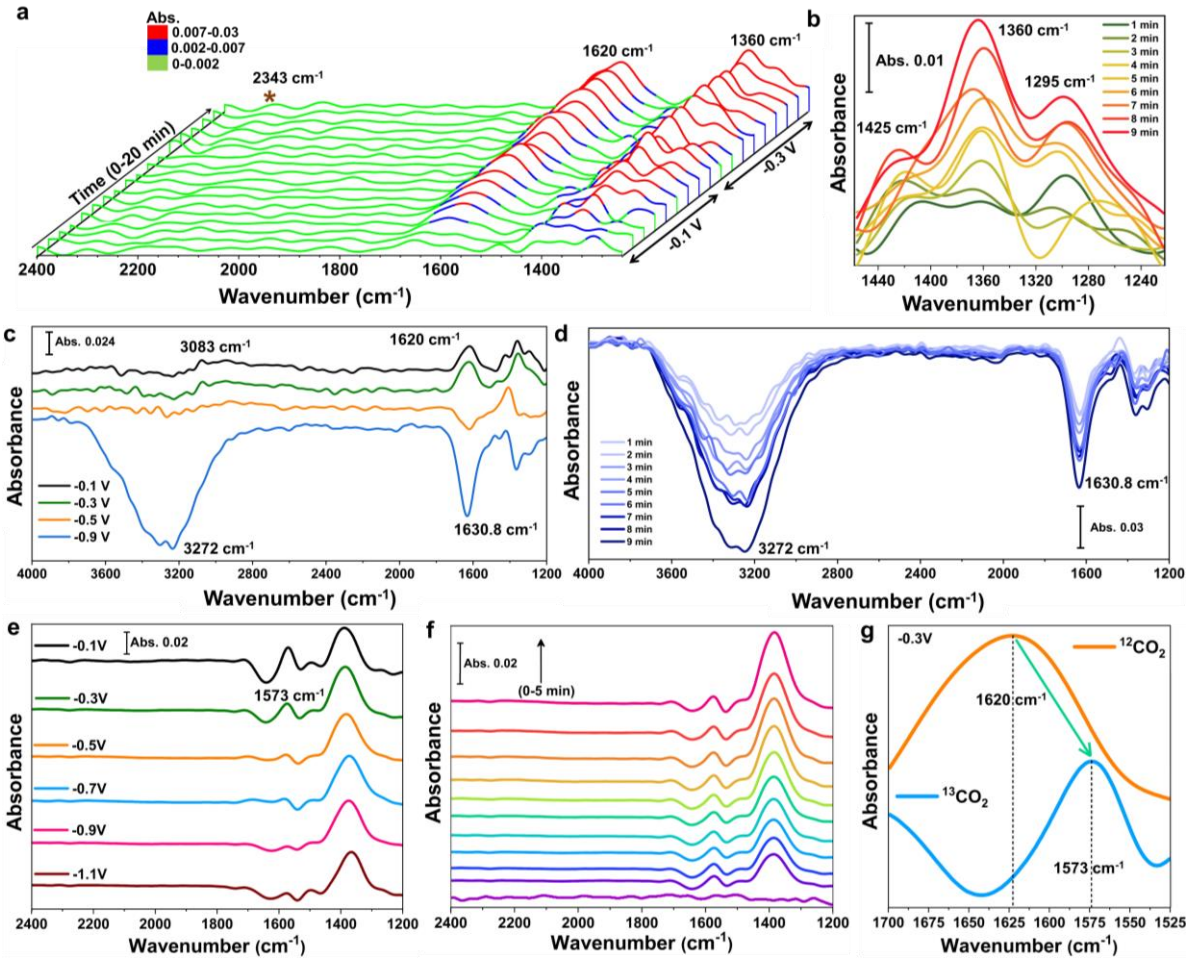

Figure 4.10. (a) In-situ IR of CO_2 reduction on Cu_1-WC@NGC catalyst along with the binding mode of different intermediates adsorbed on catalysts surface during eCO_2RR. (b) IR spectra are corresponding to $HCOO^-$ and COOH intermediate formed during eCO_2RR at a different time during CA at -0.3 V (vs. RHE). **(c)** Potential dependent in situ IR spectra taken during a chronoamperometric study done on Cu_1-WC@NGC catalyst. (d) Time-dependent in-situ infrared spectra were taken at -0.9 V (vs. RHE) in CO_2RR condition. (e) Potential dependent in situ IR spectra on Cu_1-WC@NGC catalyst during electrochemical $^{13}CO_2$RR study. (f) Time dependent evolution of IR band at -0.3V (vs. RHE) during isotope labelling in situ IR study. (g) Comparison of IR band corresponding to the major intermediate stretching of formate in electrochemical $^{12}CO_2$RR and $^{13}CO_2$RR conditions at -0.3V (vs. RHE).

In **Figure 4.10b**, the three vibrational modes of COOH viz. O-H deformation, C-O stretching, and C=O stretching are clearly visible at 1295 cm^{-1}, 1360 cm^{-1} and 1620 cm^{-1}, respectively. The IR intensity of the major peaks centered at 1620 cm^{-1} and 1360 cm^{-1} were gradually increased with the increase of the applied cathodic potentials indicating that more CO_2 was reduced at the higher cathodic potential (-0.3V) with higher FE. The intensity of HCO_3^- ions observed at 1360 cm^{-1} has been increased over the period of time, indicating that more HCO_3^- was being formed at a cathodic potential of -0.3V. The peak ~1620 cm^{-1} observed in both potentials, which can be assigned to the asymmetric O-C=C stretching mode of $HCOO^-$ ions.[51] Moreover, the two reverse peaks centered at ~1630.8 cm^{-1} and 3272 cm^{-1} appeared at relatively higher potential (**Figure 4.10c**) can be assigned to the H-O-H bending and O-H stretching, respectively, of an H_2O molecule, indicating the predominance of HER in the higher overpotential. The intensity of these two peaks was gradually increased with the increase of the electrolysis time (**Figure 4.10d)** during CA at -0.9 V (vs. RHE).[52] Furthermore, to confirm the key intermediate formed during the eCO_2RR process, the electrolysis was performed with $^{13}CO_2$, and IR spectra were analyzed. The potential and time-dependent evolution of the in situ IR spectra have been shown in **Figure 4.10e** and **4.10f,** respectively. It has been detected that there is a clear isotopic shift corresponding to the C=O stretching of the formate intermediate from 1620 cm^{-1} to 1573 cm^{-1} upon exchanging $^{12}CO_2$ with $^{13}CO_2$ (**Figure 4.10g**).[53]

In this case, we have carried out the CO_2RR reaction in the 0.1M KCl concentration instead of $KHCO_3$ to avoid the exchange of ^{13}C with the ^{12}C of during the CO_2 reduction process as the gaseous CO_2 and bicarbonate always forms equilibrium.[54] The in situ ATR-FTIR results confirm that the dissolved CO_2 was reduced predominantly at the lower overpotential (-0.1-0.3 V), but HER was dominated In the higher potential (> -0.3 V). Based on the in-situ ATR-FTIR experiments, a plausible mechanism for the formation of HCOOH and CH_3COOH can be proposed, as depicted in **Figure 4.11**.[22] The first step of reduction of CO_2 is the initial formation of the radical anion $CO_2^{\bullet-}$ and then reduced to formic through the C-bound formate pathway. After the adsorption of $CO_2^{\bullet-}$, C–O bond cleaves with the loss of an H_2O molecule. The intermediate –CHO can be further reduced until a $–CH_2OH$ species is formed on the catalyst surface. Lastly, the C-O bond in $-CH_2OH$ dissociates with the loss of another H_2O molecule forming $–CH_3$ species, which is the precursor of CH_3COOH. The adsorbed $–CH_3$ species can combine with adsorbed $CO_2^{\bullet-}$ and form CH_3COOH, or it can also undergo a nucleophilic attack from the not adsorbed $CO_2^{\bullet-}$ in the CO_2 saturated solution and form acetic acid.[55]

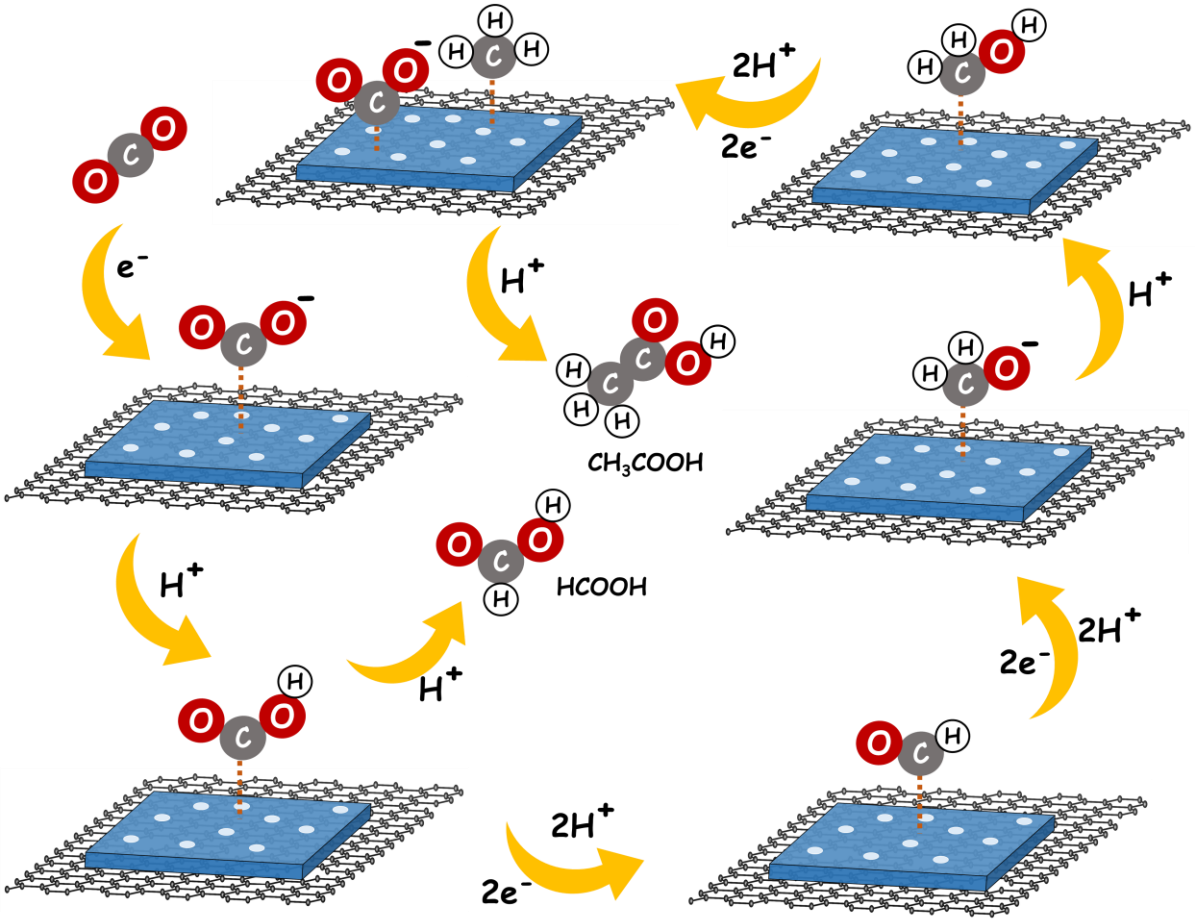

Figure 4.11. Schematic illustration of the mechanistic pathway for eCO_2RR on Cu_1-WC@NGC for the production of formic acid and acetic acid.

4.4.4. Oxidation state and Local electronic structures from Spectroscopic study

To elucidate the local structure, oxidation state, and coordination atmosphere of W and Cu in the present catalysts, X-ray absorption (XAS) study has been performed. X-ray absorption Near Edge Spectrum (XANES), shown in **Figure 4.12a**, shows an increase in the white line of L_{III}-edge of W indicates the charge transfer from W to Cu in Cu_x-WC@NGC compared to pristine WC@NGC.[56] In the higher loading of Cu, the decrease in the white line intensity of Cu *K*-edge and the photon energy of the absorption edge of Cu shifted to the lower energy indicates the lowering of the oxidation state of Cu (**Figure 4.12b**), which can be explained that atomically dispersed Cu present in Cu_1-WC@NGC has been transformed into nanoparticles upon agglomeration.[57] The k^3-weighted FT of R-space data indicates that Cu in Cu_1-WC@NGC has a peak at 1.6 Å, which can be corresponding to the bond in C coordinated atomically dispersed Cu site in WC@NGC (**Figure 4.12c**). This signature peak has been disappeared in the Cu_n-WC@NGC catalyst, where Cu is present in its elemental form, and the nature of R-space data is similar to that of Cu foil (**Figure 4.12d**).

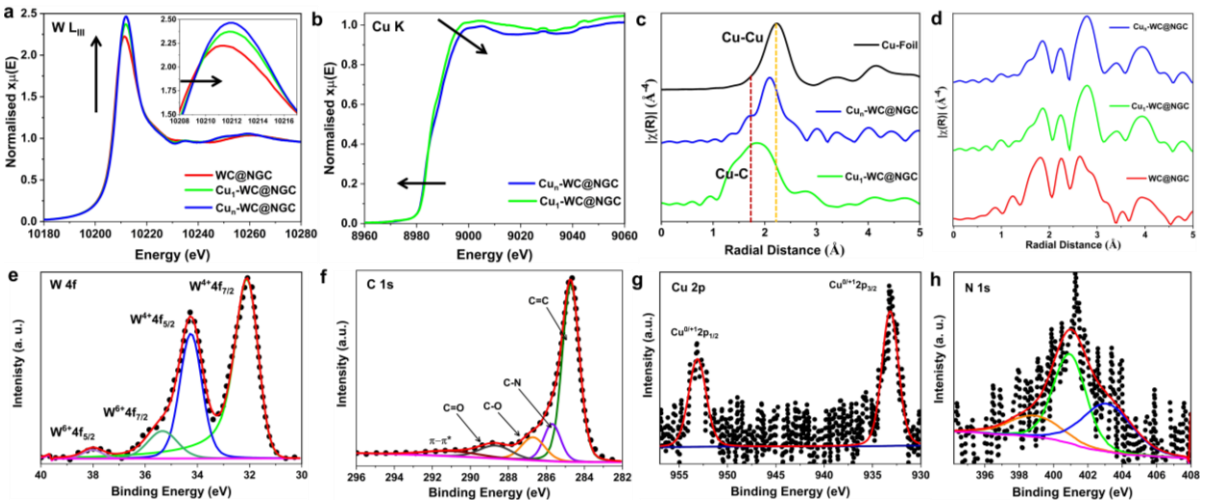

Figure 4.12. XANES spectra of (a) W L_{III}-edge and (b) Cu *K*-edge of WC@NGC, Cu_1-WC@NGC, Cu_n-WC@NGC catalysts. k^3-weighted FT EXAFS at (c) Cu *K*-edge for Cu_1-WC@NGC, Cu_n-WC@NGC, Cu foil, and (d) W L_{III} -edge for WC@NGC, Cu_1-WC@NGC, Cu_n-WC@NGC. High-resolution XPS spectra of Cu_1-WC@NGC for (e) W 4f, (f) C 1s, (g) Cu 2p, (h) N 1s.

X-ray photoelectron spectroscopy (XPS) of Cu loaded and pristine WC@NGC shows that the catalyst is constituted of W, N, Cu, N, and O elements (**Figure 4.13a-c**). The W 4f XPS spectrum consists of two major peaks at 32.13 and 34.27 eV, which are assigned to W^{4+} $4f_{7/2}$ and $4f_{5/2}$ of WC (**Figure 4.12e**). The peaks at a relatively higher binding energy (35.4 and 38 eV) are corresponding to the inevitable surface oxidation of Cu_x-WC@NGC. The C 1s XPS spectrum shows that peaks centered at 284.6 eV, 285.6 eV, 286.7 eV, 288.9 eV correspond to C-C/C=C, C-N, C-O, and C=O, respectively of the graphitic carbon sheets (**Figure 4.12f**). The Cu 2p XPS spectrum shows two peaks at 933.19 eV and 953.2 eV assigned to Cu $2p_{3/2}$ and $2p_{1/2}$, which is higher than that of Cu^{+1} and slightly lower than Cu^{+2} of CuO.[58] The absence of the satellite peak of Cu^{2+} eliminates the possibility of copper oxide formation on the surface of the catalyst.

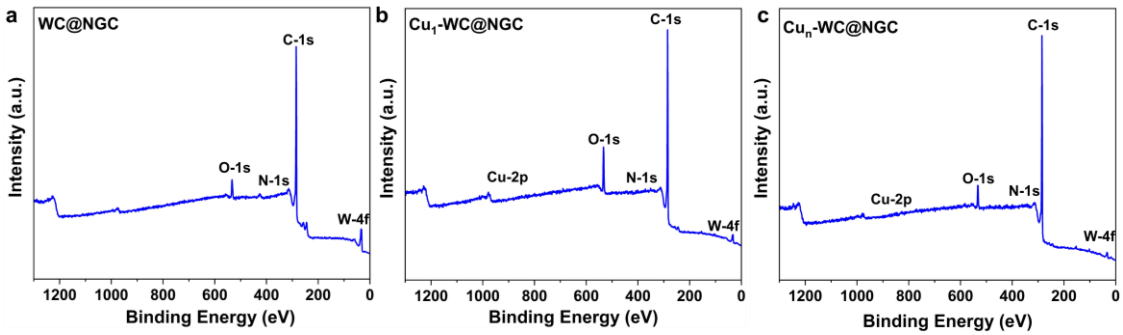

Figure 4.13. (a) XPS survey scan spectra (a) WC@NGC, (b) Cu_1-WC@NGC and (c) Cu_n-WC@NGC.

Moreover, the binding energy difference between Cu $2p_{3/2}$ and Cu $2p_{1/2}$, is 19.11 eV for Cu_1-WC@NGC catalyst, which is entirely different from that of CuO (18.4 eV), eliminate the presence of formation of CuO and indicated a different chemical environment of Cu ions in the carbide lattice.[59, 60] The typical presence of pyridinic (398.7), pyrrolic (400.8 eV), and graphitic (402.5 eV) N species in the N 1s spectra confirm the incorporation of N in the carbon matrix.[61] The binding energy of W has been shifted to the higher energy due to promotional loading of Cu, indicating an increase in the W oxidation state (**Figure 4.14**) which had also been observed in XANES analysis (**Figure 4.12a**). For Cu_1-WC@NGC, the presence of atomically dispersed Cu site (Cu_1^{x+}) greatly promotes CO_2 activation by adsorbing H_2O on Cu_1^{x+} site and adsorbing CO_2 on the neighboring W site.[39] On the other hand, the H_2O adsorption, and CO_2 activation property have been drastically reduced in the Cu_n-WC@NGC catalysts due to lowering the oxidation state of Cu.

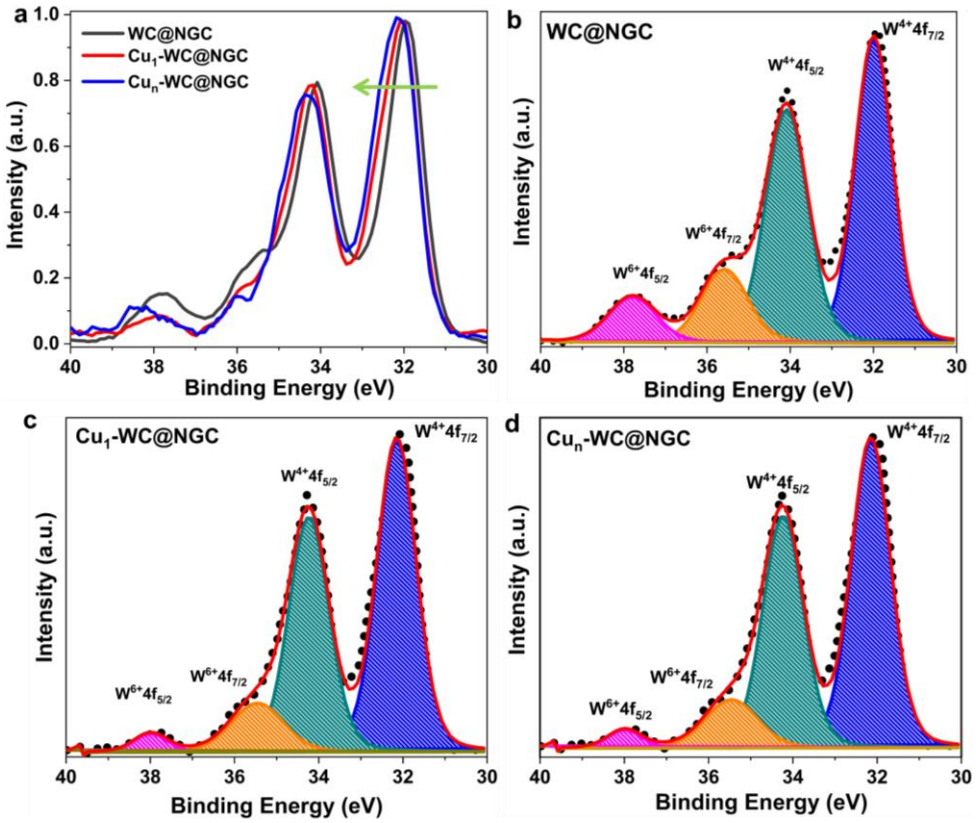

Figure 4.14. High resolution XPS spectra of W 4f of different WC@NGC and Cu-WC@NGC catalysts. (a) Relative comparison of W 4f binding energy of WC@NGC, Cu_1-WC@NGC and Cu_n-WC@NGC catalysts. Fitted W 4f XPS spectra of (b) WC@NGC, (c) Cu_1-WC@NGC and (d) Cu_nWC@NGC; W 4f 7/2 and 4f 5/2 states (of WC) are represented by the blue and dark cyan curves respectively. W 4f 7/2 and 4f 5/2 states of WO_3 have been represented by orange and magenta curves respectively.

The detailed analysis of surface composition through XPS also proves the elemental presence of W and Cu in both the Cu-loaded WC@NGC catalysts, and it was found that the atomic percentage of Cu has been increased from 2.27% (in Cu_1-WC@NGC) to 26.73% (in Cu_n-WC@NGC) (**Table 4.1**). The relative composition of WC and WO_3 has quantified by XPS analysis, and it was noticed that incorporation of copper reduces the surface WO_3 in the Cu_1-WC@NGC (**Table 4.2**). Altogether, the presence of atomically dispersed Cu sites in the catalyst unifies the distribution of the interface of WC lattice and the N-doped carbon sheet, reduces the surface WO_3, and facilitate the charge and mass transfer between Cu and WC.[62, 63]

Table 4.1. The relative amount (atomic %) of W and Cu present on the surface of different Cu-loaded WC@NGC catalysts, was obtained from XPS considering W $4f_{7/2}$ and Cu $2p_{3/2}$.

Catalyst	W (at %)	Cu (at %)
Cu_1-WC@NGC	97.73	2.27
Cu_n-WC@NGC	73.27	26.73

Table 4.2. Amount (%) of WC and WO_3 present on the surface of different Cu-loaded WC@NGC catalysts, was obtained from XPS considering W $4f_{7/2}$.

Catalyst	WC (at %)	WO_3 (at %)
WC@NGC	76.80	23.20
Cu_1-WC@NGC	85.84	14.16
Cu_n-WC@NGC	85.11	14.89

4.4.5. Post electrochemical characterization

It is very important to get an insight into the oxidation state of the active elements, surface composition, and the actual active crystallographic phase while applying potential during the electrolysis process. Ex-situ XPS (**Figure 4.15a-c**, **4.16**), ex-situ Raman (**Figure 4.15d**), and powder XRD characterization (**Figure 4.17**) of the catalyst were analyzed immediately after the electrolysis at the respective potential. **Figure 4.15a** shows the gradual increase in the formation of WO_3 upon reduction potential, which can be the reason for lowering the CO_2RR activity, and subsequently, HER becomes predominant, especially in the higher overpotential.[64, 65] The relative amount of WC and WO_3 as a function of applied potential has been plotted in **Figure 4.15b** and listed in **Table 4.3**. The formation of WO_3 on the catalyst surface can be triggered by the charge transfer from the Cu site. As a consequence that, the binding energy (BE) of Cu 2p has been shifted to lower binding energy, indicating a lowering of the oxidation state of Cu upon increasing the cathodic potential in the Cu_1-WC@NGC catalyst (Figure 4.15c).[66]

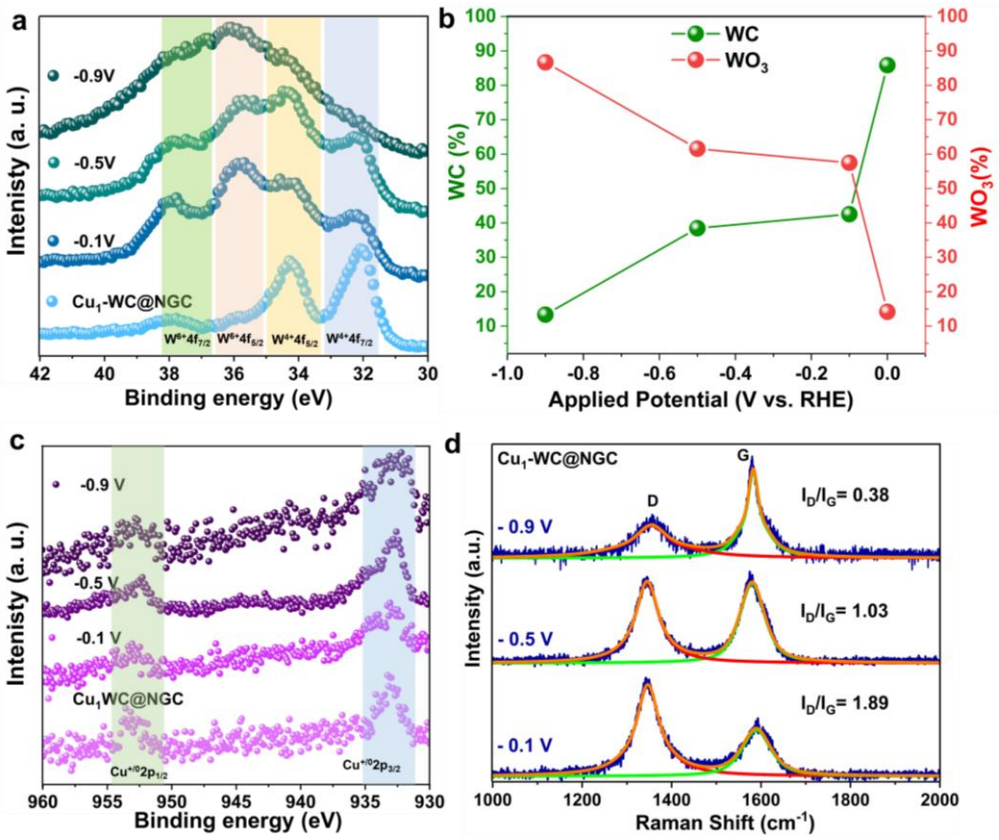

Figure 4.15. (a) High-resolution XPS spectra of (b) W 4f, (c) Cu 2p for Cu_1-WC@NGC catalysts and the catalyst coated carbon electrode after application of a potential of -0.1V, -0.5V, and -0.9V during the chronoamperometric study for eCO_2RR. (d) I_D and I_G bands in Raman spectra of Cu_1-WC@NGC as a function of potential during eCO_2RR.

Table 4.3. Amount (%) of WC and WO_3 present on the surface of Cu_1-WC@NGC at different applied potential during electrochemical CO_2RR, was obtained from XPS considering W $4f_{7/2}$.

Potential	WC (%)	WO_3 (%)
0.0 V	85.84	14.16
-0.1 V	42.53	57.47
-0.5 V	38.46	61.54
-0.9 V	13.33	86.67

The reason for lowering the electrochemical CO_2RR performance at higher potential can be attributed to the fact the CO_2 adsorption property of the catalyst has been gradually reduced on highly oxidized W site (as evident from potential dependent XPS) in the higher potential, and H_2O adsorption has been increased, which gives rise to the higher rate of hydrogen evolution. The Raman spectra of the catalyst at different applied potentials contain characteristic D and G bands at about 1348, 1579 cm^{-1}, respectively (Figure 4.15d).[67]

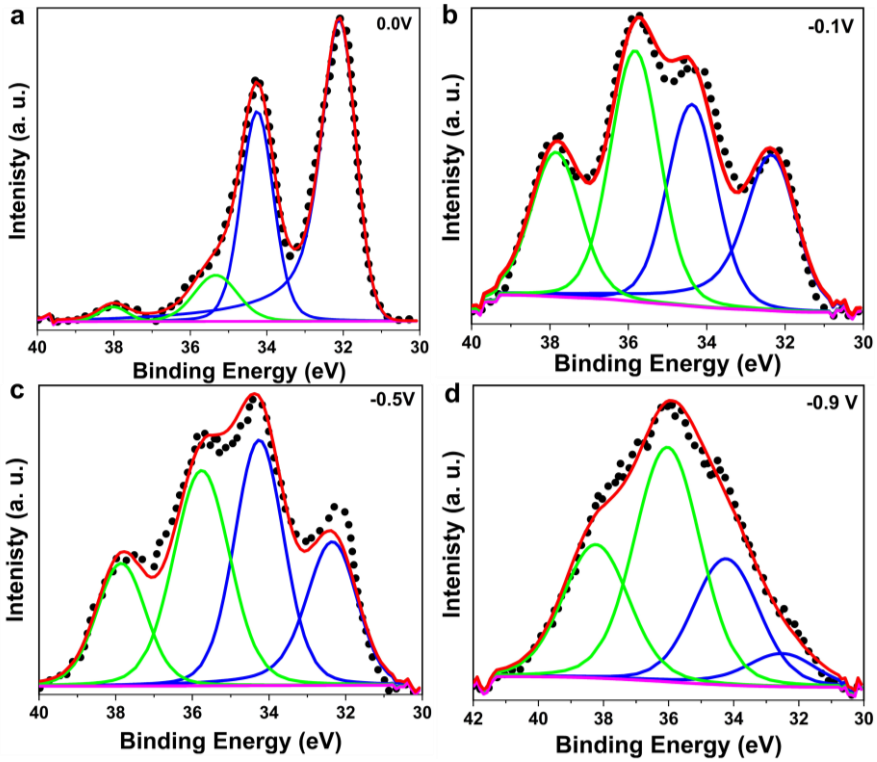

Figure 4.16. W 4f XPS spectra of (a) pristine Cu_1-WC@NGC and at (b) -0.1V, (c) -0.5V and (d) -0.9V applied potential. WC $4f_{7/2}$ and $4f_{5/2}$ states are represented by the blue curves, WO_3 $4f_{7/2}$ and $4f_{5/2}$states are represented by green curve.

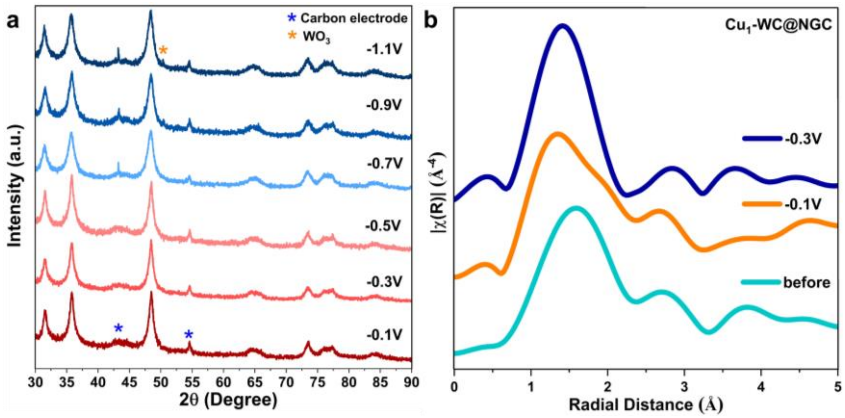

Figure 4. 17. Post electrochemical powder XRD analysis of Cu_1-WC@NGC at different applied potential. (b) In situ k^3-weighted FT XAFS at Cu K-edge for Cu_1-WC@NGC at different applied potential in the electrochemical CO_2RR condition in the CO_2 purged 0.5M $KHCO_3$ media.

The high I_D/I_G ratio in the lower potential indicates the presence of defects, which can be attributed to N doping in the graphitic matrix, one of the favorable factors for enhancing electrical conductivity, accessibility of the active site, and thereby increasing eCO_2RR performance. In the extremely reducing atmosphere, the intensity associated with the I_D band

is reduced can be correlated to the reduction of surface defects and lowering the CO_2RR activity.[68] To know the active crystallographic phase responsible for the CO_2RR activity, ex-situ powder XRD has been employed after the CA study. It is found that the major phase of WC in the catalyst is extremely stable in the entire range of negative potential with a negligible amount of WO_3 on the surface in the higher cathodic potential (**Figure 4.17a**). The in-situ XAFS study shows the the presence of Cu-single atomic site even after electrolysis at potential -0.3V (vs. RHE) as the signature bond at the radial distance of 1.4-1.5 Å for Cu-C bond persists in the operando condition in the FT XAFS spectra in **Figure 4.17b**.

4.4.6. High current density using flow cell with GDE configuration

Finally to enhance the CO_2 mass transport and get the higher current density, the Cu_1-WC@NGC has been tested in flow cell with gas diffusion electrode (GDE) configuration. PTFE-based GDE has been used in this case instead of carbon based as the former has better stability and proper diffusion of CO_2 gas which can properly maintain the gas-catalyst-electrolyte over long period of time during electrolysis.[41] In the flow cell, the current density (**Figure 4.18a**) and FE of all the CO_2 reduced products (**Figure 4.18b**) has increased than that of obtained in the H-cell suppressing the HER.[69]

4.4.7. Computational understanding of the reaction mechanism

To gain insights into the reaction mechanism, we performed density functional theory (DFT) calculations for the CO_2 reduction to the acetate on the two different structures, viz. WC and Cu_1-WC. A previous report by Asadi et al.,[48] explained the mechanism of CO_2 reduction to methane over W_2C. The present DFT result also showed a similar pathway until the formation of -CH_3 intermediate, considered as the precursor to form acetic acid.

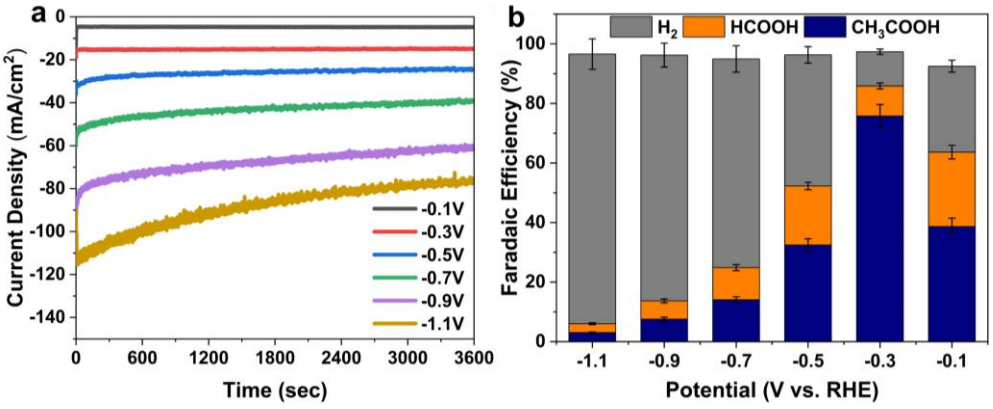

Figure 4.18. (a) Chronoamperometric study on Cu_1-WC@NGC during electrochemical CO_2RR in 1M KOH in flow cell with GDE configuration. (b) Faradaic efficiency for each CO_2 reduced products different potential as on Cu_1WC@NGC in flow cell configuration in 1M KOH using PTFE-based GDE.

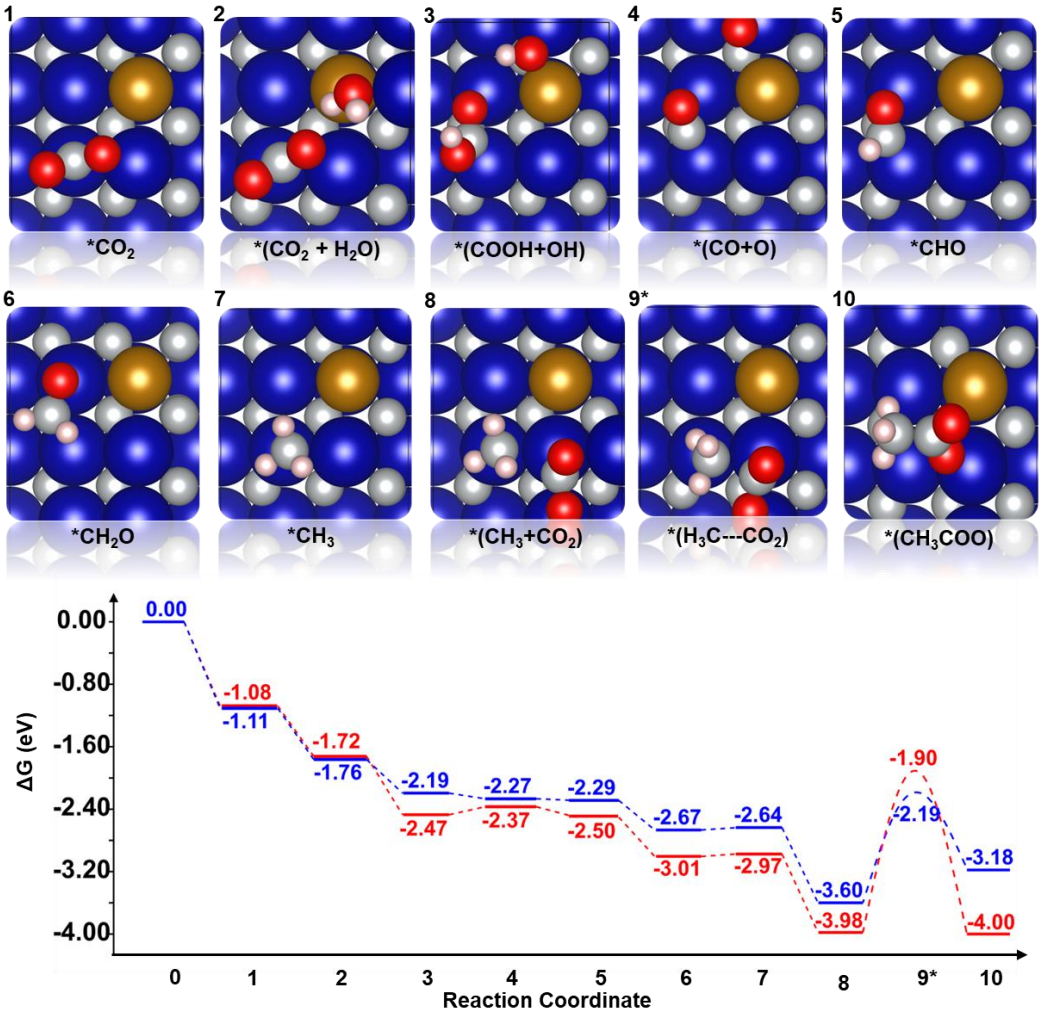

Figure 4.19. Representation of each step involved in the formation of acetic acid from CO_2 on Cu-WC surface. Blue colour represents W, orange represents C, grey denotes C, red represents O, brown colour represents H. The comparison of the Free Energy profile for CO_2 reduction to acetic acid production over bare WC and Cu-WC surfaces.

The reduction of CO_2 to $*CH_3$ is feasible on both WC and Cu_1-WC (**Figure 4.19**). The next step is the crucial C-C coupling to form the acetate intermediate. Several previous reports suggest direct coupling of $*COO^-$ with $*CH_3$ as one of the possible paths for acetate formation.[22, 70] As the d-band centre of W-atom at the surface lies nearer the Fermi level (**Figure 4.20**), it effectively captures and activates the CO_2 molecule to form $*COO^-$.

Bader charge analysis shows that there is around -1.01e charge transfer from the surface to CO_2 molecule forming the $*COO^-$ ion, which is then directly coupled with $*CH_3$ intermediate forming acetate ion. The free energy profile shows that Cu incorporation decreases the transition state barrier for the coupling which can be attributed to the small shift in d-band centre (-0.94 to -0.96 eV) after Cu-doping. It is also important to note that the proton transfer from -OH to -COOH intermediate is comparatively more accessible in the Cu_1-WC.

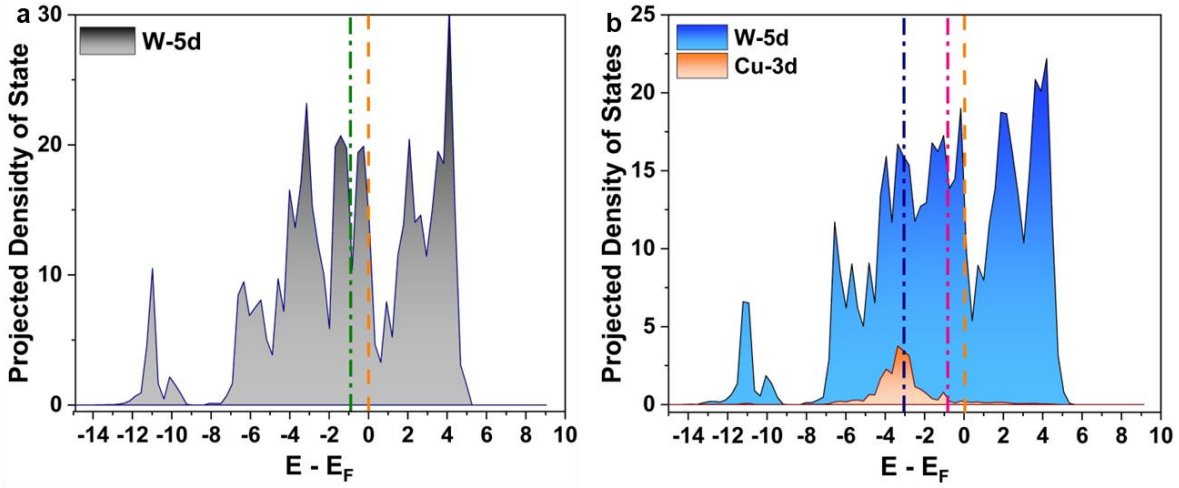

Figure 4. 20. Projected density of states (PDOS) of W 5d, and Cu 3d orbitals for (a) WC and (b) Cu-WC.

4.5. Conclusion

In conclusion, this work demonstrates a unique approach to synthesize the atomically dispersed Cu in WC@NGC catalyst, which exhibited extremely selective and robust electrochemical CO_2 performance towards the formation of acetic acid with a maximum FE of 80.03% at an ultra-low overpotential of -0.3 (vs. RHE). The superior performance of Cu_1-WC@NGC is resulted mainly because of the synergistic effect of WC lattice, atomically dispersed Cu center which activates the CO_2 and the N-doped carbon matrix for producing acetic acid. In-situ FT-IR spectroscopic study was carried out during the electrolysis process to map all the possible intermediates formed during eCO_2RR to propose the reaction mechanism. CO_2 can be easily adsorbed on WC@NGC surface and converted to $CO_2^{\bullet-}$, which can be further transformed to *CHO, OCH_3, and finally, C-C coupling happens. Post electrochemical XPS, Raman spectroscopy, and power XRD analysis reveal the potential dependent structural evolution and compositional changes, which play a crucial role in the CO_2 reduction activity and product selectivity. The major findings here is the formation of WO_3 in case of WC-based catalyst which is promoting the HER. So, to achive higher eCO_2RR selctivity at higher current density, we need to stabilise the WC species by different strategy. The facile design of electrocatalyst, unique structural features, and excellent electrochemical performance of the reported WC-based catalyst material open a new way for developing an efficient noble-metal-free catalyst for highly efficient CO_2 reduction to C_{2+} products.

4.6. References

1. Verdaguer-Casadevall, A.; Li, C. W.; Johansson, T. P.; Scott, S. B.; McKeown, J. T.; Kumar, M.; Stephens, I. E. L.; Kanan, M. W.; Chorkendorff, I., Probing the Active

Surface Sites for CO Reduction on Oxide-Derived Copper Electrocatalysts. *J. Am. Chem. Soc.* **2015,** *137*, 9808-9811.

2. Luo, W.; Nie, X.; Janik, M. J.; Asthagiri, A., Facet Dependence of CO_2 Reduction Paths on Cu Electrodes. *ACS Catal.* **2016,** *6*, 219-229.
3. Xiao, C.; Zhang, J., Architectural Design for Enhanced C_2 Product Selectivity in Electrochemical CO_2 Reduction Using Cu-Based Catalysts: A Review. *ACS Nano* **2021,** *15*, 7975-8000.
4. Zhou, Y.; Zhou, R.; Zhu, X.; Han, N.; Song, B.; Liu, T.; Hu, G.; Li, Y.; Lu, J.; Li, Y., Mesoporous PdAg Nanospheres for Stable Electrochemical CO_2 Reduction to Formate. *Adv. Mater.* **2020,** *32*, 2000992.
5. Wang, P.; Yang, H.; Xu, Y.; Huang, X.; Wang, J.; Zhong, M.; Cheng, T.; Shao, Q., Synergized Cu/Pb Core/Shell Electrocatalyst for High-Efficiency CO_2 Reduction to C_{2+} Liquids. *ACS Nano* **2021,** *15*, 1039-1047.
6. Lee, H.-E.; Yang, K. D.; Yoon, S. M.; Ahn, H.-Y.; Lee, Y. Y.; Chang, H.; Jeong, D. H.; Lee, Y.-S.; Kim, M. Y.; Nam, K. T., Concave Rhombic Dodecahedral Au Nanocatalyst with Multiple High-Index Facets for CO_2 Reduction. *ACS Nano* **2015,** *9*, 8384-8393.
7. Kim, C.; Jeon, H. S.; Eom, T.; Jee, M. S.; Kim, H.; Friend, C. M.; Min, B. K.; Hwang, Y. J., Achieving Selective and Efficient Electrocatalytic Activity for CO_2 Reduction Using Immobilized Silver Nanoparticles. *J. Am. Chem. Soc.* **2015,** *137*, 13844-13850.
8. Choukroun, D.; Pacquets, L.; Li, C.; Hoekx, S.; Arnouts, S.; Baert, K.; Hauffman, T.; Bals, S.; Breugelmans, T., Mapping Composition–Selectivity Relationships of Supported Sub-10 nm Cu–Ag Nanocrystals for High-Rate CO_2 Electroreduction. *ACS Nano* **2021,** *15*, 14858-14872.
9. Lei, F.; Liu, W.; Sun, Y.; Xu, J.; Liu, K.; Liang, L.; Yao, T.; Pan, B.; Wei, S.; Xie, Y., Metallic Tin Quantum Sheets Confined in Graphene Toward High-Efficiency Carbon Dioxide Electroreduction. *Nat. Commun.* **2016,** *7*, 12697.
10. Zhang, S.; Kang, P.; Meyer, T. J., Nanostructured Tin Catalysts for Selective Electrochemical Reduction of Carbon Dioxide to Formate. *J. Am. Chem. Soc.* **2014,** *136*, 1734-1737.
11. Bertin, E.; Garbarino, S.; Roy, C.; Kazemi, S.; Guay, D., Selective Electroreduction of CO_2 to Formate on Bi and Oxide-Derived Bi Films. *J. CO_2 Util* **2017,** *19*, 276-283.

12. Koh, J. H.; Won, D. H.; Eom, T.; Kim, N.-K.; Jung, K. D.; Kim, H.; Hwang, Y. J.; Min, B. K., Facile CO_2 Electro-Reduction to Formate via Oxygen Bidentate Intermediate Stabilized by High-Index Planes of Bi Dendrite Catalyst. *ACS Catal.* **2017,** *7*, 5071-5077.
13. Albo, J.; Sáez, A.; Solla-Gullón, J.; Montiel, V.; Irabien, A., Production of Methanol from CO_2 Electroreduction at Cu_2O and Cu_2O/ZnO-Based Electrodes in Aqueous Solution. *Appl. Catal. B* **2015,** *176-177*, 709-717.
14. Gao, S.; Sun, Z.; Liu, W.; Jiao, X.; Zu, X.; Hu, Q.; Sun, Y.; Yao, T.; Zhang, W.; Wei, S.; Xie, Y., Atomic Layer Confined Vacancies for Atomic-Level Insights into Carbon Dioxide Electroreduction. *Nat. Commun.* **2017,** *8*, 14503.
15. Ding, C.; Li, A.; Lu, S.-M.; Zhang, H.; Li, C., In Situ Electrodeposited Indium Nanocrystals for Efficient CO_2 Reduction to CO with Low Overpotential. *ACS Catal.* **2016,** *6*, 6438-6443.
16. Bitar, Z.; Fecant, A.; Trela-Baudot, E.; Chardon-Noblat, S.; Pasquier, D., Electrocatalytic Reduction of Carbon Dioxide on Indium Coated Gas Diffusion Electrodes—Comparison with Indium Foil. *Appl. Catal. B* **2016,** *189*, 172-180.
17. Wu, J.; Ma, S.; Sun, J.; Gold, J. I.; Tiwary, C.; Kim, B.; Zhu, L.; Chopra, N.; Odeh, I. N.; Vajtai, R.; Yu, A. Z.; Luo, R.; Lou, J.; Ding, G.; Kenis, P. J. A.; Ajayan, P. M., A Metal-Free Electrocatalyst for Carbon Dioxide Reduction to Multi-Carbon Hydrocarbons and Oxygenates. *Nat. Commun.* **2016,** *7*, 13869.
18. Zhang, S.; Kang, P.; Ubnoske, S.; Brennaman, M. K.; Song, N.; House, R. L.; Glass, J. T.; Meyer, T. J., Polyethylenimine-Enhanced Electrocatalytic Reduction of CO_2 to Formate at Nitrogen-Doped Carbon Nanomaterials. *J. Am. Chem. Soc.* **2014,** *136*, 7845-7848.
19. Lum, Y.; Kwon, Y.; Lobaccaro, P.; Chen, L.; Clark, E. L.; Bell, A. T.; Ager, J. W., Trace Levels of Copper in Carbon Materials Show Significant Electrochemical CO_2 Reduction Activity. *ACS Catal.* **2016,** *6*, 202-209.
20. Leverett, J.; Daiyan, R.; Gong, L.; Iputera, K.; Tong, Z.; Qu, J.; Ma, Z.; Zhang, Q.; Cheong, S.; Cairney, J.; Liu, R.-S.; Lu, X.; Xia, Z.; Dai, L.; Amal, R., Designing Undercoordinated Ni–N_x and Fe–N_x on Holey Graphene for Electrochemical CO_2 Conversion to Syngas. *ACS Nano* **2021,** *15*, 12006-12018.
21. Qiao, J.; Liu, Y.; Hong, F.; Zhang, J., A Review of Catalysts for the Electroreduction of Carbon Dioxide to Produce Low-Carbon Fuels. *Chem. Soc. Rev.* **2014,** *43*, 631-675.

22. Genovese, C.; Ampelli, C.; Perathoner, S.; Centi, G., Mechanism of C–C Bond Formation in the Electrocatalytic Reduction of CO_2 to Acetic Acid. A Challenging Reaction to Use Renewable Energy with Chemistry. *Green Chem.* **2017,** *19*, 2406-2415.
23. Medrano-García, J. D.; Ruiz-Femenia, R.; Caballero, J. A., Revisiting Classic Acetic Acid Synthesis: Optimal Hydrogen Consumption and Carbon Dioxide Utilization. In *Computer Aided Chemical Engineering*, Kiss, A. A.; Zondervan, E.; Lakerveld, R.; Özkan, L., Eds. Elsevier: 2019; Vol. 46, pp 145-150.
24. Wang, Y.; Wang, D.; Dares, C. J.; Marquard, S. L.; Sheridan, M. V.; Meyer, T. J., CO_2 Reduction to Acetate in Mixtures of Ultrasmall $(Cu)_n$,$(Ag)_m$ Bimetallic Nanoparticles. *PNAS* **2018,** *115*, 278.
25. Genovese, C.; Schuster, M. E.; Gibson, E. K.; Gianolio, D.; Posligua, V.; Grau-Crespo, R.; Cibin, G.; Wells, P. P.; Garai, D.; Solokha, V.; Krick Calderon, S.; Velasco-Velez, J. J.; Ampelli, C.; Perathoner, S.; Held, G.; Centi, G.; Arrigo, R., Operando Spectroscopy Study of the Carbon Dioxide Electro-Reduction by Iron Species on Nitrogen-Doped Carbon. *Nat. Commun.* **2018,** *9*, 935.
26. De, R.; Gonglach, S.; Paul, S.; Haas, M.; Sreejith, S. S.; Gerschel, P.; Apfel, U.-P.; Vuong, T. H.; Rabeah, J.; Roy, S.; Schöfberger, W., Electrocatalytic Reduction of CO_2 to Acetic Acid by a Molecular Manganese Corrole Complex. *Angew. Chem. Int. Ed.* **2020,** *59*, 10527-10534.
27. Liu, Y.; Chen, S.; Quan, X.; Yu, H., Efficient Electrochemical Reduction of Carbon Dioxide to Acetate on Nitrogen-Doped Nanodiamond. *J. Am. Chem. Soc.* **2015,** *137*, 11631-11636.
28. Han, N.; Yang, K. R.; Lu, Z.; Li, Y.; Xu, W.; Gao, T.; Cai, Z.; Zhang, Y.; Batista, V. S.; Liu, W.; Sun, X., Nitrogen-Doped Tungsten Carbide Nanoarray as an Efficient Bifunctional Electrocatalyst for Water Splitting in Acid. *Nat. Commun.* **2018,** *9*, 924.
29. Qiao, L.; Zhu, A.; Zeng, W.; Dong, R.; Tan, P.; Ding, Z.; Gao, P.; Wang, S.; Pan, J., Achieving Electronic Structure Reconfiguration in Metallic Carbides for Robust Electrochemical Water Splitting. *J. Mater. Chem. A* **2020,** *8*, 2453-2462.
30. do Rêgo, U. A.; Lopes, T.; Bott-Neto, J. L.; Tanaka, A. A.; Ticianelli, E. A., Oxygen Reduction Electrocatalysis on Transition Metal-Nitrogen Modified Tungsten Carbide Nanomaterials. *J. Electroanal. Chem.* **2018,** *810*, 222-231.
31. Song, L.; Wang, T.; Wang, Y.; Xue, H.; Fan, X.; Guo, H.; Xia, W.; Gong, H.; He, J., Porous Iron-Tungsten Carbide Electrocatalyst with High Activity and Stability toward

Oxygen Reduction Reaction: From the Self-Assisted Synthetic Mechanism to Its Active-Species Probing. *ACS Appl. Mater. Inter.* **2017,** *9*, 3713-3722.

32. Wan, W.; Tackett, B. M.; Chen, J. G., Reactions of Water and C_1 Molecules on Carbide and Metal-Modified Carbide Surfaces. *Chem. Soc. Rev.* **2017,** *46*, 1807-1823.
33. Li, N.; Chen, X.; Ong, W.-J.; MacFarlane, D. R.; Zhao, X.; Cheetham, A. K.; Sun, C., Understanding of Electrochemical Mechanisms for CO_2 Capture and Conversion into Hydrocarbon Fuels in Transition-Metal Carbides (MXenes). *ACS Nano* **2017,** *11*, 10825-10833.
34. Kunkel, C.; Viñes, F.; Illas, F., Transition Metal Carbides as Novel Materials for CO_2 Capture, Storage, and Activation. *Energy Environ. Sci.* **2016,** *9*, 141-144.
35. Wannakao, S.; Artrith, N.; Limtrakul, J.; Kolpak, A. M., Catalytic Activity and Product Selectivity Trends for Carbon Dioxide Electroreduction on Transition Metal-Coated Tungsten Carbides. *J. Phys. Chem. C* **2017,** *121*, 20306-20314.
36. Koverga, A. A.; Flórez, E.; Dorkis, L.; Rodriguez, J. A., Promoting Effect of Tungsten Carbide on the Catalytic Activity of Cu for CO_2 Reduction. *Phys. Chem. Chem. Phys.* **2020,** *22*, 13666-13679.
37. Cai, Y.; Fu, J.; Zhou, Y.; Chang, Y.-C.; Min, Q.; Zhu, J.-J.; Lin, Y.; Zhu, W., Insights on Forming N,O-Coordinated Cu Single-Atom Catalysts for Electrochemical Reduction CO_2 to Methane. *Nat. Commun.* **2021,** *12*, 586.
38. Yang, H.; Wu, Y.; Li, G.; Lin, Q.; Hu, Q.; Zhang, Q.; Liu, J.; He, C., Scalable Production of Efficient Single-Atom Copper Decorated Carbon Membranes for CO_2 Electroreduction to Methanol. *J. Am. Chem. Soc.* **2019,** *141*, 12717-12723.
39. Jiao, J.; Lin, R.; Liu, S.; Cheong, W.-C.; Zhang, C.; Chen, Z.; Pan, Y.; Tang, J.; Wu, K.; Hung, S.-F.; Chen, H. M.; Zheng, L.; Lu, Q.; Yang, X.; Xu, B.; Xiao, H.; Li, J.; Wang, D.; Peng, Q.; Chen, C.; Li, Y., Copper Atom-Pair Catalyst Anchored on Alloy Nanowires for Selective and Efficient Electrochemical Reduction of CO_2. *Nat. Chem.* **2019,** *11*, 222-228.
40. Roy, S.; Bagchi, D.; Vemuri, V.; Ch. Sarma, S.; Ahuja, V.; Rajaji, V.; Narayana, C.; Peter, S. C., Deconvolution of Phase–Size–Strain Effects in Metal Carbide Nanocrystals for Enhanced Hydrogen Evolution. *Nanoscale* **2020,** *12*, 15414-15425.
41. Corral, D.; Feaster, J. T.; Sobhani, S.; DeOtte, J. R.; Lee, D. U.; Wong, A. A.; Hamilton, J.; Beck, V. A.; Sarkar, A.; Hahn, C.; Jaramillo, T. F.; Baker, S. E.; Duoss, E. B.,

Advanced Manufacturing for Electrosynthesis of Fuels and Chemicals from CO_2. *Energy Environ. Sci.* **2021,** *14*, 3064-3074.

42. Kresse, G.; Furthmüller, J., Efficient Iterative Schemes for ab Initio Total-Energy Calculations Using a Plane-Wave Basis Set. *Phys.Rev. B* **1996,** *54*, 11169-11186.
43. Kresse, G.; Furthmüller, J., Efficiency of ab-Initio Total Energy Calculations for Metals and Semiconductors Using a Plane-Wave Basis Set. *Comput. Mater. Sci.* **1996,** *6*, 15-50.
44. Perdew, J. P.; Burke, K.; Ernzerhof, M., Generalized Gradient Approximation Made Simple. *Phys. Rev. Lett.* **1996,** *77*, 3865-3868.
45. Blöchl, P. E., Projector Augmented-Wave method. *Phys.Rev. B* **1994,** *50*, 17953-17979.
46. Grimme, S.; Antony, J.; Ehrlich, S.; Krieg, H., A Consistent and Accurate ab Initio Parametrization of Density Functional Dispersion Correction (DFT-D) for the 94 Elements H-Pu. *J. Chem. Phys.* **2010,** *132*, 154104.
47. Monkhorst, H. J.; Pack, J. D., Special Points for Brillouin-Zone Integrations. *Phys.Rev. B* **1976,** *13*, 5188-5192.
48. Esmaeilirad, M.; Baskin, A.; Kondori, A.; Sanz-Matias, A.; Qian, J.; Song, B.; Tamadoni Saray, M.; Kucuk, K.; Belmonte, A. R.; Delgado, P. N. M.; Park, J.; Azari, R.; Segre, C. U.; Shahbazian-Yassar, R.; Prendergast, D.; Asadi, M., Gold-Like Activity Copper-Like Selectivity of Heteroatomic Transition Metal Carbides for Electrocatalytic Carbon Dioxide Reduction Reaction. *Nat. Commun.* **2021,** *12*, 5067.
49. Xu, H.; Rebollar, D.; He, H.; Chong, L.; Liu, Y.; Liu, C.; Sun, C.-J.; Li, T.; Muntean, J. V.; Winans, R. E.; Liu, D.-J.; Xu, T., Highly Selective Electrocatalytic CO_2 Reduction to Ethanol by Metallic Clusters Dynamically formed from Atomically Dispersed Copper. *Nat. Energy* **2020,** *5*, 623-632.
50. Innocent, B.; Pasquier, D.; Ropital, F.; Hahn, F.; Léger, J. M.; Kokoh, K. B., FTIR Spectroscopy Study of the Reduction of Carbon Dioxide on Lead Electrode in Aqueous Medium. *Appl. Catal. B* **2010,** *94*, 219-224.
51. Mistry, B. J. C., A Handbook of Spectroscopic Data. **2009**.
52. Nur Hossain, M.; Chen, S.; Chen, A., Thermal-Assisted Synthesis of Unique Cu Nanodendrites for the Efficient Electrochemical Reduction of CO_2. *Appl. Catal. B* **2019,** *259*, 118096.
53. Lee, J.-E.; Yamaguchi, A.; Ooka, H.; Kazami, T.; Miyauchi, M.; Kitadai, N.; Nakamura, R., In Situ FTIR Study of CO_2 Reduction on Inorganic Analogues of Carbon Monoxide Dehydrogenase. *Chem. Commun.* **2021,** *57*, 3267-3270.

54. Dunwell, M.; Lu, Q.; Heyes, J. M.; Rosen, J.; Chen, J. G.; Yan, Y.; Jiao, F.; Xu, B., The Central Role of Bicarbonate in the Electrochemical Reduction of Carbon Dioxide on Gold. *J. Am. Chem. Soc.* **2017,** *139*, 3774-3783.
55. Zhang, P.; Wu, T.; Han, B., Preparation of Catalytic Materials Using Ionic Liquids as the Media and Functional Components. *Adv. Mater.* **2014,** *26*, 6810-6827.
56. Feng, K.; Zhong, J.; Zhao, B.; Zhang, H.; Xu, L.; Sun, X.; Lee, S.-T., $Cu_xCo_{1-x}O$ Nanoparticles on Graphene Oxide as A Synergistic Catalyst for High-Efficiency Hydrolysis of Ammonia–Borane. *Angew. Chem. Int. Ed.* **2016,** *55*, 11950-11954.
57. Ghodselahi, T.; Vesaghi, M. A.; Shafiekhani, A.; Baghizadeh, A.; Lameii, M., XPS Study of the Cu@Cu_2O Core-Shell Nanoparticles. *Appl. Surf. Sci.* **2008,** *255*, 2730-2734.
58. Bui, N. T.; Kang, H.; Teat, S. J.; Su, G. M.; Pao, C.-W.; Liu, Y.-S.; Zaia, E. W.; Guo, J.; Chen, J.-L.; Meihaus, K. R.; Dun, C.; Mattox, T. M.; Long, J. R.; Fiske, P.; Kostecki, R.; Urban, J. J., A Nature-Inspired Hydrogen-Bonded Supramolecular Complex for Selective Copper Ion Removal from Water. *Nat. Commun.* **2020,** *11*, 3947.
59. Biesinger, M. C., Advanced Analysis of Copper X-ray Photoelectron Spectra. *Surf. Interface Anal.* **2017,** *49*, 1325-1334.
60. Greczynski, G.; Hultman, L., X-ray Photoelectron Spectroscopy: Towards Reliable Binding Energy Referencing. *Prog. Mater Sci.* **2020,** *107*, 100591.
61. Kondo, T.; Guo, D.; Shikano, T.; Suzuki, T.; Sakurai, M.; Okada, S.; Nakamura, J., Observation of Landau Levels on Nitrogen-Doped Flat Graphite Surfaces without External Magnetic Fields. *Sci. Rep.* **2015,** *5*, 16412.
62. Wang, X.; Peng, Q.; Li, Y., Interface-Mediated Growth of Monodispersed Nanostructures. *Acc. Chem. Res.* **2007,** *40*, 635-643.
63. Ma, Y.-Y.; Lang, Z.-L.; Yan, L.-K.; Wang, Y.-H.; Tan, H.-Q.; Feng, K.; Xia, Y.-J.; Zhong, J.; Liu, Y.; Kang, Z.-H.; Li, Y.-G., Highly Efficient Hydrogen Evolution Triggered by a Multi-Interfacial Ni/WC Hybrid Electrocatalyst. *Energy Environ. Sci.* **2018,** *11*, 2114-2123.
64. Tian, H.; Cui, X.; Zeng, L.; Su, L.; Song, Y.; Shi, J., Oxygen Vacancy-Assisted Hydrogen Evolution Reaction of the Pt/WO_3 Electrocatalyst. *J. Mater. Chem. A* **2019,** *7*, 6285-6293.
65. Zheng, H.; Mathe, M., Hydrogen Evolution Reaction on Single Crystal WO_3/C Nanoparticles Supported on Carbon in Acid and Alkaline Solution. *Int. J. Hydrogen Energy* **2011,** *36*, 1960-1964.

66. Momose, Y.; Sato, K.; Ohno, O., Electrochemical Reduction of CO_2 at Copper Electrodes and its Relationship to the Metal Surface Characteristics. *Surf. Interface Anal.* **2002,** *34*, 615-618.
67. Wu, J.-B.; Lin, M.-L.; Cong, X.; Liu, H.-N.; Tan, P.-H., Raman Spectroscopy of Graphene-Based Materials and its Applications in Related Devices. *Chem. Soc. Rev.* **2018,** *47*, 1822-1873.
68. Gutić, S. J.; Kozlica, D. K.; Korać, F.; Bajuk-Bogdanović, D.; Mitrić, M.; Mirsky, V. M.; Mentus, S. V.; Pašti, I. A., Electrochemical Tuning of Capacitive Response of Graphene Oxide. *Phys. Chem. Chem. Phys.* **2018,** *20*, 22698-22709.
69. Niu, Z.-Z.; Chi, L.-P.; Liu, R.; Chen, Z.; Gao, M.-R., Rigorous Assessment of CO_2 Electroreduction Products in a Flow Cell. *Energy Environ. Sci.* **2021,** *14*, 4169-4176.
70. Wang, S.; Guo, S.; Luo, Y.; Qin, Z.; Chen, Y.; Dong, M.; Li, J.; Fan, W.; Wang, J., Direct Synthesis of Acetic Acid from Carbon Dioxide and Methane over Cu-Modulated BEA, MFI, MOR and TON Zeolites: a Density Functional Theory Study. *Catal. Sci. Technol.* **2019,** *9*, 6613-6626.

Chapter 5

Operando Investigation of the Origin of C-C Coupling in Electrochemical CO_2 Reduction Upon Releasing Bonding and Structural Ordering in Pd-Cu Catalyst

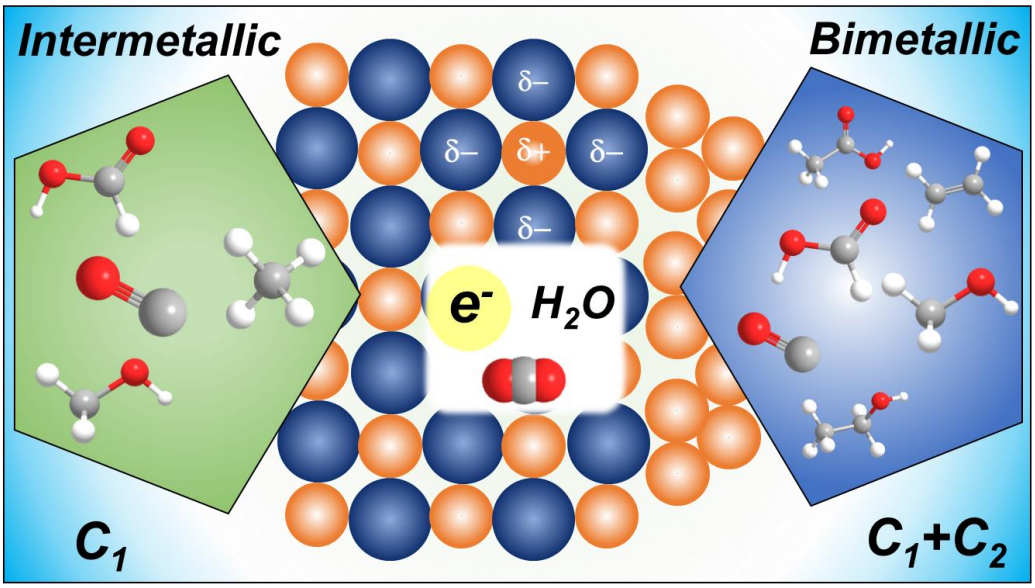

Bagchi, D.; Riyaz, M.; Churipard, S. R., Singh, A. K.; Peter, S. C. (*manuscript under preparation*)

Summary

Tuning the product selectivity is the most crucial factor for the CO_2RR process. In this chapter, we have showed how the catalyst structure plays an important role in switching the product selectivity from C_1(CO, HCOOH, CH_4) to highe energy dense and more reduced C_2 product (C_2H_4, C_2H_5OH, CH_3COOH etc.) Copper is the only metal that produces a range of alcohol and hydrocarbon after electroreduction of CO_2. But the selectivity of Cu towards a certain product is extremely poor as it forms a variety of reduced products concurrently. Controlling selectivity and overall performance depends on the modification of the copper site and local environment. This study depicts how the product selectivity can be switched from C_1 to C_2 and multicarbon products by systematic incorporation of secondary metal (Pd) into the copper lattice. Real-time in situ XAFS study showed the potential dependent evolution of Pd-Cu and Cu-Cu bonds at different PdCu-based catalysts. The detailed analysis of in situ IR and Raman also determined the adsorbed intermediate species and helped to identify the mechanism. DFT studies show the feasibility of mulicarbon product formation on bimetallic catalysts compared to alloy and intermetallic catalysts. The current density and the activity of the electrochemical CO_2 reduction have been enhanced by the utilization of the flow cell in the gas diffusion electrode configuration.

In this chapter, DB (author) has conceptualized the idea and synthesised the catalysts, performed all the electrochemical studies (both flow cell and H-cell) and other ex-situ (XRD, XPS, TEM), in-situ studies (FTIR, EXAFS), analyzed the data, and written the draft. MR performed the computational study. SRC helped to setting up GC. AKS assisted in in-situ EXAFS experiment. SCP conceptualized the idea, supervised the work, reviewed and edited the draft.

Table of Contents

5.1. Introduction 173

5.2. Experimental Details 174
5.2.1. Chemicals and reagents 174
5.2.2. Synthesis of Pd-Cu-based catalysts 174

5.3. Characterization and Experimental Methods 174
5.3.1. Powder X-ray Diffraction (PXRD) 174
5.3.2. Transmission Electron Microscope (TEM) 174
5.3.3. Inductively coupled plasma atomic emission spectroscopy (ICP-OES) 175
5.3.4. X-ray Photoelectron Spectroscopy (XPS) 175
5.3.5. X-ray Absorption Spectroscopy 175
5.3.6. Electrochemical CO_2 Reduction Reaction (eCO_2RR) 175
5.3.7. Flow cell optimization for eCO_2RR in gas diffusion electrode configuration 176
5.3.8. Gaseous product analysis. 176
5.3.9. Liquid product analysis 177
5.3.10. In situ Electrochemical Attenuated Total Reflection Fourier Transform Infrared Spectroscopy (ATR-FTIR). 177
5.3.11. Methodology of computational study 178

5.4. Results & Discussion 179

5.5. Electrochemical CO_2 reduction (eCO_2RR) 182

5.6. Mechanistic Studies 184
5.6.1. In situ ATR-FTIR spectroscopy 184
5.6.2. In situ Raman Study 186

5.7. Spectroscopic investigation of the active site 186
5.7.1. XPS study 186
5.7.2. Ex situ and in situ X-ray absorption spectroscopy 187

5.8. Computational understanding of the Reaction Mechanism 190

5.9. High current density using flow cell with GDE configuration 195

5.10. Conclusion 197

5.11. References 198

5.1. Introduction

The major challenge related to eCO_2RR is tuning the catalyst surface to achieve selective production of the specific product espeially multicarbon products. Cu-based catalysts have been extensively studied for eCO_2RR to hydrocarbons and alcohols.[1] However, monometallic Cu catalysts suffer from low selectivity towards any particular product formation.[2] It is important to modify the Cu site to gain selective and efficient production of specific alcohols or hydrocarbons. A variety of approaches have been already employed to modify the Cu surface and enhance the product selectivity, such as size,[3] shapes,[4, 5] grain boundaries[6, 7], chemical state,[8, 9], and surface modification.[10] Incorporation of secondary metal into the copper lattice is one of the important strategies to tune the electronic structure and local coordination of the Cu site and thereby modifying the intermediate species involved in the eCO_2RR so that unique product selectivity can be achieved.[11, 12] Majority of the Cu-based alloys are concentrated to disordered random alloy for examples CuAg for ethanol[13], CuAu for CO[14], CuZn for ethanol[15], CuPd for CH_4[16], etc.

Pd-based electrocatalysts are potential materials for eCO_2RR due to their extremely high conductivity as well as optimum adsorption of the key intermediates.[17] As copper has the ability to produce multi-carbon product like alcohols and hydrocarbons, Pd also binds C-bound intermediate, especially CO, strongly and thereby facilitating the C-C coupling.[18, 19] But, Pd suffers from CO-poisoning due to extreme covering of the intermediate.[20] It is important to isolate the Pd site by foreign element to enhance the catalytic activity and stability. Pd-Cu is one of the most suitable couples to tune the effect of adsorption of CO_2-derived intermediate and maximize the product selectivity. To date, some of the PdCu-based catalysts are reported in the eCO_2RR. Most of these studies are based on the effect of composition and alloying effect and have not explored much on the structural ordering effect, nature of bonding between metals, the evolution of the active sites or charge transfer kinetics, or the in situ mechanistic investigation.[16, 21, 22]

In this study, we demonstrate systematic structure-electrochemical CO_2RR activity of atomically ordered PdCu intermetallic, PdCu alloy, and PdCu bimetallic catalysts. It has been found experimentally that ordered intermetallic PdCu-catalyst selectively produces C1 products like CO, HCOOH, and CH_4. On the other hand, the alloy and bimetallic PdCu catalysts promote the C-C coupling by stabilizing the C-bound intermediate s and producing multicarbon products like ethanol. The evolution of the oxidation state, as well as local structure, have been probed by a real-time in situ XAFS study, which reveals that the Pd-Cu

bond sustains in the electrochemical atmosphere and is crucial for the C1 product selectivity. In situ XAFS also reveals that apart from Cu-O bond polarity, the combination of Cu-Cu and Cu-Pd can also promote the C-C coupling in electrochemical conditions. In situ ATR-FTIR determines the key intermediate for the formation of CO_2-reduced product on the Pd-Cu catalyst. From the computational study, we have proved that the C-C coupling is more favorable on the bimetallic catalyst than that of alloy and intermetallic due to lower activation energy for the formation of *COHCO intermediate.

5.2. Experimental Details

5.2.1. Chemicals and reagents

The following chemicals were used: copper nitrate ($Cu(NO_3)_2.3H_2O$, Alfa Aesar), palladium acetylacetonate ($Pd(acac)_2$, Alfa Aesar), sodium borohydride ($NaBH_4$, Sigma Aldrich), tetraethylene glycol (TEG, Merck). All the chemicals used were commercially available certified reagents and used without further purifications unless mentioned.

5.2.2. Synthesis of Pd-Cu-based catalysts

Palladium acetylacetonate and copper nitrate were taken in 1:1 mol ratio and dissolved in 20 mL of TEG by sonication and magnetic stirring in a 50 mL RB. After the solution was vigorously stirred at 60 °C under Ar atmosphere for 30 minutes, $NaBH_4$ freshly dissolved in 10 mL of TEG was added slowly and temperature was increased accordingly. Powders were precipitated from solution by centrifugation and were washed thoroughly with ethanol. For intermetallic compound, the reaction temperature has been increased to 240°C for 4h. For making the alloy catalyst temperature has been has been fixed to 220°C for 2hrs. For making the bimetallic catalyst the reaction ratio was 220°C for 4hrs.

5.3. Characterization and Experimental Methods

5.3.1. Powder X-ray Diffraction (PXRD)

PXRD measurements were done at room temperature on a Rigaku Miniflex X-ray diffractometer with a Cu−K_α X-ray source (λ = 1.5406 Å), equipped with a position-sensitive detector in the angular range of $10° \leq 2\theta \leq 90°$ with the step size 0.02° and a scan rate of 0.5 s/step calibrated against corundum standards. The experimental XRD patterns were compared to the patterns simulated from the data reported in the literature.

5.3.2. Transmission Electron Microscope (TEM)

TEM images and selected area electron diffraction patterns were collected using a JEOL JEM-2010 TEM instrument and color mapping was done in TECHNAI. The samples for

these measurements were prepared by sonicating the nanocrystalline powders in ethanol and drop-casting a small volume onto a carbon-coated copper grid.

5.3.3. Inductively coupled plasma atomic emission spectroscopy (ICP-OES)

ICP-OES was performed using a Perkin Elmer Optima 7000 DV instrument. The samples were digested in concentrated aqua regia, followed by dilution with distilled water. In a typical experiment, 2 mg of the sample was dissolved in 1 ml aqua regia and left overnight (12 hrs) for digestion. The digested sample was then diluted to 10 ml volume with deionized water. The solid particles were separated by thorough centrifugation before measurements.

5.3.4. X-ray Photoelectron Spectroscopy (XPS)

XPS measurements were carried out using Thermo K-alpha+ spectrometer using micro focused and monochromated Al Kα radiation with energy 1486.6 eV. The pass energy for the spectral acquisition was kept at 50 eV for individual core-levels. The electron flood gun was utilized for providing charge compensation during data acquisition. Further, the individual core-level spectra were checked for charging using C1s at 284.6 eV as standard and corrected if needed. The peak fitting of the individual core-levels was done using CASA XPS software with a Shirley type background.

5.3.5. X-ray Absorption Spectroscopy

X-ray absorption near-edge spectroscopy (XANES) and quick-Extended X-ray Absorption Fine Structure (quick-EXAFS) experiments at 300 K were performed at PETRA III, beamline P64, of DESY, Germany. Measurements of Cu-*K* and Pd-*K* at ambient pressure were performed in fluorescence as well as transmission mode using gas ionization chambers to monitor the incident and transmitted X-ray intensities. Monochromatic X-rays were obtained using a Si (111) double crystal monochromator, which was calibrated by defining the inflection point (first derivative maxima) of Cu foil as 8980.5 eV. The beam was focused by employing a Kirkpatrick-Baez (K-B) mirror optic. A rhodium-coated X-ray mirror was used to suppress higher-order harmonics. A CCD detector was used to record the transmitted signals. Pellets for the ex-situ measurements were made by homogeneously mixing the sample with an inert cellulose matrix to obtain an X-ray absorption edge jump close to one.

5.3.6. Electrochemical CO_2 Reduction Reaction (eCO_2RR)

All the electrochemical measurements were performed using a CHI 6008E electrochemical workstation. Electrochemical CO_2 reduction reaction (eCO_2RR) is carried out in a three-electrode system, which involves a working electrode (glassy carbon or carbon cloth), counter electrode (graphitic carbon rod), and reference electrode (Ag/AgCl). The cell

compartments are separated by a proton exchange membrane (Nafion 117), and the electrolyte used is 0.5M $KHCO_3$ solution. The electrolyte solutions were purged with CO_2 gas for 1 hour prior to the measurement. The electrocatalyst was prepared by dispersing 2 mg of catalyst and 0.2 mg of Vulcan (activated carbon) in 200 µL of mixed solvent solution (IPA:H_2O = 1:1 v/v) and 10 µL of 1 wt% nafion binder. From the prepared catalyst 100 µL was coated on the carbon cloth and dried. The electrochemical cell was designed to have a large electrode area (0.7 cm x 0.7 cm) and a small electrolyte volume (10 mL) in each of the two compartments, along with a gas headspace of approximately 5 mL above the electrolyte on each side of the membrane. CO_2, regulated by a mass flow controller at 10 standard cubic centimeters per minute (sccm), flowed through the working electrode compartment of the cell during electrolysis. CO_2 flow through the cell was necessary in order to see large current efficiencies for CO_2 reduction products, presumably because of mass transport limitations in a quiescent cell. The flow rate of 10 sccm was chosen to ensure sufficient CO_2 transport to the surface while preventing interference from gas bubbles striking the surface.

5.3.7. Flow cell optimization for eCO_2RR in gas diffusion electrode configuration

To increase the CO_2 diffusion and increase the overall current density, the electrochemical carbon dioxide experiments were carried out in a filter-press type Micro Flow Cell (Electrocell A/S), where a Ti sheet coated with Ir-MMO (iridium-mixed metal oxide) is used as an Anode plate (Electrocell S/A). An anionic exchange membrane (Fumasep FAB-PK-130) was employed in the case of CO_2RR in KOH medium. As discussed in **Figure 1.12**, the cell has three compartments, viz. CO_2 gas compartment, cathodic and anodic compartment (**Figure 1.13**).

The electrolyte was recirculated continuously into the cell (both in cathode and anode) by two separate peristaltic pumps (Ravel, RH-P100L-100) to accumulate liquid products. The flow of CO_2 was regulated by a mass flow controller (Brooks) at different flowrate (standard cubic centimeters per minute (sccm)) to optimize the most suitable flow rate, flowed through the working electrode compartment of the cell during electrolysis. For the final study, the gas flow is fixed to 50 sccm, and electrolyte flow was set to 20 sccm. To achieve C-based GDE, Freudenberg H23C2 has been used as the gas diffusion layer (GDL) and catalyst ink was coated with loading of 1mg/cm^2.

5.3.8. Gaseous product analysis

All the gaseous products were analyzed by online 490-Micro Gas Chromatography (GC), which has four channels for detecting different gaseous products. Each channel has a

specific column for analyzing relevant gases *viz*. Molsieve 5Å (for channel 1 and 2), Pora PLOT U (in channel 3) and CP-Sil 5 CB (for channel 4). The carrier gases were Ar and H_2. Each GC channel is equipped with a thermal conductivity detector (TCD). This detector responds to the difference in thermal conductivity between a reference cell (carrier gas only) and a measurement cell (carrier gas containing sample components).

Calculation of Faradaic Efficiency (FE) for gaseous products,

$$FE_{gas} = \frac{ppm \times flow\ rate \times \frac{number\ of\ electron \times Faradaic\ contant \times pressure}{R \times Temperature}}{I_{average}} \times 100$$

Where ppm is the concentrations detected by GC, R is a gas constant (8.31 j $K^{-1}mol^{-1}$).

5.3.9. Liquid product analysis

The liquid products were analyzed by ^1H NMR (600 MHz, JEOL). The following protocol was applied. 500 mL of the electrolyte and 30 µL of an internal standard solution were transferred into a centrifuge tube. The internal standard solution consisted of 50 mM phenol (99.5 %) and 10 mM dimethyl sulfoxide (99.9 %) made in D_2O solvent. The mixture is transferred into an NMR tube. Solvent suppression was used to decrease the intensity of the water peak.

5.3.10. In situ Electrochemical Attenuated Total Reflection Fourier Transform Infrared Spectroscopy (ATR-FTIR)

In situ electrochemical FTIR spectroscopic studies were performed using a purged VERTEX FT-IR spectrometer equipped with the A530/P accessory and a mid-band MCT detector. A silicon hemispherical window (F530-8) was used with the working electrode placed gently on top of the window as the single reflection attenuated total reflection (ATR) accessory for the FTIR study. The in situ experimental setups is depicted in **Figure 1.15**. The measurement parameters were 4 cm^{-1} resolution and 100 scans.

This setup enabled the detection of eCO_2RR intermediate formation and change of adsorption of various intermediates on the electrode surface and within the thin-layer electrolyte. In the beginning of the IR-experiment, we have taken a spectrum of the overall electrochemical cell and then take a background spectrum so that the contribution of the electrolyte can be subtracted in the next spectrum while applying the potential during performing CO_2RR. The spectra were analyzed by the OPUS software and the absorption spectra have been directly plotted at various potential and time.

5.3.11. Methodology of computational study

All DFT calculations were performed using the PWscf (Plane-Wave Self-Consistent Field) method implemented in Quantum Espresso Simulation Package.[23] The Perdew-Becke Ernzerhof (PBE)[24] exchange-correlation functional was used in combination with ultra-soft pseudopotential[25] that represents the interaction between ionic cores and valence electrons. The kinetic energy cutoff of 545 eV is applied to truncate the plane-wave basis used to represent the Kohn-Sham orbitals, and a convergence threshold of 0.03 eV/Å is accounted for forces on the atoms for ionic minimization. The correction to long-range dispersion interactions was included by employing the D3 correction method by Grimme et al.[26] The Monkhorst-Pack mesh[27] k-points of (3 × 3 × 1) for intermetallic CuPd(111), CuPd(100), and (2 × 2 × 1) for Alloy and bimetallic CuPd(111) were used. A denser k-point mesh of (5 × 5 × 1) with Hubbard correction (DFT+U)[28] with U_{eff} = 9 and 6 eV for Cu and Pd respectively was used for the density of state calculations.

To model the intermetallic surfaces, first, the bulk model of bcc CuPd was fully relaxed and then created a p(3 × 2) surface slab for PdCu (110) and p(2×2) for PdCu (111) including four atomic layers, with a vacuum thickness of 15 Å to avoid interactions between the repeating units. To create the alloy CuPd(111) surface, bulk fcc $Cu_{0.25}Pd_{0.75}$ was fully relaxed and then created a p(2 × 2) surface with four layers. The atoms in the top two layers were then allowed to relax while the bottom two layers were fixed at the bulk equilibrium distances. The bimetallic surface was modeled by adsorbing a cluster model of Cu (two-layer fcc Cu(111) containing 12 atoms) over p(2 × 2) surface of Pd with two layers.[29] During geometry optimization, the top layer of Pd and the Cu cluster were relaxed in all directions, while the bottom layer was fixed at the bulk equilibrium distances. The adsorption energy (E_{ads}) of the adsorbate was calculated as:

$$E_{ads} = E_{slab+x} - (E_{slab} + E_x)$$

Where E_{slab+x}, E_{slab} and E_x are the total energy of slab with adsorbate, the energy of bare slab and the energy of adsorbate in the gas phase respectively. The reaction free energies were approximated as:

$$\Delta G = \Delta E + \Delta ZPE - T\Delta S$$

Where ΔE is the DFT calculated change in reaction energy, ΔZPE is the zero-point energy change, and TΔS is the entropy change at 300 K. The entropy and ZPE were calculated from the frequency computed (**Table 5.1**) using phonon.x implemented in Quantum Espresso.

Table 5.1. Zero-point energies (ZPE) and entropy corrections for adsorbed intermediates and gas phase molecules. The values for gas phase molecules are taken from ref.[30]

Species	ZPE (eV)	TS (eV)	ZPE-TS
H_2	0.27	0.42	-0.15
CO_2	0.31	0.65	-0.34
CO	0.14	0.67	-0.53
H_2O	0.58	0.65	-0.07
HCOOH	0.90	1.02	-0.12
*CO_2	0.30	0.09	0.21
*COOH	0.61	0.17	0.44
*HCOOH	0.82	0.09	0.73
*CO	0.12	0.14	-0.02
*COH	0.36	0.13	0.23
*CHO	0.34	0.10	0.24
*CH_2O	0.65	0.17	0.48
*OCCHO	0.66	0.29	0.37
*OCCOH	0.66	0.24	0.32

5.4. Results & Discussion

The formation of different kinds of PdCu-based catalysts has been achieved by colloidal synthesis technique using metal precursor and $NaBH_4$ as the reducing agent. The ordered intermetallic compound (PdCu-IM) required high temperature, as it demands high kinetic energy for the better diffusion of the reactants. An increase in reaction temperature favors better thermal vibration of the atoms, which enhances the diffusion of the metals and results in the ordered compounds.[31] In this case, at elevated temperature conditions, by using a strong reducing agent ordered intermetallic phase of PdCu was obtained. PdCu-IM is a primitive cubic system crystallizes in the CsCl structure type having $Pm\bar{3}m$ space group, where all the corners were occupied by the Cu atoms (Wyckoff site 1*a*) and the body center is occupied by the Pd atoms (Wyckoff site 1*b*).[32] XRD pattern of PdCu IM contains peaks at $2\theta = 29.9°$, 42.8°, and 53.1°, which correspond to (100), (110), (111) diffractions of PdCu with a BCC structure, respectively (**Figure 5.1a**). Whereas disordered PdCu alloy (PdCu-Al) phase crystallizes in FCC structure with space group $Fm\bar{3}m$. The XRD patterns exhibit peaks at 41.04°, 47.74°, and 69.82°, which correspond to (111), (200), and (220) diffractions of FCC structures,

respectively.[33] The bimetallic analogue of PdCu (PdCu-BM) contains diffraction from the FCC lattice of both Pd and Cu (**Figure 5.1a**). The unit cell representation along with the mixing pattern of different PdCu-systems, have been depicted in **Figure 5.1b**.

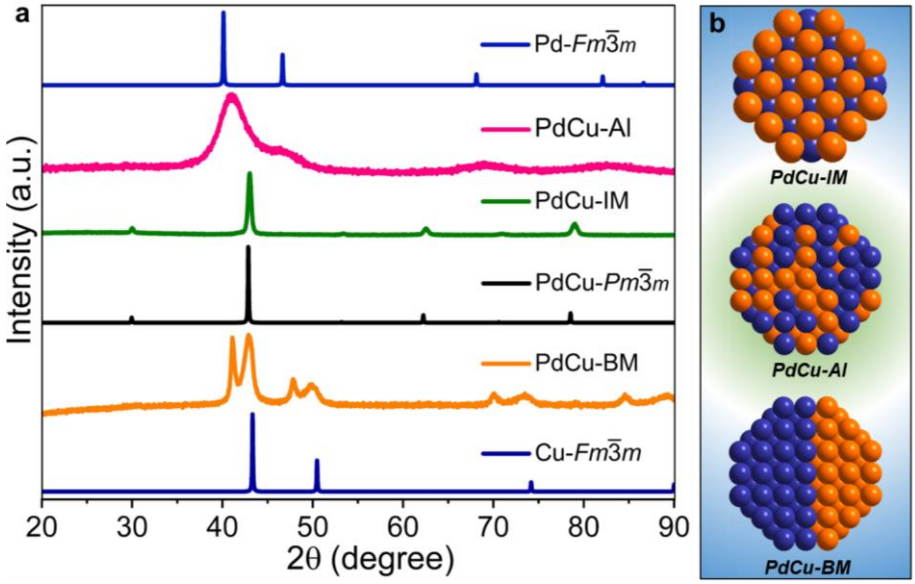

Figure 5.1. (a) Comparison of powder XRD patterns of different types of PdCu nanoparticles (PdCu-IM (intermetallic), PdCu-Al (alloy) and PdCu-BM (bimetallic)) with the corresponding simulated XRD patterns. (b) Schematic representation of PdCu-IM, PdCu-Al and PdCu-BM.

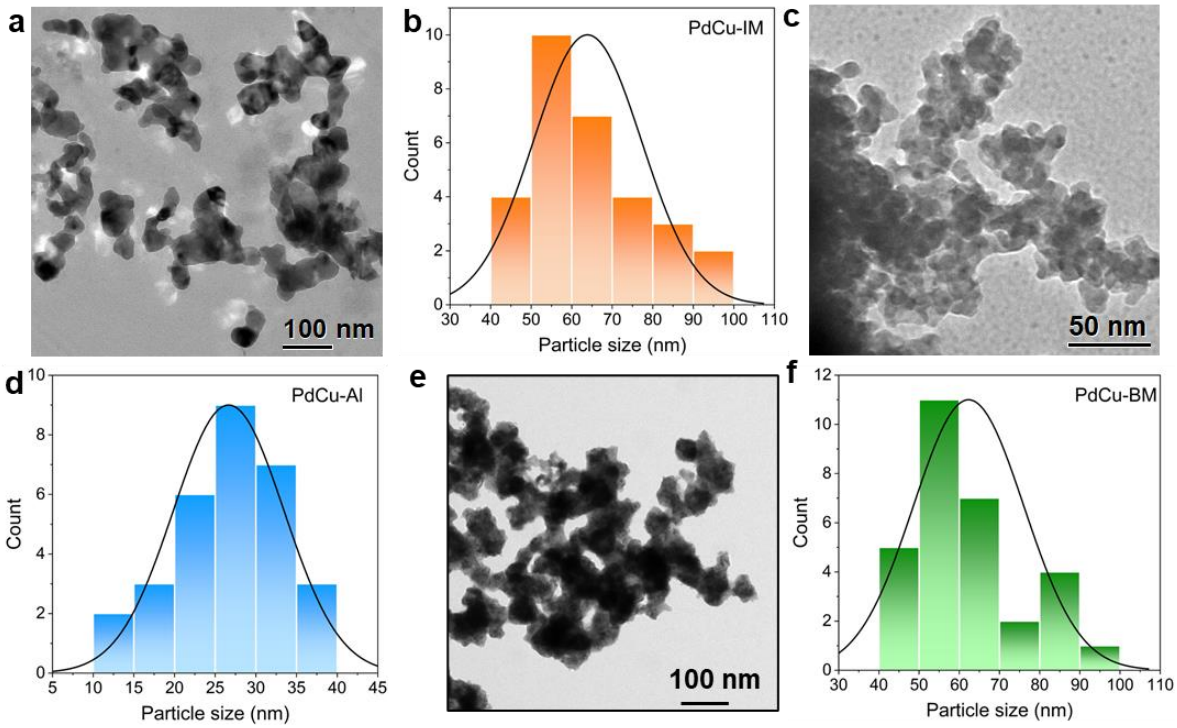

Figure 5.2. TEM images of (a) PdCu-IM and (b) the histogram profile of particle distribution. TEM images of (c) PdCu-IM and (d) the histogram profile of particle distribution. TEM images of (e) PdCu-IM and (f) the histogram profile of particle distribution.

Transmission electron microscopy (TEM) images of different PdCu nanosystems showed the uniform presence of dispersed particles all over the surface (**Figure 5.2a-e**). The average particle size of PdCu-Al has been found to be smaller than that of the PdCu-IM and PdCu-BM as the alloy has been formed at a lower temperature (**Figure 5.2a-e**).

Moreover, the selected area electron diffraction (SAED) patterns of PdCu-IM were indexed with (110), (111), and (200) planes of PdCu-ordered $Pm\bar{3}m$ structure (**Figure 5.3a**) and (111), (220) and (311) planes of PdCu-Al (**Figure 5.3b**). SAED pattern of PdCu-BM confirms the presence of crystallographic signature of both Pd and Cu lattice as presented in **Figure 5.3c**. The high-resolution (HR) TEM image of PdCu-IM depicts the presence of major crystallographic plane (110) of PdCu-IM phase having d-spacing 0.218 nm (**Figure 5.3d**). On the other hand, HRTEM image of PdCu-BM shows the exposed (111) plane of both Cu and Pd lattice (**Figure 5.3e**).

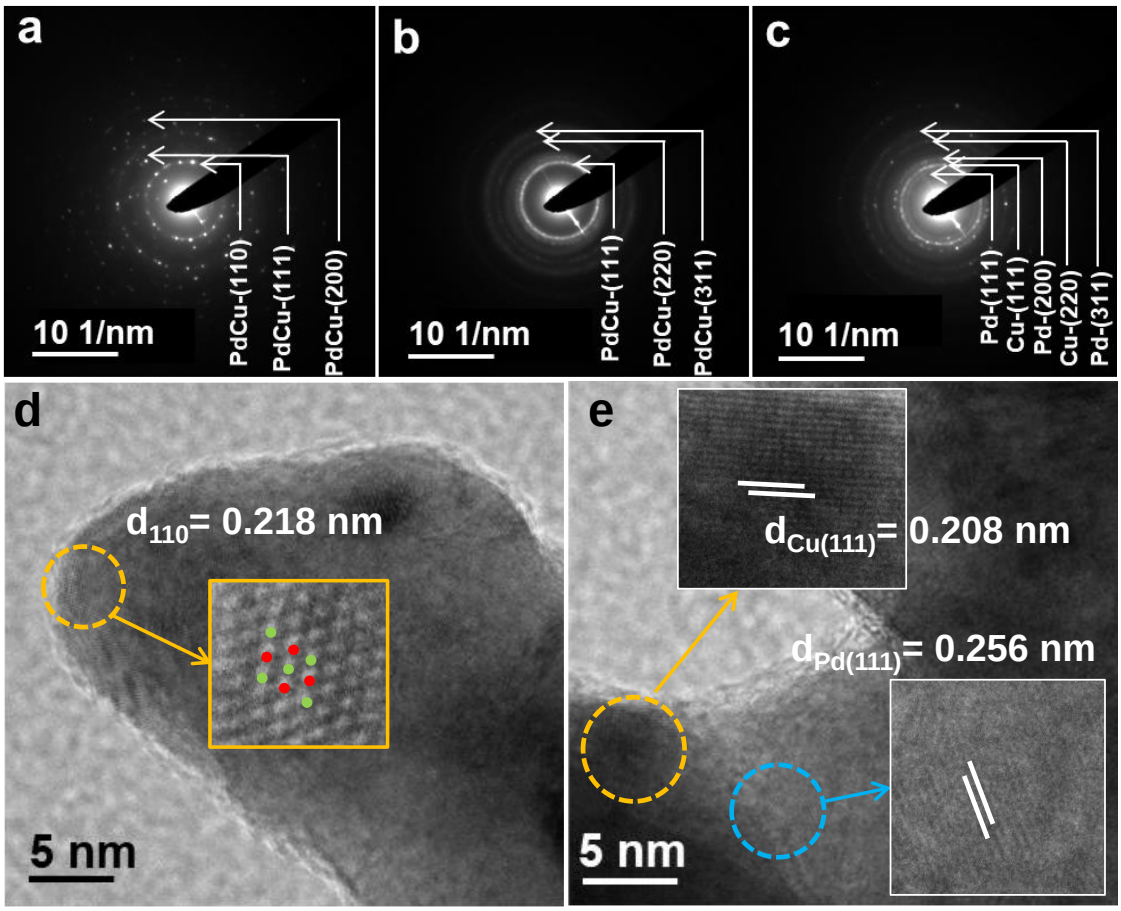

Figure 5.3. Selected area electron diffraction (SAED) pattern of (a) PdCu-IM, (b) PdCu-Al and (c) PdCu-BM nanoparticles. High-resolution TEM (HRTEM) images of (d) PdCu-IM and (e) PdCu-BM nanoparticles.

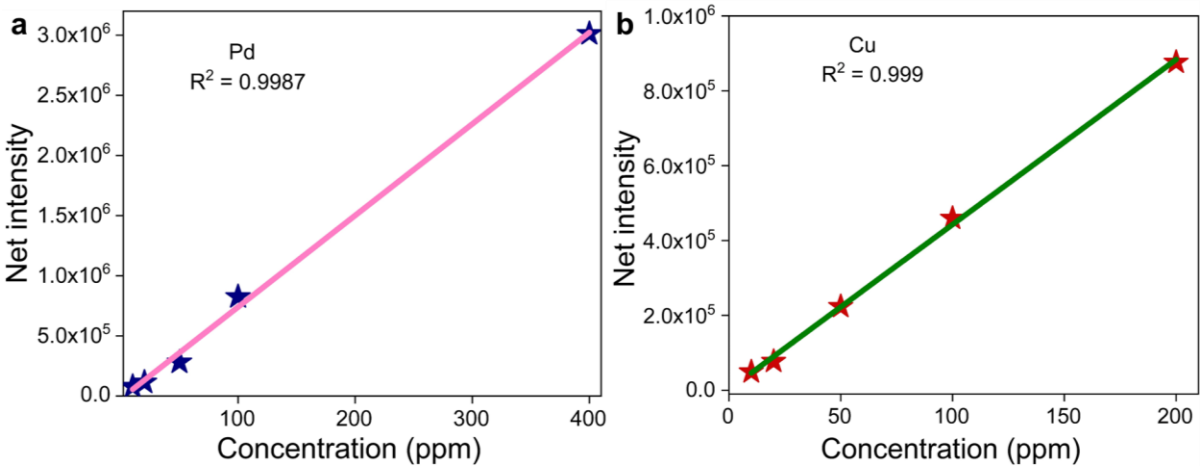

Tables 5.4. ICP-OES Calibration curves for (a) Pd and (b) Cu quantification at different concentration range.

The elemental composition of the Pd-Cu-catalysts have been determined from ICP-OES techniques (**Figure 5.4**) and tabulated in **Table 5.2**. It has been observed that the ratio of Pd and Cu have been found to be almost similar in the three different catalysts materials viz. PdCu-IM and PdCu-Al, PdCu-BM. From these observation, it can be concluded that the catalytic activity may not be controlled by the compositional effect of Pd and Cu.

Tables 5.2. Calculation of amount of Pd and Cu present in Pd-Cu-based catalysts through ICP-OES.

Catalyst	Elements	mol	Atomic %
PdCu-IM	Pd	0.0110	50.561
	Cu	0.0108	49.439
PdCu-Al	Pd	0.0172	53.569
	Cu	0.0149	46.431
PdCu-BM	Pd	0.0221	50.128
	Cu	0.022	49.872

5.5. Electrochemical CO_2 reduction (eCO_2RR)

From Linear Sweep Voltammogram (**Figure 5.5a**), it is clear that the value of current density (as a function of applied potential) is maximum in the case of PdCu-Al, and the minimum current density is obtained for PdCu-IM catalyst at any applied overpotential. The current density of the PdCu-BM is observed as the intermediate of alloy and IM (**Figure 5.5a**). So, the electrocatalytic activity for CO_2 reduction is expected to follow the same trend as the trend of current density values. It is important to mention that the contribution of the hydrogen

evolution reaction (HER) will also be there. [34] The potential-dependent evolution of all the CO_2-reduced products has been plotted in **Figure 5.5b-e.** The gaseous products like CO and H_2 have been detected and quantified from online GC analysis. The liquid product analysis of was performed by NMR, which detected the products like: formic acid (δ = 8.33, s, 1H), ethanol (δ = 1.06, t, 3H & δ = 3.53, q, 2H), methanol ((δ =3.23, s, 3H), n-propanol ((δ = 0.77, t, 3H; δ = 1.42, sextet, 2H & δ = 3.44, t, 2H).

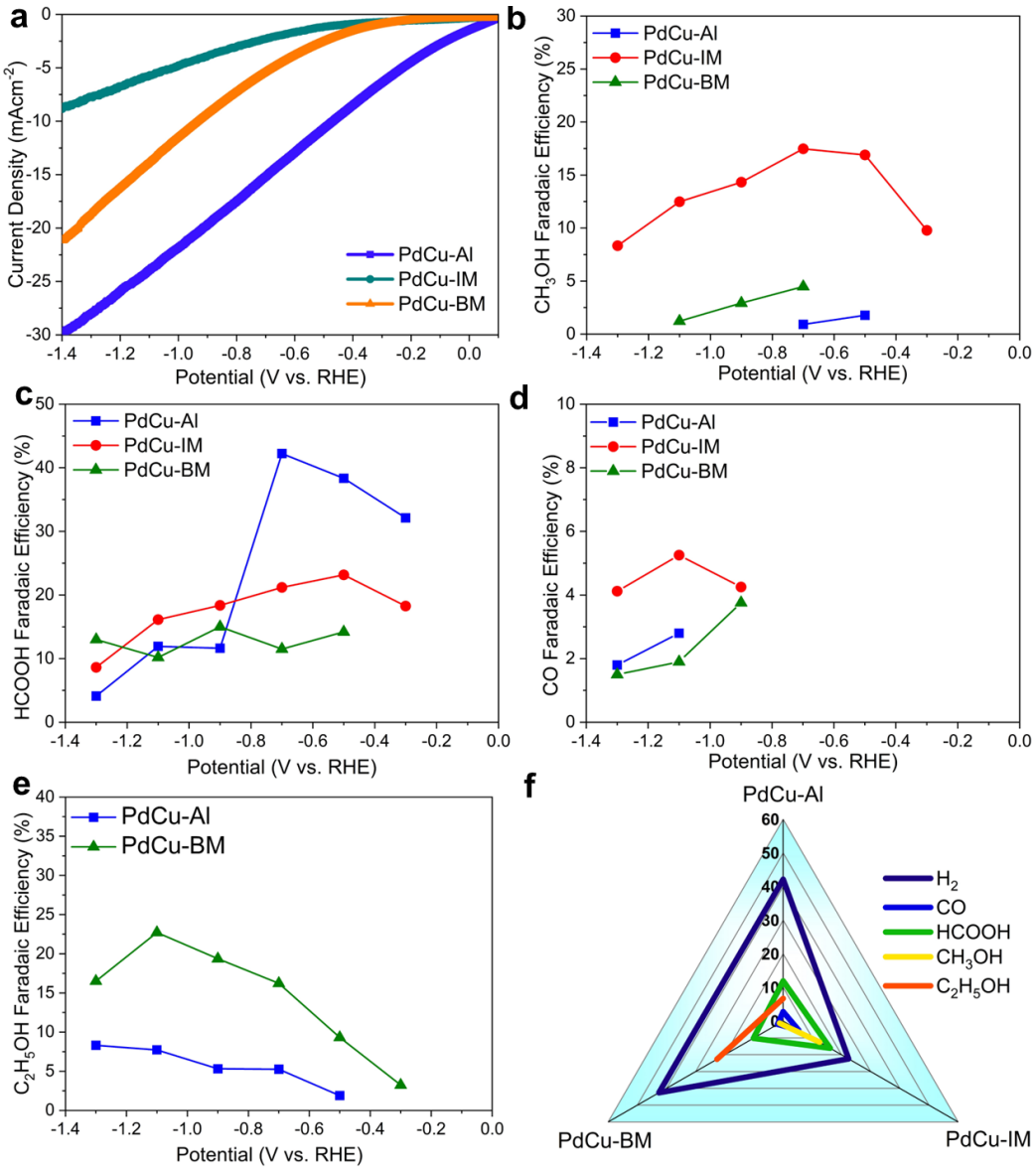

Figure 5.5. (a) Linear Sweep Voltammogram of different types of PdCu-based nanocatalyst at electrochemical CO_2RR condition in CO_2 purged 0.5 M $KHCO_3$ solution. Faradaic efficiencies (FEs) for (b) CH_3OH, (c) HCOOH, (d) CO, (e) C_2H_5OH for different kinds Pd-Cu catalysts viz. PdCu-IM, PdCu-Al, and PdCu-BM compounds. (f) Overall comparison of the FE of different products formed on different PdCu-surface. Products were analyzed after performing CA at -0.9 V vs. RHE at electrochemical CO_2RR condition.

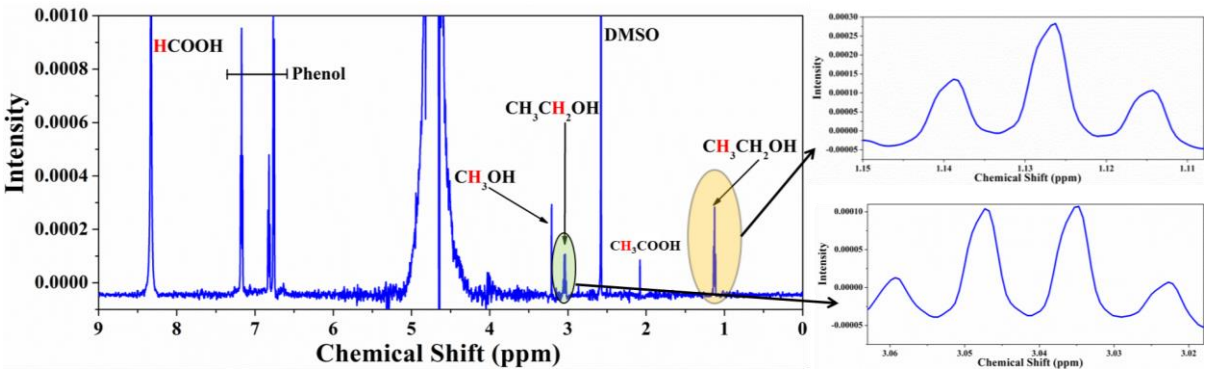

Figure 5.6. ^{1}H-NMR spectra of liquid products formed after eCO_2RR in CO_2-saturated 0.5 M $KHCO_3$ on PdCu catalyst. Zoomed ^{1}H-NMR spectra of ethanol.

The peak intensity in NMR depends on the number of protons and concentration of each product in the solution mixture, which has been used to calculate the Faradaic Efficiency of the CO_2 reduced products (**Figure 5.6**). In **Figure 5.5f**, the comparison of FE of different CO_2 reduced products for PdCu-IM, PdCu-Al and PdCu-BM compounds have been plotted while measuring chronoamperometry (CA) for 1 hour at -0.9 nV (vs. RHE). The best catalyst found for the production (FE of 22.44%) of ethanol is Pd-Cu bimetallic compound. PdCu-Al has also produced little amount of ethanol (FE 6.72%), whereas the PdCu-IM does not produce ethanol at all. PdCu-IM is more selective for the production of mono carbon products like methanol and formic acid. The data comparison suggests that the destruction of chemical bond between Pd and Cu favors the C-C coupling towards C2 product, ethanol.

5.6. Mechanistic Studies

5.6.1. In situ ATR-FTIR spectroscopy

In situ ATR-FTIR spectroscopy was carried out to detect the time and potential-dependent evolution of the key intermediates evolved during the course of eCO_2RR and to have an idea about the mechanistic pathway involved in the reaction, which was done in CO_2 saturated 0.5 M $KHCO_3$ solutions. The experimental set-up for the in situ ATR-FTIR experiment has been depicted in **Figure 1.10,** where a Si hemisphere crystal has been employed as the window. The potential-dependent IR study was performed during CO_2RR at -0.1V -0.3V, -0.5V, -0.7V, -0.9V, and -1.1V (vs. RHE), and the electrolyte (0.5M $KHCO_3$) has been saturated by continuous purging of the hugely pure CO_2 into the IR cell. **Figure 5.7a** shows the potential dependent evolution of different IR bands in the eCO_2RR condition. The negative-going signature band observed at 2338 cm^{-1} can be attributed to CO_2 consumption.[35] In the very first step of eCO_2RR is the formation of formate intermediates.[36] The key vibrational modes of COOH, like C=O stretch and O-H deformation of C-OH and are observed at 1570

cm^{-1} and 1299 cm^{-1}, respectively, for PdCu-BM catalyst (**Figure 5.7a**). The vibrational bands at 1398 cm^{-1} can corresponding to the IR absorption of the C-O bond of HCO_3^- and its intensity has been gradually increasing as the cathodic potential increases, proving higher formation of HCO_3^- species at the higher cathodic potential (-1.1V) than at the lower potential (-0.1V) (**Figure 5.7b**).[37]

Earlier studies showed that the band at around 1430 cm^{-1} represents the symmetric stretch of $*COO^-$ and C-O stretching of *COOH on the catalyst surface, which has been overlapped with the carbonate peak in the higher negative potential.[38, 39] Furthermore, the in situ ATR-FTIR study also probe stretching bands corresponding coupling intermediate for the C_2 product formation, i.e., OCCHO (1508.3 cm^{-1}) and its intensity gradually increased during chronoamperometry process (**Figure 5.7a-b**).[40]

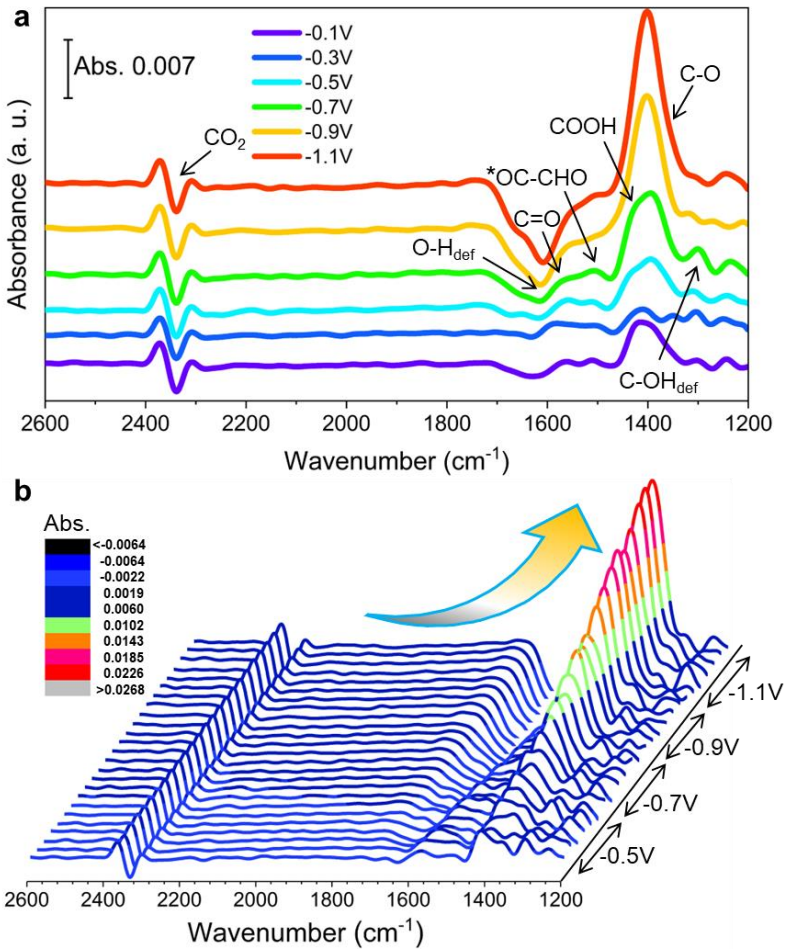

Figure 5.7. In situ ATR infrared (IR) spectra along with the binding mode of different intermediates adsorbed on catalyst surface during eCO_2RR performed on PdCu-BM. (a) Potential-dependent in situ IR spectra during the course of eCO_2RR. (b) Time-dependent evolution of in situ IR spectra taken on PdCu-BM catalyst in eCO_2RR condition on PdCu-catalyst during chronoamperometric study at -0.5V, -0.7V, -0.9V and -1.1V (vs. RHE).

5.6.2. In situ Raman Study

In situ Raman spectroscopic study has been carried out to probe the dynamic nature of the surface adsorbed intermediate during eCO_2RR. The schematic representation of the Raman set up has been demonstrated in **Figure 1.12**. The first step of the eCO_2RR is accompanied by the reduction of monodentate carbonate at ~920 cm^{-1} observed as the CO_2 reduction begins.[41] The broad band at around 1370-1400 cm^{-1} can be assigned to the bidentate carbonate species adsorbed on the catalyst surface. The potential-dependent evolution of the different metal-intermediate species and their Raman bands have been plotted in **Figure 5.8a**. The obvious presence of the metal-CO bonds has been found in the region of 1950-2000 cm^{-1}.[42] The real-time analysis of the different bands is depicted in **Figure 5.8b**. Apart from in situ IR study, operando Raman spectroscopic analyses also demonstrated the presence of key intermediates formed on the PdCu surface during the reaction.[43, 44]

5.7. Spectroscopic investigation of the active site

5.7.1. XPS study

XPS has been performed to understand the surface oxidation state of each element on PdCu-catalysts. The high-resolution XPS of Pd core level (3d) indicates the existence of metallic Pd peak at 335.82 eV for $3d_{5/2}$ in PdCu-IM along with the very little amount of surface oxides (**Figure 5.9**).[34, 45] The binding energy of Pd $3d_{5/2}$ for PdCu-Al has been found to be slightly higher (336.02 eV) than that of PdCu-IM. In the bimetallic catalyst (PdCu-BM), Pd $3d_{5/2}$ becomes lower in energy (335.92 eV). The core level Cu 2p XPS spectra suggest that both metallic (at 932.11 eV) and very less intense oxide (Cu^{2+}) (at 933.54 eV) peak of Cu $3p_{3/2}$ present in the PdCu-IM catalyst. The binding energy of Cu $3p_{3/2}$ has been obtained to be in PdCu-Al (at 932.2 eV) and PdCu-BM (at 932.66 eV).

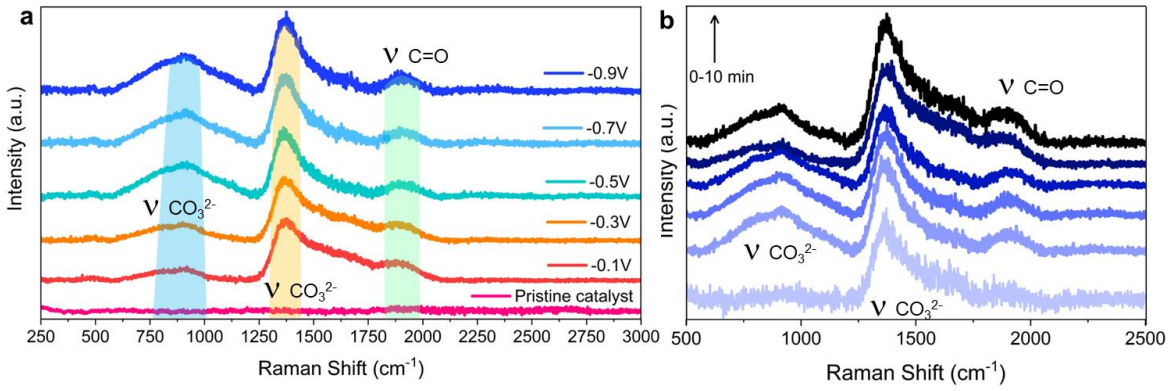

Figure 5.8. In situ Raman study on Pd-Cu catalyst in CO_2 purged $KHCO_3$ solution. (a) Evolution of different Raman bands during eCO_2RR at different potential. (b) Time-dependent in situ Raman spectra of different CO_2-reduced intermediate bound on catalyst surface.

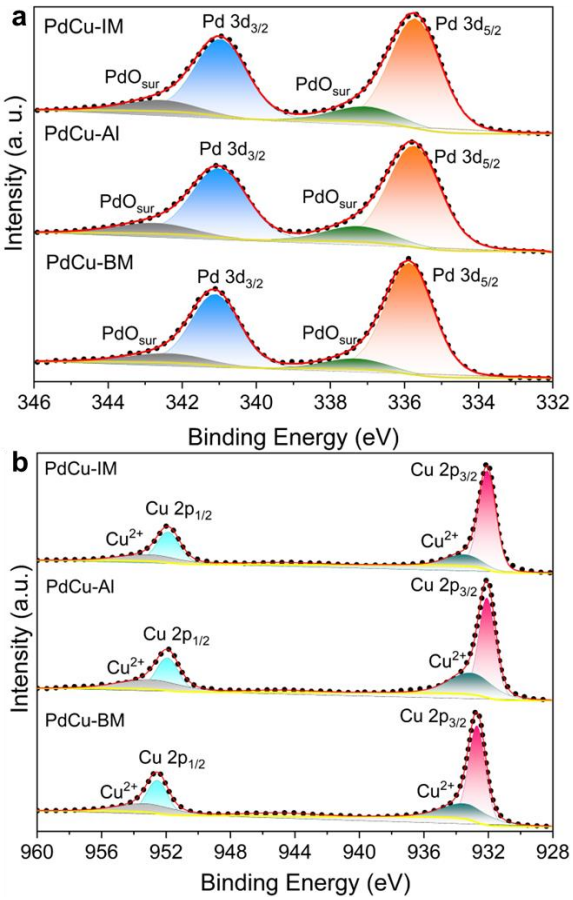

Figure 5.9. High-resolution XPS of (c) Pd 3d and (d) Cu 2p for all the PdCu-based catalysts.

From the XPS analyses, it can be concluded that the Cu site has been orderly coordinated with that of the Pd site in PdCu-IM, which leads to the lower oxidation state in PdCu-IM. On the other hand, in alloy and bimetallic, Cu is more exposed to the surface to be oxidized and found to be in a higher oxidation state.

5.7.2. Ex situ and in situ X-ray absorption spectroscopy

XAS is a very powerful tool to get an idea about the chemical state and local structural information for solid-state compounds.[46] The normalized XANES spectra of the Pd *K*-edge for all the PdCu-based catalysts indicate that the absorption edge corresponding to the 1s→4p dipole transition of the Pd K edge is very much close to that of metallic Pd (**Figure 5.10a**). The Fourier transformed (FT) R-space data of the Pd K-edge for all PdCu-catalysts have been plotted in **Figure 5.10b,** and their wavelet transform have been plotted in **Figure 5.10c, 5.10d, 5.10e,** and **Figure 5.10f** for Pd foil, PdCu-IM, PdCu-Al, PdCu-BM respectively. The FT-transform and wavelet transform XAFS data prove the clear presence of the Pd-Cu bond in both PdCu-IM and PdCu-Al at around 2.1Å.[47] On the other hand, in the PdCu-BM catalyst, both Pd-Cu and Pd-Pd bonds have been observed in the R-space data as well-as wavelet transform plots (**Figure 5.10f**).

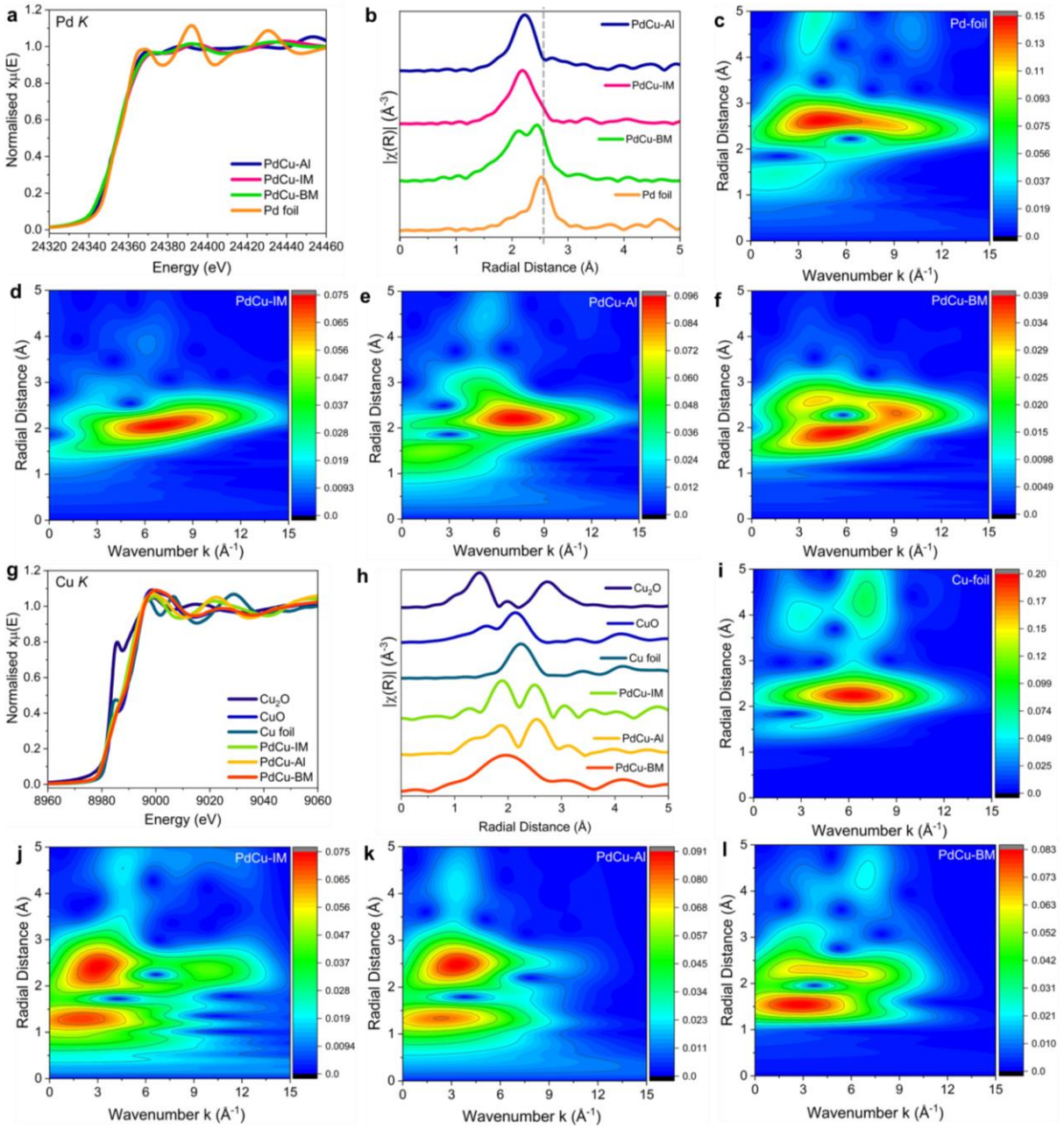

Figure 5.10. (a) Comparison of (a) normalized XANES spectra, (b) Fourier transformed (FT) R-space of Pd *K*-edge XAFS for PdCu-IM, PdCu-Al, PdCu-BM with the XANES spectra of standard Pd foil. Wavelet transform-XAFS of the Pd *K*-edge for (c) standard Pd foil, (d) PdCu-IM, (e) PdCu-Al, and (f) PdCu-BM. Comparison of (g) normalized XANES spectra and (h) Fourier transformed (FT) R-space of Cu *K*-edge of all the PdCu-based catalysts with the respective reference samples. Wavelet transform-XAFS of the Cu *K*-edge for (i) standard Pd foil, (j) PdCu-IM, (k) PdCu-Al, and (l) PdCu-BM.

The XANES spectra of Cu-edge show slightly higher absorption photon energy than that of elemental Cu foil, suggesting a relatively higher oxidation state in PdCu-catalysts. (**Figure 5.10g**). The R-space data of Cu edge XAFS in **Figure 5.10h** and from wavelet

transform plots in **Figure 5.10i-l** manifest the presence of Cu- O at a radial distance of 1.4-1.5 Å along with the Pd-Cu bond in PdCu-based catalysts.[19]

To visualize the change of local structure and oxidation state at different potential in the in the CO_2 reduction conditions, operando XAS has been performed.[48] The operando XANES spectra of Pd *K*-edge at different potential indicates that the oxidation state of Pd does not affect much upon applying negative potential (**Figure 5.11**). On the contrary, the potential depdendent in situ spectra of Cu *K*-edge XANES shows that the position of the absorption energy decreases to lower photon energy and the white line intensity also decreases as the negative potential increases in all the Pd-Cu-based catalyst (**Figure 5.12a-c**). It is important to mention that the surface copper oxide species present in the catalysts have been reduced in the reducing atmosphere under eCO_2RR condition. As a consequence, the XANES septra of Cu K edge and the absorption photon energy gradually shifted more towards the metallic state of Cu. To understand the local structure of Cu during CO_2RR condition, the potential dependent FT-EXAFS of Cu K-edge have been analysed for all the catalysts. The bond corresponding to Pd-Cu at 2.1Å is stable under reducing atmosphere for both PdCu-IM and PdCu-Al (**Figure 5.12a-b**) catalysts in the operational condition in higher reduction potential during CO_2RR.[49]

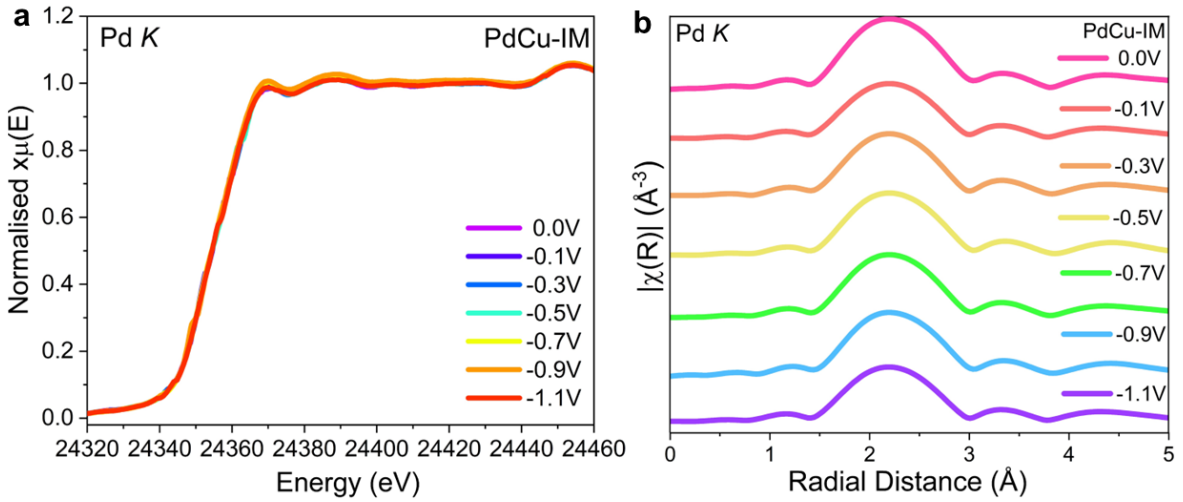

Figure 5.11. (a) Potential dependent in situ XAS in eCO_2RR conditions. (a) Comparison of normalized XANES spectra of Pd *K*-edge during in-situ XAS for PdCu-IM at different applied potential at eCO_2RR condition in 0.5M $KHCO_3$. (b) Fourier transformed R-space data of Cu *K*-edge of (d) PdCu-IM catalyst at different potential during in-situ XAS at different applied potential at eCO_2RR condition in 0.5M $KHCO_3$.

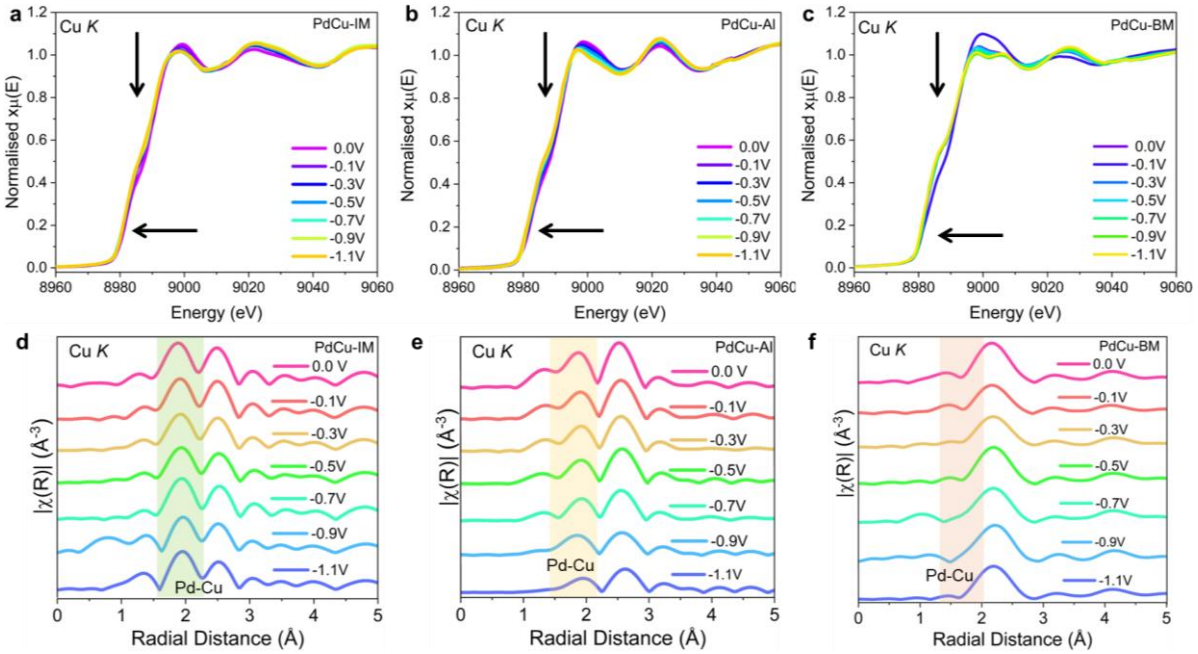

Figure 5.12. Potential dependent in situ XAS in eCO$_2$RR conditions. Comparison of normalized XANES spectra of Cu K-edge during in-situ XAS for (a) PdCu-IM, (b) PdCu-Al, and (c) PdCu-BM at the different applied potential at eCO$_2$RR condition in 0.5M KHCO$_3$. Fourier transformed R-space data of Cu K-edge of (d) PdCu-IM, (e) PdCu-Al, and (f) PdCu-BM catalyst at different potentials during in-situ XAS at different applied potentials at eCO$_2$RR condition in 0.5M KHCO$_3$.

It is noteworthy to mention that the presence of Cu-O bond is found to be higher in case of PdCu-Al than that of PdCu-BM. Still, the multicarbon formation is higher in case of PdCu-BM. This clearly signifies that the optimum presence of Pd-Cu interface is important for the coupling process in case of bimetallic catalyst, which can also trigger the formation of further multicarbon products like ethanol in this case.

5.8. Computational understanding of the Reaction Mechanism

To gain insights into the reaction mechanism, we performed density functional theory (DFT) calculations for the CO_2 reduction to HCOOH, CH_3OH, CO, and CH_3COH on the three different structures, viz. Intermetallic PdCu (111), Alloy PdCu (111), and Bimetallic PdCu(111). The current consensus regarding the CO_2 reduction on copper and copper-based catalyst surfaces is that first, it is reduced to form adsorbed CO via COOH intermediate, and our DFT calculation shows that CO_2 could be easily converted to adsorbed CO over all the structures considered. It also showed that the COOH intermediate could also be converted into HCOOH with an applied potential of less than 0.3 V on all the catalyst surfaces, which is consistent with our experimental results.

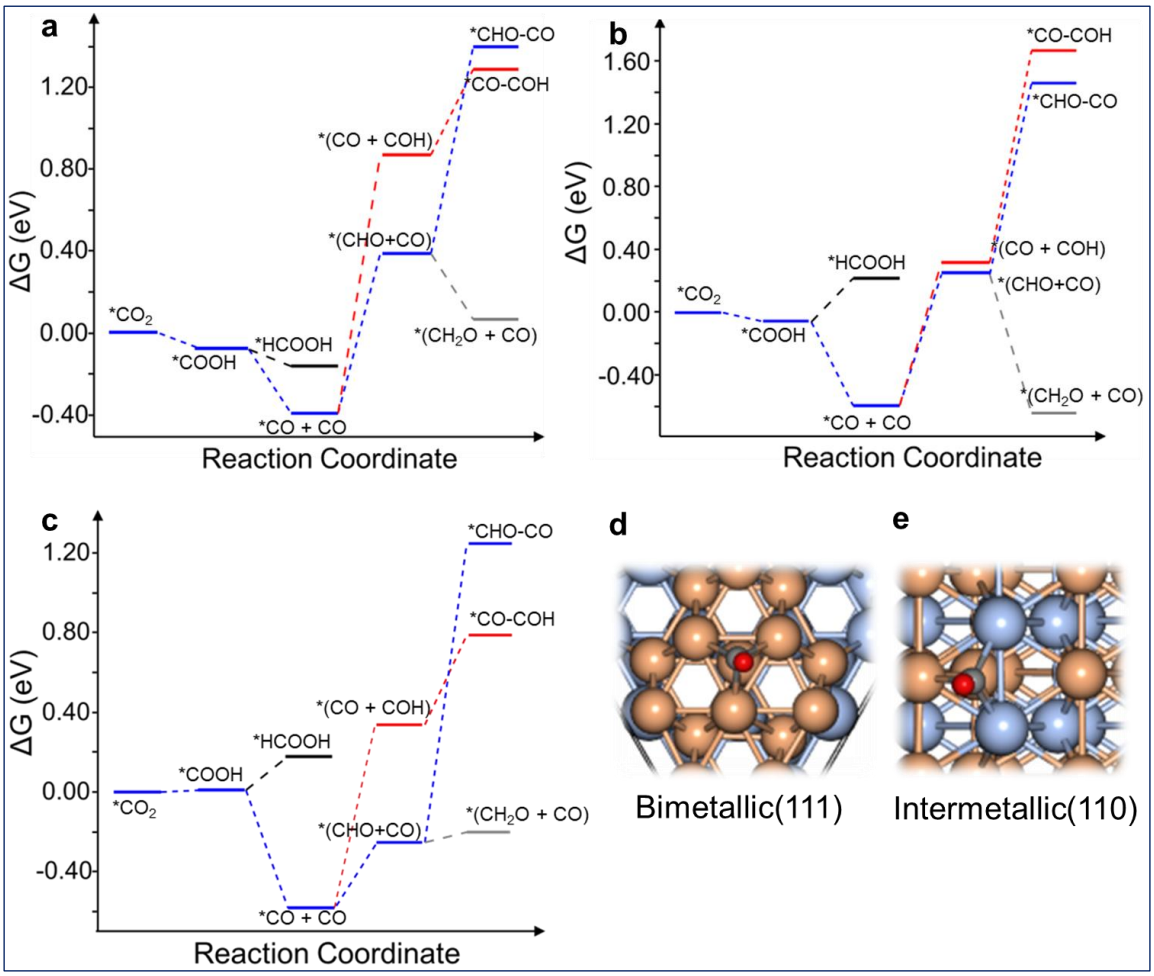

Figure 5.13. Free Energy profile for CO_2 reduction over (a) PdCu-IM (111) (b) PdCu-IM (110) (c) PdCu-Al (111). (d) and (e) shows the CO adsorption configuration on PdCu-BM and PdCu-IM surfaces respectively.

The pathway for the formation of ethanol and methanol was next investigated. After the reduction of CO_2 to CO, we first investigated the adsorption configuration of CO on the metal surface. It is noteworthy that, in the case of PdCu-Al and PdCu-IM, the CO is more prone to bind with Pd atoms. This is because the d-band center of Pd is nearer to the Fermi level than that of Cu, which causes easy charge transfer from Pd to the CO (**Figure 5.14a-c**). Due to the same reason, the CO binding energy with the surface is more in the case of intermetallic and alloy as compared to bimetallic. The C-C coupling is the next crucial step for the formation of C2 products like ethanol in this case. In the literature, OC-COH and OC-CHO are the two most common proposed intermediates formed after the coupling step. Here we also investigated these two possible pathways for the C-C coupling. The ΔG value for the formation of *CHO intermediate is lesser than *COH. Therefore *CHO can be considered as the major species on all the surfaces considered.

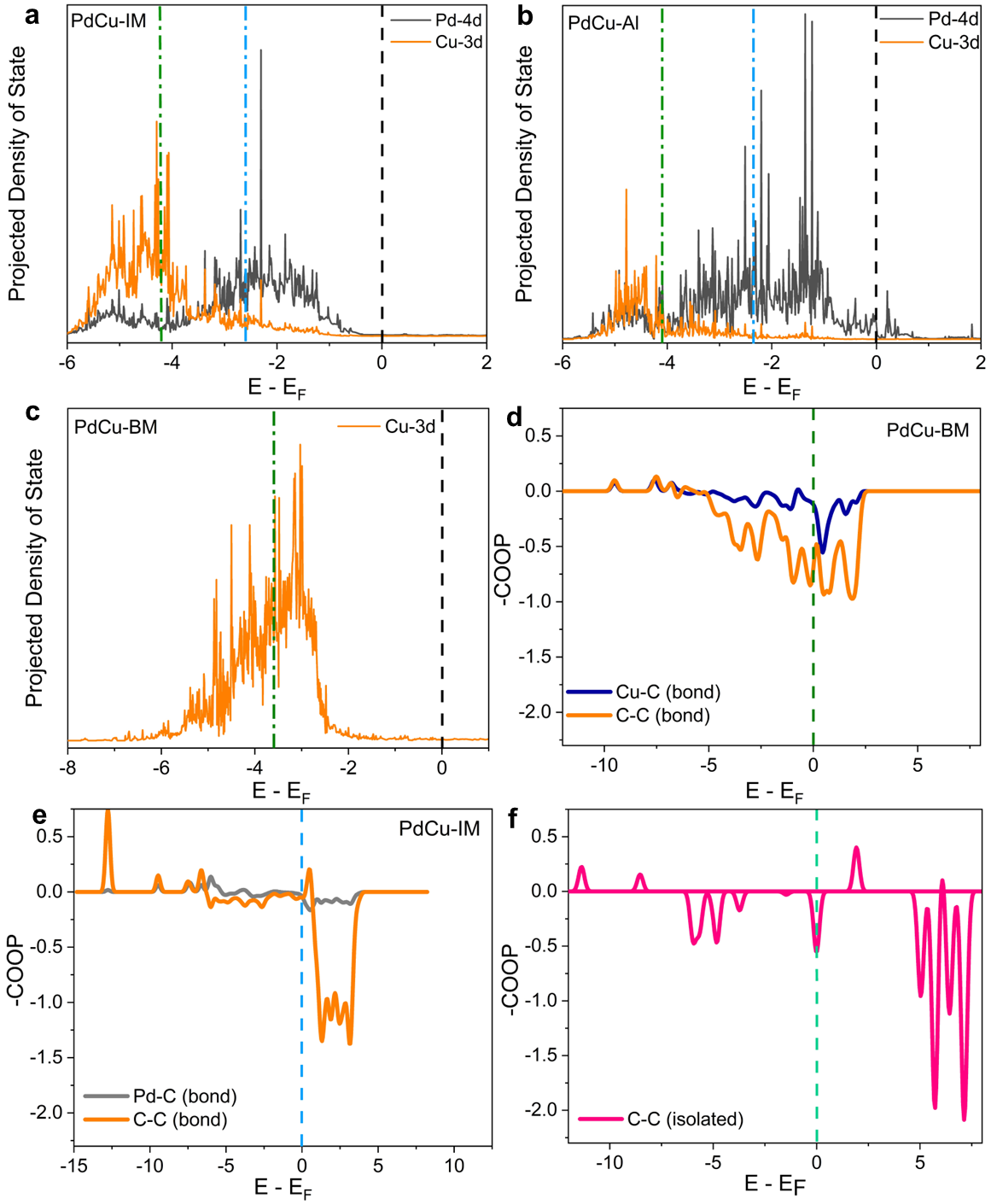

Figure 5.14. Projected density of states (PDOS) of Pd 4d, and Cu 3d orbitals for (a) PdCu-IM, (b) PdCu-Al and (c) PdCu-BM. The crystal orbital overlap populations of the C-C bond of *OC-CHO species adsorbed on (d) PdCu-BM, (e) PdCu-IM and (f) for isolated C-C bond. (g) Free Energy profile for CO_2 reduction over PdCu-IM (111), PdCu-IM (110), PdCu-Al (111). PdCu-BM (111).

From the energy profile, it can be seen that the C-C coupling on all the catalyst surfaces is endothermic. The ΔG value for the C–C coupling was found to be 0.34 eV uphill on the

bimetallic surface via the OC-CHO pathway as compared to the 1.32 eV on the intermetallic surface. To understand this difference in ΔG value, we analyze the COOP (Crystal orbital overlap population)45 curve of the C-C and M-C (M=Pd and Cu) bond shown in **Figure 5.14d-f**. The curve shows the change in the position of the antibonding orbital of the intermediate w.r.t the Fermi level. Literature reports suggested that the hollow site of the metal surface in which the C atom interacts with three metal atoms is considered most favorable for C-O adsorption (**Figure 5.13**).

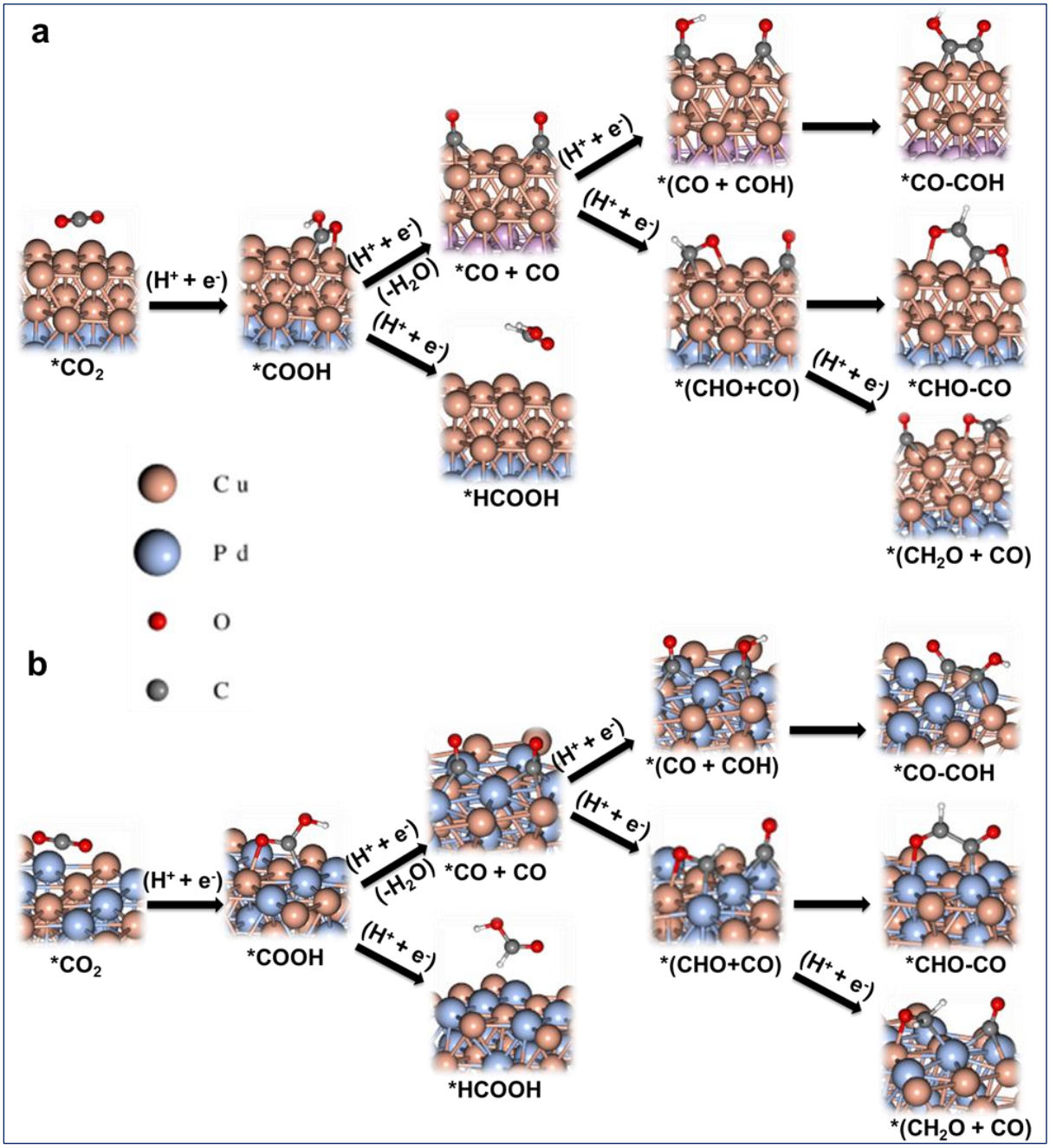

Figure 5.15. Various mechanistic pathways studied for CO_2 reduction on (a) PdCu-BM and (b) PdCu-IM surfaces.

In the case of PdCu-IM, although the antibonding bonding orbital shifted towards the Fermi level as compared to the isolated hypothetical OHC-CHO intermediate, it is still unoccupied. In the case of bimetallic, the shift of antibonding orbital is much more than the intermetallic, and it's partially occupied, which suggests that the bimetallic surface effectively captures the coupled intermediate as compared to intermetallic. This was also confirmed by Bader charge analysis,[50], which shows a charge transfer of -0.76 e from the bimetallic surface to the coupled intermediate while only –0.06 e transfer from the intermetallic surface. Another important factor that governs the C-C coupling is the binding energy of the coupling intermediates with the surface. In the case of PdCu-Al and PdCu-IM, the intermediates bind strongly with the surface, so there is higher reaction-free energy for coupling as compared to the bimetallic surface. Though the formation*CHO intermediate is more energetically favorable than *COH on the Alloy surface, the energy profile (**Figure 5.15**) suggests that for *OC-COH coupling path is more feasible for the coupled product.

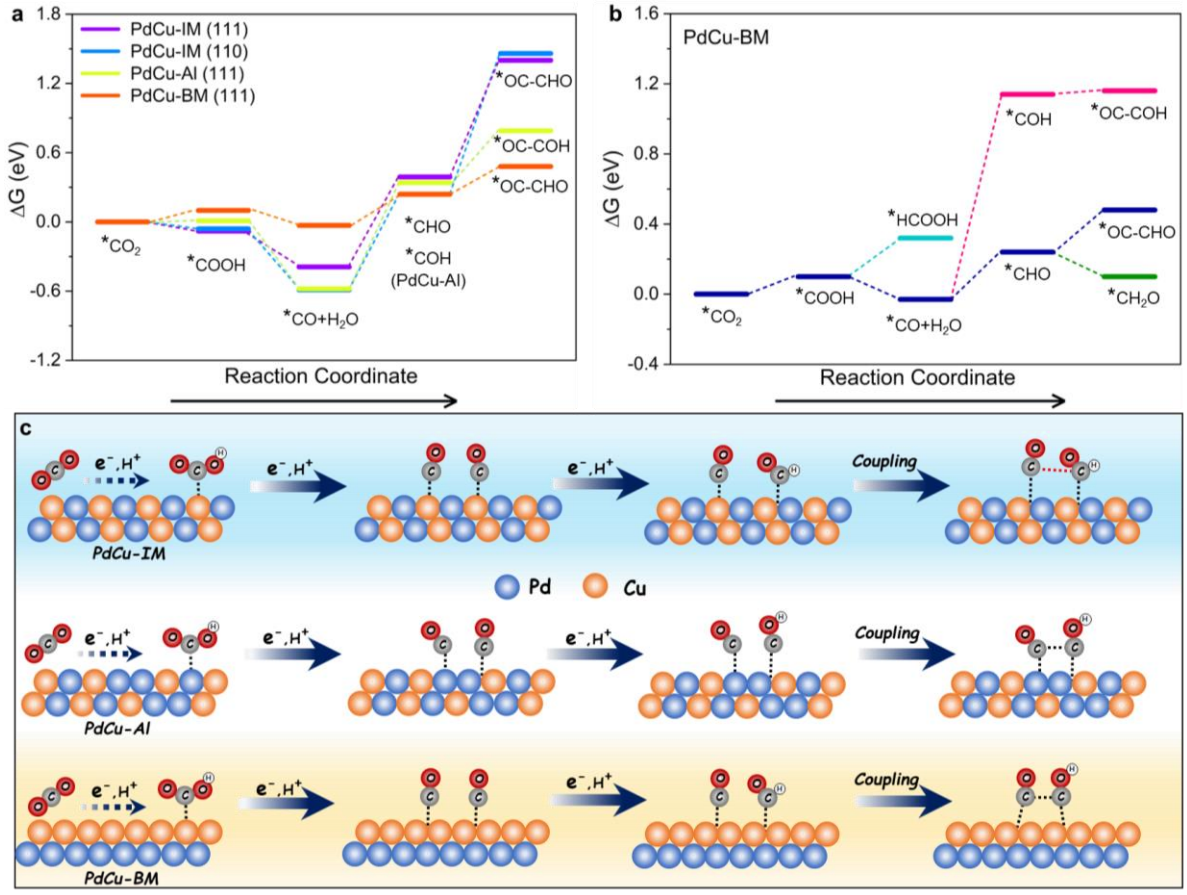

Figure 5.16. (a) Free Energy profile for CO_2 reduction over PdCu-IM (111), PdCu-IM (110), PdCu-Al (111). PdCu-BM (111). (b) The comparison of the Free Energy profile of different possible pathways for CO_2 reduction over PdCu-BM surface. (c) Mechanistic illustration of the coupling process during eCO_2RR on different PdCu-based catalyst surfaces.

Considering all the plausible pathway, the PdCu-BM surface facilitates the coupling process by lowering the activation energy of the *OC-CHO intermediate, which is further converted to a high-energy product like ethanol (**Figure 5.16a**). The coupling process is energetically less favorable in PdCu-Al and PdCu-IM surfaces. In the PdCu-BM surface, the formation of *OC-COH intermediate is not energetically favorable (**Figure 5.16b)**. Once the coupling is done, the next hydrogenation steps are generally exothermic in nature shown in a number of previous reports.[10, 51] The mechanistic pathways for CO_2RR on different PdCu surface, derived from the DFT study as well as in situ FT-IR and Raman spectroscopic analyses, is schematically represented in **Figure 5.16c**.

5.9. High current density using flow cell with GDE configuration

Finally, to increase the CO_2 mass transport and to obtain industrial-level current density, the CO_2RR performance of Pd-Cu-based catalysts has been evaluated in a flow cell with a gas diffusion electrode (GDE) configuration. **Figure 5.17** demonstrated the diffusion of CO_2 gas through the hydrophobic channel of GDE, which can properly maintain the gas-catalyst-electrolyte interface and could be able to perform CO_2 reduction efficiently.[52] In the flow cell, the current density has increased multi-fold than that obtained in the H-cell, as evident from LSV (**Figure 5.18a**) and chronoamperomtric plot (**Figure 5.18b**).[53] In the flow cell configuration, the potential dependent formation of major mono carbon products like CO and formate have been plotted in **Figures 5.19a** and **5.19b**.

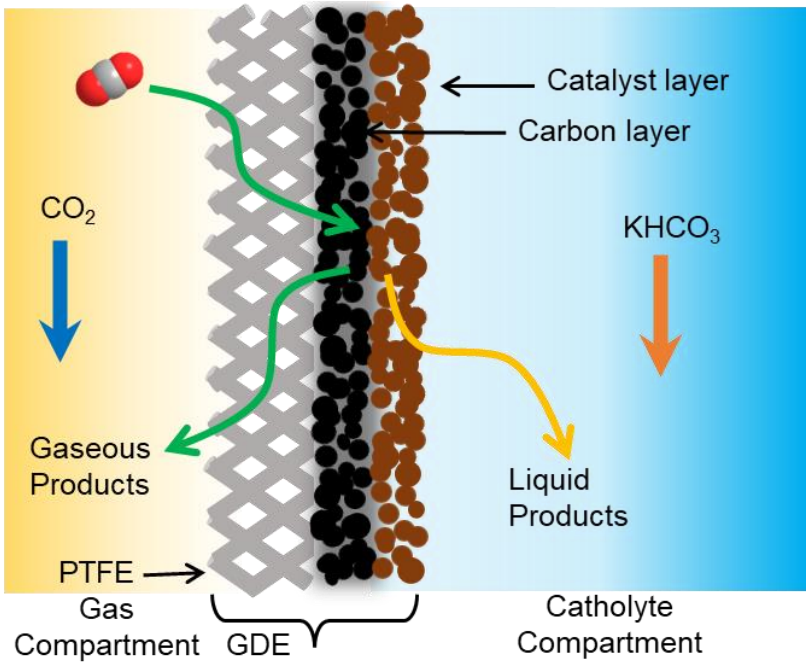

Figure 5.17. Schematic illustration of the CO_2-GDE-electrolyte interface in the flow cell configuration.

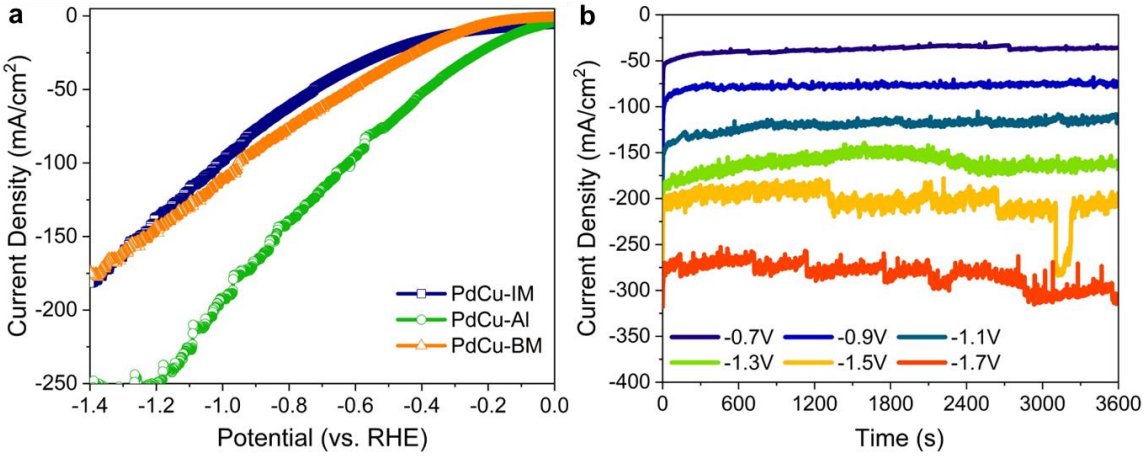

Figure 5.18. (a) Linear Sweep Voltammogram of different types of PdCu-based catalyst at eCO_2RR condition in flow cell configuration in 1M $KHCO_3$. (b) Industrial level current density obtained in the chronoamperometric study in flow cell on Pdu-BM catalyst.

It is very clear from those Figures that PdCu-IM facilitates the formation of C1 products. On the other hand, the distribution of ethylene and ethanol in **Figures 5.19c** and **5.19d** respectively, denotes that PdCu-BM promotes the multicarbon product formation especially in the higher applied potential.

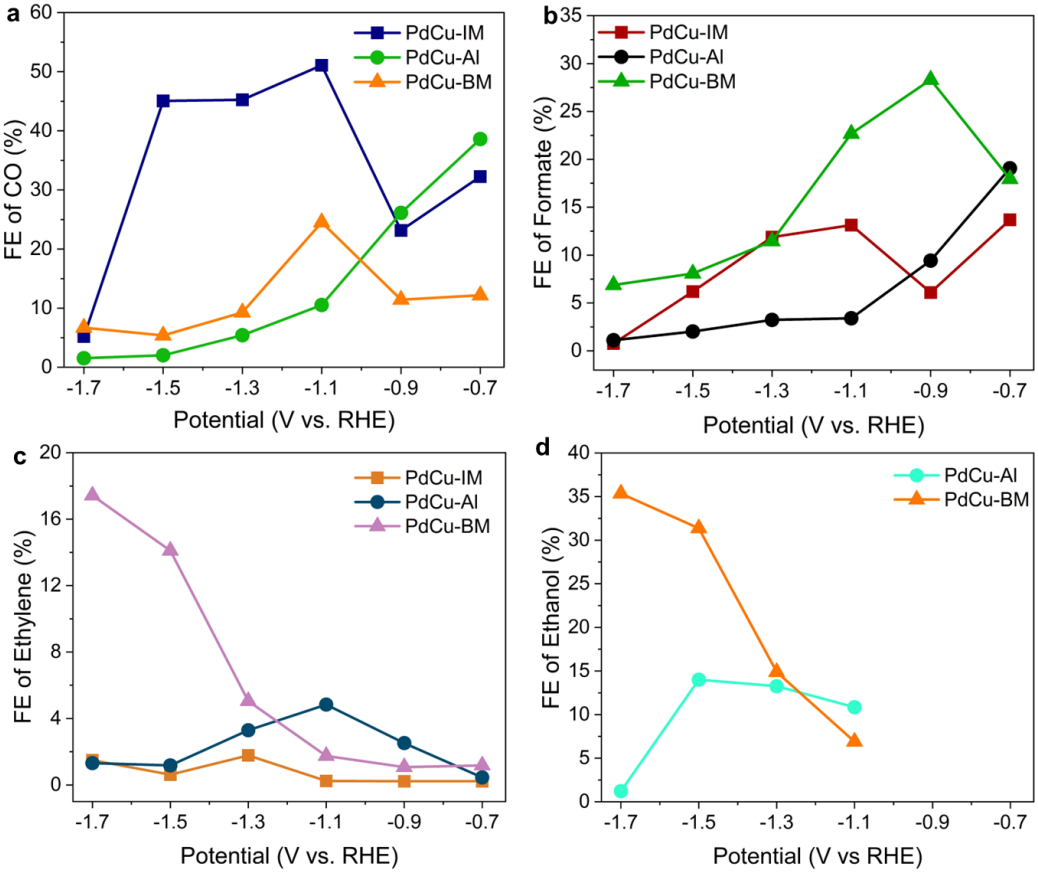

Figure 5.19. Faradaic efficiencies for (a) CO, (b) formate, (c) ethylene, and (d) ethanol for different kinds Pd-Cu catalysts.

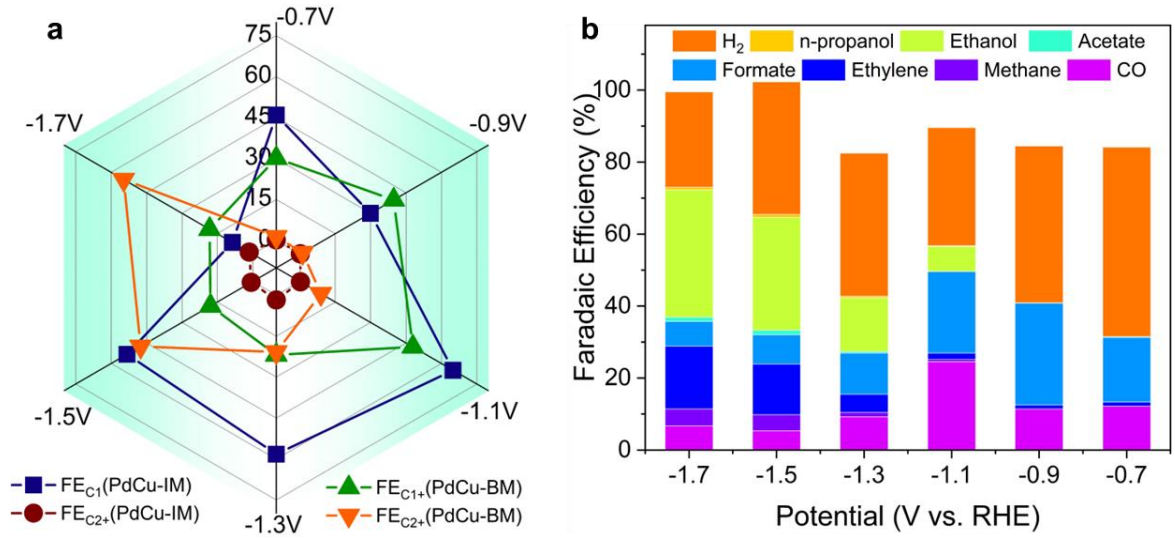

Figure 5.20. (a) Comparison of C_1 and C_{2+} selectivity of PdCu-IM and PdCu-BM at different potential. (b) Potential dependent distribution of all CO_2-reduced products on PdCu-BM catalyst in flow cell configuration.

Figure 5.20a summarises the overall product selectivity of C_1 and C_{2+} formation on PdCu-IM and PdCu-BM. It is fould that PdCu-IM shows maximum C1 selectivity of 64.95%. On the contrary, PdCu-BM displays maximum C_{2+} product selctivity of 54.69%. The FE of all the products formed during CO_2RR have been plotted in **Figure 5.20b**.

5.10. Conclusion

In conclusion, we have rationalized the bonding and structural ordering as the key parameters to tune the selective conversion of CO_2 to either C1 or C2 products on Pd-Cu based compounds. Different kinds of Pd-Cu catalysts like intermetallic, alloy, and bimetallic are generated to understand the components playing the role in selective conversion of CO_2 and reaction mechanism. The sample that consists of neighboring Cu atoms (PdCu-BM) favours the production of multicarbon products i.e. ethanol, while the sample that features the alternating Pd-Cu arrangement favors the production of monocarbon product like CO, formate and methanol. With the help of various in situ spectroscopic study like in situ ATR-FTIR, Raman spectroscopy, in situ XAFS, along with computational study, we have unraveled the reaction mechanism as well as the potential dependent active site for the PdCu-catalyst. The major finding is that the product switching from C1 to C2 selectivity depending on the careful selection of the catalyst based on similar metals. In this case we have obtained higher current density (>100 mA/cm^2) by the utilization of flow cell which is very important from industrial perspective. This concept can provide a new insight for the design of even better Pd-Cu-based

catalysts for the conversion of CO_2 to desired products. In place of Pd, other transition metals can also be giving a new structure-product selectivity trend like this work.

5.11. References

1. Nitopi, S.; Bertheussen, E.; Scott, S. B.; Liu, X.; Engstfeld, A. K.; Horch, S.; Seger, B.; Stephens, I. E. L.; Chan, K.; Hahn, C.; Nørskov, J. K.; Jaramillo, T. F.; Chorkendorff, I., Progress and Perspectives of Electrochemical CO_2 Reduction on Copper in Aqueous Electrolyte. *Chem. Rev.* **2019,** *119*, 7610-7672.
2. Wang, Y.; Liu, J.; Zheng, G., Designing Copper-Based Catalysts for Efficient Carbon Dioxide Electroreduction. *Adv. Mater.* **2021,** *33*, 2005798.
3. Reske, R.; Mistry, H.; Behafarid, F.; Roldan Cuenya, B.; Strasser, P., Particle Size Effects in the Catalytic Electroreduction of CO_2 on Cu Nanoparticles. *J. Am. Chem. Soc.* **2014,** *136*, 6978-6986.
4. Roberts, F. S.; Kuhl, K. P.; Nilsson, A., High Selectivity for Ethylene from Carbon Dioxide Reduction over Copper Nanocube Electrocatalysts. *Angew. Chem. Int. Ed.* **2015,** *54*, 5179-5182.
5. De Gregorio, G. L.; Burdyny, T.; Loiudice, A.; Iyengar, P.; Smith, W. A.; Buonsanti, R., Facet-Dependent Selectivity of Cu Catalysts in Electrochemical CO_2 Reduction at Commercially Viable Current Densities. *ACS Catal.* **2020,** *10*, 4854-4862.
6. Mariano, R. G.; McKelvey, K.; White, H. S.; Kanan, M. W., Selective Increase in CO_2 Electroreduction Activity at Grain-Boundary Surface Terminations. *Science* **2017,** *358*, 1187.
7. Chen, Z.; Wang, T.; Liu, B.; Cheng, D.; Hu, C.; Zhang, G.; Zhu, W.; Wang, H.; Zhao, Z.-J.; Gong, J., Grain-Boundary-Rich Copper for Efficient Solar-Driven Electrochemical CO_2 Reduction to Ethylene and Ethanol. *J. Am. Chem. Soc.* **2020,** *142*, 6878-6883.
8. Chou, T.-C.; Chang, C.-C.; Yu, H.-L.; Yu, W.-Y.; Dong, C.-L.; Velasco-Vélez, J.-J.; Chuang, C.-H.; Chen, L.-C.; Lee, J.-F.; Chen, J.-M.; Wu, H.-L., Controlling the Oxidation State of the Cu Electrode and Reaction Intermediates for Electrochemical CO_2 Reduction to Ethylene. *J. Am. Chem. Soc.* **2020,** *142*, 2857-2867.
9. Xiao, H.; Goddard, W. A.; Cheng, T.; Liu, Y., Cu Metal Embedded in Oxidized Matrix Catalyst to Promote CO_2 Activation and CO Dimerization for Electrochemical Reduction of CO_2. *Proc. Natl. Acad. Sci.* **2017,** *114*, 6685.

10. Ma, W.; Xie, S.; Liu, T.; Fan, Q.; Ye, J.; Sun, F.; Jiang, Z.; Zhang, Q.; Cheng, J.; Wang, Y., Electrocatalytic Reduction of CO_2 to Ethylene and Ethanol through Hydrogen-Assisted C–C Coupling over Fluorine-Modified Copper. *Nat. Catal.* **2020,** *3*, 478-487.
11. Chen, X.; Henckel, D. A.; Nwabara, U. O.; Li, Y.; Frenkel, A. I.; Fister, T. T.; Kenis, P. J. A.; Gewirth, A. A., Controlling Speciation During CO_2 Reduction on Cu-Alloy Electrodes. *ACS Catal.* **2020,** *10*, 672-682.
12. Dickinson, H. L. A.; Symes, M. D., Recent Progress in CO_2 Reduction Using Bimetallic Electrodes Containing Copper. *Electrochem. commun.* **2022,** *135*, 107212.
13. Huang, J.; Mensi, M.; Oveisi, E.; Mantella, V.; Buonsanti, R., Structural Sensitivities in Bimetallic Catalysts for Electrochemical CO_2 Reduction Revealed by Ag–Cu Nanodimers. *J. Am. Chem. Soc.* **2019,** *141*, 2490-2499.
14. Kim, D.; Resasco, J.; Yu, Y.; Asiri, A. M.; Yang, P., Synergistic Geometric and Electronic Effects for Electrochemical Reduction of Carbon Dioxide Using Gold–Copper Bimetallic Nanoparticles. *Nat. Commun* **2014,** *5*, 4948.
15. Ren, D.; Ang, B. S.-H.; Yeo, B. S., Tuning the Selectivity of Carbon Dioxide Electroreduction toward Ethanol on Oxide-Derived Cu_xZn Catalysts. *ACS Catal.* **2016,** *6*, 8239-8247.
16. Zhang, S.; Kang, P.; Bakir, M.; Lapides Alexander, M.; Dares Christopher, J.; Meyer Thomas, J., Polymer-Supported CuPd Nanoalloy as a Synergistic Catalyst for Electrocatalytic Reduction of Carbon Dioxide to Methane. *Proc. Natl. Acad. Sci.* **2015,** *112*, 15809-15814.
17. Gao, D.; Zhou, H.; Cai, F.; Wang, J.; Wang, G.; Bao, X., Pd-Containing Nanostructures for Electrochemical CO_2 Reduction Reaction. *ACS Catal.* **2018,** *8*, 1510-1519.
18. Nørskov, J. K.; Bligaard, T.; Rossmeisl, J.; Christensen, C. H., Towards the Computational Design of Solid Catalysts. *Nat. Chem.* **2009,** *1*, 37-46.
19. Ji, Y.; Chen, Z.; Wei, R.; Yang, C.; Wang, Y.; Xu, J.; Zhang, H.; Guan, A.; Chen, J.; Sham, T.-K.; Luo, J.; Yang, Y.; Xu, X.; Zheng, G., Selective CO-to-acetate Electroreduction via Intermediate Adsorption Tuning on Ordered Cu–Pd Sites. *Nat. Catal.* **2022,** *5*, 251-258.
20. Jana, R.; Bhim, A.; Bothra, P.; Pati, S. K.; Peter, S. C., Electrochemical Dealloying of $PdCu_3$ Nanoparticles to Achieve Pt-like Activity for the Hydrogen Evolution Reaction. *ChemSusChem* **2016,** *9*, 2922-2927.

21. Yin, Z.; Gao, D.; Yao, S.; Zhao, B.; Cai, F.; Lin, L.; Tang, P.; Zhai, P.; Wang, G.; Ma, D.; Bao, X., Highly Selective Palladium-Copper Bimetallic Electrocatalysts for the Electrochemical Reduction of CO_2 to CO. *Nano Energy* **2016,** *27*, 35-43.
22. Ma, S.; Sadakiyo, M.; Heima, M.; Luo, R.; Haasch, R. T.; Gold, J. I.; Yamauchi, M.; Kenis, P. J. A., Electroreduction of Carbon Dioxide to Hydrocarbons Using Bimetallic Cu–Pd Catalysts with Different Mixing Patterns. *J. Am. Chem. Soc.* **2017,** *139*, 47-50.
23. Giannozzi, P.; Baroni, S.; Bonini, N.; Calandra, M.; Car, R.; Cavazzoni, C.; Ceresoli, D.; Chiarotti, G. L.; Cococcioni, M.; Dabo, I.; Dal Corso, A.; de Gironcoli, S.; Fabris, S.; Fratesi, G.; Gebauer, R.; Gerstmann, U.; Gougoussis, C.; Kokalj, A.; Lazzeri, M.; Martin-Samos, L.; Marzari, N.; Mauri, F.; Mazzarello, R.; Paolini, S.; Pasquarello, A.; Paulatto, L.; Sbraccia, C.; Scandolo, S.; Sclauzero, G.; Seitsonen, A. P.; Smogunov, A.; Umari, P.; Wentzcovitch, R. M., Quantum Espresso: a Modular and Open-Source Software Project for Quantum Simulations of Materials. *J. Phys.: Condens. Matter* **2009,** *21*, 395502.
24. Perdew, J. P.; Burke, K.; Ernzerhof, M., Generalized Gradient Approximation Made Simple. *Phys. Rev. Lett* **1996,** *77*, 3865-3868.
25. Vanderbilt, D., Soft Self-Consistent Pseudopotentials in a Generalized Eigenvalue Formalism. *Phys. Rev. B* **1990,** *41*, 7892-7895.
26. Grimme, S.; Antony, J.; Ehrlich, S.; Krieg, H., A Consistent and Accurate ab Initio Parametrization of Density Functional Dispersion Correction (DFT-D) for the 94 Elements H-Pu. *J. Chem. Phys.* **2010,** *132*, 154104.
27. Monkhorst, H. J.; Pack, J. D., Special Points for Brillouin-Zone Integrations. *Phys. Rev. B* **1976,** *13*, 5188-5192.
28. Anisimov, V. I.; Aryasetiawan, F.; Lichtenstein, A. I., First-Principles Calculations of the Electronic Structure and Spectra of Strongly Correlated Systems: The LDA+ U Method. *J. Phys.: Condens. Matter* **1997,** *9*, 767-808.
29. Ting, L. R. L.; Piqué, O.; Lim, S. Y.; Tanhaei, M.; Calle-Vallejo, F.; Yeo, B. S., Enhancing CO_2 Electroreduction to Ethanol on Copper–Silver Composites by Opening an Alternative Catalytic Pathway. *ACS Catal.* **2020,** *10*, 4059-4069.
30. Peterson, A. A.; Abild-Pedersen, F.; Studt, F.; Rossmeisl, J.; Nørskov, J. K., How Copper Catalyzes the Electroreduction of Carbon Dioxide into Hydrocarbon Fuels. *Energy Environ. Sci.* **2010,** *3*, 1311-1315.

31. Wang, D.; Xin, H. L.; Hovden, R.; Wang, H.; Yu, Y.; Muller, D. A.; DiSalvo, F. J.; Abruña, H. D., Structurally Ordered Intermetallic Platinum–Cobalt Core–Shell Nanoparticles with Enhanced Activity and Stability as Oxygen Reduction Electrocatalysts. *Nat. Mater.* **2013,** *12*, 81-87.
32. Ashly, P. C.; Sarkar, S.; Sarma, S. C.; Kaur, K.; Gautam, U. K.; Peter, S. C., Compressive Strain Induced by Multiple Phase Distribution and Atomic Ordering in PdCu Nanoparticles to Enhanced Ethanol Oxidation Reaction Performance. *J. Power Sources* **2021,** *506*, 230168.
33. Marakatti, V. S.; Sarma, S. C.; Joseph, B.; Banerjee, D.; Peter, S. C., Synthetically Tuned Atomic Ordering in PdCu Nanoparticles with Enhanced Catalytic Activity toward Solvent-Free Benzylamine Oxidation. *ACS Appl. Mater. Inter.* **2017,** *9*, 3602-3615.
34. Bagchi, D.; Sarkar, S.; Singh, A. K.; Vinod, C. P.; Peter, S. C., Potential- and Time-Dependent Dynamic Nature of an Oxide-Derived PdIn Nanocatalyst during Electrochemical CO_2 Reduction. *ACS Nano* **2022,** *16*, 6185-6196.
35. Innocent, B.; Pasquier, D.; Ropital, F.; Hahn, F.; Léger, J. M.; Kokoh, K. B., FTIR Spectroscopy Study of the Reduction of Carbon Dioxide on Lead Electrode in Aqueous Medium. *Appl. Catal. B* **2010,** *94*, 219-224.
36. Yang, B.; Liu, K.; Li, H.; Liu, C.; Fu, J.; Li, H.; Huang, J. E.; Ou, P.; Alkayyali, T.; Cai, C.; Duan, Y.; Liu, H.; An, P.; Zhang, N.; Li, W.; Qiu, X.; Jia, C.; Hu, J.; Chai, L.; Lin, Z.; Gao, Y.; Miyauchi, M.; Cortés, E.; Maier, S. A.; Liu, M., Accelerating CO_2 Electroreduction to Multicarbon Products via Synergistic Electric–Thermal Field on Copper Nanoneedles. *J. Am. Chem. Soc.* **2022,** *144*, 3039-3049.
37. Zhu, S.; Jiang, B.; Cai, W.-B.; Shao, M., Direct Observation on Reaction Intermediates and the Role of Bicarbonate Anions in CO_2 Electrochemical Reduction Reaction on Cu Surfaces. *J. Am. Chem. Soc.* **2017,** *139*, 15664-15667.
38. Smith, E. L.; Porter, M. D., Structure of Monolayers of Short Chain n-Alkanoic Acids ($CH_3(CH_2)_nCOOH$, n = 0-9) Spontaneously Adsorbed from the Gas Phase at Silver as Probed by Infrared Reflection Spectroscopy. *J. Phys. Chem. A* **1993,** *97*, 8032-8038.
39. Fan, M.; Andrade, G. F. S.; Brolo, A. G., A Review on the Fabrication of Substrates for Surface Enhanced Raman Spectroscopy and Their Applications in Analytical Chemistry. *Anal. Chim. Acta* **2011,** *693*, 7-25.

40. Kim, Y.; Park, S.; Shin, S.-J.; Choi, W.; Min, B. K.; Kim, H.; Kim, W.; Hwang, Y. J., Time-Resolved Observation of C–C Coupling Intermediates on Cu Electrodes for Selective Electrochemical CO_2 Reduction. *Energy Environ. Sci.* **2020,** *13*, 4301-4311.
41. Moradzaman, M.; Mul, G., In Situ Raman Study of Potential-Dependent Surface Adsorbed Carbonate, CO, OH, and C Species on Cu Electrodes During Electrochemical Reduction of CO_2. *ChemElectroChem* **2021,** *8*, 1478-1485.
42. Shan, W.; Liu, R.; Zhao, H.; He, Z.; Lai, Y.; Li, S.; He, G.; Liu, J., In Situ Surface-Enhanced Raman Spectroscopic Evidence on the Origin of Selectivity in CO_2 Electrocatalytic Reduction. *ACS Nano* **2020,** *14*, 11363-11372.
43. Jiang, S.; Klingan, K.; Pasquini, C.; Dau, H., New Aspects of Operando Raman Spectroscopy Applied to Electrochemical CO_2 Reduction on Cu Foams. *J. Chem. Phys.* **2018,** *150*, 041718.
44. Zhan, C.; Dattila, F.; Rettenmaier, C.; Bergmann, A.; Kühl, S.; García-Muelas, R.; López, N.; Cuenya, B. R., Revealing the CO Coverage-Driven C–C Coupling Mechanism for Electrochemical CO_2 Reduction on Cu_2O Nanocubes via Operando Raman Spectroscopy. *ACS Catal.* **2021,** *11*, 7694-7701.
45. Militello, M. C.; Simko, S. J., Elemental Palladium by XPS. *Surf. Sci. Spectra* **1994,** *3*, 387-394.
46. Timoshenko, J.; Roldan Cuenya, B., In Situ/Operando Electrocatalyst Characterization by X-ray Absorption Spectroscopy. *Chem. Rev.* **2021,** *121*, 882-961.
47. Li, J.; Xu, A.; Li, F.; Wang, Z.; Zou, C.; Gabardo, C. M.; Wang, Y.; Ozden, A.; Xu, Y.; Nam, D.-H.; Lum, Y.; Wicks, J.; Chen, B.; Wang, Z.; Chen, J.; Wen, Y.; Zhuang, T.; Luo, M.; Du, X.; Sham, T.-K.; Zhang, B.; Sargent, E. H.; Sinton, D., Enhanced Multi-Carbon Alcohol Electroproduction from CO via Modulated Hydrogen Adsorption. *Nat. Commun* **2020,** *11*, 3685.
48. Roy, S.; Bagchi, D.; Dheer, L.; Sarma, S. C.; Rajaji, V.; Narayana, C.; Waghmare, U. V.; Peter, S. C., Mechanistic Insights into the Promotional Effect of Ni Substitution in Non-Noble Metal Carbides for Highly Enhanced Water Splitting. *Appl. Catal. B* **2021,** *298*, 120560.
49. Lin, S.-C.; Chang, C.-C.; Chiu, S.-Y.; Pai, H.-T.; Liao, T.-Y.; Hsu, C.-S.; Chiang, W.-H.; Tsai, M.-K.; Chen, H. M., Operando Time-Resolved X-Ray Absorption Spectroscopy Reveals the Chemical Nature Enabling Highly Selective CO_2 Reduction. *Nat. Commun.* **2020,** *11*, 3525.

50. Henkelman, G.; Arnaldsson, A.; Jónsson, H., A Fast and Robust Algorithm for Bader Decomposition of Charge Density. *Comput. Mater. Sci.* **2006,** *36*, 354-360.
51. Li, Y. C.; Wang, Z.; Yuan, T.; Nam, D.-H.; Luo, M.; Wicks, J.; Chen, B.; Li, J.; Li, F.; de Arquer, F. P. G.; Wang, Y.; Dinh, C.-T.; Voznyy, O.; Sinton, D.; Sargent, E. H., Binding Site Diversity Promotes CO_2 Electroreduction to Ethanol. *J. Am. Chem. Soc.* **2019,** *141*, 8584-8591.
52. Corral, D.; Feaster, J. T.; Sobhani, S.; DeOtte, J. R.; Lee, D. U.; Wong, A. A.; Hamilton, J.; Beck, V. A.; Sarkar, A.; Hahn, C.; Jaramillo, T. F.; Baker, S. E.; Duoss, E. B., Advanced Manufacturing for Electrosynthesis of Fuels and Chemicals from CO_2. *Energy Environ. Sci.* **2021,** *14*, 3064-3074.
53. Niu, Z.-Z.; Chi, L.-P.; Liu, R.; Chen, Z.; Gao, M.-R., Rigorous Assessment of CO_2 Electroreduction Products in a Flow Cell. *Energy Environ. Sci.* **2021,** *14*, 4169-4176.

Chapter 6

Unravelling the Mechanism of Higher Alcohols Production on the Ordered Intermetallic Surface During CO_2 Electroreduction

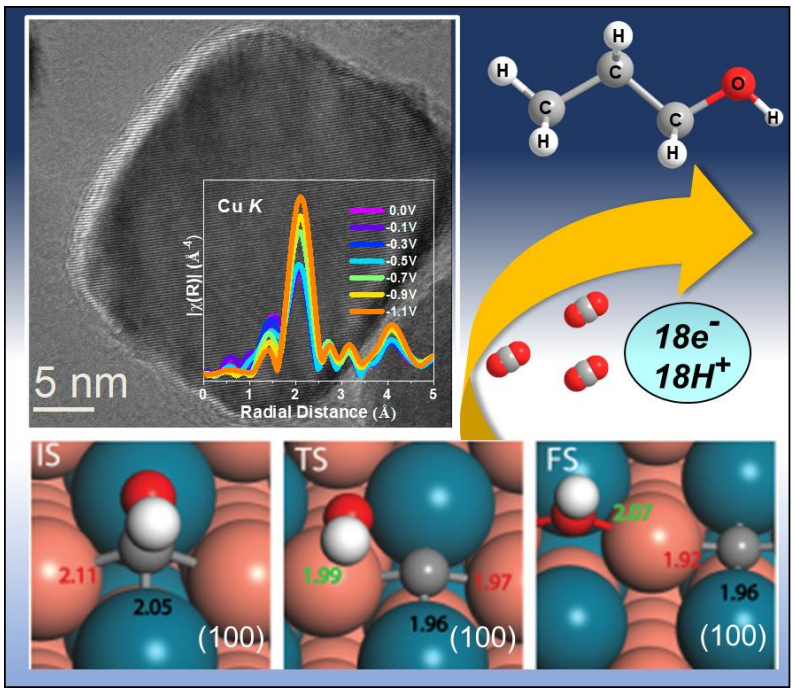

Bagchi, D.; Khan, T. S.; Iyar, J.; Singh, A. K.; Kaur, K.; Vinod, C. P.; Gautam, U. K.; Haider, M. A. Peter, S. C. (*manuscript under revision*)

Summary

Electrochemical reduction of carbon dioxide (eCO_2RR) to the higher hydrocarbons or alcohols is always desirable due to its high-energy value. In the continuation of the previous chapter, we have tried to design a similar Pd-Cu-based catalyst with 1:3 mole ratio (Pd:Cu) and obtain a structurally ordered catalyst, which can generate highly energy-dense CO_2 reduced C_3 products like n-propanol with high selectivity. We demonstrate a unique synthesis route of morphology-controlled (spherical and cubic) $PdCu_3$ ordered intermetallic nanoparticles (NPs) without using any external strong reducing agent. Structurally ordered cubic $PdCu_3$ with (100) exposed crystallographic plane exhibits enhanced selectivity towards the formation of ethanol and n-propanol compared to spherical $PdCu_3$ NPs with (111) exposed plane. This work reports the highest ever formation rate and Faradaic Efficiency (FE) towards n-propanol from CO_2 via electrochemical pathway. Density functional theory simulations are highlighting the key mechanistic route to obtain higher C_{2+} alcohol selectivity on the two different surfaces of $PdCu_3$. The product selectivity trend is attributed to the differences in active surface ensemble of Pd and Cu atoms leading to differential binding of the adsorbates and specifically to the selective activation of the C-O bond. This further establishes the important role of alloying Pd with Cu in rationally tailored surfaces for higher alcohol synthesis.

In this chapter, DB (author) has conceptualized the idea and synthesised the catalysts, performed all the electrochemical studies (both flow cell and H-cell) and other ex-situ (XRD, XPS, TEM), in-situ studies (FTIR, EXAFS), analyzed the data, and written the draft. TSK, JI and MAH performed the computational study. AKS assisted in in-situ EXAFS experiment. KK and UKG helped to take TEM images. CPV procured the XPS data. SCP conceptualized the idea, supervised the work, reviewed and edited the draft.

Table of Contents

6.1. Introduction 207

6.2. Experimental Details 209

6.2.1. Chemicals and reagents 209

6.2.2. Synthesis of $PdCu_3$ 209

6.3. Characterization and Experimental Methods…. 210

6.3.1. Powder X-ray Diffraction (PXRD) 210

6.3.2. Transmission Electron Microscope (TEM) 210

6.3.3. Inductively coupled plasma atomic emission spectroscopy (ICP-OES) 210

6.3.4. X-ray Photoelectron Spectroscopy (XPS) 210

6.3.5. Scanning electron microscopy (SEM) and Energy Dispersive Spectrum (EDAX) 211

6.3.6. X-ray Absorption Spectroscopy 211

6.3.7. Electrochemical CO_2 Reduction Reaction (eCO_2RR) 211

6.3.8. Flow cell optimization for eCO_2RR in gas diffusion electrode configuration . 212

6.3.9. Gaseous product analysis 212

6.3.10. Liquid product analysis 213

6.3.11. In situ Electrochemical Attenuated Total Reflection Fourier Transform Infrared Spectroscopy (ATR-FTIR) 213

6.3.12. Methodology of computational study 213

6.4. Results & Discussion 214

6.4.1. Electrochemical CO_2 reduction (eCO_2RR) 217

6.4.2. Faradaic efficiency (FE) of CO_2 reduced products 219

6.5. Mechanistic Studies 224

6.5.1. In-situ IR spectroscopy and XPS study 224

6.5.2. Ex situ and in situ X-ray absorption spectroscopy 226

6.5.3. Mechanistic Insight on Product Selectivity 230

6.5.4. Differential electrochemical mass spectrometry (DEMS) 240

6.6. Conclusion 241

6.7. References 241

6.1. Introduction

The previous chapters focused on the tuning the Pd-Cu-based catalyst surface so that the product selectivity can be switched from C_1 to C_{2+} hydrocarbons and alcohols. In that case also, the C_{2+} selectivity (for example n-propanol) was rescricted to very less. As a liquid product, ethanol and n-propanol has attracted significant attention because of its multi-functional usage including the chemical industry, and it can be easily stored and transported.[1] So, achieving the higher selectivity, i.e., Faradaic efficiency (FE) for ethanol and n-propanol, is one of the vital aims of CO_2RR research.[2] Copper is the only metal that can produce a plethora of hydrocarbons and alcohols upon eCO_2RR. Albeit monometallic Cu catalysts suffer from selectivity towards any particular product formation.[3, 4] Due to this a variety of techniques such as shapes,[5, 6] size,[7] oxidation state,[8, 9] and grain boundaries[10, 11] have been already employed to modify the Cu surface and enhance the product selectivity. As we discussed in chapter 5, the addition of second a second metal to Cu has become a successful approach to enhance the product selectivity by tailoring the binding energy of the intermediate on the interface of both metals. However, most of the studies are mainly focused on disordered random alloy, especially selectivity towards C_1 products with very limited reports on ordered structures.[12, 13 14] Bimetallic alloy catalysts suffer from surface poisoning and lower stability due to its disordered atomic positions which leads the random distribution of active sites and irregular surface composition.[15, 16] On other hand, it is extremely difficult to synthesize ordered intermetallic materials with Cu and 3d transition metals by a solution-phase method due to large differences in reduction potential.[17, 18] For the simultaneous reduction of Cu and other transition metals having significantly different electronegativity requires strong and ultrafast reducing agent like organoborohydrides (superhydrides) or Na naphthalide.[19] Furthermore, in most cases, post-synthetic high-temperature thermal annealing has been found to be a necessary step for the formation of ordered intermetallic phases, which often results in agglomeration followed by particle size growth.[20, 21] Therefore, it is really a challenge to control the particle size during ordered phase formation. In the previous chapter we have studied the ordering nature of Pd and Cu to tune the product selectivity. On the other hand, controlling the shape of the nanoparticle is also very crucial as it can influence the catalytic property.[22] The shape control of Cu nanoparticles has drawn great attention due to enhancement in activity and selectivity by engineering exposed crystallographic facets.[5, 6] Roberts et. al. showed that nanostructured Cu dominated by cubic surface gave enhanced ethylene selectivity.[5] Recently, Gregorie et. al. reported different shape-controlled Cu nanocrystals that exhibited ethylene

selectivity of up to 57% on Cu cubes in 1 M KOH medium.[6] However, it is still a great challenge to obtain the shape control process of Cu-based nanocrystals with ordered intermetallic nanomaterials. Moreover, Cu and Cu-based alloys are reported so far for the selective formation of ethanol.[3, 23] Carbon-based catalysts have also been reported for ethanol production, but producing relatively low current densities.[24] Recently, Cu-based catalysts have shown higher selectivity towards ethanol formation in the alkaline conditions.[25, 26] However, the disadvantage of using alkaline electrolyte is the unexpected reaction between CO_2 and OH^- to form carbonate and bicarbonate, which has detrimental effect in the long-term electrolyzer stability.[27, 28] Inspite of several efforts for CO_2 to ethanol and higher alcohols like n-propanol formation, there is no study ever reported based on stable ordered intermetallic compound. Mechanistic studies for alcohol formation on Cu in CO_2RR has led to varying conclusions. Sargent and co-workers reported the stabilization of *HCCHOH intermediate by incorporating Au into the Cu lattice.[7] Luo et al. have found *HCCOH as the key intermediate for the formation of ethanol on Cu-surface.[20] Grätzel and co-workers proposed that free CO and adsorbed *CH_3 combine to form *$COCH_3$ intermediate, which is further reduced to ethanol.[31] In general, electrochemical CO_2 reduction to hydrocarbon products proceeds via the hydrogenation of CO_2 to form surface adsorbed *COOH (or *OCHO) species and subsequently CO* species, which consists of the rate-determining step.[29] However, selectivity to various products is often determined by the preferential route for the hydrogenation of CO* species.[29-31] For the synthesis of C_{2+} alcohols (ethanol and n-propanol), the surface is essentially required to carry out C-C coupling steps in combination with selective cleavage of the C-O bond. While interpretations differ on C_{2+} product formation in ascertaining the correct intermediate and pathways,[32] C_{2+} alcohols are generally considered from the coupling of adsorbed *CO intermediates.[30, 33] The selectivity between ethanol and n-propanol is finally decided by the propensity of the surface to carry out CO insertion in adsorbed CH_3CHO* species.[29] Understandably, the desired role of the surface to produce C_{2+} alcohols is difficult to achieve in one single transition metal, following which Pd is introduced in this study along with Cu to design the catalyst surface[34] in the form of a $PdCu_3$ intermetallic which facilitates the conversion of CO_2 to C_{2+} alcohols.

In this work, we demonstrate a unique strategy for the synthesis of ordered $PdCu_3$ nanocube ($PdCu_3$-C) and $PdCu_3$ nanosphere ($PdCu_3$-S) by changing the solvent ratio of oleylamine and oleic acid without using any strong reducing agent (**Figure 6.1**). $PdCu_3$-C and $PdCu_3$-S compounds crystallize in the cubic system having the space group $Pm\bar{3}m$.

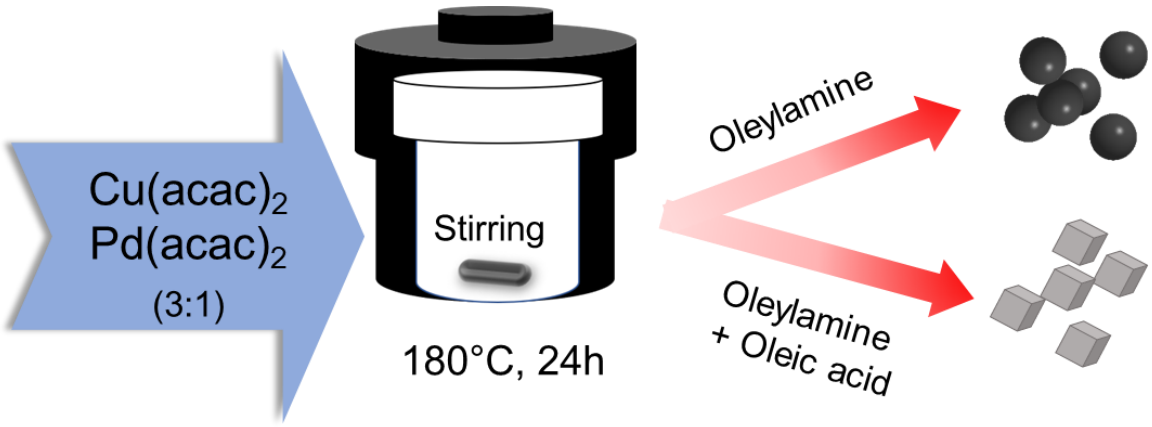

Figure 6.1. Schematic of annealing process for the solvothermal synthesis of $PdCu_3$ ordered intermetallic catalysts.

Both of these compounds have shown excellent electrochemical CO_2RR performance with ethanol and n-propanol as the major multi-carbon products. The ordered $PdCu_3$-C catalyst having (100) exposed plane has higher multi-carbon selectivity than the $PdCu_3$-S where (111) plane is exposed. The selectivity trend on the two different surfaces are elucidated in density functional theory (DFT) simulations of the mechanistic routes, originating from adsorbed CO* species, described as selectivity determining steps in CO_2RR.[29] Because of the ordered arrangement of the intermetallic catalysts, $PdCu_3$ shows excellent stability during the eCO_2RR process, as evident in the microscopic analysis elucidating the morphological evolution of the catalyst surface under applied negative potential. The rational design favored the highest ever formation rate and FE towards n-propanol.

6.2. Experimental Details

6.2.1. Chemicals and reagents

Palladium acetylacetonate ($Pd(acac)_2$) and oleylamine were purchased from Sigma-Aldrich, hexadecyltrimethylammonium bromide (CTAB) were purchased from SDFCL and copper acetylacetonate ($Cu(acac)_2$) was purchased from Alfa Aesar. All the chemicals (more than 99% purity) were used as purchased without further purification. Millipore water of conductivity 18.2 MΩcm was used for the synthesis and all other studies. Potassium bicarbonate, which has been used as the electrolyte during CO_2 reduction, was bought from Sigma Aldrich. All the chemicals used were commercially available certified reagents and used without further purifications unless mentioned.

6.2.2. Synthesis of $PdCu_3$

$PdCu_3$ intermetallic nanoparticles were synthesized in different shapes by solvothermal method. In a typical solvothermal procedure, 0.1 mmol $Pd(acac)_2$, 0.3 mmol $Cu(acac)_2$ and 75

mg CTAB were mixed together in 18 ml oleylamine with vigorous stirring and loaded in 23 ml Teflon lined autoclave. The autoclave was kept at 180 ^oC for 24 hrs. $PdCu_3$ nanocubes were obtained by changing the solvent from oleylamine to 8:1 ratio of oleylamine and oleic acid. The product was repeatedly washed several times with a 1:1 mixture of hexane and ethanol and dried in vacuum oven at 60 ^oC for 6hrs. In this chapter we have used mild reducing agent like oleylamine or oleic acid to get proper morphology controlled nanoparticle. On the other hand, in the previous case, $NaBH_4$ has been used and we obtained random sized connected nanoparticle.

6.3. Characterization and Experimental Methods

6.3.1. Powder X-ray Diffraction (PXRD)

PXRD measurements were done at room temperature on a Rigaku Miniflex X-ray diffractometer with a Cu−K_α X-ray source (λ = 1.5406 Å), equipped with a position-sensitive detector in the angular range of $10° \leq 2\theta \leq 90°$ with the step size 0.02° and a scan rate of 0.5 s/step calibrated against corundum standards. The experimental XRD patterns were compared to the patterns simulated from the data reported in the literature.

6.3.2. Transmission Electron Microscope (TEM)

TEM images and selected area electron diffraction patterns were collected using a JEOL JEM-2010 TEM instrument and color mapping was done in TECHNAI. The samples for these measurements were prepared by sonicating the nanocrystalline powders in ethanol and drop-casting a small volume onto a carbon-coated copper grid.

6.3.3. Inductively coupled plasma atomic emission spectroscopy (ICP-OES)

ICP-OES was performed using a Perkin Elmer Optima 7000 DV instrument. The samples were digested in concentrated aqua regia, followed by dilution with distilled water. In a typical experiment, 2 mg of the sample was dissolved in 1 ml aqua regia and left overnight (12 hrs) for digestion. The digested sample was then diluted to 10 ml volume with deionized water. The solid particles were separated by thorough centrifugation before measurements.

6.3.4. X-ray Photoelectron Spectroscopy (XPS)

XPS measurements were carried out using Thermo K-alpha+ spectrometer using micro focused and monochromated Al Kα radiation with energy 1486.6 eV. The pass energy for the spectral acquisition was kept at 50 eV for individual core-levels. The electron flood gun was utilized for providing charge compensation during data acquisition. Further, the individual core-level spectra were checked for charging using C1s at 284.6 eV as standard and corrected

if needed. The peak fitting of the individual core-levels was done using CASA XPS software with a Shirley type background.

6.3.5. Scanning electron microscopy (SEM) and Energy Dispersive Spectrum (EDAX)

The FESEM measurement was performed using Leica scanning electron microscopy equipped with an energy-dispersive X-ray spectroscopy (EDX) instrument (Bruker 120 eV EDAX instrument). Data were acquired by using an accelerating voltage of 15 kV, and the typical time taken for data accumulation is 100 s. The elemental analyses were performed using the P/B-ZAF standardless method (where P/B = peak to background model, Z = atomic no. correction factor, A = absorption correction factor, and F = fluorescence factor) for Cu, Ga at multiple areas on the sample coated Si wafer.

6.3.6. X-ray Absorption Spectroscopy

X-ray absorption near-edge spectroscopy (XANES) and quick-Extended X-ray Absorption Fine Structure (quick-EXAFS) experiments at 300 K were performed at PETRA III, beamline P64, DESY, Germany. Measurements of Cu-*K* and Pd-*K* at ambient pressure were performed in fluorescence as well as transmission mode using gas ionization chambers to monitor the incident and transmitted X-ray intensities. Monochromatic X-rays were obtained using a Si (111) double crystal monochromator, which was calibrated by defining the inflection point (first derivative maxima) of Cu foil as 8980.5 eV. The beam was focused by employing a Kirkpatrick-Baez (K-B) mirror optic. A rhodium-coated X-ray mirror was used to suppress higher-order harmonics. A CCD detector was used to record the transmitted signals. Pellets for the ex-situ measurements were made by homogeneously mixing the sample with an inert cellulose matrix to obtain an X-ray absorption edge jump close to one.

6.3.7. Electrochemical CO_2 Reduction Reaction (eCO_2RR)

All the electrochemical measurements were performed using a CHI 6008E electrochemical workstation. Electrochemical CO_2 reduction reaction (eCO_2RR) is carried out in a three-electrode system, which involves a working electrode (glassy carbon or carbon cloth), counter electrode (graphitic carbon rod), and reference electrode (Ag/AgCl). The cell compartments are separated by a proton exchange membrane (Nafion 117), and the electrolyte used is 0.5M $KHCO_3$ solution. The electrolyte solutions were purged with CO_2 gas for 1 hour prior to the measurement. The electrocatalyst was prepared by dispersing 2 mg of catalyst and 0.2 mg of Vulcan (activated carbon) in 200 µL of mixed solvent solution (IPA:H_2O = 1:1 v/v) and 10 µL of 1 wt% nafion binder. From the prepared catalyst 100 µL was coated on the carbon cloth and dried. The electrochemical cell was designed to have a large electrode area (0.7 cm

x 0.7 cm) and a small electrolyte volume (10 mL) in each of the two compartments, along with a gas headspace of approximately 5 mL above the electrolyte on each side of the membrane. CO_2, regulated by a mass flow controller at 10 standard cubic centimeters per minute (sccm), flowed through the working electrode compartment of the cell during electrolysis. CO_2 flow through the cell was necessary in order to see large current efficiencies for CO_2 reduction products, presumably because of mass transport limitations in a quiescent cell. The flow rate of 10 sccm was chosen to ensure sufficient CO_2 transport to the surface while preventing interference from gas bubbles striking the surface.

6.3.8. Flow cell optimization for eCO_2RR in gas diffusion electrode configuration

To increase the CO_2 diffusion and increase the overall current density, the electrochemical carbon dioxide experiments were carried out in a filter-press type Micro Flow Cell (Electrocell A/S), where a Ti sheet coated with Ir-MMO (iridium-mixed metal oxide) is used as an Anode plate (Electrocell S/A). An anionic exchange membrane (Fumasep FAB-PK-130) was employed in the case of CO_2RR in KOH medium. The electrolyte was recirculated continuously into the cell (both in cathode and anode) by two separate peristaltic pumps (Ravel, RH-P100L-100) to accumulate liquid products. The flow of CO_2 was regulated by a mass flow controller (Brooks) at different flowrate (standard cubic centimeters per minute (sccm)) to optimize the most suitable flow rate, flowed through the working electrode compartment of the cell during electrolysis. For the final study, the gas flow is fixed to 50 sccm, and electrolyte flow was set to 20 sccm. To achieve C-based GDE, Freudenberg H23C2 has been used as the gas diffusion layer (GDL) and catalyst ink was coated with loading of 1mg/cm^2.

6.3.9. Gaseous product analysis

All the gaseous products were analyzed by online 490-Micro Gas Chromatography (GC), which has four channels for detecting different gaseous products. Each channel has a specific column for analyzing relevant gases *viz*. Molsieve 5Å (for channel 1 and 2), Pora PLOT U (in channel 3) and CP-Sil 5 CB (for channel 4). The carrier gases were Ar and H_2. Each GC channel is equipped with a thermal conductivity detector (TCD). This detector responds to the difference in thermal conductivity between a reference cell (carrier gas only) and a measurement cell (carrier gas containing sample components).

Calculation of Faradaic Efficiency (FE) for gaseous products,

$$FE_{gas} = \frac{ppm \times flow\ rate \times \frac{number\ of\ electron \times Faraday\ contant \times pressure}{R \times Temperature}}{I_{average}} \times 100$$

Where ppm is the concentrations detected by GC, R is a gas constant (8.31 j $K^{-1}mol^{-1}$).

6.3.10. Liquid product analysis

The liquid products were analyzed by ^{1}H NMR (600 MHz, JEOL). The following protocol was applied. Five hundred mL of the electrolyte and 30 µL of an internal standard solution were transferred into a centrifuge tube. The internal standard solution consisted of 50 mM phenol (99.5%) and 10 mM dimethyl sulfoxide (99.9%) made in D_2O solvent. The mixture is transferred into an NMR tube. Solvent suppression was used to decrease the intensity of the water peak.

6.3.11. In situ Electrochemical Attenuated Total Reflection Fourier Transform Infrared Spectroscopy (ATR-FTIR)

In situ electrochemical FTIR spectroscopic studies were performed using a purged VERTEX FT-IR spectrometer equipped with the A530/P accessory and a mid-band MCT detector. A silicon hemispherical window (F530-8) was used with the working electrode placed gently on top of the window as the single reflection attenuated total reflection (ATR) accessory for the FTIR study. The measurement parameters were 4 cm^{-1} resolution and 100 scans. This setup enabled the detection of eCO_2RR intermediate formation and change of adsorption of various intermediates on the electrode surface and within the thin-layer electrolyte. In the beginning of the IR-experiment, we have taken a spectrum of the overall electrochemical cell and then take a background spectrum so that the contribution of the electrolyte can be subtracted in the next spectrum while applying the potential during performing CO_2RR. The spectra were analyzed by the OPUS software and the absorption spectra have been directly plotted at various potential and time.

6.3.12. Methodology of computational study

DFT simulations on the two different facets of $PdCu_3$ intermetallic alloy are carried out in the framework of the plane-wave basis set code available in Vienna Ab initio Simulation Package (VASP, version 6.2.0).[35] The intermetallic alloy structure is drawn on replacing the 1 Cu atom with Pd in the fcc unit cell and thereby, geometrically optimizing the lattice to obtain the bulk structure. The two different facets of the $PdCu_3$ alloy are created by cleaving the bulk structure in (111) and (100) directions. A periodic supercell of size 4x4 is drawn with a vacuum size of 20 Å in the z-direction to represent the catalyst surface, where reactants in vacuum are adsorbed and reacted to form products.

Overall, four layers of the metal in the surface model structure are representing the bulk, sub-surface and surface of the catalyst, in which bulk layers are kept fixed, while the surface and sub-surface layers are allowed to relax in structure optimization to represent surface

restructuring in catalytic reactions. The plane-wave basis set, expanded to an energy cut off value of 396 eV, is applied to calculate the electron density. Kohn-sham equations are solved with a pseudopotential approximation using revised Perdew-Burke-Ernzerhof (RPBE)[36] exchange-correlation functional in the Irreducible Brillouin Zone to estimate the ground-state energy of the structure. In this iterative process, the electronic structure of the surface model is converged to obtain a self-consistent field of the electron density. To simplify integrations in the reciprocal lattice, 3x3x1 k-points are applied in the Monkhorst-Pack scheme. Once ground state-energy of the structure is estimated, the force on the structure is directly derived following the Hellman and Feynman Theorem.[37] For geometry optimization, energy and forces on the structures are converged to a value of 10^{-6} eV and 0.05 eV/Å respectively using RMM-DIIS algorithm[38] on the potential energy surface (PES). Binding energy of the adsorbates are calculated as the difference in the energy of the adsorbed structure on the surface with the sum of energies of the clean surface and gas phase energy of the adsorbate.

In order to estimate the activation energies of the elementary reaction step, transition state (TS) structures are identified on the minimum energy path (MEP) using a Climbing Image Nudged Elastic Band (NEB) method.[39] Structures of the initial and final states are estimated from geometry optimization as local minima on the PES, which are subsequently connected by 15 linearly interpolated images to construct an estimated reaction coordinate. The MEP is realized, when the structures connecting the reactant and product states are obtained with perpendicular forces converged to 0.1 eV/Å following the RMM-DIIS algorithm. In the Climbing Image NEB, the structure with maximum energy on the MEP is allowed to climb up and represent the TS, with restoring forces (minima) in all other directions. Activation energy of the reaction step is estimated as the difference in energies of the TS and initial state (IS) structures. Similarly, reaction energy is calculated as the difference in the final state (FS) and IS.

6.4. Results & Discussion

$PdCu_3$ crystallizes in a cubic space group with lattice parameter a = 3.722 Å.[40] **Figure 6.2** shows the comparison of the experimental powder XRD with the simulated pattern of the $PdCu_3$ ($Pm\bar{3}m$) confirming the formation of ordered phase. Pure Pd metal crystallizes in a face-centered cubic crystal structure ($Pm\bar{3}m$) (a = 3.8902 (3) Å), where all the corners and faces are occupied by the Pd atoms (Wyckoff no. 4a) (**Figure 6.3a)**. While in $PdCu_3$ the Pd atoms occupy the corner positions (Wyckoff no. 1a) and the Cu atoms occupy half of the octahedral holes (Wyckoff no. 3c).

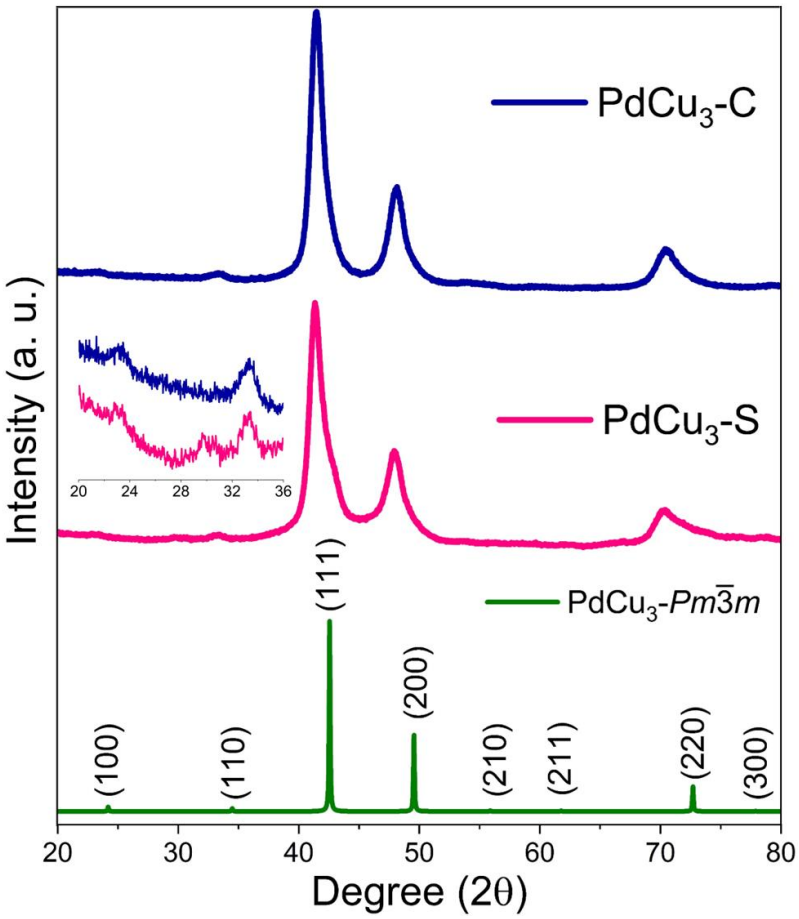

Figure 6.2. Comparison of Powder XRD patterns of as synthesized $PdCu_3$-C and $PdCu_3$-S intermetallic nanoparticles with simulated powder patterns of $PdCu_3$. The peaks which appear due to ordering of Pd and Cu are marked with *.

Such an ordered arrangement of Cu atoms within the lattice of Pd is expected to increase the catalytic activity.[41-43] The $PdCu_3$ nanocrystals, which are having exposed 100 lattice planes tend to form the cubic nanoparticle, and those are having 111 exposed planes gives rise to spherical nanoparticle as represented in **Figure 6.3a**. Transmission electron microscopic (TEM) images show the spherical (**Figure 6.3b**) and cubic (**Figure 6.3c**) shaped nanocrystals of the $PdCu_3$ uniformly distributed on the surface and we named them as $PdCu_3$-S and $PdCu_3$-C, respectively. From the high-resolution TEM images (**Figures 6.3d** and **6.3e**), the d-spacing was found to be 0.213 nm and 0.356 nm, respectively, for $PdCu_3$-S and $PdCu_3$-C nanoparticles which are matching with the lattice spacing of the (111) and (100) planes of ordered $PdCu_3$. The selected area electron diffraction (SAED) pattern of $PdCu_3$-S (**Figure 6.3f**) and $PdCu_3$-C (**Figure 6.3g**) nanoparticles shows the representative ring pattern of (111), (200), (210), (311) crystallographic planes in the case of $PdCu_3$-S and (100), (200), (210), (220) in case of $PdCu_3$-C.[40]

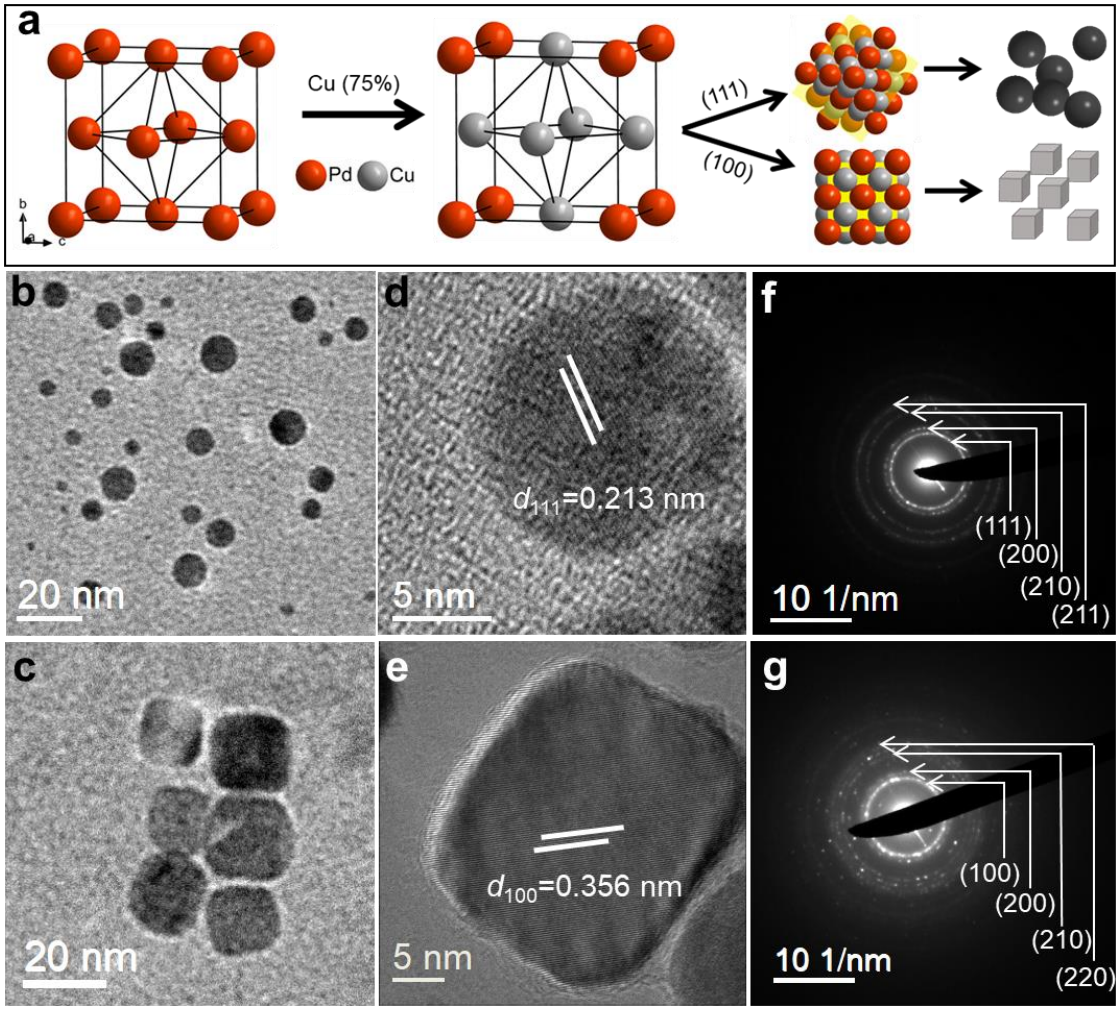

Figure 6.3. (a) Schematic illustration of formation of $PdCu_3$-S and $PdCu_3$-C from its crystal structure. Transmission Electron Microscopy (TEM) images of (b) $PdCu_3$-S and (c) $PdCu_3$-C. High resolution (HR) TEM of (d) $PdCu_3$-S and (e) $PdCu_3$-C. Selected area electron diffraction (SAED) pattern of (f) $PdCu_3$-S and (g) $PdCu_3$-C.

Table 6.1. Elemental composition of Pd and Cu in PdCu3-intermetallic catalysts from ICP-OES experiment.

Sample	Elements	mg/L	Atomic %
$PdCu_3$-S	Pd	66.73	25.402
	Cu	117.0	74.598
$PdCu_3$-C	Pd	86.5	24.669
	Cu	157.5	75.33

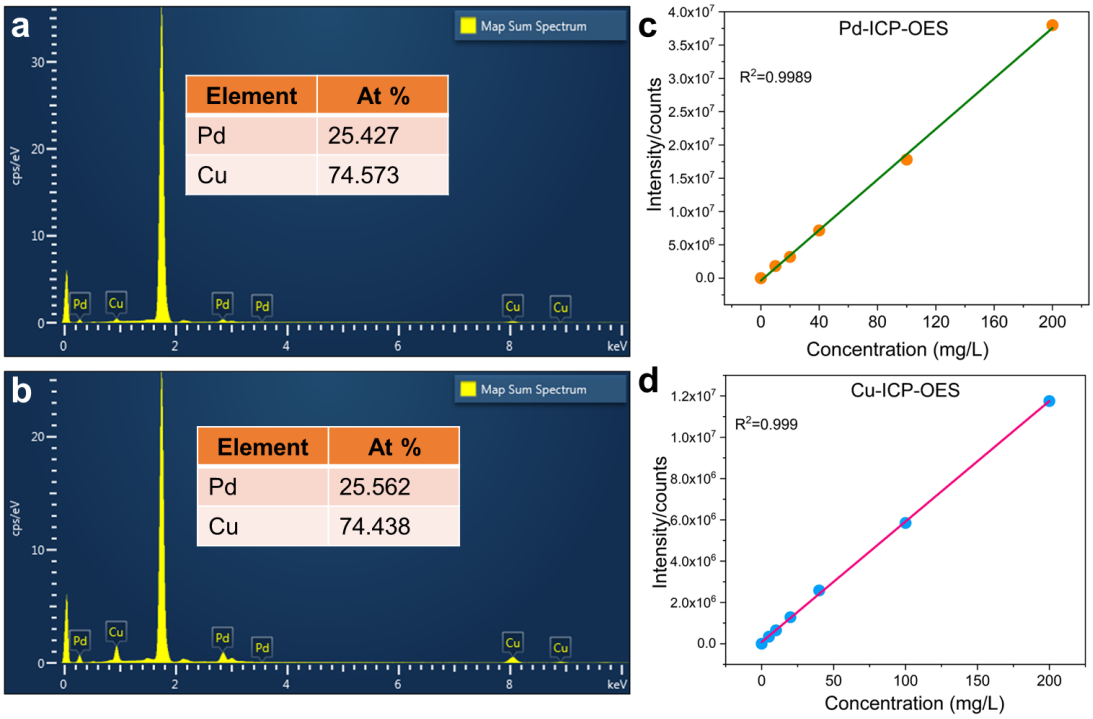

Figure 6.4. SEM-EDS spectra and elemental composition of (a) $PdCu_3$-C and (b) $PdCu_3$-S catalysts. ICP-OES Calibration curves for (c) Pd and (d) Cu quantification at different concentration range.

The morphological tuning from the sphere to the cube has been achieved by the systematic control of the solvent used during the solvothermal reaction. It is well-reported that oleylamine having $–NH_2$ group binds onto the (100) crystal facet and hinders the growth along (100).[44] On the contrary, the –COOH group of oleic acid can bind on the (111) facet and favors the growth of (100).[45] CTAB plays an important role in the co-reduction of Pd^{II}/Pd (0.915V vs. SHE) and Cu^{II}/Cu (0.34V vs. SHE),[46] which would not have been possible in the presence of weak reducing agent oleylamine. The elemental composition of both $PdCu_3$ nanoparticles has been verified from SEM-EDS as well as ICP-OES study (**Figure 6.4, Table 6.1**).

6.4.1. Electrochemical CO_2 reduction (eCO_2RR)

Electrochemical CO_2RR studies were carried out on both $PdCu_3$ catalysts in 0.5 M $KHCO_3$ with continuous CO_2 purging at 20 sccm flow rate in the customized cell. Catalysts were coated on toray carbon paper as the working electrode, which is having a surface area of 1 cm^2. Firstly, a linear sweep voltammetric study has been performed in the CO_2RR potential region, and it was observed that in the CO_2 atmosphere, both the $PdCu_3$-S and $PdCu_3$-C catalysts provide much lower onset potentials and higher current densities than those in N_2-saturated 0.5 M $KHCO_3$, indicating that the catalytic activity is originated from CO_2 reduction process (**Figure 6.5a**).

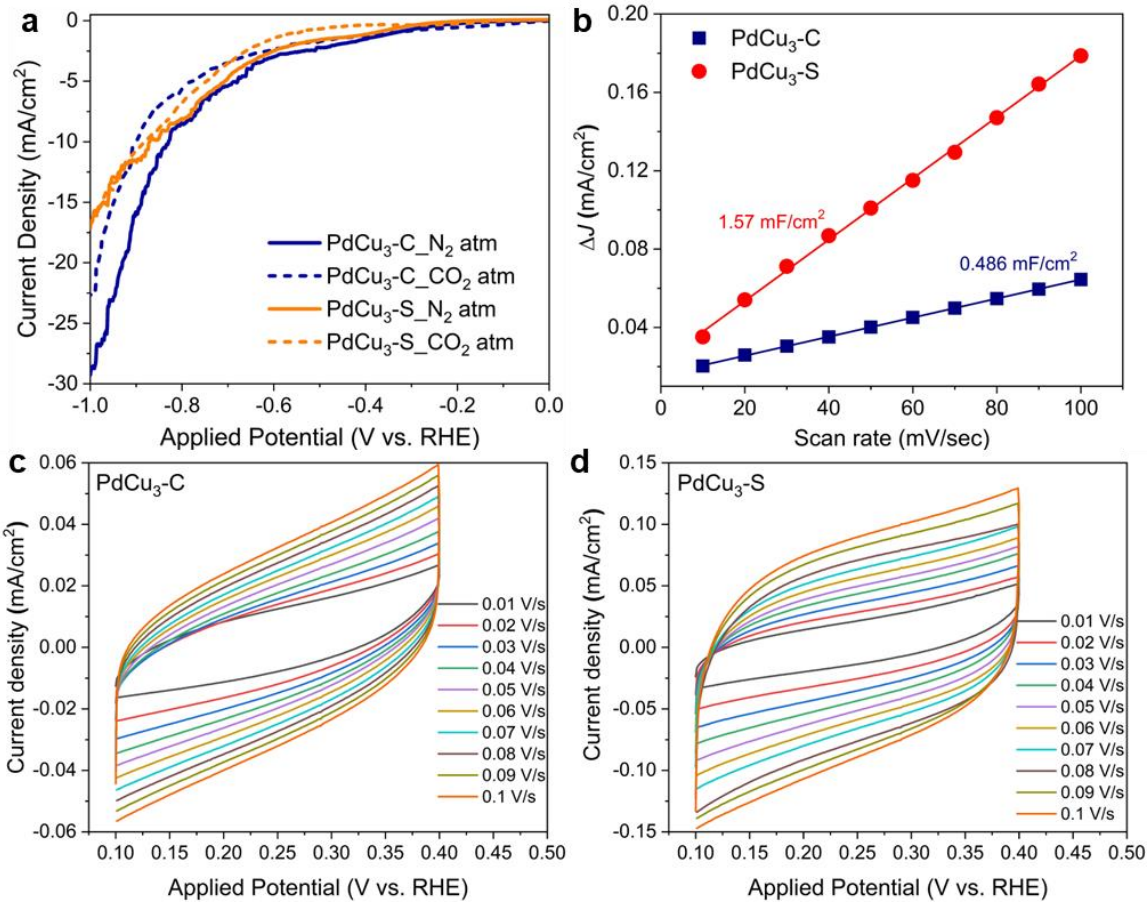

Figure 6.5. (a) Comparison of linear sweep voltammogram at CO_2 and N_2 atmosphere in same potential window. (b) Plots of ΔJ vs. scan rate where the slope of the fitted line gives the corresponding C_{dl} values. Cyclic voltammograms (CVs) of (c) $PdCu_3$-S, (d) $PdCu_3$-C, sweeping over the potential area from 0.1 V (vs. RHE) to 0.4 V (vs. RHE) for the determination of double-layer capacitance (C_{dl}) and thereby estimation if effective surface area (ECSA).

Electrochemically active surface area (ECSA) is one of the most critical factors influencing the activity of any electrocatalytic reaction. To understand the role of ECSA in activity enhancement, double layer capacitances (C_{dl}) of the catalysts are determined (**Figure 6.5b**). As shown in **Figure 6.5c-d**, $PdCu_3$-S catalyst (1.57 mF/cm^2) displayed larger C_{dl} values than the $PdCu_3$-C catalyst (0.486 mF/cm^2), indicates the CO_2RR activity does not directly correlate with the electrochemically active surface area, rather the electronic factor is playing a crucial role here.[32] For the evaluation of the electrochemical behavior and the quantification of CO_2-reduced products, chronoamperometric test at different potentials (-0.1 V, -0.3 V, -0.5 V, -0.7 V, -0.9 V, and -1.1 V vs. RHE) was performed in CO_2 saturated 0.5 M $KHCO_3$ solution for 1h under the CO_2 flow of 20 sccm. The flat nature of chronoamperometry curves on both

the intermetallic catalysts indicates good electrochemical stability during CO_2RR conditions (**Figure 6.6**).

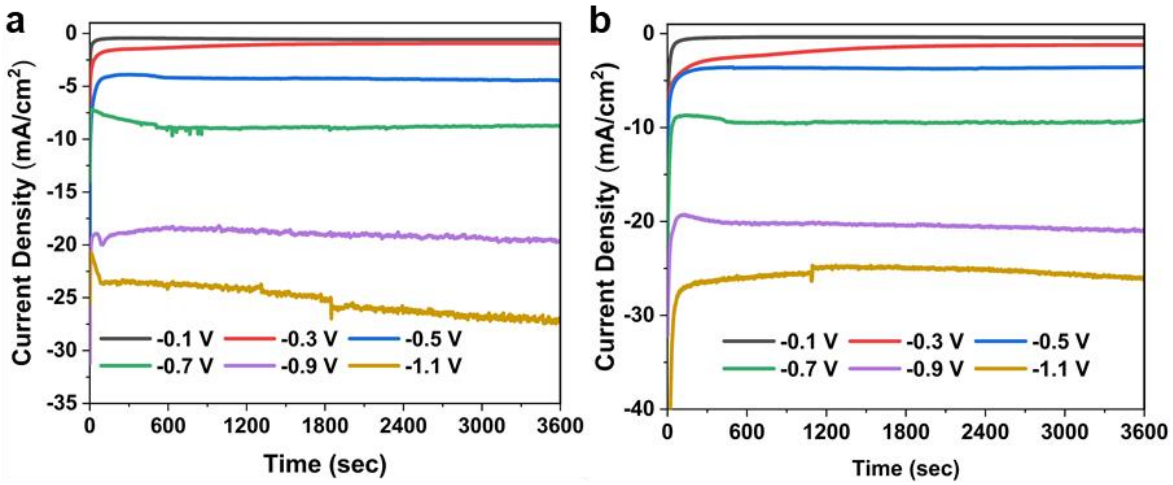

Figure 6.6. Chronoamperometric study (current density as function of time) on (a) $PdCu_3$-C and (b) $PdCu_3$-S ordered intermetallic catalysts during electrochemical CO_2RR in 0.5 M $KHCO_3$.

6.4.2. Faradaic efficiency (FE) of CO_2 reduced products

After every chronoamperometric study at each potential (**Figure 6.7a**), all the CO_2-reduced products were detected and quantified to evaluate the CO_2 reduction performance and product selectivity. The gaseous products were analyzed by the gas chromatographic (GC) technique, and the liquid products were quantified by High Performance Liquid Chromatography (HPLC) and Nuclear magnetic resonance. **Figure 6.7b-d** displays the formation rate of different products along with their respective FEs as a function of applied potentials from −0.1 V to −1.1 V over $PdCu_3$-S and $PdCu_3$-C catalysts. Both the $PdCu_3$-S and $PdCu_3$-C catalysts exhibit almost a similar trend of potential dependency towards CO formation (**Figure 6.7b**). The rate of CO formation, as well as FEs, have been increased as the potential reduction increases. $PdCu_3$-S has shown higher CO formation rate than that of $PdCu_3$-C, producing maximum 32.85 $\mu molh^{-1}cm^{-2}mg^{-2}$ with FE of 8.82% at a reduction potential -1.1 V (vs. RHE) whereas the CO production rate in the case of $PdCu_3$-C is 17.76 $\mu molh^{-1}cm^{-2}mg^{-1}$ with FE of 4.10%. The formation rate of formic acid has also been found to be higher in the case of $PdCu_3$-S than that of $PdCu_3$-C. At relatively higher overpotential (-1.1V), $PdCu_3$-S has exhibited 28.29 $\mu molh^{-1}cm^{-2}mg^{-1}$ production rate of HCOOH (**Figure 6.7c**). On the other hand, at the same potential $PdCu_3$-C has shown a formation rate of 20.27 $\mu molh^{-1}cm^{-2}mg^{-1}$ for HCOOH. From these observations, it is evident that the formation of monocarbon product like

CO and HCOOH are preferably at the (111) surface ($PdCu_3$-S) than that on (100) surface ($PdCu_3$-C). On the other hand, $PdCu_3$-C has shown higher selectivity towards ethanol with maximum formation rate of 0.75 $\mu molh^{-1}cm^{-2}mg^{-1}$, which is much higher than that of $PdCu_3$-S catalyst (0.302 $\mu molh^{-1}cm^{-2}mg^{-1}$) at -1.1V (vs. RHE) (**Figure 6.7d**). From these controlled studies, it can be concluded that $PdCu_3$-C having (100) facet facilitates the multi-carbon product formation upon C-C coupling. On the other hand, $PdCu_3$-S favours the production of higher amount of monocarbon products, which means the intermediate forms on the surface immediately desorbs as the C1 product and hamper the C-C coupling process to form ethanol and other multicarbon product.[6] To minimize the mass transport limitations in the H-cell mentioned and to obtain higher current density as well as better CO_2RR performance the experiments have benn conducted in a flow cell. The GDE configuration has been optimized with different loadings of catalyst and ionomer (Nafion) to obtain a proper gas diffusion layer and to restrict electrolyte flooding. The carbon-based gas diffusion electrode (GDE) that contains a microporous carbon black layer and a fiber-based PTFE bounded backbone is used as catalyst support to increase the conductivity of the working electrode to enhance the overall current density.[47, 48]

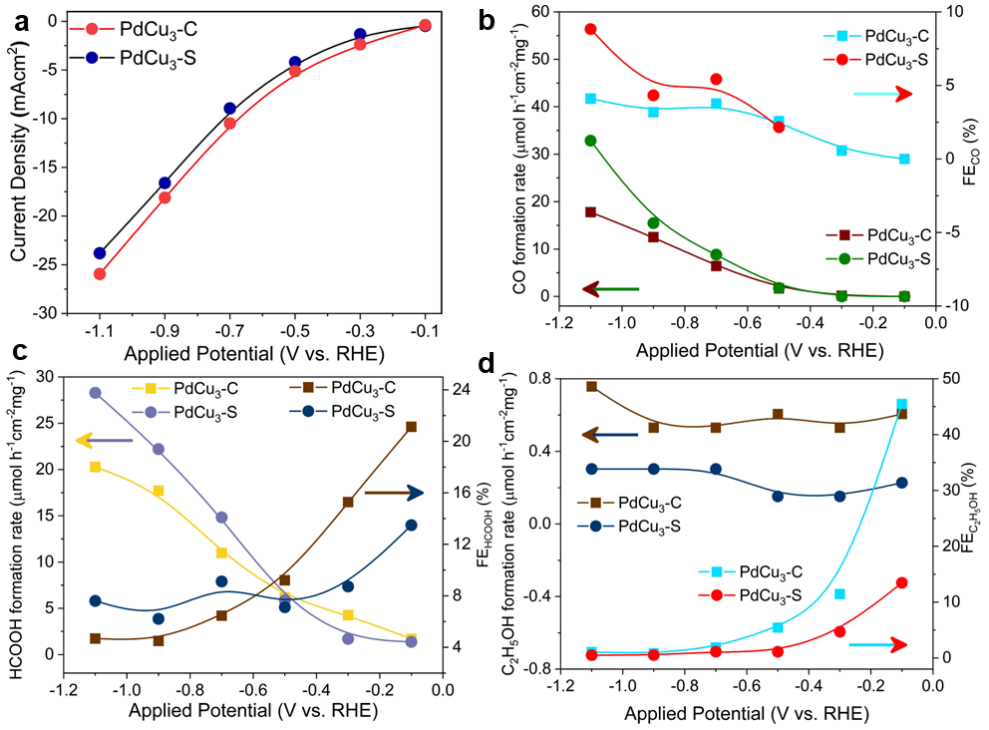

Figure 6.7. ECO_2RR performance of $PdCu_3$-C and $PdCu_3$-S catalysts. (a) Current density at different applied potential during the chronoamperometric study. The rate of formation of CO_2 reduced product at different applied potential along with corresponding Faradaic efficiency for (b) CO, (c) HCOOH, and (d) C_2H_5OH.

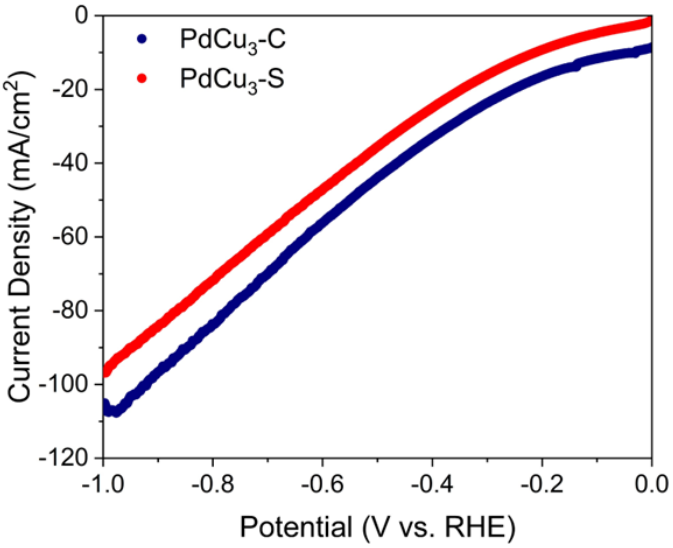

Figure 6.8. Comparison of linear sweep voltammogram of $PdCu_3$-C and $PdCu_3$-S in 0.5M $KHCO_3$ in the flow cell configuration with GDE.

Linear sweep voltammograms on both catalysts (**Figure 6.8a)** suggesting a multi-fold increment in the higher current density (~100 mA/cm^2 @-1.0V) achieved in the flow cell compared to the traditional H-cell. In the flow cell condition, the current density achieved in 0.5M $KHCO_3$ has been enhanced 4-5 times than that of H-cell and the current density is found to be slightly higher on $PdCu_3$-C catalyst than that of $PdCu_3$-S (**Figure 6.9a-b**).

Figure 6.10a and **Figure 6.10b** showed the potential dependent formation rate and FE of ethanol and n-propanol, respectively. It is noteworthy to mention that the use of flow cell not only enhances the current density but the multicarbon product n-propanol has also been produced in a significant amount which was not at all in detectable quantity in the case of H-cell.

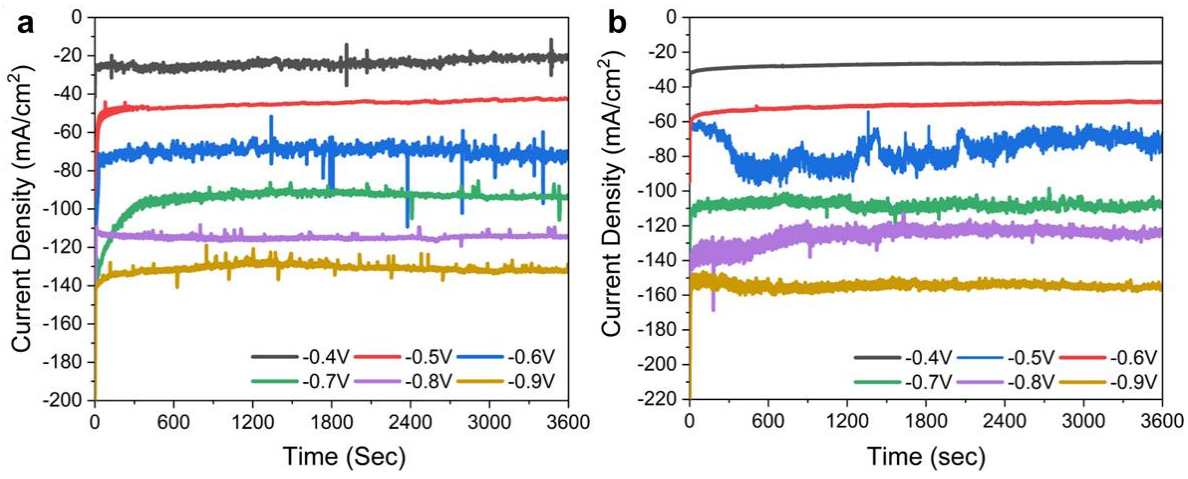

Figure 6.9. Chronoamperometric study (current density as function of time) on (a) $PdCu_3$-S and (b) $PdCu_3$-C catalysts during eCO_2RR in 0.5 M $KHCO_3$.

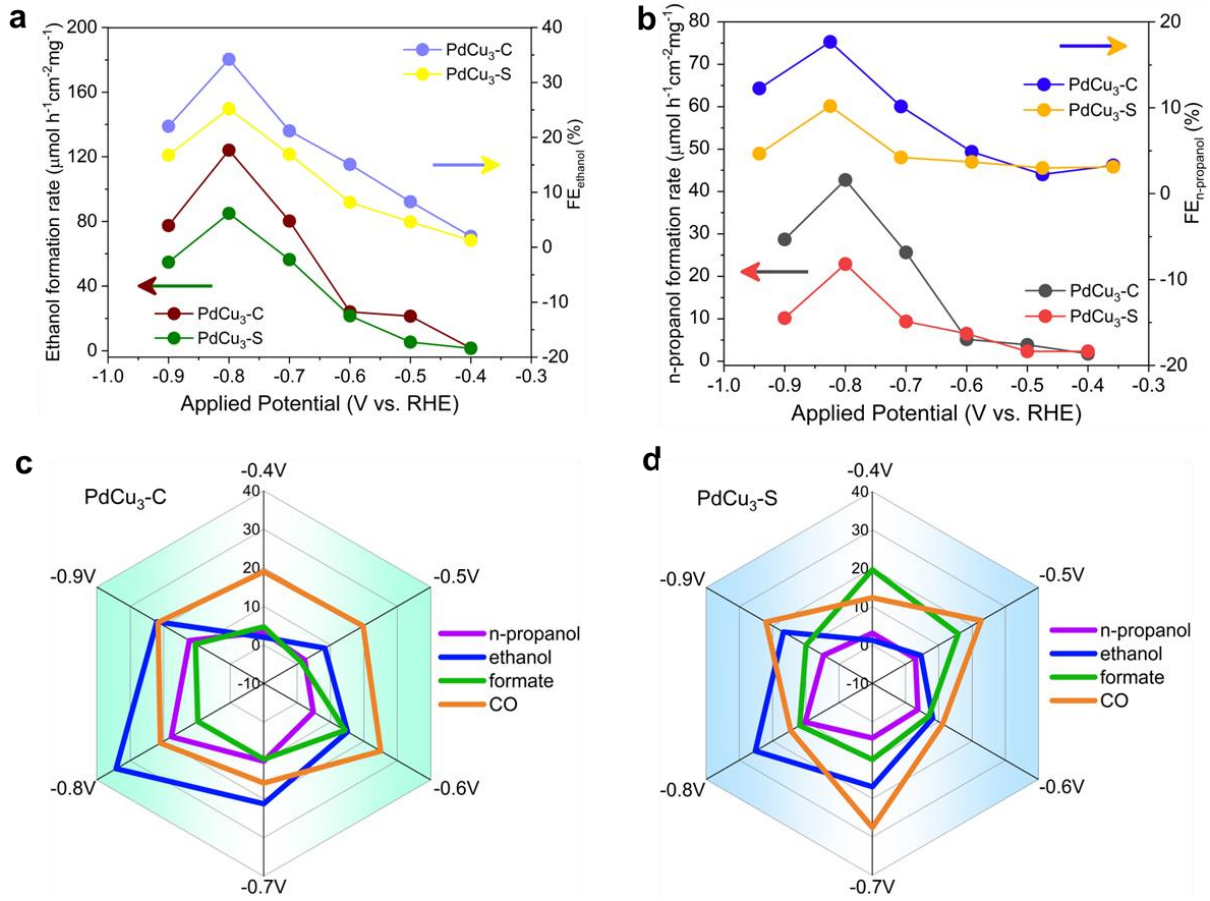

Figure 6.10. ECO$_2$RR experiments on PdCu$_3$-C and PdCu$_3$-S catalysts in a flow cell. The comparison of rate of formation of the major product at different applied potential along with corresponding FEs on PdCu$_3$-C and PdCu$_3$-S for (a) ethanol and (b) n-propanol. Comparison of Faradaic efficiency (FE) of all the CO_2 reduced products formed on (c) PdCu$_3$-C and (d) PdCu$_3$-S during ECO$_2$RR performed in the flow cell in 0.5M $KHCO_3$.

The potential-dependent NMR spectra of liquid products and the corresponding chemical shift of different CO_2-reduced products has been depicted in **Figure 6.11-6.12**. In the flow cell configuration, a small amount of formic acid has been detected even in the anodic compartment as presented in the NMR spectra due to the cross-over through the anion-exchange membrane (**Figure 6.13**). The formation rate and FE of the major multi-carbon product, ethanol, and n-propanol, have been found to be higher on PdCu$_3$-C than that of PdCu$_3$-S. The FE of all the CO_2 reduced products along with hydrogen have been plotted for PdCu$_3$-C in the **Figure 6.10c** and for PdCu$_3$-S in **Figure 6.10d**. The maximum FE of ethanol is found to be 34.2% and formation rate of 124.1 $mmolh^{-1}cm^{-2}mg^{-2}$ at -0.8V. The FE of n-propanol is observed 17.66% with a formation rate of 42.72 $mmolh^{-1}cm^{-2}mg^{-2}$ on PdCu$_3$-C catalyst with the overall current density of 125.6 mA/cm^2, which is found to be higher than most of the n-propanol producing catalysts reported in the literature.

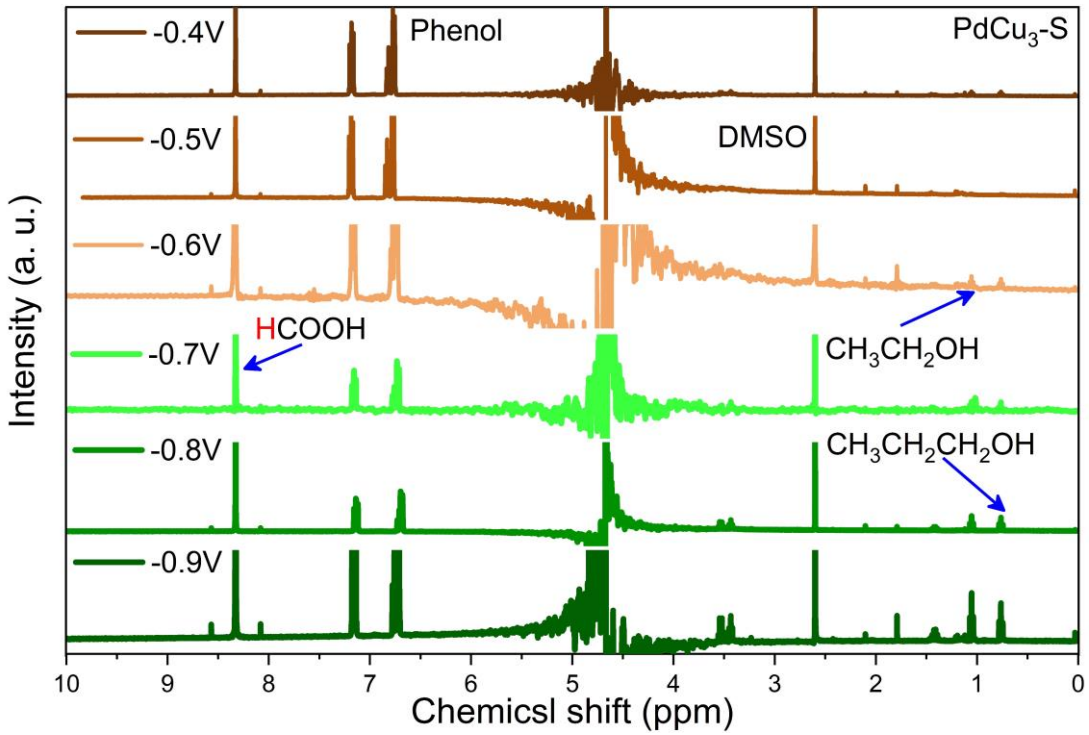

Figure 6.11. NMR spectra of the catholyte obtained from the CO_2 reduction at each individual potential in flow cell configuration. Experimental conditions: $PdCu_3$-S as working electrode with 0.5 M $KHCO_3$ electrolyte at the end of CA measured at different potentials.

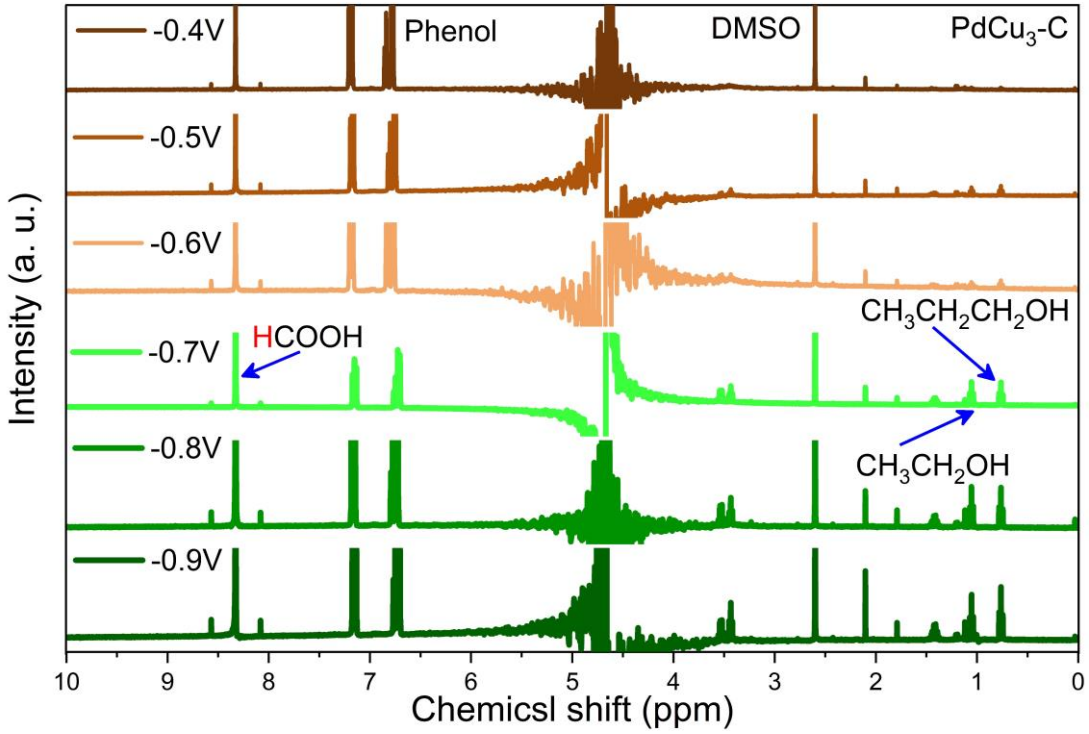

Figure 6.12. NMR spectra of the catholyte obtained from the CO_2 reduction at each individual potential in flow cell configuration. Experimental conditions: $PdCu_3$-C as working electrode with 0.5 M $KHCO_3$ electrolyte at the end of CA measured at different potentials.

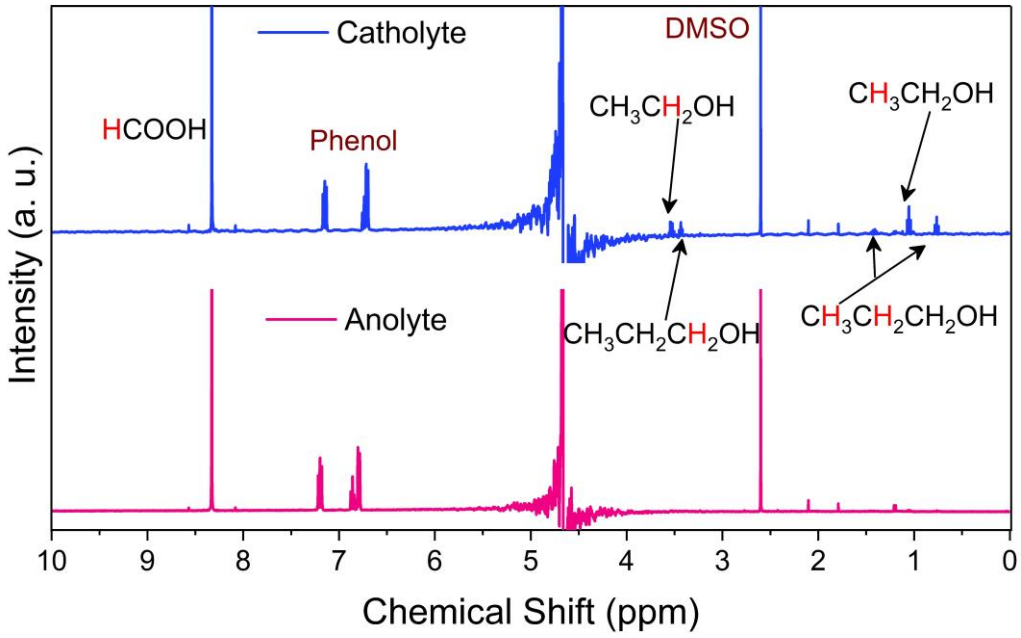

Figure 6.13. NMR spectra of the catholyte and anolyte obtained from the CO_2 reduction at -0.8 V (vs. RHE) in flow cell configuration. Experimental conditions: $PdCu_3$-C as working electrode with 0.5 M $KHCO_3$ electrolyte at the end of CA.

6.5. Mechanistic Studies

6.5.1. In-situ IR spectroscopy and XPS study

To investigate the reaction mechanism of the electrochemical reduction of CO_2 and to detect the important intermediates formed during eCO_2RR on the $PdCu_3$ catalysts, in-situ ATR-FTIR spectroscopy was performed in CO_2 saturated 0.5 M $KHCO_3$ solution at different reduction potentials. **Figures 6.14a** and **6.14b** display the potential dependent spectra taken while CO_2RR was performed at -0.1V -0.3V, -0.5V, -0.7V, -0.9V, -1.1V (vs. RHE) on $PdCu_3$-S and $PdCu_3$-C catalysts, respectively. During CO_2 electrolysis, the electrolyte (0.5M $KHCO_3$) was saturated by continuously purging high purity CO_2 into the IR cell. The negative-going band observed at 2343 cm^{-1} appeared at all the applied potentials, can be attributed to the CO_2 consumption.[49] Major vibrational modes of COOH (which is the first adsorbed intermediate during CO_2RR) like O-H deformation and C=O stretch are clearly visible at 1622 cm^{-1}, and 1220 cm^{-1}, respectively for $PdCu_3$-S (**Figure 6.14a**). Similar stretching peaks are observed for $PdCu_3$-C at 1641 cm^{-1} and 1232 cm^{-1}. As displayed in **Figures 6.14a** and **6.14b**, the IR intensity of the major peaks corresponding to different vibrational modes of the COOH group was gradually increased with the increase of the applied cathodic potentials as the reaction proceeds further, indicating that more CO_2 was being reduced at the higher cathodic potential (-1.1V), where the FE of the CO_2 reduced product was found to be higher than -0.1V clearly indicates

the higher formation of HCOOH in the higher overpotential. The bands centered at 1408 cm^{-1} for $PdCu_3$-S and 1382.3 cm^{-1} for $PdCu_3$-C can be denoted to the IR absorption of HCO_3^- and its intensity is increased over the period of time as we increase the cathodic potential, indicating that more HCO_3^- was being formed at the higher cathodic potential (-0.3V) than at the lower potential (-01V).[50] The peak oberved at ~1620 cm^{-1} in both the potential can be corroborated to the asymmetric O-C=O stretching mode of $HCOO^-$ ions.[51]

Moreover, two reverse peaks centered at ~1622.6 cm^{-1} and 3280 cm^{-1} for $PdCu_3$-S and 1641 cm^{-1} and 3285 in the case of $PdCu_3$-C have also been evolved during CO_2 reduction, which can be ascribed to the H-O-H bond bending and O-H stretching, respectively, of H_2O molecule due to competing hydrogen evolution reaction.[52]

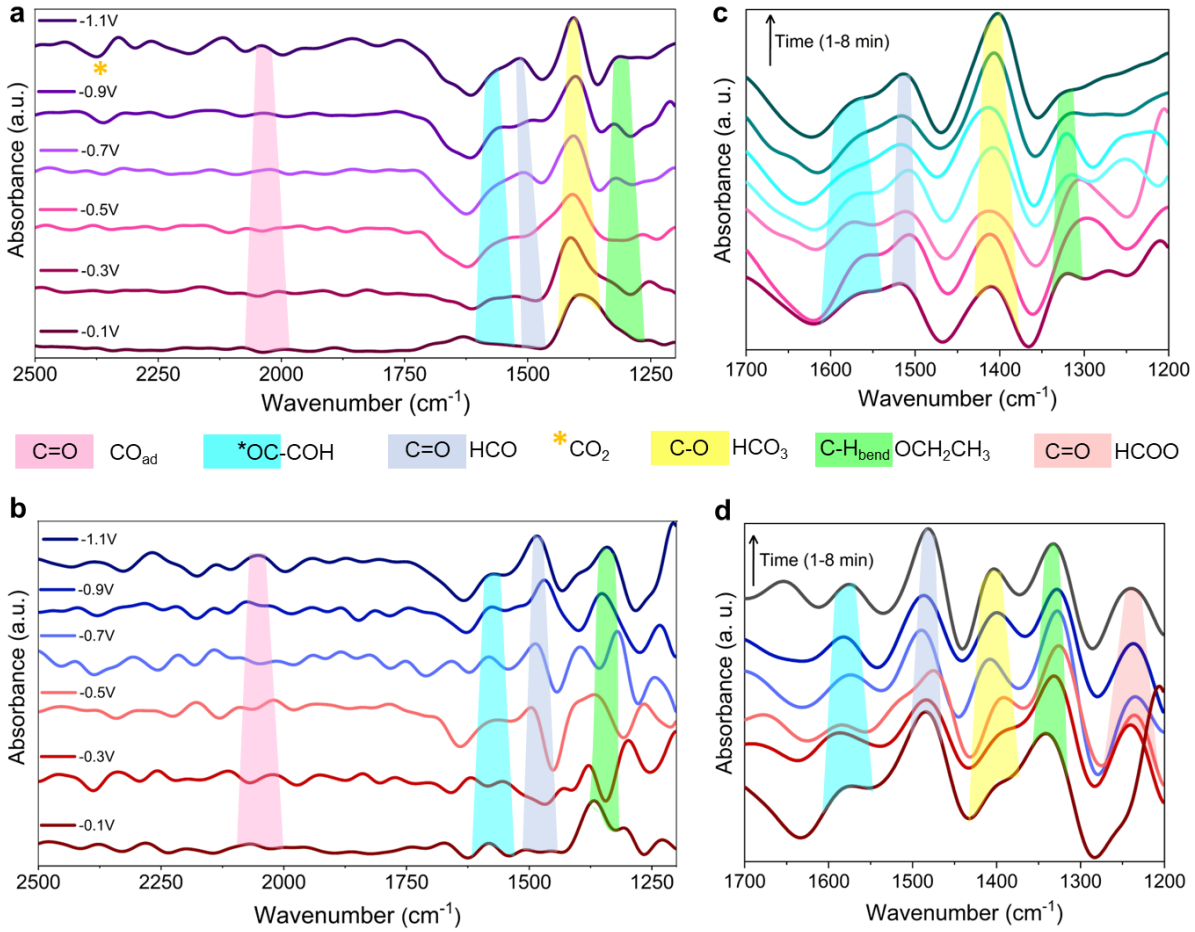

Figure 6.14. Mechanistic investigation of CO_2RR by in-situ IR study. Potential dependent IR spectra obtained during the eCO_2RR on (a) $PdCu_3$-S catalyst and (b) $PdCu_3$-C catalyst. IR spectra were taken at a different time on (c) $PdCu_3$-S catalyst and (d) $PdCu_3$-C catalyst during CA at -1.1 V (vs. RHE). High resolution XPS of (e) Pd 3d and (f) Cu 2p for $PdCu_3$-C before and after performing electrochemical study.

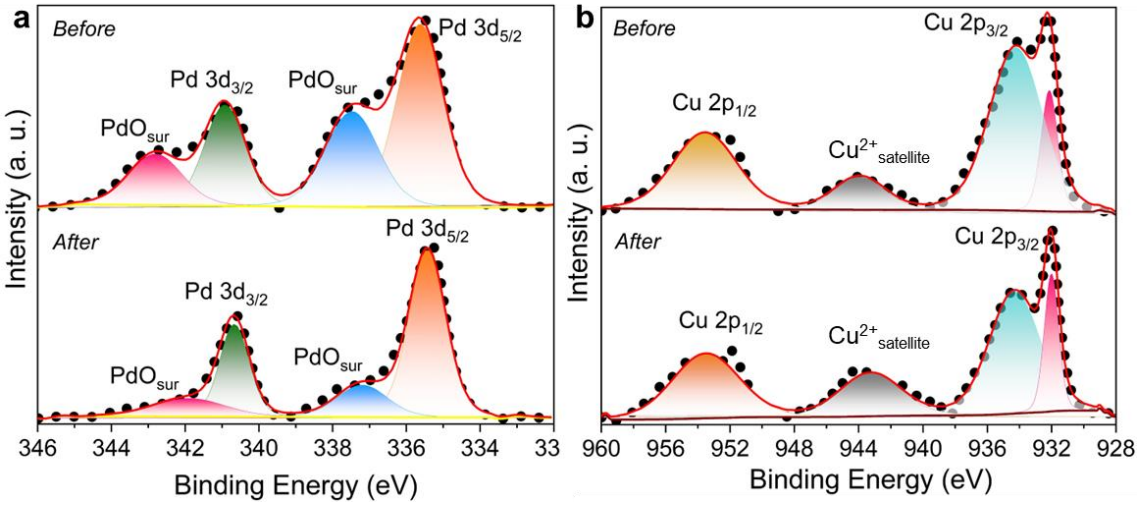

Figure 6.15. High resolution XPS of (a) Pd 3d and (b) Cu 2p for $PdCu_3$-C before and after performing electrochemical study.

As can be seen from **Figures 6.14c** and **6.14d**, bands due to water bending mode are less prominent in the case of $PdCu_3$-C than $PdCu_3$-S indicate predominant CO_2RR selectivity over $PdCu_3$-C surface. In addition to the IR bands related to formate intermediate, the in situ ATR FT-IR also detects CO stretching bands at 2039 cm^{-1} on $PdCu_3$-S and 1254 cm^{-1} on $PdCu_3$-C.[50, 53] Based on the previously reported DFT study, observed peaks at around 1320−1330 cm^{-1} for both the catalysts can be attributed to the CH bending of $O_{bound}OCH_2CH_{3,ad}$ intermediate species.[54] Most importantly, stretching bands corresponding coupling intermediate for the C2 product formation, i.e., OC-COH (1560.3 cm^{-1} on $PdCu_3$-S) and (1575.2 cm^{-1} on $PdCu_3$-C) were observed CO_2 reducing atmosphere, and its intensity gradually increased during chronoamperometry process.[55]

XPS of Pd core level (3d) showed the existence of metallic Pd peak at around 335.62 eV along with some amount of surface oxides, which has been decreased after electrolysis process as mentioned in **Figure 6.15a**.[56] The Cu 2p XPS spectra suggest that both metallic (at 932.15 eV) and oxide (Cu^{2+}) (at 934.29 eV) peak of Cu $3p_{3/2}$ present in the $PdCu_3$ catalyst. But the Cu is so susceptible to the aerial oxidation that the existence of coper oxide sustains even after the electrolysis process (**Figure 6.15b**).[57] So, to probe the surface of the catalyst during the real time electrochemical condition, in situ XAFS was carried out.

6.5.2. Ex situ and in situ X-ray absorption spectroscopy

XAS has been performed to understand the oxidation state and local chemical atmosphere for both Cu and Pd.[58] The normalized XANES spectra of Pd *K*-edge for both $PdCu_3$-C and $PdCu_3$-S show that the absorption edge corresponding to the 1s→4p dipole

transition of Pd K edge is very much close to that of metallic Pd (**Figure 6.16a**). On the other hand, the absorption energy of the Cu shifted slightly to the higher absorption energy than that of elemental Cu foil, indicating the higher oxidation state of Cu in both $PdCu_3$-C and $PdCu_3$-S (**Figure 6.16b**). The Fourier transformed (FT) R-space data suggests that the Pd K-edge contains the signature peak of the Pd-Cu bond at around 2.1Å. It is reported that the metal-oxide have been found to play an important role in CO_2RR selectivity.[59, 60] In order to detect small amounts of metal-oxygen species, both Pd-O and Cu-O, proper analysis of the XAFS data by wavelet-transform have been performed, which is presented in the **Figures 6.16c-d**. It is found that $PdCu_3$-C contains little amount of surface CuO and Pd is in the elemental state in both the $PdCu_3$-C and $PdCu_3$-S (**Figure 6.16a-b)**.[61] $PdCu_3$-S also has Pd in elemental oxidation state and the major bond corresponding to Pd-Cu is prominent in **Figure 6.17a-b**.

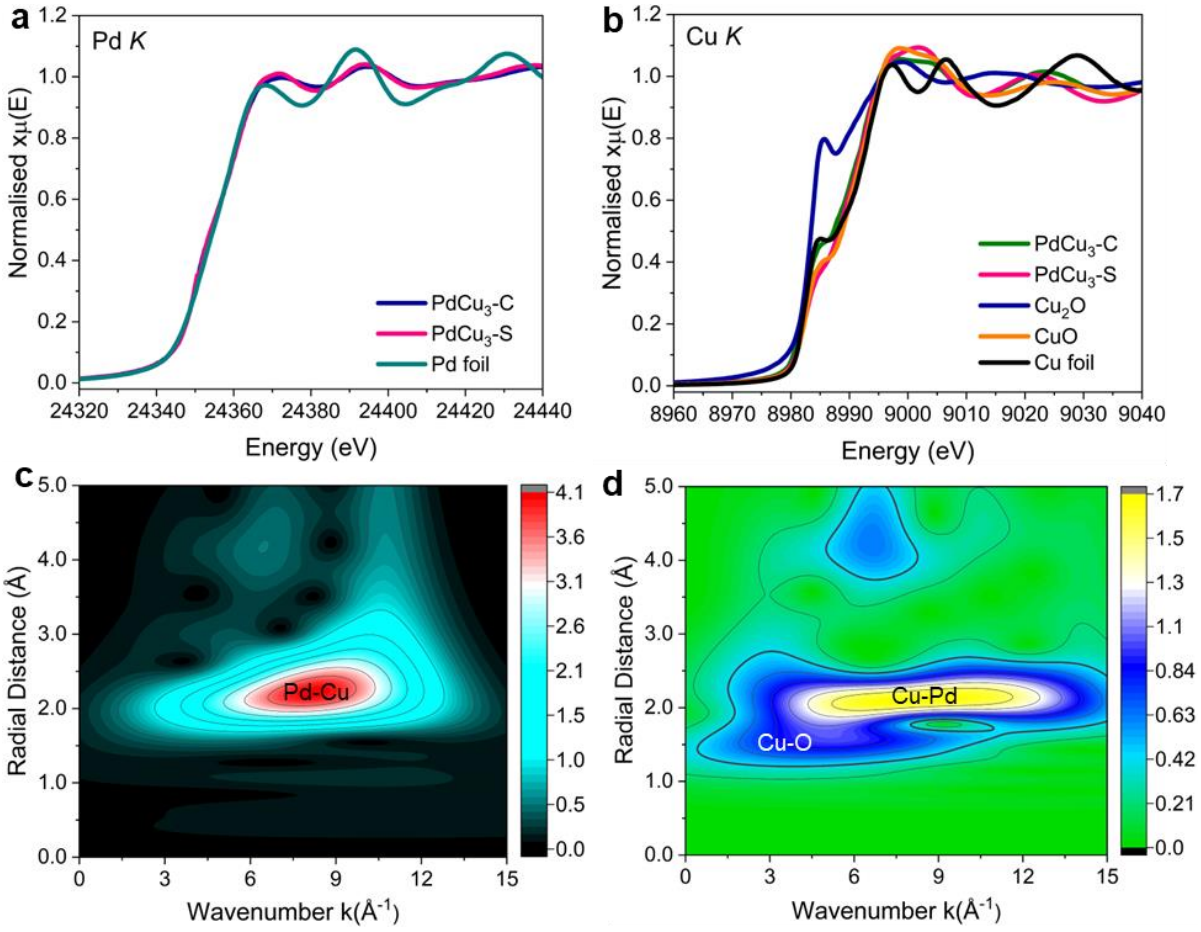

Figure 6.16. Ex situ XAS analysis of $PdCu_3$-C and $PdCu_3$-S catalysts. (a) Comparison of normalized XANES spectra of Pd *K*-edge. (b) Cu *K*-edge with the respective reference samples. Wavelet transform-EXAFS of the synthesized $PdCu_3$-C catalyst for (c) Pd *K*-edge, (d) Cu *K*-edge.

The presence of surface copper oxide is more in case of $PdCu_3$-S as indicated in the wavelet-transform of Cu *K*-edge (**Figure 6.17d**).

With the aim of analyzing the local structure and oxidation state at different applied potential in the CO_2 reduction conditions, we have carried out operando XAS.[62] The potential dependent XANES spectra of Pd *K*-edge shows that the oxidation state of Pd has slightly decreases upon applying negative potential (**Figure 6.18a**).

On the otherhand, the in situ spectra of Cu K XANES shows that the absorption energy significantly decreases to photon energy and subsequently the white line intensity also decreases as the applied potential increases. In the higher negative potential the XANES septra of Cu K edge gradually becomes more likely to be the metallic Cu having lower oxidation state in the $PdCu_3$-C catalysts (**Figure 6.18b**). The potential dependent FT-EXAFS of Pd K-edge showed the major peak at 2.1 Å does not alter much upon applied potential (**Figure 6.18c**).

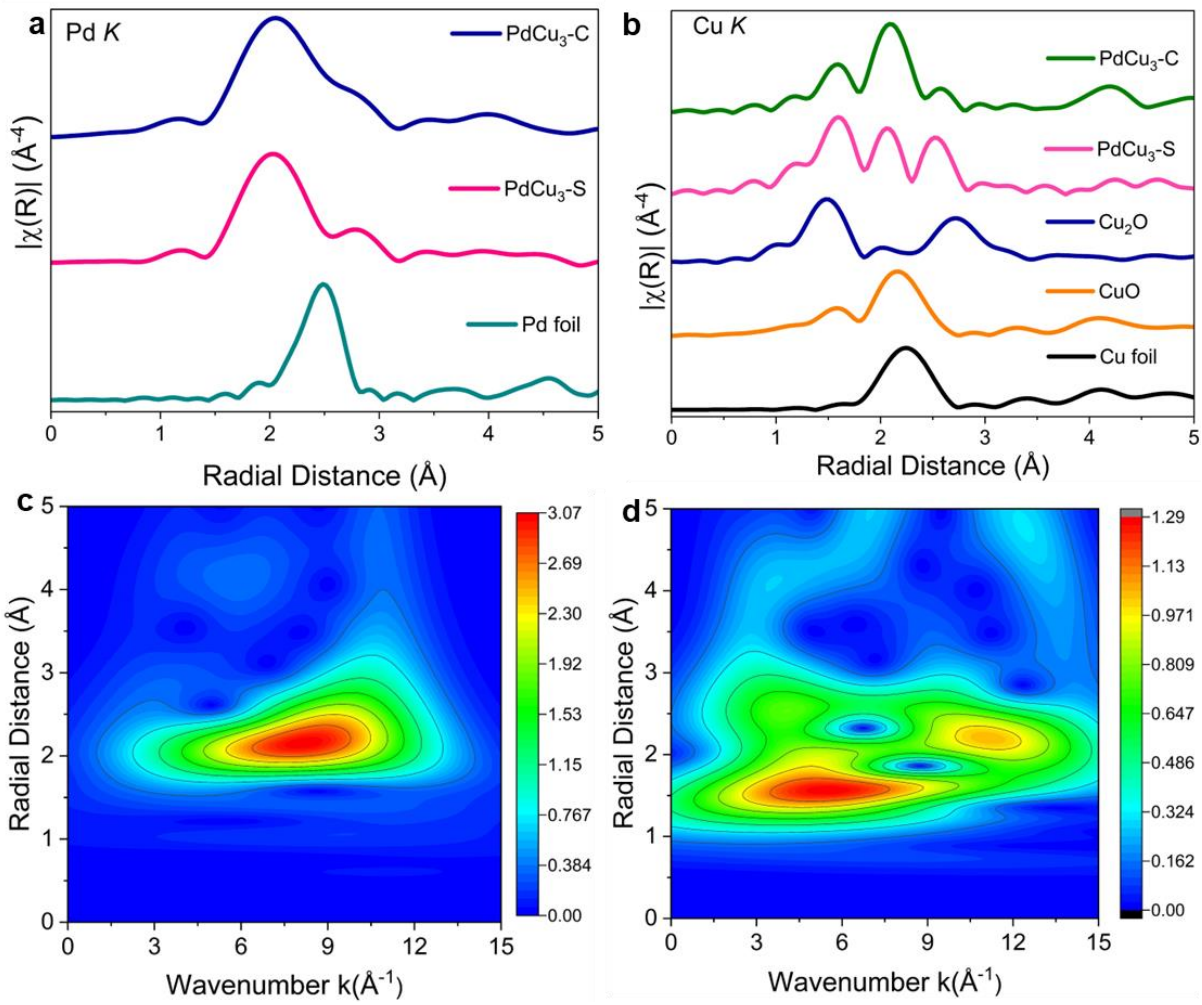

Figure 6.17. Fourier transformed R-space data of (a) Pd *K*-edge and (b) Cu *K*-edge of $PdCu_3$-C and $PdCu_3$-S and compared with the standard metal foil and oxide samples. Wavelet transform-EXAFS of the synthesized $PdCu_3$-C catalyst for (c) Pd *K*-edge, (d) Cu *K*-edge.

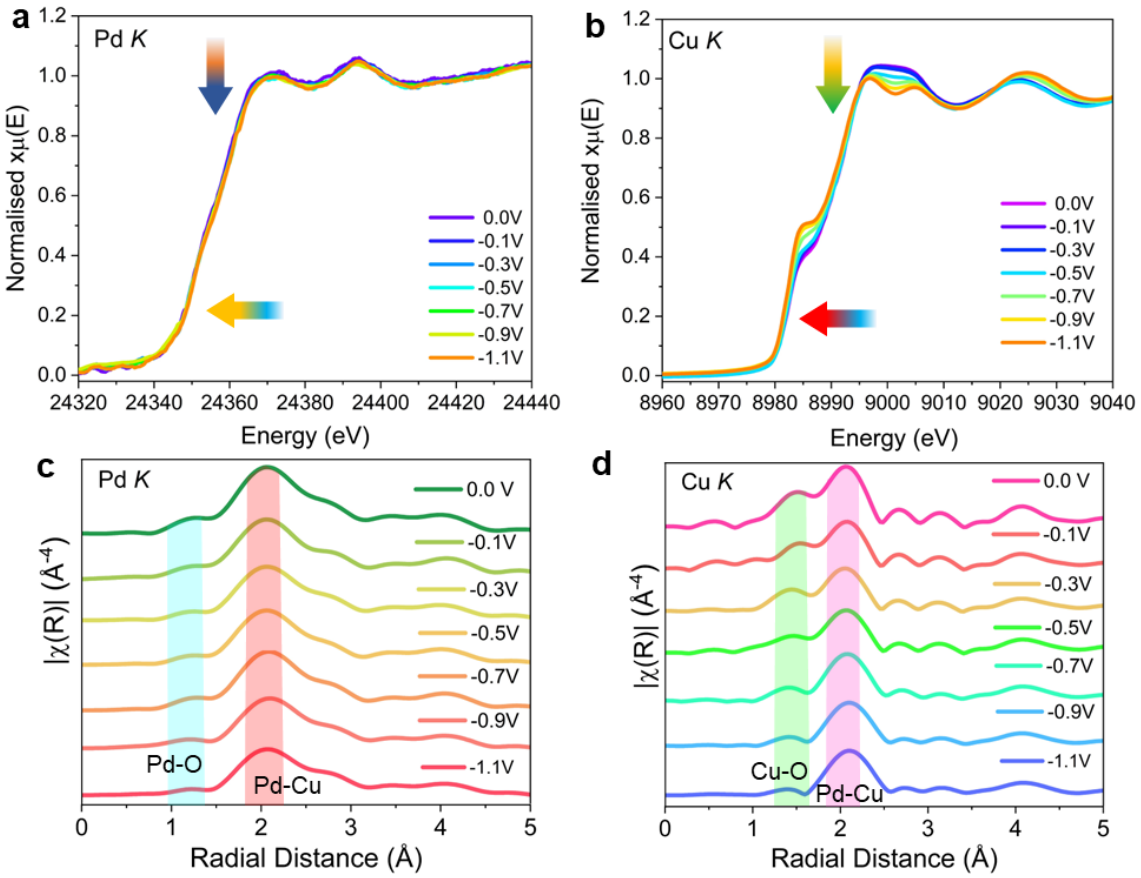

Figure 6.18. Potential dependent in situ XAS of $PdCu_3$-C in the eCO_2RR conditions. Comparison of normalized XANES spectra of (a) Pd *K*-edge (b) Cu *K*-edge at different applied potential during in-situ XAS in the eCO_2RR condition. Fourier transformed R-space data of (c) Pd K-edge and (d) Cu K-edge of $PdCu_3$-C catalyst at different potential during in-situ XAS.

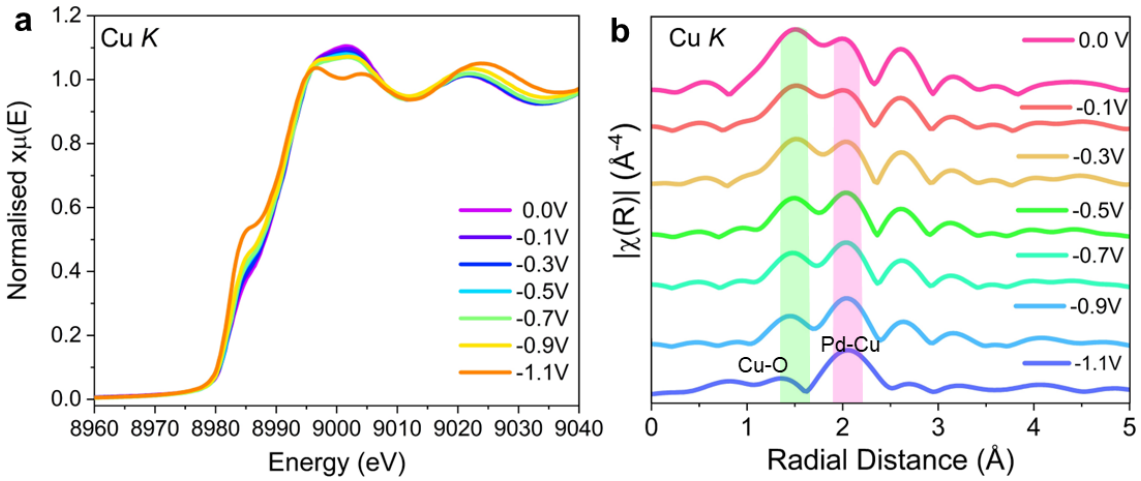

Figure 6.19. Potential dependent in situ XAS in the eCO_2RR conditions on $PdCu_3$-S catalyst. (a) Comparison of normalized XANES spectra of Cu *K*-edge at different applied potential during in-situ XAS in the eCO_2RR condition. (b) Fourier transformed R-space data of Cu K-edge at different potential during in-situ XAS.

In the case of Cu *K*-edge R-space spectra, the bond corresponding to Cu–Cu at 2.3 Å is stable under a reduced atmosphere, But the intensity of the bond related to Cu–O at 1.6 Å decreases its intensity as the negative potential increases, indicates the prominence of metallic nature in the CO_2RR atmosphere of the intermetallic surfaces (**Figure 6.18d**). For $PdCu_3$-S, the potential dependent FT-EXAFS of Pd K-edge also showed the gradual disappearnce of the Cu-O bond and the exposure of the metallic Cu-Pd bond as the negative potential increases (**Figure 6.19a-b)**. From these observation, it can be concluded that both Cu and Pd got rid of its surface oxidised species in the operational condition in higher reduction potential during CO_2RR.[60]

6.5.3. Mechanistic Insight on Product Selectivity

Since both Cu and Pd are reduced to the metallic state in CO_2RR, a model surface representing the intermetallic composition of $PdCu_3$ is drawn to study CO* hydrogenation steps. **Figure 6.20a** and **6.20b** are showing the DFT calculations for the mechanistic routes to synthesize C_{2+} alcohols on the (100) and (111) facets of $PdCu_3$. The CO dimerization route to produce C_2 species (CO-CO*), which may act as a precursor for alcohol formation on CuS[63] and Cu[33] is calculated to be an endothermic step on both the (111) and (100) surfaces (214.2, kJ/mol and 299.1 kJ/mol, respectively). Interestingly, in acidic conditions, Sargent and co-workers have estimated a relatively reduced Gibb's free energy difference (~50 kJ/mol) between the reactant CO* and product OC-CO* species on PdCu bimetallic surface.[33] Authors have further pointed towards significant variation in C_{2+} selectivity on PdCu, ascribing it to the electronic effect of Pd as available in isolated Pd single-atoms, bimetallic configurations and aggregated dimers or trimers.

This further establishes the importance of synthesizing ordered intermetallic of $PdCu_3$ for C_{2+} alcohol synthesis. Moreover, on the model intermetallic surface, direct CO dissociation appears to be unlikely with high (>200 kJ/mol on both facets) endothermicity. Following which, adsorbed CO* species are hydrogenated to form *COH species with activation energies of around 200 kJ/mol on both the surfaces. Formation of *COH is considered a key step in methanol synthesis on Cu.[29, 31] From *COH a direct C-O bond activation route followed by CO* insertion is considered for C_{2+} alcohol synthesis. As compared to direct CO dissociation, the energy barrier for *C-OH dissociation is significantly reduced. On the (111) surface this barrier is reduced to 260.5 kJ/mol, while on the (100) surface this is calculated to be 160 kJ/mol.

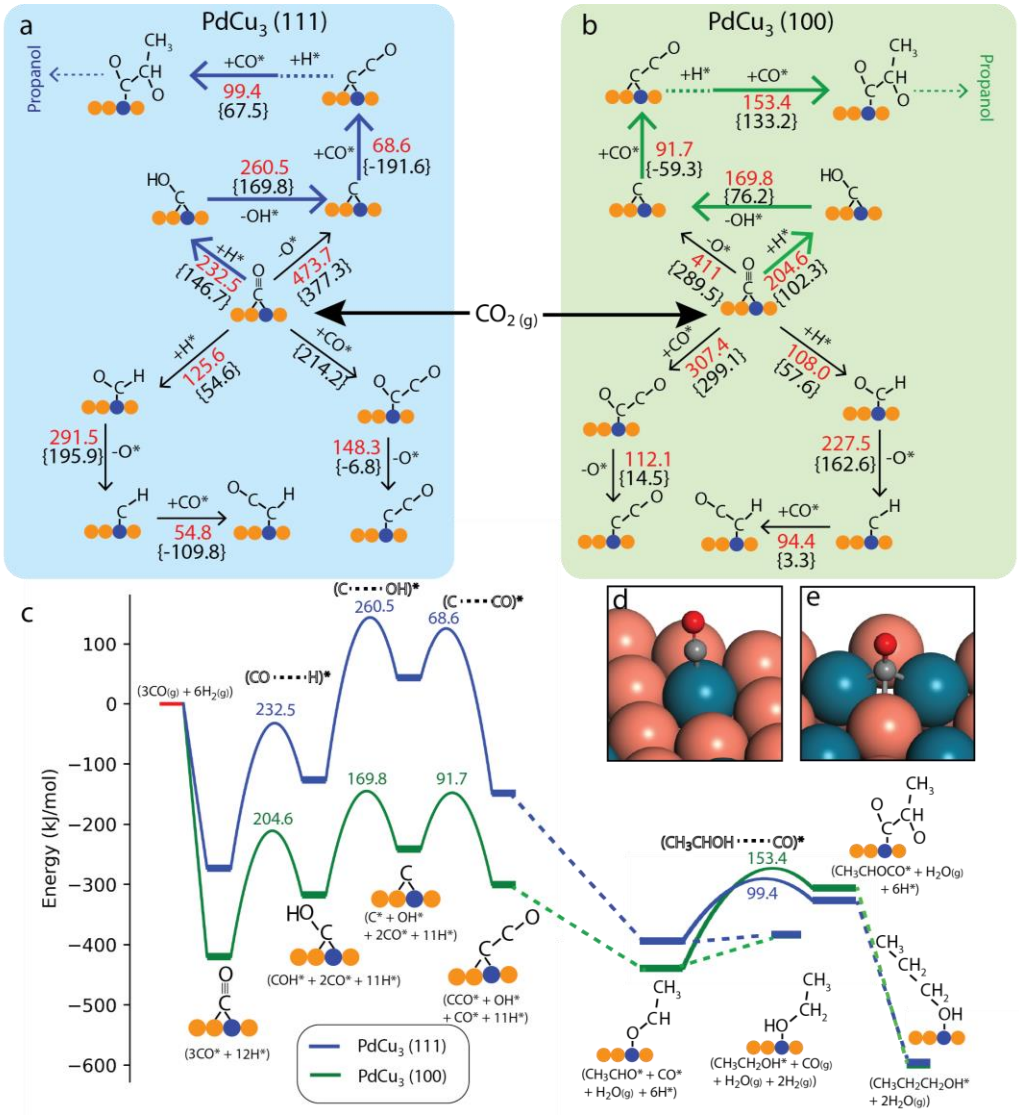

Figure 6.20. Mechanistic routes for CO_2 reduction to produce ethanol and n-propanol on (a) $PdCu_3$ (111) and (b) $PdCu_3$ (100) surfaces. DFT calculations of the key steps in CO* hydrogenation pathways are enumerated as the activation energy (kJ/mol) in red color and reaction energy (kJ/mol) in black color. The corresponding reaction diagram comparing the two selective pathways (blue and green arrows Figure **a** and **b**) for ethanol and n-propanol formation on the (111) and (100) facets of $PdCu_3$ is shown in **(c)**. The cartoon representation of the $PdCu_3$ surface is depicting Cu in orange and Pd in blue color, where binding of the intermediate with Cu or Pd atoms is marked. The reaction diagrams for all the pathways analyzed in Figure **6.20a** and **6.20b** is presented in **Figure 6.22-6.24**. Detailed binding geometry of the intermediates is available in later figures (**Figure 6.24-6.34**). Energy values mentioned at the transition state is the estimated activation energy of the intrinsic reaction step. The important role of Pd alloying on Cu is highlighted in the coordination environment for CO adsorption on the (d) $PdCu_3$ (111) and (e) $PdCu_3$ (100) facets.

However, on the reaction diagram (**Figure 6.20c**), the TS energy for *COH dissociation lies at the maximum with respect to the reference on both the surfaces, suggesting this to be a likely rate determining step in C_{2+} alcohol synthesis. **Figure 6.25** is showing corresponding Gibbs free energy diagram at an overpotential of -0.8V, where also a similar trend in energies of the key intermediates and TS structures are observed, suggesting the possibility of the same rate-limiting step in the range of overpotential studied. **Figure 6.21a** is showing the IS and TS structures of *COH dissociation steps. One may observe an ensemble of 4 surface atoms (2 Cu and 2 Pd) interacting with adsorbed *COH species on the (100) surface, while this ensemble is formed with 3 atoms (2 Cu and 1 Pd) on (111). The striking difference in the number of Pd atoms involved in the interaction with *COH intermediate, leads to the difference in calculated activation energies for the C-O bond dissociation step. Greater the number of Pd atoms involved in interaction, lesser is the activation energy of C-O bond dissociation, as observed in the case of (100) versus (111) surfaces of $PdCu_3$ (160 kJ/mol versus to 260.5 kJ/mol respectively). Since Pd is actively participating in cleaving the C-O bond, the d-band center of Pd on the $PdCu_3$ (100) and (111) surfaces are estimated and this is shown in the partial density of states (PDOS) plot (**Figure 6.21b**). The d-band center of Pd varies from -2.49 eV in $PdCu_3$ (111) to -2.01 eV in $PdCu_3$ (100) with respect to the Fermi level. Since Pd d-band center in $PdCu_3$ (100) is significantly closer to the Fermi level, $PdCu_3$ (100) is highly reactive and strongly binding with the hydrocarbon species as compared to the (111) surface. The next important step in alcohol formation is the C-C coupling step. Adsorbed CO* species could directly insert in C* forming the backbone C-C-O* species which may act as the precursor to form ethanol.

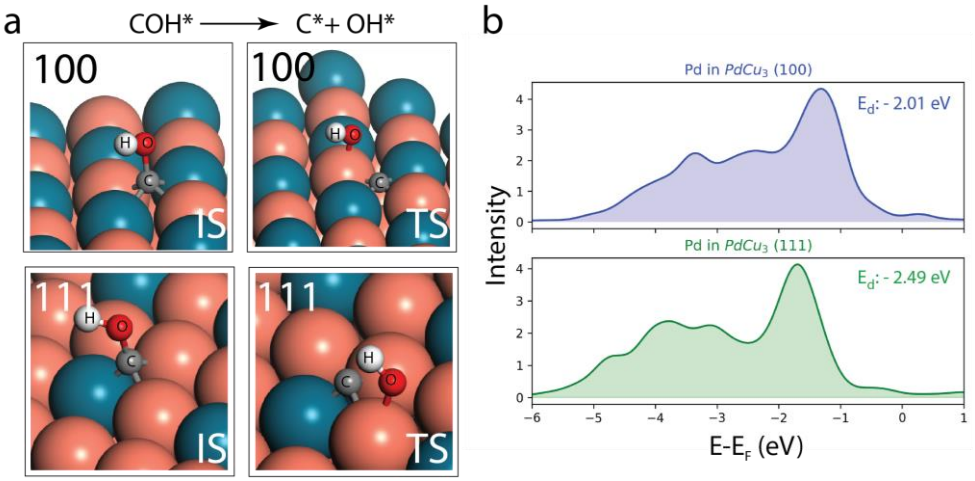

Figure 6.21. Structures of the initial state (IS) and transition state (TS) for (a) COH* dissociation and (b) changes in the d-band of Pd on the (100) and (111) surfaces of $PdCu_3$.

On the reaction energy diagram (**Figure 6.20c**), adsorbed ethanol lies at a lower energy as compared to *CCO species, suggesting exothermic proton coupled electron transfer reactions. Interestingly, activation barriers for the C-C coupling steps are estimated higher on the (100) surface (91.7 kJ/mol, **Figure 6.20b**) as compared to the (111) surface (E_a = 68.5 kJ/mol, **Figure 6.20a**). This is likely due to strongly adsorbed C* and *CO species on (100) vis-à-vis to (111), **Figure 6.20c**. Both ethanol and n-propanol are likely produced from the same intermediate, CH_3CHO*.[29] Ethanol is produced on subsequent hydrogenation of CH_3CHO*, while an insertion of CO* in CH_3CHO* followed by dehydration and hydrogenation reaction yields propanol on the surface.[29] The barriers for CO* insertion step in CH_3CHO* are marked in Figure 6c. Similar to the trend in the first CO* insertion step to C*, the (100) surface calculated a higher activation energy (153.4 kJ/mol) for the C-C coupling reaction of CH_3CHO*-CO*. In contrast, this barrier is significantly reduced on the (111) surface (99.4 kJ/mol). Interestingly, the TS structure [CH_3CHO---CO]* lies nearly at the same energy level for both the surfaces with respect to the reference in the energy diagram (**Figure 6.20c**). Thus the slight shift in selectivity in propanol formation on the two facets is likely due to the differences in the transformation of CH_3CHO*.

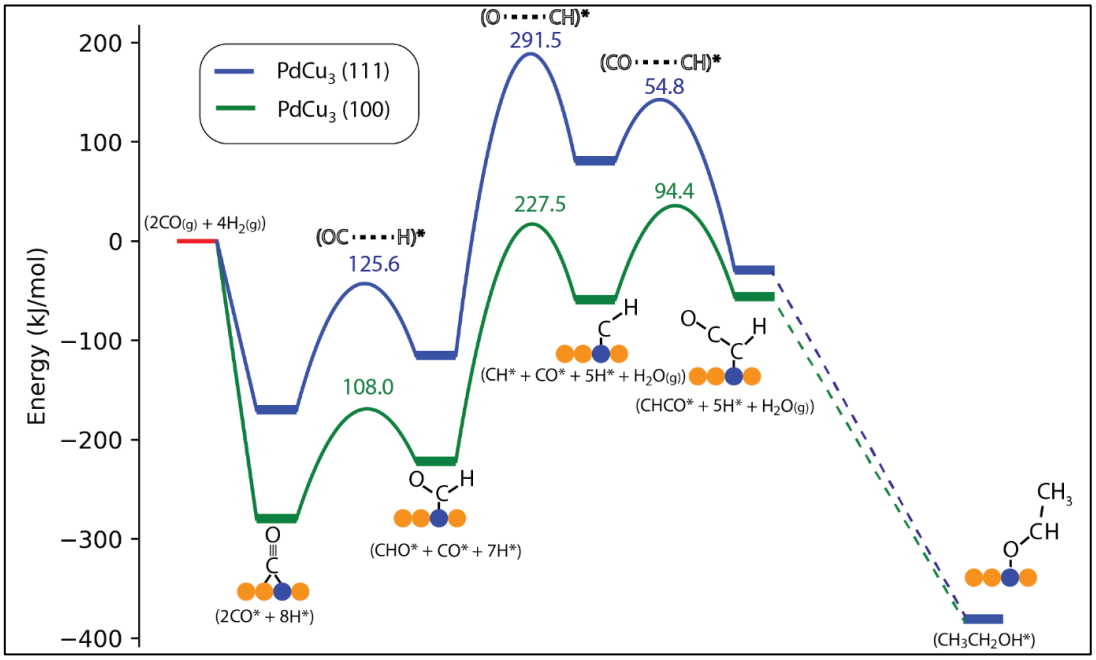

Figure 6.22. CHO dissociation pathway. The reaction diagram representing CHO dissociation pathway for ethanol formation is compared over 111 and 100 surfaces. Here, the energies in the reaction diagram are referenced to $2CO_{(g)}$ and $4H_{2(g)}$. The values over the maxima represent the activation barrier for the corresponding step. The transition state is represented over maxima with *.

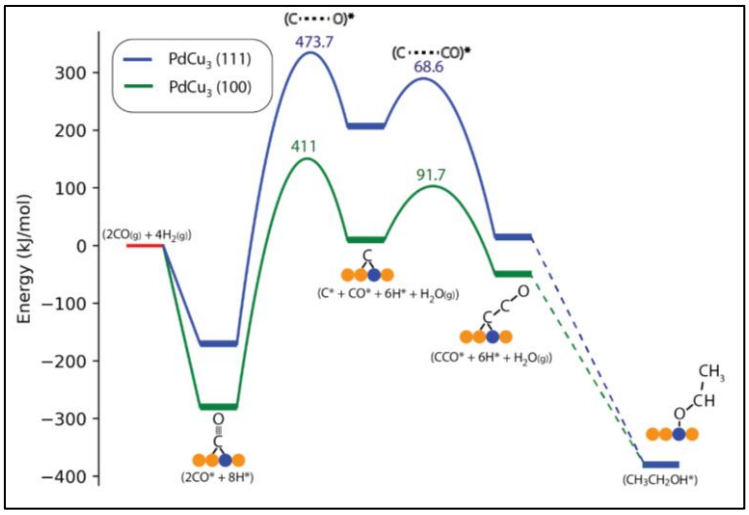

Figure 6.23. CO dissociation pathway. The reaction diagram representing CO dissociation pathway for ethanol formation is compared over 111 and 100 surfaces. Here, the energies in the reaction diagram are referenced to $2CO_{(g)}$ and $4H_{2(g)}$. The values over the maxima represent the activation barrier for the corresponding step. The transition state is represented over maxima with *.

On the contrary, ethanol selectivity is clearly decided by the C-O bond activated TS structure [C---OH]*, which lies significantly higher in energy for (111) as compared to (100). This may be the reason $PdCu_3$ cubes are producing ethanol with significantly higher selectivity as compared to spheres which contain majority (111) sites.[29]

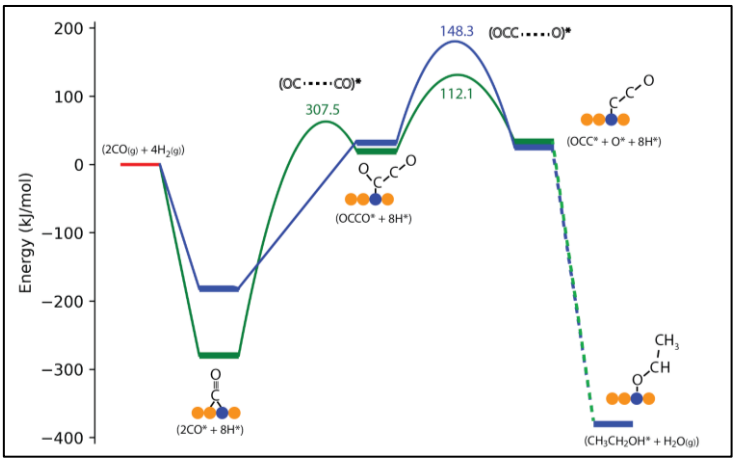

Figure 6.24. OCCO pathway. The reaction diagram representing CO-CO coupling pathway for ethanol formation is compared over 111 and 100 surfaces. Here, the energies in the reaction diagram are referenced to $2CO_{(g)}$ and $4H_{2(g)}$. The values over the maxima represent the activation barrier for the corresponding step. The transition state is represented over maxima with *.

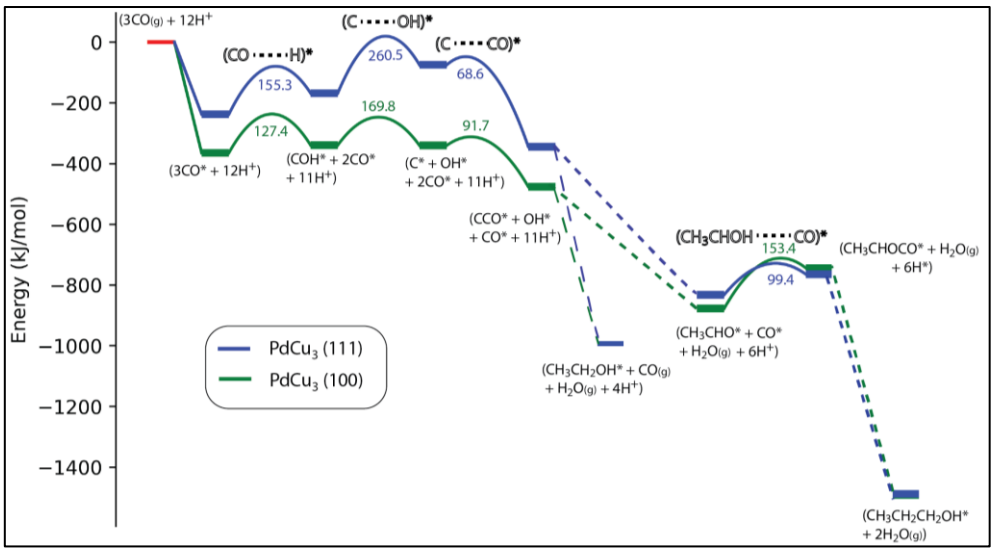

Figure 6.25. COH dissociation pathway at overpotential -0.8 V. The reaction diagram representing COH dissociation pathway for ethanol formation is compared over 111 and 100 surfaces. Here, the energies in the reaction diagram are referenced to $3CO_{(g)}$ and $12H^{+}_{(g)}$. The values over the maxima represent the activation barrier for the corresponding step. The transition state is represented over maxima with *.

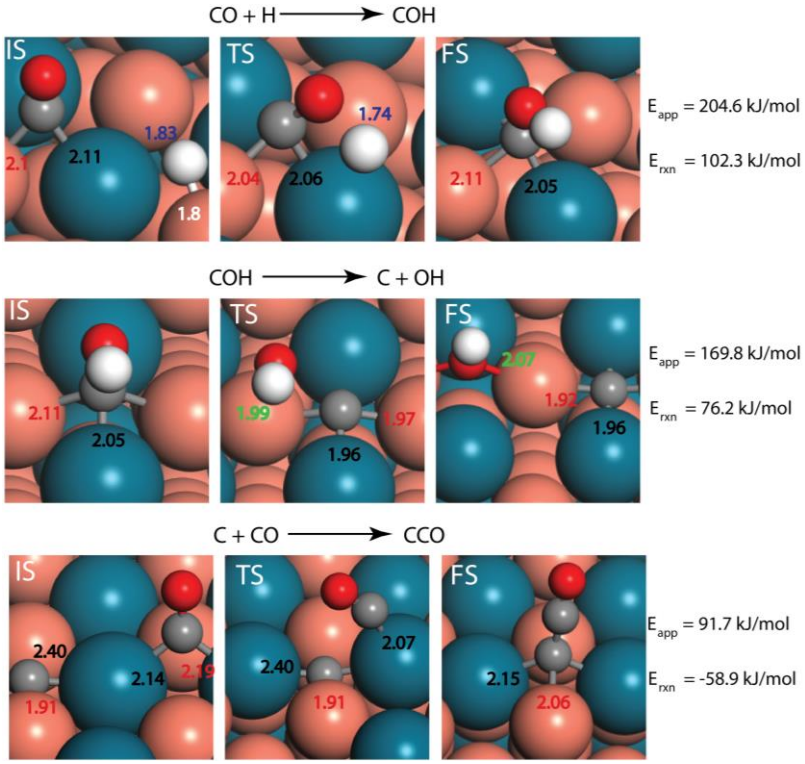

Figure 6.26. The structures of the initial (IS), transition (TS) and final (FS) state of the elementary reaction steps in COH dissociation pathway for CCO products over $PdCu_3$ (100). The numbers in red, black, blue and green represent Cu–C, Pd–C, Pd–H and Cu–O bond distances. All the bond distances are in Å.

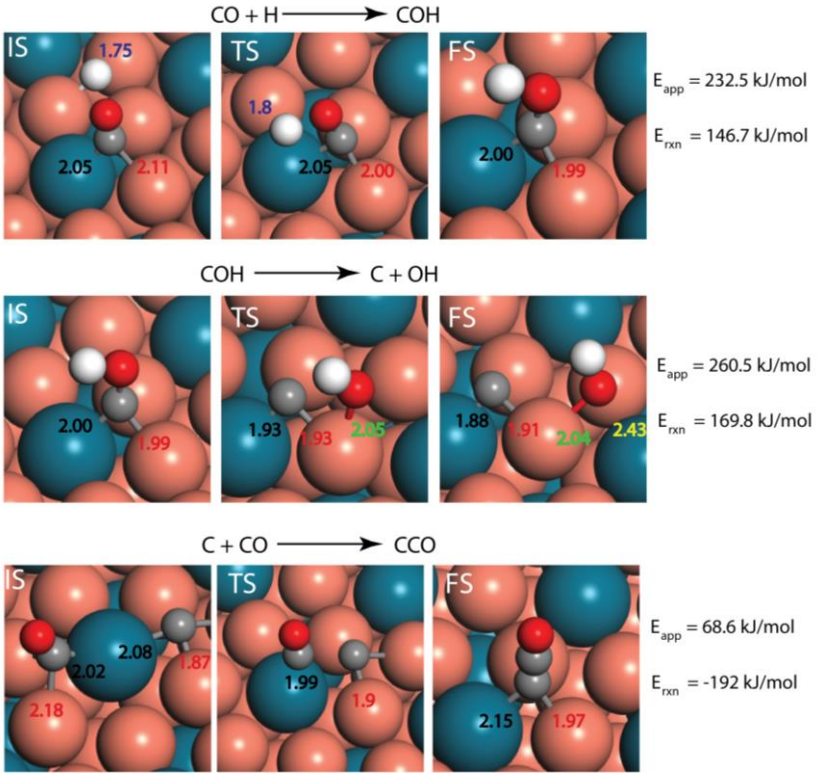

Figure 6.27. The structures of the initial (IS), transition (TS) and final (FS) state of the elementary reaction steps in COH dissociation pathway for CCO products over $PdCu_3$ (111). The numbers in red, black, blue, yellow and green represent Cu–C, Pd–C, Pd–H, Pd–O and Cu–O bond distances. All the bond distances are in Å.

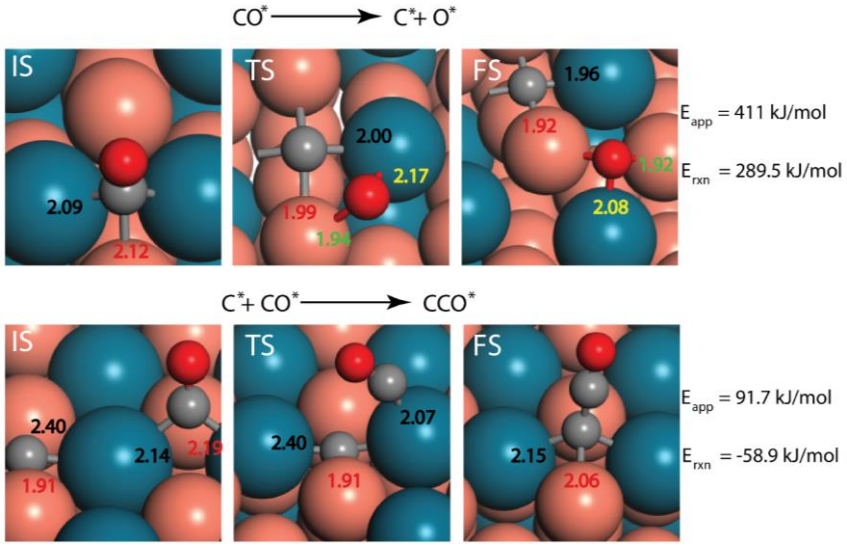

Figure 6.28. The structures of the initial (IS), transition (TS) and final (FS) state of the elementary reaction steps in CO dissociation pathway for CCO products over $PdCu_3$ (100). The numbers in red, black, yellow and green represent Cu–C, Pd–C, Pd–O and Cu–O bond distances. All the bond distances are in Å.

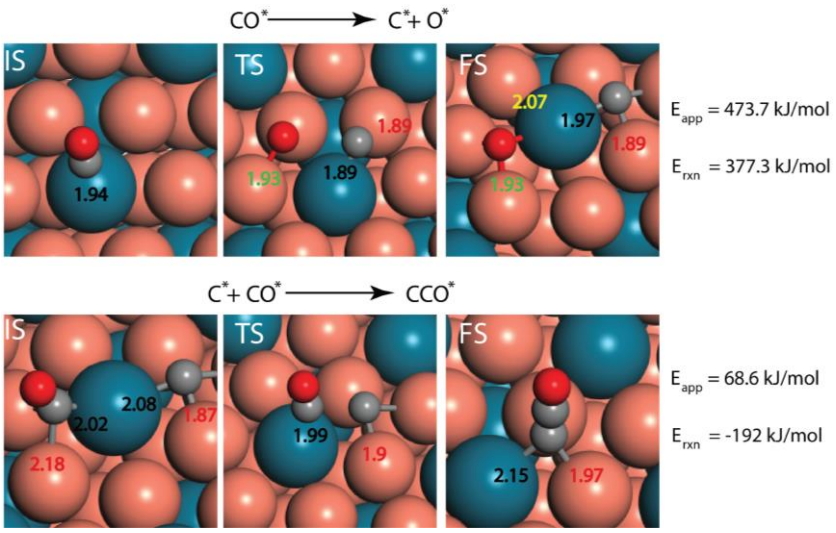

Figure 6.29. The structures of the initial (IS), transition (TS) and final (FS) state of the elementary reaction steps in CO dissociation pathway for CCO products over $PdCu_3$ (111). The numbers in red, black, yellow and green represent Cu–C, Pd–C, Pd–O and Cu–O bond distances. All the bond distances are in Å.

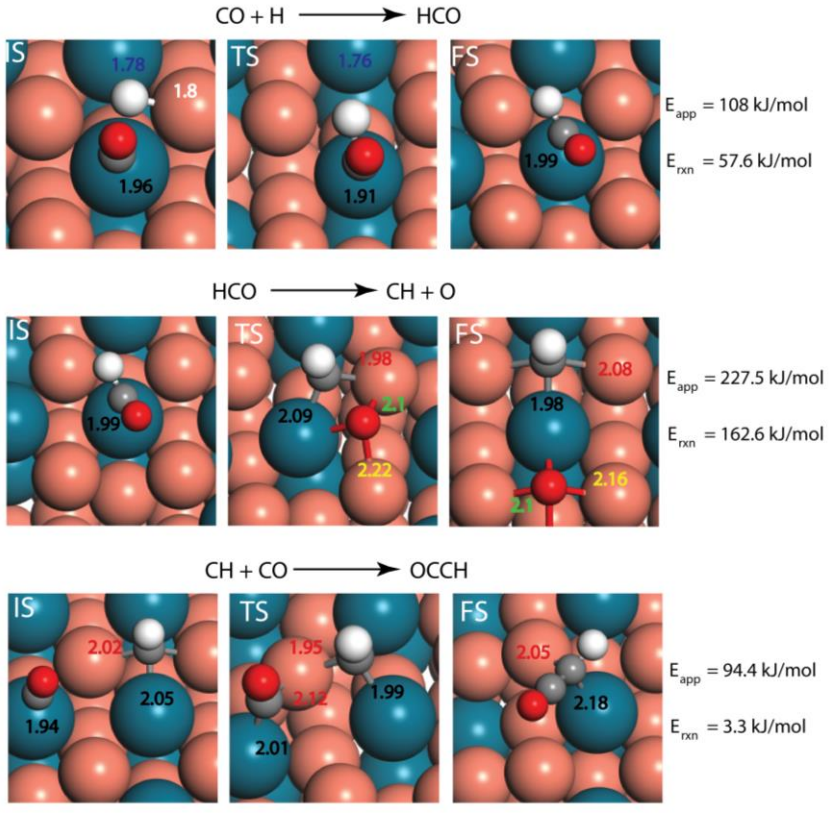

Figure 6.30. The structures of the initial (IS), transition (TS) and final (FS) state of the elementary reaction steps in HCO dissociation pathway for CCO products over $PdCu_3$ (100). The numbers in red, black, blue, yellow and green represent Cu–C, Pd–C, Pd–H, Pd–O and Cu–O bond distances. All the bond distances are in Å.

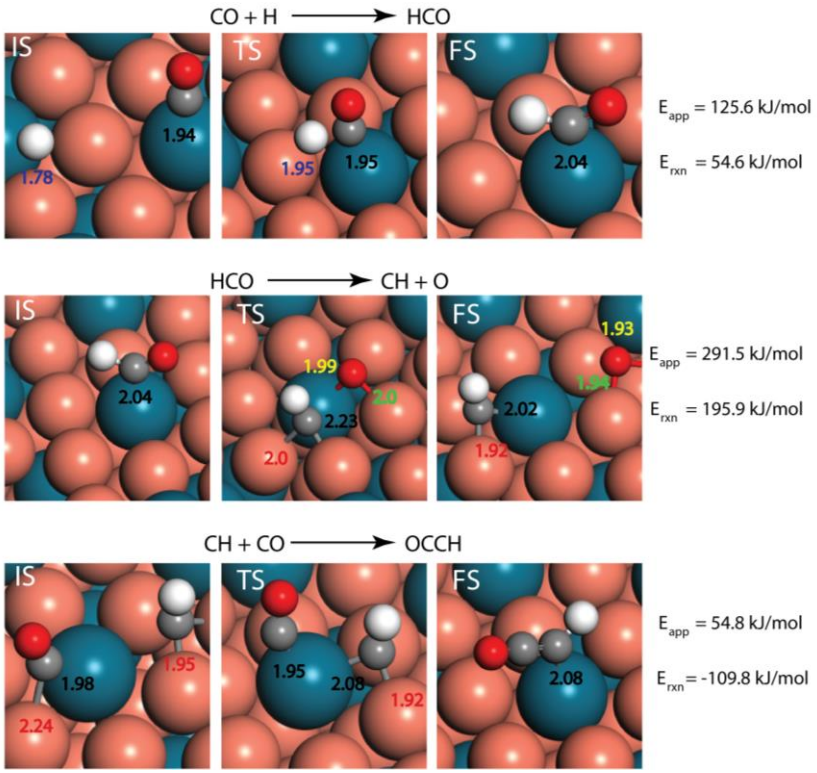

Figure 6.31. The structures of the initial (IS), transition (TS) and final (FS) state of the elementary reaction steps in HCO dissociation pathway for CCO products over $PdCu_3$ (111). The numbers in red, black, blue, yellow and green represent Cu–C, Pd–C, Pd–H, Pd–O and Cu–O bond distances. All the bond distances are in Å.

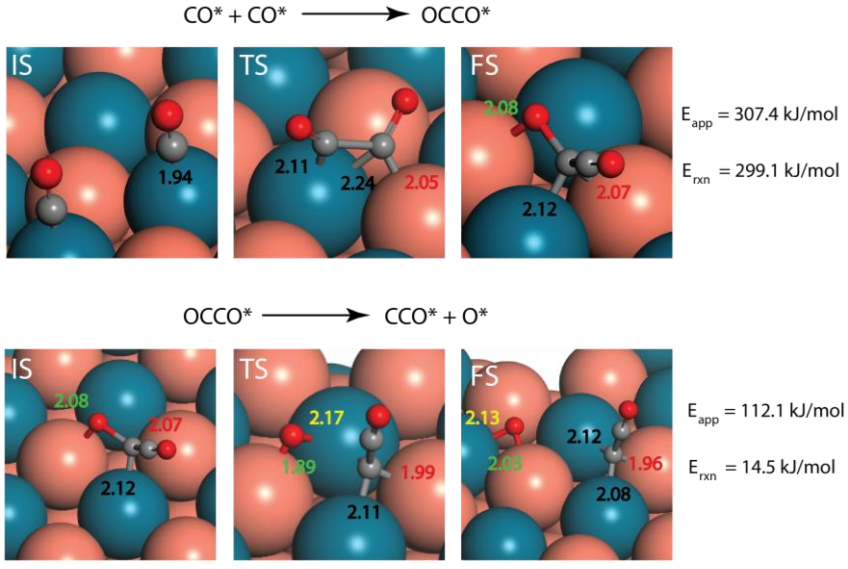

Figure 6.32. The structures of the initial (IS), transition (TS) and final (FS) state of the elementary reaction steps in CO+CO association pathway for CCO products over $PdCu_3$ (100). The numbers in red, black, yellow and green represent Cu–C, Pd–C, Pd–O and Cu–O bond distances. All the bond distances are in Å.

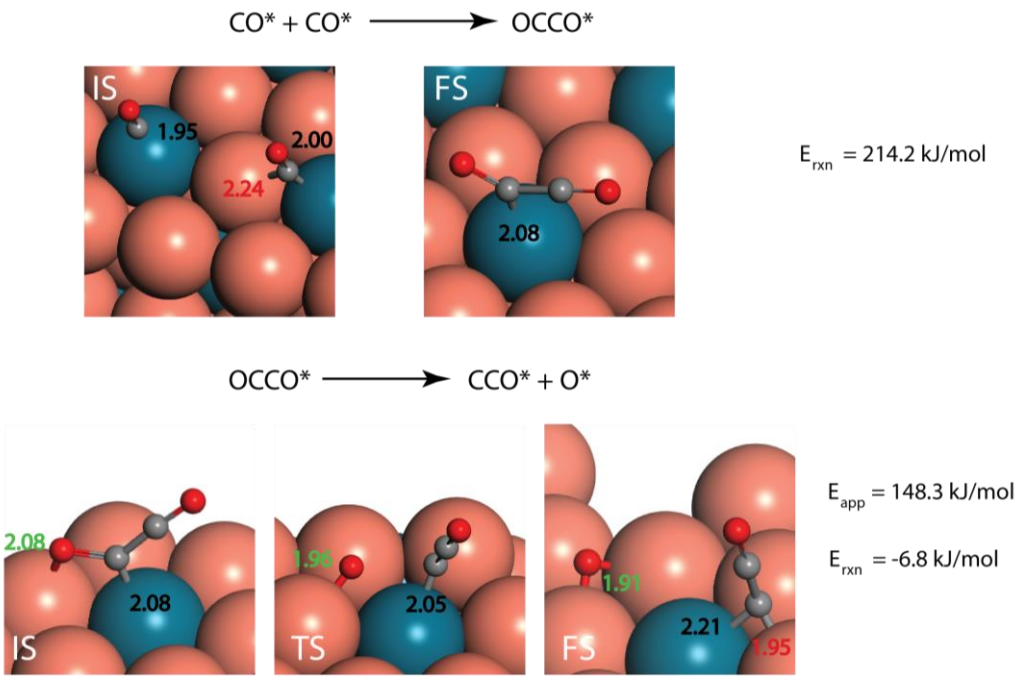

Figure 6.33. The structures of the initial (IS), transition (TS) and final (FS) state of the elementary reaction steps in CO+CO association pathway for CCO products over $PdCu_3$ (111). The numbers in red, black and green represent Cu–C, Pd–C and Cu–O bond distances. All the bond distances are in Å.

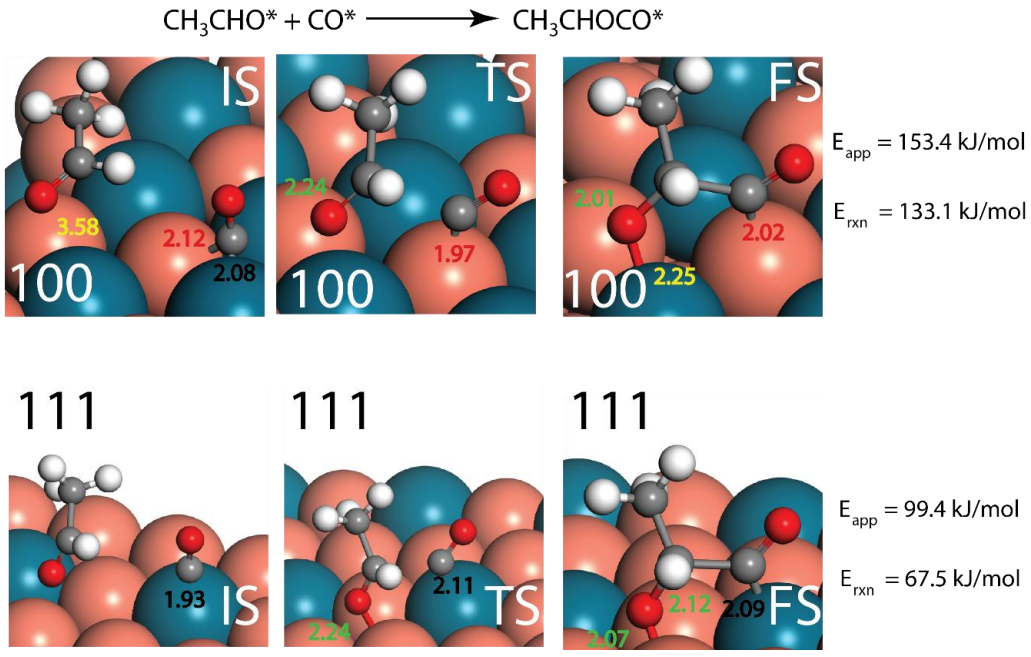

Figure 6.34. The structures of the initial (IS), transition (TS) and final (FS) state of the elementary reaction steps in C_3 product formation pathway from CH_3CHO over $PdCu_3$ (100) and (111) surfaces. The numbers in red, black, yellow and green represent Cu–C, Pd–C, Pd–O and Cu–O bond distances. All the bond distances are in Å.

6.5.4. Differential electrochemical mass spectrometry (DEMS)

We have also carried out the DEMS study to probe the local product distribution directly form the surface of the electrode. We have optimized our DEMS set-up by calibrating the instrument with respect to the composition of air (**Figure 6.35a**). The instrument was also standardized with respect to the hydrogen evolution reaction on 20% Pt/C catalyst (**Figure 6.35b-c**).

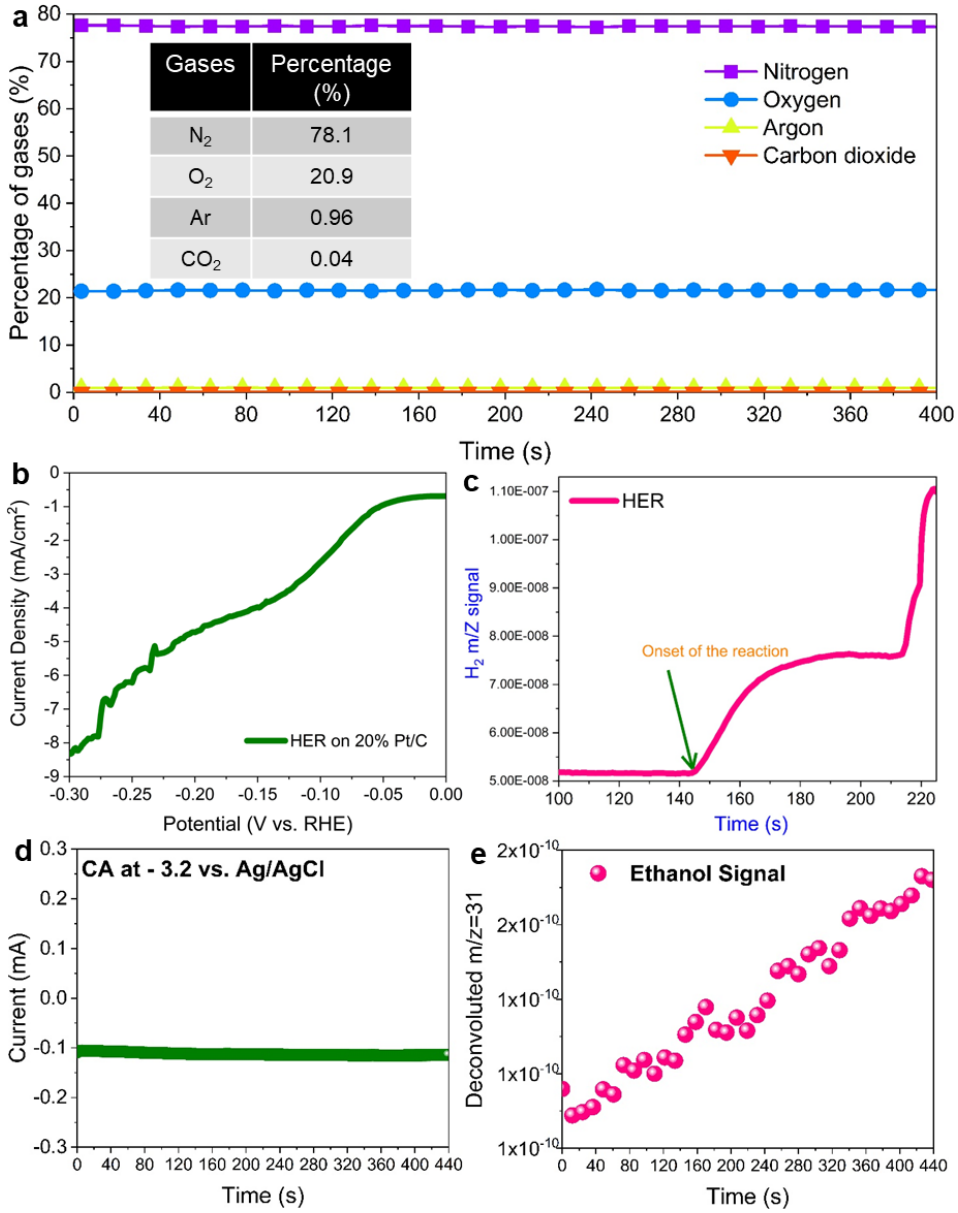

Figure 6.35. (a) Calibration different gas components present in air. (b) Linear sweep voltammogram (LSV) during hydrogen evolution reaction on 20% Pt/C in 0.1M $KHCO_3$. (C) Ion currents for m/z = 2 recorded during LSV in in 0.1M $KHCO_3$. (d) chronoamperometric (CA) study performed in CO_2 purged 0.1M $KHCO_3$ for $PdCu_3$-C catalyst. (e) Ion currents for m/z = 31 to probe ethanol signal during CA in CO_2 purged 0.1M $KHCO_3$.

From the mass ion current corresponding to m/Z=2, the electrolysis time for the formation of hydrogen that is the onset of the reaction can be calculated (**Figure 6.35c**). Similarly, eCO_2RR has also been performed on $PdCu_3$-C catalyst in CO_2 purged 0.1M $KHCO_3$ solution. Study. The m/Z=31 corresponds to the CO_2 reduced product ethanol has been monitored during the CA (**Figure 6.35d**). Time-dependent monitoring of the m/Z=31 signal clearly shows the evolution of ethanol during electrolysis process over $PdCu_3$-C (**Figure 6.35e)**. The flow of the electrolyte was kept 1ml/min during performing DEMS study in CO_2RR condition.

6.6. Conclusion

In this work, we have demonstrated a facile one-step low-temperature synthesis technique for shape control formation of $PdCu_3$ ordered intermetallic catalyst where oleylamine acts as a solvent, surfactant, and reducing agent. The $PdCu_3$-C catalyst exposing (100) facet has shown enhanced selectivity towards ethanol and n-propanol production from CO_2 compared to (111) plane exposed spherical $PdCu_3$-S. The reaction mechanism and adsorbed intermediate have been probed by in situ ATR FT-IR technique and two important intermediates such as OCH_2CH_3 and OCCO during the formation of ethanol have been detected.The in-situ EXAFS study probes the potential-dependent evolution of the local structure and coordination atmosphere of both Cu and Pd metal-site in eCO_2RR conditions. DFT studies also predict that (100) has optimum binding energy for multicarbon product formation. Finally, utilization of flow cell with GDE not only enhances the current density (>100 mA/cm^2) but produces that multicarbon, especially n-propanol in substantial quantity. This study focuses on an important aspect of facet-dependent electrochemical CO_2 reduction activity for ordered intermetallic catalysts and its mechanistic investigation through in situ studies.

6.7. References

1. Li, Y. C.; Wang, Z.; Yuan, T.; Nam, D.-H.; Luo, M.; Wicks, J.; Chen, B.; Li, J.; Li, F.; de Arquer, F. P. G.; Wang, Y.; Dinh, C.-T.; Voznyy, O.; Sinton, D.; Sargent, E. H., Binding Site Diversity Promotes CO_2 Electroreduction to Ethanol. *J. Am. Chem. Soc.* **2019,** *141*, 8584-8591.
2. Khan, T. S.; Jalid, F.; Haider, M. A., First-Principle Microkinetic Modeling of Ethanol Dehydrogenation on Metal Catalyst Surfaces in Non-oxidative Environment: Design of Bimetallic Alloys. *Top. Catal.* **2018,** *61*, 1820-1831.

3. Kuhl, K. P.; Cave, E. R.; Abram, D. N.; Jaramillo, T. F., New Insights into the Electrochemical Reduction of Carbon Dioxide on Metallic Copper Surfaces. *Energy Environ. Sci.* **2012,** *5*, 7050-7059.
4. Marakatti, V. S.; Sarma, S. C.; Joseph, B.; Banerjee, D.; Peter, S. C., Synthetically Tuned Atomic Ordering in PdCu Nanoparticles with Enhanced Catalytic Activity toward Solvent-Free Benzylamine Oxidation. *ACS Appl. Mater. Inter.* **2017,** *9*, 3602-3615.
5. Roberts, F. S.; Kuhl, K. P.; Nilsson, A., High Selectivity for Ethylene from Carbon Dioxide Reduction over Copper Nanocube Electrocatalysts. *Angew. Chem. Int. Ed.* **2015,** *54*, 5179-5182.
6. De Gregorio, G. L.; Burdyny, T.; Loiudice, A.; Iyengar, P.; Smith, W. A.; Buonsanti, R., Facet-Dependent Selectivity of Cu Catalysts in Electrochemical CO_2 Reduction at Commercially Viable Current Densities. *ACS Catal.* **2020,** *10*, 4854-4862.
7. Reske, R.; Mistry, H.; Behafarid, F.; Roldan Cuenya, B.; Strasser, P., Particle Size Effects in the Catalytic Electroreduction of CO_2 on Cu Nanoparticles. *J. Am. Chem. Soc.* **2014,** *136*, 6978-6986.
8. Chou, T.-C.; Chang, C.-C.; Yu, H.-L.; Yu, W.-Y.; Dong, C.-L.; Velasco-Vélez, J.-J.; Chuang, C.-H.; Chen, L.-C.; Lee, J.-F.; Chen, J.-M.; Wu, H.-L., Controlling the Oxidation State of the Cu Electrode and Reaction Intermediates for Electrochemical CO_2 Reduction to Ethylene. *J. Am. Chem. Soc.* **2020,** *142*, 2857-2867.
9. Bagchi, D.; Raj, J.; Singh, A. K.; Cherevotan, A.; Roy, S.; Manoj, K. S.; Vinod, C. P.; Peter, S. C., Structure-Tailored Surface Oxide on Cu–Ga Intermetallics Enhances CO_2 Reduction Selectivity to Methanol at Ultralow Potential. *Adv. Mater.* **2022,** *34*, 2109426.
10. Mariano, R. G.; McKelvey, K.; White, H. S.; Kanan, M. W., Selective Increase in CO_2 Electroreduction Activity at Grain-Boundary Surface Terminations. *Science* **2017,** *358*, 1187.
11. Chen, Z.; Wang, T.; Liu, B.; Cheng, D.; Hu, C.; Zhang, G.; Zhu, W.; Wang, H.; Zhao, Z.-J.; Gong, J., Grain-Boundary-Rich Copper for Efficient Solar-Driven Electrochemical CO_2 Reduction to Ethylene and Ethanol. *J. Am. Chem. Soc.* **2020,** *142*, 6878-6883.
12. Kim, D.; Xie, C.; Becknell, N.; Yu, Y.; Karamad, M.; Chan, K.; Crumlin, E. J.; Nørskov, J. K.; Yang, P., Electrochemical Activation of CO_2 through Atomic Ordering Transformations of AuCu Nanoparticles. *J. Am. Chem. Soc.* **2017,** *139*, 8329-8336.

13. Ren, D.; Deng, Y.; Handoko, A. D.; Chen, C. S.; Malkhandi, S.; Yeo, B. S., Selective Electrochemical Reduction of Carbon Dioxide to Ethylene and Ethanol on Copper(I) Oxide Catalysts. *ACS Catal.* **2015,** *5*, 2814-2821.
14. Kim, D.; Resasco, J.; Yu, Y.; Asiri, A. M.; Yang, P., Synergistic Geometric and Electronic Effects for Electrochemical Reduction of Carbon Dioxide Using Gold–Copper Bimetallic Nanoparticles. *Nat. Commun.* **2014,** *5*, 4948.
15. Aricò, A. S.; Bruce, P.; Scrosati, B.; Tarascon, J.-M.; van Schalkwijk, W., Nanostructured Materials for Advanced Energy Conversion and Storage Devices. *Nat. Mater.* **2005,** *4*, 366-377.
16. Rößner, L.; Armbrüster, M., Electrochemical Energy Conversion on Intermetallic Compounds: A Review. *ACS Catal.* **2019,** *9*, 2018-2062.
17. Alden, L. R.; Roychowdhury, C.; Matsumoto, F.; Han, D. K.; Zeldovich, V. B.; Abruña, H. D.; DiSalvo, F. J., Synthesis, Characterization, and Electrocatalytic Activity of PtPb Nanoparticles Prepared by Two Synthetic Approaches. *Langmuir* **2006,** *22*, 10465-10471.
18. Chai, G. S.; Yoon, S. B.; Yu, J.-S.; Choi, J.-H.; Sung, Y.-E., Ordered Porous Carbons with Tunable Pore Sizes as Catalyst Supports in Direct Methanol Fuel Cell. *J. Phys. Chem. B* **2004,** *108*, 7074-7079.
19. Takasu, Y.; Fujiwara, T.; Murakami, Y.; Sasaki, K.; Oguri, M.; Asaki, T.; Sugimoto, W., Effect of Structure of Carbon-Supported PtRu Electrocatalysts on the Electrochemical Oxidation of Methanol. *J. Electrochem. Soc.* **2000,** *147*, 4421.
20. Kodiyath, R.; Ramesh, G. V.; Koudelkova, E.; Tanabe, T.; Ito, M.; Manikandan, M.; Ueda, S.; Fujita, T.; Umezawa, N.; Noguchi, H.; Ariga, K.; Abe, H., Promoted C–C bond Cleavage over Intermetallic $TaPt_3$ Catalyst toward Low-Temperature Energy Extraction from Ethanol. *Energy Environ. Sci.* **2015,** *8*, 1685-1689.
21. Cui, Z.; Chen, H.; Zhou, W.; Zhao, M.; DiSalvo, F. J., Structurally Ordered Pt_3Cr as Oxygen Reduction Electrocatalyst: Ordering Control and Origin of Enhanced Stability. *Chem. Mater.* **2015,** *27*, 7538-7545.
22. Huang, J.; Buonsanti, R., Colloidal Nanocrystals as Heterogeneous Catalysts for Electrochemical CO_2 Conversion. *Chem. Mater.* **2019,** *31*, 13-25.
23. Hori, Y.; Murata, A.; Takahashi, R., Formation of Hydrocarbons in the Electrochemical Reduction of Carbon Dioxide at a Copper Electrode in Aqueous Solution. *J. Chem. Soc., Faraday Trans. 1* **1989,** *85*, 2309-2326.

24. Lv, K.; Fan, Y.; Zhu, Y.; Yuan, Y.; Wang, J.; Zhu, Y.; Zhang, Q., Elastic Ag-Anchored N-Doped Graphene/Carbon Foam for the Selective Electrochemical Reduction of Carbon Dioxide to Ethanol. *J Mater. Chem. A* **2018,** *6*, 5025-5031.
25. Ren, D.; Gao, J.; Pan, L.; Wang, Z.; Luo, J.; Zakeeruddin, S. M.; Hagfeldt, A.; Grätzel, M., Atomic Layer Deposition of ZnO on CuO Enables Selective and Efficient Electroreduction of Carbon Dioxide to Liquid Fuels. *Angew. Chem. Int. Ed.* **2019,** *58*, 15036-15040.
26. Luo, M.; Wang, Z.; Li, Y. C.; Li, J.; Li, F.; Lum, Y.; Nam, D.-H.; Chen, B.; Wicks, J.; Xu, A.; Zhuang, T.; Leow, W. R.; Wang, X.; Dinh, C.-T.; Wang, Y.; Wang, Y.; Sinton, D.; Sargent, E. H., Hydroxide Promotes Carbon Dioxide Electroreduction to Ethanol on Copper via Tuning of Adsorbed Hydrogen. *Nat. Commun.* **2019,** *10*, 5814.
27. Schulz, K. G.; Riebesell, U.; Rost, B.; Thoms, S.; Zeebe, R. E., Determination of the Rate Constants for the Carbon Dioxide to Bicarbonate Inter-Conversion in pH-Buffered Seawater Systems. *Mar. Chem.* **2006,** *100*, 53-65.
28. König, M.; Vaes, J.; Klemm, E.; Pant, D., Solvents and Supporting Electrolytes in the Electrocatalytic Reduction of CO_2. *iScience* **2019,** *19*, 135-160.
29. Guzmán, H.; Russo, N.; Hernández, S., CO_2 Valorisation towards Alcohols by Cu-Based Electrocatalysts: Challenges and Perspectives. *Green Chem.* **2021,** *23*, 1896-1920.
30. Peng, C.; Luo, G.; Zhang, J.; Chen, M.; Wang, Z.; Sham, T.-K.; Zhang, L.; Li, Y.; Zheng, G., Double Sulfur Vacancies by Lithium Tuning Enhance CO_2 Electroreduction to n-Propanol. *Nat. Commun.* **2021,** *12*, 1580.
31. Peterson, A. A.; Abild-Pedersen, F.; Studt, F.; Rossmeisl, J.; Nørskov, J. K., How Copper Catalyzes the Electroreduction of Carbon Dioxide into Hydrocarbon Fuels. *Energy Environ. Sci.* **2010,** *3*, 1311-1315.
32. Xu, H.; Rebollar, D.; He, H.; Chong, L.; Liu, Y.; Liu, C.; Sun, C.-J.; Li, T.; Muntean, J. V.; Winans, R. E.; Liu, D.-J.; Xu, T., Highly Selective Electrocatalytic CO_2 Reduction to Ethanol by Metallic Clusters Dynamically Formed from Atomically Dispersed Copper. *Nat. Energy* **2020,** *5*, 623-632.
33. Zhuang, T.-T.; Liang, Z.-Q.; Seifitokaldani, A.; Li, Y.; De Luna, P.; Burdyny, T.; Che, F.; Meng, F.; Min, Y.; Quintero-Bermudez, R.; Dinh, C. T.; Pang, Y.; Zhong, M.; Zhang, B.; Li, J.; Chen, P.-N.; Zheng, X.-L.; Liang, H.; Ge, W.-N.; Ye, B.-J.; Sinton, D.; Yu, S.-H.; Sargent, E. H., Author Correction: Steering Post-C–C Coupling Selectivity

Enables High Efficiency Electroreduction of Carbon Dioxide to Multi-Carbon Alcohols. *Nat. Catal.* **2022,** *5*, 578-579.

34. Porwal, G.; Gupta, S.; Sreedhala, S.; Elizabeth, J.; Khan, T. S.; Haider, M. A.; Vinod, C. P., Mechanistic Insights into the Pathways of Phenol Hydrogenation on Pd Nanostructures. *ACS Sustain. Chem. Eng.* **2019,** *7*, 17126-17136.
35. Kresse, G.; Furthmüller, J., Efficiency of ab-Initio Total Energy Calculations for Metals and Semiconductors Using a Plane-Wave Basis Set. *Comput. Mater. Sci.* **1996,** *6*, 15-50.
36. Hammer, B.; Hansen, L. B.; Nørskov, J. K., Improved Adsorption Energetics Within Density-Functional Theory Using Revised Perdew-Burke-Ernzerhof Functionals. *Phys. Rev. B* **1999,** *59*, 7413-7421.
37. Feynman, R. P., Forces in Molecules. *Phys. Rev.* **1939,** *56*, 340-343.
38. Pulay, P., Convergence Acceleration of Iterative Sequences. the Case of scf Iteration. *Chem. Phys. Lett.* **1980,** *73*, 393-398.
39. Henkelman, G.; Uberuaga, B. P.; Jónsson, H., A Climbing Image Nudged Elastic Band Method for Finding Saddle Points and Minimum Energy Paths. *J. Chem. Phys.* **2000,** *113*, 9901-9904.
40. Wang, C.; Chen, D. P.; Sang, X.; Unocic, R. R.; Skrabalak, S. E., Size-Dependent Disorder–Order Transformation in the Synthesis of Monodisperse Intermetallic PdCu Nanocatalysts. *ACS Nano* **2016,** *10*, 6345-6353.
41. Ashly, P. C.; Sarkar, S.; Sarma, S. C.; Kaur, K.; Gautam, U. K.; Peter, S. C., Compressive Strain Induced by Multiple Phase Distribution and Atomic Ordering in PdCu Nanoparticles to Enhanced Ethanol Oxidation Reaction Performance. *J. Power Sources* **2021,** *506*, 230168.
42. Jana, R.; Bhim, A.; Bothra, P.; Pati, S. K.; Peter, S. C., Electrochemical Dealloying of $PdCu_3$ Nanoparticles to Achieve Pt-like Activity for the Hydrogen Evolution Reaction. *ChemSusChem* **2016,** *9*, 2922-2927.
43. Ma, S.; Sadakiyo, M.; Heima, M.; Luo, R.; Haasch, R. T.; Gold, J. I.; Yamauchi, M.; Kenis, P. J. A., Electroreduction of Carbon Dioxide to Hydrocarbons Using Bimetallic Cu–Pd Catalysts with Different Mixing Patterns. *J. Am. Chem. Soc.* **2017,** *139*, 47-50.
44. Yang, H.; Ogawa, T.; Hasegawa, D.; Takahashi, M., Synthesis and Magnetic Properties of Monodisperse Magnetite Nanocubes. *J. Appl. Phys.* **2008,** *103*, 07D526.
45. Xiao, J.; Qi, L., Surfactant-Assisted, Shape-Controlled Synthesis of Gold Nanocrystals. *Nanoscale* **2011,** *3*, 1383-1396.

46. Xia, B. Y.; Wu, H. B.; Wang, X.; Lou, X. W., One-Pot Synthesis of Cubic $PtCu_3$ Nanocages with Enhanced Electrocatalytic Activity for the Methanol Oxidation Reaction. *J. Am. Chem. Soc.* **2012,** *134*, 13934-13937.
47. Dinh, C.-T.; Burdyny, T.; Kibria, M. G.; Seifitokaldani, A.; Gabardo, C. M.; García de Arquer, F. P.; Kiani, A.; Edwards, J. P.; De Luna, P.; Bushuyev, O. S.; Zou, C.; Quintero-Bermudez, R.; Pang, Y.; Sinton, D.; Sargent, E. H., CO_2 Electroreduction to Ethylene via Hydroxide-Mediated Copper Catalysis at an Abrupt Interface. *Science* **2018,** *360*, 783.
48. Niu, Z.-Z.; Chi, L.-P.; Liu, R.; Chen, Z.; Gao, M.-R., Rigorous Assessment of CO_2 Electroreduction Products in a Flow Cell. *Energy Environ. Sci.* **2021,** *14*, 4169-4176.
49. Innocent, B.; Pasquier, D.; Ropital, F.; Hahn, F.; Léger, J. M.; Kokoh, K. B., FTIR Spectroscopy Study of the Reduction of Carbon Dioxide on Lead Electrode in Aqueous Medium. *Appl. Catal. B* **2010,** *94*, 219-224.
50. Zhu, S.; Jiang, B.; Cai, W.-B.; Shao, M., Direct Observation on Reaction Intermediates and the Role of Bicarbonate Anions in CO_2 Electrochemical Reduction Reaction on Cu Surfaces. *J. Am. Chem. Soc.* **2017,** *139*, 15664-15667.
51. Mistry, B. J. C., A handbook of spectroscopic data. **2009**.
52. Nur Hossain, M.; Chen, S.; Chen, A., Thermal-Assisted Synthesis of Unique Cu Nanodendrites for the Efficient Electrochemical Reduction of CO_2. *Appl. Catal. B* **2019,** *259*, 118096.
53. Wuttig, A.; Liu, C.; Peng, Q.; Yaguchi, M.; Hendon, C. H.; Motobayashi, K.; Ye, S.; Osawa, M.; Surendranath, Y., Tracking a Common Surface-Bound Intermediate during CO_2-to-Fuels Catalysis. *ACS Cent. Sci.* **2016,** *2*, 522-528.
54. Katayama, Y.; Nattino, F.; Giordano, L.; Hwang, J.; Rao, R. R.; Andreussi, O.; Marzari, N.; Shao-Horn, Y., An In Situ Surface-Enhanced Infrared Absorption Spectroscopy Study of Electrochemical CO_2 Reduction: Selectivity Dependence on Surface C-Bound and O-Bound Reaction Intermediates. *J. Phys. Chem. C* **2019,** *123*, 5951-5963.
55. Wang, P.; Yang, H.; Tang, C.; Wu, Y.; Zheng, Y.; Cheng, T.; Davey, K.; Huang, X.; Qiao, S.-Z., Boosting Electrocatalytic CO_2–to–Ethanol Production via Asymmetric C–C Coupling. *Nat. Commun.* **2022,** *13*, 3754.
56. Bagchi, D.; Sarkar, S.; Singh, A. K.; Vinod, C. P.; Peter, S. C., Potential- and Time-Dependent Dynamic Nature of an Oxide-Derived PdIn Nanocatalyst during Electrochemical CO_2 Reduction. *ACS Nano* **2022,** *16*, 6185-6196.

57. Shah, A. H.; Wang, Y.; Hussain, S.; Akbar, M. B.; Woldu, A. R.; Zhang, X.; He, T., New Aspects of C_2 Selectivity in Electrochemical CO_2 Reduction over Oxide-Derived Copper. *PCCP* **2020,** *22*, 2046-2053.
58. Mondal, S.; Bagchi, D.; Riyaz, M.; Sarkar, S.; Singh, A. K.; Vinod, C. P.; Peter, S. C., In Situ Mechanistic Insights for the Oxygen Reduction Reaction in Chemically Modulated Ordered Intermetallic Catalyst Promoting Complete Electron Transfer. *J. Am. Chem. Soc.* **2022,** *144*, 11859-11869.
59. Arán-Ais, R. M.; Rizo, R.; Grosse, P.; Algara-Siller, G.; Dembélé, K.; Plodinec, M.; Lunkenbein, T.; Chee, S. W.; Cuenya, B. R., Imaging Electrochemically Synthesized Cu_2O Cubes and their Morphological Evolution under Conditions Relevant to CO_2 Electroreduction. *Nat. Commun.* **2020,** *11*, 3489.
60. Lin, S.-C.; Chang, C.-C.; Chiu, S.-Y.; Pai, H.-T.; Liao, T.-Y.; Hsu, C.-S.; Chiang, W.-H.; Tsai, M.-K.; Chen, H. M., Operando Time-Resolved X-Ray Absorption Spectroscopy Reveals the Chemical Nature Enabling Highly Selective CO_2 Reduction. *Nat. Commun.* **2020,** *11*, 3525.
61. K, R.; N, P.; C.P, V.; Khan, T. S.; Gupta, S.; Haider, M. A.; Jagadeesan, D., CuO as a Reactive and Reusable Reagent for the Hydrogenation of Nitroarenes. *Appl. Catal. B-Environ.* **2021,** *297*, 120417.
62. Roy, S.; Bagchi, D.; Dheer, L.; Sarma, S. C.; Rajaji, V.; Narayana, C.; Waghmare, U. V.; Peter, S. C., Mechanistic Insights into the Promotional Effect of Ni Substitution in Non-Noble Metal Carbides for Highly Enhanced Water Splitting. *Appl. Catal. B* **2021,** *298*, 120560.
63. Peng, L.; Karube, K.; Taguchi, Y.; Nagaosa, N.; Tokura, Y.; Yu, X., Dynamic Transition of Current-Driven Single-Skyrmion Motion in a Room-Temperature Chiral-Lattice Magnet. *Nat. Commun.* **2021,** *12*, 6797.

SUMMARY & FUTURE OUTLOOK

The inspiration of this thesis is to develop cost-effective, stable, and scalable transition metal-based electrocatalysts for the efficient conversion of CO_2 to useful fuels and chemicals. This strategy can be expanded in the broader field of the electrochemistry community to design sustainable catalyst materials for other electrochemical processes as well. A plethora of catalysts were synthesized by various synthesis techniques like solid-state high temperature, ball milling process, solvothermal synthesis, colloidal synthesis, multi-step chemical reduction process, etc. In this work, different solid-state catalyst materials like monometallic, bimetallic, alloy, intermetallic, metal-oxide, and metal carbide have been properly synthesized. All of these materials have been well-characterized by different classical and advanced spectroscopic and microscopic techniques. The evaluation of the electrocatalytic performances has been examined by the utilization of both traditional H-type cell as well as the flow cell in the gas diffusion configuration to enhance the catalytic performance and the current density. We have also tried to unravel the reaction mechanism and to determine the active site by various advanced in situ spectroscopic techniques like ATR-FTIR, Raman, XAFS, and DEMS. With the help of all of these studies, we have not only obtained the idea about the real-time electronic and structural evolution of the catalyst, we could also be able to identify underlying structure-property relationships which can help in designing more efficient catalysts in the future.

The thesis is divided into 6 chapters, with Chapter 1 discussing environmental issues associated with CO_2 emissions and its probable solutions to overcome these issues. Chapters 2-6 mainly focus on the discovery of novel solid-state materials as the efficient electrocatalysts for the conversion of CO_2 to selective production of CO (chapter 2), methanol (chapter 3), acetic acid (chapter 4), ethanol and ethylene (chapter 5) and n-propanol (chapter 6). In the second chapter, the dynamic interface made by In_2O_3 and PdIn alloy has been investigated during eCO_2RR. One interesting observation has been found that the product selectivity towards CO not only depends on the applied potential but also dependent on the time of electrolysis. With the help of XRD, XAFS, XPS, and Raman spectroscopic techniques, it has been concluded that In_2O_3 acts as protecting oxide layer for PdIn alloy and restricts the surface oxidation of Pd. The production of CO has been improved by the optimization of flow cell parameters in gas diffusion electrode configuration, and a higher current density has been achieved.

In the next chapter, for the first time, we have explored two entirely new ordered intermetallic catalysts, Cu_9Ga_4 and $CuGa_2$, for the eCO_2RR. In the combination of in situ XAFS, FT-IR, and XPS, it has been proven that the surface gallium oxide (Ga_2O_3)is the crucial active

site for the production of methanol via eCO_2RR. The unique 2D flake-type structure of $CuGa_2$ has promoted the formation of higher amount of surface Ga_2O_3, which is responsible for the higher catalytic performance (FE of methanol: 77.26%) than that of Cu_9Ga_4, which has 3D spherical morphology hindering the surface oxide formation.

In the fourth chapter, we report a useful strategy to stabilize the copper single-site tungsten carbide (WC) nanoparticles embedded on N-doped graphitic carbon (NGC), which has shown excellent activity towards the formation of acetic acid at significantly lower potential during eCO_2RR. The presence of an atomically dispersed Cu site ($Cu_1^{\delta+}$) greatly promotes CO_2 activation by adsorbing H_2O on the $Cu_1^{\delta+}$ site and adsorbing CO_2 on the neighboring W site. On the other hand, the H_2O adsorption and CO_2 activation property have been drastically reduced in the higher loading of Cu into carbide WC@NGC catalyst due to the lowering of the oxidation state of Cu. Advanced electronic microscopic and in situ spectroscopic techniques provide detailed information about the potential-dependent structure and the catalytic property.

In the fifth chapter, we have systematically synthesized different combinations of Pd-Cu-based catalysts, viz. ordered intermetallic, alloy, and bimetallic, by a simple solution process synthesis approach and studied their eCO_2RR activity. It has been found that the ordered intermetallic catalyst (PdCu-IM) selectively produces C1 products like CO, HCOOH, and CH_3OH. On the other hand, alloy and bimetallic catalysts could convert CO_2 to a multi-carbon product like ethanol and ethylene. In situ Raman spectroscopy, in situ XAFS, along with computational study, we have unravelled the reaction mechanism for the coupling process as well as the potential dependent active site for the PdCu-catalyst. Considering all the plausible pathways, the PdCu-BM surface (where selectivity is most towards multi-carbon production) facilitates the coupling process by lowering the activation energy of the *OC-CHO intermediate, which is further converted to a high-energy product like ethanol.

In the continuation of the previous work, we have demonstrated a unique strategy for the synthesis of ordered intermetallic $PdCu_3$ nanocube ($PdCu_3$-C) and $PdCu_3$ nanosphere ($PdCu_3$-S) by simply changing the solvent ratio of oleylamine and oleic acid without using any strong reducing agent. The ordered $PdCu_3$-C catalyst having (100) exposed plane has higher multi-carbon selectivity than $PdCu_3$-S where (111) plane is exposed. With the help of flow cell in gas diffusion electrode configuration, we could be able to achieve FE of n-propanol is observed 17.66% with a formation rate of 42.72 $mmolh^{-1}cm^{-2}mg^{-2}$ on $PdCu_3$-C catalyst with the overall current density of 125.6 mA/cm^2, which is found to be higher than most of the n-propanol from CO_2 producing catalysts reported in the literature. The evolution of the active

sites or charge transfer kinetics or the in situ mechanistic investigations are also one of those extremely important findings of the present work, which has not been explored in the literature. From the computational study, it has been found that the C-O dissociation step on the $PdCu_3$ surface is the most crucial step for the further coupling process and formed n-propanol.

In conclusion, this thesis has succeeded in the development of a variety of transition metal-based electrocatalysts, which could able to convert selectivity to various useful fuels and chemicals. Summary of the work presented in this thesis schematically given in **Figure 7.1.** Throughout the thesis, a plethora of fundamental concepts of tuning the catalytic property has been used, like controlling metal-surface oxide, alloying, structural ordering, the role of a single atomic site and the effect of exposed facet. The progress of CO_2 reduction research is strongly dependent on the design of efficient catalysts to achieve higher activity and selectivity towards the desired product. In view of this, the content of this thesis can be used as a handbook for those who are working in this area. Not only the design of the catalyst, the systematic developments of the flow cell reactor along with gas diffusion electrode design can also be very useful for future CO_2 electroreduction technology. The standardization and optimization of the various component involved in the in situ studies like ATR-FTIR, Raman, XAFS, and DEMS could be beneficial for understanding the real-time picture of the reaction mechanism and the active sites involved in eCO_2RR. Overall, the strategies used in this thesis may be exploited for developing product selective, sustainable catalysts for the commercial CO_2 conversion technology, which can really find a solution to the global issues related to energy and the environment.

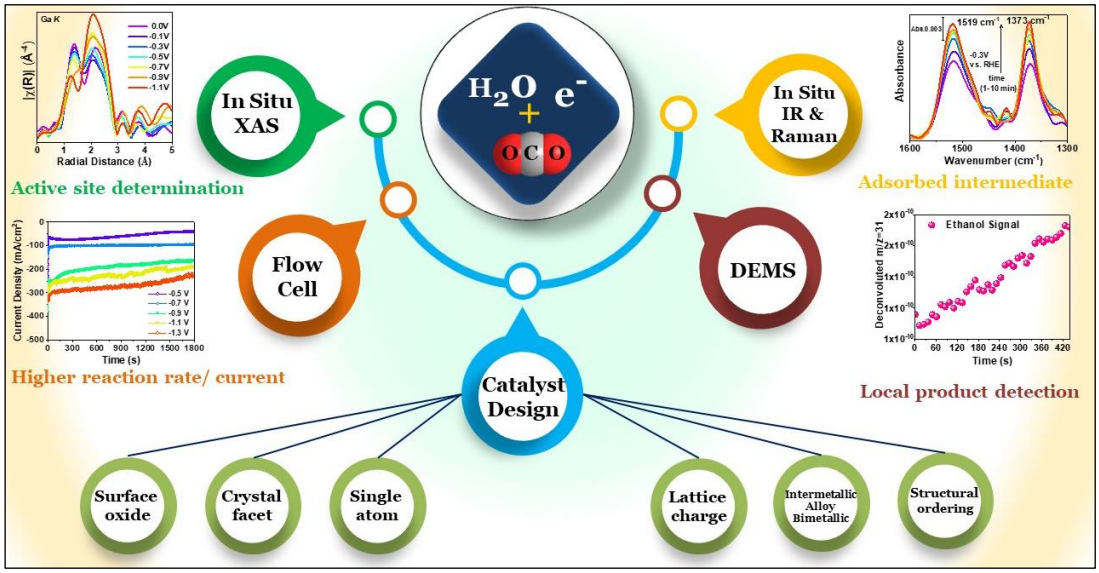

Figure 7.1. Schematic illustration describing the contents of the thesis.

LIST OF PUBLICATIONS

▪ Published

1. Structure-Tailored Surface Oxide on Cu–Ga Intermetallics Enhances CO_2 Reduction Selectivity to Methanol at Ultralow Potential. **D. Bagchi**, J. Raj, A. K. Singh, A. Cherevotan, S. Roy, K. S. Manoj, C. P. Vinod and S. C. Peter, *Adv. Mater.*, 2022, **34**, 2109426.
2. Potential- and Time-Dependent Dynamic Nature of an Oxide-Derived PdIn Nanocatalyst during Electrochemical CO_2 Reduction. **D. Bagchi**, S. Sarkar, A. K. Singh, C. P. Vinod and S. C. Peter, *ACS Nano*, 2022, **16**, 6185–6196.
3. Chemical Modulation of Active Sites in Ordered Pd_2Ge Lattice Triggering Kinetics and Complete Electron Transfer Mechanism of Oxygen Reduction Reaction. S. Mondal, **D. Bagchi**, M. Riyaz, S. Sarkar, A. K. Singh, C. P. Vinod, S. C. Peter. *J. Am. Chem Soc*., 2022, **144**, 11859–11869.
4. An Integrated Material Design and Catalytic Perspective on Electrochemical CO_2 Reduction. **D. Bagchi**, S. Roy, S. C. Sarma and S. C. Peter. *Adv. Funct. Mater.* 2022, 2209023.
5. Morphology Tuned Pt_3Ge Accelerates Water Dissociation to Industrial Standard Hydrogen Production in wide pH Range. S. Mondal, S. Sarkar, **D. Bagchi**, T. Das, R. Das, A. K. Singh, P. K. Prasanna, C. P. Vinod, S. Chakraborty and S. C. Peter. *Adv. Mater.*, 2022, 2202294.
6. Optimized Metal Deficiency Induced Operando Phase Transformation Enhances Charge Polarization Promoting Hydrogen Evolution Reaction. **D. Bagchi**, A. K. Singh, S. Sarkar, S. Ch. Sarma, D. Mumbaraddi, S. D. Ramarao, S. C. Peter. Chem. Mater. 2022, **34**, 8999–9008.
7. Strain Induced Phase Transformation in Iron Oxide for Enhanced Production of Higher Alcohols from CO_2. Devender Goud, S. R. Churipard, **D. Bagchi**, A. K. Singh, M. Riyaz, C. P. Vinod, and S. C. Peter. *ACS Catal*. 2022, **12**,11118–11128.
8. Tuning Hybridization and Charge Polarization in Metal Nanoparticles Dispersed over Schiff Base Functionalized SBA-15 Enhances CO_2 Capture and Conversion to Formic Acid. A. Cherevotan, B. Ray, A. Yadav, **D. Bagchi**, A. K. Singh, M. Riyaz, S. R.

Churipard, V. Naral, K. Kaur, U. K. Gautam, C. P. Vinod, and S. C. Peter, *J. Mater. Chem. A*, 2022, **10**, 18354-18362.

9. Work in Tandem: Unusual Improvement in OER Performance of NiFe LDH Grown in Presence of 1T rich MoS_2. S. Chakraborty, Shivanna Marappa, S. Agarwal, **D. Bagchi**, A. Rao, C.P. Vinod, S. C. Peter, A. Singh and M. Eswaramoorthy. *ACS Appl. Mater. Inter*., 2022, **14**, 31951–31961.
10. Ultralow Non-Noble Metal Loaded MOF Derived Bi-Functional Electrocatalysts for the Oxygen Evolution and Reduction Reactions. **D. Bagchi**, N. Phukan, S. Sarkar, R. Das, B. Ray, P. Bellare, N. Ravishankar and S. C. Peter, *J. Mater. Chem. A*, 2021, **9**, 9319-9326
11. Mechanistic Insights into the Promotional Effect of Ni Substitution in Non-Noble Metal Carbides for Highly Enhanced Water Splitting. **D. Bagchi,** S. Roy, L. Dheer, S. C. Sarma, V. Rajaji, C. Narayana, U. V. Waghmare and S. C. Peter, *Appl. Catal. B.*, 2021, **298**, 120560
12. Deconvolution of Phase–Size–Strain Effects in Metal Carbide Nanocrystals for Enhanced Hydrogen Evolution. S. Roy, **D. Bagchi**, V. Vemuri, S. Ch. Sarma, V. Ahuja, V. Rajaji, C. Narayana and S. C. Peter, *Nanoscale*, 2020, **12**, 15414-15425.
13. Synergetic Effect of Ni-Substituted Pd_2Ge Ordered Intermetallic Nanocomposites for Efficient Electrooxidation of Ethanol in Alkaline Media. A. R. Rajamani, P. C. Ashly, L. Dheer, S. C. Sarma, S. Sarkar, **D. Bagchi**, U. V. Waghmare and S. C. Peter, *ACS Appl. Energy Mater.*, 2019, **2**, 7132-7141.

- **Under Review**

1. Atomically Dispersed Copper on WC@NGC Boosts the Conversion of CO_2 to Acetic Acid. **D. Bagchi,** M. Riyaz, J. Raj, S. Roy, A. K. Singh, A. Cherevotan, C. P. Vinod and S. C. Peter.
2. Understanding the Effect of Lattice Charge on Multi-Carbon CO_2 Reduction Products. **D. Bagchi**, S. Ch. Sarma, J. Raj, S. Roy, S. Raj, V. Mishra, D Gouda and S. C. Peter.
3. Induced Structural Ordering Enhances Highly Selective Production of Acetic Acid from CO_2 at Ultra-Low Potential. **D. Bagchi**, S. Sarkar, J. Raj, A. Cherevotan, C. P. Vinod, S. C. Peter.
4. Operando Generated Medium Entropy Intermetallic and Oxygen Deficient Metal Oxide Synergistically Enhance the Conversion of Carbon Dioxide to Methanol. A.

Cherevotan, A. Yadav, A. K. Singh, **D. Bagchi**, S. R. Churipard, B. Ray, K. Kaur, U. K. Gautam, C. P. Vinod, and S. C. Peter.

5. Unravelling the Mechanism of Higher Alcohols Production on the Ordered Intermetallic Surface During CO_2 Electroreduction. **D. Bagchi**, T. Khan, J. Iyer, A. K. Singh, K. Kaur, C. P. Vinod, U. K. Gautam, A. Haider and S. C. Peter.
6. Oxygen Generation Catalysis by interfacial charge transfer at mono-atomic Co sites secured on ordered intermetallic surface. S. Mondal, **D. Bagchi**, M. Riyaz, A. K. Singh, C. P. Vinod, and S. C. Peter.
7. In-situ Surface Reconstruction Upon Aliovalent Substitution in ZnS to $CuGaS_2$ Selectively Converting CO_2 to Ethylene Photochemically. S. Chakraborty, R. Das, K. Das, A. K. Singh, **D. Bagchi**, C. P. Vinod, and S. C. Peter.

- ## Manuscript under preparation

1. Operando Investigation of the Origin of C-C Coupling in Electrochemical CO_2 Reduction Upon Releasing Bonding and Structural Ordering in Pd-Cu Catalyst. **D. Bagchi**, M. Riyaz, S. R. Churipard, A. K. Singh, and S. C. Peter.
2. Probing the active sites for electrochemical CO_2 reduction on oxide-derived high entropy alloy. **D. Bagchi**, N. Dutta, C. P. Vinod and S. C. Peter.

About the Author

I was born and raised at Karimpur, a small village in West Bengal. I completed my B. Sc. (Honours in Chemistry) at Ramakrishna Mission Vidyamandira, Belur Math, and pursued M. Sc. from Indian Institute of Technology, Madras. The quest for science I developed since my childhood instigated me to invest my entire career in exploring the mysteries of science. This urged me to opt for doing Ph.D. in Chemistry, specifically in materials chemistry where the implementation is towards the benevolent nature. Currently, I am working on designing catalyst materials and mechanistic investigation for electrochemical conversion of carbon dioxide to valuable fuels and chemicals. Throughout my research carrier I am privileged to gain experience in several spectroscopic and microscopic techniques like XRD, XPS, XAFS, ATR-FTIR, Raman, EPR, DEMS, GC, HPLC, NMR, GC-MS, UV, ICP-OES, TEM, SEM, HAADF-STEM, AFM etc. I have also gained knowledge about learning different fundamental and advanced electrochemical techniques along with reactor designing and optimization of different in situ techniques. Besides research, I love playing cricket, watching movies and very much enthusiastic about fitness.

"*I expand PhD as **P**erseverance **h**onoured with **D**edication. I wish my knowledge gained awakens the empathetic soul within me. My degree will gain success if implemented ever for mankind*."